NUREG/CP-0105
Vol. 3

Proceedings of the U.S. Nuclear Regulatory Commission

Seventeenth Water Reactor Safety Information Meeting

Volume 3
- Primary Systems Integrity
- Plant Performance, Testing and Analysis
- Piping and NDE
- Plant Aging

Held at
Holiday Inn Crowne Plaza
Rockville, Maryland
October 23–25, 1989

U.S. Nuclear Regulatory Commission

Office of Nuclear Regulatory Research

Proceedings prepared by
Brookhaven National Laboratory

Available from

Superintendent of Documents
U.S. Government Printing Office
P.O. Box 37082
Washington D.C. 20013-7082

and

National Technical Information Service
Springfield , VA 22161

NUREG/CP-0105
Vol. 3
R1, R5, R9, RD,
RF, RM, RV

Proceedings of the U.S. Nuclear Regulatory Commission

Seventeenth Water Reactor Safety Information Meeting

Volume 3
- Primary Systems Integrity
- Plant Performance, Testing and Analysis
- Piping and NDE
- Plant Aging

Held at
Holiday Inn Crowne Plaza
Rockville, Maryland
October 23–25, 1989

Date Published: March 1990

Compiled by: Allen J. Weiss

Office of Nuclear Regulatory Research
U.S. Nuclear Regulatory Commission
Washington, DC 20555

Proceedings prepared by
Brookhaven National Laboratory

ABSTRACT

This three-volume report contains 84 papers out of the 111 that were presented at the Seventeenth Water Reactor Safety Information Meeting held at the Holiday Inn Crowne Plaza, Rockville, Maryland, during the week of October 23-25, 1989. The papers are printed in the order of their presentation in each session and describe progress and results of programs in nuclear safety research conducted in this country and abroad. Foreign participation in the meeting included ten different papers presented by researchers from France, Germany, Japan, Norway and the United Kingdom. The titles of the papers and the names of the authors have been updated and may differ from those that appeared in the final program of the meeting.

PROCEEDINGS OF THE
17th WATER REACTOR SAFETY INFORMATION MEETING

October 23-25, 1989

Published in Three Volumes

GENERAL INDEX

VOLUME 1

VOLUME 2

VOLUME 3

REGISTERED ATTENDEES (NON-NRC)
17th WATER REACTOR SAFETY INFORMATION MEETING

S. ADDITON
TENERA
7101 WISCONSIN AVE.
BETHESDA, MD 20814
USA

M. AIKINS
GILBERT COMMONWEALTH INC.
P.O. BOX 1498
READING, PA 19603
USA

K. AKAGANE
JAPAN INST. OF NUCLEAR SAFETY
3-17-1 TURANOMON
MINATO-KU, TOKYO
JAPAN

T. AKIYOSHI
NUPEC-NUCLEAR POWER ENG. TEST CENTER
FUJITA KANKO TORANOMON BLDG-3-17-1
MINATO-KU, TOKYO, 105
JAPAN

P. ALBRECHT
UNIVERSITY OF MARYLAND
DEPT. OF CIVIL ENGINEERING
COLLEGE PARK, MD 20742
USA

A. ALONSO
MADRID POLYTECHNICAL UNIVERSITY
JOSE GUTIERREZ ABASCAL, 2
MADRID, 28006
SPAIN

H. ALSMEYER
KERNFORSCHUNGSZENTRUM, PHDR
PO BOX 3640
KARLSRUHE, FRG D7500
FRG

D. AMICK
EBASCO SERVICES INC.
2211 W. MEADOWVIEW RD
GREENSBORO, NC 27407
USA

D. ARMSTRONG
WASHINGTON PUB. PWR. SUPPLY SYS.
3000 GEORGE WASHINGTON
RICHLAND, WA 99352
USA

H. ASCHER
NAVAL RESEARCH LABORATORY
CODE 5326
WASHINGTON, DC 20375
USA

V. ASMOLOV
I. V. KURCHATOV INST. OF ATOMIC ENERGY
KURCHATOV SQUARE
MOSCOW, 123182
USSR

M. AZARM
BROOKHAVEN NATIONAL LABORATORY
BUILDING 130
UPTON, NY 11973
USA

J. BAEK
MPR ASSOCIATES, INC
1050 CONNECTICUT AVE, NW
WASHINGTON, DC 20036
USA

T. BAKER
INSTITUTE FOR CIRCADIAN PHYSIOLOGY
677 BEACON STREET
BOSTON, MA 02215
USA

K. BANDYOPADHYAY
BROOKHAVEN NATIONAL LABORATORY
BUILDING 129
UPTON, NY 11973
USA

A. BANERJEE
STONE & WEBSTER ENGINEERING CORP
245 SUMMER STREET
BOSTON, MA 02107
USA

V. BARNES
BATTELLE-HARC
P.O. BOX C - 5395
SEATTLE, WA 98155
USA

J. BARON
MADRID POLYTECHNICAL UNIVERSITY
JOSE GUTIERREZ ABASCAL, 2
MADRID, 28006
SPAIN

M. BARRETT
DUKE POWER COMPANY
P.O. BOX 33189
CHARLOTTE, NC 28242
USA

G. BARTHOLOMÉ
SIEMENS AG / UB KWU
HAMMERBACHERSTR. 12+14
ERLANGEN, D-8520
FRG

S. BASSOLS
EDF/SEPTN
12-14 AVENUE DUTRIEVOZ
VILLEURBANNE, CEDEX 69628
FRANCE

J. BASURTO
CNSNS
INSURGENTES SUR 1776
MEXICO CITY, D.F. 01030
MEXICO

K. BAUMGAERTEL
GESELLSCHAFT FUR REAKTORSICHERHEIT
SCHWERTNERGASSE 1
D-5000 COLOGNE, 1
FRG

P. BAZIN
CEA FRENCH ATOMIC ENERGY COMMISSION
AVENUE DES MATYRS - 85 X
GRENOBLE, CEDEX 38041
FRANCE

A. BEHBAHANI
SINGER LINK-MILES
McGRAW ROAD
COLUMBIA, MD 21045
USA

S. BELICZEY
GESELLSCHAFT FUR REAKTORSICHERHEIT
SCHWERTNERGASSE 1
D-5000 COLOGNE, 1
FRG

C. BENHARDT
WESTINGHOUSE SAVANNAH RIVER COMPANY
SAVANNAH RIVER SITE
AIKEN, SC 29801
USA

K. BERGERON
SANDIA NATIONAL LABORATORIES
P.O. BOX 5800, DIVISION 6429
ALBUQUERQUE, NM 87185
USA

R. BINGHAM
MPR ASSOCIATES, INC
1050 CONNECTICUT AVE, NW
WASHINGTON, DC 20036
USA

W. BINNER
AUSTRIAN RESEARCH CENTER SEIBERSDORF
1010 KRAMERGASSE 1
VIENNA, A-1010
AUSTRIA

D. BIRMINGHAM
BABCOCK & WILCOX CO.
1562 BEESON STREET
ALLIANCE, OH 44601
USA

D. BLEY
PICKARD, LOWE & GARRICK, INC.
2260 UNIVERSITY DRIVE
NEWPORT BEACH, CA 92660
USA

M. BOHN
SANDIA NATIONAL LABORATORIES
1515 EUBANK AVE.
ALBUQUERQUE, NM 87123
USA

M. BONACA
NORTHEAST UTILITIES
P.O. BOX 270
HARTFORD, CT 06141-0270
USA

E. BOUCHERON
SANDIA NATIONAL LABORATORIES
P.O. BOX 5800, DIVISION 6418
ALBUQUERQUE, NM 87185
USA

B. BOYACK
LOS ALAMOS NATIONAL LABORATORY
P.O. BOX 1663, MS K551
LOS ALAMOS, NM 87545
USA

S. BREWER
AMERICAN ELECTRIC POWER SERVICE CORP.
1 RIVERSIDE PLAZA
COLUMBUS, OH 43215
USA

T. BRITT
WESTINGHOUSE SAVANNAH RIVER COMPANY
SAVANNAH RIVER SITE
AIKEN, SC 29801
USA

I. BRITTAIN
AEA TECHNOLOGY, WINFRITH
WINFRITH TECHNOLOGY CENTER
DORCHESTER, DORSET DT2 8DH
UK

A. BROWN
EG&G IDAHO, INC.
P.O. BOX 1625
IDAHO FALLS, ID 83415
USA

C. BUCHHOLZ
GE NUCLEAR ENERGY
175 CURTNER AVENUE M/C 754
SAN JOSE, CA 95125
USA

L. BUFFARDI
GEORGE MASON UNIVERSITY
4400 UNIVERSITY DR.
FAIRFAX, VA 22030
USA

N. BUTTERY
NATIONAL POWER DIVISION OF CEGB
BOOTHS HALL, CHELFORD ROAD
KNUTSFORD, CHESHIRE WA16 8QG
UK

R. BYE
HMNII-HEALTH & SAFETY EXECUTIVE
ST. PETERS HOUSE, BALLIOL
BOOTLE, MERSEYSIDE L20 3LZ
UK

R. CALLAWAY
NUMARC
1776 I ST., NW
WASHINGTON, DC 20006
USA

A. CAMP
SANDIA NATIONAL LABORATORIES
P.O. BOX 5800, DIVISION 6412
ALBUQUERQUE, NM 87185
USA

D. CARLSON
SANDIA NATIONAL LABORATORIES
P.O. BOX 5800, DIVISION 6521
ALBUQUERQUE, NM 87185
USA

B. CARLUCCI
ATOMIC ENERGY OF CANADA LTD
CHALK RIVER LABORATORIES
CHALK RIVER, ONTARIO, CA K0J1P0
CANADA

R. CARTER
OAK RIDGE NATIONAL LABORATORY
P.O. BOX 2008
OAK RIDGE, TN 37831-6360
USA

D. CASADA
OAK RIDGE NATIONAL LABORATORY
P.O. BOX 2009
OAK RIDGE, TN 37831-8057
USA

M. CASE
DUKE ENGINEERING & SERVICES
526 S. CHURCH ST., P.O. BOX 36911
CHARLOTTE, NC 28236
USA

L. CATALANI
FRAMATOME
TOUR FIAT CEDEX 16
PARIS-LA-DEFENSE, 92084
FRANCE

S. CHAKRABORTY
PAUL SCHERRER INSTITUTE
WURENLINGEN + VILLIGEN
WUERENLINGEN, CH5303
SWITZERLAND

U. CHANDRA
EBASCO SERVICES INC.
2211 W. MEADOWVIEW RD
GREENSBORO, NC 27407
USA

J. CHANG
U. S. DEPARTMENT OF ENERGY
1000 INDEPENDENCE AVE.
WASHINGTON, DC 20545
USA

N. CHAPMAN
BECHTEL POWER CORPORATION
15740 SHADY GROVE ROAD
GAITHERSBURG, MD 20877-1454
USA

T. CHARRAS
CEA FRENCH ATOMIC ENERGY COMMISSION
CEN SACLAY
GIF, YVETTE 91191
FRANCE

T. CHEN
ANF
PO BOX 130
RICHLAND, WA 99352
USA

R. CHEVERTON
OAK RIDGE NATIONAL LABORATORY
P.O. BOX 2009, BLDG 9204-1
OAK RIDGE, TN 37831-8057
USA

S. CHIANG
TAIWAN POWER COMPANY
242 ROOSECELT ROAD, SECT. III
TAIPEI, TAIWAN 10763
ROC

K. CHIKAMOTO
JAPAN NUS
7-1 NISHI-SHINJU 2 CHOME
NISHI-SHINJUKU, TOKYO 163
JAPAN

O. CHOPRA
ARGONNE NATIONAL LABORATORY
9700 S. CASE AVENUE
ARGONNE, IL 60439
USA

C. CHOU
LAWRENCE LIVERMORE NATIONAL LAB
P.O. BOX 8, L-198
LIVERMORE, CA 94550
USA

H. CHOW
ADVANCED NUCLEAR FUELS CORP.
2101 HORN RAPIDS RD
RICHLAND, WA 99352
USA

J. CHRISTENSEN
BATTELLE-PACIFIC NORTHWEST LABS.
P.O. BOX 999
RICHLAND, WA 99352
USA

J. CHURCH
WESTINGHOUSE SAVANNAH RIVER COMPANY
SAVANNAH RIVER SITE
AIKEN, SC 29808
USA

J. CLOSE
EG&G IDAHO, INC.
P.O. BOX 1625
IDAHO FALLS, ID 83415
USA

M. CONEY
NATIONAL POWER TECH. & ENVIR. CENTRE
NPTEC, KELVIN AVENUE
LEATHERHEAD, SURREY KT24 5NR
UK

J. CONINE
KAPL-GENERAL ELECTRIC CO.
P.O. BOX 1072
SCHENECTADY, NY 12301-1072
USA

W. CORWIN
OAK RIDGE NATIONAL LABORATORY
P.O. BOX 2009, BLDG 9204-1
OAK RIDGE, TN 37831-8056
USA

M. COURTAUD
CEA FRENCH ATOMIC ENERGY COMMISSION
AVENUE DES MATYRS - 85 X
GRENOBLE, CEDEX 38041
FRANCE

B. COWARD
MPR ASSOCIATES, INC
1050 CONNECTICUT AVE, NW
WASHINGTON, DC 20036
USA

K. COZENS
NUMARC
1776 I ST., NW
WASHINGTON, DC 20006
USA

A. CRONENBERG
ENGINEERING SCIENCE AND ANALYSIS
545 SHOUP AVE, SUITE 336
IDAHO FALLS, ID 83402
USA

R. CUSHMAN
NIAGARA MOHAWK POWER CORPORATION
301 PLAINFIELD ROAD
SYRACUSE, NY 13203
USA

R. DAIL
APTECH ENGINEERING SERVICES, INC
601 N. FAIRFAX STREET, SUITE 420
ALEXANDRIA, VA 22314
USA

R. DALLMAN
EG&G IDAHO, INC.
P.O. BOX 1625, MS 2508
IDAHO FALLS, ID 83415
USA

P. DAMERELL
MPR ASSOCIATES, INC
1050 CONNECTICUT AVE, NW
WASHINGTON, DC 20036
USA

B. DARLASTON
NATIONAL POWER TECH. & ENVIR. CENTRE
BERKELEY NUCLEAR LABORATORIES
BERKELEY, CLOS GL13 9PB
UK

N. DAVIES
AEA TECHNOLOGY, NRL RISLEY
WARRINGTON
CHESHIRE, WA3 6AT
UK

P. DAVIS
PRD CONSULTING
1935 SABIN DRIVE
IDAHO FALLS, ID 83406
USA

J. DELGADO
CNSNS
INSURGENTES SUR 1806
MEXICO CITY, D.F. 01030
MEXICO

R. DERUAZ
CEA FRENCH ATOMIC ENERGY COMMISSION
AVENUE DES MATYRS - 85 X
GRENOBLE, CEDEX 38041
FRANCE

K. DeWALL
EG&G IDAHO, INC.
P.O. BOX 1625
IDAHO FALLS, ID 83415
USA

R. deWIT
NATL INST. OF STANDARDS & TECHNOLOGY
ROOM A153, MATERIALS BUILDING
GAITHERSBURG, MD 20899
USA

D. DIAMOND
BROOKHAVEN NATIONAL LABORATORY
BUILDING 130
UPTON, NY 11973
USA

M. DIMARZO
UNIVERSITY OF MARYLAND
DEPT. OF MECHANICAL ENGINEERING
COLLEGE PARK, MD 20742
USA

S. DOCTOR
BATTELLE-PACIFIC NORTHWEST LABS.
P.O. BOX 999
RICHLAND, WA 99352
USA

C. DODD
OAK RIDGE NATIONAL LABORATORY
P.O. BOX 2008
OAK RIDGE, TN 37831-6158
USA

A. DOWLING
NATIONAL POWER DIVISION OF CEGB
BARNETT WAY
BARNWOOD, GLOUCESTER GL4 7RS
UK

M. DROUIN
SCIENCE APPLICATIONS INTL. CORP.
2109 AIR PARK RD., S. E.
ALBUQUERQUE, NM 87106
USA

S. DUA
GE NUCLEAR ENERGY
175 CURTNER AVENUE
SAN JOSE, CA 95125
USA

J. DUCO
CEA FRENCH ATOMIC ENERGY COMMISSION
DAS/SASC,CEN/FAR,BP NO 6
FONTENAY-AUX-ROSES CEDEX, CEDEX 92265
FRANCE

R. DUFFEY
EG&G IDAHO, INC.
P.O. BOX 1625
IDAHO FALLS, ID 83415
USA

J. DUKELOW
BATTELLE-PACIFIC NORTHWEST LABS.
P.O. BOX 999
RICHLAND, WA 99352
USA

D. EISSENBERG
OAK RIDGE NATIONAL LABORATORY
P.O. BOX 2009, MS 8057
OAK RIDGE, TN 37831
USA

G. EMBLEY
KAPL-GENERAL ELECTRIC CO.
P.O. BOX 1072
SCHENECTADY, NY 12301-1072
USA

P. ERICSSON
SWEDISH NUCLEAR POWER INSPECTORATE
P.O. BOX 27106
STOCKHOLM, S-102 52
SWEDEN

S. ERIXON
SWEDISH NUCLEAR POWER INSPECTORATE
P.O. BOX 27106
STOCKHOLM, S-102 52
SWEDEN

M. EVANS
NUS CORPORATION
901 CLAPPER RD.
GAITHERSBURG, MD 20878
USA

R. FALK
GROVE ENGINEERING
15215 SHADY GROVE ROAD
ROCKVILLE, MD 20850
USA

A. FIELDEN
AEA TECHNOLOGY, NRL RISLEY
WARRINGTON
CHESHIRE, WA3 6AT
UK

R. FIELDS
NATL INST. OF STANDARDS & TECHNOLOGY
A154/223
GAITHERSBURG, MD 20899
USA

R. FONTAINE
KAPL-GENERAL ELECTRIC CO.
P.O. BOX 1072
SCHENECTADY, NY 12301-1072
USA

E. FOX
OAK RIDGE NATIONAL LABORATORY
P.O. BOX 2009
OAK RIDGE, TN 37831
USA

A. FRESCO
BROOKHAVEN NATIONAL LABORATORY
BUILDING 130
UPTON, NY 11973
USA

B. FRYER
ANF
PO BOX 130
RICHLAND, WA 99352
USA

R. FUJITA
LOS ALAMOS NATIONAL LABORATORY
P.O. BOX 1663, MS K557
LOS ALAMOS, NM 87545
USA

T. FUKETA
JAERI/SNL
P.O. BOX 5800, ABQ
ALBUQUERQUE, NM 87185
USA

P. GEORGE
CENTRAL ELECTRICITY GENERATING BOARD
BOOTHS HALL, CHELFORD ROAD
KNUTSFORD, CHESHIRE WA16 8QG
UK

J. GIESEKE
BATTELLE COLUMBUS
505 KING AVE.
COLUMBUS, OH 43201
USA

J. GLEASON
WYLE LABORATORIES
P.O. BOX 077777
HUNTSVILLE, AL 35807-7777
USA

D. GOLDEN
EG&G IDAHO, INC.
PO BOX 1625
IDAHO FALLS, ID 83415
USA

M. GOMOLINSKI
CEA FRENCH ATOMIC ENERGY COMMISSION
CEN/FAR BP NO. 6
FONTENAY-AUX-ROSES, CEDEX 92265
FRANCE

T. GRANT
BATTELLE
400 N.E. 41ST. ST., P.O. BOX C-5395
SEATTLE, WA 98105
USA

B. GUNTHER
BROOKHAVEN NATIONAL LABORATORY
BUILDING 130
UPTON, NY 11973
USA

J. GUPPY
BROOKHAVEN NATIONAL LABORATORY
BUILDING 475B
UPTON, NY 11973
USA

S. HABER
BROOKHAVEN NATIONAL LABORATORY
BUILDING 130
UPTON, NY 11973
USA

G. HAEHNEL
GESELLSCHAFT FUR REAKTORSICHERHEIT
SCHWERTNERGASSE 1
D-5000 COLOGNE, 1
FRG

F. HAGGAG
OAK RIDGE NATIONAL LABORATORY
P.O. BOX 2008, 4500S, MS 6151
OAK RIDGE, TN 37831-6151
USA

A. HALL
HMNII-HEALTH & SAFETY EXECUTIVE
ST. PETERS HOUSE, BALLIOL
BOOTLE, MERSEYSIDE L20 3LZ
UK

P. HALL
NATIONAL POWER DIVISION OF CEGB
BARNETT WAY
BARNWOOD, GLOUCESTER GL4 7RS
UK

C. HALLER
MPR ASSOCIATES, INC
1050 CONNECTICUT AVE, NW
WASHINGTON, DC 20036
USA

L. HANES
WESTINGHOUSE SCIENCE & TECHNOLOGY
1310 BEULAH ROAD
PITTSBURGH, PA 15228
USA

W. HANNUM
TENNESSEE VALLEY AUTHORITY
1N-77B BLUE RIDGE PLACE
CHATTANOOGA, TN 37421
USA

D. HANSON
EG&G IDAHO, INC.
P.O. BOX 1625
IDAHO FALLS , ID 83415
USA

J. HARDY
OAK RIDGE NATIONAL LABORATORY
P.O. BOX 2008
OAK RIDGE, TN 37831-6003
USA

D. HARRISON
MPR ASSOCIATES, INC
1050 CONNECTICUT AVE, NW
WASHINGTON, DC 20036
USA

R. HARVEY
YANKEE ATOMIC ELECTRIC COMPANY
580 MAIN STREET
BOLTON, MA 01740
USA

K. HASHIMOTO
JAPAN ATOMIC ENERGY RES. INST
TOKAI-MURA, NAKA-GUN
IBARAKI-KEN, 319-11
JAPAN

K. HAUGSET
OECD HALDEN REACTOR PROJECT
P.O. BOX 173
HALDEN, 1751
NORWAY

J. HAWTHORNE
MATERIALS ENGINEERING ASSOCIATES
9700-B M. L. KING HWY
LANHAM, MD 20706
USA

H. HAYNES
OAK RIDGE NATIONAL LABORATORY
P.O. BOX 2009
OAK RIDGE, TN 37831-8057
USA

F. HEUSER
GESELLSCHAFT FUR REAKTORSICHERHEIT
LIEGNITZER STR. 8
5063 OVERATH,
FRG

J. HEYMAN
NASA LANGLEY RESEARCH CENTER
INST. RESEARCH DIV., MS-231
HAMPTON, VA 23665
USA

D. HICKS
UKAEA/WRPD
B.329, HARWELL LABORATORY
OXFORDSHIRE, OX11 ORA
UK

J. HIGGINS
BROOKHAVEN NATIONAL LABORATORY
BUILDING 130
UPTON, NY 11973
USA

P. HILL
PENNSYLVANIA POWER & LIGHT
TWO NORTH NINTH STREET
ALLENTOWN, PA 18101
USA

J. HINTON
WESTINGHOUSE SAVANNAH RIVER COMPANY
SAVANNAH RIVER SITE
AIKEN, SC 29808
USA

T. HIRONS
LOS ALAMOS NATIONAL LABORATORY
P.O. BOX 1663, MS E581
LOS ALAMOS, NM 87545
USA

R. HOCKENBURY
RENSSELAER POLYTECHNIC INSTITUTE
JEC 5048
TROY, NY 12180
USA

C. HOFMAYER
BROOKHAVEN NATIONAL LABORATORY
BUILDING 129
UPTON, NY 11973
USA

G. HOLMAN
LAWRENCE LIVERMORE NAT'L LAB
PO BOX 808
LIVERMORE, CA 94550
USA

K. HORIKAMI
JAPAN ATOMIC ENERGY RES. INST
TOKAI-MURA, NAKA-GUN
IBARAKI-KEN, 319-11
JAPAN

D. HORSCHEL
SANDIA NATIONAL LABORATORIES
P.O. BOX 5800, DIVISION 6523
ALBUQUERQUE, NM 87185
USA

T. HSU
VIRGINIA POWER
5000 DOMINION BLVD
GLEN ALLEN, VA 23060
USA

E. HUGHES
BECHTEL POWER CORPORATION
15740 SHADY GROVE ROAD
GAITHERSBURG, MD 20877-1454
USA

R. HUMPHREYS
UKAEA
CULHAM
ABINGTON, OXFORDSHIRE OX14 3DB
UK

S. HUMPHRIES
SCIENTECH, INC.
11821 PARKLAWN DRIVE
ROCKVILLE, MD 20852
USA

M. HYNES
AEATECHNOLOGY, SRD
SRD, WIGSHAW LANE, CULCHETH
WARRINGTON, CHESHIRE WA3 4NE
UK

S. HYTEN
WYLE LABORATORIES
P.O. BOX 077777
HUNTSVILLE, AL 35807-7777
USA

M. ICHIKAWA
JAPAN ATOMIC ENERGY RES. INST
TOKAI-MURA, NAKA-GUN
IBARAKI-KEN, 319-11
JAPAN

T. IGUCHI
JAPAN ATOMIC ENERGY RES. INST
TOKAI-MURA, NAKA-GUN
IBARAKI-KEN, 319-11
JAPAN

L. INNES
ATOMIC ENERGY CONTROL BOARD
270 ALBERT STREET
OTTAWA, ONTARIO K1P 5S9
CANADA

T. IWAMURA
JAPAN ATOMIC ENERGY RES. INST
TOKAI-MURA, NAKA-GUN
IBARAKI-KEN, 319-11
JAPAN

J. IZQUIERDO
CONSEJO SEGURIDAD NUCLEAR
4 JUSTO DORADO 11
MADRID, 28003
SPAIN

M. JACOBUS
SANDIA NATIONAL LABORATORIES
P.O. BOX 5800, DIVISION 6419
ALBUQUERQUE, NM 87185
USA

J. JANSKY
BTB-LEONBERG
GERLINGER STRASSE 151
LEONBERG, 7250
FRG

R. JENKS
LOS ALAMOS NATIONAL LABORATORY
P.O. BOX 1663, MS K555
LOS ALAMOS, NM 87545
USA

J. JO
KAERI-NUCLEAR SAFETY CENTER
P.O. BOX 7, DMEDUK DANJI
TAEJON, 302-353
KOREA

A. JOHNSON
BATTELLE-PACIFIC NORTH-WEST LABS.
P.O. BOX 999, MS P8-10
RICHLAND, WA 99352
USA

W. JOHNSON
UNIVERSITY OF VIRGINIA
NUCL. ENG. DEPT., REACTOR BLDG.
CHARLOTTESVILLE, VA 22901
USA

R. JONES
ELECTRIC POWER RESEARCH INSTITUTE
3412 HILLVIEW AVE, P.O. BOX 10412
PALO ALTO, CA 94303
USA

M. KALSI
KALSI ENGINEERING, INC
745 PARK TWO DRIVE
SUGAR LAND, TX 77478
USA

T. KANZLEITER
BATTELLE INSTITUTE FRANKFURT
AM ROMERHOF 35
FRANKFORT, D-6000
FRG

R. KARIMI
SCIENCE APPLICATIONS INTL. CORP.
1710 GOODRIDGE DR.
MC LEAN, VA 22102
USA

W. KASTENBERG
UCLA
5532 BOELTER HALL
LOS ANGELES, CA 90024-1597
USA

Y. KATAOKA
ERL HITACHI LTD.
1186 MORIYAMA-CHO
HITACHI, JAPAN 316
JAPAN

W. KATO
BROOKHAVEN NATIONAL LABORATORY
BUILDING 197C
UPTON, NY 11973
USA

G. KATZENMEIER
KERNFORSCHUNGSZENTRUM, PHDR
PO BOX 3640
KARLSRUHE, FRG D7500
FRG

S. KAWAKAMI
NUPEC-NUCLEAR POWER ENG. TEST CENTER
SHUWA-KAMIYACHO BLDG TORANOMON -3-13-4
MINATO-KU, TOKYO, 105
JAPAN

D. KELLY
EG&G IDAHO, INC.
P.O. BOX 1625
IDAHO FALLS, ID 83415
USA

J. KELLY
SANDIA NATIONAL LABORATORIES
P.O. BOX 5800, DIVISION 6418
ALBUQUERQUE, NM 87185
USA

M. KHATIB-RAHBAR
ENERGY RESEARCH
7831 WHITERIM TERRACE
POTOMAC, MD 20854
USA

H. KIM
KAERI-NUCLEAR SAFETY CENTER
P.O. BOX 7, DMEDUK DANJI
TAEJON, 302-353
KOREA

S. KINNERSLY
AEA TECHNOLOGY,WINFRITH
WINFRITH TECHNOLOGY CENTER
DORCHESTER, DORSET DT2 8DH
UK

W. KIRK
LOS ALAMOS NATIONAL LABORATORY
P.O. BOX 1663, MS E561
LOS ALAMOS, NM 87545
USA

R. KIRK
S. AFRICA SCIENCE & TECHNOLOGY OFFICE
COUNCIL FOR NUCLEAR ENERGY, BOX 7106
HENNUPSMEER, 0046
S. AFRICA

C. KIZER
AIR TRANSPORT ASSOCIATION OF AMERICA
1709 NEW YORK AVENUE, N.W.
WASHINGTON, DC 20006
USA

H. KNOEDLER
BECHTEL-KWU ALLIANCE
15740 SHADY GROVE ROAD
GAITHERSBURG, MD 20877-1454
USA

C. KOT
ARGONNE NATIONAL LABORATORY
9700 CASS AVENUE, BLDG. 335
ARGONNE, IL 60439
USA

K. KUROIWA
COMPUTER SOFTWARE DEVEL. CO., LTD.
4-1, SHIBAKOEN 2-CHOME
MINATOO-KU, TOKYO 105
JAPAN

R. KURTZ
BATTELLE-PACIFIC NORTHWEST LABS.
P.O. BOX 999
RICHLAND, WA 99352
USA

K. KUSSMAUL
MPA STUTTGART
PFAFFENWALDRING 32
STUTTGART 80, 7000
FRG

O. KYMÄLÄINEN
IMATRAN VOIMA OY
P.O. BOX 112
VANTAA, 01601
FINLAND

A. LAKNER
VIKING SYSTEMS INTERNATIONAL
101 CHESTNUT STREET
GAITHERSBURG, MD 20879
USA

W. LANIER
KAPL-GENERAL ELECTRIC CO.
P.O. BOX 1072
SCHENECTADY, NY 12301-1072
USA

CHIP LARSON
BATTELLE-PACIFIC NORTHWEST LABS.
P.O. BOX 999
RICHLAND, WA 99352
USA

L. LARSON
WESTINGHOUSE - BETTIS
2895 O'NEIL
BETHEL PARK, PA 15102
USA

B. LEE
U. S. DEPARTMENT OF ENERGY
EH 351
GERMANTOWN, MD 20874
USA

S. LEE
MPR ASSOCIATES, INC
1050 CONNECTICUT AVE, NW
WASHINGTON, DC 20036
USA

J. LEHNER
BROOKHAVEN NATIONAL LABORATORY
BUILDING 130
UPTON, NY 11973
USA

K. LEIGH
AEA TECHNOLOGY, SRD
SRD, WIGSHAW LANE, CULCHETH
WARRINGTON, CHESHIRE WA3 4NE
UK

G. LI
TAIWAN POWER COMPANY
67, LANE 144, KEELUNG RD., SEC. 4
TAIPEI, TAIWAN 10772
ROC

L. LIAO
INSTITUTE OF NUCLEAR ENERGY
P.O. BOX 3-3
LUNG TAN, TAIWAN 32500
ROC

R. LIBBY
BATTELLE-PACIFIC NORTHWEST LABS.
P.O. BOX 999, K6-42
RICHLAND, WA 99352
USA

K. LIESCH
GESELLSCHAFT FUR REAKTORSICHERHEIT
FORSCHUNGSGELANDE
GARCHING, 8046
FRG

C. LIN
EBASCO SERVICES INC.
2 WORLD TRADE CTR., 89TH FL
NEW YORK, NY 10048
USA

M. LINDSTROEM
SWEDISH NUCLEAR POWER INSPECTORATE
P.O. BOX 27106
STOCKHOLM, S-102 52
SWEDEN

B. LIPFORD
MPR ASSOCIATES, INC
1050 CONNECTICUT AVE, NW
WASHINGTON, DC 20036
USA

M. LIVOLANT
CEA FRENCH ATOMIC ENERGY COMMISSION
CEN/FAR - DRSN
FONTENAY-AUX-ROSES, CEDEX 92265
FRANCE

G. LLOYD
AEA TECHNOLOGY, NRL RISLEY
WARRINGTON
CHESHIRE, WA3 6AT
UK

F. LOBBIN
GENERAL PHYSICS CORPORATION
6700 ALEXANDER BELL DRIVE
COLUMBIA, MD 21046
USA

F. LOSS
MATERIALS ENGINEERING ASSOCIATES
9700-B M. L. KING HWY
LANHAM, MD 20706
USA

W. LUCKAS, JR.
BROOKHAVEN NATIONAL LABORATORY
BUILDING 130
UPTON, NY 11973
USA

P. MACDONALD
EG&G IDAHO, INC.
P.O. BOX 1625
IDAHO FALLS, ID 83415-2507
USA

I. MADNI
BROOKHAVEN NATIONAL LABORATORY
BUILDING 830
UPTON, NY 11973
USA

A. MADONNA
ENEA-DISP
VIA V. BRANCATI, 48
ROME, 00144
ITALY

H. MAGLEBY
EG&G IDAHO, INC.
P.O. BOX 1625
IDAHO FALLS, ID 83415
USA

A. MARCUS
UNIVERSITY OF MINNESOTA
271 19TH AVE, S.
MINNEAPOLIS, MN 55113
USA

C. MARKUS
PGE-TROJAN NUCLEAR PLANT TNB-1 NSRD
71760 COLUMBIA RIVER HIGHWAY
RAINIER, OR 97048
USA

P. MARSILI
ENEA-DISP
VIA V. BRANCATI, 48
ROME, 00144
ITALY

R. MARTIN
EG&G IDAHO, INC.
P.O. BOX 1625 MS 2404
IDAHO FALLS, ID 83415
USA

R. MASSE
U.S. GEOLOGICAL SURVEY
P.O. BOX 25046 DFC, MS-967
DENVER, CO 80225
USA

L. MATTILA
TECHNICAL RSCH CTR OF FINLAND
P.O. BOX 169
HELSINKI, SF-00181
FINLAND

B. MAVKO
IJS
JAMOVA 39
LJUBLJANA, 61000
YUGOSLAVIA

D. McCLOSKEY
SANDIA NATIONAL LABORATORIES
P.O. BOX 5800, DIVISION 6400
ALBUQUERQUE, NM 87185
USA

N. McDONALD
OECD NUCLEAR ENERGY AGENCY
38 BLD SUCMET
PARIS, 75016
FRANCE

K. McKAY
WESTINGHOUSE - BETTIS.
BETTIS LABORATORY P.O. BOX 79
W. MIFFLIN, PA 15122-0079
USA

C. MEDICH
SIET
VIA NINO BIXIO 27
PIACENZA, 29100
ITALY

O. MERCIER
PAUL SCHERRER INSTITUTE
WURENLINGEN + VILLIGEN
VILLIGEN PSI, CH5232
SWITZERLAND

M. MERILO
ELECTRIC POWER RESEARCH INSTITUTE
3412 HILLVIEW AVE, P.O. BOX 10412
PALO ALTO, CA 94303
USA

E. MERRICK
APTECH ENGINEERING SERVICES, INC
901 THREADNEEDLE SUITE 100
HOUSTON, TX 77079
USA

D. METLAY
BROOKHAVEN NATIONAL LABORATORY
BUILDING 130
UPTON, NY 11973
USA

Y. MEYZAUD
FRAMATOME
TOUR FIAT CEDEX 16
PARIS-LA-DEFENSE, 92084
FRANCE

D. MIRKOVIC
BROOKHAVEN NATIONAL LABORATORY
BUILDING 130
UPTON, NY 11973
USA

D. MODEEN
NUMARC
1776 EYE STREET NW, SUITE 300
WASHINGTON, DC 20006
USA

S. MODRO
EG&G IDAHO, INC.
P.O. BOX 1625
IDAHO FALLS, ID 83415
USA

F. MOODY
GE NUCLEAR ENERGY
175 CURTNER AVENUE
SAN JOSE, CA 95125
USA

D. MOORE
SOUTHERN COMPANY SERVICES, INC.
P.O. BOX 2625
BIRMINGHAM, AL 35202
USA

T. MOSKAL
BABCOCK & WILCOX CO.
1562 BEESON STREET
ALLIANCE, OH 44601
USA

D. MOULIN
CEA FRENCH ATOMIC ENERGY COMMISSION
CEN SACLAY
GIF, 91191
FRANCE

R. MURALIDHARAN
GE NUCLEAR ENERGY
175 CURTNER AVENUE
SAN JOSE, CA 95125
USA

Y. MURAO
JAPAN ATOMIC ENERGY RES. INST
TOKAI-MURA, NAKA-GUN
IBARAKI-KEN, 319-11
JAPAN

N. NAKAJIMA
JAPAN ATOMIC ENERGY RES. INST
TOKAI-MURA, NAKA-GUN
IBARAKI-KEN, 319-11
JAPAN

R. NANSTAD
OAK RIDGE NATIONAL LABORATORY
P.O. BOX 2008, MS6151
OAK RIDGE, TN 37831-6151
USA

B. NASSERSHARIF
TEXAS A&M UNIVERSITY
MAIL STOP 3363
COLLEGE, TX 77843
USA

C. NEGIN
GROVE ENGINEERING
15215 SHADY GROVE ROAD
ROCKVILLE, MD 20850
USA

D. NEITZEL
BATTELLE-PACIFIC NORTHWEST LABS.
P.O. BOX 999, P7-50
RICHLAND, WA 99352
USA

A. NELSON
U.S. GEOLOGICAL SURVEY
P.O. BOX 25046 DFC, MS-966
DENVER, CO 80225
USA

E. NIEUWLAND
N.V. PZEM
P.O. BOX 5048
MIDDELBURG, 4330 KA
THE NETHERLANDS

C. NOBLE
U.S. DEPARTMENT OF ENERGY - IDAHO
785 DOE PLACE
IDAHO FALLS, ID 83402
USA

Y. NOGUCHI
CHUBU ELECTRIC POWER CO. INC
900 17TH STREET, N.W., SUITE 714
WASHINGTON, DC 20006
USA

S. NOMURA
NUCLEAR MATERIAL CONTROL CENTER
2-17-13 NAGATA-CHO
TOKYO, CHIYODA-KU 100
JAPAN

P. NORTH
EG&G IDAHO, INC.
P.O. BOX 1625
IDAHO FALLS, ID 83415-2507
USA

H. NOURBAKHSH
BROOKHAVEN NATIONAL LABORATORY
BUILDING 130
UPTON, NY 11973
USA

J. O'HARA
BROOKHAVEN NATIONAL LABORATORY
BUILDING 130
UPTON, NY 11973
USA

P. O'REGAN
YANKEE ATOMIC ELECTRIC COMPANY
580 MAIN STREET
BOLTON, MA 01740
USA

M. OAKDEN
AEA TECHNOLOGY, SRD
SRD, WIGSHAW LANE, CULCHETH
WARRINGTON, CHESHIRE WA3 4NE
UK

A. OHNUKI
JAPAN ATOMIC ENERGY RES. INST
TOKAI-MURA, NAKA-GUN
IBARAKI-KEN, 319-11
JAPAN

H. OLSON
WESTINGHOUSE SAVANNAH RIVER COMPANY
SAVANNAH RIVER SITE
AIKEN, SC 29808
USA

K. ONISHI
JAPAN ELECTRIC POWER INFORMATION CTR.
1726 M STREET, NW - SUITE 403
WASHINGTON, D. C. 20036
USA

R. OSTERRIEDER
WESTINGHOUSE ELECTRIC
P.O. BOX 355
PITTSBURGH, PA 15230
USA

T. OYAMA
SUMISHO ELECTRONICS CO. LTD.
3-11 KANDA NISHIKI-CHO, CHIYODA-KU
TOKYO, 101
JAPAN

I. OZAWA
JAPAN INSTITUTE OF NUCLEAR SAFETY
FUJITA KANKOU TORANOMON BLDG-3-17-1
MINATO-KU, TOKYO, 105
JAPAN

H. ÖLANDER
SWEDISH NUCLEAR POWER INSPECTORATE
P.O. BOX 27106
STOCKHOLM, S-102 52
SWEDEN

C. PAIK
FAUSKE & ASSOCIATES, INC.
16W070 WEST 83RD STREET
BURR RIDGE, IL 60521
USA

P. PAN
LOS ALAMOS NATIONAL LABORATORY
P.O. BOX 1663
LOS ALAMOS, NM 87545
USA

J. PAN
UNIVERSITY OF MICHIGAN
MECHANICAL ENGINEERING DEPT
ANN ARBOR, MI 48109
USA

F. PANISKO
BATTELLE-PACIFIC NORTHWEST LABS.
P.O. BOX 999
RICHLAND, WA 99352
USA

M. PARKS
SANDIA NATIONAL LABORATORIES
P.O. BOX 5800, DIVISION 6523
ALBUQUERQUE, NM 87185
USA

C. PARLAVANTZAS
COLENCO AG
PARKSTRASSE 27
BADEN, 5400
SWITZERLAND

W. PENNELL
OAK RIDGE NATIONAL LABORATORY
P.O. BOX 2009
OAK RIDGE, TN 37831-8058
USA

G. PETRANGELI
ENEA-DISP
VIA V. BRANCATI, 48
ROME, 00144
ITALY

G. POSAKONY
BATTELLE-PACIFIC NORTHWEST LABS.
P.O. BOX 999
RICHLAND, WA 99352
USA

T. PRATT
BROOKHAVEN NATIONAL LABORATORY
BUILDING 130
UPTON, NY 11973
USA

D. PRELEWICZ
ENSA, INC.
15025 SHADY GROVE RD, STE 170
ROCKVILLE, MD 20850
USA

J. PRUETT
OAK RIDGE NATIONAL LABORATORY
P.O. BOX 2008
OAK RIDGE, TN 37831-6135
USA

J. PUGA
UNESA
FRANCISCO GERVAS, 3
MADRID, 28020
SPAIN

C. PUGH
OAK RIDGE NATIONAL LABORATORY
P.O. BOX 2008
OAK RIDGE, TN 37831-6135
USA

E. PURVIS
U.S. DEPARTMENT OF ENERGY
NE-14
WASHINGTON, DC 20545
USA

L. RAU
NEW HAMPSHIRE YANKEE
P.O. BOX 300
SEABROOK, NH 03874
USA

M. REIK
TÜV BAYERN
POSTFACH 210420
D-8000 MUNICH 21,
FRG

D. RENY
EG&G IDAHO, INC.
P.O. BOX 1625
IDAHO FALLS, ID 83415
USA

M. REOCREUX
CEA FRENCH ATOMIC ENERGY COMMISSION
CEN/FAR BP NO. 6
FONTENAY-AUX-ROSES, CEDEX 92265
FRANCE

L. RIB
AECL TECHNOLOGIES
15400 CALHOUN DRIVE, SUITE 100
ROCKVILLE, MD 20855
USA

B. RICE
TU ELECTRIC
400 N. OLIVE, LB 81; 24 SLIC
DALLAS, TX 75201
USA

D. RICHARDS
ATOMIC ENERGY OF CANADA LTD
WHITESHELL NUCLEAR RES. ESTABLISH.
PINAWA, MANITOBA ROE 1L0
CANADA

J. RICHARDSON
LOS ALAMOS NATIONAL LABORATORY
P.O. BOX 1663, MS K555
LOS ALAMOS, NM 87545
USA

B. RIEGEL
GESELLSCHAFT FUR REAKTORSICHERHEIT
FORSCHUNGSGELANDE
GARCHING, 8046
FRG

M. RIGAMONTI
SIET
VIA NINO BIX10 27
PIACENZA, 29100
ITALY

A. ROBERTS
HMNII-HEALTH & SAFETY EXECUTIVE
HEALTH & SAFETY EXECUTIVE
SHEFFIELD, S. YORKSHIRE S3 7HQ
UK

U. ROHATGI
BROOKHAVEN NATIONAL LABORATORY
BUILDING 475B
UPTON, NY 11973
USA

A. ROMANO
BROOKHAVEN NATIONAL LABORATORY
BUILDING 197C
UPTON, NY 11973
USA

S. ROSINSKI
SANDIA NATIONAL LABORATORIES
P.O. BOX 5800, DIVISION 6521
ALBUQUERQUE, NM 87185
USA

E. ROTH
WESTINGHOUSE SCIENCE & TECHNOLOGY
1310 BEULAH ROAD
PITTSBURGH, PA 15235
USA

P. ROTHE
CREARE INC
P.O. BOX 71
HANOVER, NH 03755
USA

P. SAMANTA
BROOKHAVEN NATIONAL LABORATORY
BUILDING 130
UPTON, NY 11973
USA

J. SANCHEZ
INSTITUTE OF NUCLEAR ENERGY RES. (ININ)
SALAZAR EDO DE MEXICO
11000, MEXICO CITY, D.F.
MEXICO

O. SANDERVAG
SWEDISH ENERGY RESEARCH CENTRE
S-611 82
NYKÖPING, 61182
SWEDEN

F. SCHMID
TÜV BAYERN
WESTENDSTRASSE 199 - POSTFACH 210420
D-8000 MUNICH 21,
FRG

M. SCHMIDT
BECHTEL-KWU ALLIANCE
15740 SHADY GROVE RD.
GAITHERSBURG, MD 20877
USA

K. SCHNEIDER
SIEMENS AG / UB KWU
HAMMERBACHERSTR. 12+14
ERLANGEN, D-8520
FRG

G. SCHWAB
FLUOR DANIEL INC
200 W. MONROE STREET
CHICAGO, IL 60606
USA

F. SCIACCA
SCIENCE & ENGINEERING ASSOCIATES, INC.
8100 UPTOWN BLVD. NE, SUITE 700
ALBUQUERQUE, NM 87110
USA

D. SCIAUDONE
KAPL-GENERAL ELECTRIC CO.
P.O. BOX 1072
SCHENECTADY, NY 12301-1072
USA

J. SCOBEL
WESTINGHOUSE
HAYMAKER-NORTHERN PIKE
MONROEVILLE, PA 15146
USA

W. SCOTT
BATTELLE-PACIFIC NORTHWEST LABS.
P.O. BOX 999
RICHLAND, WA 99352
USA

P. SECKER
ARIZONA PUBLIC SERVICE
11202 N.24TH AVE
PHOENIX, AZ 85029
USA

B. SEHGAL
ELECTRIC POWER RESEARCH INSTITUTE
3412 HILLVIEW AVE, P.O. BOX 10412
PALO ALTO, CA 94303
USA

R. SENEMEAUD
CEA FRENCH ATOMIC ENERGY COMMISSION
CEN/FAR BP NO. 6
FONTENAY-AUX-ROSES, CEDEX 92265
FRANCE

S. SETH
MITRE CORP.
7525 COLSHIRE DR.
MCLEAN, VA 22102
USA

W. SHA
ARGONNE NATIONAL LABORATORY
9700 CASS AVENUE, BLDG. 335
ARGONNE, IL 60439
USA

W. SHACK
ARGONNE NATIONAL LABORATORY
9700 CASS AVENUE, BLDG. 212
ARGONNE, IL 60439
USA

V. SHAH
EG&G IDAHO, INC.
P.O. BOX 1625
IDAHO FALLS, ID 83415
USA

G. SHERWOOD, JR.
U.S. DEPARTMENT OF ENERGY
3509 BASFORD ROAD
FREDERICK, MD 21701
USA

D. SHIFLETT
AECL TECHNOLOGIES
15400 CALHOUN DRIVE, SUITE 100
ROCKVILLE, MD 20855
USA

D. SIEBE
LOS ALAMOS NATIONAL LABORATORY
P.O. BOX 1663, MS K555
LOS ALAMOS, NM 87545
USA

E. SILVER
OAK RIDGE NATIONAL LABORATORY
P.O. BOX 2009 M.S. 8065
OAK RIDGE, TN 37831
USA

E. SILVERMAN
ARD CORPORATION
9151 RUMSEY ROAD
COLUMBIA, MD 21045
USA

F. SIMONEN
BATTELLE-PACIFIC NORTHWEST LABS.
P.O. BOX 999
RICHLAND, WA 99352
USA

J. SIMONS
MPR ASSOCIATES, INC
1050 CONNECTICUT AVE, NW
WASHINGTON, DC 20036
USA

U. SINHA
EG&G IDAHO, INC.
P.O. BOX 1625, MS 2406
IDAHO FALLS, ID 83415
USA

G. SLAUGHTER
OAK RIDGE NATIONAL LABORATORY
P.O. BOX 2008, 4500S, MS 6152
OAK RIDGE, TN 37831-6152
USA

J. SMOTREL
BABCOCK & WILCOX CO.
P.O. BOX 10935
LYNCHBURG, VA 24501
USA

B. SPENCER
ARGONNE NATIONAL LABORATORY
9700 S. CASE AVENUE
ARGONNE, IL 60439
USA

J. SPIESS
WESTINGHOUSE - BETTIS
BETTIS LABORATORY P.O. BOX 79
W. MIFFLIN, PA 15122-0079
USA

H. STADTKE
JOINT RESEARCH CENTER
ISPRA ESTABLISHMENT
ISPRA, VARESE I21020
ITALY

F. STALLMANN
OAK RIDGE NATIONAL LABORATORY
P.O. BOX 2008, BLDG 3001
OAK RIDGE, TN 37831-6028
USA

R. STARCK
MPR ASSOCIATES, INC
1050 CONNECTICUT AVE, NW
WASHINGTON, DC 20036
USA

R. STEELE
EG&G IDAHO, INC.
P.O. BOX 1625
IDAHO FALLS, ID 83415
USA

H. STEINBERG
U.S. DEPARTMENT OF ENERGY
MAIL STOP EH-321
GERMANTOWN, MD 20545
USA

P. STOOP
NETHERLANDS ENERGY RES. FOUNDATION
WESTERDUINWEG 3
PETTEN, 1755 ZG
THE NETHERLANDS

W. STOPPLER
MPA STUTTGART
PFAFFENWALDRING 32
STUTTGART 80, 7000
FRG

D. STRAWSON
MPR ASSOCIATES, INC
1050 CONNECTICUT AVE, NW
WASHINGTON, DC 20036
USA

E. STUBBE
TRACTEBEL
1 PLACE DU TRONE
BRUSSELS,
BELGIUM

H. STUMPF
LOS ALAMOS NATIONAL LABORATORY
P.O. BOX 1663
LOS ALAMOS, NM 89545
USA

M. SUBUDHI
BROOKHAVEN NATIONAL LABORATORY
BUILDING 130
UPTON, NY 11973
USA

T. SUEMURA
JAPAN ATOMIC ENERGY RES. INST
TOKAI-MURA, NAKA-GUN
IBARAKI-KEN, 319-11
JAPAN

S. SUK
KOREAN ADVANCED ENERGY RSCH
21-D RACEBROOK E.
E. HARTFORD, CT 06108
USA

V. SUKHORUCHKIN
I.V. KURCHATOV INST. OF ATOMIC ENERGY
KURCHATOV SQUARE
MOSCOW, 123182
USSR

H. SULLIVAN
LOS ALAMOS NATIONAL LABORATORY
P.O. BOX 1663, MS K557
LOS ALAMOS, NM 87545
USA

J. SUTTON
YANKEE ATOMIC ELECTRIC COMPANY
100 MAIN ST.
BOLTON, MA 01740
USA

H. SUWA
JAPAN NUS
7-1 NISHI-SHINJU 2 CHOME
NISHI-SHINJUKU, TOKYO 163
JAPAN

S. SUZUKI
JAPAN INSTITUTE OF NUCLEAR SAFETY
FUJITA KANKOU TORANOMON BLDG-3-17-1
MINATO-KU, TOKYO, 105
JAPAN

B. SWAN
GEOMATRIX CONSULTANTS
ONE MARKET PLAZA,SPEAR ST. TOWER
SAN FRACISCO, CA 94131
USA

H. TADA
FUYO DATA PROCESSING & SYS. DEV., LTD.
2-12, KAIGAN 3 CHOME
MINATO-KU,TOKYO, 108
JAPAN

M. TAEB
SINGER LINK-MILES
McGRAW ROAD
COLUMBIA, MD 21045
USA

A. TALLMAN
WESTINGHOUSE HANFORD CO.
P.O. BOX 1970 H5-53
RICHLAND, WA 99352
USA

C. TALLY
BABCOCK & WILCOX CO.
PO BOX 10935
LYNCHBURG, VA 24506
USA

O. TAMPONE
ENEA-DISP
ORE CASACCIA VIA ANGUILLARESE 301
ROME, 00060
ITALY

J. TANJI
JAPAN INSTITUTE OF NUCLEAR SAFETY
FUJITA KANKOU TORANOMON BLDG-3-17-1
MINATO-KU, TOKYO, 105
JAPAN

K. TASAKA
JAPAN ATOMIC ENERGY RES. INST
TOKAI-MURA, NAKA-GUN
IBARAKI-KEN, 319-11
JAPAN

J. TAYLOR
BROOKHAVEN NATIONAL LABORATORY
BUILDING 130
UPTON, NY 11973
USA

P. THIESS
AMECS
P.O. BOX 1189
WASHINGTON, DC 20013
USA

R. THOMPSON
AMES LAB, IOWA STATE UNIV.
108 OFFICE & LABORATORY
AMES, IOWA 50011
USA

M. TING
ATOMIC ENERGY COUNCIL, EXECUTIVE YUAN
67, LANE 144, KEELUNG RD., SEC. 4
TAIPEI, TAIWAN 10772
ROC

A. TINGLE
BROOKHAVEN NATIONAL LABORATORY
BUILDING 130
UPTON, NY 11973
USA

N. TODREAS
MASS. INSTITUTE OF TECHNOLOGY
77 MASS. AVE
CAMBRIDGE, MA 02168
USA

A. TOIVOLA
INDUSTRIAL POWER CO. LTD -TVO
27160 OLKILUOTO
SUOMI, SF-27160
FINLAND

J. TRAVIS
LOS ALAMOS NATIONAL LABORATORY
P.O. BOX 1663, GROUP N-6, MS - K557
LOS ALAMOS, NM 87544
USA

J. TROTTER
GROVE ENGINEERING
15215 SHADY GROVE ROAD
ROCKVILLE, MD 20850
USA

A. TURNER
DOMINION ENGINEERING
6862 ELM ST.
MC LEAN, VA 22101
USA

M. TUTTLE
LAMONT-DOHERTY GEOL. OBSERVATORY
COLUMBIA UNIVERSITY
PALISADES, NY 10964
USA

S. UNWIN
BATTELLE
505 KING AVE
COLUMBUS, OH 43201
USA

F. URBANUS
WESTINGHOUSE - BETTIS
P.O. BOX 79
W. MIFFLIN, PA 15122
USA

R. VALENTIN
ARGONNE NATIONAL LABORATORY
9700 CASS AVENUE, BLDG. 308
ARGONNE, IL 60439
USA

K. VALTONEN
FINNISH CENTRE FOR RAD. & NUCL. SAFETY
P.O. BOX 268
HELSINKI, 00101
FINLAND

D. VAN DUYNE
STONE & WEBSTER ENGINEERING CORP
245 SUMMER STREET, P.O. 2325
BOSTON, MA 02107
USA

F. van IDDEKINGE
DUTCH NUCLEAR SAFETY DEPT.
P.O. BOX 67
VOORBURG, 2270 MA
THE NETHERLANDS

W. VESELY
SCIENCE APPLICATIONS INTL. CORP.
2941 KENNY ROAD
COLUMBUS, OH 43221
USA

A. VIEIRA
BECHTEL POWER CORPORATION
15740 SHADY GROVE ROAD
GAITHERSBURG, MD 20877-1454
USA

M. VILLARAN
BROOKHAVEN NATIONAL LABORATORY
BUILDING 130
UPTON, NY 11973
USA

I. WALL
ELECTRIC POWER RESEARCH INSTITUTE
3412 HILLVIEW AVE, P.O. BOX 10412
PALO ALTO, CA 94303
USA

T. WALTERS
MPR ASSOCIATES, INC
1050 CONNECTICUT AVE, NW
WASHINGTON, DC 20036
USA

R. WEEMS
U.S. GEOLOGICAL SURVEY
MAIL STOP 928
RESTON, VA 22092
USA

A. WEISS
BROOKHAVEN NATIONAL LABORATORY
BUILDING 197C
UPTON, NY 11973
USA

P. WEISS
SIEMENS AG / UB KWU
HAMMERBACHERSTR. 12+14
ERLANGEN, D-8520
FRG

J. WELLS
LAWRENCE LIVERMORE NATIONAL LAB
P.O. BOX 8, L-196
LIVERMORE, CA 94550
USA

T. WHEELER
SANDIA NATIONAL LABORATORIES
P.O. BOX 5800, DIVISION 6412
ALBUQUERQUE, NM 87185
USA

G. WILKOWSKI
BATTELLE COLUMBUS
505 KING AVE.
COLUMBUS, OH 43201
USA

K. WILLIAMS
SCIENCE APPLICATIONS INTL. CORP.
2109 AIR PARK RD., S. E.
ALBUQUERQUE, NM 87106
USA

G. WILSON
EG&G IDAHO, INC.
P.O. BOX 1625
IDAHO FALLS, ID 83415
USA

B. WIMPENNY
ROLLS-ROYCE AND ASSOCIATES LTD
P.O. BOX 31, RAYNESWAY
DERBY, DE2 8BJ
UK

K. WINEGARDNER
BATTELLE-PACIFIC NORTHWEST LABS.
P.O. BOX 999
RICHLAND, WA 99352
USA

L. WOLF
KERNFORSCHUNGSZENTRUM, PHDR
PO BOX 3640
KARLSRUHE, FRG D7500
FRG

A. WOLFORD
EG&G IDAHO-INEL
P.O. BOX 1625
IDAHO FALLS, ID 83415
USA

K. WOOTEN
SOUTHERN COMPANY SERVICES, INC.
P.O. BOX 2625
BIRMINGHAM, AL 35202
USA

J. WREATHALL
SCIENCE APPLICATIONS INTL. CORP.
2941 KENNY ROAD
COLUMBUS, OH 43221
USA

W. WULFF
BROOKHAVEN NATIONAL LABORATORY
BUILDING 475B
UPTON, NY 11973
USA

K. XANTHOPOULOS
SWEDISH NUCLEAR POWER INSPECTORATE
P.O. BOX 27106
STOCKHOLM, S-102 52
SWEDEN

H. YAMADA
MITSUBISHI ATOMIC POWER IND. INC
4-1, SHIBAKOUEN 2-CHOME, MINATO-KU
TOKYO, 105
JAPAN

Y. YEH
ATOMIC ENERGY COUNCIL, EXECUTIVE YUAN
67, LANE 144, KEELUNG RD., SEC. 4
TAIPEI, TAIWAN 107
ROC

M. YOKOTA
TOKYO ELECTRIC POWER CO. INC
1901 L STREET, N.W., SUITE 720
WASHINGTON, DC 20036
USA

R. YOUNG
AEA TECHNOLOGY, SRD
SRD, WIGSHAW LANE, CULCHETH
WARRINGTON, CHESHIRE WA3 4NE
UK

R. YOUNGBLOOD
BROOKHAVEN NATIONAL LABORATORY
BUILDING 130
UPTON, NY 11973
USA

V. YRJÖLÄ
TECHNICAL RSCH CTR OF FINLAND
P.O. BOX 169
HELSINKI, SF-00181
FINLAND

H. ZEILE
EG&G IDAHO, INC.
P.O. BOX 1625
IDAHO FALLS, ID 83415
USA

M. ZEYA
ONTARIO HYDRO - NED
700 WASHINGTON AVE., H11 D23
TORONTO, ONTARIO M5G 1X6
CANADA

G. ZIGLER
SCIENCE & ENGINEERING ASSOCIATES, INC.
6100 UPTOWN BLVD. NE, SUITE 700
ALBUQUERQUE, NM 87110
USA

R. ZIPPER
GESELLSCHAFT FUR REAKTORSICHERHEIT
SCHWERTNERGASSE 1
D-5000 COLOGNE, 1
FRG

P. ZMOLA
C&P ENGINEERING
5409 NEWINGTON RD.
BETHESDA, MD 20816
USA

R. ZOGRAN
MPR ASSOCIATES, INC
1050 CONNECTICUT AVE, NW
WASHINGTON, DC 20036
USA

PROCEEDINGS OF THE
SEVENTEENTH WATER REACTOR SAFETY INFORMATION MEETING
October 23-25, 1989

TABLE OF CONTENTS - VOLUME 3

Plant Performance, Testing and Analysis (Cont'd)

Piping and NDE

Chairman: C. Serpan

Plant Aging

Chairman: W. Farmer

✓Plant Aging
Chairman: J. Vora

HEAVY SECTION STEEL TECHNOLOGY PROGRAM FRACTURE ISSUES*

W. E. Pennell
Oak Ridge National Laboratory
Oak Ridge, TN 37831

Abstract

Large scale fracture mechanics tests have resulted in the identification of a number of fracture technology issues. Identification of additional issues has come from the reactor vessel materials irradiation test program and from reactor operating experience. This paper provides a review of fracture issues with an emphasis on their potential impact on a reactor vessel pressurized thermal shock (PTS) analysis. Mixed mode crack propagation emerges as a major issue, due in large measure to the poor performance of existing models for the prediction of ductile tearing. Rectification of ductile tearing technology deficiencies may require extending the technology to include a more complete treatment of stress state and loading history effects. The effect of cladding on vessel fracture remains uncertain to the point that it is not possible to determine at this time if the net effect will be positive or negative. Enhanced fracture toughness for shallow flaws has been demonstrated for low strength structural steels. Demonstration of a similar effect in reactor pressure vessel steels could have a significant beneficial effect on the probabilistic analysis of reactor vessel fracture. Further development of existing fracture mechanics models and concepts is required to meet the special requirements for fracture evaluation of circumferential flaws in the welds of ring forged vessels. Fracture technology advances required to address the issues discussed in this paper are the major objective for the ongoing Heavy Section Steel Technology (HSST) program at ORNL.

1. Introduction

Fracture prevention requirements for steel nuclear reactor pressure vessels in commercial nuclear power stations are defined in Section *10 CFR 50* of the Code of Federal Regulations (Ref. 1). National consensus standards developed by the American Society of Mechanical Engineers (ASME) for fracture prevention in nuclear reactor vessels (Refs. 2 & 3) and by the

*Research sponsored by the Office of Nuclear Regulatory Research, U.S. Nuclear Regulatory Commission under Interagency Agreement 1886-8011-9B with the U.S. Department of Energy under Contract DE-AC05-840R21400 with Martin Marietta Energy Systems, Inc.

American Society for Testing Materials are incorporated into the requirements of *10 CFR 50* by reference. Guidance for performing the irradiation effects evaluation and the pressurized thermal shock (PTS) safety analyses required by *10 CFR 50* is provided in *Regulatory Guides 1.99* (Ref. 4) and 1.154 (Ref. 5) respectively.

Requirements outlined in the previous paragraph have as their common objectives (a) assuring that steel reactor vessels are constructed of materials that will provide an adequate margin of protection against failure by either brittle fracture or ductile tearing and (b) assuring that the effects of aging during reactor service do not reduce the fracture prevention margins below an acceptable level. The aging effect of primary concern is that produced by irradiation induced hardening and loss of ductility in the reactor vessel materials. The emphasis in this paper is on the fracture mechanics technology advances required to more accurately assess the effects of irradiation aging on pressure vessel fracture prevention margins.

Identification of the need for fracture prevention technology advances has come from large scale fracture technology validation experiments, materials irradiation test programs and from nuclear power plant operating experience. Existing technology for the analysis of mixed mode (cleavage-tearing) crack propagation has not performed well in predicting the response of heavy section vessels in pressurized thermal shock tests (Ref. 6). Predictions of cleavage fracture initiation toughness for heavy section wide-plate crack-arrest specimens have been significantly less than values obtained in subsequent tests (Ref. 7). These same tests have produced crack arrest toughness values significantly in excess of the limiting values incorporated into the crack arrest toughness curves of Ref. 3. Fracture toughness tests on beam specimens with varying flaw depths have given indications of enhanced fracture toughness for shallow flaws (Ref. 8). These test results indicate a need for further development of some of the basic elements of existing mixed-mode fracture mechanics technology.

Post-irradiation fracture toughness data have been obtained for the ASTM A533-B material commonly used in reactor vessel construction (Ref. 9), low-upper-shelf-weld (LUSW) material found in reactor vessels fabricated by Babcock and Wilcox (Ref. 10) and for the stainless steel cladding used as a corrosion protection coating in all pressurized water reactors in the USA (Ref. 11). Results from tearing tests on the A533-B and LUSW materials show the anticipated relationship between ductile tearing initiation toughnesses, with J_{Ic} values for the LUSW material being approximately half those for A533-B. This well known result is responsible in part for the special irradiation exposure limitations placed on the subset of reactor vessels containing LUSW material. Test data for irradiated cladding material however show it to have a ductile tearing initiation toughness very similar to that of LUSW material. The inference of this finding is that the existence of a coating with low tearing initiation toughness must be considered in the fracture evaluation of a much broader segment of the reactor vessel population. Cladding material, which was frequently neglected as a structural element in pressure vessel fracture evaluations, must now be considered as a potential initiation point for ductile tearing.

Operating experience with commercial nuclear power plants serves to accentuate the need for near term resolution of the reactor vessel fracture prevention technology issues. The NRC is in process of amending the PTS rule of 10 CFR 50.61 to be consistent with the requirements of Reg. Guide 1.99 Rev 2. When evaluated in conformance with the amended PTS rule, five plants are predicted to reach the pressurized thermal shock screening criteria before the end of their licensed life (Ref. 12). Refined PTS analysis technology may be required in the near term therefore to support a plant-specific PTS analysis of these plants. Violation of the 50 ft.lb. minimum allowable Charpy energy requirement of Ref. 1 exists at this time in five plants, of which four use ring forging construction (Ref. 13). Evaluation of these plants requires that existing fracture prevention technology, which was developed to deal primarily with axial flaws in longitudinal weld seams, be adapted and extended to deal with the special conditions relevant to the analysis of flaws in circumferential welds.

The intent in this paper is to explore the origin of some of the more significant fracture technology issues existing today, and indicate the potential impact their resolution may have on reactor vessel safety analysis results. Action to resolve these issues is in progress in the HSST program at ORNL, in companion NRC sponsored R&D programs within the USA and in a number of foreign national and international programs.

2. Issue Assessment Model Selection

Assessments of the impact of irradiation damage on reactor pressure vessel fracture prevention margins are based upon the changes produced by irradiation in the vessel material Charpy fracture energy curve. Principal features of the fracture margin assessment process for irradiated reactor vessels are summarized in Fig. 1. Parameters used in the irradiation damage assessment are (a) changes in the temperature at which a Charpy impact energy of 30 ft.lb. is achieved (ΔRT_{NDT}) and (b) Changes in the Charpy curve upper-shelf energy (ΔUSE). Increases in the reference temperature for nil-ductility-transition (RT_{NDT}) have impact on the cleavage fracture behavior of the pressure vessel material. These changes influence both the pressure-temperature limits incorporated into the plant Technical Specifications and the cleavage crack initiation and arrest properties used in the plant PTS analysis.

Decreases in the Charpy curve upper-shelf-energy are associated with a decreased resistance to failure by ductile tearing. This decreased tearing toughness must also be factored into the plant PTS analysis.

Rules of *10 CFR 50* Appendix G require demonstration "that lower values of upper shelf energy will provide margins of safety against fracture equivalent to those required by Appendix G of the ASME Code" when the upper-shelf-energy drops below 50 ft.lb. Specific guidelines for providing the required demonstration of fracture margin retention are not currently included in either 10 CFR 50 or the ASME Code. Work is in progress however within the ASME Section XI Fracture Assessment Committee to determine under what conditions reactor vessels may be permitted to operate with Charpy impact energies below the current 50 ft.lb. limit. It is to be anticipated

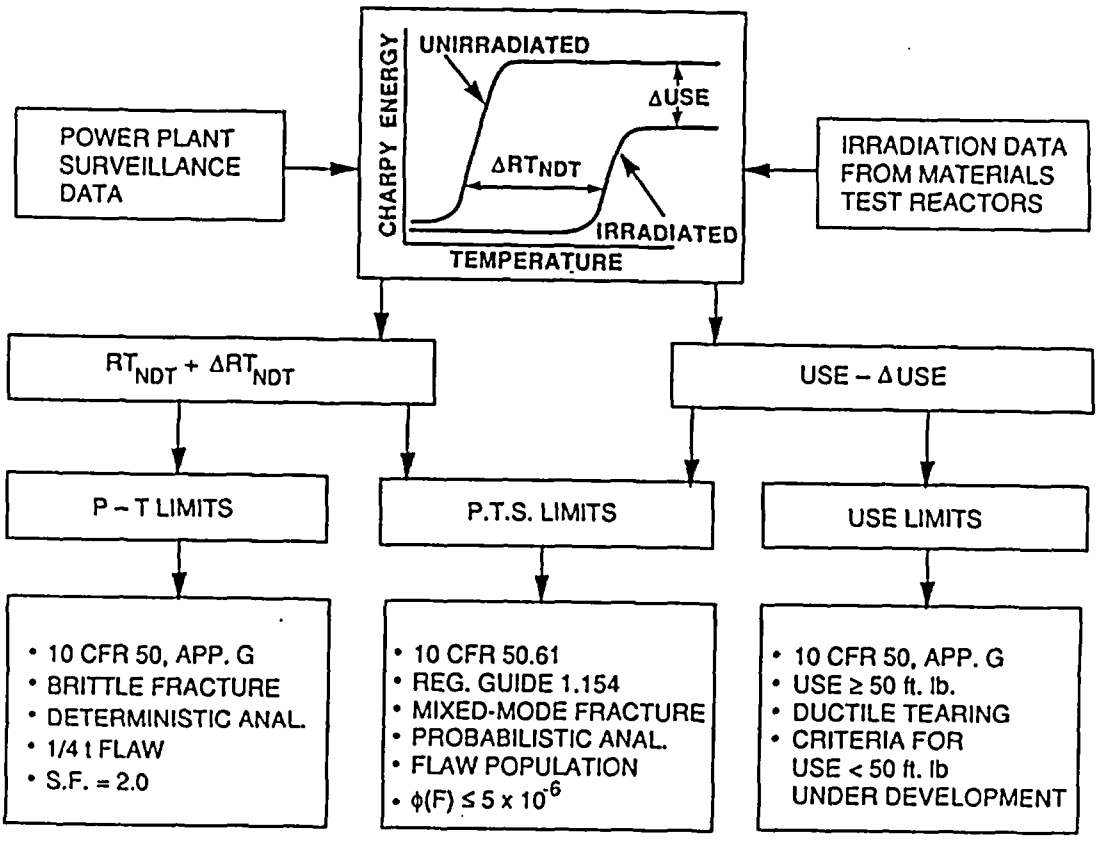

Fig. 1. Summary of the regulatory process used to assure retention of adequate fracture prevention margins in irradiated reactor pressure vessels.

therefore that ductile tearing considerations may in the near future be factored into the definition of the plant P-T limits.

At the present time, the plant PTS evaluation is the only application of materials irradiation data in a reactor vessel failure margin assessment in which the effects of irradiation induced changes in both the cleavage fracture and ductile tearing toughness of the material must be jointly included in a quantitative manner. This makes the reactor vessel PTS analysis model an attractive vehicle for assessing the potential impact of fracture technology uncertainties.

A further reason for selecting the reactor vessel PTS analysis model to evaluate the effect of uncertainties derives from the nature of the analysis and the characteristics of the associated flaws. Analysis used to define the plant P-T limits is based on an assumed 1/4t flaw. It is to be expected that the results of this analysis would be little influenced by consideration of surface effects such as those associated with shallow flaws and cladding. The PTS analysis in contrast requires consideration of a flaw distribution which includes shallow surface flaws. The PTS analysis model is thus sensitive to the full range of fracture technology uncertainties.

3. PTS Analyses Model Characteristics

Analysis of the behavior of postulated flaws in irradiated pressure vessel material during a PTS transient is performed using the OCA-P computer program (Ref. 14). OCA-P calculates the conditional probability of a through-wall fracture of the pressure vessel using a given input PTS transient and a probabilistic definition of the vessel wall flaw population. Our review of the potential impact of current fracture issues on reactor vessel fracture prevention margins can be accomplished however without consideration of the probabilistic elements of the OCA-P analysis. Principal features of the deterministic analysis performed by OCA-P at each time step throughout the PTS transient are illustrated in Figs. 2 and 3.

Time history definitions of the PTS transient boundary conditions on the vessel inner surface are input to the program and the resulting transient through-wall temperature gradients and combined pressure thermal stress distributions are calculated at selected time intervals throughout the transient. The calculated through-wall temperature and combined pressure-thermal stress curves for a selected time in the PTS transient are shown in Fig. 2. The vessel wall stress distribution is used to calculate crack tip stress intensity factors (K_I) for a range of flaw depths. A plot of the applied K_I as a function of flaw depth is also shown in Fig. 2.

Irradiation fluence data for a given point in the vessel operating history is input to OCA-P in the form of a vessel wall fluence profile. The

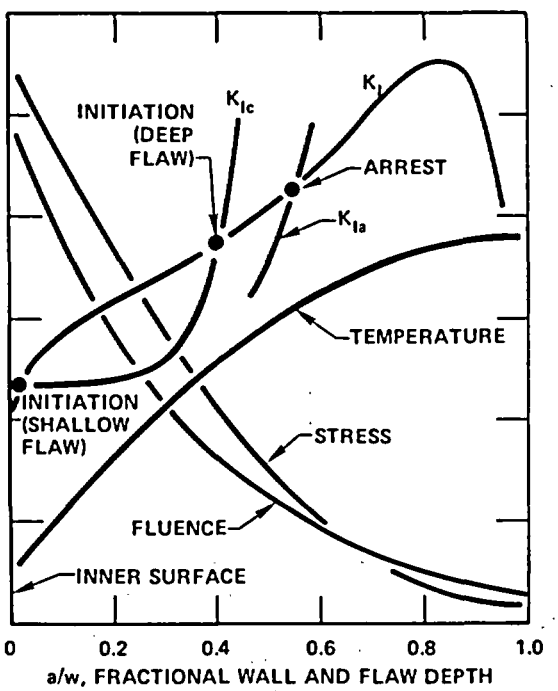

Fig. 2. Temperature, stress and fluence profiles in a reactor pressure vessel wall at a given instant in time during a PTS transient with the associated fracture toughness (K_{Ic} and K_{Ia}) and applied stress-intensity factor (K_I) curves.

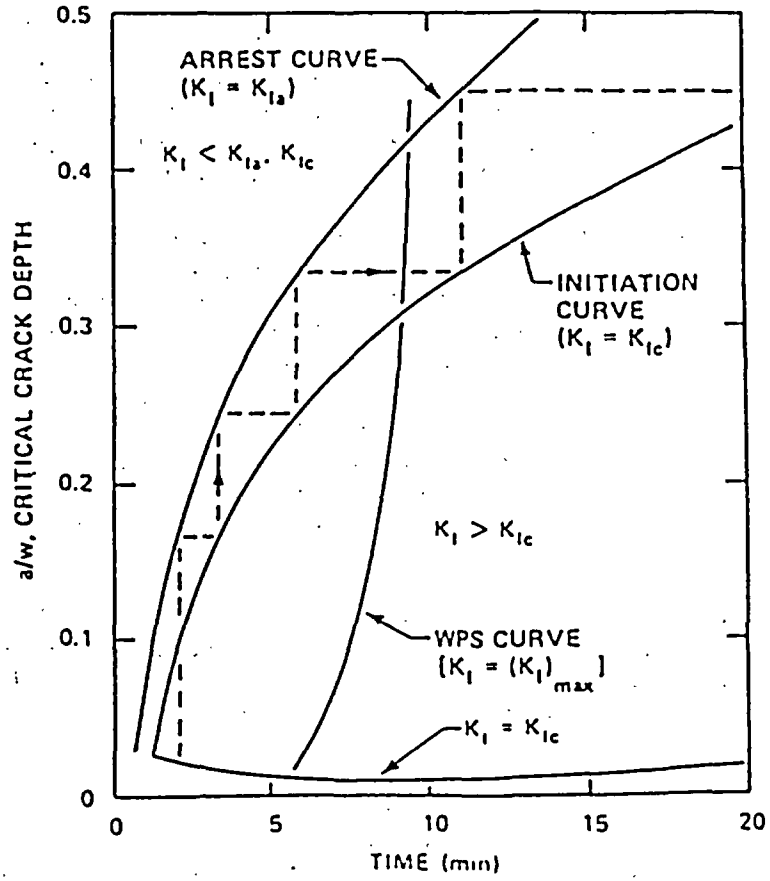

Fig. 3. Critical crack depth curves defined by plotting the locus of crack initiation and crack-arrest values as a function of time during a PTS transient.

fluence profile is used in conjunction with material dependent fluence-ΔRT_{NDT} curves to generate a through-wall ΔRT_{NDT} profile. Adding the irradiation induced ΔRT_{NDT} to the initial material NDT_o and subtracting the result from the local vessel wall temperature gives the quantity $T - RT_{NDT}$ required to define the point of entry into the material cleavage crack initiation (K_{Ic}) and crack arrest (K_{Ia}) curves. Material crack initiation and crack arrest toughness curves derived in this manner are shown superimposed on the applied K_I curve in Fig. 2.

Points of intersection of the applied K_I curve with the material K_{Ic} and K_{Ia} curves define the critical crack depths for crack initiation and arrest at a given point in time during the PTS transient. Note that the curves of Fig. 2 show two such intersections with the K_{Ic} curve, one for shallow and one for deep flaws. This characteristic of a typical PTS analysis is responsible for the special interest in fracture technology issues which could influence the initiation and propagation of surface and near surface flaws.

Output from the PTS analysis at a given point in time during the transient is in the form of critical crack depths for cleavage crack initiation and arrest. These results are extracted from analyses performed at specified time intervals throughout the transient and plotted to form curves of time-dependant critical cleavage crack initiation and arrest depths. An example of the resulting "critical crack depth" curves is given in Fig. 3.

Propagation of a crack initiating from a shallow flaw is indicated by the broken line in Fig. 3. The crack propagates in a series of cleavage initiation-arrest events. In the example given, crack propagation is terminated when the crack propagation path intersects the warm-prestress curve. This curve defines the point in time for each point through the thickness of the section at which the calculated crack tip stress intensity factor reaches its maximum value. Thereafter the calculated K_I falls with time. Testing has shown that a cleavage crack will not initiate when the crack tip K_I is decreasing. For the example given in Fig. 3 therefore, cleavage crack propagation would cease at approximately 33% penetration of the vessel wall.

The final step in the PTS analysis is to determine if the arrested crack is stable. Crack stability is checked by considering two additional failure modes. These are (a) instability of the remaining ligament under pressure induced membrane loading and (b) continued crack propagation by ductile tearing.

In order to assure a realistic assessment of the potential impact of fracture technology uncertainties, the "Rancho Seco" PTS transient was used as input to the OCA-P computer program for the generation of critical crack depth curves. The bulk coolant pressure-temperature history representing the Ranch Seco transient is shown in Fig. 4. While the critical crack depth

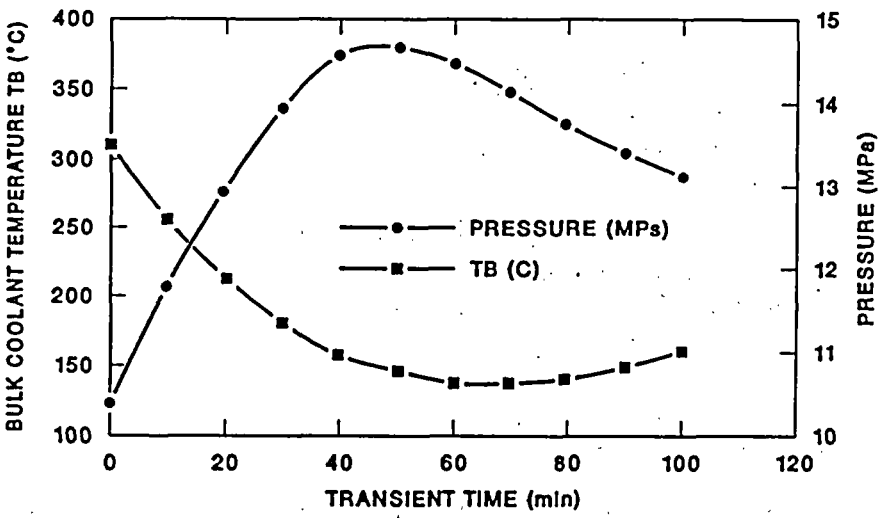

Fig. 4. Pressure-temperature time histories used in the fracture-issue evaluations. This PTS transient is based on an idealization of the Rancho Seco transient.

diagram produced using the input of Fig. 4 is clearly realistic, it is important to recognize when considering the evaluation of uncertainties that this transient is one of a large family of potential PTS transients, some of which could have significantly differing characteristics.

Critical crack depth curves produced using the Rancho Seco transient and an end-of-license-period irradiation conditioning are shown in Fig. 5 together with the warm prestress curve and the ligament stability limit. In this base case analysis result, the fracture window is defined by the segment of the K_{Ic} curve lying to the left of the warm prestress curve. This is so because a cleavage crack, once initiated, would not encounter the crack arrest curve before reaching the ligament stability limit. The width of the fracture window is a useful parameter with which to measure the potential impact of a fracture technology uncertainty. It is important to recognize however that the true significance of the fracture window derives from the segment of the vessel flaw population included within its bounds. In the case of the base case analysis of Fig. 5 the flaw population between points A and D on the a/w axis are included in the window.

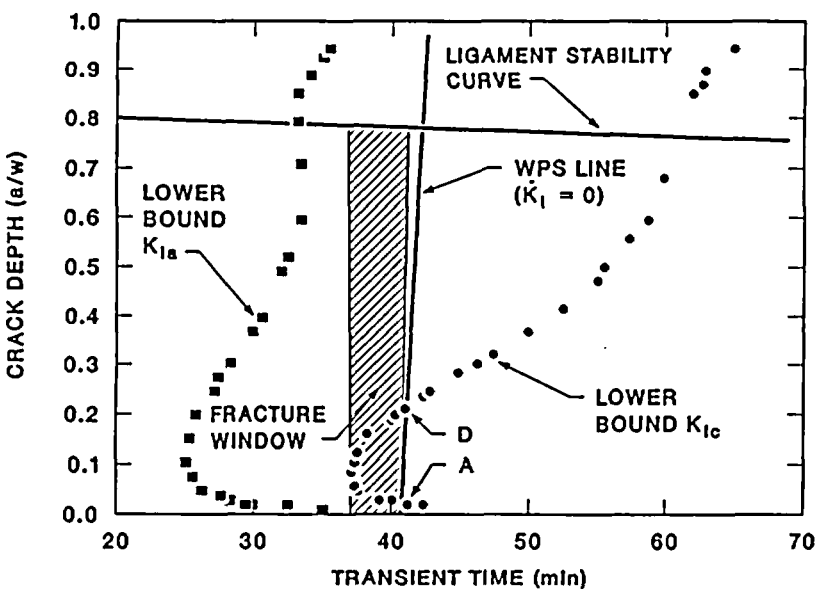

Fig. 5. Base case critical crack depth curves and the associated fracture window obtained using lower-bound K_{Ic} and K_{Ia} fracture-toughness input.

4. Fracture Issue Assessments

Mixed mode crack propagation involves crack initiation, propagation and arrest in both the cleavage fracture and ductile tearing modes. Uncertainties exist in the analytical models and materials data used in a number of critical areas of this analysis.

4.1 Cleavage Crack Initiation and Arrest

Cleavage crack initiation data obtained from wide plate tests of A533-B material are summarized in the bar chart of Fig. 6 (Ref. 7). The crack tip stress intensity factors were calculated using a 3D finite element model which accurately represented the geometry of the crack tip region. The test specimen geometry was such that plane strain constraint at the crack tip was not maintained. It was to be expected therefore that the plane stress fracture initiation toughness (K_c) obtained in these tests would be higher than the plane strain toughness (K_{Ic}) obtained at the same temperature from small specimen tests. What was not expected was the magnitude of the K_c/K_{Ic} ratio. The average measured K_c value was converted to an equivalent K_{Ic} value using Irwin's β conversion equation (Eq. 1) as implemented in Ref. 15.

where

$$K_c^2 = K_{Ic}^2[1 + 1.4\beta_{Ic}^2]$$
$$\beta_{Ic} = \frac{1}{B}\left(\frac{K_{Ic}}{\sigma_{ys}}\right)^2 \qquad (1)$$

The resulting equivalent average K_{Ic} value is approximately 60% higher than the value predicted from small scale plane strain K_{Ic} tests.

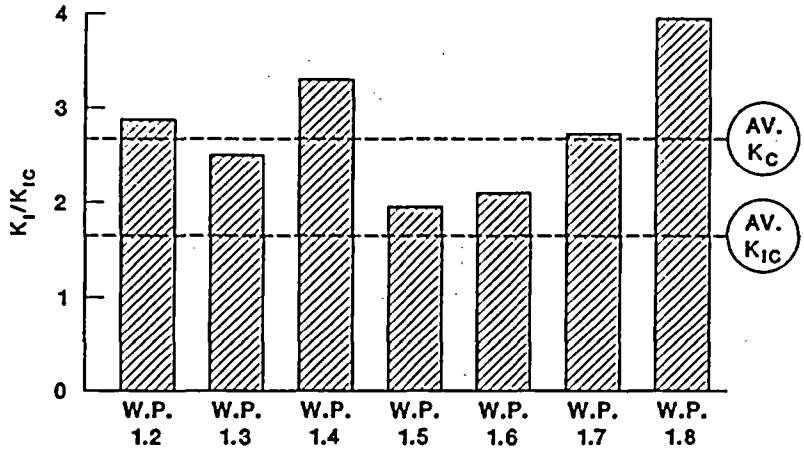

Fig. 6. Plane stress cleavage fracture initiation toughness data obtained from the A533B wide-plate tests expressed as a function of K_I/K_{Ic}.

An explanation for the crack initiation fracture toughness discrepancy described in the previous paragraph is not yet available. It would be inappropriate at this time to infer a basic increase in crack initiation fracture toughness for large scale plate specimens. The tests results do

however indicate a need to consider the potential effect of an enhanced cleavage crack initiation toughness on the response of a reactor pressure vessel to a PTS transient. In an effort to indicate an upper bound to this effect, The OCA-P analysis of the Rancho Seco PTS transient was run using a lower bound K_{Ic} curve 60% higher than that given in Ref. 3.

Cleavage crack arrest data from a number of large scale tests are shown superimposed on the crack arrest fracture toughness (K_{Ia}) curve of Section XI of the ASME Boiler and Pressure Vessel Code (Ref. 3) in Fig. 7. These data indicate the lower bound crack arrest fracture toughness curve can be extended considerably beyond the 220 MPa·$\sqrt{m}$ limit incorporated into the curves of Ref. 3.

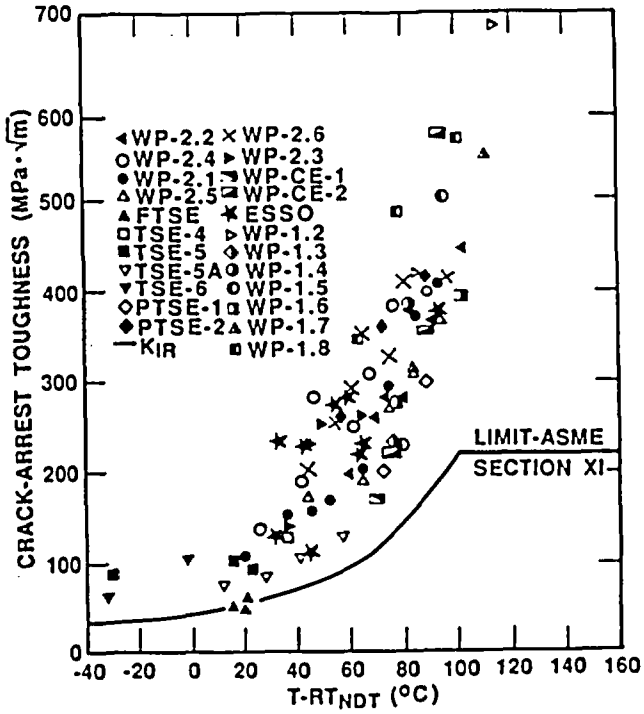

Fig. 7. Crack-arrest fracture toughness (K_{Ia}) data obtained from large specimen and wide-plate tests on A533B and simulated LUS weld material.

The data of Fig. 7 were corrected for the effect of crack tip tunneling, which occurred in some of the tests, and a lower bound curve was fitted. This enhanced crack arrest curve was used, together with the enhanced crack initiation toughness curve described above, in an OCA-P analysis to determine the effect of enhanced cleavage fracture properties on the reactor vessel response to a PTS transient.

Results from the OCA-P analysis using enhanced fracture toughness properties are shown superimposed on the base case results in Fig. 8. The

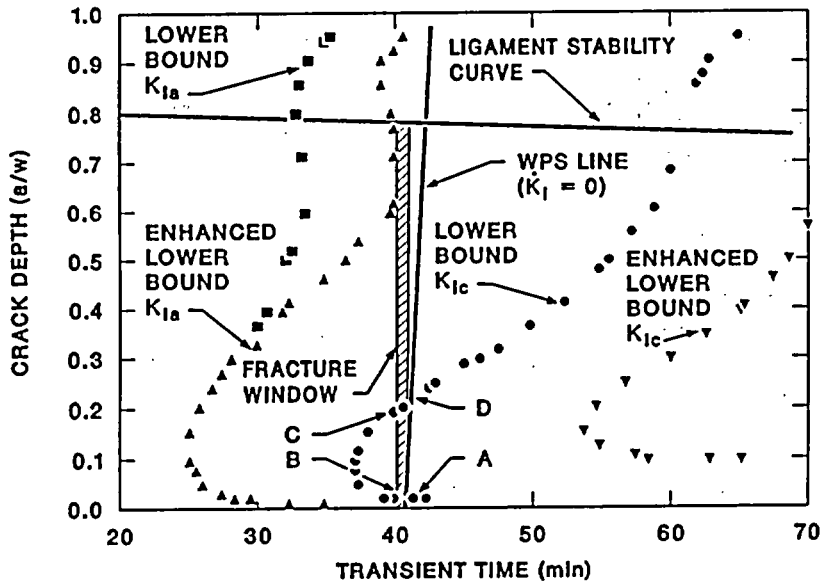

Fig. 8. Critical crack depth curves incorporating enhanced lower-bound fracture-toughness input, showing the effect on the width of the fracture window.

critical crack depth curve for crack initiation, corresponding to the enhanced K_{Ic} input, is seen to lay to the right and above the base case curve. The fact that the entire curve lays to the right of the warm prestress line indicates that cleavage crack initiation would not occur for the transient considered. It is appropriate to note however that the critical crack depth curves move to the left with increasing irradiation exposure due to the increasing ΔRT_{NDT}. This could occur for instance in the event of a plant life extension. Should this occur, the fact that the enhanced K_{Ic} critical crack depth curve lays above the base case curve could become important since it would effectively preclude crack initiation from shallow flaws.

The analysis results summarized in Fig. 8 show no negative effects of an enhanced cleavage crack initiation toughness. For the PTS transient analyzed the benefits, if any, of an enhanced K_{Ic} curve would be realized only in the event of a plant life extension.

Critical crack depth results given in Fig. 8 for the enhanced crack arrest toughness input show a more immediate benefit. The enhanced lower bound K_{Ia} input has the effect of moving the upper portion of the crack arrest curve to the right, where it overlaps a portion of the lower bound crack initiation curve. This overlap has the effect of reducing the width of the fracture window.

The width of the fracture window is measured in units of time, but the impact of a reduced fracture window width is evident if one considers its effect on the population of flaws from which a potential cleavage fracture failure could initiate. In the base case critical crack depth curves of

Fig. 5, a through-wall cleavage fracture can be initiated from the population of initial flaws between points A and D on the crack depth axis. The enhanced K_{Ia} results of Fig. 8 however show that through wall cracks can initiate only from those segments of the initial flaw population between points A and B and between points B and C. The segment of the initial flaw population between points B and C is effectively removed as a source of a through-wall cleavage fracture.

Reducing the initial flaw population from which a through-wall cleavage fracture can initiate will act to reduce the predicted failure rate. Other factors must be considered however before the true value of this reduction can be assessed. In particular, the introduction into the PTS analysis of an enhanced cleavage crack initiation toughness for shallow flaws would serve to accentuate the advantages associated with an enhanced lower bound K_{Ia} curve. In contrast, consideration of ductile tearing failure modes could mitigate the advantage, particularly in low-upper-shelf weld material with low tearing resistance.

4.2 Ductile Tearing

Ductile tearing initiation toughness data for A533-B material and low-upper shelf weld material are shown in the plots of Fig. 9. These data were obtained from the test series reported in Refs. 9 and 10. At a temperature of 200°C the ductile tearing initiation toughness of the low-upper-shelf weld material is less than half that of A533-B. The reduced tearing initiation toughness of LUSW material makes ductile tearing a credible mechanism for fracture initiation. An OCA-P analysis was run to determine the range of flaw depths over which ductile tearing fracture initiation could occur.

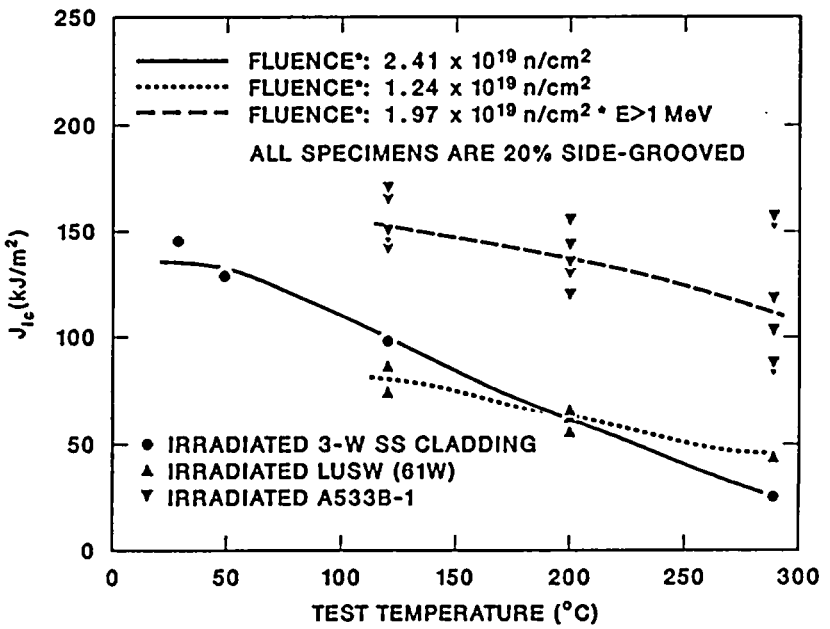

Fig. 9. Ductile tearing initiation-toughness curves (J_{Ic}) for A533B, LUS weld material and cladding in the irradiated condition.

Ductile tearing fracture initiation data (J_{Ic}) of Fig. 9 were converted to equivalent cleavage crack initiation values for use in the OCA-P computer program, using the J_{Ic}-K_{Ic} relationship of equation 2 (Ref. 16).

$$J_{Ic} = \frac{(1 - \nu^2)K_{Ic}^2}{E} \qquad (2)$$

Ductile tearing initiation curves generated in this analysis are shown superimposed on the base case critical crack depth curves in Fig. 10. The curve for LUSW material dips from an initial value of a/w = 0.36 to an a/w value of approximately 0.1. The low point in the curve lays to the left of the warm prestress line and therefore represents a condition in which crack propagation initiated in a ductile tearing mode could convert to cleavage fracture.

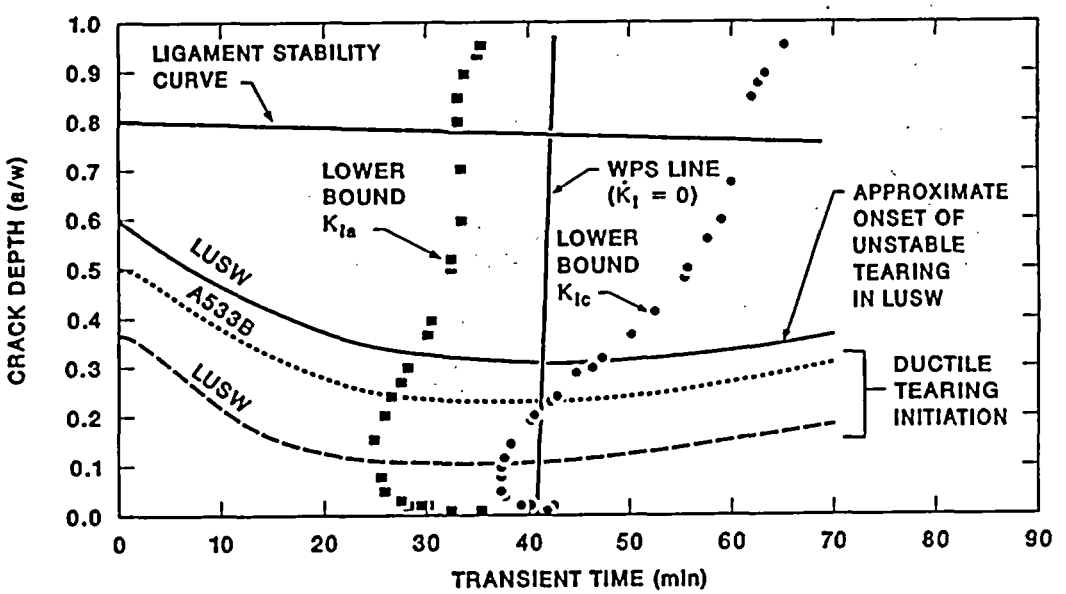

Fig. 10. Ductile tearing initiation and instability boundaries superimposed on the base case critical crack-depth curves.

Crack initiation and propagation data for a heavy section steel vessel containing a low-upper-shelf plate insert were obtained in pressurized thermal shock tests at ORNL (Ref. 6). Results from this test confirm the ductile tearing crack initiation and mixed mode crack propagation response potential indicated in Fig. 10. A photograph of the fracture surface from the PTSE-2 test is shown in Fig. 11. It shows that in the initial transient, which included a warm prestressing event, ductile tearing initiated at the tip of the test flaw (14 mm deep) and extended its depth by approximately 50% before converting to cleavage fracture.

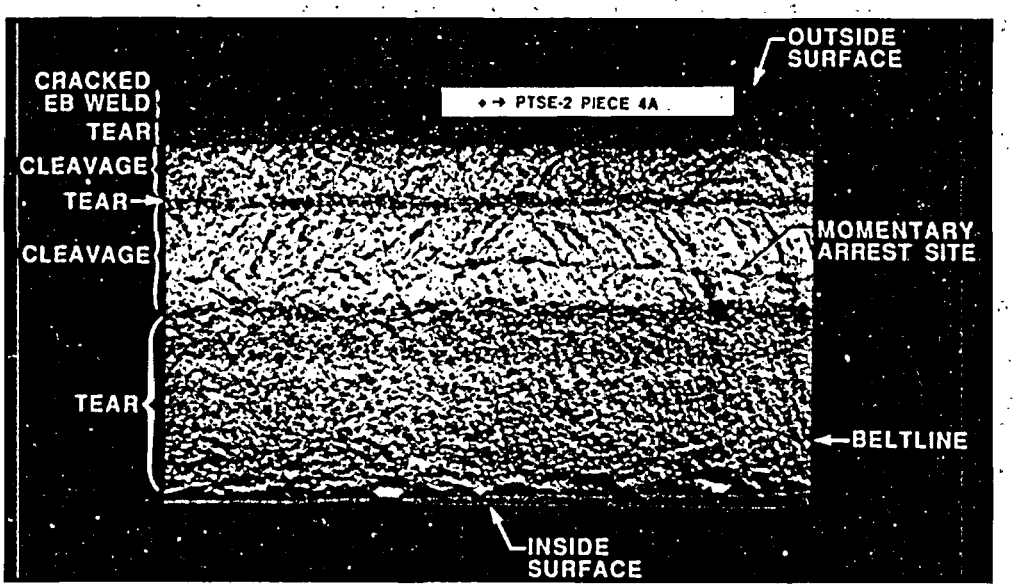

Fig. 11. Fracture surface from the PTSE-2 test on a vessel with a LUS insert, showing a 50% increase in crack depth due to ductile tearing prior to the initiation of cleavage fracture.

Results discussed above indicate a need to extend the treatment of ductile tearing behavior in PTS probabilistic fracture analysis models. The present generation (OCA/USA) of PTS analysis computer programs include an evaluation of the influence of ductile tearing on the stability of an arrested cleavage crack, but do not include any representation of ductile tearing in advance of the initiation of cleavage fracture. PTS analysis model extension requirements include (a) crack initiation by ductile tearing and (b) crack propagation by both ductile tearing and tearing conversion to cleavage fracture.

Tearing dependent ligament stability assessments, in addition to their role in a mixed mode PTS vessel fracture analysis, are of interest in defining the bounds within which enhanced cleavage crack arrest data could influence the PTS analysis result. J-R curve data for representative irradiated samples of A533-B and LUSW material were extracted from Refs. 9 and 10 respectively. Curves fitted to those data are reproduced in Fig. 12. The data sets selected were for test temperatures close to 200°C, since this represents a temperature which could exist near the crack tip when the crack tip J integral reaches its maximum value.

Validity limits defined by the criteria of ASTM E1152 (Ref. 17) are shown superimposed on the curves of Fig. 12. In the case of the LUSW material the curve rises very little beyond the ASTM E1152 validity limit. The upper bound asymptotic value from the LUSW material curve is therefore a reasonable value to use for the purpose of defining an upperbound limit of effectiveness of enhanced cleavage crack arrest toughness in LUSW material.

A curve representing an upper bound limit to the onset of unstable tearing in LUSW material is shown superimposed on the critical crack depth

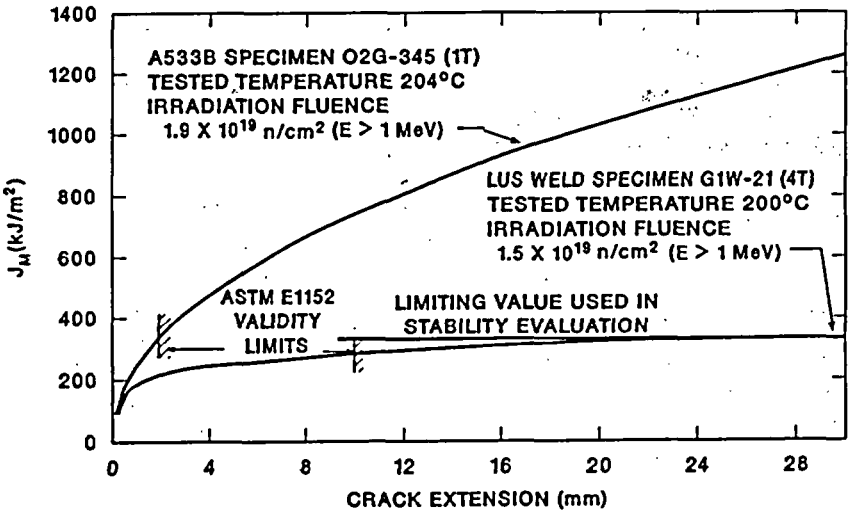

Fig. 12. J-R curves for irradiated A533 B and LUS weld material, showing the asymptotic J_M value used to estimate the upper bound of tearing instability for the LUS weld material.

curves in Fig. 10. This curve was generated using a K_c equivalent upper bound Jm value in the OCA-P computer program. The curve is seen to intersect the critical K_{Ia} curve at an a/w value of 0.33. The curves of Fig. 8 show the enhanced K_{Ia} curve to depart from the base case K_{Ia} curve at about the same a/w value. It appears unlikely therefore that enhanced cleavage crack arrest data would have any significant effect on the PTS analysis of reactor vessels containing LUSW material.

A ligament tearing instability analysis for A533-B material, similar to that described above for the LUSW material, is not currently available. The nature of the J-R curve for A533-B does not support the use of a simplified bounding analysis such as was used for the LUSW material. Large scale testing experience has called into question the adequacy of existing ductile tearing technology for the prediction of ductile tearing crack propagation to depths of practical interest for a ligament tearing stability analysis. The magnitude of the difference between the Jm curves for A533-B and LUSW material however suggests that the previously discussed advantages deriving from an enhanced crack arrest fracture toughness could remain valid for the A533-B material. In that connection, an estimate of the ligament tearing instability curve for A533-B would be particularly valuable in that it would define an upper bound for the useful extension of an enhanced K_{Ia} curve.

4.3 Mixed Mode Crack Propagation

Nowhere are pressure vessel fracture prevention technology issues more evident than in the analysis of mixed mode crack propagation in circumstances involving a significant degree of ductile tearing. Pretest predictions of ductile tearing crack extension in large scale tests have been

substantially in error for tests performed both in the USA and abroad (Refs. 6 and 18). To date no consistent pattern has emerged from the evaluation of prediction errors. Predictions for the PTSE-2 (Ref. 6) test underestimated the amount of ductile crack growth while the opposite was true for the British spinning cylinder test (Ref. 18).

Results from the PTSE-2 test will serve to illustrate the nature of the crack growth prediction errors encountered. In the first PTSE-2 test the pressure-temperature transient was tailored to produce a warm prestressing event after an initial ductile tearing event. The transient started from a uniform vessel temperature of close to 300°C but the extensive temperature monitoring instrumentation showed that tearing started when the temperature was close to 100°C. One would expect therefore that the material J-R curves for 100°C test temperatures would give the most accurate prediction of tearing behavior in this test.

J-R curves obtained in 100°C tests using material cut from undamaged segments of the LUS insert after the PTS test, are given in Fig. 13 (Ref. 6). Both deformation J (Jd) and modified J (Jm) formulations were used to interpret the test data. Calculated crack tip J values were then used to define the position on the vertical axis for measured crack extensions obtained in the test. It is evident from Fig. 13 that pretest predictions based on either the Jd or Jm versions of the J-R curve will substantially underestimate the amount of tearing actually observed.

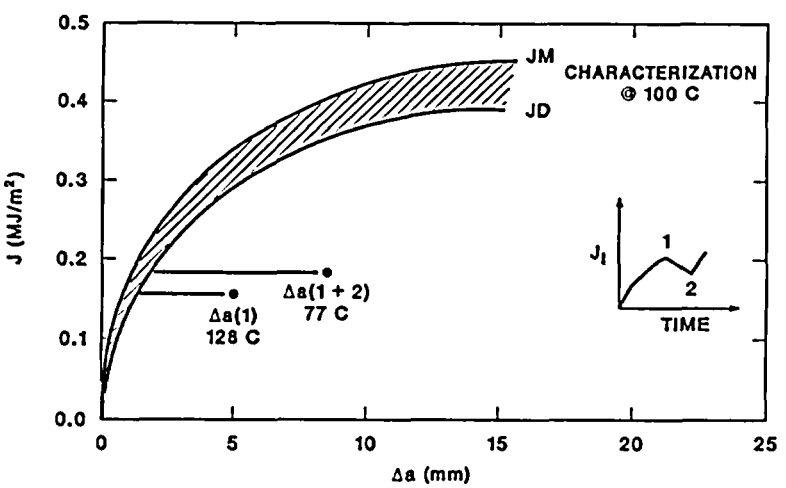

Fig. 13. Ductile tearing crack-extension data from the PTSE-2 test showing the discrepancy between measured and predicted results.

There is currently no consensus of opinion on the cause of tearing prediction discrepancies such as those illustrated in Fig. 13. Since tearing involves considerable plastic flow, a possible influence of the hydrostatic/deviatoric stress ratio suggests itself with both constraint induced and far-field stress states influencing the magnitude of plastic flow prior

to fracture. Early tube burst tests with varying stress ratios have demonstrated a strong influence of far-field biaxial stress ratio on plastic flow prior to fracture (Ref. 19). More recently, analysis of J-R data obtained from specimens with varying degrees of crack tip constraint have shown a relationship between the J-R curve and the constraint induced crack tip hydrostatic/deviatoric stress ratio (Ref. 20).

An element of the PTSE-2 test result of particular interest is the increase in the crack ductile tearing extension obtained when the specimen was reloaded after a load reduction for warm prestressing. The reload took the crack tip calculated J value to slightly above that associated with completion of the first tearing event. This action produced a second tearing increment equal to approximately 60% of that produced in the first event. This result strongly suggests that load history effects may be important in the prediction of ductile tearing behavior in reactor vessels subjected to the complex loading history which could be associated with a possible lifetime sequence of PTS events.

A need for further development of the technology for predicting the ductile tearing and tearing-cleavage fracture response of reactor vessels to a PTS transient is evident. This need appears to extend beyond the bounds of the ongoing evaluation of Jd and Jm as parameters for the representation of material ductile tearing behavior.

4.4 Shallow Cracks

A probabilistic fracture mechanics analysis of potential pressurized thermal shock events for the H. B. Robinson nuclear plant is reported in Ref. 21. The distribution of crack initiations obtained in the analysis of Ref. 21 is plotted in Fig. 14 as a function of the initial crack depth. Results summarized in Fig. 14 illustrate the dominant influence of shallow flaws on the number of crack initiations predicted in a probabilistic PTS analysis. To a large extent the crack initiation distribution is a reflection of the assumed initial flaw distribution used in the analysis, in which shallow flaws are numerically dominant. The results do serve to emphasize however the potentially significant impact of any fracture mechanics development which would influence the material fracture toughness to be associated with shallow flaws.

Shallow crack fracture behavior in A36, a low strength structural steel, has been investigated by W. A. Soren at the University of Kansas (Ref. 8). The investigation included both elastic-plastic finite element analysis and CTOD fracture toughness testing of beam specimens containing both deep ($a/w = 0.5$) and shallow ($a/w = 0.15$) cracks.

Results from the analytical portion of the study showed that for shallow cracks ($a/w \leq 0.15$), the yield zone at fracture extended behind the crack front to the free surface of the beam specimen, thereby reducing the level of crack tip constraint. Loss of crack tip constraint is associated with increased plastic flow and blunting of the crack prior to fracture. The elastic-plastic analysis results would therefore predict an increased fracture toughness for shallow cracks.

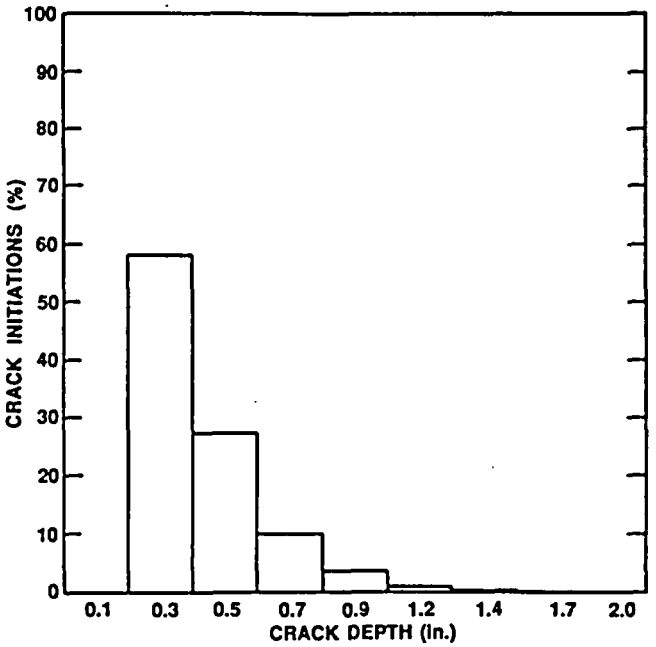

Fig. 14. Crack initiation distribution obtained in a reactor vessel failure probability analysis performed at ORNL for the H. B. Robinson Unit 2 Nuclear Power Plant.

Data from the deep crack and shallow crack tests of Ref. 8 are reproduced in Fig. 15. The data confirm the lower bound fracture toughness trends predicted by the elastic-plastic analysis. At a given temperature, the CTOD value at fracture for the shallow crack (a/w = 0.15) is approximately 2.5 times that for a deep crack (a/w = 0.5).

The 31.8mm wide specimens used in the A36 shallow crack tests would produce plane stress rather than plane strain lateral constraint conditions at the crack front. The results of Fig. 15 are therefore indicative of an increase in plane stress fracture toughness with decreasing crack depth. It appears reasonable to suppose however that a similar trend would be obtained using test specimen widths associated with plane strain lateral constraint conditions.

Investigations completed to date provide a clear indication that enhanced fracture toughness properties are associated with shallow flows in A36 material. A36 is a low yield strength carbon steel with a relatively high strain hardening exponent (σy = 36 ksi : UTS = 58 - 80 ksi : ε_T = 23%). It is appropriate therefore to question the relevance of the shallow crack trends observed in A36 to quenched and tempered alloy steels such as A533B, Class 1 (σy = 50 ksi : UTS = 80 - 100 ksi : ε_T = 18%).

Ongoing shallow crack fracture toughness testing of high strength A517 quenched and tempered alloy steel plate (σy = 100 ksi : UTS = 115 - 135 ksi, ε_T = 14%) , performed at the University of Kansas under the direction of Professor S. J. Rolfe, have shown a trend of increasing fracture

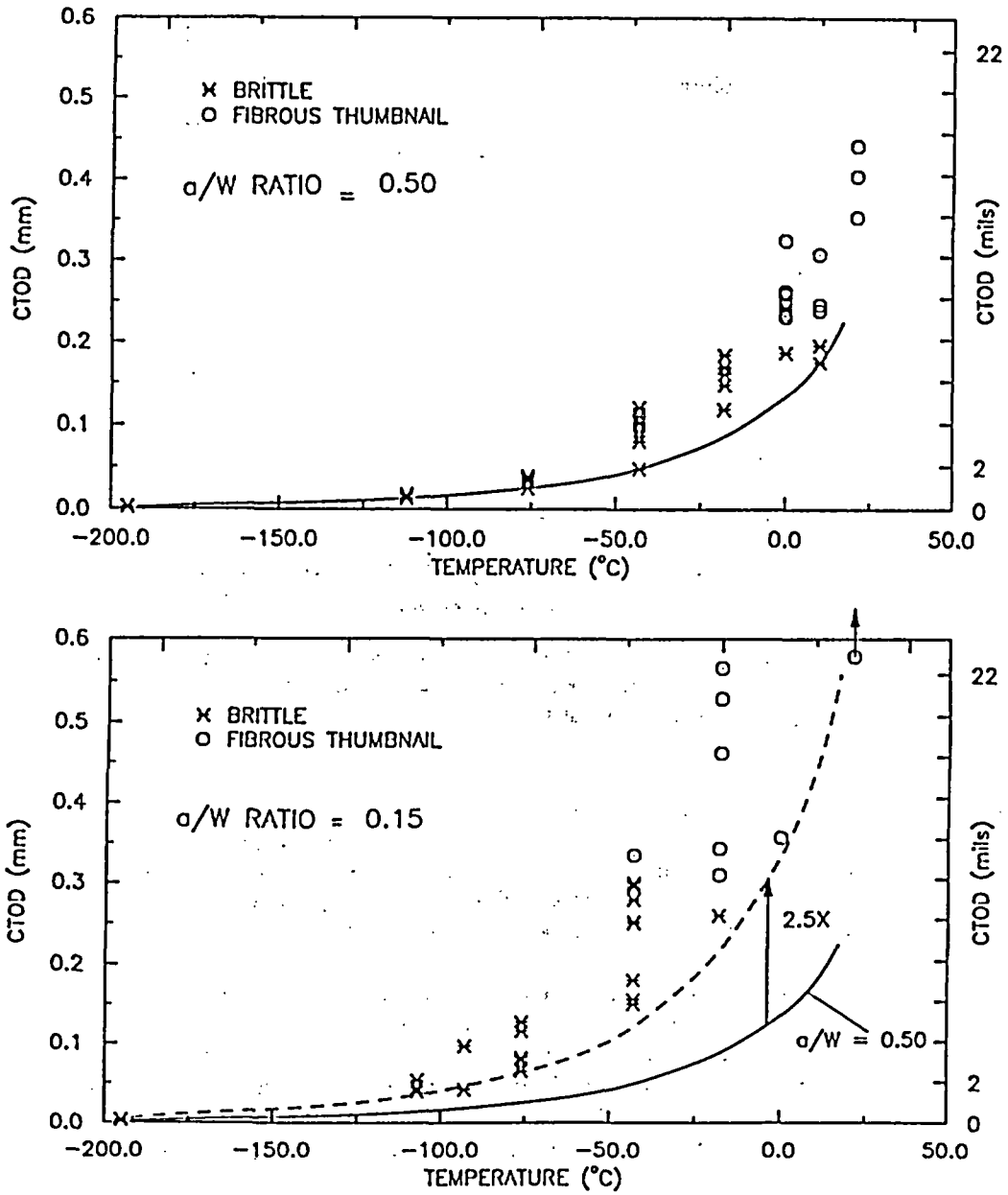

Fig. 15. Shallow flaw CTOD fracture-toughness data for A36 generated by the University of Kansas (Ref. 16).

toughness with decreasing crack depth compatible with that observed in A36. Mechanical properties of A36 and A517 straddle those of A533B. It appears reasonable therefore to anticipate an enhanced fracture toughness for shallow flaws in A533B material.

An international shallow flaw testing project headed by the Edison Welding Institute in the USA and the Welding Institute in the UK is

scheduled to produce standardized testing procedures and data interpretation methods towards the end of 1990. The potential beneficial impact of enhanced shallow flaw fracture toughness data on the PTS analysis is such that early application of the shallow flaw testing technology to reactor pressure vessel steels is planned within the HSST program.

4.5 Cladding

Stainless steel cladding is used as a corrosion protection barrier on all commercial water cooled reactors licensed by the NRC. Any effect of cladding which could influence the fracture characteristics of a pressure vessel wall is therefore of special interest because of the large population of vessels affected.

Beneficial effects of cladding in providing an insulating layer on the inside surface of the reactor vessel are included in analysis performed by the OCA-P program. Potential additional benefits deriving from the concept of cladding as a tough surface medium producing surface forces which act to reduce the crack tip stress intensity factor in subsurface flaws or tunneling cracks (Fig. 16a), have long been recognized. Tests on clad plate have shown that under certain conditions cladding can act to inhibit the surface propagation of a fast running cleavage crack (Ref. 22). The tests also showed however substantial propagation of the cleavage crack by sub-surface tunneling. It is not clear at this time what net benefit to pressure vessel

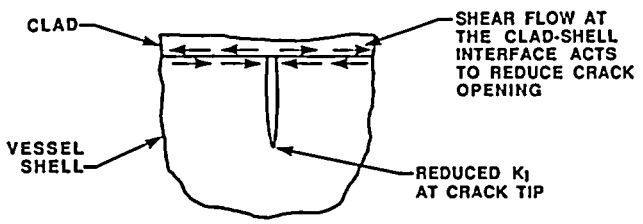

(a) POSITIVE CLAD POTENTIAL FOR SUB-CLAD FLAWS

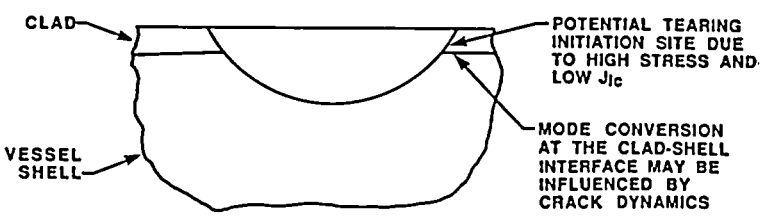

(b) NEGATIVE CLAD POTENTIAL

Fig. 16. Illustration of the potential role of cladding in (a) reducing the crack tip stress-intensity factor for a submerged or tunneling crack and (b) acting as a trigger point for initiation of a tearing/cleavage fracture.

integrity would be derived from the cladding, and the associated toughened surface layer of vessel plate material, once a fast running cleavage crack had been initiated in the vessel wall.

Recently reported results on the fracture properties of irradiated cladding show the cladding to have low resistance to ductile tearing toughness (Ref. 11). A J_{Ic} curve for the irradiated cladding is shown superimposed on the curves for A533-B and LUSW material in Fig. 9. J_{Ic} properties of the cladding are seen to be similar to those of LUSW material.

Low ductile tearing toughness in irradiated cladding raises the issue of cladding as the potential site for tearing initiation of a propagating flaw. The flaw configuration of concern in connection with cladding initiated tearing is illustrated in Fig. 16b. Tearing in the cladding itself would be of little importance since the mechanical contribution of the cladding to the overall pressure vessel wall strength is negligible. The concern for tearing initiating in the cladding is associated with the possibility of initiating a fast running crack in the vessel wall material once the tearing fracture in the cladding reaches the clad-vessel interface. Beam bending tests on irradiated specimens of clad A533-B have shown that ductile tearing of the cladding at both in-clad and through-clad flaws can convert to cleavage fracture once the crack front reaches the reactor vessel structural material (Ref. 23). Additional testing will be required to fully characterize the tearing and mixed mode crack propagation behavior under the 1 : 1 stress ratio conditions produced by the thermal stress element of the PTS transient.

It is evident from the discussion above that the issues associated with cladding are such that it is not possible to predict at this time if their resolution will have a net positive or negative impact on pressure vessel fracture prevention margins and failure probabilities.

4.6 Ring Forged Vessels

Ring forged construction eliminates the longitudinal welds in a reactor pressure vessel and thereby eliminates the welds with the highest pressure induced stresses which have been the primary focus of attention in the development of pressure vessel fracture prevention technology as it exists today. These vessels must however be analyzed to demonstrate compliance with the fracture prevention Requirements of Ref. 1. Issues arise relative to the applicability of fracture prevention technology developed for longitudinal welds for application to circumferential welds. Of particular concern are the assumptions and boundary conditions built into the technology to give a conservative evaluation of longitudinal welds. These same assumptions and boundary conditions may not necessarily give a conservative result when applied to circumferential welds. The need for early resolution of these issues is accentuated by the fact that 4 out of the 5 reactor vessels which currently violate the minimum Charpy upper-shelf requirement of Ref. 1 are of ring forged construction (Ref. 13).

A primary concern is the applicability of ductile tearing toughness data generated under conditions of plane strain constraint, for application to conditions where the plane strain boundary conditions no longer apply, and are in fact non conservative. Plane strain, as interpreted in fracture

toughness testing and analysis, translates to zero strain. Axial strains in a pressure vessel under internal pressure loading are close to zero. Fracture toughness data generated under conditions of plane strain constraint are thus directly applicable to the fracture analysis of longitudinal flaws under hoop stress dominated loading.

Loss of plane strain constraint results in a Poisson's Ratio induced contraction along the crack front and an associated increase in fracture toughness. In the case of a circumferential crack however the strains parallel to the crack front produced by the pressure induced hoop loading are positive. This condition is illustrated in Fig. 17. Since a negative strain parallel to the crack front has been demonstrated to be associated with an increase in fracture toughness it appears reasonable to suppose that a positive strain parallel to the crack front may be associated with a decrease in fracture toughness.

Data required to resolve the issue of ductile tearing toughness in the presence of a positive strain parallel to the crack front are not currently available, due in large measure to the difficulty of performing the large scale biaxial fracture toughness tests required for their generation. Current investigations of this issue are focused on analysis of existing fracture toughness data obtained under conditions of varying degrees of plane strain constraint. The objective of this work is to identify a reliable stress state and/or strain state parameter for correlation with the fracture toughness data. Once the required correlation parameter is identified and verified the plan is to use it to extrapolate trends from the existing fracture toughness data base. If this extrapolation indicates a reduced fracture toughness for conditions with a positive strain parallel to the crack

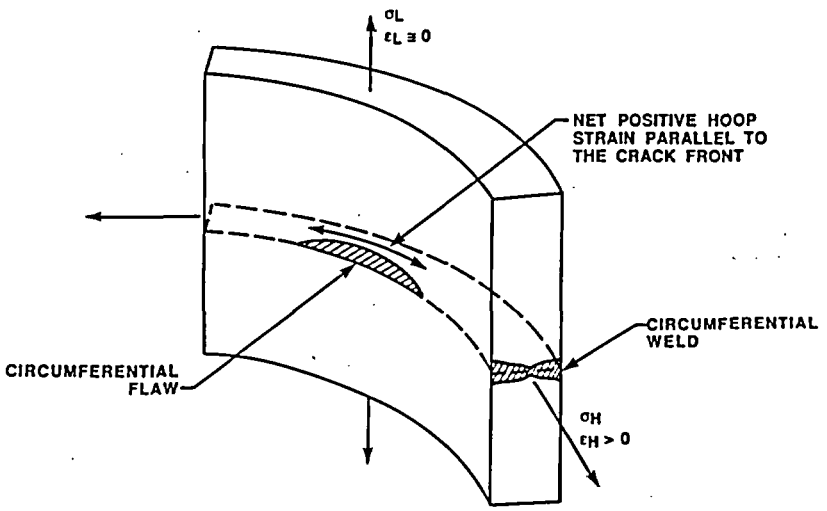

Fig. 17. Configuration of a circumferential flaw in the weld of a ring-forged reactor vessel showing positive tensile hoop strains parallel to the crack front.

front, consideration will be given to performing some large scale exploratory fracture toughness tests under biaxial loading conditions representative of those encountered in the circumferential welds of pressure vessels.

The foregoing discussion of stress/strain state effects on fracture toughness was focused on the ductile tearing behavior of the material where the connection between stress state and the strains at fracture is well established (Ref. 19). Consideration must be given however to the possible impact of these same parameters on the cleavage fracture behavior of the material.

An assumption incorporated into models used for the PTS analysis of axial flaws is that of a uniform distribution of fully mixed coolant in the reactor vessel downcomer annulus. This is an acceptable assumption in the case of an axial flaw since it tends to produce the maximum calculated thermal strains in the hoop direction and also permits the use of a simplified thermal stress analysis model. These same simplifying assumptions however are not acceptable for the PTS analysis of circumferential cracks since they tend to produce a non conservative result. Specifically, the additional constraint to axial thermal expansion produced when the incoming cool fluid flow is confined to a plume below the inlet nozzle, must be incorporated into the analysis. The coolant flow pattern of concern is illustrated in Fig. 18.

Large scale thermal transient tests have been performed in Germany using the HDR reactor vessel as a test article. Test objectives were to

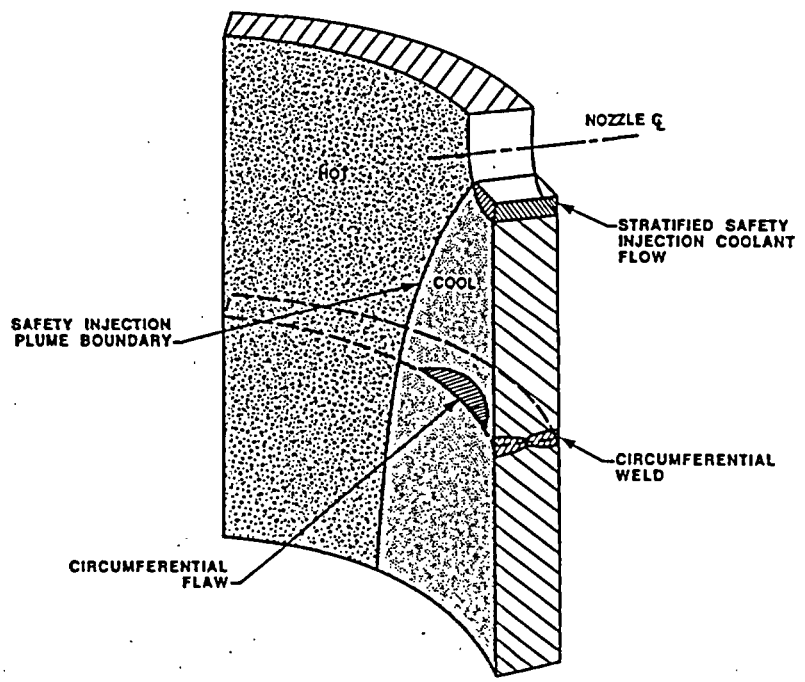

Fig. 18. Idealized representation of potential coolant flow stratification and streaming effects during a safety injection transient.

determine the profile of the downcomer plume during a simulated safety injection transient and measure the associated strain distribution in the reactor vessel. Results recently reported from these tests (Ref. 24) indicate a pronounced cold plume effect with associated axial thermal strains considerably greater than those generated in the hoop direction. These test results reinforce the need for a refined treatment of thermal-hydraulic boundary conditions in the PTS analysis of cracks in circumferential welds.

5. Conclusions

Large scale fracture mechanics tests and irradiation tests have resulted in the identification of a number of issues relating to the adequacy of the existing technology in use to assure fracture prevention in nuclear pressure vessels. Analysis performance discrepancies encountered in the application of the technology used to predict ductile tearing behavior makes this an area of particular concern. Development tasks aimed at resolving these issues are in progress within the HSST and HSSI programs at ORNL, in companion NRC funded programs within the USA and in a number of foreign national and international programs. Timely resolution of the fracture technology issues is required to support near term regulatory actions relating to operating nuclear power plants which have violated, or are close to violating, the irradiation damage limits set in *10 CFR 50* to provide protection against fracture of the reactor pressure vessel. Additional impetus for the resolution of these issues derives from the need to provide support for upcoming regulatory action on plant life extension applications.

Acknowledgments

The author wishes to acknowledge contributions made by B. R. Bass, R. D. Cheverton, W. R. Corwin, F. M. Haggag, J. G. Merkle, C. E. Pugh, R. K. Nanstad and D. J. Naus (numerous discussions of fracture issues and test data), T. L. Dickson (OCA-P analysis), J. R. Gordon of the Edison Welding Institute and Professor S. J. Rolfe of the University of Kansas (CTOD test data and background discussions) and M. E. Mayfield (HSST Program Monitor) and C. Z. Serpan (Chief, Materials Engineering Branch) of the NRC for suggesting and supporting this review of fracture issues.

6. References

Ref. No.	Title
1	Code of Federal Regulations, Title 10, Part 50, Section 50.61 and Appendix G
2	The American Society of Mechanical Engineers, Boiler and Pressure Vessel Code, Section III, Nuclear Power Plant Components — Division 1, Appendix G — Protection Against Non Ductile Failure, 1986 Edition

3 The American Society of Mechanical Engineers, Boiler and Pressure Vessel Code, Section XI, Rules for Inservice Inspection of Nuclear Power Plant Components, Appendix A – Analysis of Flaws, 1986 Edition

4 Radiation Embrittlement of Reactor Vessel Materials, Regulatory Guide 1.99 (Rev. 2), U.S. Nuclear Regulatory Commission, Washington, DC, May 1988

5 Format and Content of Plant-Specific Pressurized Thermal Shock Safety Analysis Reports for Pressurized Water Reactors, Regulatory Guide 1.154 U.S. Nuclear Regulatory Commission, Washington, DC, January 1987

6 R. H. Bryan et al., Pressurized-Thermal Shock Test of 6-in Thick Pressure Vessels. PTSE-2: Investigation of Low Tearing Resistance and Warm Prestressing, NUREG/CR-4888 (ORNL-6377), December 1987

7 D. J. Naus et al., SEN Wide-Plate Crack-Arrest Tests Using A 533 Grade B Class 1 Material: WP-CE Test Series, NUREG/CR-5408 (ORNL/TM-11269), to be published in 1989.

8 William A. Soren, The effect of specimen size and crack depth on the elastic-plastic fracture toughness of a low-strength high-strain hardening steel. Phd dissertation, University of Kansas, May 1989. Research sponsored by the Pressure Vessel Research Committee and the American Iron and Steel Institute.

9 J. J. McGowan et al., Characterization of Irradiated Current-Practice Welds and A533 Grade B Class 1 Plate for Nuclear Pressure Vessel Service, NUREG/CR-4880 (ORNL-6484/V1 & V2), July 1988

10 A. L. Hiser et al., J-R Curve Characterization of Irradiated Low Upper Shelf Welds, NUREG/CR-3506 (MEA-2028), April 1984

11 F. M. Haggag et al., Effects of Irradiation on the Fracture Properties of Stainless Steel Weld Overlay Cladding, SMIRT Power Conference Seminar Number 2, Monterey, California, August 21-22, 1989

12 Enclosure 3, Regulatory Analysis, Revision 2 to Regulatory Guide 1.99, Radiation Embrittlement of Reactor Vessel Materials, November 1987, Available from the U.S. Nuclear Regulatory Commission public document room, Washington, DC

13 Minutes of the Advisory Committee on Reactor Safeguards (ACRS) Subcommittee on Materials and Metallurgy Meeting at Bethesda, Maryland, June 20, 1989

14 R. D. Cheverton and D. G. Ball, OCA-P, A Deterministic and Probabilistic Fracture-Mechanics Code for Application to Pressure Vessels, NUREG/CR-3618 (ORNL-5991), May 1984

15 J. G. Merkle, An Examination of the Size Effects and Data Scatter Observed in Small-Specimen Cleavage Fracture Toughness Testing, NUREG/CR-3672 (ORNL/TM-9088), April 1984

16 S. T. Rolfe and J. M. Barsom, Fracture and Fatigue Control in Structures: Applications of Fracture Mechanics, Prentice-Hall Inc., Englewood, New Jersey. 1977

17 Standard Test Method for Determining J-R Curves, ASTM E1152, Annual Book of ASTM Standards, Volume 03.01, July 1989.

18 D. J. Lacey and R. E. Leckenby, Determination of Upper Shelf Fracture Resistance in the Spinning Cylinder Test Facility, Transactions of the 10th International Conference on Structural Mechanics in Reactor Technology, Volume F, LWR Pressure Components, June 1989

19 B. F. Langer, Applied Mechanics in the Nuclear Industry: Applications of Stress Analysis, Westinghouse Electric Corporation Scientific Paper 67-1DO-CODES-P1

20 H. Kordisch, E. Sommer and W. Schmitt, The Influence of Triaxiality on Stable Crack Growth, Fraunhofer-Institute Fur Werkstoffmechanic (IWM), Freiburg, Fed. Rep. Germany, Nuclear Engineering and Design, 112 (1989) 27-35

21 R. D. Cheverton and D. G. Ball, "Chapter 5, Probabilistic Fracture Mechanics Analysis of Potential Overcooling Sequences for H. B. Robinson Unit 2." pp. 263-306 in Pressurized Thermal Shock Evaluation of the H. B. Robinson Nuclear Power Plant, NUREG/CR-4183, Vol. 1 (ORNL/TM-9567/VI), Martin Marietta Energy Systems Inc., Oak Ridge National Lab. (September 1985)

22 S. K. Iskander, G. C. Robinson and C. B. Oland, Flaw Behavior in Mechanically Loaded Clad Plates, Oak Ridge National Laboratory, Proceedings of the SMIRT Power Conference No. 2, Monterey, California, August 21-22, 1989

23 D. E. McCabe, Fracture Resistance of Irradiated Stainless Steel Clad Vessels, MEA-2260 Materials Engineering Associates Inc., 9700-B Martin Luther King Jr. Highway, Lanham, MD 20706-1837, Proceedings of the U.S. Nuclear Regulatory Commission Fifteenth Water Reactor Safety Meeting, Volume 2, October 26-29, 1987.

24 H. Kordisch et al., Analysis of the Initiation and Growth of a Circumferential Crack in the HDR-RPV-Cylinder Under Pressurized Thermal Shock, Fh-IWM, Freiburg, FR Germany, VTT, Helsinki, Finland and KfK/PHDR, Karlsruhe, FR Germany: SMIRT-10, Post Conference Seminar No. 2, Monterey, California, August 21-22, 1989.

Heavy-Section Steel Irradiation Program Summary*

W. R. Corwin, R. K. Nanstad, S. K. Iskander, and F. M. Haggag

Oak Ridge National Laboratory
Oak Ridge, Tennessee 37831

ABSTRACT

In light-water-cooled nuclear power plants, a steel reactor pressure vessel (RPV) forms the primary containment boundary for the nuclear fuel assembly. Since a failure of the RPV carries the potential of major contamination release and severe accident, it is imperative to safe reactor operation to understand and be able to accurately predict realistic failure models of the vessel material. A major known risk arises from irradiation-induced degradation of the RPV fracture resistance which occurs as a result of normally occurring neutron flux during the service life of the reactor. Better understanding of the irradiation degradation of the vessel material will provide better input to improve the engineering models vital for prediction of RPV integrity and safe service life.

For this reason, the Heavy-Section Steel Irradiation (HSSI) Program has been established with its primary goal to provide a thorough, quantitative assessment of the effects of neutron irradiation on the material behavior, and in particular the fracture toughness properties, of typical pressure vessel steels as they relate to light-water RPVs. The program includes the direct continuation of irradiation studies previously conducted within the Heavy-Section Steel Technology Program augmented by enhanced examinations of the accompanying microstructural changes. Effects of specimen size, material chemistry, product form and microstructure, irradiation fluence, flux, temperature and spectrum, and postirradiation annealing are being examined on a wide range of fracture properties including fracture toughness (K_{Ic} and J_{Ic}), crack-arrest toughness (K_{Ia}), ductile tearing resistance (dJ/da), Charpy V-notch impact energy, dropweight nil-ductility temperature (NDT), and tensile properties. Models based on observations of radiation-induced microstructural changes using field ion and high-resolution transmission electron microscopy provide a firmer basis for extrapolating the measured changes in fracture properties to wider ranges of irradiation conditions. The principal materials examined within the HSSI Program are high-copper welds since their postirradiation properties are most frequently limiting in the continued safe operation of commercial RPVs. In addition,

a limited effort will focus on stainless steel weld overlay cladding, typical of that used on the inner surface of RPVs, since its postirradiation fracture properties have the potential for strongly affecting the extension of small surface flaws during overcooling transients.

Results from the HSSI studies will be integrated to aid in resolving major regulatory issues facing the U.S. Nuclear Regulatory Commission which involve RPV irradiation embrittlement such as pressurized-thermal shock, operating pressure-temperature limits, low-temperature overpressurization, and the specialized problems associated with low upper-shelf welds. Taken together the results of these studies also provide guidance and bases for evaluating both the aging behavior and the potential for plant life extension of light-water RPVs.

---

*Research sponsored by the Office of Nuclear Regulatory Research, U.S. Nuclear Regulatory Commission under Interagency Agreement DOE 1886-8109-8L with the U.S. Department of Energy under Contract DE-AC05-84OR21400 with Martin Marietta Energy Systems, Inc.

INTRODUCTION

The degrading effects of neutron irradiation on carbon and low-alloy pressure vessel steels have been recognized and investigated since the early 1950s. In those steels at light-water-reactor (LWR) operating temperature (288°C), radiation damage is produced when neutrons of sufficient energy displace atoms from their lattice sites. The defects formed in the steel as a result of those displacements typically cause hardening and a decrease in toughness. Tensile behavior exhibits an increase in yield strength, a decrease in the ultimate to yield strength ratio, and a loss of ductility as measured by specimen elongation. The decrease in toughness is most commonly represented by an increase in the ductile-brittle transition temperature and a decrease of the ductile shelf energy as measured by the Charpy V-notch (CVN) impact test.

While it was soon recognized that the effects of irradiation could degrade pressure vessel materials, definitive effects on their fracture properties, especially in thick sections, were not available. Therefore, when the Heavy-Section Steel Technology (HSST) Program was initiated in 1967, irradiation effects was designated as one of the major topics of investigation. Over the past two decades much information on irradiation effects on fracture in thick sections has been developed within the HSST Program.[1] In 1989, the U.S. Nuclear Regulatory Commission (NRC) decided to transfer all irradiation effects studies from the HSST Program into a new but separate companion program, the Heavy-Section Steel Irradiation (HSSI) Program. The HSSI Program includes the direct continuation of all irradiation studies previously planned or conducted within the HSST program augmented by enhanced examinations of the accompanying microstructural changes. To minimize confusion, all nomenclature including irradiation series numbering used previously within the HSST Program has been adopted within the HSSI Program.

Title 10, Part 50 of the Code of Federal Regulations[2] (10CFR50) includes requirements for fracture toughness of reactor pressure vessels. Those requirements include surveillance testing; CVN specimens are required, tensile specimens are recommended, and fracture toughness specimens are required if the surveillance materials are predicted to exhibit marginal properties. Furthermore, 10CFR50 requires prediction of radiation effects using *Regulatory Guide 1.99* (Rev. 2)[3] and, if those predictions indicate unacceptable end-of-life toughness, the vessel must be designed to accommodate thermal annealing. Additionally, criteria are specified for toughness transition temperatures which, if attained by the surveillance tests, require plant-specific analyses to demonstrate adequate protection against pressurized thermal shock. As part of those requirements, 10CFR50 refers to the *ASME Boiler and Pressure Vessel Code*, Sections III and XI,[4] for fracture toughness requirements and ASTM Standard E 185 for surveillance testing and analysis as well as application of the test results. The irradiation investigations within the HSSI Program address and

provide support for validating and, if needed, revising virtually all of the above regulations. This paper summarizes the current and planned irradiation investigations which compose the HSSI Program.

Results from the HSSI studies will be integrated to aid in resolving major regulatory issues the U.S. Nuclear Regulatory Commission has recognized as high priority[5] which involve reactor pressure vessel (RPV) irradiation embrittlement such as pressurized-thermal shock, operating pressure-temperature limits, low-temperature overpressurization, postirradiation annealing, and the specialized problems associated with low upper-shelf welds. Taken together the results of these studies also provide guidance and bases for evaluating both the aging behavior and the potential for plant life extension of LWR pressure vessels.

PROGRAM SCOPE

The principal focus of the HSSI Program is irradiation effects in high-copper weld metal since the postirradiation properties of these materials are most frequently limiting in the continued safe operation of commercial RPVs. In addition, a limited effort will focus on stainless steel weld overlay cladding, typical of that used on the inner surface of RPVs, since its postirradiation fracture properties have the potential for strongly affecting the extension of small surface flaws during overcooling transients.

The current investigations of high-copper weldments fall into two major categories: first, the amount of the irradiation-induced shifts and any accompanying changes in shape of both the ASME K_{Ic} and K_{Ia} curves in welds which maintain relatively high resistance to ductile fracture, and second, the determination of the overall degree of post-irradiation embrittlement for low upper-shelf (LUS) welds in which the resistance to ductile tearing falls to particularly low levels following irradiation. The Fifth and Sixth Irradiation Series, addressing the shifts in the K_{Ic} and K_{Ia} curves, respectively, are both examining two identical high-copper, high upper-shelf weldments. The results of the Fifth Series, which is virtually complete, have shown that the shape of the irradiated K_{Ic} curve can change such that its actual shift is slightly greater than that predicted by small specimens. Ongoing testing of the irradiated crack-arrest specimens from the Sixth Series, exposed under the same conditions as the fracture toughness specimens in the Fifth, will be completed this year. Preliminary results have shown the shift in the irradiated K_{Ia} curve to be about the same as that obtained with small specimens.

The Tenth Irradiation Series will begin an extensive evaluation of irradiation-induced embrittlement in LUS welds by examining the beltline fabrication weld from the Midland Unit No. 1 RPV which was abandoned prior to start-up. The submerged-arc weld is typical of many LUS welds actually in service. The series will include an

extensive initial characterization of chemistry and fracture properties in the unirradiated condition and a full range of postirradiation fracture tests on specimens up to 102 mm (4 in.) thick in both the transition and upper-shelf regimes, including an assessment of irradiation-rate and saturation effects. Further examinations of LUS material are planned for subsequent irradiation series including detailed evaluations of the shifts in their K_{Ic} and K_{Ia} curves (Series 8) and the degree of recovery and rate of re-embrittlement of their fracture toughness following postirradiation annealing (Series 9).

Two new initiatives have been included within the HSSI Program to provide better support and utilization of the results from the major irradiation experiments. The first of these is an effort to produce a physically based model of irradiation damage to allow more accurate interpolations and extrapolations of existing data to be made. Initial efforts will center on LUS weld metal and utilize the atom probe field ion microscope for examination of irradiation-induced defects in irradiated LUS welds. The second initiative is the expansion of existing hot cell facilities to provide a cost-effective fabrication and evaluation unit capable of machining and examining test specimens of activated material which has been irradiated during actual service. The testing of such in-service aged material will further augment available information concerning effects of irradiation spectrum and rate on fracture properties.

ONGOING IRRADIATIONS OF HIGH-COPPER WELDS

SERIES 5, K_{Ic} CURVE SHIFT AND SHAPE

The primary objective of Series 5 is to validate the temperature shift and shape of the ASME Code Section XI K_{Ic} curve for irradiated reactor vessel materials. Appendix G of 10CFR50 requires determination of the unirradiated RT_{NDT} using CVN and drop-weight (DWT) specimens as specified in Section III of the ASME Code. Appendix A of Section XI contains the K_{Ic} curve which is normalized on the temperature scale to the RT_{NDT}. For determination of the adjusted RT_{NDT}, 10CFR50 refers to ASTM E 185 which specifies the method for using surveillance test results. Standard E 185 specifies that a minimum of 12 CVN specimens be used to obtain a "full" Charpy energy vs test temperature curve and to determine the transition temperature shift at an energy value of 41 J (30 ft-lb) using the average curve fits to both the unirradiated and irradiated results. The 41-J shift is then added to the unirradiated RT_{NDT} to obtain the adjusted RT_{NDT}. Thus, the K_{Ic} curve for irradiated material would simply be shifted to higher temperatures by an amount equal to the CVN 41-J shift. The implicit assumptions in this procedure are that: (1) the CVN 41-J temperature shift represents the RT_{NDT} shift, (2) the K_{Ic} shift is the same as the CVN

shift, and (3) the shape of the K_{Ic} curve does not change for irradiated materials. Furthermore, E 185 does not contain any distribution requirements (in terms of test temperature) for testing of the CVN surveillance specimens, nor does it discuss statistical variation in test results.

Series 5 was conceived to verify the postirradiation K_{Ic} curve to as high a fracture toughness level as practicable. Additionally, a comparison of the K_{Ic}, CVN, and DWT NDT shifts are supporting objectives within a framework of multiple tests for statistical analyses. The test materials are two submerged-arc welds with relatively high but different copper contents. The weld wire was specially produced with copper in the melt to minimize copper variability in the fabricated welds. The welds were fabricated by Combustion Engineering, Inc., in 216-mm-thick (8.5-in.) plate using Linde 124 welding flux. Table 1 gives the chemical composition of the two welds, designated HSSI 72W and 73W, and shows they have virtually identical composition except for copper contents of 0.23 and 0.31 wt %, respectively. About 14 lin m of each weldment were fabricated in approximately 1.3-m (4-ft) lengths and postweld heat treated at 621°C for 40 h. The largest specimens utilized, 4TCS in the irradiated conditions and 8TCS in the unirradiated condition were both expected to allow maximum valid Klc values (according to ASTM Standard E 399) of about 130 MPa $\sqrt{m}$, given the yield strength of the materials and their expected increase due to irradiation.

Table 1. Chemical compositions of the two submerged-arc welds in HSSI Irradiation Series 5.

	Composition, wt %									
Material	C	Mn	P	S	Si	Cr	Ni	Mo	Cu	V
72W	0.093	1.60	0.006	0.006	0.44	0.27	0.60	0.58	0.23	0.003
73W	0.098	1.56	0.005	0.005	0.45	0.25	0.60	0.58	0.31	0.003

The irradiations were conducted at the poolside facility of the Oak Ridge Research Reactor (ORR) from May 1984 to December 1985. Irradiation temperatures were controlled at 288°C and the target neutron fluence (>1 MeV) was 1.75×10^{19} neutrons/cm^2. The temperature control was excellent considering the large numbers of specimens contained in the small specimen capsules. Greater than 90% of the CVN, tensile, and 1TCS were 288 ± 9°C, while the 4TCS were 288 ± 4°C. The tensile, CVN, and compact specimens show an average fluence of about 1.5×10^{19} neutrons/cm^2 (>1 MeV). Two groups of DWT specimens were used and designated primary and scoping. The scoping groups had an average irradiation temperature and fluence of about 276°C and 1.5×10^{19} neutrons/cm^2, respectively. The primary

groups had averages of 291°C and 1.0 x 10^{19} neutrons/cm^2, respectively. The primary groups were so designated because they were irradiated at about the target temperature. Due to placement in the capsules, however, they received less exposure than the CVN specimens and fluence adjustments are discussed later. Dosimetry, neutronics, etc., are discussed in refs. 6, 7, and 8.

The effects of irradiation on yield and ultimate tensile strength resulted in the yield strength increases ranging from about 22 to 32%, depending on test temperature. Weld 73W experienced greater strengthening, as expected, due to its higher copper concentration. Figures 1 and 2 show the CVN energy results for welds 72W and 73W, respectively. The 41-J transition temperature shifts were 72 and 82°C, respectively, and, again, reflect the difference in copper contents. The shifts were determined using hyperbolic tangent curve fits to the data for each weld. The results of CVN and DWT testing are summarized in Table 2. The actual 41-J shifts for both welds were substantially less than the predictions of *Regulatory Guide 1.99* (Rev. 2) and a model developed by Materials Properties Council Subcommittee 6.[9] It is also noted that the 68-J (50 ft-lb) shifts for the two welds show greater difference than do the 41-J shifts; this will be discussed later. The primary group of DWT specimens showed somewhat lesser NDT shifts but, as mentioned earlier, the fluence of those specimens was much less than that of the CVN specimens. The scoping group of DWT specimens showed greater shifts than those of the primary group, but a comparison is difficult because the fluences and, especially, irradiation temperatures are significantly different. Table 3 shows the results of applying a linear adjustment scheme to the primary DWT data. The adjustment is made by normalizing the actual observations to the *Regulatory Guide 1.99* predictions and accounting for the fluence differences by assuming a linear material sensitivity to irradiation over the relatively small fluence range from 1.0 to 1.51 x 10^{19} neutrons/cm^2. As shown in the table, the adjusted NDT shifts of 69 and 80°C are very close to the observed CVN shifts of 72 and 82°C for welds 72W and 73W, respectively. Thus, the conclusion from these tests is that the CVN 41-J shifts represent the DWT NDT shifts for these materials. This conclusion is in agreement with results shown previously by experiments at the Naval Research Laboratory.[10]

The fracture toughness results for unirradiated and irradiated specimens are summarized in Figures 3 and 4. All of the K_{JC} values shown were calculated from the J-integral value at the onset of cleavage as previously described.[1] The unirradiated data are depicted by range bars and the irradiated K_{IC} curves were constructed by shifting the unirradiated curves upward in temperature according to the CVN 41-J shifts as specified by E 185. Both figures note "pop-in" values which represent cleavage events which occurred but did not fracture the specimen. The two results

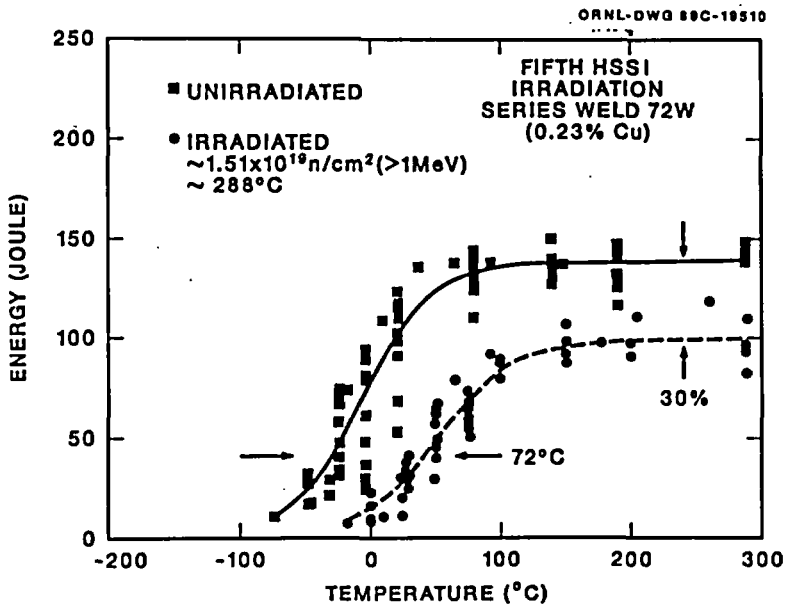

Fig. 1. Charpy impact energy vs test temperature for HSSI weld 72W before and after irradiation at ~288°C to an average fluence (>1 MeV) of 1.75 x 10^{19} neutrons/cm^2. The slope of the curve appears to have changed only slightly as a consequence of irradiation.

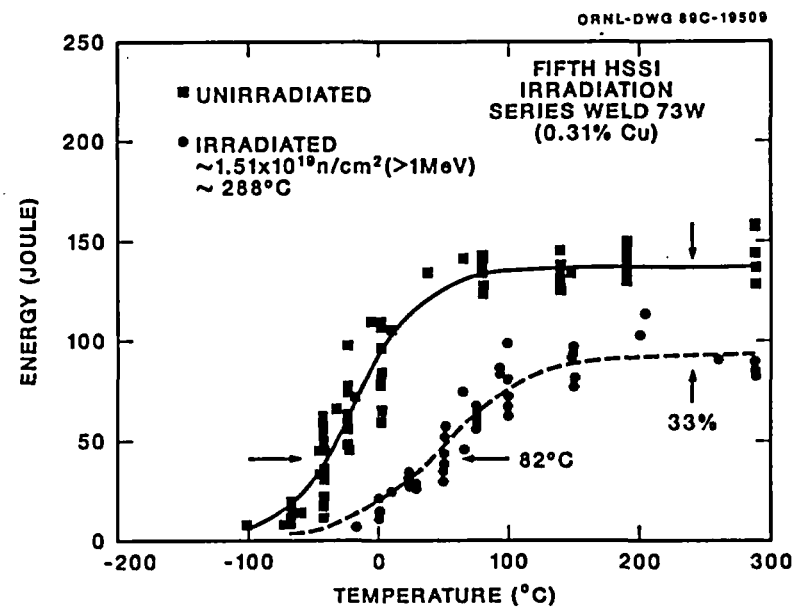

Fig. 2. Charpy impact energy vs test temperature for HSSI weld 73W before and after irradiation at ~288°C to an average fluence (>1 MeV) of 1.75 x 10^{19} neutrons/cm^2. The slope of the curve has substantially decreased after irradiation compared to that for weld 72W.

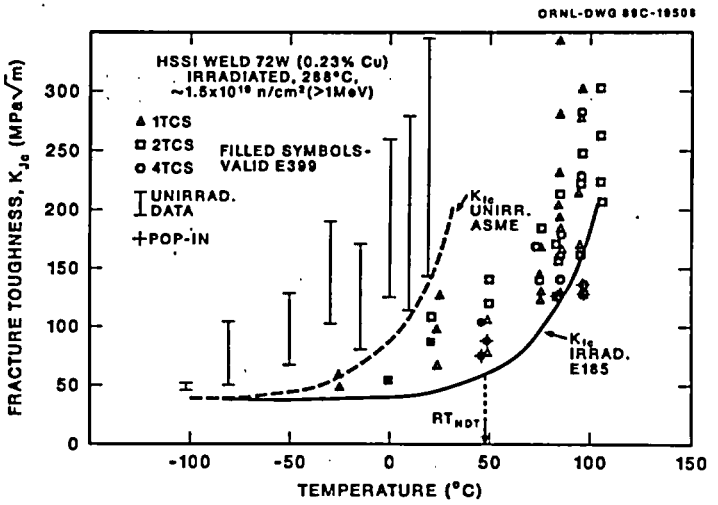

Fig. 3. Fracture toughness, K_{JC}, vs test temperature for HSSI weld 72W irradiated at ~288°C to an average fluence (>1 MeV) of 1.5 x 10^{19} neutrons/cm^2. The K_{IC} curve has been shifted 72°C, equal to the Charpy 41-J shift, as required by ASTM E 185. Two K_{JC} values determined at the onset of cleavage pop-ins lie below the shifted curve.

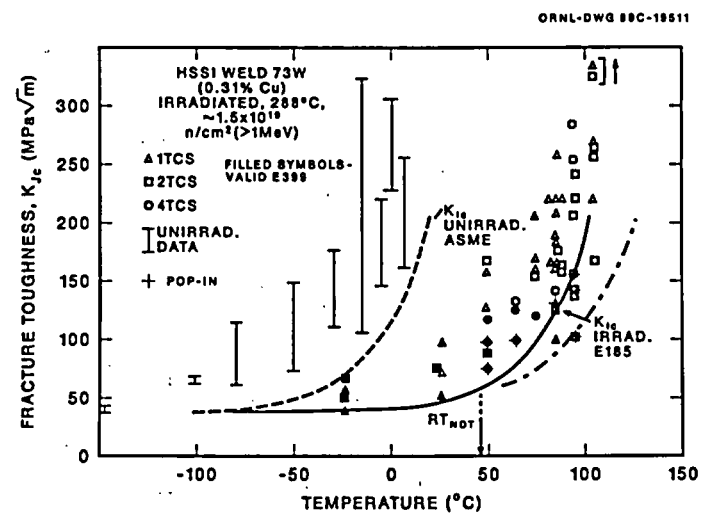

Fig. 4. Fracture toughness, K_{JC}, vs test temperature for HSSI weld 73W irradiated at ~288°C to an average fluence (>1 MeV) of 1.5 x 10^{19} neutrons/cm^2. The K_{IC} curve has been shifted 82°C, equal to the Charpy 41-J shift, as required by ASTM E 185. Five K_{JC} values lie below the curve, three results which fractured the specimens and two values determined at the onset of cleavage pop-ins. The dashed line drawn to the right of the K_{IC} curve was constructed as a preliminary lower bound curve to the irradiated data and indicates a change in the shape of the curve.

Table 2. Effects of irradiation on Charpy V-notch and drop-weight transition temperatures for welds 72W and 73W.

Charpy transition temperature shift (°C)					Drop-weight NDT[a] temperature shift (°C)			
41 J					Primary[b]		Scoping[c]	
Actual	MPC-6[d]	Draft RG 1.99 Rev. 2[e]	0.89 mm	Fracture appearance	Actual	Draft RG 1.99 Rev. 2[e]	Actual	Draft RG 1.99 Rev. 2[e]
Weld 72W, 0.23% Cu, 0.60% Ni								
72	90	105	92	59	61	93	72	105
Weld 73W, 0.31% Cu, 0.60% Ni								
82	123	123	115	70	72	110	94	123

[a] Nil-ductility temperature.
[b] Average irradiation temperature of 291°C, fluence (>1 MeV) = 1 x 10^{19} neutrons/cm^2.
[c] Average irradiation temperature of 275°C, fluence (>1 MeV) = 1.5 x 10^{19} neutrons/cm^2.
[d] Materials Properties Council Subcommittee 6 on Nuclear Materials.
[e] *Regulatory Guide 1.99* (Rev. 2).

Table 3. Charpy impact ΔTT_{41} and drop-weight ΔNDT for HSSI Irradiation Series 5 Welds after adjusting for fluence differences.

Charpy impact			Drop-weight				
Fluence	TT_{41} (°C)	Draft RG 1.99 Rev. 2[b] (°C)	Actual fluence (n/cm^2)	Actual ΔNDT (°C)	Draft RG 1.99 Rev. 2[b] (°C)	Adjusted fluence (n/cm^2)	Adjusted ΔNDT (°C)
Weld 72W, 0.23% Cu, 0.60% Ni							
1.51 x 10^{19}	72	105	1.0 x 10^{19}	61	93	1.51 x 10^{19}	69
Weld 73W, 0.31% Cu, 0.60% Ni							
1.51 x 10^{19}	82	123	1.0 x 10^{19}	72	110	1.51 x 10^{19}	80

[a] Weld 73W adjustment: RG 1.99 (1.51 - 1.0) = 13°C
(72/110) x 13 = 8°C
72 + 8 = 80°C
Adjusted ΔNDT = 80°C
[b] *Regulatory Guide 1.99* (Rev. 2).

which fall below the K_{Ic} curve for 72W are both pop-ins, while the five results which fall below the curve for 73W are represented by two pop-ins and three specimen failures. As with the unirradiated results, the large specimens (4TCS) do not always define the lowest results at a given test temperature. The shift of the lower-bound K_{Ic} curve for weld 72W is similar to that of the CVN 41-J shift, but that for weld 73W appears to be substantially greater than the CVN shift. For this purpose, a K_{Ic} value of 125 MPa $\sqrt{m}$ was chosen for the comparison and the shift was determined to be about 101°C for weld 73W. That compares to a CVN 41-J shift of 82°C and, interestingly, a CVN 68-J shift of 104°C. The better comparison with the 68-J shift is reflective of the previously noted shape change of the CVN curve for the irradiated weld 73W.

It is clear that the interpretation of the significance of cleavage pop-ins to conclusions regarding the shift and shape of the postirradiation K_{Ic} curve is crucial. Various schemes for such an interpretation have been discussed within the technical community and are being applied to these results. In that context, it is noted that a total of about 12 pop-ins were observed in the irradiated tests while only one was observed in the unirradiated tests. Thus, an investigation of such a preponderance of pop-ins in the irradiated condition is certainly warranted. It is also clear that a reasonable construction of postirradiation curves will involve the use of fracture toughness data outside the range of linear elastic fracture mechanics as defined by ASTM E 399. The use of fracture toughness data determined by elastic-plastic fracture mechanics techniques in the transition temperature region will involve consideration of specimen size effects, stable ductile tearing preceding cleavage, and statistical analyses such as the Weibull method.

The preliminary observations from Series 5 are summarized as follows:

1. The scatter in fracture toughness and CVN results is large; statistical analyses and elastic-plastic fracture mechanics are required for interpretation.

2. The irradiated CVN shifts are about the same as the DWT NDT temperature shifts.

3. The lower-bound K_{Ic} (at 125 MPa $\sqrt{m}$) curve shift for weld 73W is greater than that of the CVN 41-J shift, about 101°C compared to 82°C. It is similar, however, to the CVN 68-J shift of 104°C.

4. The shape of the lower-bound K_{Ic} curve changed for weld 73W, but the change is similar to that for the CVN curve.

5. The evaluation of cleavage pop-ins is significant to conclusions regarding the K_{Ic} curve shift and shape.

SERIES 6, K_{Ia} CURVE SHIFT AND SHAPE

The primary objective of Series 6 is to validate the temperature shift and shape of the ASME Section XI crack-arrest toughness, K_{Ia}, curve for irradiated reactor vessel materials. Because the K_{Ia} curve also describes the reference fracture toughness K_{IR} curve in Section III of the ASME Code, Series 6 is directly applicable to the shift and shape of the K_{IR} curve. The available data base for crack-arrest toughness of RPVs is very limited compared to that for initiation fracture toughness. Thus, an important supporting objective of Series 6 is to expand both the unirradiated and irradiated data bases for prototypic reactor vessel steels. The current known available data base for irradiated crack-arrest toughness consists of only 19 data points for base metal and 17 data points for weldments.

The materials for this series are the identical welds used for Series 5, 72W and 73W. The irradiations were conducted at the poolside facility of the ORR from December 1985 to May 1986 using the same capsule irradiation facilities and with the same target irradiation temperature and fluence as described for Series 5. Two capsules, each containing 30 crack-arrest specimens of various types, were irradiated. As was the case in the companion Series 5, the temperature control of the specimens was excellent. Irradiation temperatures of 75% of the specimens was 288°C ± 2°C with the remaining specimens irradiated at 283°C ± 3°C. The average and standard deviation for the specimen fluence were 1.8 and 0.3 x 10^{19} neutrons/cm^2 (>1 MeV), respectively.

The largest specimens used were 33 and 50 mm thick in the irradiated and unirradiated conditions, respectively. Given the current validity limits of ASTM standard E 1221 on crack-arrest testing, a 33-mm-thick compact crack-arrest (CCA) specimen (1.3TCCA) of 73W can measure a valid K_{Ia} value of about 150 MPa $\sqrt{m}$. In the unirradiated condition, a 2TCCA specimen is required to achieve the same measuring capacity. In addition to the standard CCA specimen which uses a starter notch located in a brittle weld material, duplex specimens are included in this series. The duplex specimen consists of a crack starter hole located in a section of hardened 4340 steel which has been electron beam welded to a section of the test material. For both types of specimens, the crack starter only serves to provide the driving force necessary to drive the crack well into the test material prior to arrest. The use of the duplex design allows tests to be conducted at higher temperatures than with weld-embrittled specimens of the same thickness. Thus, multiple tests are being performed at each of several temperatures within about 50°C below and above the RT_{NDT}. Weld-embrittled specimens are used primarily in the lower part of that range while duplex specimens would be primarily used at the higher temperatures.

Most of the unirradiated K_{Ia} specimens[11] and all of the irradiated weld-embrittled crack-arrest specimens have been tested for both welds. Figures 5 and 6 show those results for welds 72W and 73W relative to the ASME K_{Ia} curves which are

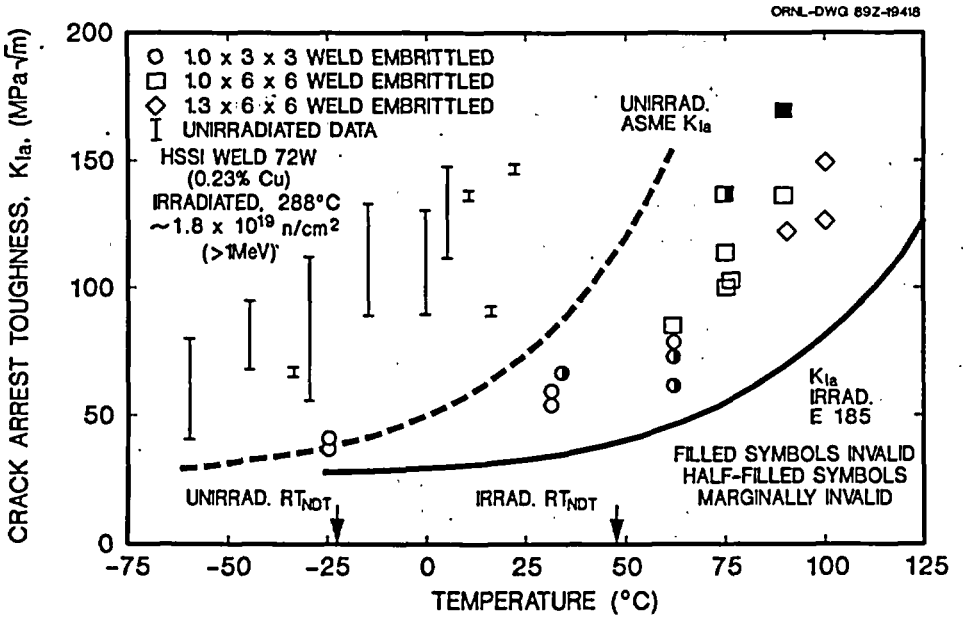

Fig. 5. Preliminary crack-arrest toughness, K_{Ia}, vs test temperature for HSSI weld 72W irradiated at ~288°C to an average fluence (>1 MeV) of 1.8 x 10^{19} neutrons/cm^2. The K_{Ia} curve has been shifted 72°C, equal to the Charpy 41-J shift, as required by ASTM E 185.

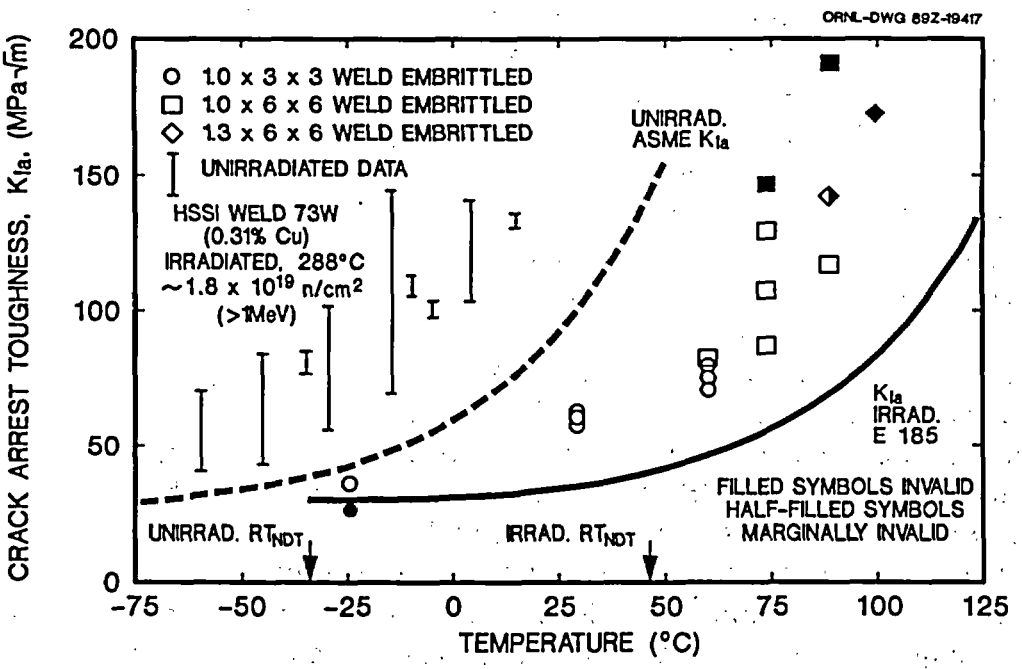

Fig. 6. Preliminary crack-arrest toughness, K_{Ia}, vs test temperature for HSSI weld 73W irradiated at ~288°C to an average fluence (>1 MeV) of 1.8 x 10^{19} neutrons/cm^2. The K_{Ia} curve has been shifted 82°C, equal to the Charpy 41-J shift, as required by ASTM E 185.

appropriately indexed to the correct unirradiated or irradiated RT_{NDT} values. Most of the test results are either strictly valid or only marginally invalid according to ASTM E 1221. While both data sets are incomplete and the individual results within them still preliminary, it appears that the shift in the crack-arrest toughness behavior is similar to the 41-J shift in the corresponding CVN impact curves. It is also interesting to note that the lowest K_{Ia} data lay further above the curve than do the corresponding K_{Ic} data above the K_{Ic} curve. Firm conclusions about the amount of shift and any changes in shape in the K_{Ia} curve must be reserved until the remaining specimens have been tested and all results thoroughly analyzed.

INVESTIGATIONS OF POSTIRRADIATION EMBRITTLEMENT IN LOW UPPER-SHELF WELDS

Seventeen U.S. reactors contain RPVs with potential LUS primary fabrication welds. All the LUS welds are in vessels fabricated by the Babcock and Wilcox Company using the submerged-arc welding process. The welds were all made using copper-coated welding wire and the Linde 80 welding flux and all suffer from the problem of a relatively low resistance to failure from ductile tearing. Their low tearing resistance stems primarily from the combination of a high concentration of fine inclusions associated with high oxygen levels in the weld metal in conjunction with enhanced radiation sensitivity due to the high copper contents. Current projections predict that the Charpy upper-shelf impact energy in 15 of the 17 reactor vessels containing these welds will drop below the 68-J regulatory limit before their scheduled end-of-life. Operators of plants with vessels containing steel with upper-shelf energy of less than 68-J must show adequate margins of safety for continued plant operation through detailed plant specific analysis or shutdown. To provide a better basis for the preparation and evaluation of such plant-specific analyses, in particular, and expand the data base on LUS welds in general, the HSSI Program will conduct three additional irradiation series which will exclusively address irradiation-induced degradation in LUS welds. Series 8 will address the shifts and changes in shape in the K_{Ic} and K_{Ia} curves in LUS materials in a fashion similar to that used in Series 5 and 6 to investigate high upper-shelf materials. Series 9 will examine effects of section size on the annealing and reirradiation response of LUS welds. Series 10 will extensively examine fracture behavior in both the upper shelf and ductile-to-brittle transition range of a commercially produced weld removed from an actual pressure vessel. Due to availability of material and the pressing need for results, Series 10 will be conducted first.

SERIES 10, IRRADIATION EFFECTS IN A COMMERCIAL LOW UPPER-SHELF WELD

The primary objective of Series 10 is to investigate the post-irradiation fracture toughness of the submerged-arc weld from the beltline region of the Midland Unit 1 reactor vessel. This PWR is owned by Consumers Power Company and was cancelled prior to start-up. The weld from that vessel is of considerable interest because it carries the Babcock and Wilcox designation WF-70, a submerged-arc weld fabricated with a specific heat of weld wire and specific lot of flux. Welds with the WF-70 designation are the controlling materials (regarding irradiation effects) in five operating nuclear plants. The WF-70 weld was fabricated using copper-coated wire and Linde 80 flux and is known to be a low upper-shelf, high-copper weld. The fact that this particular weld exists in numerous operating reactors is the primary motivation for this series. The material from the Midland reactor was initially considered for Series 8 for detailed determinations of K_{Ic} and K_{Ia}, but concerns about the copper variability resulted in its inclusion in a separate irradiation series. An important supporting objective is the determination of local and global copper variation. Another specific supporting objective is a complete unirradiated characterization to include determination of the RT_{NDT} and the CVN upper-shelf energy. Fracture toughness specimens will be used to examine size effects in J-R curve testing with this material. A long-term irradiation capsule will also be included to investigate irradiation rate effects.

The planning for Series 10 is virtually complete, and will include irradiation of CVN, tensile, DWT, crack-arrest, and fracture toughness specimens up to 4TCS. All those specimens would be irradiated at 288°C to a fluence of about 1×10^{19} neutrons/cm^2 (>1 MeV). Three scoping capsules containing CVN, tensile, and 0.5TCS will be irradiated to fluences of 5×10^{18}, 1×10^{19}, and 5×10^{19} neutrons/cm^2 (>1 MeV) to investigate irradiation saturation and provide information for irradiation of the primary capsules containing the larger specimens. Those irradiations will be performed under usual test reactor conditions. Additionally, a complement of tensile, CVN, and 0.5TCS will be irradiated at a relatively low neutron flux to investigate irradiation rate effects. The scoping capsules will be irradiated in the 2-MW University of Buffalo Reactor (UBR). It is not yet known which irradiation facility will be used for the primary capsules but discussions are ongoing with operators of appropriate reactors in the U.S. and Europe to determine which will be most suitable for the irradiations.

About 12 lin m of weld from the pressure vessel installed in Unit 1 of the now abandoned Midland Power Plant has been obtained for Series 10. Initial characterization of the unirradiated material has begun. Initial testing has revealed a relatively wide range of transition temperatures and upper-shelf energies for the unirradiated condition which vary with position within the weld. Preliminary values of

RT_{NDT} ranging from -15°C to 17°C have been determined to date. Preliminary median values of the upper-shelf impact energy for the material range from 88 to 103 J (65 to 76 ft-lb). These variations in fracture properties and similar anticipated ones in material chemistry will need to factored into the detailed irradiation plan for this material. Current plans call for the initiation of the scoping irradiations in 1990 to be followed by the primary irradiations in 1991.

SERIES 8, K_{Ic} and K_{Ia} CURVE SHIFTS AND SHAPE CHANGES IN LOW UPPER-SHELF WELDS

The primary objective of Series 8 is to validate the postirradiation temperature shift and shape of the ASME Code Section XI K_{Ic} and K_{Ia} curves for LUS, high-copper welds. Considerable testing was performed with prototypic LUS welds in HSST Series 2 and 3, but only CVN tests were performed in the transition temperature region.[11] All fracture toughness tests were performed on the ductile-shelf and no crack-arrest tests were performed. This series is closely related to Series 5 and 6 in its objectives except for the specific material of interest. The existing data base for K_{Ic} and K_{Ia} data of low upper-shelf welds is sparse and inadequate for determining the postirradiation temperature shift and shape of the fracture toughness and crack-arrest toughness curves. The high concentration of inclusions which promote void formation and coalescence leading to low-energy tearing on the ductile shelf will likely result in different behavior in the ductile-brittle transition region as well. It is the effects of irradiation on the transition region fracture behavior of these materials which is of concern in Series 8, and direct comparisons will be made with the results of Series 5 and 6. Series 8 is currently in the planning stage; thus, specific materials and irradiation conditions cannot be reported. However, because the materials of concern in commercial LWRs are the LUS welds with high copper contents, it is anticipated that one or more weldments with copper content in the range 0.20 to 0.40 wt % will be utilized. The possibility of obtaining welds from existing reactor vessels (see discussion of Series 10) has been investigated but, because the known LUS, high-copper welds which might be appropriate in terms of properties and chemical composition were fabricated with copper-coated welding wire, they are probably not acceptable for this research project. The range of copper concentration reported in typical welds fabricated with copper flashing on the welding wire, even when only one lot of wire is used, is very wide. Because the irradiation sensitivity of these materials is strongly dependent on copper content, and the scatter of fracture toughness is high in the transition region, a wide specimen-to-specimen copper variation would exacerbate the variations and confound the results relative to determinations of curve shifts and shapes. The limited examination of the Midland weld has confirmed that the amount of scatter in fracture properties of at least one commercial weld would limit its

usefulness in making definitive determination of shifts and changes in shape in K_{Ic} and K_{Ia} curves. Thus, it is likely that high-copper weld wire would be manufactured for this series as it was for Series 5 and 6, with welding flux and procedures used to commercially fabricate LUS welds. The specimen complement will be similar to that for Series 5 and 6 with the possible exception of 4TCS. The results of Series 5, which provide a direct comparison of irradiated 2TCS and 4TCS, will be used as the basis for determination of the need for the larger specimens. Because only two 4TCS will fit in a capsule compared to 18 2TCS, the economic and statistical advantages are obvious. However, because this series will likely use the same material as Series 9, some 4TCS will be irradiated; it is the number of specimens which is yet to be determined.

The irradiation conditions for this series will be similar to those of Series 5 and 6; an irradiation temperature of 288°C and a target fluence of 1.5 to 2.0 x 10^{19} neutrons/cm^2 (>1 MeV). It is not yet known which irradiation facility will be used but it is likely to be the same as that selected for Series 10. Although no firm schedules are established, this series will probably begin about 1992.

SERIES 9, THERMAL ANNEALING IN THICK SECTIONS

The primary objective of Series 9 is to validate the effectiveness of thermal annealing in reducing irradiation-induced degradation of thick-section reactor vessel steels and investigate their reirradiation response. It has been well established that postirradiation thermal annealing at temperatures in excess of the irradiation temperature can result in significant recovery of mechanical properties. Thermal annealing is being examined in specific cases as a means to restore reactor vessel safety margins; and, in fact, 10CFR50 requires that PWRs predicted to reach the pressurized-thermal-shock (PTS) screening criteria before design end-of-life be designed for incorporation of a thermal annealing procedure. Guidelines for in-service annealing of LWR vessels are contained in ASTM standard E 509. Furthermore, annealing is one potential factor in plant life extension considerations. Annealing studies reported to date have used small specimens, e.g., CVN, 0.5TCS, and 1TCS. There are concerns that the larger amount of constraint in thick sections may affect the operative micromechanisms controlling fracture in postirradiation annealed microstructures. Series 9 would, therefore, directly compare the annealing response of small and large fracture mechanics specimens. An important aspect of the study would be a direct comparison of the reirradiation behavior of small and large specimens. It is considered particularly important that understanding of the mechanisms controlling radiation damage, annealing recovery, and reirradiation damage be pursued to allow for better management of annealing programs based on limited test specimens in commercial reactor surveillance programs. Fracture

toughness in the transition temperature and ductile-shelf regions will be investigated. Series 9 is currently in the planning stages; thus, specific materials and irradiation conditions cannot be reported. The materials likely to result in decisions to thermally anneal a reactor vessel are the LUS, high-copper welds. Thus, such a weld would be the primary candidate material for this series. Furthermore, if sufficient material were procured for Series 8, the same weld could be used for Series 9 with considerable savings in that unirradiated characterization and initial irradiations would have been performed. If that were the case, specimens would be needed only for the annealing and reirradiation phases. The specimen complement has not been planned for this series but would, of course, include CVN, tensile, and fracture toughness specimens up to 4TCS.

The initial irradiation conditions for Series 9 will probably be the same as for Series 5, 6, and 8, with an irradiation temperature of 288°C and a target fluence from 1.5 to 2.0 x 10^{19} neutrons/cm^2 (>1 MeV). The thermal annealing temperature will likely be in the range 399 to 454°C (750 to 850°F). Reirradiation would be performed at 288°C with the target fluence dependent on annealing results. The irradiation facility will probably be the same as that for Series 8. Although there is no firm schedule for Series 9, it is not likely that annealing studies would commence before 1995.

REACTOR VESSEL STAINLESS STEEL CLADDING

SERIES 7, IRRADIATION EFFECTS ON STAINLESS STEEL CLADDING

The objective of Series 7 is to evaluate the postirradiation mechanical properties, including fracture toughness, of the stainless steel cladding applied to the inside surfaces of LWR vessels. Cladding is applied to reactor vessels primarily to protect the coolant from contamination by corrosion products. Analyses of certain thermal shock scenarios have been inhibited by a lack of information regarding the fracture resistance of the cladding, but the little information available in the literature indicated that austenitic stainless steel cladding may undergo severe embrittlement as a consequence of neutron irradiation.[12] Series 7 was conceived to investigate irradiation effects on stainless steel claddings representative of those used in early PWRs that are being examined for their fracture resistance under overcooling situations. The series was conducted in two phases with the phases being distinguished primarily by the cladding fabrication method.

The materials were austenitic stainless steel claddings deposited on A533 grade B class 1 steel plate using two weld cladding procedures. The fabrication techniques and postweld heat treatments duplicate commercial procedures as closely as possible. However, to permit fabrication of mechanical test specimens of the

cladding, multilayer depositions were utilized to provide a cladding thickness of approximately 20 mm. This is thicker than the usual reactor vessel cladding (4 to 6 mm), but it should represent multilayer cladding, and test specimens were machined with regard to location within the cladding. The two weld cladding procedures chosen for Series 7 are the single-wire oscillating submerged-arc procedure (Phase 1) and the three-wire series-arc procedure (Phase 2).

In Phase 1, the first layer of cladding was deposited using type 309 weld wire and subsequent layers using type 308. The materials were given a postweld heat treatment equivalent to 40 h at 621°C. Very high heat input during application of the first layer resulted in substantial base metal dilution (up to 50%), and the effects on properties were significant. Specimens for unirradiated characterization and irradiation testing were carefully machined from the different layers. Charpy V-notch and tensile specimens were irradiated by Materials Engineering Associates (MEA) in the core of the 2-MW UBR from June to July 1985 at a nominal temperature of 288°C to a fluence of about 2×10^{19} neutrons/cm^2 (>1 MeV). All testing was conducted at ORNL. CVN and tensile tests showed that the highly diluted cladding layer (adjacent to the base metal) experienced substantial radiation damage, while the cladding layers not diluted with base metal showed almost no effects of irradiation.[13,14] Significant observations were reported in this study regarding the ductile-brittle transition behavior exhibited by the stainless steel cladding, and detailed discussions have been presented concerning the important role of the delta-ferrite phase to the fracture process in the weld metal.[15]

In Phase 2, a three-wire series-arc procedure was used in which weld wires of types 308, 309, and 304 stainless steels were independently fed into the welding arc to obtain the desired cladding composition. Combustion Engineering, Inc., modified the procedure they had used in vessel manufacture to produce a characterization block with three layers of cladding which was fabricated such that all three layers had nominally the same mechanical properties. Furthermore, the three-wire series-arc process resulted in very little base metal dilution. Ferrite numbers varied from 7.5 to 10 throughout the three layers of the cladding. Following fabrication, the material was given a postweld heat treatment equivalent to 40 h at 621°C. All irradiations were performed by MEA in the core of the UBR from September to December 1985 at a nominal temperature of 288°C. Tensile and CVN specimens were irradiated to fluences of about 2 and 5×10^{19} neutrons/cm^2. Compact specimens (0.5TCS) were machined from both the three-wire and single-wire cladding. Specimens from the single-wire cladding were machined from the highly diluted type 309 layer and from the type 308 layer. The 0.5TCS were all irradiated to about 2×10^{19} neutrons/cm^2 (>1 MeV).

Tensile and CVN specimens of the three-wire cladding were tested from -125 to 288°C and showed that yield strength increased about 20% (about the same for both fluences) at room temperature, while ultimate strength and tensile elongation were

essentially unaffected by irradiation. The CVN energy of the three-wire cladding exhibited transition temperature shifts of 13 and 28°C at 2 and 5 x 10^{19}, respectively. The CVN upper-shelf energy decreased by 15 and 20% at the low and high fluences, respectively. The effect of irradiation of the CVN lateral expansion was substantial on the ductile upper shelf, the transition region, and the brittle lower shelf. The 0.5TCS were tested from -75 to 288°C. Figures 7 and 8 show consistent irradiation-induced decreases in both the J_{Ic} and the tearing modulus. This is in agreement with the reduction in both the CVN upper-shelf energy and lateral expansion.[16] The low values of J_{Ic} and tearing modulus of the irradiated specimens raise concern about the potential adverse impact of the stainless steel cladding on the integrity of a pressure vessel during an overcooling transient in which the growth of small surface flaws can have a significant effect on the probability of vessel failure. The lowest value of an irradiated specimen was 23 kJ/m^2 which is considerably less than the lowest value of 43 kJ/m^2 for the LUS welds examined in the Second and Third HSST Irradiation Series.[1]

The results of Series 7 can be summarized as follows:

1. Yield strength of both single-wire and three-wire series-arc stainless claddings were increased by irradiation at prototypic LWR conditions.
2. The CVN toughness of good quality stainless steel claddings is somewhat degraded by irradiation while highly diluted cladding exhibits very poor toughness and is significantly degraded by irradiation.
3. Irradiation exposure reduced both the J_{Ic} and the tearing modulus of both single-wire and three-wire cladding.

Additional work in the area of irradiation effects on stainless steel cladding will focus on the effects of in-service exposure. Sections of trepans, which contain the layer of cladding, removed from the decommissioned Gundremmingen reactor vessel in the Federal Republic of Germany have been obtained. Current plans include the examination of their tensile, impact, and microstructural properties through the use of subsize specimen technology. The results from their examination will provide additional insight into the effects of irradiation rate and spectrum on the degradation of fracture resistance of stainless steel weld overlay cladding. It is anticipated that the utilization of the additional machining capability being developed as a part of the new in-service aged materials evaluation facility will result in substantially enhanced cost-effectiveness in specimen fabrication of the irradiated cladding.

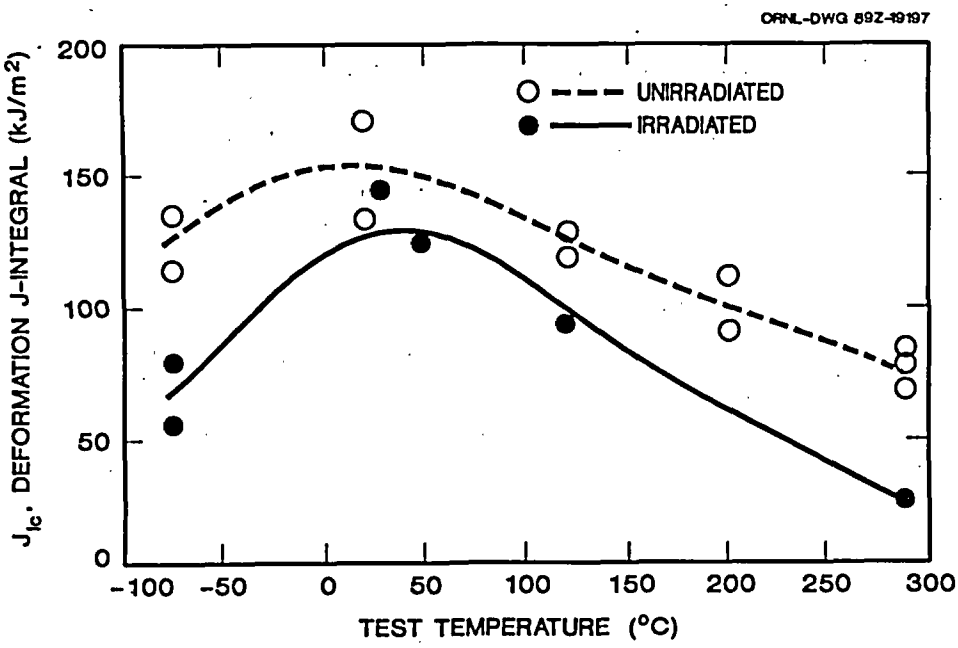

Fig. 7. Effect of irradiation on J_{Ic}, initiation fracture toughness, vs test temperature on three-wire series-arc stainless steel weld-overlay cladding irradiated at ~288°C to an average fluence (>1 MeV) of 2 x 10^{19} neutrons/cm^2.

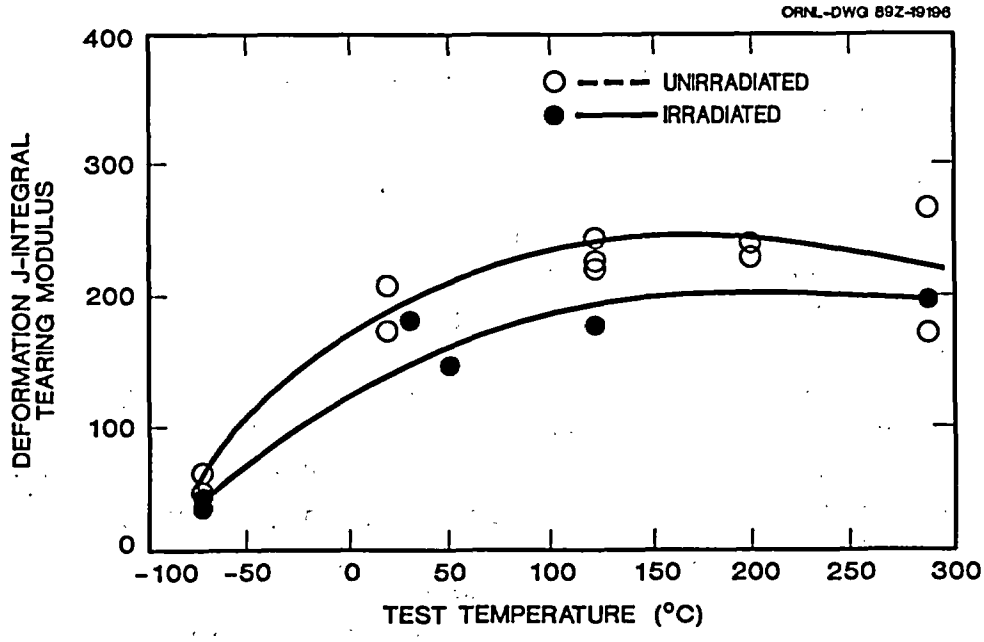

Fig. 8. Effect of irradiation on the tearing modulus vs test temperature on three-wire series-arc stainless steel weld-overlay cladding irradiated at ~288°C to an average fluence (>1 MeV) of 2 x 10^{19} neutrons/cm^2.

INITIATIVES IN MICROSTRUCTURAL ANALYSIS AND MODELING

The capability to accurately predict the remaining fracture resistance of pressure vessel materials is becoming more acute as vessels receive increasing exposures. Materials in many U.S. vessels are already expected to exceed the transition temperature screening criteria or drop below the 68 J upper-shelf impact energy limit before their scheduled end of life and many more will reach those limits if extended operating licenses can be obtained. Clearly, the degree of uncertainty and associated potential error margins involved in predicting and evaluating radiation-induced damage must be reduced to allow continued safe operation as the window narrows between possible and permissible conditions of operation. The unknowns inherent in the multidimensional interpolation and extrapolation of radiation damage pose a very difficult challenge to not only current but even the most sophisticated empirically based methods to accurately predict behavior under conditions removed very far from the existing data base. Too many combinations of material chemistry, product form and microstructure, irradiation fluence, flux, temperature and spectrum, and postirradiation annealing and reirradiation exist to be able to generate a data base which adequately covers all conditions of interest.

To provide a better basis for meeting the needs of increased accuracy in predictions of irradiation-induced damage, the HSSI Program has initiated a task with the ultimate goal of producing a predictive model based on the operative micromechanisms of irradiation damage. Detailed examination of irradiated materials from other tasks by atom probe field ion microscopy (APFIM), with some assistance from analytical electron microscopy (AEM) for conditions where defects can be resolved by this technique, will be conducted in parallel with an analysis of the existing radiation hardening data base. The APFIM and AEM studies will provide the detailed microstructural information necessary to build and calibrate the rate theory based model on a sound physical basis. An initial model for the evolution of self-defect/solute clusters and other microstructures based on radiation-induced defect reactions will be developed to describe the kinetics of hardening in ferritic steels. Initial variables of interest in the rate theory work will include solute concentration, irradiation temperature, damage rate, and fluence. The microstructural model will be used to predict shifts in the nil-ductility transition temperature as a function of the irradiation dose and temperature. Ongoing analysis of available data from test reactor and LWR surveillance programs will provide a test of the model's validity and predictive capability and provide a basis for its revision and improvement.

The initial focus of the microstructural examination and modeling effort will be LUS weld metal. Unirradiated and irradiated specimens from both the Second and Third HSST Irradiation Series[1] and the Tenth HSSI Irradiation Series will be examined by APFIM and AEM as well as more traditional methods. These

observations will be augmented in the future with those on similar material irradiated under prototypic conditions in power reactors, if such can be obtained, to provide a much wider base for establishing effects of irradiation rate and spectrum on irradiation-induced damage in LUS weld metal.

SUMMARY

The HSSI Program irradiation effects studies will continue and expand upon the more than two decades of HSST investigations which have sought to understand irradiated reactor vessel behavior. The HSSI studies are providing an enhanced data base for the evaluation of irradiation effects on the integrity of pressure vessel materials. HSSI Irradiation Series 5, 6, and 8 are determining the detailed changes to the fracture toughness and arrest toughness curves for low and high upper-shelf materials. Irradiation Series 10 will provide a detailed examination of the effects of irradiation including rate and saturation effects on both the ductile fracture and transition behavior of a commercial LUS weld. Irradiation Series 7 is evaluating effects of irradiation on stainless steel weld overlay cladding. Irradiation Series 9 will provide a basis for evaluating the effects of annealing and reirradiation in the section sizes of interest to pressure vessel operation.

In addition to supplying enhanced information on irradiation effects, the results of the HSSI Program are directly targeted to provide bases for a number of regulatory products. These include the ASME Code Sections III, Appendix G (toughness) and 10CFR50 Appendices G and H (toughness and surveillance program requirements); fracture toughness curves for the ASME Code Section III, Appendix G and Section XI, Appendix A; 10CFR50.61, Fracture Toughness Requirements for Protection Against Pressurized Thermal Shock Events; *Regulatory Guide 1.99,* Radiation Damage to Reactor Vessel Materials; Unresolved Safety Issue A-11, Low Upper Shelf Toughness; establishment of the new appendix to the ASME Code Section XI dealing with LUS toughness criteria; and numerous ASTM standards dealings with subjects ranging from surveillance programs to specimen test methods.

Irradiation effects is a central issue in the safe operation of existing nuclear reactor vessels, for effective design of future vessels, and for potential extension of design lifetimes. Continued research to further understanding of irradiation effects and the underlying mechanisms of radiation damage is essential.

ACKNOWLEDGMENTS

The author acknowledges D. D. McCoy for preparation of the final manuscript and D. J. Alexander and D. J. McGuire for their helpful reviews. The financial support and guidance provided by the U.S. Nuclear Regulatory Commission and Alfred Taboada, Technical Monitor, are greatly appreciated.

REFERENCES

1. R. K. Nanstad, "Summary of the Heavy-Section Steel Technology Program Irradiation Series," pp. 314-354 in *Proceedings of the U. S. Nuclear Regulatory Commission Sixteenth Water Reactor Safety Information Meeting,* USNRC Conference Proceeding, NUREG/CP-0097, Vol. 2, March 1989.

2. Title 10, *Code of Federal Regulations,* Parts 0 to 199, U.S. Government Printing Office, Washington, D.C., January 1987.

3. "Radiation Embrittlement of Reactor Vessel Materials," *Regulatory Guide 1.99* (Rev. 2), U.S. Nuclear Regulatory Commission, Washington, D.C., May 1988.

4. *ASME Boiler and Pressure Vessel Code, An American National Standard,* American Society of Mechanical Engineers, New York, 1986.

5. C. Z. Serpan and P. N. Randall, "Irradiation Effects in Reactor Pressure Vessel Steels: A Nuclear Regulatory Commission Perspective," pp. 5-12 in *Radiation Embrittlement of Nuclear Pressure Vessel Steels: An International Review (Second Volume),* ASTM STP 909, L. E. Steele, Ed., American Society for Testing and Materials, Philadelphia, 1986.

6. M. L. Williams, I. Remec, and F. B. K. Kam, Martin Marietta Energy Systems, Inc., Oak Ridge Natl. Lab., *Neutron Spectral Characterization for the Fifth Heavy-Section Steel Technology (HSST) Irradiation Series,* "Neutronics Calculations," NUREG/CR-4031, Vol. 2 (ORNL/TM-9423/V2), March 1985.

7. I. Remec, F. W. Stallman, and F. B. K. Kam, Martin Marietta Energy Systems, Inc., Oak Ridge Natl. Lab., *Neutron Spectral Characterization for the Fifth Heavy-Section Steel Technology (HSST) Irradiation Series,* "Neutronics Exposure Parameters," NUREG/CR-4031, Vol. 3 (ORNL/TM-9423/V3), March 1985.

8. L. F. Miller, C. A. Baldwin, F. W. Stallman, and F. B. K. Kam, Martin Marietta Energy Systems, Inc., Oak Ridge Natl. Lab., *Neutron Exposure Parameters for the Metallurgical Test Specimens in the Fifth Heavy-Section Steel Technology Irradiation Series Capsules,* NUREG/CR-5019 (ORNL/TM-10582), March 1988.

9. Materials Properties Council Subcommittee 6 on Nuclear Materials, "Prediction of the Shift in the Brittle-Ductile Transition Temperature of Light-Water Reactor (LWR) Pressure Vessel Materials," *J. Test. Eval.* **11**(4), 237-60 (July 1983).

10. J. R. Hawthorne and L. E. Steele, *The Effect of Neutron Irradiation on the Charpy V and Drop-Weight Test Transition Temperatures of Various Steels and Weld Metals*, NRL Report 5479, Naval Research Laboratory, Washington, D.C., May 1960.

11. "Sixth HSST Irradiation Series: Crack Arrest," pp. 185-190 in *Heavy-Section Steel Technology Program Semiann. Prog. Rep. April-September 1986,* NUREG/CR-4219, Vol. 3, No. 2 (ORNL/TM-9593/V3&N2), December 1986.

12. W. R. Corwin, Martin Marietta Energy Systems, Inc., Oak Ridge Natl. Lab., *Assessment of Radiation Effects Relating to Reactor Pressure Vessel Cladding,* NUREG/CR-3671 (ORNL-6047), July 1984.

13. W. R. Corwin, R. G. Berggren, and R. K. Nanstad, Martin Marietta Energy Systems, Inc., Oak Ridge Natl. Lab., *Charpy Toughness and Tensile Properties of a Neutron-Irradiated Stainless Steel Submerged Arc Weld Cladding Overlay*, NUREG/CR-3927 (ORNL/TM-9309), September 1984.

14. W. R. Corwin, R. G. Berggren, and R. K. Nanstad, "Charpy Toughness and Tensile Properties of a Neutron-Irradiated Stainless Steel Submerged-Arc Weld Cladding Overlay," pp. 951-971 in *Effects of Radiation on Materials: Twelfth International Symposium,* ASTM STP 870, American Society for Testing and Materials, Philadelphia, 1985.

15. W. R. Corwin, R. G. Berggren, R. K. Nanstad, and R. J. Gray, "Fracture Behavior of a Neutron-Irradiated Stainless Steel Submerged Arc Welding Cladding Overlay," *Nucl. Eng. Des.* **89**, 199-221 (1985).

16. F. M. Haggag and S. K. Iskander, "Results of Irradiated Cladding Tests and Clad Plate Experiments," pp. 355-370 in *Proceedings of the U. S. Nuclear Regulatory Commission Sixteenth Water Reactor Safety Information Meeting*, USNRC Conference Proceeding, NUREG/CP-0097, Vol. 2, March 1989.

USE OF J/J_M-R CURVES IN ASSESSING THE FRACTURE BEHAVIOR OF LOW UPPER SHELF TOUGHNESS MATERIALS

By

E.M. Hackett
David Taylor Research Center (DTRC)
Annapolis, Maryland 21402

J.A. Joyce
United States Naval Academy (USNA)
Annapolis, Maryland 21402

ABSTRACT

The objective of this investigation was to evaluate the use of small specimen J/J_M-R curves in assessing the fracture resistance behavior of reactor vessels containing low upper shelf (LUS) toughness weldments. As required by 10 CFR, Part 50, reactor vessel beltline materials must maintain an upper shelf Charpy V-Notch (CVN) energy of at least 50 ft-lbs throughout vessel life. If CVN values from surveillance specimens fall below this value, the utility must demonstrate to the NRC that the lower values will provide "margins of safety against fracture equivalent to those required by Appendix G of the ASME Boiler and Pressure Vessel Code." This paper will present recommendations regarding the material fracture resistance aspects of this problem and outline an analysis procedure for demonstrating adequate fracture safety based on CVN values.

It is recommended that the deformation formulation of the J-integral be used in the analysis described above. For cases where J-integral fracture toughness testing will be required, the ASTM E1152-87 procedure should be followed, however data should be taken to 50% to 60% of the specimen remaining ligament. Extension of the crack growth validity limits for J-R curve testing, as described in E1152-87, can be justified on the basis of a "singularity zone" analysis which shows an engineering basis for J-control to 25% to 40% of the specimen remaining ligament. If J-R curve extrapolations are required for the analysis, a simple power law fit to data in the extended validity region should be used. The example analysis performed for low upper shelf LINDE 80 weld material, showed required CVN values for a reactor vessel with a 7.8 inch thick wall ranging from 32 ft-lbs to 48 ft-lbs, depending on the magnitude of the thermal stress component.

INTRODUCTION

In November 1987, a J/J_M working group was established, consisting of technical experts in the area of elastic-plastic fracture mechanics (EPFM), to resolve the issue of which parameter (J or J_M) was appropriate for fracture mechanics analyses of nuclear components. Such fracture mechanics analyses can involve instability calculations at large amounts (>0.6 inches) of crack extension, where the validity of EPFM assumptions is doubtful.

Work by the group in this area over the last 2 years has indicated that the choice of parameter was only one of several technical issues in need of resolution to provide the basis for fracture safety analyses of nuclear components. These technical issues included: (1) Methods for Obtaining J-R Curve Data, (2) J-R Curve Validity Limits, and (3) J-R Curve Fitting Procedures and Extrapolations. These issues will be addressed in separate sections of this report. It has also become apparent that resolution of the choice of parameter, J or J_M, will require substantially more research, particularly as regards numerical modeling similar to that which was performed for development of the ASTM J-R curve standard (E1152-87) [Booth, et al, 1985]. The more basic research issue of constraint effects on J-R curves also remains to be adequately addressed. Future efforts of the working group will be focused predominantly on the constraint issue.

The purpose of this paper is to report recommendations on use of J-R curves in fracture safety analyses of low upper shelf (LUS) LINDE 80 weld metal used in certain reactor vessels. Details on the background of this specific application are provided below.

BACKGROUND

The focus of this report is to address the problem of the material fracture resistance aspects of low upper shelf (LUS) toughness weldments in reactor vessel beltline regions. This problem relates to reactor vessels which were fabricated with copper-coated electrodes and LINDE 80 fluxes which produced weldments especially susceptible to neutron irradiation embrittlement. The upper shelf impact toughness of these welds, as measured by the Charpy V-notch (CVN) test, tends to degrade with long term irradiation. In 1980, The Nuclear Regulatory Commission (NRC) designated this problem as unresolved safety issue A-11, "Reactor Vessel Materials Toughness", and published NUREG 0744 [July, 1982] to provide guidance in performing fracture safety analyses of LUS materials. At the same time, the NRC requested the American Society of Mechanical Engineers (ASME) Boiler and Pressure Vessel Code Subcommittee, Section XI, to address the margin(s) of safety required for such analyses. The problem was assigned to the Working Group on Flaw Evaluation.

For purposes of the above analyses, LUS CVN performance was defined as 50 ft-lbs. or less. As amended in 1983, federal regulation 10 CFR 50 requires reactor vessel beltline materials to maintain an upper shelf CVN of at least 50 ft-lbs throughout the life of the vessel. If upper shelf CVN energies below 50 ft-lbs are measured from surveillance specimens, the utility must

demonstrate to the Nuclear Regulatory Commission (NRC) that the "lower values of upper shelf energy will provide margins of safety against fracture equivalent to those required by Appendix G of the American Society of Mechanical Engineers (ASME) Boiler and Pressure Vessel Code."

In NUREG 0744 [1982] it was noted that linear elastic fracture mechanics (LEFM) methods were inapplicable under vessel operating conditions, and that EPFM methods would be required. The document described the use of J-R curves as the material property in an elastic-plastic analysis for resistance to unstable ductile tearing. NUREG 0744 pre-dated the publication which documented the development of J_M [Ernst, 1983]. In 1987, controversy over the calculation of the J-integral for extended crack growth developed and led to questions as to whether J or J_M was the more appropriate parameter to use under such conditions. The ASME Section XI Working Group on Flaw Evaluation (WGFE) was tasked to further examine the LUS issue and to develop an updated A-11 document to outline an approach to solving such a problem. This document, entitled, "Development of Criteria for Assessment of Reactor Vessels with Low Upper Shelf Welds", provides details of an EPFM methodology for assessing the flaw tolerance of an LUS vessel. As details of the materials resistance aspects of the problem were beyond the charter of the WGFE, the NRC formed the J/J_M working group to provide guidance on the material fracture resistance aspects of the LUS problem. This paper provides specific recommendations for the fracture resistance aspects of the LUS LINDE 80 weld metal issue.

METHODS FOR OBTAINING J-R CURVE DATA

The basic procedure to be followed for generation of J-R curve data is the ASTM Standard Test Method for Determining J-R Curves, E1152-87. This Standard describes an elastic compliance procedure for J-R curve determination. Other methods are allowed (Direct Current Potential Drop [DCPD], Alternating Current Potential Drop [ACPD], etc.) if equivalent crack length accuracy can be demonstrated. Inaccuracy in the predicted versus actual final crack length measurement can cause problems such as "tailing-up" or negative slopes on J-R curves. ASTM E1152 requires an accuracy of 15% on predicted versus actual final crack length up to a crack extension maximum of $0.1 \times b_o$ (b_o = initial specimen remaining ligament). It is recommended that J-R curve data be taken far beyond this limit, up to 50% to 60% of b_o. J-R curve data obtained using an elastic compliance method on several steel alloys has been shown to be within the 15% limit, even at such large crack extensions [NUREG CR 5143, 1988].

For J-R curve data where predicted versus actual crack extensions are outside the 15% accuracy limit, normalization analysis, such as that described by Herrera and Landes [1988], may be employed to correct the R curve data. Normalization analysis uses the calibration curve in which the flow properties of a material for stationary crack growth provide the relationships between load, displacement and crack length.

J-R CURVE VALIDITY LIMITS

Restrictions placed on the amount of valid crack growth for J-R curve tests in ASTM E1152-87 (crack extension < 0.1 x b_o) limit the usefulness of this standard in generating materials resistance information for nuclear components, where large crack extensions are required. Extension of the crack growth validity limits for J-R curve testing was investigated by DTRC using both fatigue precracked and blunt notched specimens to determine if deformation plasticity conditions prevailed to large crack extensions.

Blunt notch tests of 1T compact specimens were conducted and the final loads and J values were compared with results from corresponding fatigue precracked elastic compliance J-R curve tests. For deformation plasticity conditions to prevail, the final loads and J values between the blunt notch and J-R curve tests should be in good agreement. A summary of the comparisons performed with A533B, A710 and 3%-Ni steels is presented in Table 1. This comparison shows good agreement for the A533B and 3%-Ni steels and poor agreement for the A710 steel. The A710 steel specimens were characterized by larger deformations than either the A533B or 3%-Ni steels at similar amounts of crack growth. The blunt notch tests for materials other than the highly ductile A710 alloy indicate that deformation theory is applicable for the medium-to-high strength steels investigated, even when large crack extensions and corresponding material unloading has occurred. This provides support for extension of J-R curve crack growth validity limits beyond that currently provided in ASTM E1152-87. Complete details of the J-R curve and blunt notch testing are provided in NUREG/CR-5143 [1988].

Subsequent to the blunt notch testing, an analysis, aimed at quantifying the extent of the J-singularity controlled region of crack growth in a laboratory specimen, was developed. It was observed that real (engineering) limits to the applicability of the J-integral were apparent in a plot of the plastic component of crack opening displacement versus crack extension. Such a plot is shown for a 3%-Ni steel 1/2T compact specimen in Figure 1. This plot shows a region of initial crack blunting, a region of singularity controlled crack growth, and finally, a gradual return to crack blunting. While the presence of a singularity is difficult to verify experimentally, it is known that it should produce the most intense conditions for crack growth. The plot in Figure 1 shows the most intense crack growth occurring in the central linear region. The presence of blunting in the beginning of the test and the weakening of the singularity as the test progresses are reflected by the fact that the increment of crack growth per increment of plastic displacement is greatly reduced in these regions. The delineations between these zones are much more apparent on this plot than on a standard J-R curve. The limit of the singularity controlled crack growth region is taken to be at a 5% deviation from the linear region shown on the plot. Application of this type of analysis to several materials investigated by DTRC (A533B, A106, 3% Ni steels and LINDE 80 weld metal) has shown the loss of singularity controlled growth to be in the range of 25% to 40% of the specimen remaining ligament. This loss of singularity region has also been found to be consistent with the beginning of the upward sweep observed in J_M-R curves. The specimen size dependence demonstrated by the modified J, therefore, appears to be a clear

indicator of a loss of singularity in these specimens. Details of the development of the singularity zone analysis were provided in NUREG/CR-5238 [1989]. It is recommended that this analysis be conducted for all specimens used to provide materials resistance information for LUS LINDE 80 weld metal and that full use be made of the extended validity range when considering extrapolations if these are necessary.

J-R CURVE FITTING PROCEDURES AND EXTRAPOLATIONS

The experimental singularity zone defined above extends the applicable region of the J resistance curve well beyond the present limits of ASTM E1152-87. As shown above, the results indicate that crack extensions of up to 40% of the initial remaining ligament can be justified by the singularity limit defined directly from experimental data.

When even this extended J-R curve data is not adequate to address crack growth resistance, it is proposed that an extrapolation can be made in the following manner. First, only small specimen data in the singularity zone should be utilized. Second, a simple power law of the form

$$J = C(\Delta a)^m \qquad (1)$$

where C and m are fitting parameters and Δa is the amount of crack extension, should be fit to the small specimen singularity zone data for purposes of extrapolation.

This analysis was applied to J-R curve data from LUS LINDE 80 weld metal from the Babcock & Wilcox Company. This data is shown in Figure 2. On first examination, the small specimen data of Figure 2 appear to be grossly conservative in comparison with the 2T C(T) result. Utilizing only the data in the singularity zone for each small specimen, however, and fitting a simple power law to the data, provides the comparison shown in Figure 3. Here it is shown that extrapolations of the small specimen data (0.394T to 1T) produce accurate to conservative estimates of the large specimen (2T) behavior. Similar extrapolations performed using J_M-R curves have produced accurate to non-conservative estimates of the large specimen behavior. Setting limits to J-R curve extrapolations for this material will require statistical examination of large specimen (> 4T) data which was not available for this report.

CHOICE OF PARAMETER (J/J_M)

As stated in the introduction, the resolution of which parameter, J or J_M, more adequately addresses large crack extensions in laboratory specimens or structures will require further research. For the present, the deformation J formulation as specified in ASTM E1152-87, with the extended validity region and methods of extrapolation described above, appears adequate to address the LUS LINDE 80 weld metal issue. Moreover, familiarity with the concepts of J-integral tearing instability theory, which was based on the deformation J

formulation, will be useful in the fracture safety analyses required by 10 CFR 50. An important aspect of future research on J/J_M will be performance of numerical analyses with simulated crack growth, to evaluate which parameter more accurately describes material fracture behavior at large crack extensions and deformations.

PROPOSED CRITERIA FOR FRACTURE SAFETY ANALYSIS OF REACTOR VESSELS CONTAINING LOW UPPER SHELF TOUGHNESS WELDS

Criteria that have been proposed by NRC and ASME to address the fracture safety of low upper shelf weld metal in reactor vessels, have included evaluation of fracture toughness at an arbitrary amount of crack extension (0.1 inches), and evaluation for tearing instability at extended crack growth. A proposed criteria for the arbitrary tearing is

$$J_{material} > J_{applied} \text{ at:}$$

Pressure (P) = 1.25 P_{design} = 3125 psi
Crack Extension = 0.1 inches
$J_{material}$ evaluated from a two sigma lower bound J-R curve for the available data ($J_{material} = J_{mean} - 2$ sigma)

A proposed criteria for the tearing instability analysis is the following:

Pressure (P) = 1.5(P_{design}) = 3750 psi
The slope of the J-R curve (dJ/da) is calculated from a two sigma lower bound J-R curve.

EXAMPLE FRACTURE SAFETY ANALYSIS FOR LINDE 80 WELD MATERIAL

The following problem is utilized as an example analysis demonstrating the application of the above proposed criteria. A reactor vessel with a 7.8 inch thick wall was selected for this example.

A. Considerations for Determination of Driving Force For Fracture

Structure

Thick Walled Pressure Vessel
Thickness (t) = 7.8 inches
Inner radius (r_i) = 10t
Outer Radius (r_o) = r_i + t
Pressure = P
Stress = σ

$$\sigma = P[(r_i + ((r_o^2 r_i^2)/r^2))/(r_o^2 - r_i^2)] \qquad (2) \quad \text{[Popov, 1976]}$$

$$\text{where,} \quad r = 0.25t \qquad (3)$$

Flaw Analysis

For a semi-elliptical flaw, 1/4t in depth with a depth to length ratio (a/l) of 0.167, the value for the J-integral due to pressure stress may be estimated from a modified Newman-Raju [1980] equation proposed by Bloom [1985]:

$$J_P = (\sigma_f^2 a)(Y^2)[\Pi(\sigma/\sigma_f)^2/(1 - (Y^2/\beta)(\sigma/\sigma_f)^2)]/E' \qquad (4)$$

where,

a = Flaw Depth
σ_f = Flow Stress
β = 6 (Plane Strain)
$E' = E/(1-\upsilon^2)$
Y, M, Q are flaw shape and geometry factors

The K value due to the pressure stress can be obtained from J by using the expression:

$$K_P = (J_P * E')^{1/2} \qquad (5)$$

Thermal Analysis

The K value due to thermal stress may be estimated from [EPRI, 1989]:

$$K_T = 1363(a_e)^{1.72} - 1419(a_e) + 35(a_e)^{2.38}(CR-10)^{0.99} \qquad (6)$$

where,

$$a_e = 0.25t + 0.053(JE'/\sigma_f^2) \qquad (7)$$

CR = Cooling Rate, (0^oF/Hr, 50^oF/Hr or 100^oF/Hr) (8)

The total driving force for fracture is obtained by combining the pressure and thermal stress components using the following expression:

$$J_{TOTAL} = (K_T + K_P)^2/E' \qquad (9)$$

B. Considerations for Determination of Fracture Resistance

Material and Fracture Properties

Flow Stress - σ_f - 85000 psi
Elastic Modulus - E - 29 x 10^6 psi
Poisson's Ratio - υ - 0.3

The material fracture resistance is expressed in terms of the 2 sigma lower bound J-R curve referred to previously. For purposes of this example analysis, the lower bound J-R curve was obtained by a correlation with CVN energy values which is described in a recent EPRI report [1989]. $J_{material}$ is obtained from a power law representation of the J-R curve: $J_{material} = A(\Delta a)^n$ with A and n as fitting functions from the J-CVN correlation in terms of CVN toughness.

C. Fitness for Service Analysis in Terms of CVN Toughness

As with any fracture mechanics fitness-for-service analysis, the determination of the suitability of the component for continued service is based on a comparison of the driving force for fracture with the material fracture resistance. This section describes the combined analysis.

The essential postulate of the first criteria proposed in the previously (tearing limit at 0.1 inches of crack extension) is that $J_{material}$ be greater than $J_{applied}$ at; (1) a pressure of 1.25 x P_{design} (3125 psi), (2) crack extension of 0.1 inches, and (3) $J_{material}$ represented by a 2 sigma lower bound J-R curve ($J_{material} = J_{mean} - 2$ Sigma).

At 3125 psi, a 7.8 inch thick reactor vessel with a 1/4t flaw is subject to the following J_{total} values calculated from equation (9):

Cooldown Rate (°F/Hr)	J_{total} (in-lbs/sq in)	CVN Toughness (ft-lbs)
0	277	32
50	335	38
100	400	44

Applying the lower bound CVN correlation suggested in the EPRI report [1989] yields the CVN results shown above. An example interpretation is that at 100°F/Hr, a CVN toughness of 44 ft-lbs is required to demonstrate an adequate margin of safety to allow the plant to remain in operation.

The second criteria referred to in the previous section involves a tearing instability analysis at a pressure of 1.5 x P_{design} (3750 psi) with the slope of the J-R curve (dJ/da) determined from the 2 sigma lower bound J-R curve. As above, an evaluation point is chosen at a crack extension of 0.1 inches. the applied dJ/da and J at 0.1 inches of crack extension is evaluated and the

resulting plot is shown in Figure 4 for all three cooldown rates. The J-CVN correlation is performed at the 0.1 inch evaluation point for each CVN value and is plotted on identical axes as shown in Figure 5. The intersections of the curves of Figures 4 and 5 imply identical power law functions meaning that the intersection CVN value is a delineator between stable and unstable vessel performance. These intersection values are tabulated below and compared with the results of the first criteria.

Cooldown Rate (°F/Hr)	CVN Tearing Limit (ft-lbs)	CVN Instability Limit (ft-lbs)
0	32	38
50	38	43
100	44	48

In this example problem, the tearing instability criteria would govern fitness-for-service requirements for the vessel.

CONCLUSIONS

The following conclusions can be drawn from the data and analyses presented in this report. These conclusions are specific to the problem of low upper shelf (LUS) toughness LINDE 80 weldments in reactor vessel beltline regions of certain commercial nuclear plants.

(1) For generation of J-R curve data, the deformation formulation of the J-integral, as specified in ASTM E1152-87, should be used. J-R curve test data should be acquired out to crack extensions of 50% to 60% of the specimen initial remaining ligament.

(2) A "singularity zone" analysis, as described herein, can be used to define a region of extended validity for J-R curve data. This extended validity region can range from 25% to 40% of the specimen initial remaining ligament.

(3) Extrapolations of J-R curve data, where needed, should be performed by fitting a simple power law to the data in the extended validity region.

(4) An example problem, combining analysis for a tearing limit and tearing instability for the LUS LINDE 80 weld metal, produced required CVN values for safe operation in the range of 32 ft-lbs to 48 ft-lbs for a 1/4t flaw in a reactor vessel with a 7.8 inch thick wall. Variation in the range is caused by consideration of the magnitude of the thermal stress component. For the conditions described in the example analysis, the tearing instability criterion governs the fitness-for-service requirements for the vessel.

REFERENCES

Bloom, J.M., "Extensions of the Failure Assessment Diagram Approach - Semi-Elliptical Flaw in Pressurized Cylinder, ASME Pressure Vessel and Piping Technology Journal, Vol. 107, February, 1985.

Booth, B.C. and Newman, J.C., Jr., and Shivakurman, K.N., "An Elastic-Plastic Finite Element Analysis of the J-Resistance Curve Using a CTOD Criterion," ASTM STP 945, American Society for Testing and Materials, Philadelphia, PA, 1985, pp. 665-685.

EPRI Report, "Evaluation of Upper Shelf Toughness Requirements for Reactor Pressure Vessels," Prepared for Electric Power Research Institute, Palo Alto, California 94303, Volume 2, Detailed Report, October, 1989

Ernst, H.A., "Material Resistance and Instability Beyond J-Controlled Crack Growth," ASTM STP 803, American Society for Testing and Materials, Philadelphia, PA, 1983, pp. I-191-I-213.

Herrera, R. and Landes, J.D., "A Direct J-R Curve Analysis of Fracture Toughness Tests," presented at the ASTM 21st Symposium on Fracture Mechanics, Annapolis, MD, June 1987.

Newman, J.C. and Raju, I.S., "Stress Intensity Factors for Internal Surface Cracks in Cylindrical Pressure Vessels," Trans. ASME Journal of Pressure Vessel Technology, Vol. 102, November, 1980.
NUREG 0744, Vol. 2, Rev. 1, "Resolution of the Task A-11 Reactor Vessel Materials Toughness Safety Issue," U.S. Nuclear Regulatory Commission, Washington, D.C. 20555, 1982

NUREG CR/5143, "Application of the J-Integral and Modified J-Integral to Cases of Large Crack Extension," J.A. Joyce, D.A. Davis, E.M. Hackett and R.A. Hays, U.S. Nuclear Regulatory Commission, Washington, D.C. 20555, 1988

NUREG CR/5238, "Development of an Engineering Definition of the Extent of J Singularity Controlled Crack Growth," J.A. Joyce and E.M. Hackett, U.S. Nuclear Regulatory Commission, Washington, D.C. 20555, 1989

Popov, E.P., Mechanics of Materials, Second Edition, Prentice-Hall, Inc., Publishers, Englewood Cliffs, New Jersey, 1976

MATERIAL/ SPECIMEN	TEST TYPE	FINAL LOAD (pounds)	FINAL J (lbs/in)	% DIFF LOAD (%)	%DIFF J (%)	CRACK EXTENSION (inches)
3-Ni STEEL						
FYB-A3	BLUNT-NOTCHED	8100	1700	-4	-2	
FYB-A12	J-R CURVE	8400	1667			0.107
FYB-A7	BLUNT-NOTCHED	6000	2205	-5	0	
FYB-A11	J-R CURVE	6300	2216			0.202
FYB-A6	BLUNT-NOTCHED	4000	2435	-13	-1	
FYB-A10	J-R CURVE	4500	2405			0.3
A533B						
E74	BLUNT-NOTCHED	6880	2907	0	-6	
E71	J-R CURVE	6870	2749			0.096
E72	BLUNT-NOTCHED	5130	4463	-1	-1	
E75	J-R CURVE	5190	4401			0.209
E73	BLUNT-NOTCHED	3900	4278	-8	-2	
E76	J-R CURVE	4200	4208			0.274
A710						
GFF-J13	BLUNT-NOTCHED	8150	7150	-7	1	
GFF-J11	J-R CURVE	8700	7210			0.1
GFF-J14	BLUNT-NOTCHED	5800	9512	-17	6	
GFF-J10	J-R CURVE	6800	10170			0.207
GFF-J12	BLUNT-NOTCHED	3600	9450	-39	16	
GFF-J9	J-R CURVE	5000	11204			0.298
GFF-J6	BLUNT-NOTCHED	2400	10750	-50	19	
GFF-J5	J-R CURVE	3600	13250			0.387

Table 1 - Summary of J-R Curve and Blunt-Notched Tests

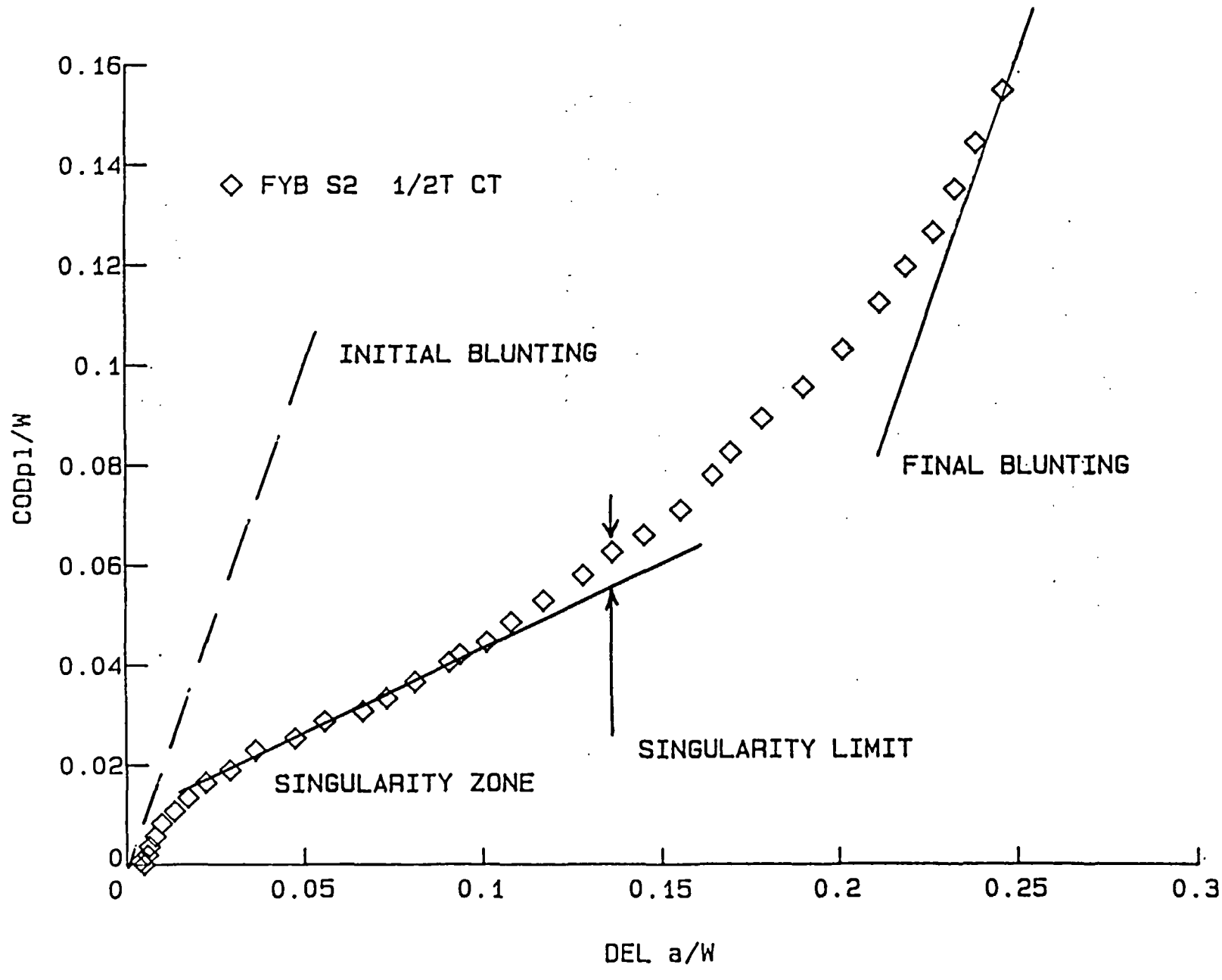

Figure 1 - "Singularity Zone" Analysis for 1/2T Compact Specimen of 3%-Ni Steel

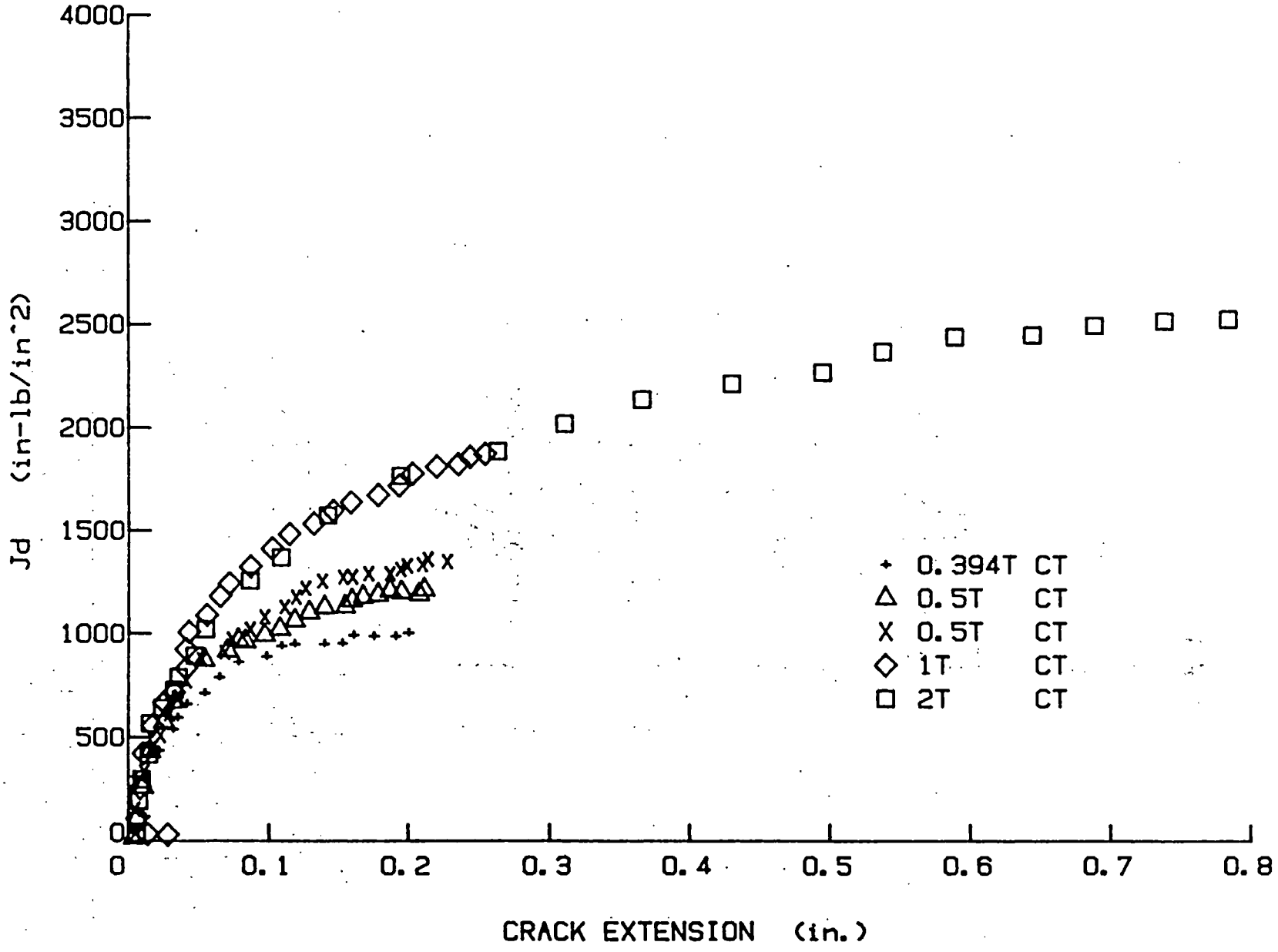

Figure 2 - J-R Curves for LINDE 80 Welds

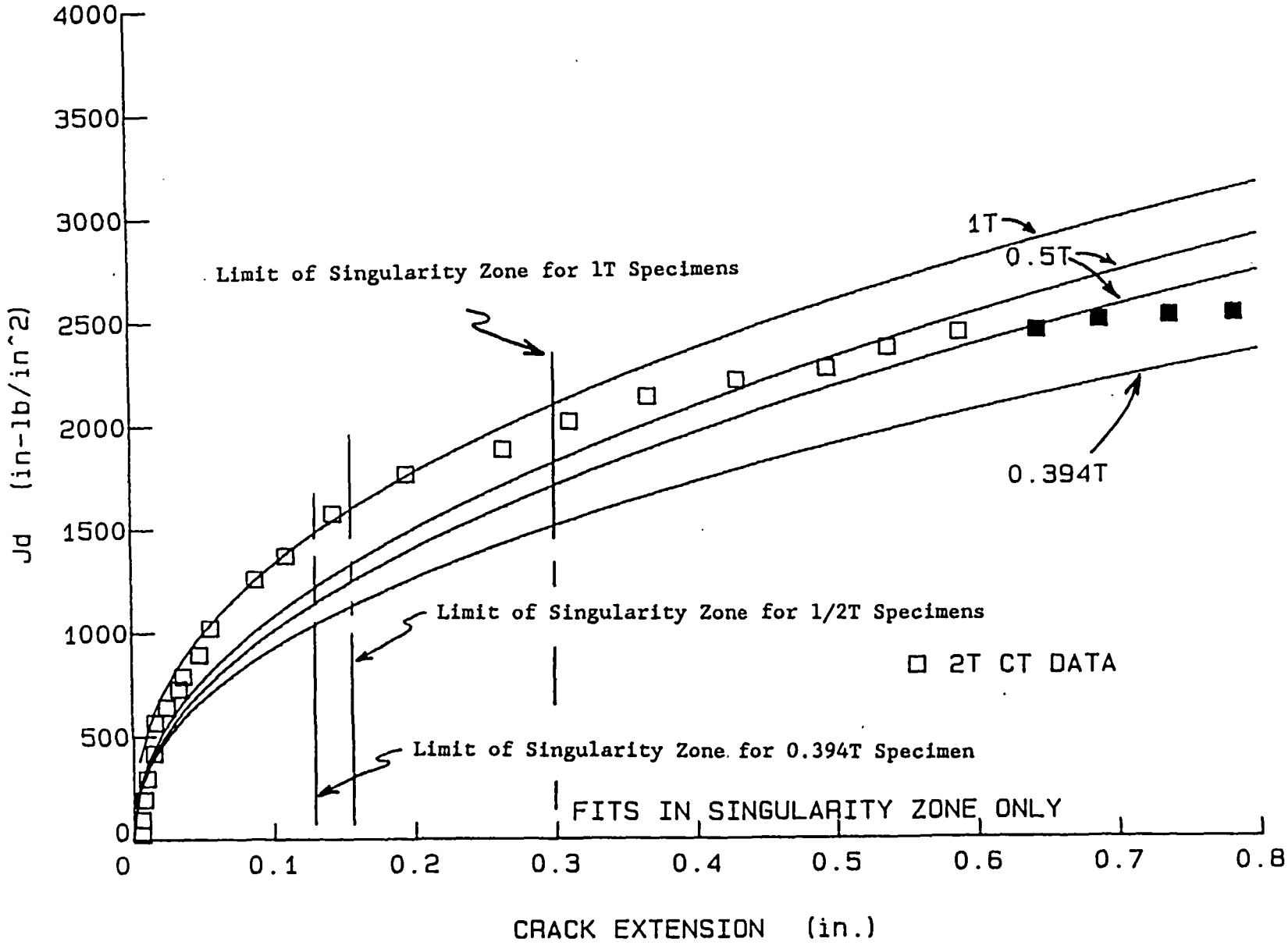

Figure 3 - Extrapolations on Small Specimen J-R Curves - Linde-80 Welds

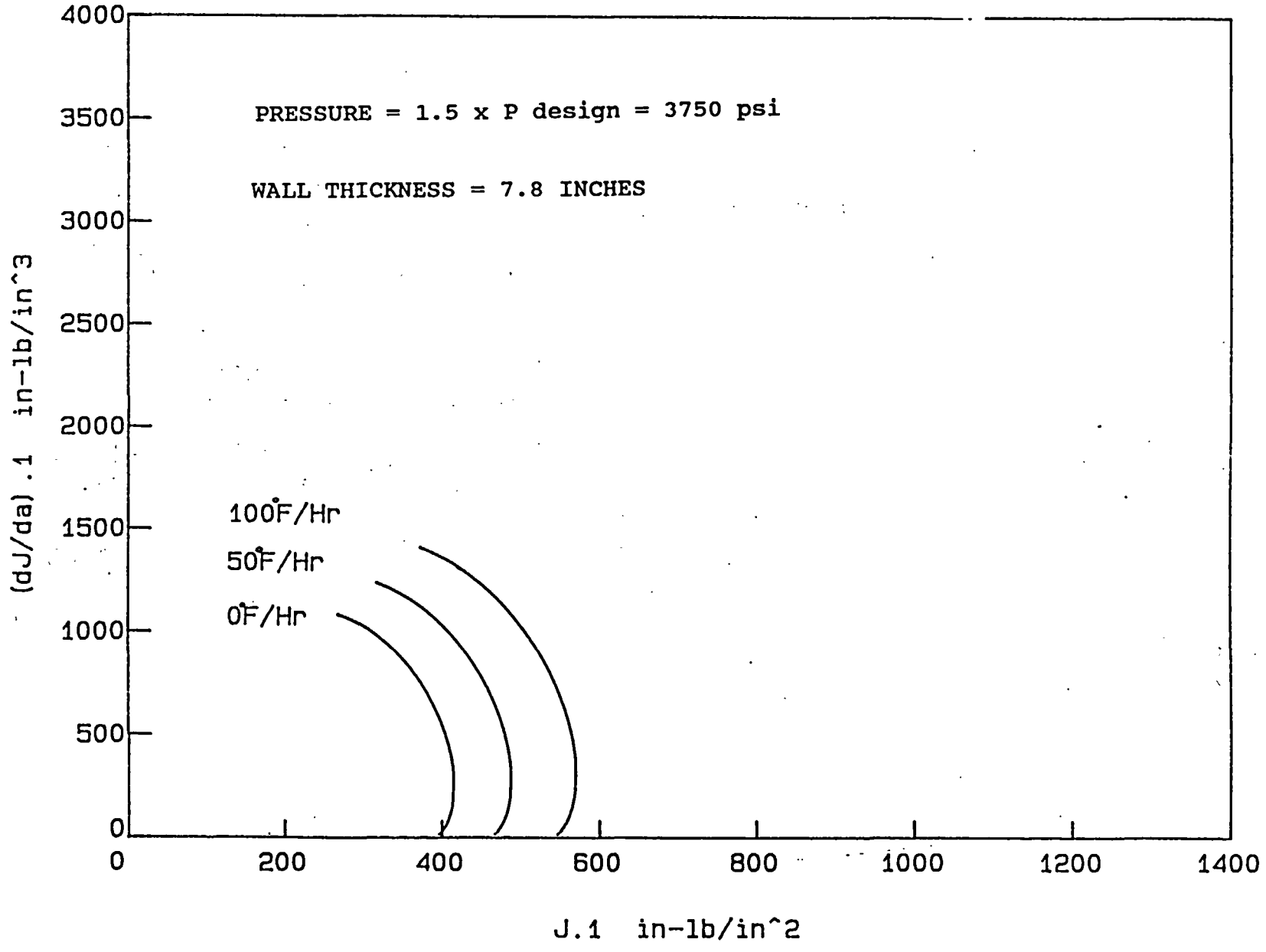

Figure 4 - Fracture Driving Force Diagram for Tearing Instability Analysis Showing Curves for Three Separate Cooldown Rates

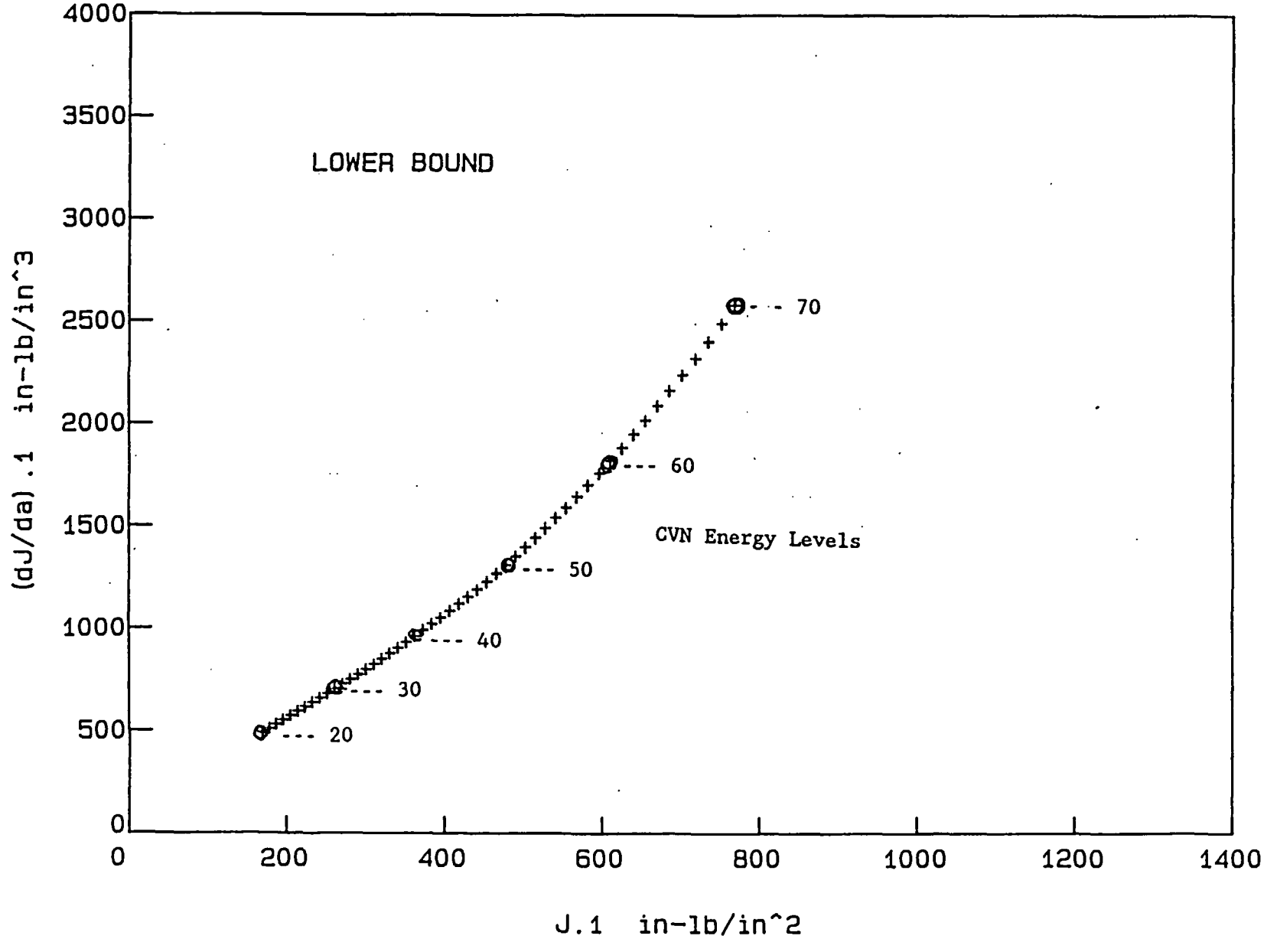

Figure 5 - Lower Bound J-CVN Correlation for Low Upper Shelf Weld Metal [EPRI, 1989]

POWER REACTOR EMBRITTLEMENT DATA BASE*

F. B. K. Kam, F. W. Stallmann, and J. A. Wang
Oak Ridge National Laboratory
Oak Ridge, Tennessee 37831

INTRODUCTION

Regulatory and research evaluations of embrittlement prediction models and of vessel integrity under load can be greatly expedited by the use of a well-designed, computerized embrittlement data base. The Power Reactor Embrittlement Data Base (PR-EDB) is a comprehensive collection of data from surveillance reports and other published reports of commercial nuclear reactors. The uses of the data base require that as many different data as available are collected from as many sources as possible with complete references and that subsets of relevant data can be easily retrieved and processed.

The objectives of this NRC-sponsored program are the following:

1. to compile and to verify the quality of the PR-EDB;

2. to provide user-friendly software to access and process the data;

3. to explore or confirm embrittlement prediction models; and

4. to interact with standards organizations to provide the technical bases for voluntary consensus standards that can be used in regulatory guides, standard review plans, and codes.

To achieve these goals, the data base architecture was designed after much discussion and planning with prospective users, namely, material scientists and members of the research staff.

The current compilation of the PR-EDB (Version 1) contains results from surveillance capsule reports of 78 reactors with 381 data points for 110 different irradiated base materials (plates and forging) and 161 data points for 79 different welds. Results from heat-affected zone materials are also listed. Menu-driven software programs have been written to facilitate maintenance, processing, and evaluations of the data. The time and effort required to process and evaluate different types of data in the PR-EDB have been drastically reduced from previous data bases.

*Research sponsored by the Office of Nuclear Regulatory Research, Division of Engineering, U.S. Nuclear Regulatory Commission under interagency Agreement DOE 1886804158 with the U.S. Department of Energy under contract De-AC05-84OR21400 with Martin Marietta Energy Systems, Inc.

The PR-EDB is designed for use at any personal computer that runs under the DOS system. This feature makes its use independent from large mainframe systems and provides better protection against data corruption and breaches of security than is possible in a centralized system in which many customers have access. Updates will be issued periodically to authorized users. The data files in the PR-EDB are in dBASE format and can be accessed with any version of dBASE or compatible software, such as Clipper. A customized software package that handles most routine tasks has been distributed with the data base and will also be periodically updated.

The Electric Power Research Institute (EPRI), reactor vendors, and utilities are in the process of providing back-up quality assurance checks of PR-EDB and will be supplementing the data base with additional data and documentation. Also EPRI, the BWR-OG Supplemental Material Surveillance Committee, and General Electric have agreed to release the boiling water reactor data for insertion into the PR-EDB. This effort and coordination with the NRC research staff, EPRI, and industry have led to the adoption of PR-EDB as the basis for an industry-wide data base by the EPRI Reactor Vessel Embrittlement Management Project.

DESIGN AND PROCEDURES

The design philosophy behind the PR-EDB is to collect the data in many, relatively small data files that closely mirror the data formats in the surveillance reports and other data sources. This is the main difference from earlier data bases, such as the ones published by MPC, which provide, essentially, one single table. The types of data that will be collected in such a table are predetermined, and each row in the table contains an entry for every data type, leading to a large number of empty entries and duplications. The main problem with this approach is that it requires a major redesign whenever new types of data are to be added to the data base. It is also fairly difficult to accommodate in such a structure multiple determinations of the same quantity, such as chemistry, and to provide complete references, if the data that are combined in the same row come from different reports. In the PR-EDB there is a different input file (raw data file) for each type of data, and the data are transcribed to the appropriate input file directly from the given source material preserving most of the original format, such as units. New types of data can be easily accommodated by simply creating a new file without disturbing the existing ones. Different determinations of the same quantity are simply added as new records and each record is referenced to its source document including page number(s). All data are entered as "characters" (i.e., no numerical format needs to be specified, and special notations such as <0.001 can be accommodated). Blank spaces indicate missing data.

In order to connect data from different files and to identify different determinations of the same quantity, unique "key identifiers" are assigned to materials and reactors. Figures 1 and 2 give a rough overview over the types of data contained in the PR-EDB and how they are connected with the material and reactor keys. In addition, each data set contains a reference identifier that identifies the source of the data. A complete bibliographic listing for each reference identifier is given in a reference file containing author, title,

that identifies the source of the data. A complete bibliographic listing for each reference identifier is given in a reference file containing author, title, report number, and time of publication. Extreme care must be exercised in assigning the correct key identifier, otherwise connections between data from different files cannot be made or are made incorrectly. The exacting standards imposed in this way have the additional advantage of repeated cross-checking which reveals many mistakes that had eluded direct proofreading.

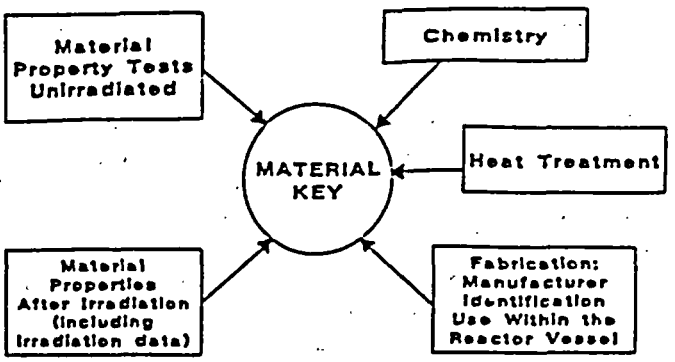

Fig. 1. Data related to the material key identifier in the PR-EDB.

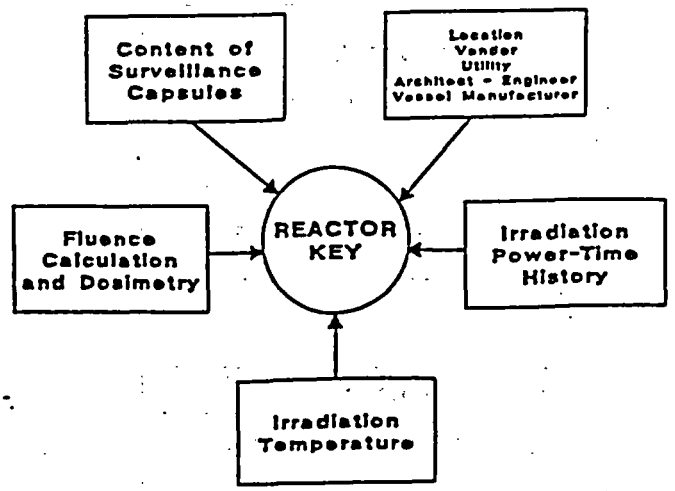

Fig. 2. Data related to the reactor key identifier in the PR-EDB.

Conventional proofreading is, of course, applied to all data entries after transcription from the source documents. Additional checks for consistency are made by cross-linking the different raw data files with each other. Mistakes are also frequently detected when the data are processed and analyzed for specific applications, such as the ones mentioned in the section on results. As with any good tool, the PR-EDB improves with use, which in turn requires that such use is encouraged by fast and friendly software. In addition to the in-house data checking, a comprehensive review of the PR-EDB is presently being done by EPRI. Corrected and updated versions of the PR-EDB will be released periodically. Records of all changes and additions are kept in our files. Also, copies of all source documents are collected in our special library.

For any specific application, the data from the raw data files are selected, combined, and put into tables or graphs. Often the data are fitted to a particular model, such as the hyperbolic tangent function, which is used to determine transition temperature and upper shelf energy from a set of Charpy impact tests. To provide the necessary software is a very important part of the PR-EDB program because data alone are useless without convenient tools to process them. Details will be discussed in the section on software. A schematic overview of the data flow in the PR-EDB is given in Fig. 3.

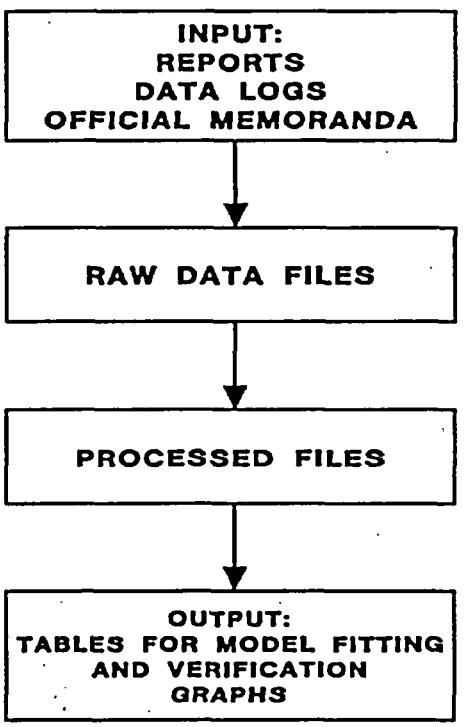

Fig. 3. Data flow in the PR-EDB.

SOFTWARE

All raw data files in the PR-EDB are in dBASE format and can be processed with any version of the original Ashton-Tate dBASE software or any compatible processor, such as Clipper. The latter was used to write a custom-tailored software package that provides the tools for many frequently performed processing steps. The program is menu-driven, that is, the user selects a particular processing step from a number of options displayed on the screen. This minimizes the learning process but is, by its nature, restricted to the more commonly used procedures. Continuing software development will increase the number of choices whenever new applications arise and after feedback from users. Processes that are not covered by the custom software can always be handled by a sequence of dBASE commands (if the user has the necessary expertise).

The following tasks can be performed by the custom software:

1. retrieve and select data from any data files;

2. display selected data to screen, printer, or graph;

3. perform calculations for any combination of data and store results;

4. rearrange data in any specified manner;

5. fit sets of raw Charpy data to hyperbolic tangent functions; and

6. select unique values from multiple determinations of the same quantity (e.g., copper content from several chemistry determinations) and combine selected unique data into special-purpose processed files.

Step 6 has not yet been released; however, it is operational and has been used to obtain some of the results listed in the next section.

RESULTS

The computerized PR-EDB and associated software have been successfully applied to the following three evaluations:

1. *Analysis of the A302B and A533B Standard Reference Materials in Surveillance Capsules of Commercial Power Reactors*, NUREG/CR-4947 (Figs. 4 and 5);
2. *Comparison of Surveillance Data in PR-EDB with "Trend Curves" in Regulatory Guide* 1.99, Revision 2 (Figs. 6 and 7); and
3. Comparison of the increase in the brittle-to-ductile transition temperature and the reduction in the Charpy-V upper-shelf energy for specimens fabricated in the LT orientation with those in the TL orientation. The data contain only pairs with the same fluence in the same capsule (Figs. 8 and 9).

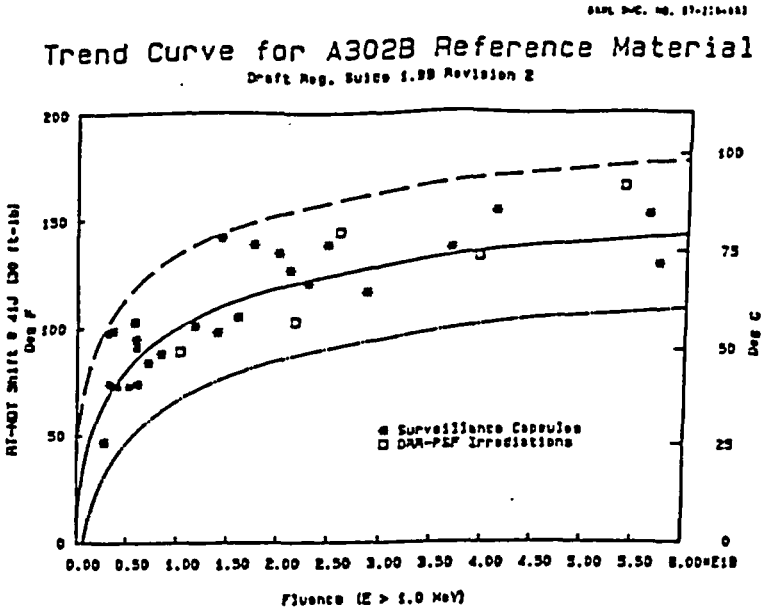

Fig. 4. Embrittlement of the A302B reference material relative to the draft Regulatory Guide 1.99, Rev. 2. The upper and lower curves are the 34°F uncertainty bounds (2σ) specified by Regulatory Guide 1.99.

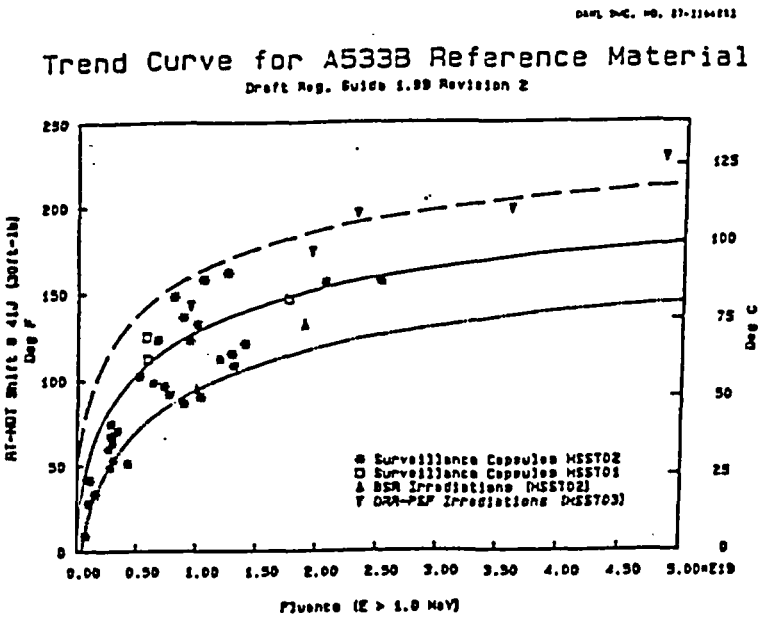

Fig. 5. Embrittlement of the A533B reference material relative to the draft Regulatory Guide 1.99, Rev. 2. The values for HSST01 and HSST03 plates are adjusted relative to HSST02 plate to account for differences in chemistry. The upper and lower curves are the 34°F uncertainty bounds (2σ) specified by Regulatory Guide 1.99.

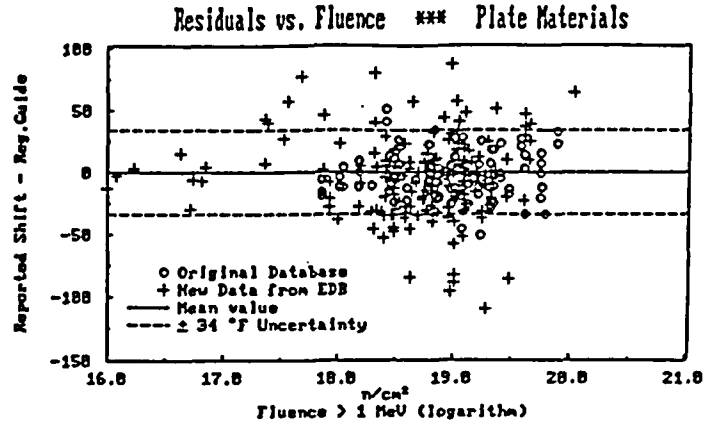

Fig. 6. Comparison of results from surveillance reports (*plate material*) with the trend curves as given in Regulatory Guide 1.99, Rev. 2. The new data show larger scatter than the original data from which the Regulatory Guide trend curve was obtained, but the scatter appears to be purely random.

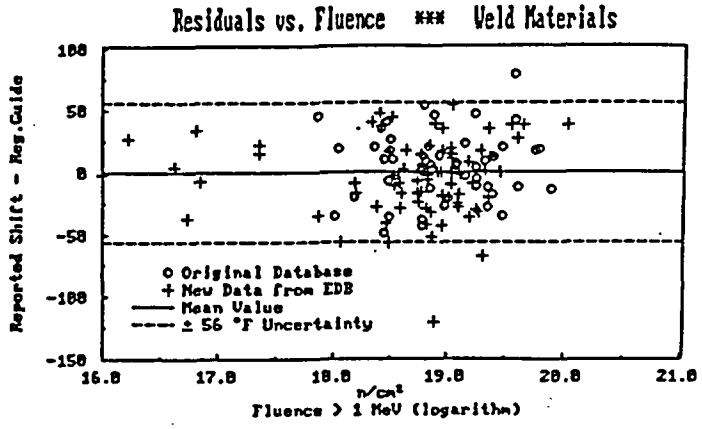

Fig. 7. Comparison of results from surveillance reports (*weld materials*) with the trend curves as given in Regulatory Guide 1.99, Rev. 2. The scatter of the new data is of the same magnitude as that of the original data and, as in Fig. 6, purely random.

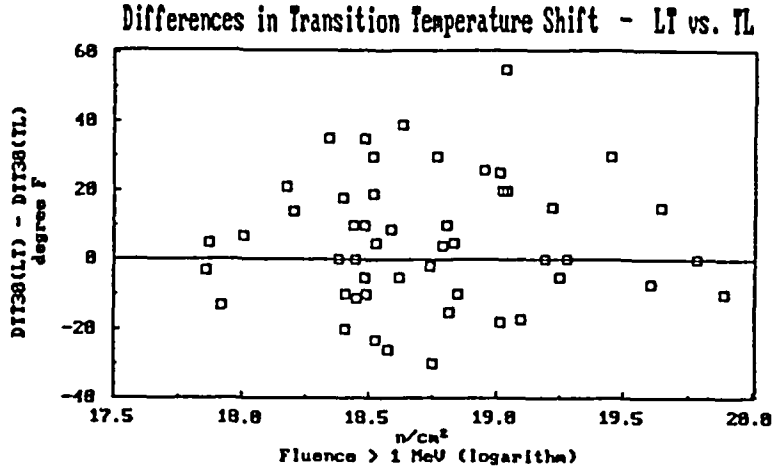

Fig. 8. Plot of results of a study to determine whether the sensitivity against radiation damage depends on the orientation of the test specimen. [The answer appears to be *negative for transition temperature shift* since the differences show no discernible bias although the scatter is fairly large.]

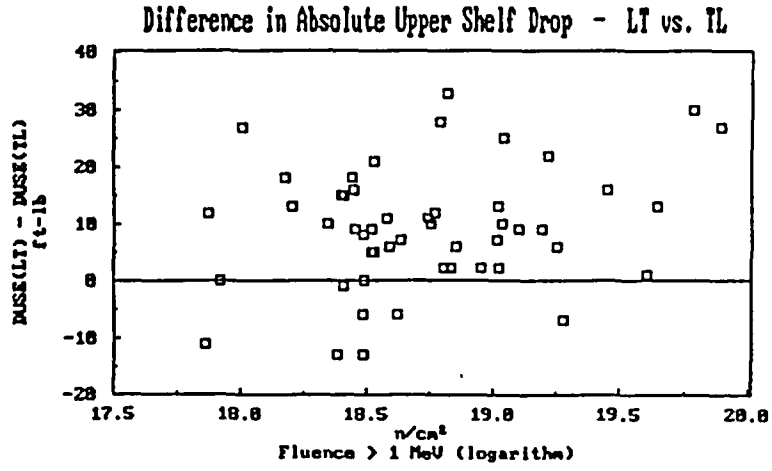

Fig. 9. Plot of results of a study to determine whether the sensitivity against radiation damage depends on the orientation of the test specimen. [Here a *bias can clearly be seen, indicating a smaller upper-shelf drop* in the average for the TL as compared to the LT orientation.]

FUTURE

The Embrittlement Data Base is designed as a continuing program. This means first of all that any data from new surveillance reports will be added as soon as they are in our possession. In addition, a vast number of test reactor data from the MPC data base, the HSST program, the ORR-PSF program, and experiments at KFA, Juelich, Germany, have been collected and will be integrated to a larger Embrittlement Data Base (EDB). Also collected, but not yet officially integrated, are data from CT and WOL specimen in the surveillance capsules and results from instrumented Charpy tests, including digitized graphic representations of instrumented curves. Detailed results from reactor physics calculations, given in 20 to 47 energy groups, are also available as well as power time histories of many reactors. Such data are important for the study of the dependency of radiation damage on fluence spectra and fluence rates. Only through continuing efforts in the maintenance and updating of data as well as software can the Embrittlement Data Base preclude obsolescence and continue to remain the effective tool for which it was designed.

ACCELERATED IRRADIATION TEST OF GUNDREMMINGEN REACTOR VESSEL TREPAN MATERIAL

J. R. Hawthorne

Materials Engineering Associates, Inc.
9700-B Martin Luther King, Jr. Hwy.
Lanham, Maryland 20706

Abstract

Initial mechanical properties tests of beltline material trepanned from the decommissioned KRB-A pressure vessel and archive material irradiated in the UBR test reactor revealed a major anomaly in relative radiation embrittlement sensitivity. Poor correspondence of material behavior in test vs. power reactor environments was observed for the weak test orientation (ASTM L-C) whereas correspondence was good for the strong orientation (ASTM C-L). To resolve the anomaly directly, Charpy-V specimens from a low (essentially-nil) fluence region of the vessel were irradiated together with archive material at 279°C in the UBR test reactor.

Properties tests before UBR irradiation revealed a significant difference in 41-J transition temperature and upper shelf energy level between the materials. However, the materials exhibited essentially the same radiation embrittlement sensitivity (both orientations), proving that the anomaly is not due to a basic difference in material irradiation resistances. Possible causes of the original anomaly and the significance to NRC Regulatory Guide 1.99 are discussed.

Introduction

The 250-MW boiling water Gundremmingen Reactor, KRB-A, located in the Federal Republic of Germany (FRG) was decommissioned by the utility owners in 1977. Prior to its decommissioning, the reactor vessel operated at a nominal temperature of ~288°C and had an inner wall fluence of about 3×10^{18} n/cm^2, E > 1 MeV (Ref. 1). In 1984, a remnant of a forging believed to be from the vessel construction was located by the U. S. Nuclear Regulatory Commission (NRC). The availability of this "archive" material and the service-degraded vessel material presented a unique opportunity for qualifying the effects of long-term irradiation on a prototypic reactor pressure vessel (RPV) steel. Specifically, the materials allowed direct tests of the effect of fluence rate (dose rate) on the degradation of Charpy-V (C_v) notch ductility and fracture toughness properties and the elevation of yield strength by neutron radiation. In addition, the materials permitted verification tests of present prediction methods for radiation-induced embrittlement (Ref. 2,3) and the attenuation of radiation effects through the vessel thickness (Ref. 2). The NRC subsequently put in place a joint USA/FRG program to (a) investigate the vessel's properties and (b) conduct accelerated irradiation tests of the archive material for power vs. test reactor comparisons. Materials Engineering Associates (MEA) and Material Pruefungsanstalt (MPA) are the lead laboratories for the two countries, respectively.

Qualification tests of the archive material located in storage at the General Electric Company provided evidence which, when coupled with vessel documentation, led to conclusions by MEA and MPA that (a) the base metal and Vessel Forging No. 7.1 were from the same steel melt and (b) the base metal is representative of the vessel forging as first placed in service (Ref. 4). This material was in the form of two circumferentially-welded ring segments; the weld is suspected of being a portion of the weld made for the reactor vessel surveillance program. One ring segment, approximately 119-mm thick and weighing about 1450 kg, was used for the primary MEA investigations of irradiation behavior. It is identified in this report as the Code GEB material. The chemical composition of the GEB base material and that of the vessel's Forging Ring No. 7 are given in Table 1 and are identical for practical purposes. Composition test results for the base metal used in the reactor surveillance program also are indicated. The reactor surveillance program was in place at the commencement of initial commercial operations; however, only ASTM C-L orientation base metal specimens (strong orientation) were included in the surveillance capsules along with the weld metal and heat affected zone (HAZ) specimens. This was the recommendation of ASTM Practice E 185 in the early 1960's.

The Anomaly

Tests of the irradiated trepan material by MPA and initial tests of UBR test reactor-irradiated archive material by MEA provided a major anomaly (Ref. 1,4). The archive material was in the form of ASTM L-C orientation (weak) C_v specimens only; the specimens had been irradiated to ~8.8×10^{18} n/cm^2, E > 1 MeV, at 288°C. These exposure parameters reflect FRG best estimates of the vessel operating conditions and its end-of-life (EOL) exposure at program initiation in 1984. (Both parameters were later revised downward based on new information supplied to MPA.) As illustrated in Figure 1, the service-induced embrittlement appeared to be much greater than

Table 1 Chemical Compositions of Archive Material GEB, KRB-A Vessel Trepan G and Surveillance Program Base Metal (Ref. 4)

Material	Composition (wt-%)												
	C	Mn	Si	P	S	Ni	Cr	Mo	Cu	Hs	Sn	Sb	V
GEB (Side 2) (MEA)	0.24	0.71	0.21	0.015	0.018	0.79	0.37	0.67	0.15	0.021	0.021	0.008	0.031
KRB-A (Trepan G) (MPA)[a]	0.22	0.71	0.22	0.013	0.012	0.75	0.38	0.62	0.16	0.02	0.03	<0.01	0.04
GEB (Side 1) (MPA)[a]	0.23	0.71	0.23	0.013	0.012	0.75	0.38	0.65	0.16	0.02	0.03	<0.01	0.04
Surveillance[b] Base Metal (MEA)	0.23	0.71	0.25	0.023	0.016	0.85	0.37	0.64	0.16	—	—	—	—

[a] MPA composition determination by Quantovac Spectroscopy.

[b] Average of tests of three surveillance specimens.

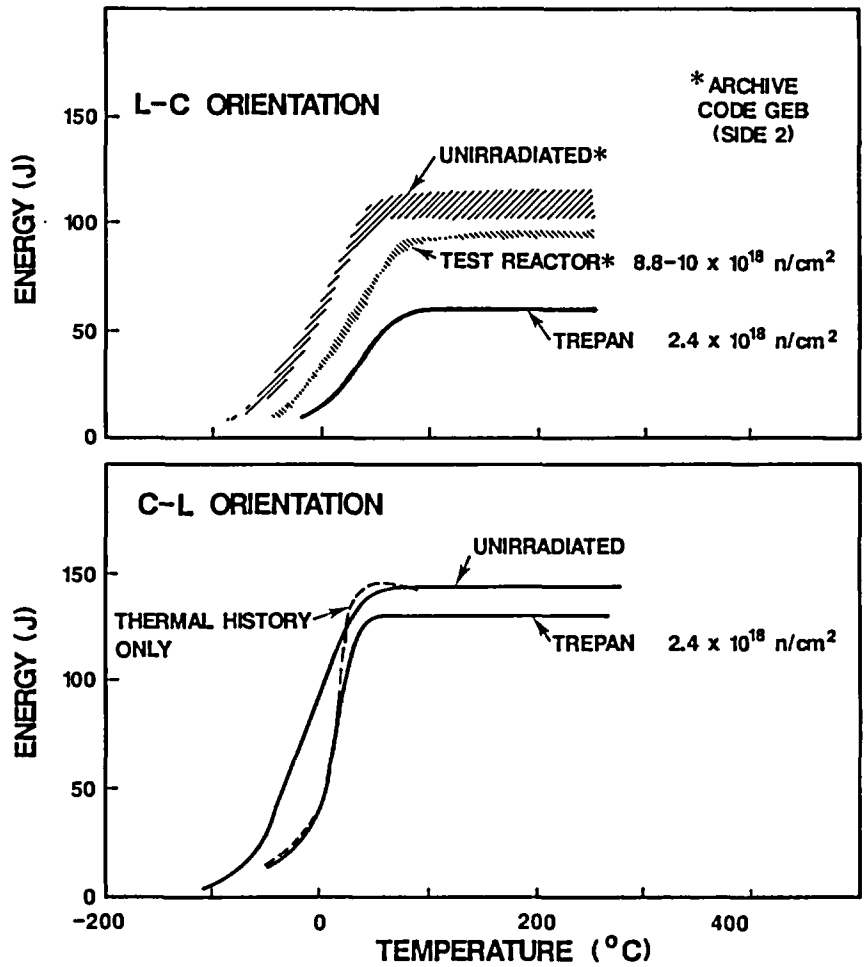

Fig. 1 Charpy-V notch ductility of KRB-A vessel material before and after irradiation service. Data from accelerated (test reactor) irradiations of the archive material by MEA and the Harwell Laboratory are indicated in the upper graph by the trend band; the dashed line in the lower graph shows the effect of long-term thermal conditioning (years) without irradiation (Ref. 1).

that produced by the UBR irradiation. Notice that the fluence to the trepan specimens (MPA determination) was approximately 2.4 x 10^{18} n/cm^2 or about one-third that received by the archive material. A second observation suggested by the data is that the trepan C-L orientation suffered much less embrittlement than the L-C orientation. The cited L-C orientation vs. C-L orientation data comparison for relative induced-embrittlement, constitutes the anomalous behavior.

Prior experience in test reactor irradiation studies and the few L-C vs. C-L orientation data comparisons available from RPV surveillance programs (both orientations were in the same capsule) have led investigators to expect roughly-comparable elevations in 41-J transition temperature. Table 2, an excerpt from the NRC embrittlement data base (Ref. 5) lists many of the comparison data available from surveillance. A companion expectation is a greater "absolute" reduction in upper shelf energy level by that orientation having the higher preirradiation C_v energy level, that is, the "strong" test orientation. The preirradiation difference must be pronounced for this observation. This is one reason that estimation procedures of NRC Regulatory Guide 1.99 for the upper shelf reduction is in terms of percentage decrease rather than an absolute change for a given fluence. A follow-on 288°C UBR irradiation of the archive material using both L-C and C-L orientation specimens, removed from the 1/8T thickness location, demonstrated that the GEB material conforms to both expectations (see Fig. 2, Ref. 4). The target fluence was 2.7 x 10^{18} n/cm^2 to better approximate the vessel inner wall (1/8 T) condition.

Mechanistic explanations are not at hand to explain the suggested difference in radiation sensitivity between test orientations. Embrittlement mechanisms identified from empirical data and experimental tests, in combination with theory by-in-large involve precipitation phenomena either enhanced or induced by irradiation (Ref. 6-11). Primarily the scenarios involve copper-rich precipitates or phosphorus-rich precipitates. A precipitation phenomenon would not explain the test orientation dependence (directionality) of radiation embrittlement sensitivity suggested by the KRB-A trepan data (Fig. 1).

The directionality, if verified, could have a major impact on the application of Regulatory Guide 1.99 and the growing consideration of possible plant lifetime extensions (PLEX). To verify (or disprove) the anomaly, the present irradiation test was proposed.

Approach

The approach centers on the simultaneous irradiation of archive and trepan material specimens in one UBR assembly. The target irradiation temperature (279°C) and the fluence level (2.6 x 10^{18} n/cm^2) were to match, as closely as practical, that of the vessel trepans at their 1/8T location. A key aspect of the approach was the use of samples from outer layers of the trepans which had received a considerably lower fluence than the inner layers in prior service. The samples for the UBR assembly had received 8-9 x 10^{17} n/cm^2 beforehand. MPA kindly provided the samples in the form of finish-machined C_v specimens, under the auspices of the continuing USA/FRG joint program.

Table 2 Comparison of LT vs. TL Orientation Embrittlement Data from RPV Surveillance (Ref. 5)

Entry	C_v Upper Shelf Energy Reduction[a] in ft-lb		
	LT Orientation	TL Orientation	Difference (LT-TL)
1	24	11	13
2	14	25	-11
3	24	17	7
4	35	2	33
5	20	5	15
6	19	3	16
7	24	18	6
8	30	8	22
9	26	10	16
10	12	0	12
11	36	26	10
12	28	19	9
13	22	9	13
14	33	22	11
15	71	44	27
16	40	12	28
17	25	10	15
18	0	13	-13
19	3	-19	22
20	22	-6	28
21	20	12	8
22	25	13	12
23	60	30	30
24	43	18	25
25	16	7	9
26	14	13	1
27	23	10	13
28	17	15	2
29	33	22	11
30	15	2	13
31	18	0	18
32	24	14	10
33	16	6	10
34	4	11	-7
35	8	14	-6
36	14	8	6

[a] Fluence range represented is 7.27×10^{17} to 7.85×10^{19} n/cm^2, E > 1 MeV.

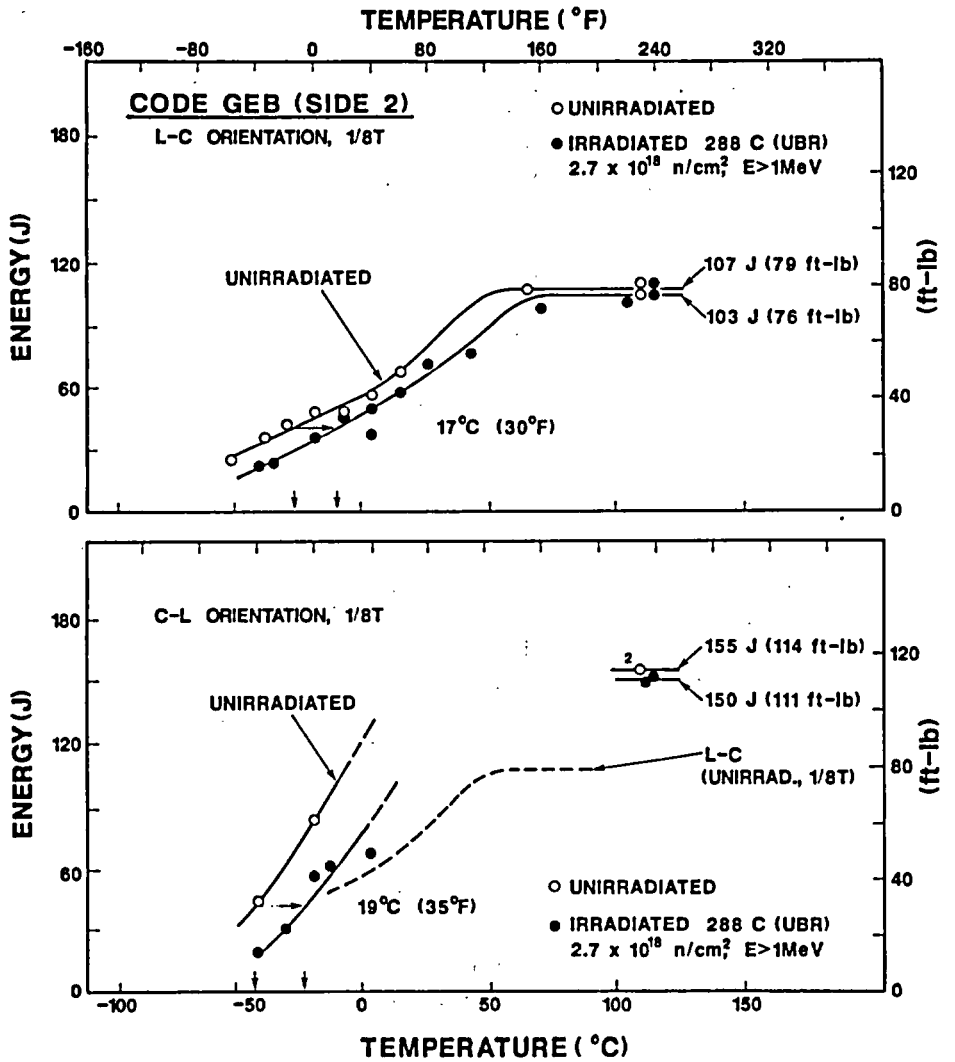

Fig. 2 Embrittlement of the archive material by a fluence matching that received by the KRB-A vessel in service (MEA Experiment Assembly UBR-78) (Ref. 4).

Material Sampling For The UBR Irradiation Test

Trepan Material

The specimens for UBR-irradiation were cut from Trepan P as illustrated in Figure 3. Layer 10 and 11 provided the samples for the L-C orientation assessments; Layers 8, 9, 10 and 11 provided the samples for the C-L orientation assessments. The fluences received by the various layers from KRB-A service are listed in Table 3. Table 3 also gives the fluences received by these layers in the companion Trepans C, D and G from which samples were taken earlier for MPA's reference condition tests. In this report, the reference condition of Forging Ring No. 7.1 is that condition at the time of the KRB-A decommissioning.

The diameter of the trepans was 107 mm. The trepans were cut from the reactor vessel in a 3 (vertical) x 4 (circumferential) array, at a location somewhat below the reactor mid-plane. Trepan C and D were in the row nearest the reactor mid-plane; Trepan G was in the middle row; Trepan P was in the row furthest from the mid-plane. The specimens were removed by electrical-discharge machining. The V-notch was produced by a milling machine cutter; no further machining was required.

Archive Material

C_v samples and tension test samples were cut for both irradiation tests and check tests. The specimens were saw cut from the 1/8-T thickness layer indexed to the original inner diameter, that is, the as-forged surface. Samples for check tests of the unirradiated condition were taken from the same forging location as samples for the irradiation. As will be evident below, the check test data agree very well with the initial forging qualification data (Ref. 4).

Material Irradiation

The specimens were irradiated in MEA Assembly UBR-83A in the UBR B-4 fuel lattice position. The irradiation time was 81.0 hours. Irradiation temperatures were monitored continuously with thermocouples welded to the specimen mid-lengths and were controlled externally by automatic instrumentation.

To preclude any exposure condition differences, the specimens of the two materials were randomized within the assembly. Iron, nickel, copper and titanium dosimeter wires were placed within the specimen array and arranged over its length for fast neutron fluence (n/cm^2, $E > 1$ MeV) and fluence-gradient determinations. Two ^{238}U neutron dosimeters were also placed within the specimen array. For thermal fluence determinations, Co-Al and Ag-Al dosimeter wires were used. Fluence values ($E > 1$ MeV) reported here are based on the calculated neutron energy spectrum for the irradiation facility (Ref. 12,13,14). The values can be converted to displacements per atom (dpa) exposure values by:

$$\text{dpa} = \text{calculated spectrum fluence, } E > 1 \text{ MeV } (1.47 \times 10^{-21}) \qquad (1)$$

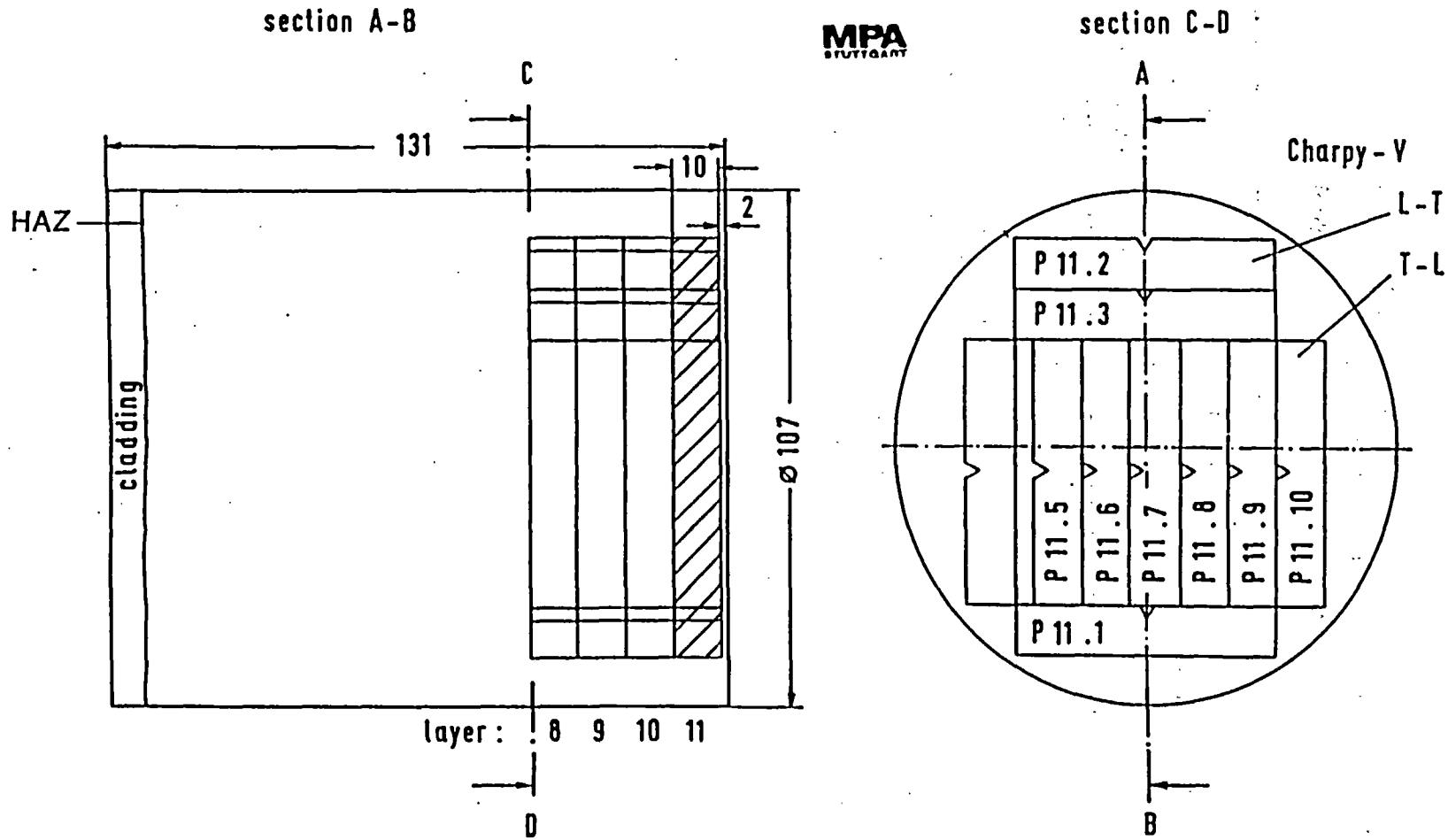

Fig. 3 Schematic illustration showing the Charpy-V specimen cutting plan for Trepan P. Not all of the specimens were irradiated in Experiment Assembly UBR-83A.

Table 3 Neutron Fluences received by Specimen Layers 8 to 11 of Trepans P, C, D and G in KRB-A Service (Courtesy MPA)

Specimen Layer	Neutron Fluence (n/cm^2, $E > 1$ MeV)			
	Trepan P[a]	Trepan C	Trepan D	Trepan G
8	1.202	1.356	1.448	1.285
9	1.047	1.179	1.261	1.118
10	0.906	1.022	1.081	0.969
11	0.782	0.882	0.942	0.836

[a] The UBR irradiation test involved L-C orientation samples from Layers 10 and 11 (only) and C-L orientation samples from Layers 8 to 11 of Trepan P.

The uncertainties in fluence rates from the iron, nickel and ^{238}U dosimetry are judged by the counting laboratory, EG&G Idaho, Inc. to be ±8, ±7 and ±5% for the 1 σ confidence level, respectively. These values do not include the uncertainties that would be associated with actual spectrum averaged cross-sections of the irradiation fields or with burnout of the reaction products of interest. The uncertainty in cross-sections from the neutron spectrum calculation is less than 15%.

Because the trepan specimens had a residual radioactivity from prior KRB-D service the irradiation assembly was final-fabricated on-site at the UBR which is located in the Buffalo Materials Research Center. A standard MEA irradiation assembly design nonetheless was used and standard MEA QA procedures were followed.

Postirradiation Testing

The C_V specimens were broken on a 407-J (300 ft-lb) capacity Tinius Olsen impact tester equipped with Dynatup instrumentation for recording applied load vs. time-of-fracture information during each test. The same machine was used by MEA for the irradiated, unirradiated and reference condition specimens. The machine was calibration-tested per ASTM Standard Method E 23 just before testing the present group of specimens (Ref. 15).

Results

Archive Material

Table 4 summarizes the results for the archive material and the trepan material. The C_V test data for the former are illustrated in Figure 4. The transition temperature elevations for the L-C and C-L orientations were, respectively, 20°C (35°F) and 17°C (30°F). Figure 5 compares the postirradiation data to that from the earlier irradiation test (UBR-78) at 288°C to the same nominal fluence. Excellent agreement is observed. UBR irradiations of L-C orientation samples of GEB2 at 275°C and 288°C to a much higher fluence, ~8.6 x 10^{18} n/cm^2, revealed an essentially-nil sensitivity of the material to irradiation temperature differences in this range (Ref. 4). In turn, the excellent agreement of the data found in Figure 5 confirms the high reproduceability of results from UBR irradiation tests. Only a slight difference in transition trend curve is discernable in the region between ~75 J (55 ft-lb) and the upper shelf regime. This may be simply a facet of the scatter pattern for the limited data available.

The observed reproduceability of postirradiation properties rules out the possibility (remote) that the anomaly under investigation is some manifestation of the UBR irradiation procedure or postirradiation test procedures. Good reproduceability of data with UBR irradiations has been shown by other RPV materials (Ref. 16).

Trepan Material

The L-C and C-L orientation data for the Trepan P material in Assembly UBR-83A are illustrated in Figure 6. Postirradiation data trends for the archive material from Figure 5 are also shown for comparison.

Table 4 Charpy-V Notch Ductility Determinations for Archive Material GEB and KRB-A Vessel Trepan Material Before and After UBR Irradiation

Material	Specimen Orientation[a]	UBR Exp.	C_v 41-J Temperature						C_v Upper Shelf Energy					
			Initial		Irradiated		Increase		Initial		Irradiated		Reduction	
			°C	°F	°C	°F	Δ°C	Δ°F	J	ft-lb	J	ft-lb	ΔJ	Δft-lb
Archive (GEB2)	L-C[b]	—	-29	-20	—	—	—	—	103	76	—	—	—	—
	L-C[c]	UBR-78	(-26)	(-15)	(-9)	(15)	(17)	(30)	(107)	(79)	(103)	(76)	(4)	(3)
	C-L[c]	UBR-78	(-40)	(-40)	(-21)	(-5)	(19)	(35)	(155)	(114)	(151)	(111)	(4)	(3)
	L-C[d]	UBR-83	-29	-20	-9	15	20	35	107	79	103	76	4	3
	C-L[d]	UBR-83	-40	-40	-23	-10	17	30	153	113	144	106	9	7
Trepan P (KRB-A)	L-C (8)[e]	—	21	70	—	—	—	—	80	59	—	—	—	—
	L-C (9)	—	23	73	—	—	—	—	83	61	—	—	—	—
	L-C (10)	—	18	65	—	—	—	—	85	63	—	—	—	—
	L-C (10,11)	UBR-83	18	65	29	85	11	20	85	63	80	59	5	4
	C-L (8)	—	-7	20	—	—	—	—	160	118	—	—	—	—
	C-L (9)	—	-9	15	—	—	—	—	157	116	—	—	—	—
	C-L (10)	—	-9	15	—	—	—	—	153	113	—	—	—	—
	C-L (8-11)	UBR-83	-9	15	4	40	14	25	153	113	134	99	19	14
Trepan P[f] (Indexed to GEB)	L-C (10,11)	UBR-83	-29	-20	29	85	58	105	107	79	80	59	27	20
	C-L (8-11)	UBR-83	-40	-40	4	40	44	80	153	113	134	99	19	14

[a] 1/8T thickness location unless noted.

[b] Specimen Set No. 1.

[c] Specimen Set No. 2.

[d] Specimen Set No. 3.

[e] Trepan thickness layer.

[f] Unirradiated Archive GEB (Side 2) vs. UBR-irradiated Trepan P.

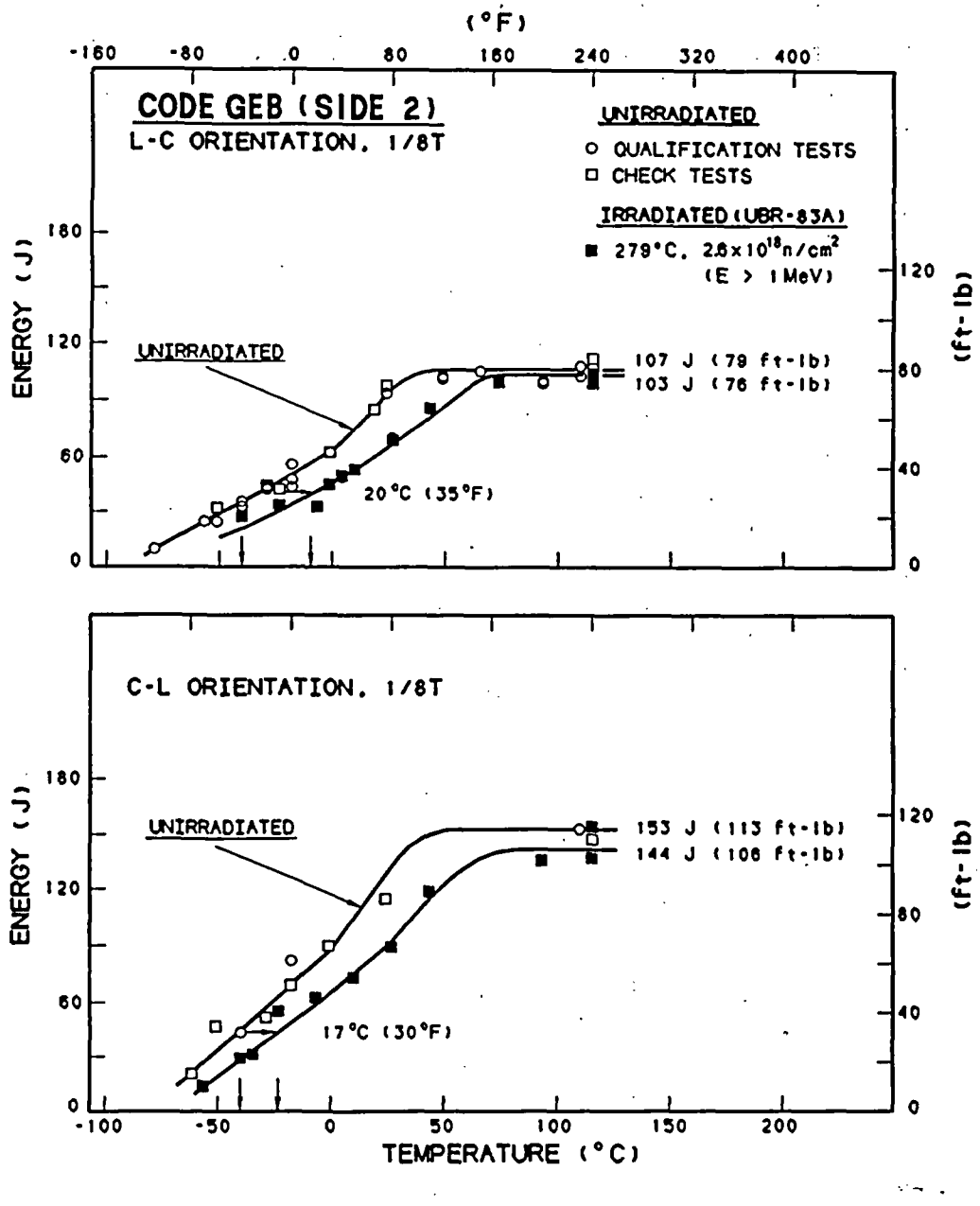

Fig. 4 Charpy-V notch ductility of the archive material before and after irradiation in Experiment Assembly UBR-83A. The unirradiated condition check test specimens and the specimens for irradiation were in close proximity to one another in the forging stock.

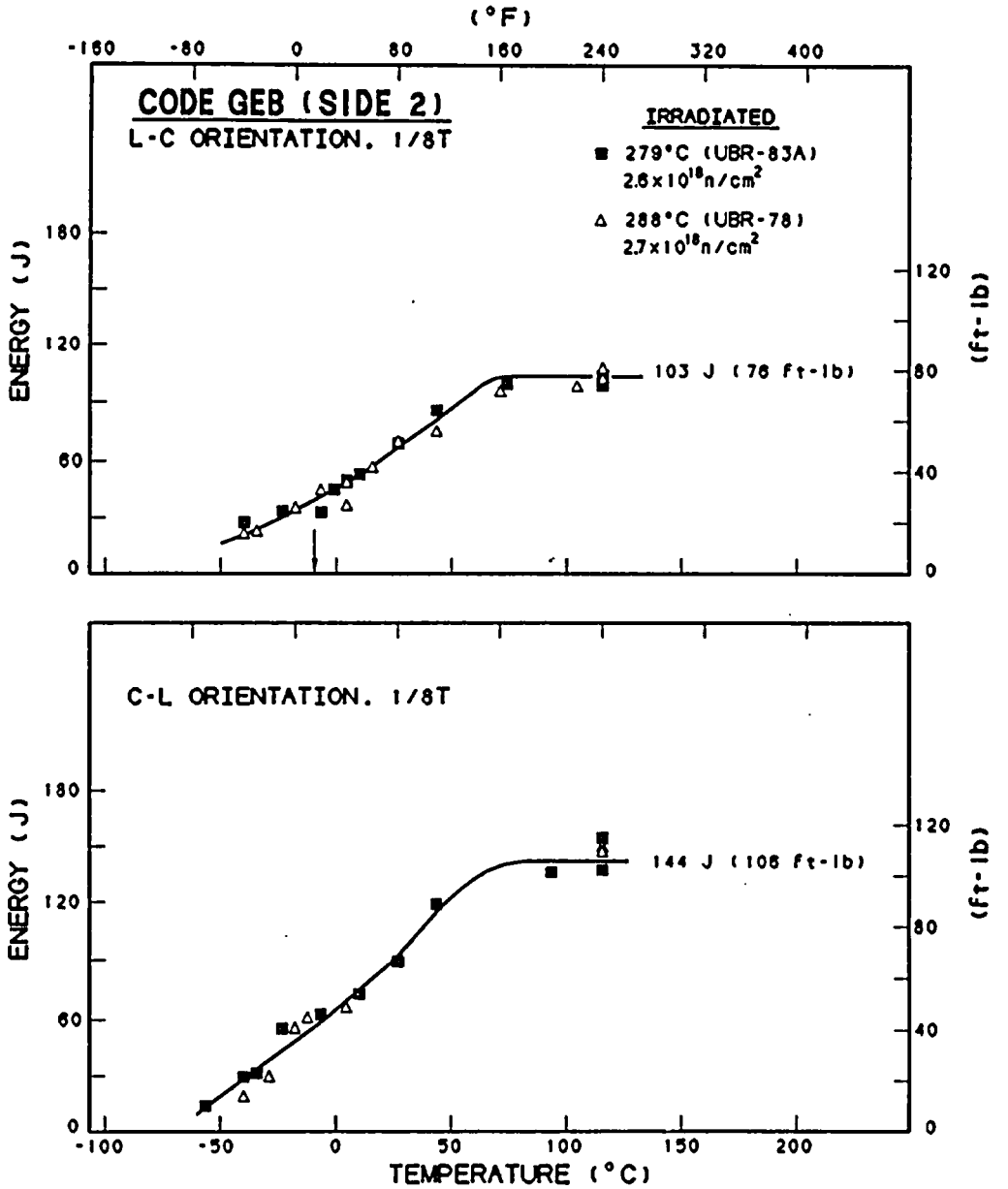

Fig. 5 Postirradiation Charpy-V data for the archive material from two UBR experiment assemblies showing the reproduceability of postirradiation properties. The irradiation temperature difference (279°C vs. 288°C) was shown not significant by other tests.

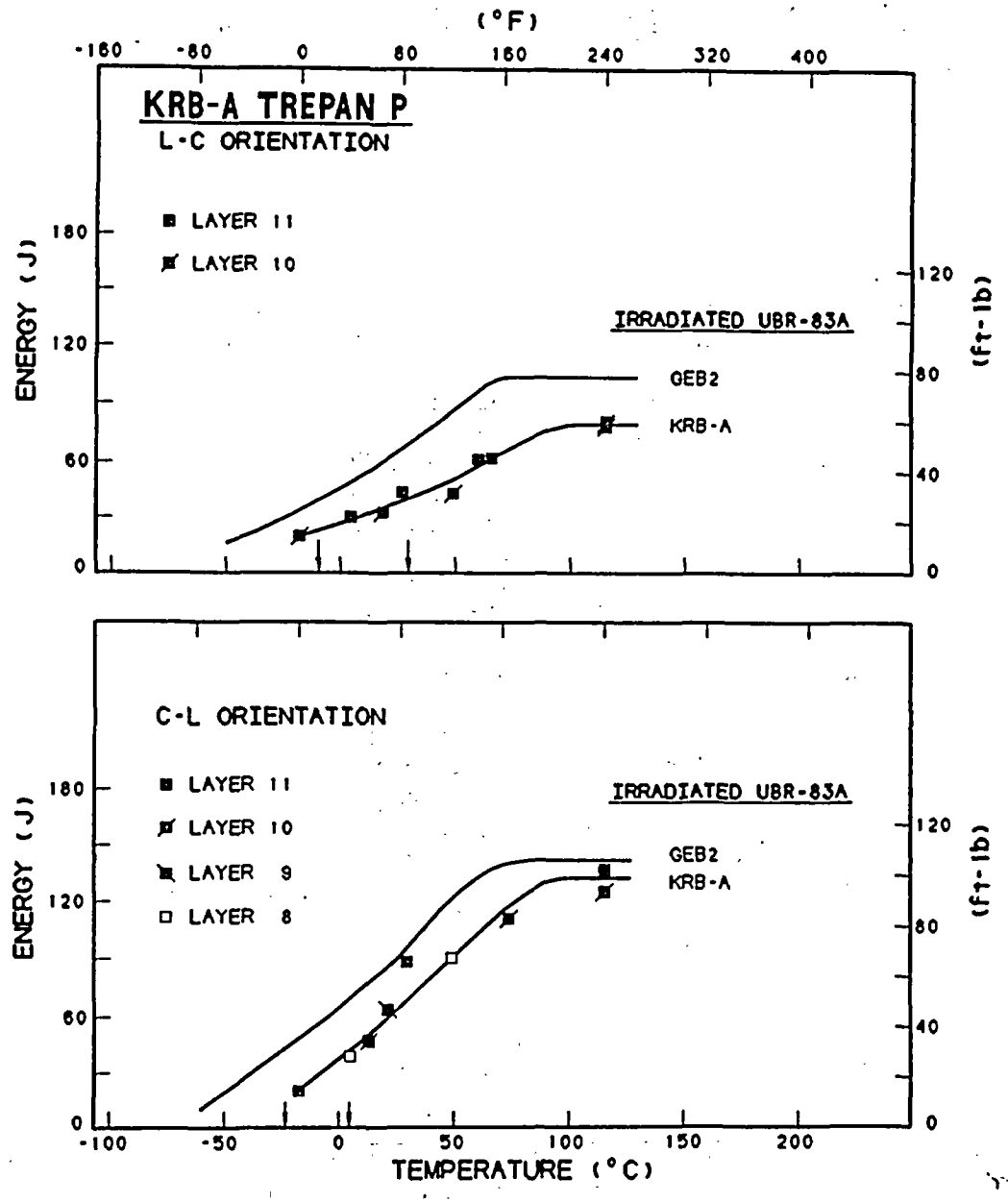

Fig. 6 Charpy-V notch ductility of the trepan material and the archive material after irradiation in Experiment Assembly UBR-83A.

Initial inspection of the trepan data reveals no particular difference in postirradiation notch ductility due to thickness location in the trepan or the associated service-related fluence. The extent of data scatter is small; only one postirradiation test point in each plot could be considered an outlier.

Trepan vs. Archive Material

The positions of the transition temperature curves for trepan vs. archive materials in Figure 6 mirror the data which originally suggested an anomaly. The trepan curves fall to the right and below the archive material curves which could be construed as a manifestation of a material radiation sensitivity difference. Also, the transition temperature elevation and the upper shelf reduction for the trepan L-C orientation is greater than those for the trepan C-L orientation. However, the indexing of the UBR-83A test results to the MPA data base for the reference condition, (tests of Trepans C, G and D) presents a different picture (Fig. 7). Such indexing indicates transition temperature elevations of only 11°C and 14°C for the L-C and C-L orientations, respectively, not the elevations of 58°C (105°F) and 44°C (80°F) found when the data are indexed to the preirradiation properties of the archive material (Fig. 6). Likewise, the difference in upper shelf energy reduction is 5 J, not 27 J for the L-C orientation. For the C-L orientation, an upper shelf reduction of 19 J is described by both indexing methods.

The 11°C and 14°C transition temperature elevations for the UBR irradiation of the trepan material agree well with the 20°C and 17°C transition temperature elevations found for the archive material. (The 9°C difference for the L-C orientation is considered not significant). The upper shelf energy reductions for the trepan material likewise agree well with those for the archive material. If the reasonable assumption is made that the properties of Trepan C, D and G represent well those of Trepan P, it can be concluded that the radiation embrittlement sensitivity of the trepan material, at least that of Layers 10 and 11 and quite possibly Layers 8 and 9, is the same as that of the 1/8T thickness location of the archive material for the accelerated-irradiation exposure case.

The difference in pre-UBR exposure properties of the trepan material vs. the archive material could stem from one or more of the following sources:

(1) Across-forging difference in unirradiated condition properties. The archive material represents one end of the forging while the trepan material depicts a location well-displaced (axially and/or circumferentially) from the archive material locus in the forging.

(2) An undocumented difference in material heat treatments, particularly in stress relief heat treatment(s) after welding. It can be envisaged that the duration of the heat treatment of the archive weldment made for the surveillance program is quite different from that of the vessel's Forging Ring No. 7.1 as placed in service.

(3) The long time-at-temperature of the vessel (years) during its service life. As noted in Figure 1, coupons of the archive material suspended in the vessel well away from the fuel core did show a significant change in transition temperature for the C-L orientation due to a temperature effect alone. The archive material was not similarly aged.

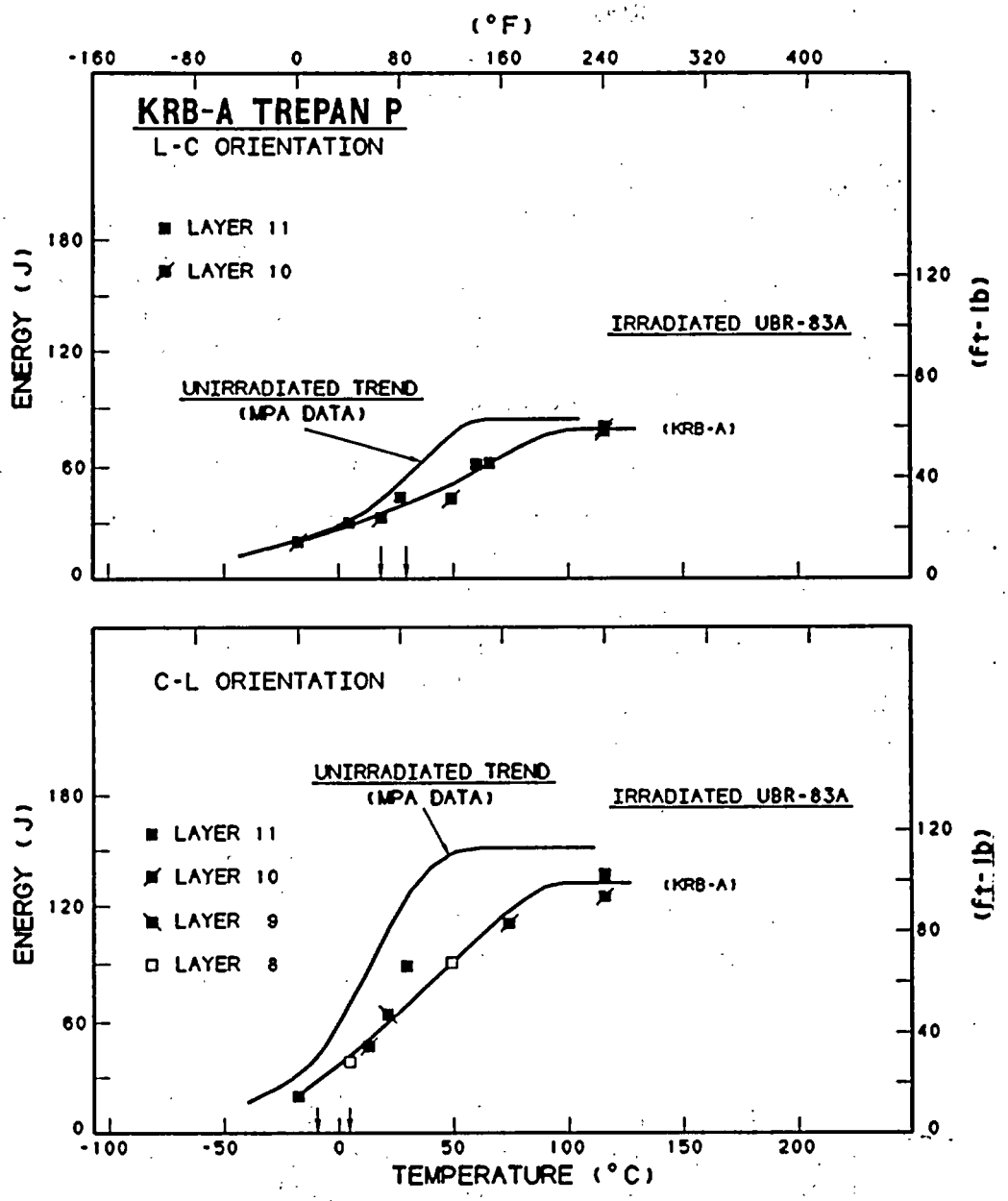

Fig. 7 Charpy-V notch ductility of the trepan material after irradiation in Experiment Assembly UBR-83A indexed to the post KRB-A service condition indicated by MPA test results.

(4) Contrary to the extensive evidence and archive material markings, the archive material was not from the same steel melt as the vessel's Forging Ring No. 7.1.

(5) Some aspect of trepan removel, specimen blanking or specimen machining altered the properties of the material.

The above possibilities are reviewed in the Discussion Section below relative to their potential impact on Regulatory Guide 1.99 applications and RPV surveillance programs. It is MEA's opinion that the first and third possibilities are the strongest in this case. Again, it is stated that the apparent radiation sensitivity of the two materials shown in the UBR irradiation was the same. Accordingly, the anomaly cannot be ascribed to some basic difference in material resistance to a 279°C nuclear environment.

Trepan Data (Inner Wall vs. Outer Wall Layers - Preservice Condition)

The MPA data for Layers 8 to 10 of Trepans C, D and G are illustrated in Figure 8. Plotting the data by individual layers, 41-J transition temperatures and upper shelf levels could be established. Superposition of the curves showed very little through-thickness differences in either property. In tests of the archive material, a good correspondence of 1/4T, vs. 1/8T and 7/8T thickness location upper shelf properties was also observed. Only a small difference in 41-J temperature (11°C) was noted for 1/4T vs. 1/8T (or 7/8T thickness) locations. With this evidence, it is assumed here for discussion purposes that the 1/8T and 7/8T properties of the vessel as placed in service were the same.

Trepan Data (Inner Wall-Postservice vs. Outer Wall-UBR Irradiated)

Figure 9 compares the data for the UBR irradiation of the trepan (outer wall) to the data for the service-irradiated trepan (inner wall).. Referring to the lower graph and temporarily ignoring the shapes of the curves, one observes that the upper shelf energy levels (and the 41-J transition temperatures) are about the same. This correspondence suggests no fluence-rate effect between the two reactors (KRB-A vs. UBR).

In contrast, the L-C orientation data yield two curves that are in general agreement up to an energy absorption level of about 61 J (45 ft-lb) but diverge above this level, that is, above 71°C (160°F). At 71°C (160°F), both the C-L orientation curve and the L-C orientation curve for the UBR irradiation of the trepan specimens have a positive slope. The curves do not show an onset of upper shelf behavior until about 104°C (220°F). The onset of upper shelf behavior for the UBR-irradiated outer-wall material at 104°C vs. much lower temperatures for the service-irradiated inner-wall material in spite of the similarity in 41-J temperatures, is in itself an anomaly.

Of further puzzlement is the relative positions and shapes of the KRB-A service-irradiated inner-wall material vs. outer-wall material in the transition region (C-L orientation). The lower portion of the curve for the inner-wall material lies to the right of that for the outer-wall material (expected relationship). But the upper portion of the curve for the inner-wall material lies well to the left of that for the outer-wall material

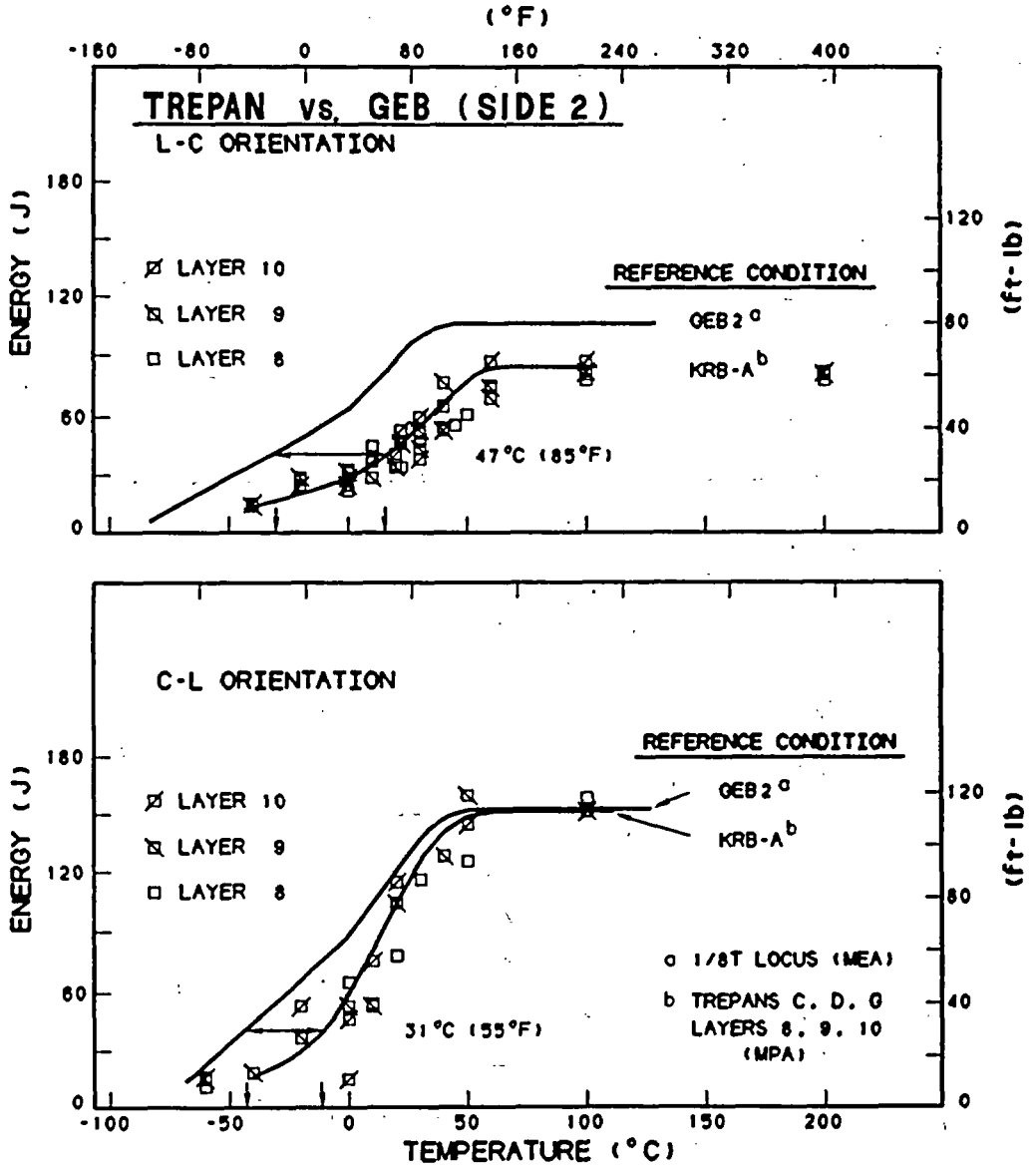

Fig. 8 Comparison of the notch ductility of the trepan material and the archive material before irradiation in the UBR. Notice the agreement of data for the three trepan layers; the trend curves are based on Layer 9 and 10 data primarily.

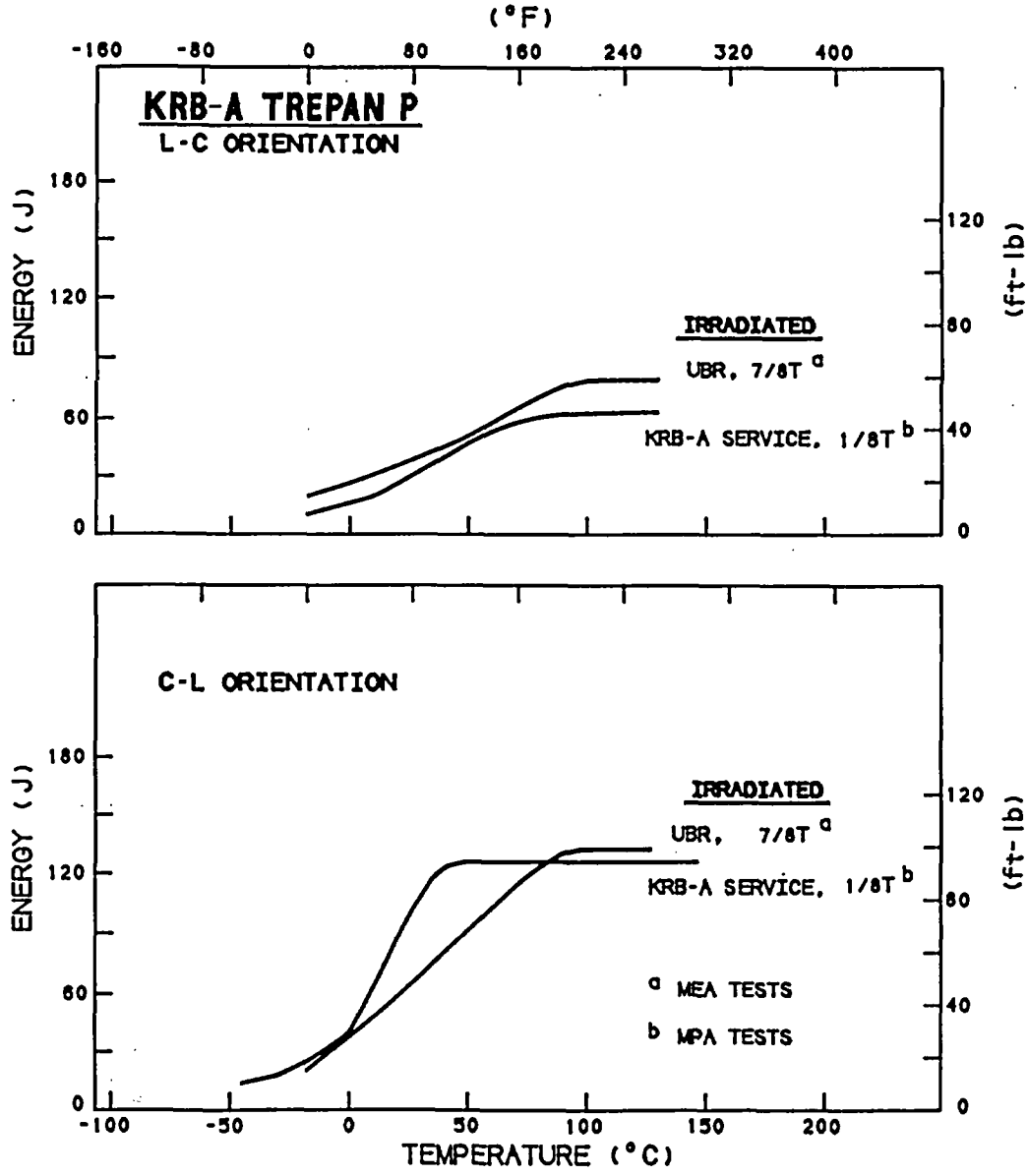

Fig. 9 Charpy-V notch ductility of the trepan material after KRB-A service irradiation (inner-wall location) and after the UBR accelerated irradiation (outer-wall location). Good agreement in upper shelf energy level is observed for the C-L orientation data but not the L-C orientation data.

(signifying better notch ductility and less radiation-induced embrittlement - unexpected). For the outer-wall material, since both orientations in the service-irradiated condition and the UBR-irradiated condition describe an internally-consistent family of curves, it can be concluded that they are reasonable accurate depictions of the properties. (A change in slope of curves by irradiation has been observed with other materials.) An explanation for the particular shape of the transition curve for the inner-wall material cannot be offered at this time. While both Trepan C and G supplied inner-wall location specimens for development of this curve, no pronounced properties difference due to sample location was reported by MPA (Ref. 1).

Of the two unusual data patterns cited above, the pattern of most concern is the difference in postirradiation upper shelf levels for the L-C orientation. Two observations may provide a clue. The upper shelf energy decreases for the inner-wall location indexed to the outer-wall location (postservice condition) are essentially the same, that is, 26 J (C-L) and 23 J (L-C). Whether or not this is significant is unknown. Similarly, it is observed that the upper shelf levels for the C-L orientation and L-C orientation commence at roughly 16°C and 77°C, respectively. A mechanistic explanation for this large temperature difference is absent.

Discussion

The present investigation has proven that the initially-reported anomaly (Ref. 1,4) is not due to a basic difference in radiation-embrittlement sensitivity between the test materials. That is, the archive GEB material and the Trepan P material (outer-wall layers) exhibited comparable embrittlement after simultaneous irradiation in the UBR test reactor.

A large difference in notch ductility between the archive material (preirradiation condition) vs. the trepan material (post-service reference condition, outer-wall layer) is apparent with one exception: the C-L orientations of these materials have about the same upper shelf energy level. Analyses of the data provide the following concerns. If the "cause" of the overall difference in reference properties is due to the difference in forging locations represented by the materials and not to a low fluence effect and/or a thermal aging effect, the implication is one of a general problem for forgings and their sampling. In this scenario, the archive material selected for surveillance may not be providing the worst-case properties for the vessel material and in fact, may lead to underestimates of the actual 41-J temperature and overestimates of the actual upper shelf energy level by significant margins. Conversely, if the cause is the low level fluence exposure of the outerwall layer and not some across-forging variability, the 31 to 47°C difference in 41-J temperature suggests that we have not been attaching proper significance to the effects of this fluence regime. Likewise, it could be that long-term thermal aging effects have been underestimated. Fortunately, this second scenario does not impact the validity of surveillance capsule data except for the possibility of large disparities between surveillance capsule time-at-temperatures and vessel wall time-at-temperatures. With a 3:1 lead factor, for example, a surveillance capsule might have only 3 years at temperature vs. a 9 year time at temperature for the vessel. Little is known about time-at-temperature effects for those very long periods of time equated to RPV design lifetimes and PLEX operations.

The comparison made of UBR-irradiated trepan material (outer wall layers) vs. the service-irradiated trepan material (inner wall layers) has reduced the scope of the original anomaly to the question of the low upper shelf energy level of the L-C orientation. The possibility of the anomaly being the result of some heretofore unobserved dose rate effect that is test-orientation dependence, cannot be dismissed on the basis of the latest UBR irradiation comparison of the archive vs. trepan materials. The outer wall layer of the vessel material and the archive material describe higher upper shelf energy levels after UBR irradiation.

The answer may reside in the seeming inconsistencies in the trepan inner-wall notch ductility properties relative to outer-wall properties, for example, the large disparity in upper shelf level between 1/8T and 7/8T locations for the L-C but not the C-L orientation. It is believed that the explanation will not be found simply though additional mechanical property testing. Instead, the plan is to examine the trepan and archive materials with state-of-the-art microscopy focusing on those aspects governing upper shelf energy absorption. To help expedite resolution, the materials have been offered to the International Group on Radiation Damage Mechanisms in Pressure Vessel Steels (IG-RDM). The IG-RDM was formed to accelerate the identification and modeling of radiation damage mechanisms. Mechanisms identification is important to better understand and project in-service embrittlement behavior and PLEX capabilities (Ref. 17).

Conclusions

The findings from the simultaneous test reactor irradiation of the trepan material from the Gundremmingen KRB-A reactor vessel and the archive material has greatly reduced the uncertainties regarding the cause(s) of the originally reported anomalous property differences between the materials in the post-irradiation condition. The important observations and determinations from this investigation can be enumerated:

(1) The UBR irradiation at 279°C produced 41-J transition temperature elevations of 11°C and 14°C for the trepan material (L-C and C-L orientation, respectively) vs. 20°C and 17°C for the archive material.

(2) The UBR irradiation at 279°C produced upper shelf energy reductions of 5 J and 19 J for the trepan material (L-C and C-L orientation, respectively) vs. 4 J and 9 J for the archive material.

(3) From (1) and (2), the radiation embrittlement sensitivities of the trepan material (outer wall region) and the archive material (1/8T region) are essentially the same. This proves that the originally-observed anomalous differences are not due to a basic difference between material radiation resistances.

(4) The pre-UBR irradiation C_v properties of the trepan and archive materials are not the same. For the L-C orientation, the 41-J temperature of the trepan material was 47°C (85°F) higher and the upper shelf energy level was 22 J (16 ft-lb) lower than those of the archive material. For the C-L orientation, the 41-J temperature of the trepan material was 31°C (55°F) higher than that for the archive material but the upper shelf energy levels were the same ~153 J (113 ft-lb).

(5) More than one cause may be responsible for the differences in preirradiation properties cited in (4).

(6) The properties dissimilarities in (4) would explain some (but not all) of the apparently greater radiation embrittlement found for the trepan material (inner wall, L-C orientation) compared to UBR-irradiated archive material.

(7) For both L-C and C-L orientations, the 41-J transition temperatures of the service-irradiated trepan material (inner wall) and the UBR-irradiated trepan material (outer wall) are about the same, illustrating an absence of a fluence rate effect on this property.

(8) The upper shelf energy levels of the service-irradiated trepan material (inner wall) and the UBR-irradiated trepan material (outer wall) are about the same in the C-L orientation (strong) but differ greatly in the L-C orientation (weak).

(9) Metallurgical or mechanistic explanations for the L-C orientation difference of (8) are not yet available; a heretofore unobserved fluence-rate effect may be responsible. Seeming inconsistent notch ductility relationships which may constitute clues to the remaining anomalous data indications, are identified.

Acknowledgements

This investigation was part of the joint USA/FRG/UK program on postservice property investigations for the Gundremmingen KRB-A Reactor Vessel.

The author thanks Dr. J. Fohl (MPA) for his personal efforts toward securing the Trepan P specimens for the investigation and for the trepan reference condition data supplied. The author also expresses his appreciation to J. W. Rogers (EG&G Idaho, Inc.) for his personal efforts on neutron dosimetry for the Experiment Assembly UBR-83A. He thanks G. Lohr and H. Sanders for their contributions in experiment construction, D. Schaffer for his efforts in postirradiation testing, and T. Krueger for her efforts in the preparation of this report.

References

1. K. Kussmaul, J. Fohl and T. Weissenberg, "Assurance of the Pressure Vessel Integrity with Respect to Irradiation Embrittlement - Activities in The Federal Republic of Germany (FRG)," Proceedings NEA/CSNI-UNIPEDE Specialist Meeting on Regulatory and Life-Limiting Aspects of Core Internals and Pressure Vessels, CSNI Report No. 146, pp.489-538, September 1988.

2. "Radiation Embrittlement of Reactor Vessel Materials," USNRC Regulatory Guide 1.99, Rev. 2, U. S. Nuclear Regulatory Commission, Washington, DC, May 1988.

3. "Standard Guide for Predicting Neutron Radiation Damage to Reactor Vessel Materials," E 900-87, Book of ASTM Standards, American Society for Testing and Materials, Philadelphia, PA, Volume 12.02, pp. 689-695, 1987.

4. J. R. Hawthorne and A. L. Hiser, "Experimental Assessments of Gundremmingen RPV Archive Material for Fluence Rate Effects Studies," USNRC Report NUREG/CR-5201, U. S. Nuclear Regulatory Commission, Washington, DC, October 1988.

5. F. W. Stallmann, C. A. Baldwin, F. B. K. Kam and B. J. Taylor,"Description of the Power Reactor Embrittlement Data Base," USNRC Report NUREG/CR-4816, Nuclear Regulatory Commission, Washington, DC, (in press, estimated publication date June 1989).

6. M. K. Miller, M. G. Hetherington and M. G. Burke, "Atom Field Ion Microscopy: A Technique for Microstructural Characterization of Irradiated Materials on the Atom Scale," presented at the TMS/ASM Fall Meeting, Chicago, IL, September 1988.

7. M. G. Burke and M. K. Miller, "Solute Clustering and Precipitation in Pressure Vessel Steels under Low Fluence Irradiation Conditions," Journal de Physique, Vol. 49-C6, pp. 283-288, November 1988.

8. F. Frisius, R. Kampmann, R. Wagner and P. A. Beaven, "SANS Analysis of Irradiated and Unirradiated Fe Alloys Containing Cu, Ni, P: Final Report," MEA Report 2296, Materials Engineering Associates, Inc., Lanham, MD, March 1988.

9. P. A. Beaven, F. Frisius, R. Kampmann, R. Wagner and J. R. Hawthorne, "SANS Investigation of Irradiated A 533-B Steels doped with Phosphorus," Radiation Embrittlement of Nuclear Reactor Pressure Vessel Steels: An International Review, 3rd Volume, ASTM STP 1011, American Society for Testing and Materials, Philadelphia, PA, pp. 243-256, 1989.

10. M. Valo, H. Huomo, P. Nyberg and P. Hautojarvi, "Positron Lifetime Characterization of Irradiated Pressure Vessel Model Alloys," Radiation Embrittlement of Nuclear Reactor Pressure Vessel Steels: An International Review, 3rd Volume, ASTM STP 1011, American Society for Testing and Materials, Philadelphia, PA, pp. 257-261, 1989.

11. G. R. Odette and G. E. Lucas, "Irradiation Embrittlement of Reactor

Pressure Vessel Steels: Mechanisms and Models and Data Correlations," Radiation Embrittlement of Reactor Pressure Vessel Steels, ASTM STP 909, American Society for Testing and Materials, Philadelphia, PA, pp. 206, 1986.

12. E. P. Lippincott, "Buffalo Light Water Reactor Calculation," Letter Communication Serial No. 7754977, Hanford Engineering Development Laboratory, Richland, WA, to J. R. Hawthorne dated November 16, 1977.

13. E. P. Lippincott, L. S. Kellogg, W. N. McElroy, and C. A. Baldwin, "Evaluation of Neutron Exposure Conditions for the Buffalo Reactor," Proceedings of the Fifth International ASTM-Euratom Symposium, Geesthacht, Federal Republic of Germany, September 24-28, 1984.

14. G. Prillinger, E. D. McGarry and J. R. Hawthorne, "Neutron Spectra Calculations for Ex-Core Irradiation Experiments at the Buffalo Reactor," Proceedings of the ASTM Fourteenth International Symposium on Effects of Radiation on Material, Andover, MA, June 27-30, 1988.

15. R. Pasternak, Letter Report, U. S. Army Laboratory Command, to J. R. Hawthorne, May 26, 1989.

16. J. R. Hawthorne, "An Exploratory Study of Element Interactions and Composition Dependencies in Radiation Sensitivity Development: Final Report," USNRC Report NUREG/CR-5357, Nuclear Regulatory Commission, Washington, DC, April 1989.

17. J. R. Hawthorne, "Mechanisms of Irradiation Damage for Reactor Vessel Steels," Compilation of Contract Research for the Materials Engineering Branch, Division of Engineering - Annual Report for FY 1988, U. S. Nuclear Regulatory Commission, NUREG-0975, Vol. 7, pp. 82-84, April 1989.

EMBRITTLEMENT OF THE SHIPPINGPORT REACTOR SHIELD TANK*

O. K. Chopra and W. J. Shack

Materials and Components Technology Division, Argonne National Laboratory,
9700 South Cass Avenue, Argonne, IL 60439, U.S.A.

Abstract

The irradiation embrittlement of the Shippingport neutron shield tank material has been characterized. Irradiation increases the Charpy transition temperature (CTT) by ~25°C (45°F) and decreases the upper shelf energy. The shift in CTT is not as severe as that observed in the HFIR surveillance specimens. However, the actual value of CTT is higher than that for the HFIR data and the toughness at service temperature is low. The increase in yield stress is 51 MPa (7.4 ksi), which is comparable to the HFIR data. The results also indicate a low impact strength and higher transition temperature for the TL orientation than that for the LT orientation. Some effects of the location across the thickness of the wall are also observed for the LT specimens; CTT is slightly greater for the specimens from the inner region of the wall. The data agree well with results from high-flux test reactors. Annealing studies indicate complete recovery of embrittlement after a 2-h anneal at 400°C. The transition curve for the annealed inner wall specimens is virtually identical to that for the as-received outer wall. The results for weld specimens from the inner and outer walls are also presented.

1. Introduction

Surveillance specimens from the high flux isotope reactor (HFIR) at Oak Ridge National Laboratory showed an very high degree of embrittlement compared with data obtained on similar materials in materials testing reactors .[1-3] One explanation of the difference between the HFIR data and the test reactor data is that, for a given irradiation level, embrittlement is greater at lower flux. Since current NRC guidelines for the assessment of the embrittlement of the pressure vessel support structures of commercial light water reactors do not consider flux, the HFIR results raise the possibility that they may not be sufficiently conservative.

To help resolve this issue, a program was initiated to characterize the irradiation embrittlement of the neutron shield tank (NST) from the decommissioned Shippingport reactor. The Shippingport NST, which operated at 55°C (130°F), was fabricated from rolled A212 grade B firebox steel similar to that used for the HFIR vessel. The inner wall of the NST was exposed to a total maximum fluence of ~6×10^{17} n/cm^2 (E>1 MeV) over a life of 9.25 effective-full-power years. This corresponds to a fast flux of 2.1×10^9 n/cm^2·s. In comparison the HFIR surveillance specimens were exposed at the inner surface of the pressure vessel at a temperature of 50°C (122°F) over a period of ~17 effective-full-power years; the flux of fast neutrons was ~2×10^8 n/cm^2 s.[1]

---

* RSR FIN Budget No. A2256; RSR Contact: E. Woolridge.

2. Material Characterization

The effort to obtain samples from the NST was sponsored jointly by the NRC and the DOE Plant Life Extension Program (PLEX) at Sandia National Laboratories. The actual sampling was performed by personnel from Battelle Pacific Northwest Laboratory. Eight ~155 mm (~6 in) disc samples of the base metal and three weld samples were obtained from the inner wall, along with the corresponding samples from the outer wall. The layout for the sample locations from the inner wall is shown in Fig. 1. The inner wall is constructed from four plates ~25.4-mm (1 in) thick, welded after assembly. Thus, specimen locations 13, 14, and 15 contain vertical welds; the other locations represent the base metal from the four plates. The total fluence varied among the various locations; the maximum vertical fluence occurred at an elevation of 211.07 m (692.5 ft), whereas the maximum azimuthal fluence occurred at the 20 and 200° positions. The estimated fluence was ~6×10^{17} n/cm^2 (E>1 MeV) for locations 3 and 9, and ~4×10^{17} n/cm^2 for locations 2 and 8.* The outer wall was constructed from two plates joined together by vertical welds at azimuthal positions 0 and 180°. A weld sample was obtained from the outer wall at location 1. No effect of irradiation is expected at the extremely low levels of irradiation for the outer wall; therefore, the outer wall samples were used to determine the unirradiated baseline data.

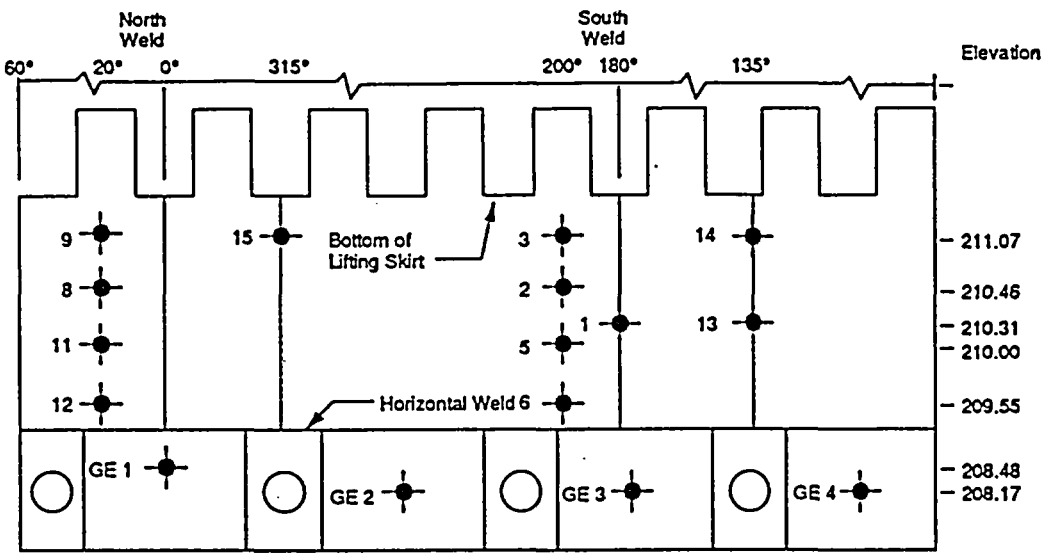

Fig. 1. Layout of Sample Location in the Shippingport Neutron Shield Tank Inner Wall.

Metallurgical characterization and chemical analyses of samples taken from each of the plates strongly suggest that both the inner and outer walls of the NST were fabricated from a single heat. Typical chemical analyses for the plate and weld metal are given in Table 1. Metallographic examination of the NST material indicates that the rolling direction is horizontal. Micrographs of the grain structure along the rolling and transverse directions are shown in Fig. 2. The surfaces shown in the micrographs are designated by the direction

* L. James, Bettis Atomic Power Laboratory, private communication (April 1989).

Table 1. Typical Chemical Compositions (wt.%) of the A212 Grade B Plate and Weld Metal from the Shippingport Neutron Shield Tank

Element	Plate	Weld
C	0.23	0.065
Mn	0.76	0.93
P	0.02	-
S	0.03	-
Si	0.27	0.73[1]
Cu	0.05	0.06[2]
Ni	0.04	0.02
Cr	0.04	0.03
O	0.01	-
N	0.004	-
Ti	<0.005	0.025
V	<0.005	0.019
Zr	<0.005	<0.005
Mo, Ca, Al	<0.01	<0.01
B, Se, Sn	<0.01	<0.01

[1]0.86 for inner-wall weld from location 14.

[2]0.07 for outer-wall weld and 0.04 for inner-wall weld from location 15.

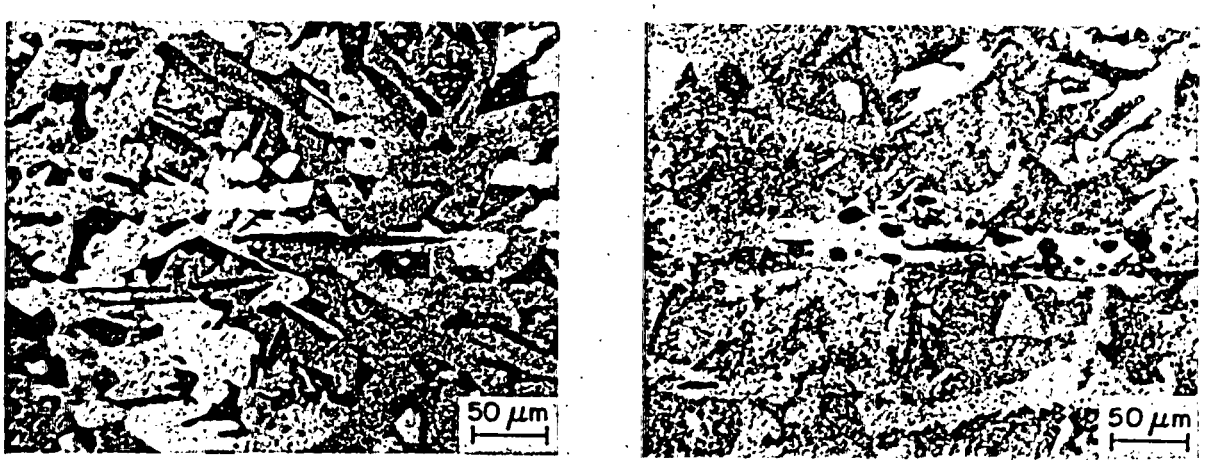

Fig. 2. Micrographs of the NST Material Along the (a) Transverse and (b) Rolling Sections.

normal to that surface. The transverse section shows some elongated grains and all the inclusions are elongated in the rolling direction. The inclusions in the rolling section are globular or flat.

There are significant variations in hardness across the thickness of the wall. A typical hardness profile (Rockwell B) for the outer wall is shown in Fig. 3. (The depth is measured from the inner surface of the plate, i. e., the surface towards the reactor core.) The hardness values of the inner and outer regions of the plate are ~10% higher than those of the plate center. However, no measurable change in grain size was observed across the thickness of the wall; the average through-wall grain size was ~12 μm. Although irradiation increases the hardness of the material, the V-shape profile is maintained at most locations, Fig. 3.

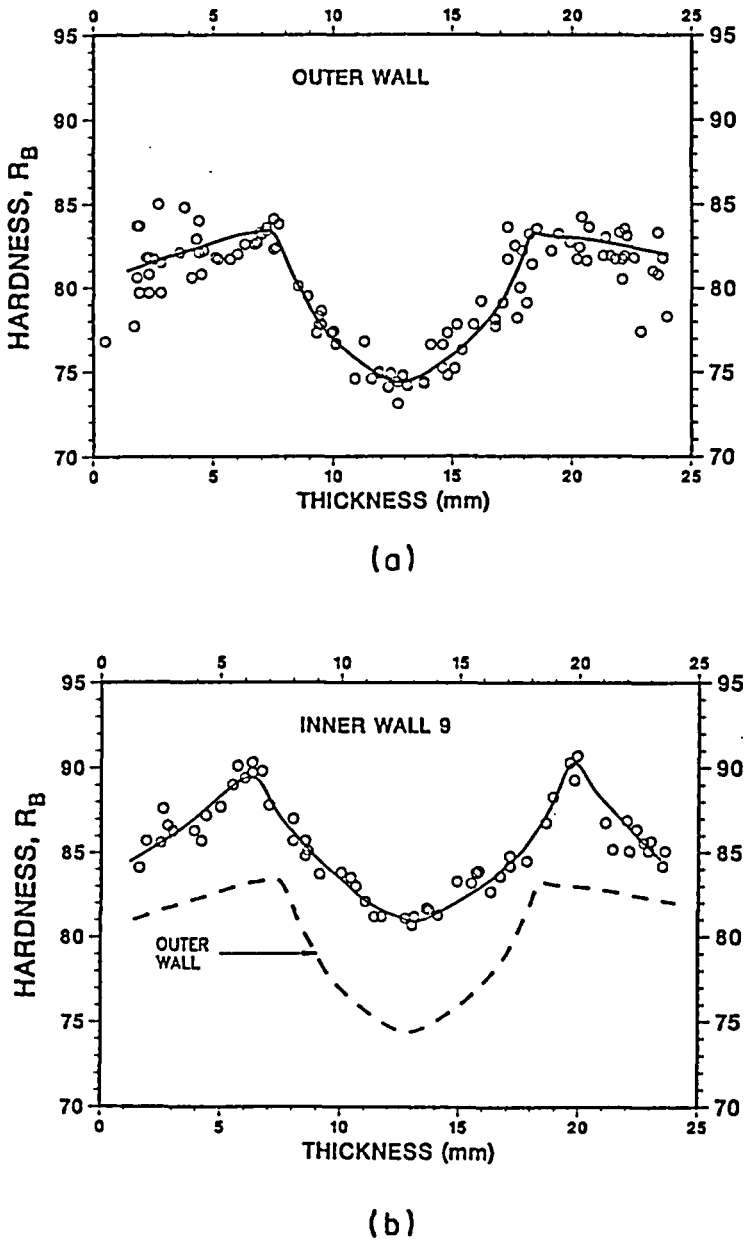

Fig. 3. Hardness Profile across the Thickness of the NST Outer Wall and Location 9 of the NST Inner Wall.

3. Irradiation Embrittlement

The irradiation embrittlement has been characterized by Charpy impact and tensile tests. Specimens were obtained in the LT and TL orientations* from three regions, i.e., inner, center, and outer 10-mm-wide regions, across the thickness of the NST wall. A typical layout for the base metal specimens from the inner and outer walls is shown in Fig. 4. Material from the outer wall, which was protected by ~0.9 m (3 ft) of water and hence had a six-order-of-magnitude lower fluence than the inner wall, was used to obtain baseline data for unirradiated material.

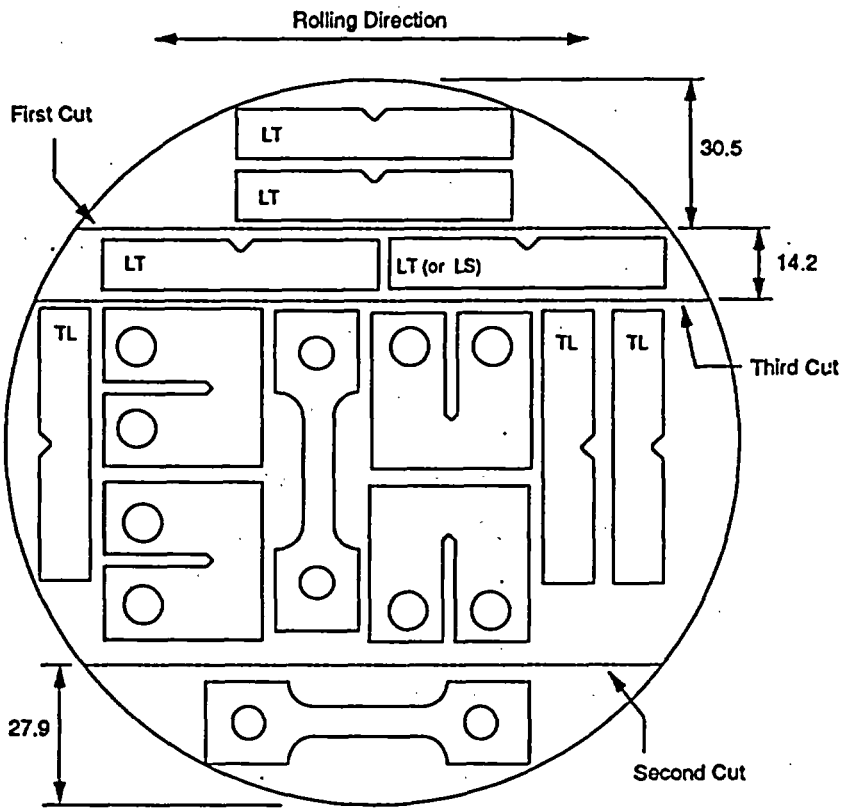

Note: Diagram based on an assumed diameter of 146 mm
All Dimensions in mm.

Fig. 4. Cutting Diagram for Base Metal Samples from the NST Inner and Outer Walls.

* The first digit designates the direction normal to the plane of the crack; the second digit represents the direction of crack propagation. L = longitudinal or rolling direction and T = transverse direction.

Charpy impact tests were conducted on standard Charpy V-notch specimens machined according to ASTM specification E 23. A Dynatup Model 8000A drop weight impact machine with an instrumented tup and data readout system was used for the tests. Tensile tests were performed on dog bone specimens, with a cross section of 4 x 5 mm and a gauge length of 20 mm.

3.1 Base Metal

Charpy transition curves for the LT and TL specimens from different regions of the NST outer wall are shown in Fig. 5. The results indicate that the variation in the transition curves with vertical and azimuthal position is very slight. However, the TL orientation is weaker than the LT orientation. The Charpy transition temperature (CTT) at the 20.3-J (15 ft·lb) level is higher, and the upper-shelf energy (USE) is lower for the TL specimens. The CTT and USE, respectively, are 16°C (61°F) and 98 J/cm^2 (~58 ft·lb) for LT specimens and 19°C (66·F) and 56 J/cm^2 (~33 ft·lb) for TL specimens. The differences in impact strength are attributed primarily to differences in the structure of the material. The plane of the crack for TL orientation, i.e., transverse section shown in Fig. 2, contains elongated inclusions.

The results also indicate some effect of position through the thickness of the wall; impact energies for specimens from the inner and outer regions of the wall are comparable, whereas those for the center specimens are slightly higher, Fig. 5b. The CTT and USE for the center specimens are 9°C (48°F)and 104 J/cm^2 (~61 ft·lb), respectively. This correlates with the differences in the hardness of the material. The hardness of the center region is R_B ~75 (142 DPH) and that of the inner or outer regions is R_B ~83 (159 DPH).

The transition curves for the LT and TL specimens from different positions on the NST inner wall, are shown in Fig. 6. The irradiated inner wall specimens show a higher CTT and lower USE relative to those from the unirradiated outer wall. The transition curves are almost independent of vertical position, which suggests that a factor of two in the variation of fluence has relatively little effect. For example, the impact energies for specimens from locations 2 and 8 (~4 x 10^{17} n/cm^2 fluence) are comparable to those for specimens from locations 3 and 9 (~6 x 10^{17} n/cm^2 fluence). For LT specimens, some differences are observed for those from the inner and outer regions of the wall; the shift in CTT is slightly greater for the inner region. The values of CTT are 37°C (99°F) for the outer region and 41°C (106°F) for the inner region, a shift of ~21 and 25°C (~38 and 45°F) for the outer and inner regions, respectively. The USE can not be established from the data in Figs. 6a and 6b. However, the specimens tested at 55°C show 100% shear fracture; thus, the impact energies for these specimens are representative of USE.

The shift in CTT of the inner-wall TL specimens is also 25°C (45°F), similar to that for the LT specimens. However, the actual value of the CTT is higher, 44°C(111°F). The effects of material hardness are minimal for the TL specimens. The impact energies for the center specimens are comparable to specimens from the inner and outer region, although the hardness is significantly different, e.g., R_B ~82 and 88 (156 and 176 DPH) for the center and inner or outer regions, respectively.

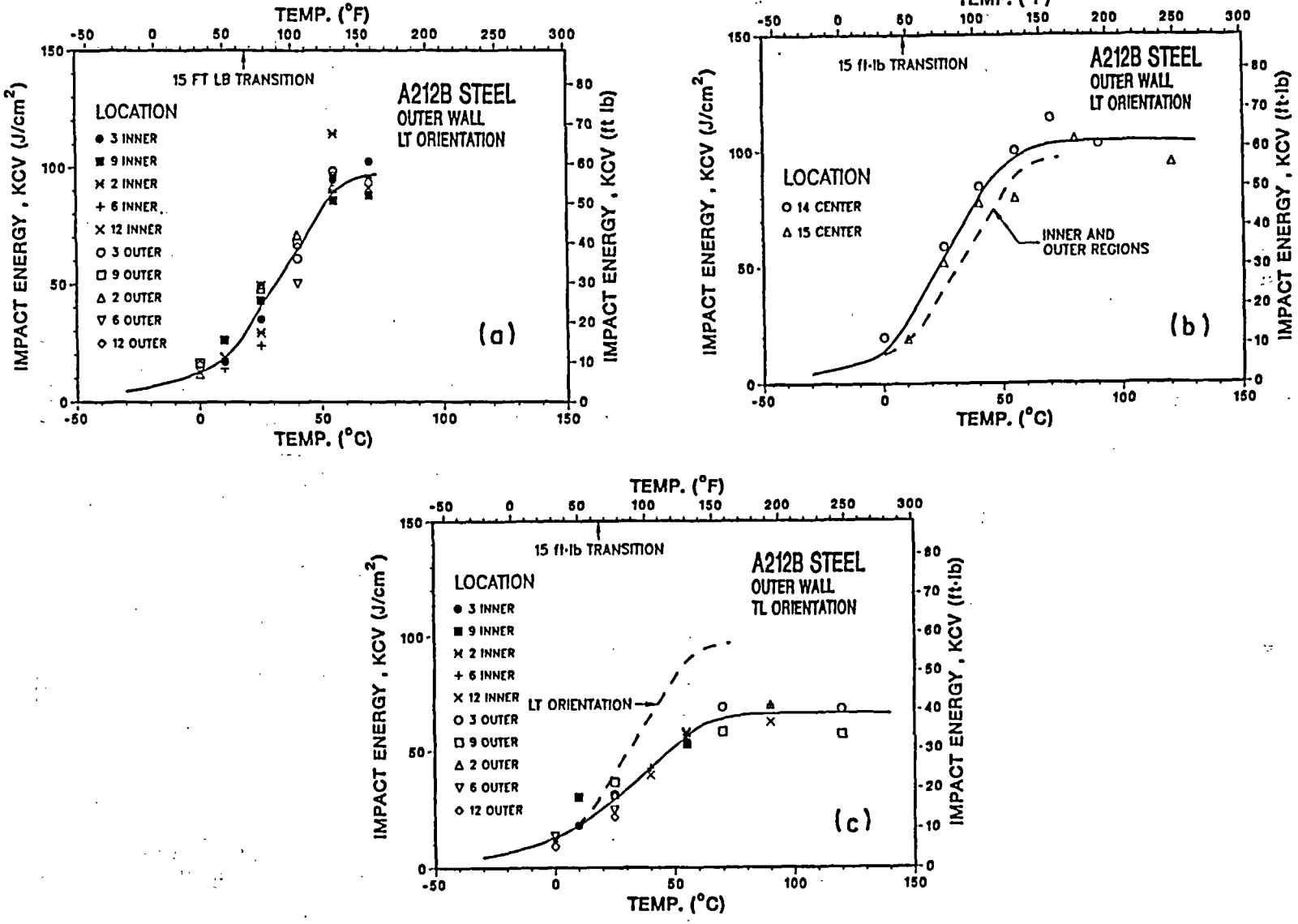

Fig. 5. Charpy Impact Test Data for the NST Outer Wall. LT specimens from (a) inner and outer regions and (b) center region. TL specimens from (c) inner and outer regions.

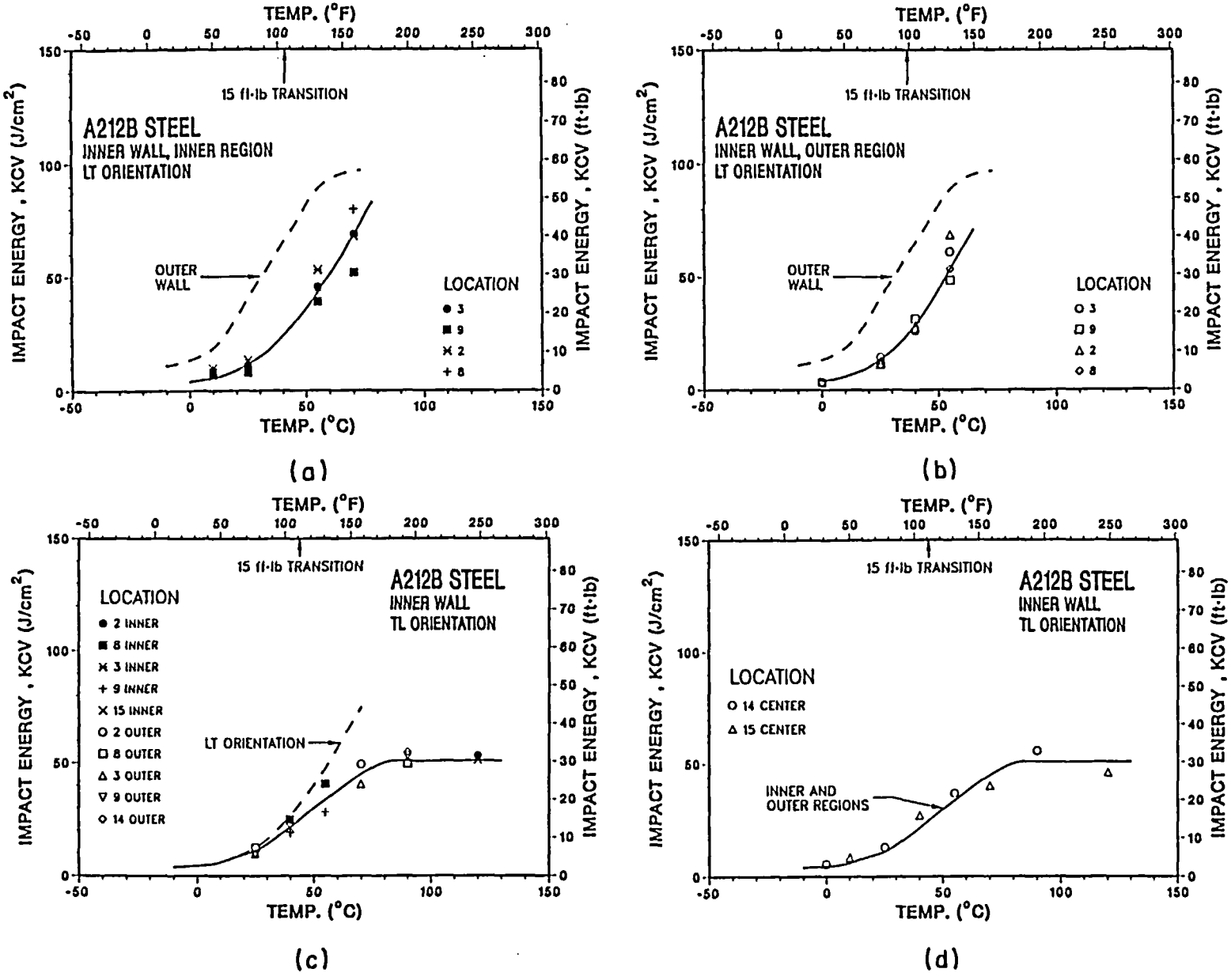

Fig. 6. Charpy Impact Test Data for the NST Inner Wall. LT specimens from (a) inner and (b) outer region. TL specimens from (c) inner and outer regions and (d) center region.

Tensile tests on LT specimens from several locations of the NST inner and outer walls were conducted at room temperature and at 55°C (131°F). The results indicate a higher yield stress for the inner wall relative to the outer wall, whereas the ultimate stress is approximately the same. The increase in yield stress is ~51 MPa (7.4 ksi) at room temperature and ~40 MPa (5.8 ksi) at 55°C. The tensile strength for locations 2 and 8 (~4 x 10^{17} n/cm^2 fluence) is comparable to that for locations 3 and 9 (~6 x 10^{17} n/cm^2 fluence).

Hardness influences the tensile properties at both test temperatures, i.e., the yield stress for the specimen from the center of the wall is always lower than that for the specimens from inner or outer regions. The difference is ~30 MPa (4.4 ksi) at room temperature and ~15 MPa (2.2 ksi) at 55°C. However, the increase in yield stress due to irradiation is the same for specimens from the center and from the inner or outer regions of the walls.

The tensile properties of the NST material were also estimated from the Charpy impact data. For dynamic loading, the yield stress is estimated from the expression

$$\sigma_y = AP_yB/Wb^2, \quad (1)$$

taken from Ref. 4, where P_y is the yield load obtained from the load-time traces of the instrumented Charpy tests, W is the specimen width, B is the specimen thickness, b is the uncracked ligament, and A is a constant. The constant A was obtained by comparing the tensile and Charpy data for LT specimens tested at room temperature and at 55°C. The best value of the constant was 1.73. The yield loads and the estimated yield stresses for the outer and inner walls are shown in Fig. 7. The measured yield stresses are compared with the estimated values. The results show the expected decrease in yield stress with an increase in test temperature. In the lower-shelf temperature regime, cleavage occurs before general yielding; therefore, the yield loads are very low. For the Charpy impact tests, cleavage fracture occurs when the yield loads are ~13 kN. Irradiation increases the yield stress at all test temperatures and, therefore, the CTT shifts to higher temperatures. Irradiation hardening is greater at room temperature than at higher temperatures.

3.2 Weld Metal

Weld samples were obtained at one position on the outer wall and three positions on the inner wall, i.e., locations 14 and 15 with ~3 x 10^{17} n/cm^2 fluence and location 13 with ~2 x 10^{17} n/cm^2 fluence. All the welds were transverse to the plate rolling direction. Charpy impact test specimens were machined perpendicular to the weld and from the inner and outer regions across the thickness of the plate. The impact strength of the outer-wall weld is significantly higher than that of the base metal, Fig. 8a. The 41-J (30 ft·lb) CTT and USE of the weld are -2°C (28°F) and 182 J/cm^2 (107 ft·lb), respectively. Location through the thickness of the weld has little or no effect on the transition curve.

The inner wall specimens show significant effect of position around the wall as well as through the thickness of the wall. The impact energies of weld specimens from the outer region of positions 13, 14, and 15 are comparable but slightly higher than those of the outer-wall weld specimens, Fig. 8b. The transition curves for the inner region of the inner-wall welds are shown in Figs. 8c and 8d. The 41-J (30 ft·lb) CTT is 8°C (46°F) for welds at locations 13 and 15 and 23°C (73°F) for the weld at location 14, i.e., a shift of 10 and 25°C (18 and 45°F), respectively.

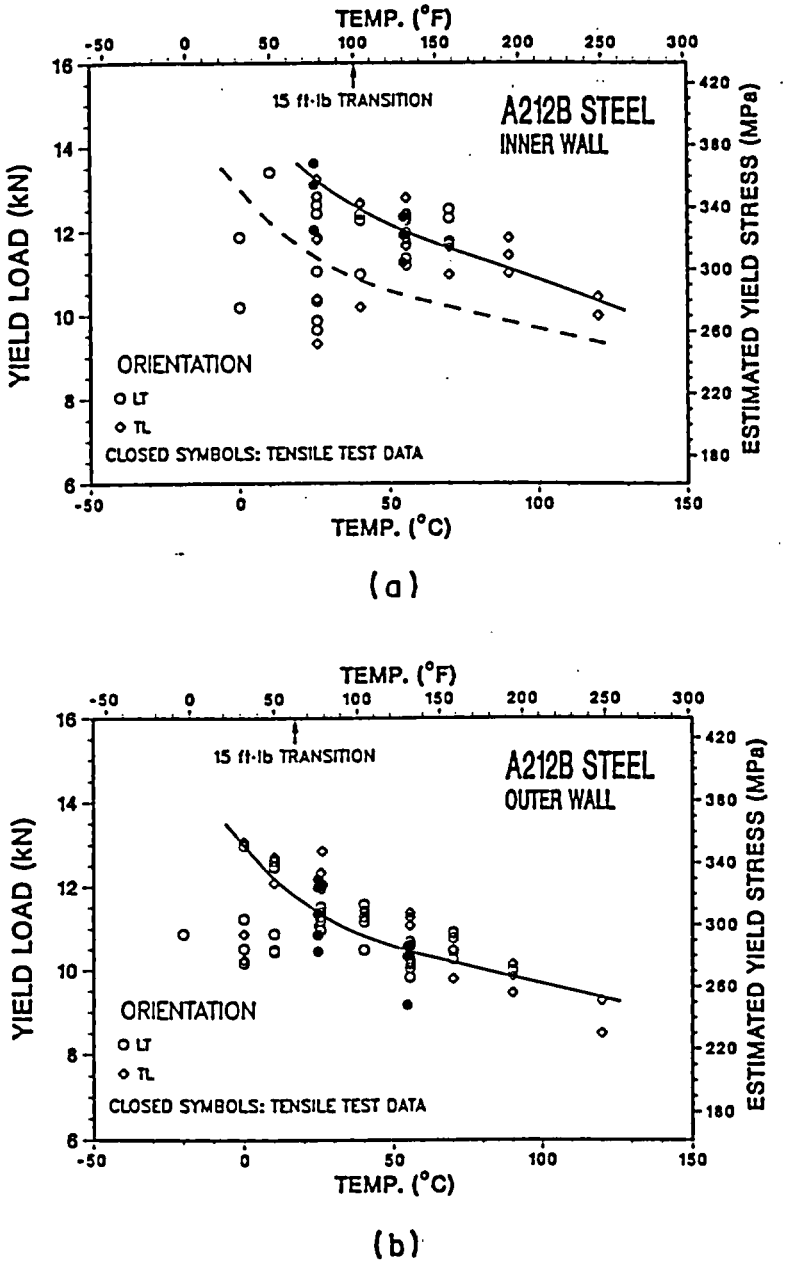

Fig. 7. Yield Stress Estimated from the Charpy Impact Data for the NST (a) Inner and (b) Outer Walls.

for the two data sets. The results for the outer weld may not be representative of the unirradiated inner-wall welds. The chemical composition of weld metals from different locations indicates only minor variations in silicon and copper content, Table 1. Additional tests and metallographic characterization of the welds are being performed to better establish the transition curves. Annealing studies, to obtain baseline data and determine the embrittlement behavior of the welds, are also planned.

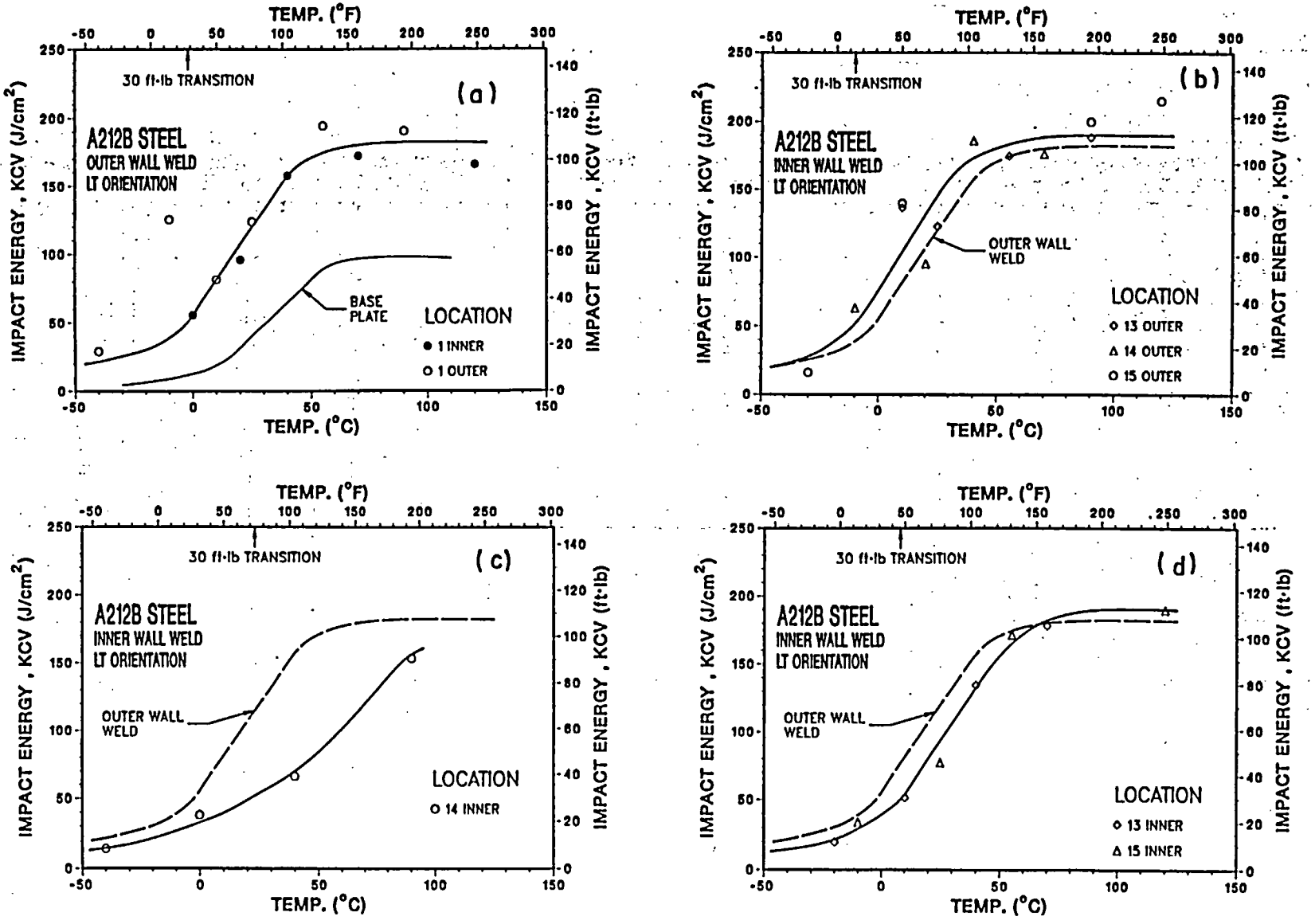

Fig. 8. Charpy Impact Test Data for Weld Metal Specimens from 9a) NST Outer Wall, (b) Inner Wall Outer Region, and (c) and (d) Inner Wall Inner Region.

4. Recovery Annealing

Annealing studies were conducted on material from the NST inner and outer walls to study the recovery behavior of embrittled material. Specimens were annealed at 400°C for up to 154 h and the annealing behavior was characterized by hardness measurements. The results indicate that the hardness of irradiated material from the inner shell decreases after annealing, whereas the hardness of the outer-shell material increases. Annealing for 1 h at 400°C (752°F) was sufficient for recovery; only a very slight increase in hardness of both the inner- and outer-shell materials occurs after annealing for longer times. The changes in hardness of material from inner and outer shells, shown in Fig. 9, reflect the differences in the fluence and flux levels of the different locations, i.e., the decrease for locations 3 and 9 is greater than for location 8.

Charpy impact data for TL specimens from the NST inner and outer walls, annealed for 2 h at 400°C, are shown in Fig. 10. The results indicate a complete recovery from irradiation embrittlement, i.e., the transition curve of the annealed specimens from the inner wall is identical to that of the outer wall. Annealing has little or no effect on the transition curve of the outer wall, Fig. 10.

5. Discussion

Charpy impact and tensile data for the Shippingport NST indicate that the shift in CTT is not as severe as would be expected on the basis of the changes seen in HFIR surveillance samples. In Fig. 11, Charpy transition curves for the outer and inner walls of the NST are compared with the results for unirradiated and irradiated HFIR surveillance samples.

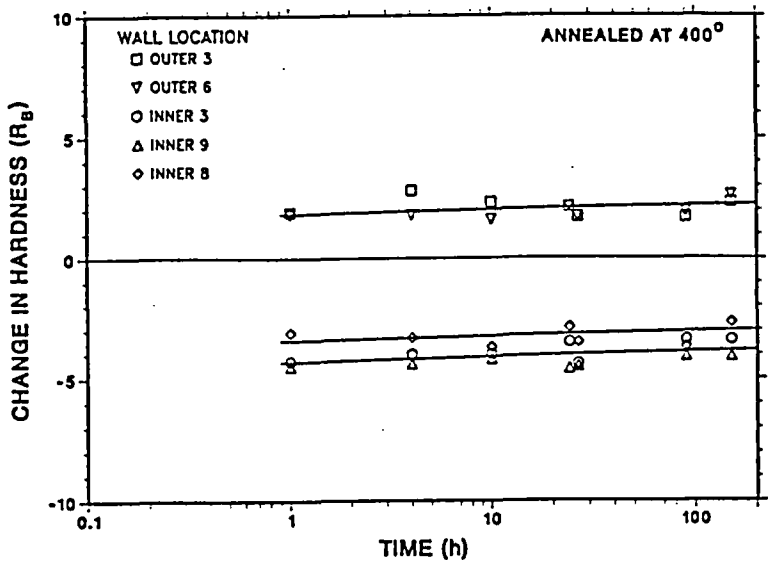

Fig. 9. Change in Hardness of the Neutron Shield Material from Inner and Outer Walls after Annealing at 400°C.

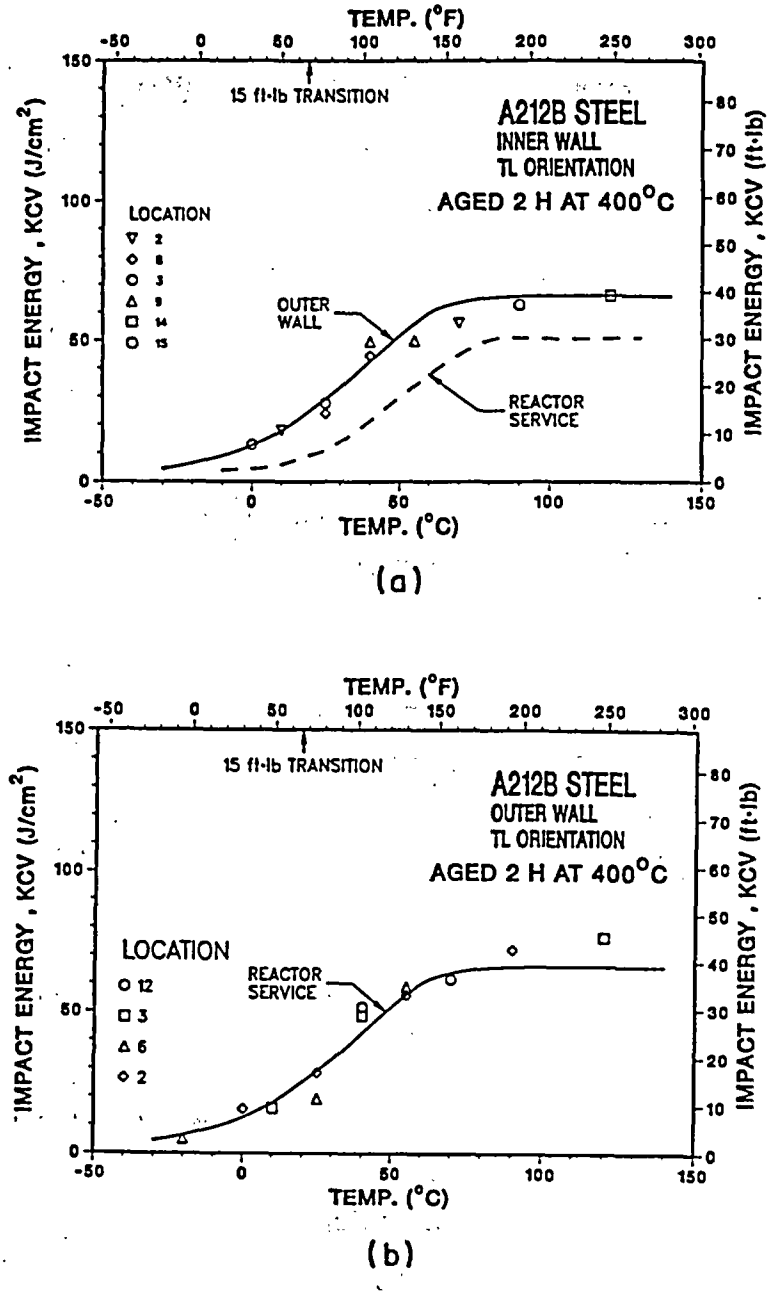

Fig. 10. Charpy Impact Test Data for Annealed TL Specimens from (a) Inner Wall and (b) Outer Wall.

Although the shift is smaller, the actual CTT of the NST material is significantly higher than that of the HFIR material. The impact energy of the NST inner wall is very low, ~40 J/cm^2 (24 ft·lb), at the service temperature of 55°C (131°F).

Except for minor differences in copper and nickel content, the chemical composition of the two materials is comparable. The concentrations of copper and nickel are 0.15 and 0.20 wt.%, respectively, for HFIR material and 0.05 and 0.04 wt.% for NST. Although the HFIR material is tougher than the NST material, the tensile strength of the HFIR material is greater

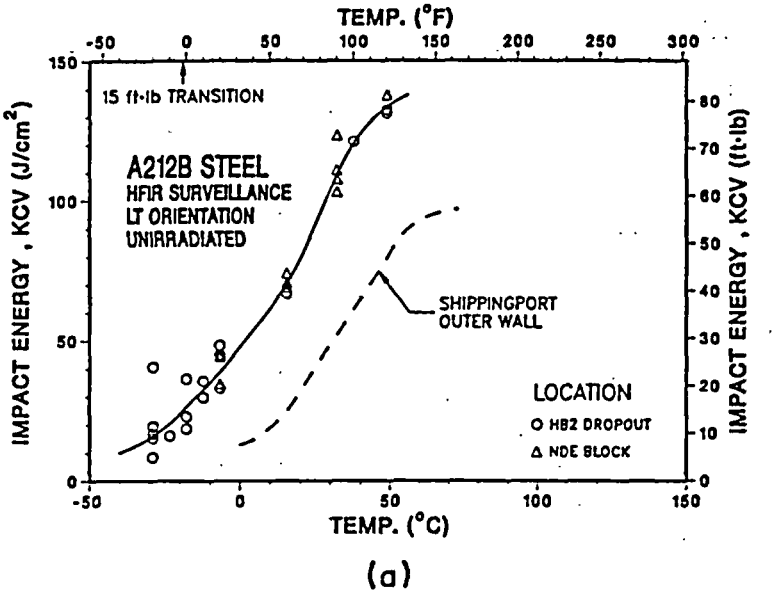

(a)

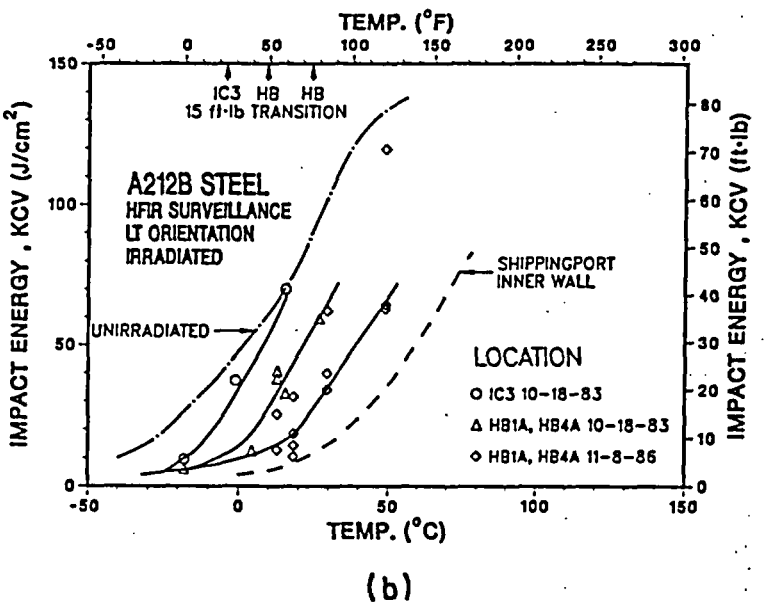

(b)

Fig. 11. Comparison of Charpy Impact Data for (a) Unirradiated and (b) Irradiated Shippingport NST and HFIR Surveillance Samples.

than that of the NST material. The yield strength and hardness, respectively, are 355 ± 11 MPa (~51 ± 2 ksi) and 170 DPH for the HFIR material[2] and 305 ± 19 MPa (44 ± 3 ksi) and 159 DPH for NST. The difference in the transition curves of the two unirradiated materials is most likely due to microstructural factors, such as the amount and distribution of inclusions.

When the shifts in CTT of the NST material are compared with the results obtained from the HFIR material irradiated in the ORR and other A212B steels irradiated in high-flux test reactors, Fig. 12, the results from the Shippingport NST are consistent with the test reactor data. The results for the NST material also agree very well with correlations for the shift in CTT, the increase in tensile yield stress, and the increase in hardness that were developed for pressure vessel steels.[5-7] The shift in transition temperature, ΔT, with an increase in tensile yield stress, $\Delta\sigma_y$, is expressed as

$$\Delta T\ (°C) = C\Delta\sigma_y\ (MPa), \tag{2}$$

where C ~0.5°C/MPa for plate material, and 0.65°C/MPa for welds. The change in yield stress with hardness, ΔDPH, is given by the relation

$$\Delta\sigma_y\ (MPa) = 3.5\Delta DPH. \tag{3}$$

The shift in the CTT of both LT and TL specimens is 25°C and the increase in yield stress is 51 MPa. The increase in hardness due to irradiation is difficult to obtain because of the variation in hardness across the thickness of the wall. However, annealing studies indicate that the irradiation-induced hardness change, represented by the decrease in hardness after annealing at 400°C for 2 h, is ~4.3 R_B (14 DPH) for locations 3 and 9. This is consistent with Eq. (3). The change in hardness is slightly lower, i.e., ~3.5 R_B (10 DPH), for location 8.

The results from the present study suggest that the unexpectedly high embrittlement of the HFIR surveillance samples may be due to factors other than flux effects. The minor differences in copper and nickel content between the two materials are not expected to have any effect at the low irradiation temperatures of Shippingport NST and the HFIR. Analytical studies are in progress at ANL to investigate radiation damage measures to determine whether a unified picture of embrittlement in HFIR, ORR, and Shippingport can be achieved. High-flux irradiation experiments will be performed for materials from the Shippingport NST and the HFIR vessel to confirm the analysis and evaluate the possible effects of metallurgical differences between the two materials.

6. Conclusions

Characterization of material from the Shippingport NTS indicates that the embrittlement of A212 grade B steel in a low-temperature, low-flux environment is consistent with that expected from the current NRC regulatory guidelines. However, the shifts in CTT are not as great as those of the HFIR surveillance samples. The reasons for this difference are not well understood.

The data on the weld samples from the NST indicate that the weld metal is tougher than the plate material. The results, however, show significant scatter, and irradiation embrittlement could not be characterized. Annealing studies to investigate the recovery behavior of the weld metal and to obtain additional information on the shift in CTT are planned.

Acknowledgments

This work was supported by the Office of Nuclear Regulatory Research, U. S. Nuclear Regulatory Commission. The authors are grateful to W. F. Burke and G. M. Dragel for their contributions to the experimental effort and to A. Sather for conducting the mechanical tests.

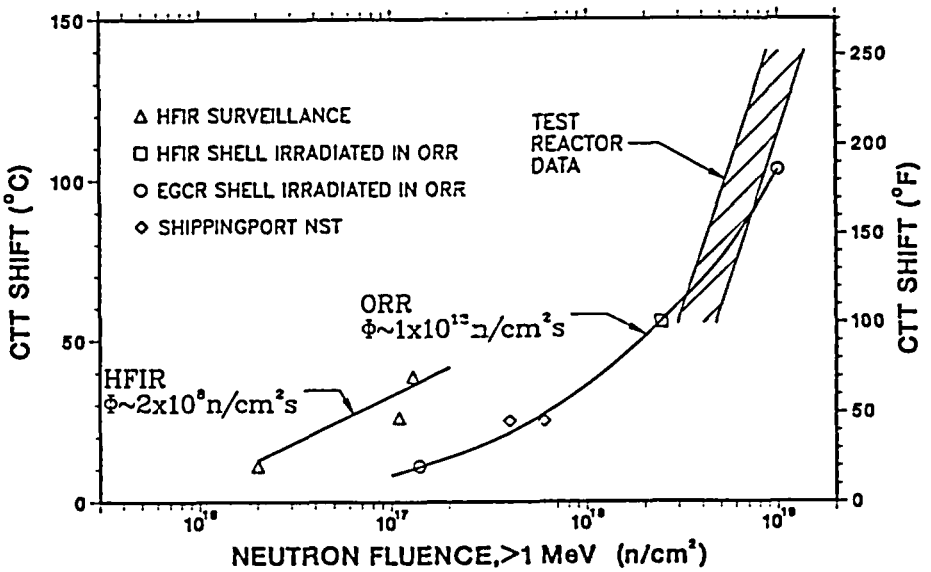

Fig. 12. Comparison of Transition Temperature Shifts for Shippingport NST with HFIR Surveillance Results and A212B data from High-Flux Test Reactors.

References

1. R. K. Nanstad, K. Farrel, D. N. Braski, and W. R. Corwin, "Accelerated Neutron Embrittlement of Ferritic Steels at Low Fluence: Flux and Spectrum Effects", J. Nucl. Mater. **158**, 1 (1988).
2. R. D. Cheverton, J. G. Merkle, and R. K. Nanstad, Evaluation of HFIR Pressure Vessel Integrity Considering Radiation Embrittlement, Oak Ridge National Laboratory Report, ORNL/TM-10444 (April 1988).
3. J. R. Hawthorne, "Studies of Radiation Effects and Recovery of Notch Ductility of Pressure Vessel Steels", British Nuclear Energy Conference, Iron and Steel Institute, London, England (1960).
4. W. L. Server, "Impact Three-Point Bend Testing for Notched and Precracked Specimens", J. Testing and Evaluation **6**, 29 (1978).
5. G. R. Odette and G. E. Lucas, Irradiation Embrittlement of LWR Pressure Vessel Steels, EPRI Report NP-6114 (January 1989).
6. G. R. Odette and G. E. Lucas, "Irradiation Embrittlement of Reactor Pressure Vessel Steels: Mechanisms, Models and Data Correlation", ASTM-STP-909, American Society for Testing and Materials, Philadelphia, 206 (1986).
7. G. E. Lucas and G. R. Odette, "Recent Advances in Understanding Radiation Hardening and Embrittlement Mechanisms in Pressure Vessel Steels", in *Proc. Second Int. Symp. on Environmental Degradation of Materials in Nuclear Power Systems - Water Reactors*, American Nuclear Society, TMS-AIME-NACE, Monterey, CA, 345 (September 1985).

FUTURE PLANS FOR NRC THERMAL-HYDRAULIC RESEARCH

Louis M. Shotkin, Chief
Reactor and Plant Systems Branch
Division of Systems Research
Office of Nuclear Regulatory Research

Water Reactor Safety Information Meeting
October, 1989

I. INTRODUCTION

The principal products of thermal-hydraulic (T/H) research are computer codes which have been assessed against data and which are capable of analyzing the behavior of the reactor coolant system under transient and accident conditions. The NRC has been developing thermal-hydraulic Systems Codes and sponsoring test programs for 15+ years. The test programs have been successfully completed. Based on code comparisons with these test data and extensive code use, closure on code development has been achieved. The codes have now reached an acceptable level of accuracy and maturity for current generation LWRs. Further development is not likely to produce major changes in our understanding of plant performance or the consequences of initiating events. Thus, it is now possible to bring the thermal-hydraulic code development program to a successful conclusion. NRC's current objective is to define the appropriate level of effort to maintain capability for thermal-hydraulic analysis in order to apply these developed codes to reactor issues in both operating reactors and advanced reactors.

II. RECENT PLANNING AND REVIEWS

An NRC Program Plan for Thermal-Hydraulic Research was published in July 1988 (Reference 1). In that NUREG report, research programs were divided into three categories: 1) major programs planned for completion by 1991/1992; 2) ongoing base programs; and 3) new programmatic initiatives. This program plan has been followed in the research activities for FY88 through FY90, and is being used to formulate plans

for FY91. After an internal review of all its programs, the Office of Research published the results of a prioritization exercise (December, 1988) which confirmed the approach outlined in the program plan. During 1988, management and staff from the NRC offices of RES, NRR and AEOD reviewed future thermal-hydraulic needs. This review concluded that thermal-hydraulic related issues will continue to arise with regularity and that the NRC staff will continue to need independent expertise and analytical capability for addressing transients in LWRs. Thus, the principal analysis codes (TRAC-PWR, TRAC-BWR, RELAP5, RAMONA, COBRA and HIPA) should be maintained for active use. To accomplish this it was suggested that a set of about 25 qualified input decks should be developed for selected codes and representative plants. The research program was reviewed by the ACRS in May and June of 1989 (Reference 3), and their recommendations to continue a four-part research program (outlined below) were agreed to by the staff (Reference 4), with the exception that the staff did not feel a new systems computer code was needed. The Commission was briefed on the status and plans for the research program (Reference 5) in early August 1989, and a Staff Requirements Memorandum (SRM) was issued by the Commission in late August (Reference 6). The SRM stressed the need to preserve and transmit the knowledge base already accumulated in the field of thermal-hydraulic research.

The staff is now preparing an update to the Research Program Plan (Reference 1) for research activities in FY92 and beyond. This paper will outline these updated plans in terms of the following research categories:

1. Computer Codes
2. Experiments
3. Data Analysis
4. Applications Research

III. FUTURE PLANS FOR T/H RESEARCH (FY92 AND BEYOND)

1. Computer Codes

The final versions of TRAC-PWR (TRAC-PF1/MOD2) and RELAP (RELAP5/MOD3), to be completed in early FY90, are expected to have an acceptable level of accuracy such that further development is not likely to produce major changes in our understanding of plant performance and accident consequences. These final code versions, plus other NRC codes already completed (RAMONA-3B, HIPA, TRAC-BWR and COBRA-NC) will provide NRC with sufficient analytical capability to meet its future needs, including any needed analyses of extended plant transients involving interaction of plant systems. These final code versions will be assessed by the International Code Assessment Program (ICAP) through 1991 when ICAP ends. It is expected that the international community of code users will continue to review new information to see if it invalidates the current understanding of code accuracy. As a result of that continuing review and code use, minor improvements and user-oriented features will be identified. NRC is discussing with ICAP members the possibility of cooperatively funding code maintenance and development activities, after ICAP ends. DOE labs have estimated 1 to 4 staff are needed per code, depending on improvements required and how actively it is used. Depending on international support and NRC requirements these codes will be maintained at appropriate DOE labs until their support can eventually be consolidated into the Thermal-Hydraulic Research Center at INEL (to be discussed further below).

Three important uses by NRC of these computer codes over the next several years are: 1) analysis of events and postulated transients in operating LWRs; 2) analysis of safety issues in advanced LWRs and other reactor designs that may be considered for use by the nuclear industry; and 3) accident management.

It is believed that existing codes are adequate for use in evaluating accident management strategies; thus, no new software development is planned for the front-end of severe accidents calculated by existing codes.

For advanced LWRs and other designs, the NRC is initiating a program to evaluate the applicability of current codes to analyze these different geometries and flow conditions. The effort will initially concentrate on the 600 MW PWR and BWR designs selected for further development by DOE. Later, if CANDU, PIUS or other designs are considered for use by the industry, the codes' applicability will be further investigated.

In the past, the scope of thermal-hydraulic research has been dominated by loss of coolant accidents and operational transients involving the reactor coolant system. The ACRS has suggested (Reference 2) that thermal-hydraulic research should have a broader perspective in the thermal sciences to include thermal and fluid transport issues related to reactor safety. Thus, the staff is considering research in areas such as fire and smoke propagation, flow effects on erosion/corrosion in pipes, and others. If any of these areas warrants further research, it is expected that existing software will be used, with only minor modifications required.

2. Experiments

Long-term research plans in experimentation fall into three areas: a) experimental facilities at universities; b) fundamental testing; and c) cooperative testing in international facilities. A fourth area, cooperative testing with domestic industry, has been successful in the past and may occur in the future. However, no specific plans exist at present.

a) Experimental facilities at universities.
Based on the favorable experience with the low-pressure, scaled

B&W loop at the University of Maryland, other small-scale loops are being planned at universities to provide experimental data and models in the future. Separate effects facilities will be considered, as required. Since it would be inappropriate to build several such facilities at one time, a gradual approach is warranted. The first such new facility might be one that would incorporate features of the advanced LWR designs. In any event, NRC staff will completely assess the benefit that has been obtained from tests with the University of Maryland facility mentioned above before proceeding with these plans. We intend to clearly define what we expect from any new test facilities at universities before any proposals to perform this research are issued. These university facilities will be actively coordinated with similar research ongoing at the T/H Research Center at INEL. For example, INEL will evaluate current code capabilities to analyze specific LWR designs and will suggest tests to assess these codes in the university facilities. This interaction will allow the skills and creative thinking which exists at the T/H Research Center to be useful in training the next generation of nuclear engineers. A useful by-product of this program is to sustain the nation's academic nuclear engineering programs and encourage top quality faculty and students to participate. For example: the criteria for evaluating proposals for additional experimental test-loop facilities will include the beneficial effects on the proposing institution's students and faculty working in areas important to the nuclear industry.

b) Fundamental Testing

It is planned to continue a small activity in fundamental testing through the existing grants program. The scope will be expanded to include research in the broader field of thermal sciences. The staff plans to first discuss with the ACRS and other experts what research topics would be most appropriate for the NRC to support.

Then a Broad Agency Announcement will be considered soliciting proposals in these areas.

c) International Facilities

It is anticipated that NRC will retain involvement in international thermal-hydraulic activities provided the resource commitment is minimized and there is substantial benefit to NRC. The NRC no longer supports any major thermal-hydraulic test facilities in the U.S. Other countries (Germany, Japan, and France) are continuing testing in facilities which formed the basis for past cooperative programs with the NRC. As these international programs (UPTF, ROSA and BETHSY) become more focussed toward issues in accident management, the NRC will consider continuing participation to a limited extent. It is expected that discussions on the scope of this participation will take place over the next year.

3. Data Analysis

A concern has been raised by both the ACRS and the Commission about how best to preserve our research results for use by "future generations" of reactor safety experts. The NRC already supports an experimental data bank, code maintenance programs, and publishes research synthesis reports on special topics. However, these existing programs may not fully address this new concern. The staff plans to review its current capabilities and identify any ways it can improve on putting completed research into the most useable form. These proposed improvements will be discussed with the ACRS and Commission to obtain a consensus on the best approach. We will first concentrate on programs recently completed (2D/3D, MIST, ROSA). Testing programs completed several years ago will pose special problems if they need to be revisited.

4. Applications Research

This is the most important element of the planned T/H program in that it applies assessed computer codes, and other completed research, to the resolution of regulatory issues that arise in operating reactors. It will also address issues identified with the advanced LWRs and other reactor designs. It is not possible to predict what scenario and which plant design will give rise to the next T/H-related regulatory issue in the 100 or so operating reactors. In anticipation of these future events, this research is being planned so that NRC will have the technical basis to respond quickly and authoritatively. What is needed are computer codes that are ready to be applied, and trained people available to apply them. The actual maintenance of the computer codes has been covered above in Section III.1. Maintaining a cadre of experts will be covered below in Section IV. The research being planned under this element addresses the actual applications and use of the codes.

Preparation for this future use involves two key activities. First is the development of qualified plant input decks for a representative set of reactor designs. These are needed to start the computer analysis of the particular transient in that particular plant, or a plant of similar design. Second, is the qualification of the computer code for its scalability, applicability and uncertainty (CSAU) when applied to selected scenarios and designs. Such CSAU studies better define the classes of reactor geometries and accident scenarios for which specific computer codes are presently applicable. This would help to assure that code performance is well understood. Accident scenarios that will be considered for these CSAU studies involve those for which code uncertainty is considered to be the dominant uncertainty, as compared with human actions and equipment reliability.

Implementation of these plans will provide the NRC with an expanded applications capability to systematically assess reactor behavior in operating LWRs, advanced LWRs, CANDU and PIUS reactors.

IV. Maintenance of Expertise

Many regulatory issues revolve around the ability to timely supply coolant to the reactor vessel, steam generators (in PWRs), and important secondary systems. NRC intends to maintain a cadre of experts (contractor and in-house) to perform thermal-hydraulic analysis of LWRs such as those required for operating reactor events (e.g., Davis-Besse, LaSalle), licensing issues, and generic research (e.g., front-end of severe accident sequences). The challenge is to provide interesting and important research activities to assure that the most competent personnel remain involved.

The primary institution for maintaining T/H expertise is the Thermal-Hydraulic Research Center at INEL (Reference 7). Expertise will be maintained at other DOE labs, if appropriate. Since much of the planned research is most suitable for a university environment, long-term research programs will be established at selected universities, and short-term programs will be funded at many others. It is also recognized that NRC staff expertise must also be maintained in the field of thermal-hydraulics. This will be accomplished by allotting more time for staff to perform in-house research and analysis that was formerly delegated to contractors.

V. Summary

The NRC has completed over 15 years of successful thermal-hydraulic research. Final versions of the T/H system codes, TRAC and RELAP, are being released. These will be assessed and maintained by an international group of users. All major testing programs have also been completed (i.e., Semiscale, LOFT, 2D/3D, MIST, FIST, etc.).

Because of the importance of thermal-hydraulics to many of the regulatory issues that periodically face this agency, the NRC intends to

maintain a vigilant posture of preparation in order to resolve future T/H-related issues.

The total level of support being planned is 6 to 7M $/year (Reference 5). Over half (3.5 to 3.8M) of this would be for applications research to provide direct support for resolution of regulatory issues in operating LWRs, as well as in advanced LWRs. The rest would provide for new research in data analysis and thermal sciences (1.5M), with an equal amount (1.5M) for computer code maintenance and fundamental testing.

This total level would support about 15 to 20 people at the T/H Research Center, an additional 5 to 10 individuals at other DOE labs and about 10 to 15 graduate students at universities.

References

1. Nuclear Power Plant Thermal-Hydraulic Performance Research Program Plan, NUREG-1252, July 1988.
2. A Prioritization of Research Activities, J. Pittman, NUREG-1319, December 1988.
3. Letter, D. Ward, ACRS, to L. Zech, NRC, "NRC Thermal-Hydraulic Research Program," June 15, 1989.
4. Letter V. Stello, NRC to D. Ward, ACRS, "NRC Thermal-Hydraulic Research Program," July 24, 1989.
5. SECY 89-219, "Status and Plans for T/H Research Conducted by the Office of Nuclear Regulatory Research," July 24, 1989.
6. Staff Requirements Memorandum, M890803, S. Chilk, Secretary, to J. Taylor, Acting Executive Director for Operations, August 21, 1989.
7. Plan for Integrating Technical Activities within the USNRC and its Contractors in the area of thermal-hydraulics, NUREG-1244, April 1987.

THE UK CONTRIBUTION TO IMPROVEMENTS IN TRAC AND RELAP5

by

I.Brittain (AEA Technology, Winfrith, Dorset)

and

M.Coney (National Power Technology & Environmental Centre, Leatherhead)

SUMMARY

This paper describes the work that has been performed in the UK on the improvement of the advanced thermal-hydraulic codes TRAC-PF1 and RELAP5. This work is part of an internationally co-ordinated effort organised by the USNRC via the International Code Assessment and Applications Program (ICAP).

The present paper describes a new reflood model for TRAC, which includes modifications to the modelling of both the heat transfer and the hydraulics. There is also an option to calculate the quench front progression using an analytic method. The use of the the present finite difference method for calculating the effects of steep axial and transverse temperature gradients in the cladding has also been investigated in some depth and has improved our understanding of the limitations of this method. Another significant improvement to the TRAC code is the development of a model to represent external thermocouples. This is important because of the central role that the LOFT experiments play in the validation of computer codes for large break LOCA analysis.

The UK contribution to improvement of the RELAP5 code has been focussed on the area of interphase drag under wet-wall conditions. Much of the work performed over the last year has been on developmental assessment, and this has led to some changes to the model. Finally, the paper describes work done to overcome problems in the RELAP5 modelling of counter-current flow in a PWR hot leg.

1.INTRODUCTION

Work has continued in the UK on both code assessment and code improvement and studies have been performed with both existing and new versions of RELAP5 and TRAC-PF1. As explained in a paper to this meeting a year ago (Brittain & Coney, 1988) it is intended that RELAP5 will be used in the UK for the formal assessment of licensing calculations concerning small break LOCA and pressurized transients in the Sizewell B plant, while TRAC-PF1 will be used for the assessment of large break LOCA calculations. The licensing calculations themselves will be performed using Westinghouse codes.

The present paper focusses on the work performed by UK staff on the development of the new versions (RELAP5/MOD3 and TRAC-PF1/MOD2) within the framework of the ICAP Code Improvement Plan. As stated in the 1988 paper, the UK contribution to the ICAP Code Improvement Plan is in three areas. The first and largest of these is the problem of post-CHF heat transfer and quenching in large break LOCA. The UK effort has been directed at the TRAC code for this case. The second area is that of interphase drag under wet wall conditions, which is of particular interest in small breaks and intact circuit faults, where it is very important to provide an accurate calculation of the mixture level in the core and in the steam-generators. The third area is the implementation of an improved offtake model in order to make better predictions of the flow and quality from a junction or a break in a horizontal pipe, such as the PWR hot leg, where stratified conditions might exist. The interphase drag and offtake model improvements have both been directed at the RELAP5 code. Although the UK developments have been aimed at TRAC or RELAP in accordance with our planned usage of the codes, the broad intention was that the improvements would be adopted for both codes.

The present paper includes an outline of a new reflood model that has been developed for TRAC-PF1/MOD2. This consists of a reflood hydraulics model, which aims to provide a much closer correspondence in terms of physical behaviour to that observed in separate effect reflood experiments. In particular, a much less oscillatory flow of entrained liquid is expected. Another development, which is implemented as an option, is an analytic model for quench progression, which is based on axial conduction theory and on experimental data from a wide range of reflood and other quench experiments. This model should provide a more accurate prediction of quench behaviour without requiring an extremely fine numerical mesh to represent the cladding temperatures in the quench front region.

The paper also contains a description of a model to represent the external thermocouples, which has also been implemented in TRAC-PF1/MOD2. This should allow the direct use of the important LOFT large break data in code validation, without having to make separate (and controversial) judgements on the effects of the external thermocouples in particular transients.

The new interphase drag model which has been implemented in RELAP5/MOD3 is described and an outline is given of the significant amount of assessment that has been carried out on this model over the last year. The offtake model, which has also been implemented in RELAP5/MOD3, has previously been described and assessed (Brittain & Coney, 1988), so there is no further discussion of this

work in the present paper. However the paper does include a report on an investigation of possible improvements to RELAP5 which would overcome deficiencies in the modelling of counter-current flows in a PWR hot leg. These deficiencies came to light during analysis of previously published data from the Upper Plenum Test Facility (UPTF).

Implementation of Improvements

Most of the development work for the new models was carried out using versions of TRAC-PF1/MOD1 and RELAP5/MOD2. However an essential part of the programme has been the implementation of new models in the mainstream versions of TRAC-PF1/MOD2 and RELAP5/MOD3. This was done during temporary attachments of five UK staff to the Idaho National Engineering Laboratory (INEL) or the Los Alamos National Laboratory (LANL) during the past year.

2. A REVISED REFLOOD MODEL FOR THE TRAC-PF1/MOD2 CODE

2.1 Reflood Model Description

The new reflood model was put together first as a stand-alone reflood program, and then implemented into TRAC-PF1/MOD2 (LANL version 4.4, including updates). For the vessel component in TRAC, the geometry can be either cylindrical or Cartesian. In either case, with a vertical vessel, the cells are arranged in columns, side by side. Each of these columns is modelled separately by the UK reflood model and is here termed a channel. In each channel, at any particular time, the model imposes one of the two 1-D steady state flow patterns shown in Figure 1. These are characterised by the two parameters ZTLC and ZQF, the heights of the top of the liquid column and the quench front respectively. These parameters move in time, hence the model is termed quasi-steady.

The height of the quench front is determined by one of two methods, the choice of which is user-specified. The first method is by finding the lowest point on a fuel rod such that its outer surface temperature is at the quenching temperature. The second uses an analytic quench front progression model, which is described later.

The top of the liquid column (ZTLC) is the lowest point at which one of the following three situations occur:

1. The void fraction exceeds a critical value
2. All the available liquid has been used up
3. The film Weber number exceeds a critical value (inverted annular flow)

Detailed steady state flow models are applied to each channel. In the region below both the quench front and the top of the liquid column, bubbly flow is modelled using the Chexal-Lellouche (1986) drift flux correlation for void fraction, and the Chen (1966) correlation for nucleate boiling heat transfer. Between the quench front and the top of the liquid column, a region of either annular flow or inverted annular flow is modelled, as shown in figure 1. Inverted annular flow is represented by the Denham (1983) model. This involves a pressure balance between the vapour film and the liquid "core", and a modified Bromley correlation for the heat transfer. The Chexal-Lellouche correlation is again used to determine the void fraction in the liquid "core". In the annular

flow region, the movement of the film is ignored and the entrained droplets are modelled in the same way as for dispersed droplet flow (see below). The Chen correlation is used for the heat transfer. In the region above both the quench front and the top of the liquid column there is dispersed droplet flow. The modelling here is based on that used for the reflood analysis code BERTHA, (Pearson & Cooper, 1985).

2.2 Interfacing the Reflood Model to the Main TRAC Scheme

The equations describing the flow regions are solved on a fine reflood mesh, similar to that used for the heat transfer in the standard version of the code. The flow conditions (mass flow rates, enthalpies) at the base of the channel are taken from the TRAC main solution and the equations describing the model solved by marching up this mesh, using the old time rod temperatures. Within each of the flow regions the equations are strictly steady state (ie. the total mass flow rate of liquid and vapour is independent of axial height), but this is not true at the top of the liquid column where a significant amount of liquid may be accumulating. Thus just above this point (at the start of annular or dispersed droplet flow) the mass flow rates must be separately specified. The vapour mass flow rate is taken to be continuous, while the liquid mass flow is chosen in such a way as to make the total liquid in the channel equal to that in the TRAC main solution at the last time step. The model provides heat transfer coefficients directly for the fine mesh used for the rod and these are averaged, by conserving heat flux, to provide coefficients for the coarse hydraulic mesh of the main TRAC solution. The void profile output by the model on the fine mesh is also transferred to the coarse mesh. A comparison of these void fractions and the TRAC old time void fractions provides a relationship between the liquid and vapour flow rates, which under steady conditions would make the two void fractions consistent. This relationship is used in a back-calculation of interphase friction coefficient (from the TRAC momentum equations) which is then put into the TRAC main solution. In this way the only input changes to the TRAC main solution are the heat transfer and interphase friction coefficients, so that there is no interference with the conservation of mass, energy and momentum in that solution.

The UK reflood model is implemented as an option. Checks are made to ensure that the reflood model is only applied to vertical rods that lie within a single vessel. Currently only one fuel rod may lie within each channel. Implementation of the reflood model into the TRAC-PF1/MOD2 scheme was made difficult by the segregation of the heat structure and the fluid calculations within the vessel and it was necessary to change the order in which some of the calculations were performed.

2.3 Quench Front Progression using the Analytic Method

In order to improve accuracy and avoid the problems of having very fine axial mesh intervals and time steps, the option of an analytic quench front model to define the rate of progression has been implemented in the code. The method requires information on the temperature of the wall a short distance ahead of the quench front and the local temperature of the water. The physical properties of the cladding, gas gap and fuel are also required. A heat transfer correlation, which is valid for the narrow region of the order of 3 or 4 mm on the wet side of the quench front, is also required. The correlation employed

is that proposed by Yu et al (1977), who examined a wide range of separate effect quenching experiments. This information defines the boundary conditions for the analytic problem, the solutions of which are represented in the code in the form of fitted curves. These curves enable the quench front velocity to be evaluated as a function of the current boundary conditions.

The analytic method therefore predicts where the quench front should move to at the next time step. This information is utilised in the TRAC calculation by appropriate modification of the heat transfer coefficients in the immediate vicinity of the quench front elevation as predicted by the analytic model. Heat transfer coefficients above the predicted quench elevation are constrained to values appropriate to film boiling, whereas the coefficients below the quench front are given values appropriate to nucleate boiling. This fairly simple modification ensures that the main TRAC solution keeps in step with the predictions of the analytic method.

2.4 Developmental Assessment

Little assessment of the model has been possible to date due to the initial difficulties of implementation and the problems of debugging and assessing a code on the LANL computer a few thousand miles away. However, a Winfrith Post Dryout (hot patch) experiment has been modelled, and an ACHILLES forced reflood experiment is currently being run on the Los Alamos computer system from Winfrith. The Winfrith Post Dryout heat transfer rig is a metre long heated tube with a 'hot patch' at the inlet and at the outlet. Coolant water is injected at a constant rate into the tube, and the hot patch causes dryout so that the inverted annular and dispersed droplet flow regions can be investigated. In the calculations using the TRAC code, the tube was modelled by a hollow rod with no axial conduction. The power profile along the rod was taken from the experimental data. Initially the tube was full of steam, and then the coolant was injected at a constant rate until steady state conditions were obtained. At this stage the temperature and void profiles of the experiment and calculations were compared. Figures 2 and 3 give the results of the first of the experiments to be modelled. Figure 2 shows the TRAC void profiles calculated by

1. The main TRAC solution in the UK version
2. The reflood model in the UK version
3. Version 4.4, (which does not contain the new reflood model)

A comparison of curves 1 and 2 confirms that the use of the interphase friction and heat transfer coefficients calculated by the UK model leads to consistent void profiles between the TRAC main solution and the reflood model but indicates significant differences from the void profile calculated by version 4.4. Figure 3 is a comparison of the temperature profiles. In this case experimental data are available. It is seen that there is an improvement in the prediction of the temperatures by the UK version compared to version 4.4.

3. EFFECT OF TIME AND SPACE DISCRETIZATION ON QUENCH PROGRESSION

3.1 Background

TRAC sensitivity studies have shown that, under slow reflood conditions, the quench front speed increases as the mesh size is reduced (see Brittain & Coney,1988 or O'Mahoney,1989). A mesh size of 0.1mm or 0.05mm is required for convergence, and gives a quench velocity some 50% greater than a mesh of 2.5mm, which is the minimum size commonly used. It was also shown that the apparent quench temperature increases as the mesh size decreases. Because the axial conduction solution in TRAC is explicit, there is a stability limit on the time step and in these studies the code automatically reduces the time step when the finer mesh is used. It was found that some 80% of the effect on quench velocity could be achieved using the coarser mesh but with time steps limited to the smaller fine mesh values. Further studies have been carried out to understand this puzzling result, and are reported below.

3.2 Recent Investigations

The first point to note is that the TRAC surface-to-fluid heat transfer coefficient is evaluated explicitly. That is to say, the value appropriate to conditions at the start of a time step is applied throughout the time step. A second point is that smoothing and limiting techniques are applied. The actual coefficient is taken to be 45% of the new value plus 55% of the old-time value, subject to the restriction that the result is not greater than twice the old-time value. These techniques are applied on a time-step basis and not per unit time, thus some time step dependency must occur. These two points combine to give an heat transfer coefficient which is less than the theoretical value evaluated directly from the code correlations during transients in which the heat transfer coefficient increases with time, as in reflood. The previously reported calculations on the reflooding of a hot nuclear rod in a vertical PIPE component have been re-examined to determine the magnitude of the deviation from the theoretical values. Figure 4 shows a snapshot from a calculation with a 0.25mm mesh where the actual values used by TRAC are compared with the theoretical correlation. It can be seen that the peak value in this case is underestimated by some 25% and the temperature at which the peak occurs is shifted downwards by some 20 deg.K.

The effect of removing the smoothing and limiting model is shown in Fig.5. This reduces the deviation from the theoretical curve and by chance in this case, the peak actual value is very close to the peak theoretical value. The step-wise nature of the actual heat transfer coefficient is also indicated for 4 consecutive time steps at one mesh point. It was found in the earlier study that a "converged " result was obtained when the time step was reduced to 0.3 ms. Fig.6 shows that indeed the actual and theoretical heat transfer surfaces are in close agreement when the time step is artificially held at this level. Thus, the previously reported sensitivity to quench speed and apparent quench temperature to time and space step sizes is largely explained by these errors due to finite differencing. It is not easy to suggest an improved calculational method. A fully implicit evaluation would be very time-consuming and would introduce errors in the opposite direction (though peak values would not be overestimated). The effects on stability of a fully or partially implict scheme are also not known.

3.3 Relative Importance of Axial and Radial Heat Flux Terms

A by-product of the current study is a more detailed examination of the relative sizes of the axial and radial heat flux terms during the quenching process. We can write the clad surface temperature equation in the simple form:

$$\text{TOTAL}\,\frac{\partial T}{\partial t} = \text{RADIAL}\,\frac{\partial T}{\partial t} + \text{AXIAL}\,\frac{\partial T}{\partial t}$$

where RADIAL $\frac{\partial T}{\partial t}$ is the rate of change of temperature caused by the net radial heat flux and AXIAL $\frac{\partial T}{\partial t}$ is the corresponding axial term. Fig.7 shows the magnitudes of these terms from a snapshot of the TRAC calculation. It can be seen that the magnitude of the radial term is about 50% larger than that of the axial term at around 460 deg.K, but that virtually all the temperature change above 570 deg.K is accounted for by the axial term.

Although the actual heat transfer coefficients, and hence heat fluxes, are time-step dependent, the quench velocity is found to be insensitive to time step when the axial conduction is artificially suppressed. The reduction in heat transfer coefficients by differencing effects causes a reduction in the amount of heat removed by axial conduction from regions at higher temperatures. If the axial conduction term is removed, this heat cannot be removed and therefore the sensitivity to space and time discretization disappears.

4. MODELLING OF EXTERNAL CLAD THERMOCOUPLES IN TRAC

4.1 Background

The LOFT experiments on large break LOCA form an important part of the integral test data-base available for code validation. In these experiments clad temperatures were measured using external thermocouples spot-welded at intervals along the rods. Previous studies (eg. Gill & Coddington, 1988) have shown that these thermocouples are thermally decoupled from the clad and therefore do not precisely indicate actual cladding temperatures. The deviation will be at a maximum in rapid transients, and during the blowdown quenching phase of large break LOCA there will be positions in the core where the thermocouple will quench but the clad, although cooled, will not quench. A 3-dimensional finite element model has been developed by Gill & Coddington (1988) which reproduces at least semi-quantitatively the behaviour of external thermocouples. An approximation to this model has now been developed by Coddington (1989) within the TRAC-PF1/MOD2 code and is described below.

4.2 Description of the New TRAC Model

The rod conduction solution in the MOD2 version allows two heat flux paths between the solid structure and the fluid, normally used to represent two-sided heat structures. In the UK modification, one heat flux path is from the normal rod surface while the other is from the surface of the attached thermocouple. The geometry is indicated in Figure 8, where it is seen that the (1-dimensional) radial mesh extends 1 mesh point beyond the clad surface to give a single mesh representation of the thermocouple. A parameter, KP/D, which includes uncertain properties of the thermocouple weld, is used to tune the predictions. (K is the thermal conductivity of the weld, P is the contact perimeter and D is the weld thickness). It is found that values from the earlier 3-dimensional study are appropriate in the TRAC model also. The heat transfer from the thermocouple

surface is treated in exactly the same way as that from the rod surface. The modifications to TRAC are not extensive and the additional computation time is negligible.

4.3 Assessment of the TRAC External Thermocouple Model

To date, the assessment and application of the model is limited. LOFT test support Facility (LTSF) tests using SEMISCALE, FEBA (solid) and REBEKA (gas-gapped) rods have been examined. Fig.9 shows TRAC results for both FEBA (solid) and REBEKA (gas-gapped) rods. There is good agreement with the experimental clad temperature in the case of the solid FEBA rods, on which there was no external thermocouple. The predicted behaviour of the external thermocouple on the REBEKA rod indicates a rapid fall to 700K in about 4 seconds for both the values of KP/D shown in the figure. Subsequent behaviour is determined by the choice of this parameter. The experimental behaviour (not shown) indicated similar behaviour to that predicted with KP/D = 1 W/m/K, with a rapid cooldown and quench in under 4 seconds.

This model is now available in TRAC-PF1/MOD2 and can be used to carry out more detailed studies of the thermocouple effects, including estimation of biases, extent of quenching and prediction of centre-line thermocouple readings. Of course, the accuracy of such calculations depends on the provision of an appropriate heat transfer package and a proper treatment of quench establishment and progression.

5.INTERPHASE FRICTION MODEL IMPROVEMENTS TO RELAP

5.1 Need for the Improvements

Assessments of the performance of RELAP5/MOD2 showed that the code had a marked tendency to overpredict the void-fraction in rod bundle geometries. This had implications concerning the calculation of level swell and boildown in a reactor core. There was also concern that the model used for the calculation of voidage in large diameter vertical pipes was not appropriate as it assumed that slug flow would occur. Evidence was available that slugs are unstable in these large pipes and that they disintegrate into cap bubbles. The assumption of slug flow could therefore lead to an under-prediction of interfacial friction under these conditions.

5.2 Basis of the New Model

The RELAP5/MOD2 interphase friction model assumed knowledge of fundamental parameters such as the interfacial area, average and maximum bubble sizes, and the interfacial friction which corresponds to these dimensions. In reality these parameters were not known at all well and it was necessary to tune the various coefficients to obtain what was thought to be a reasonable fit to the data.

The new model takes the more pragmatic approach of using well-established void-fraction correlations to derive the steady-state coefficients. The same coefficients are also used to calculate the void fraction under non-steady conditions (as is also done in the original code). It will be seen that the new approach results in a significant improvement in the accuracy of the predictions.

5.3 Profile Slip and the Definition of Interfacial Coefficients

It is well known that there are essentially two forms of slip between phases flowing in a pipe. Local slip refers to the effects of the buoyancy on the lighter phase. Profile slip arises from the fact that the distribution of the phases across the pipe is not uniform and that wall friction forces act predominantly on the fluid nearest the wall. In the new model, a clear distinction is made between interphase drag, which refers to the local drag forces on bubbles or droplets, and interphase shear which refers to the forces arising from the velocity gradients within each phase. The interphase drag coefficient is defined in terms of the local buoyancy and the local relative velocity. The interphase shear coefficients are defined in terms of the wall friction forces and the average velocities of the two phases. The relationship between the local relative velocity and the individual average phase velocities is calculated using the distribution parameter, which is a necessary part of all drift flux correlations, which are used to predict the voidage.

In the original model implemented in RELAP5/MOD2, interfacial friction forces were calculated assuming that the local phase velocities were the same as the void-fraction weighted area average. This is equivalent to ignoring the effects of profile slip.

The new formulation incorporates known physical effects in an elegant, but pragmatic way. An important reason for choosing this method was to avoid the occurrence of negative or infinite interfacial friction coefficients which can arise if empirical drift-flux correlations are used for the derivation with inappropriate average velocities.

5.4 Selection of Void Fraction Correlations

The choice of void fraction correlations is shown in Figure 10. This selection has some differences from the original proposals of Putney (1988). All the correlations now have the form of a drift flux model. The changes to the previous selection are:

- The Kataoka-Ishii correlation is now used for low flows in both intermediate and large diameter pipes.
- At low vapour fluxes in intermediate and large diameter pipes, a churn-turbulent bubbly flow correlation is now used instead of the Kataoka-Ishii correlation.
- The original RELAP5/MOD2 model has been retained for horizontal pipes, since it is believed to be adequate for this purpose.

5.5 Counter-Current Flow Limit (CCFL)

It is intended that the new interphase friction models should be applicable to any flows in straight uniform flow channels, including counter-current flow. To ensure that the correlations do not predict drift velocities which imply a breach of known limits on counter-current flow, a CCFL correlation applicable to uniform channels is used to derive a limiting value of the drift velocity for counter-current flows. It should be noted that the counter-current form of the EPRI correlation is not used, since it was developed for a non-uniform

flow channel and because solution of the equations would be computationally expensive.

RELAP5/MOD3 also contains a separate CCFL model to deal with singularities in the flow geometry. The coefficients in this case are supplied by the user.

5.6 Comparison against Separate Effect Tests

Various tests have been used to evaluate the performance of the new model in comparison to the original RELAP5/MOD2 model and to exercise all the correlations (see Putney, 1989). Numerical problems, which affected both the standard and the new models, were encountered in some of the calculations. In particular it was sometimes necessary to reduce the time-step below that required by the Courant limit to avoid voidage oscillations. Also it was found in some instances that the Reverse Void Profile model introduced oscillatory behaviour or caused poor predictions. This model was disabled for many of the calculations described below and it is understood that it will not be implemented in the release version of RELAP5/MOD3.

Rod Bundle Tests: A comparison was made with ORNL experiments (Anklam, Miller & White, 1982) concerning level swell in a heated rod bundle at 40-45 bars. Two tests with different voidage profiles were simulated The new model gave a substantial improvement for both of the test predictions. Figure 11 shows the comparison for one of these cases, and it is seen that the new model gives excellent agreement with the data. There was some loss of accuracy when the axial nodalization was reduced from 24 volumes to 6, but the improved accuracy of the new model was still very obvious.

Forced Convection in an Unheated Tube: Agostini et al (1969) describe a series of experiments performed at CISE, involving forced convection in an unheated 9mm diameter tube. Four tests at pressures of 30 and 50 bars and flow rates between 388 and 3504 kg.m-2.s-1 were simulated and comparisons made. Putney (1989) shows that the standard model gives reasonable predictions for these cases, but the predictions of the new model are still a distinct improvement.

Phase Separation in a Vessel: Wilson et al (1965) describe a number of experiments in which steam was bubbled through a stagnant pool in a 45cm diameter vessel. One test at 69 bars was simulated. The standard model under-predicted the void-fraction by a significant margin, since it assumed that there was slug flow in the vessel. The new model gave an accurate prediction.

Depressurization of Liquid in Vessels: Findlay and Sazzi (1981) describe void fraction measurements in two vessels, both 4.27m in height, which were depressurized by simulated top breaks. Two tests were calculated, the first involving a 30cm diameter vessel which was depressurized from 70 bars to 11 bars in 200s. The standard model gives a good prediction of this test, which was used for the developmental assessment of RELAP5/MOD2. The new model also gives a good prediction, providing the Reverse Void Profile model is disabled.

A much faster depressurization (73 to 20 bars in 20s) in a larger vessel (119 cm diameter) was also simulated. In this case, both the standard model and the new model underpredict the voidage, by a significant margin as seen in Figure

12. One explanation for this is that the flashing of liquid results in the transient formation of bubbles, which are smaller than the maximum-sized cap bubbles represented by the Kataoka-Ishii correlation. To investigate this, another calculation was done in which the churn-turbulent regime was assumed to exist at high as well as low vapour fluxes. Figure 12 shows that this gives a much better agreement with the data for this test. The question of whether transient effects should be taken into account in determining flow regimes and interphase friction coefficients may well merit further investigation.

Atmospheric Pressure Level Swell in a Tube: Costigan, Ralph & Wade (1986) describe steady-state level swell tests carried out in a heated 1.25cm diameter tube at atmospheric pressure. One test was simulated using 20 axial volumes to represent the 3m test-section. The new model showed a significant improvement of the voidage predictions, but both code versions predicted a mixture level at a somewhat lower elevation than the experiment.

6. RELAP5 CALCULATIONS OF CCFL IN A PWR HOT LEG

6.1 Background

Among the tests carried out at the Upper Plenum Test Facility (UPTF) was test 11, a Hot Leg Separate Effects Test, in which was measured the runback of saturated liquid from the steam generator inlet plenum to the reactor vessel against a countercurrent flow of steam (Damerell et al, 1987). As reported by Dillistone (1989), the test has been modelled at Winfrith Technology Centre using cycle 36.05 of RELAP5/MOD2, as part of an assessment of that code's ability to model horizontal countercurrent flow.

The RELAP5 nodalisation of the test (Figure 13) consisted of a simple representation of the pressure vessel and steam-generator inlet plenum as large vertical pipes, and an inclined riser and horizontal hot leg modelled with 10 cells and an appropriate reduction in flow area to take into account the hot leg ECCS injection pipe (Hutze). The system pressure was 15 bar.

6.2 Results

The flooding-curve predicted by RELAP5 for the test is curve I in Figure 14. As can be seen, the code underestimated by a factor of more than three the steam flow-rate at the flooding-point (i.e. complete turnaround of the liquid flow), and allowed almost no partial flow of liquid. It was found that the predicted abrupt change from full to almost zero liquid flow coincided with a transition from slug flow to annular flow in the two cells representing the hot leg riser. This transition is already known to coincide with the code's prediction of flooding in vertical counter-current flow (Dillistone & Richards, 1988) and in RELAP5 is effectively determined by steam flow-rate (and not void fraction as might be expected).

6.3 Effect of Code Modifications

The slug-annular transition should not be a factor in predicting horizontal flooding, which generally coincides with a transition from stratified to slug flow. The failure of RELAP5 to allow full liquid flow when it existed in the experiment was due to its failure to predict stratified flow in the hot leg riser at low steam flow-rates. It turns out that such a prediction is impossible

for standard RELAP5, because for any pipe inclined at more than 15 degrees to the horizontal the code uses a vertical flow-regime map, which does not have a stratified flow region. In the light of this, a small modification was made to the code's horizontal flow-regime map to allow stratified flow in inclined pipes generally, and the tests were rerun with the modified code.

Modified to allow stratified flow in the riser, the code predicted quite well the flooding-point steam flow-rate, but overestimated the liquid flow badly at lower steam flows and still allowed no partial liquid flow (curve II in Figure 14). The reasons for this are not fully understood, but an important factor is believed to be the fact that the code predicted the wrong qualitative behaviour of the liquid level in the hot leg, regarded as a function of distance from the foot of the riser. At that point the liquid depth was predicted to be below the critical depth, and so should have increased with distance along the hot leg; a real, steady flow under the same conditions would increase in depth and form a hydraulic jump at some point along the hot leg. The flow predicted by the code, however, decreased steadily in depth (and consequently accelerated) all the way along the hot leg to the pressure vessel. As a result, the code must have underestimated quite considerably the maximum depth of liquid in the hot leg, which would lead to it overestimating the liquid flow even if all other factors were calculated correctly.

The failure of the code to predict even qualitatively the stratified liquid level is believed to be a consequence of the form of the momentum flux gradient terms in the code's momentum equations, together with the effect of the upwind differencing scheme on these terms. There is also the fact that the code was able to predict a highly supercritical liquid velocity at the hot leg outlet to the pressure-vessel where conventional hydraulic theory expects approximately critical flow - a problem which was also noticed in RELAP5 calculations of TPTF horizontal flow experiments (Kukita et al, 1987). It is not clear whether either of these problems has a satisfactory solution, and further investigation is intended.

6.4 Results of Stand-Alone Calculations

To see what improvement might be possible if the problems were corrected, a stand-alone program was written to tabulate, for given liquid flow, the maximum liquid depth that would occur in the hot leg as a function of steam flow-rate, assuming steady one-dimensional flow, critical depth at the exit to the pressure vessel and the same models for wall and interphase friction as appear in RELAP5/MOD2. The Taitel and Dukler (1976) criterion for stratified-slug transition, as coded in RELAP5, was then used to tabulate as a function of steam flow-rate, for the same fixed liquid flow, the liquid depth at which the stratified-slug transition would occur. A theoretical flooding-curve (curve III in Figure 14) was then deduced by assuming that the limiting steam flow for a given liquid flow was that for which the maximum liquid depth in the hot leg just matched the depth for stratified-slug transition. As can be seen from Figure, the shape of this curve is much more like that of the experimental data than either of the RELAP5 predictions (although the closeness of fit is probably fortuitous). So it is possible, although by no means certain, that RELAP5 would be able to predict horizontal counter-current flow better if it were able to predict correctly the maximum depth of liquid in horizontal stratified flow.

6.5 Effects of the Reverse Void Profile Model

Finally, it was noticed in a particularly long run using the standard version of the code that the predicted liquid flow was affected by the liquid level in the steam generator inlet plenum, something which other similar experiments indicate is not a physical effect. This was found to be a consequence of the code's "Reverse Void Profile" model, which reduces interphase friction whenever it detects a low void above a high void. This model has already been shown to have an adverse effect on the code's ability to model vertical counter-current flow (Dillistone & Richards, 1988) and it is believed that the model has been removed from the successor code RELAP5/MOD3.

7. CONCLUDING REMARKS

1. A reflood model, which is believed to represent observed physical behaviour more closely, has been implemented in TRAC-PF1/MOD2. This model includes the option of an analytic quench progression model as an alternative to the fine mesh temperature calculation. So far, very little assessment of the new reflood model has been performed.

2. An investigation has been performed into the problem of convergence of the quench front advance even when very small time steps and mesh sizes are used. This is now understood, but there appears to be no clear way of achieving an accurate prediction of the quench front advance (by the fine mesh method), without adding significantly to the computer run time.

3. A model to represent external cladding thermocouples has been implemented into TRAC-PF1/MOD2. This is expected to be useful for the quantification of thermocouple effects in the LOFT large break tests.

4. A new interphase drag model has been implemented into RELAP5/MOD3 and a sufficient amount of assessment has been performed to exercise all the correlations used. The results indicate that the new model gives a substantial improvement in some situations, and never gives significantly worse predictions than the original model.

5. Suggestions are made for the correction in RELAP5/MOD3 of certain faults with the MOD2 modelling of CCFL in horizontal pipes. In particular, it is suggested that:

   a. The criterion for stratified flow in inclined pipes should be changed.

   b. The "Reverse Void Profile" model should be modified or removed.

   c. There should be an improvement in the method of predicting liquid level in horizontal stratified flow.

6. The collaboration with the USA and other countries within the auspices of the ICAP agreement continues to form an important part of the UK's activities on LOCA code improvement and validation. It is hoped that this fruitful collaboration will continue for several years to come.

8. ACKNOWLEDGEMENTS

The authors wish to acknowledge the efforts of all staff who contributed to the work described in this paper and particularly Dr.J.M.Putney, Dr.W.M.Bryce, Dr.P.I.R.Jones, Mr.N.Newman and Dr.P.Coddington who have implemented code improvements at INEL or LANL.

This paper is published by permission of AEA Technology and of National Power (currently a division of the CEGB).

REFERENCES

Agostini,G., Era,A. and Premoli,A.,1969, Density measurements of steam-water mixtures flowing in a tubular channel under adiabatic and heated conditions, CISE-R-291.

Anklam,T.M., Miller,R.F. and White,M.D.,1982, Experimental investigations of uncovered-bundle heat transfer and two-phase mixture-level swell under high-pressure low heat-flux conditions, NUREG/CR-2456

Brittain,I. and Coney,M.W.E.,1988, The UK Contribution to Improvements in TRAC and RELAP, Paper to 16th WRSM, NUREG/CP0097-Vol.4.

Chen,J. C.,1966, A Correlation for Boiling Heat Transfer to Saturated Fluids in Convective Flow, Process Design Development, Vol 5, pp 322-327.

Chexal,B. and Lellouche,G.,1986, A full-range drift-flux correlation for vertical flows (Revision 1), EPRI NP-3989-SR

Coddington,P.,1989, Implementation of an External Thermocouple Model into TRAC-PF1/MOD2, AEEW-R2547 (to be published)

Costigan,G., Ralph,J.C. and Wade,C.D.,1986, Boiling and dryout studies on water in a partially filled vertical tube, AERE-R12472

Damerell,P.S., Ehrich,N.E. and Wolfe,K.A.,1987, Use of full-scale UPTF data to evaluate scaling of downcomer (ECC bypass) and hot-leg flow phenomena. 15th WRSM, Gaithersburg. NUREG/CP 0091, Vol.4.

Denham,M.K.,1983, Inverted Annular Film Boiling and the Bromley Model AEEW-R1590

Dillistone,M.J.,1989, Analysis of the UPTF separate effects test No.11 (steam-water counter-current flow limitation in the broken loop hot leg) using RELAP5/MOD2, AEEW-M2555

Dillistone,M.J. and Richards,C.G.,1988, Modelling vertical counter-current flow limitation using RELAP5/MOD2, AEEW-M2512

Findlay,J.A. and Sazzi,O.L.,1981, BWR refill-reflood program - model qualification task plan, EPRI NP-1527, NUREG/CR-1899, GEAP-24898.

Gill,C.R. and Coddington,P.,1989,"Analysis of Heat Transfer from Fuel Rods with Externally Attached Thermocouples" AEEW-R2352.

Kataoka,I. and Ishii,M.,1987, Drift flux model for large diameter pipe and new correlation for pool void fraction, Int. J. Heat Mass Trans. 30, 1927-1939.

Kukita,Y., Anoda,Y., Nakamura,H. and Tasaka,K.,1987, Assessment and improvement of RELAP5/MOD2 code's interfacial drag models, Heat Transfer - Pittsburgh 1987, AIChE Symposium Series 83, 212-217.

O'Mahoney,R.,1989, A study of axial effects in the TRAC-PF1/MOD1 heat conduction solution during quenching. AEEW-M2552.

Pearson,K.G. and Cooper,C.A.,1985, BERTHA : A Programme for the Thermal/Hydraulic Analysis of Reflooding Experiments, AEEW-R1874

Putney,J.M.,1988, Proposals for improving interphase drag modelling for the bubbly and slug regimes in RELAP5, CERL Report No. RD/L/3306/R88

Putney,J.M.,1989, Development of a new bubbly-slug interfacial friction model for RELAP5 - Final Report. National Power Report ESTD/L/0075/R89.

Taitel,Y. and Dukler,A.E.,1976, A model for predicting flow regime transitions in horizontal and near horizontal gas-liquid flow AIChE Journal Vol.22 no.1.

Wilson,J.F., Littleton,W.E., Yant,H.W. and Meyer,W.C.,1965, Primary separation of steam and water by natural separation: Part I, Allis Chalmers Atomic Energy Division, Report ACNP-65002.

Yu,S.K.W., Farmer,P.R. and Coney,M.W.E.,1977, Methods and correlations for prediction of quenching rates on hot surfaces, Int.J.Multiphase Flow, Vol.3, pp415-443.

Zuber,N., Staub,F.W., Bijwaard,G. and Kroeger,P.G.,1967 Steady-state and transient void fraction in two-phase flow systems, General Electric Report GEAP-5417

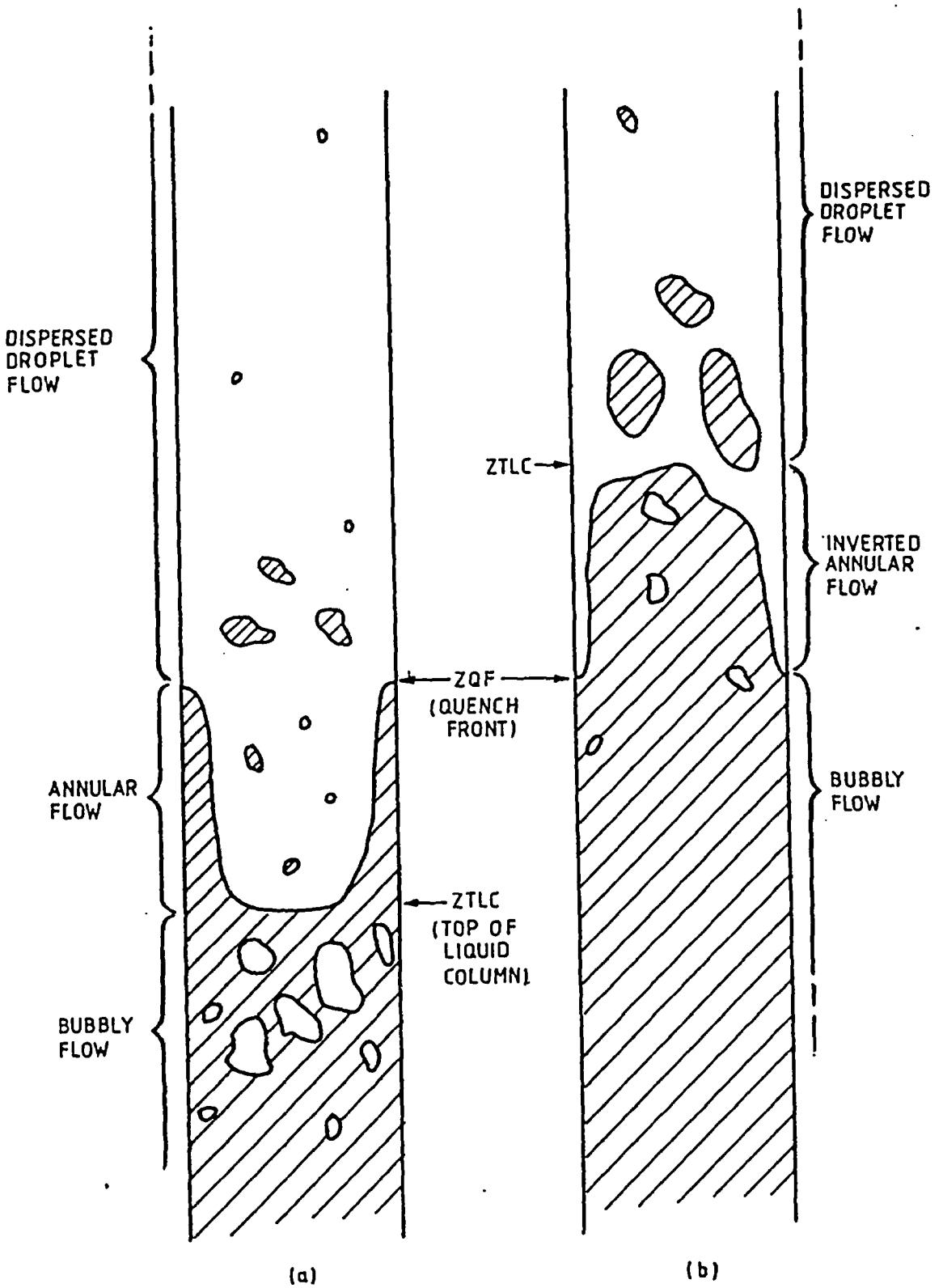

FIG. 1 FLOW PATTERNS IMPOSED DURING REFLOOD

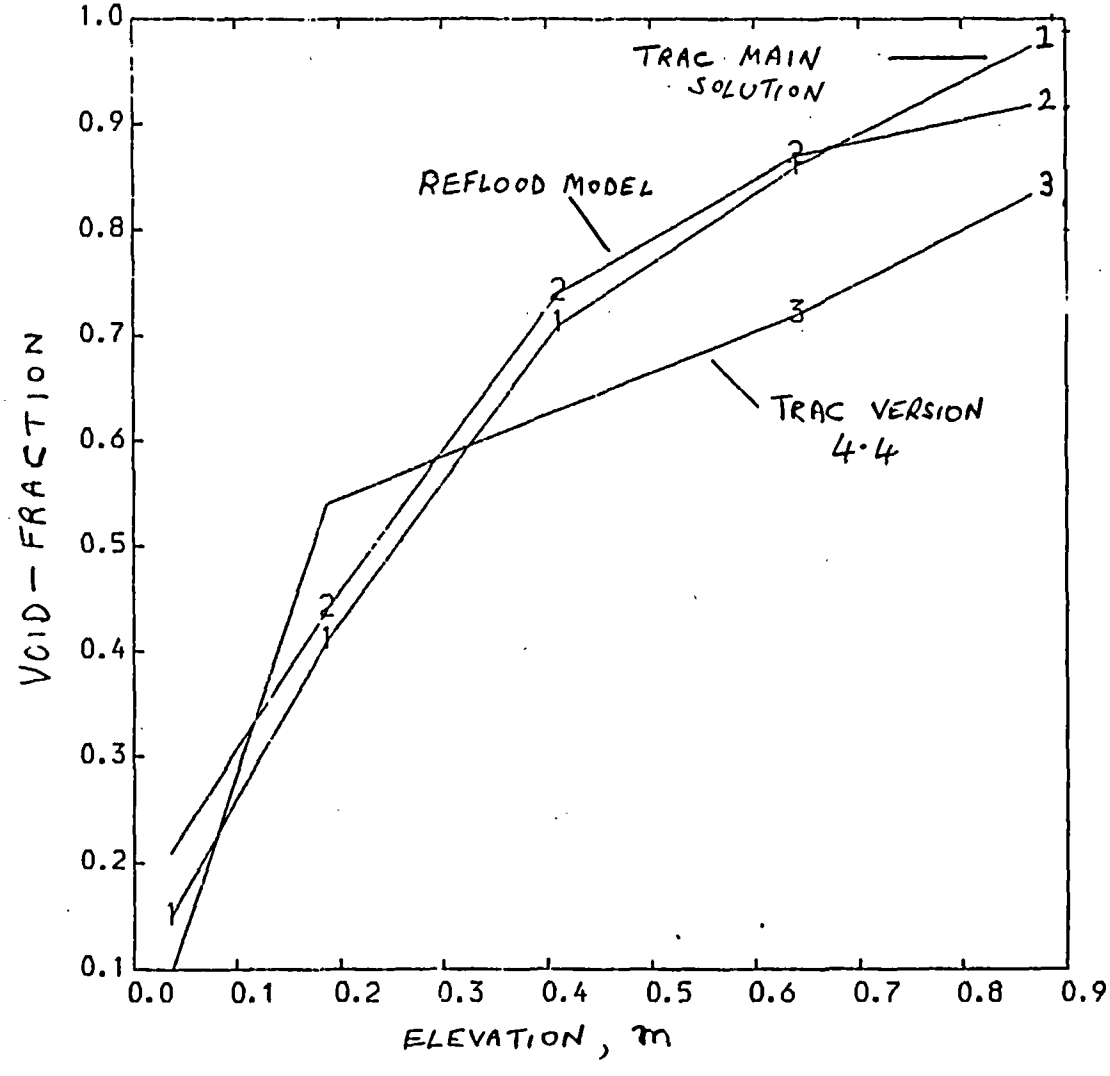

FIG 2. COMPARISON OF VOID FRACTION PREDICTIONS FOR WINFRITH POST-DRYOUT TEST

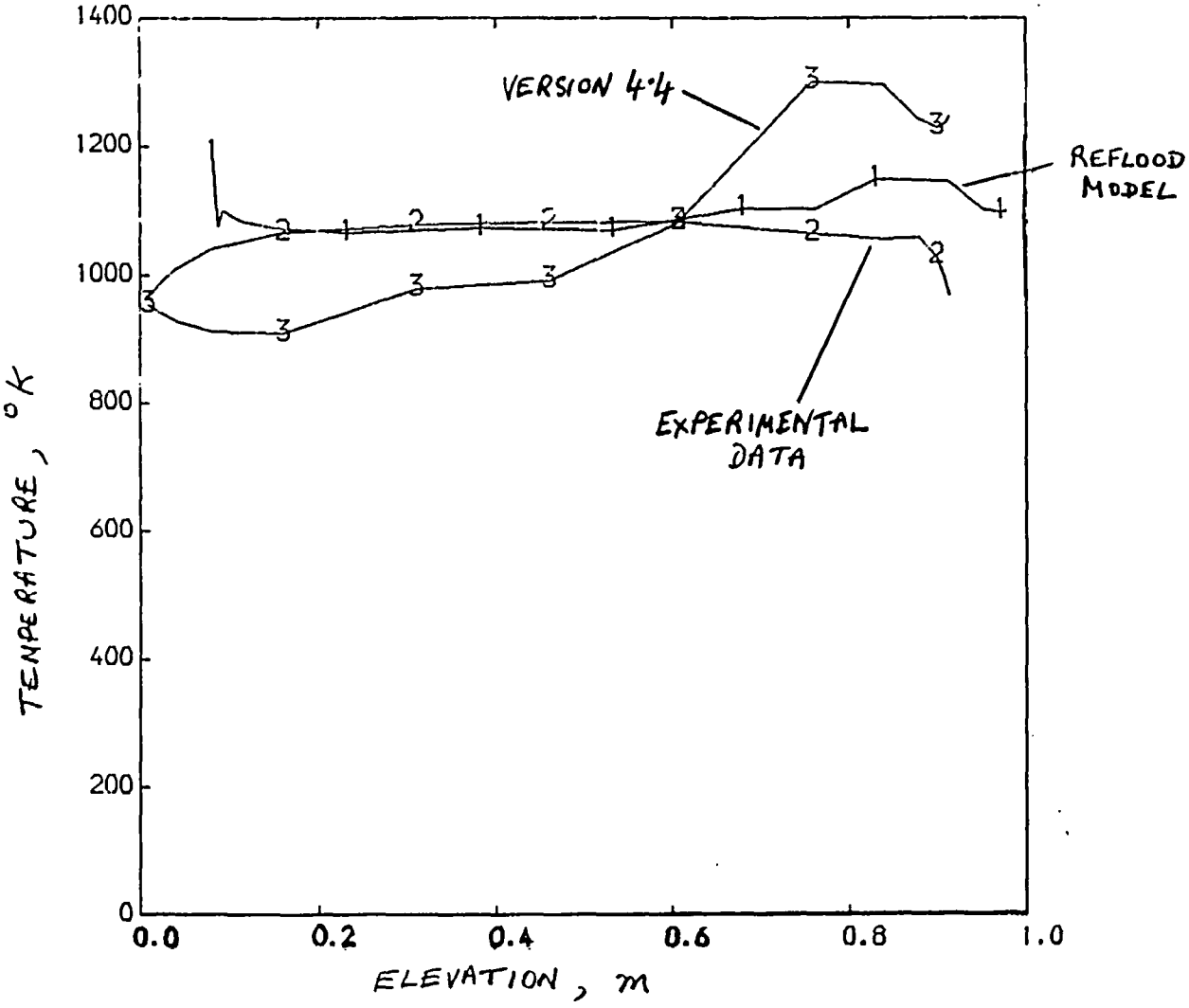

FIG. 3. COMPARISON OF CALCULATED AND MEASURED TEMPERATURES FOR WINFRITH POST-DRYOUT TEST

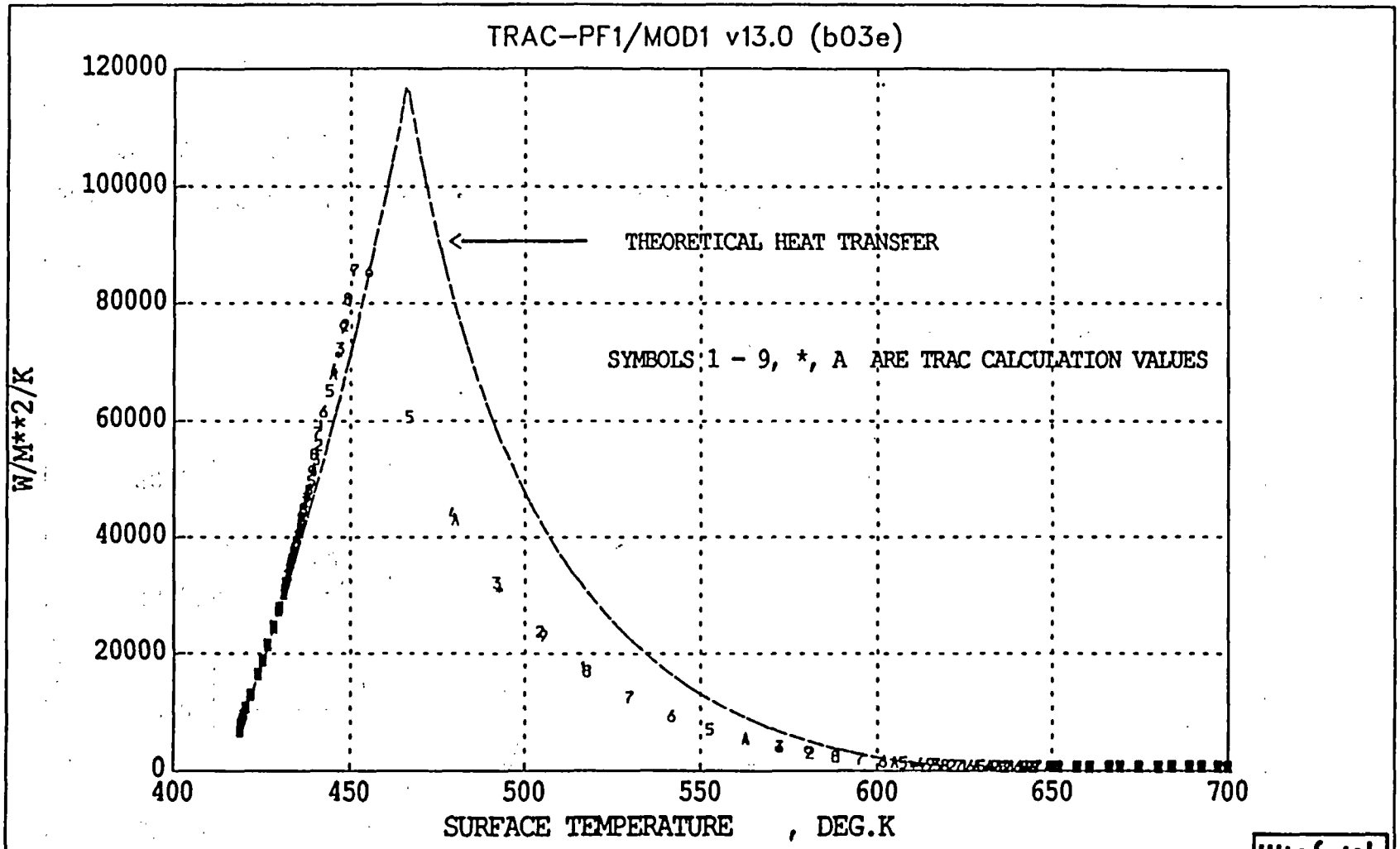

FIGURE 4

SURFACE-TO-FLUID HEAT TRANSFER COEFF. VS TEMPERATURE, AT 20 SECONDS
TRAC CALCULATION WITH 0.25MM MIN MESH + THEORETICAL HEAT TRANSFER

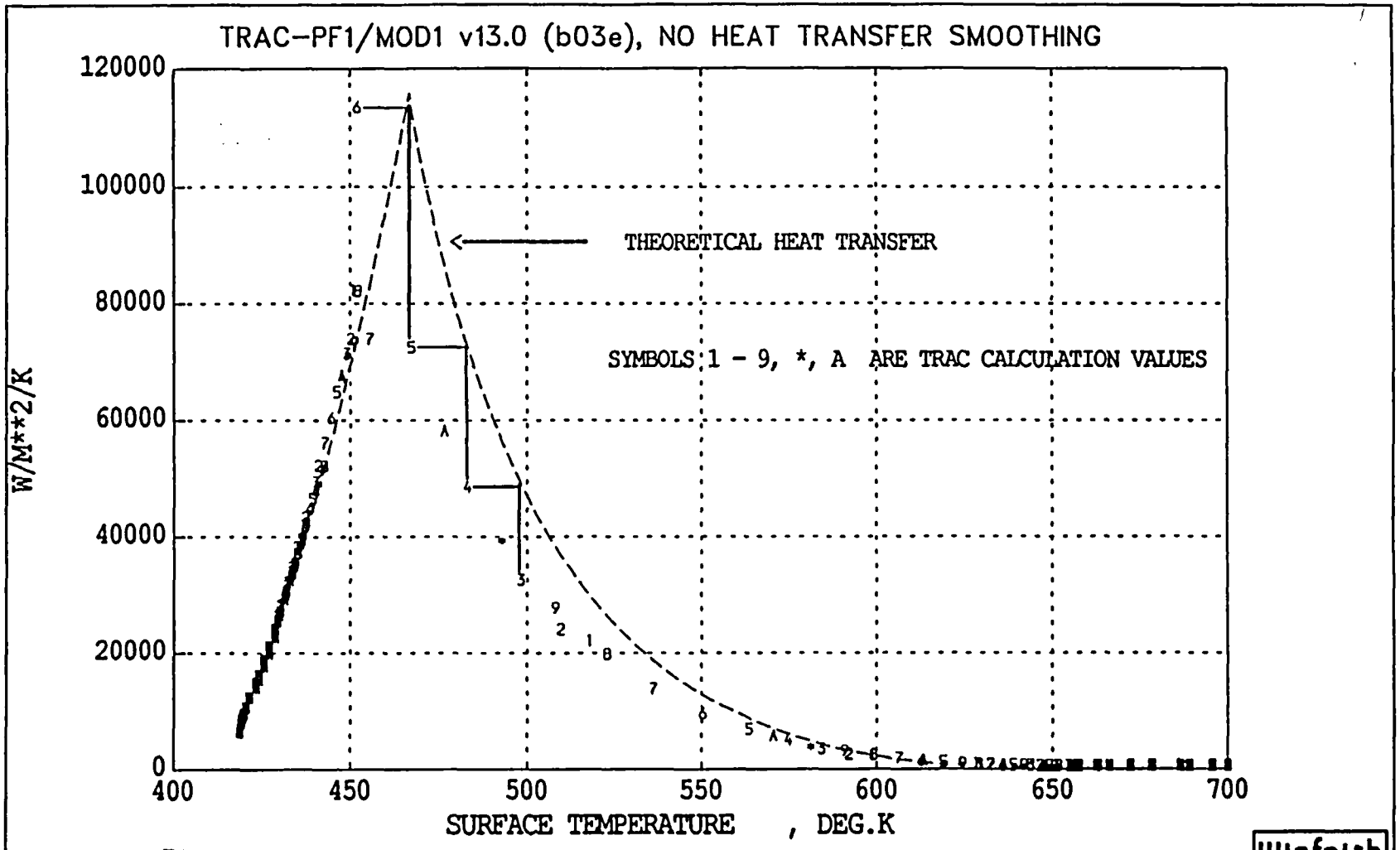

FIGURE 5

SURFACE-TO-FLUID HEAT TRANSFER COEFF. VS TEMPERATURE, AT 20 SECONDS
TRAC CALC. WITH 0.25MM MIN MESH, NO SMOOTHING + THEORETICAL H. T.

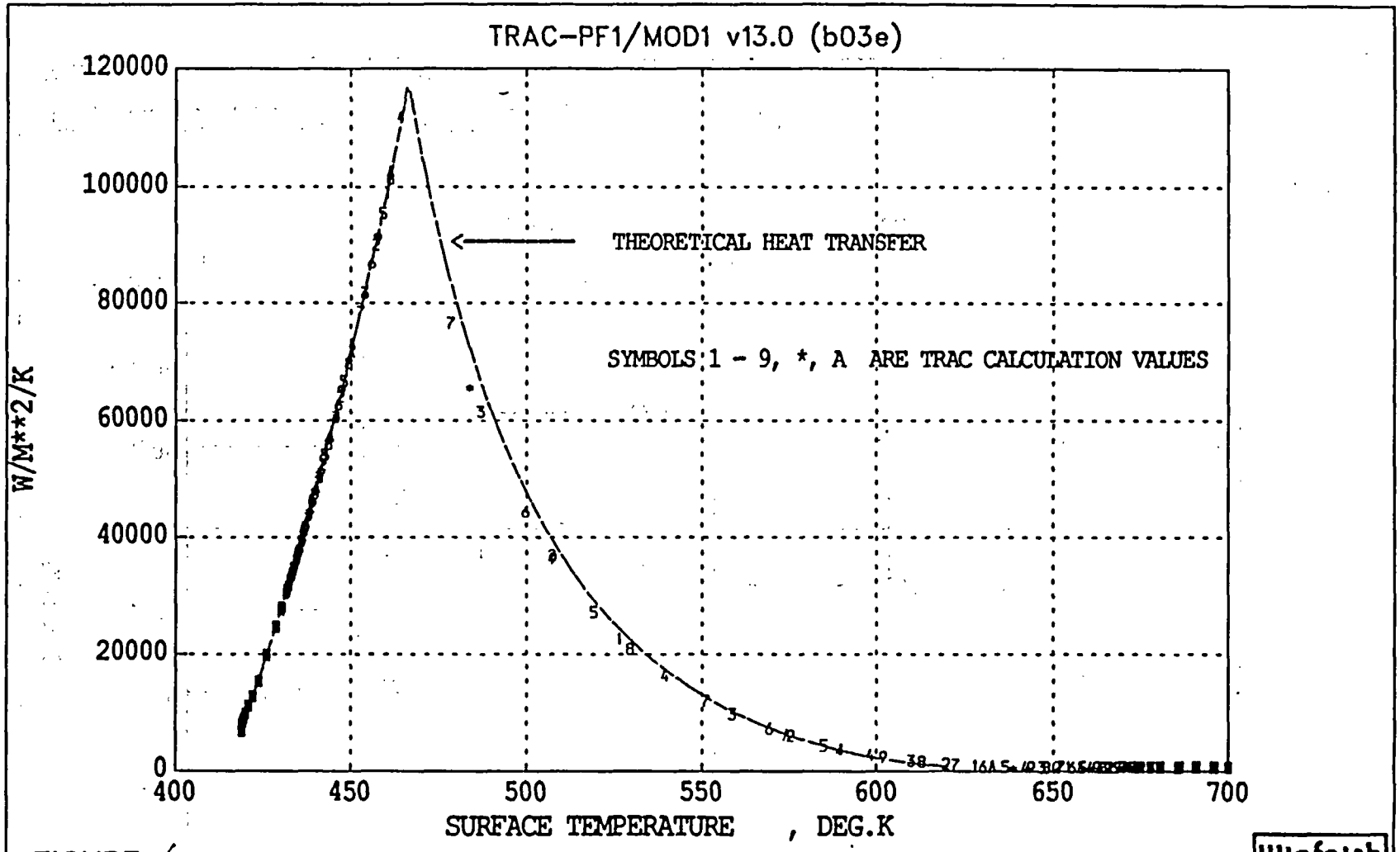

FIGURE 6

SURFACE-TO-FLUID HEAT TRANSFER COEFF. VS TEMPERATURE, AT 20 SECONDS
TRAC CALC. WITH 0.25MM MIN MESH, 0.3MS TIMESTEP + THEORETICAL H.T.

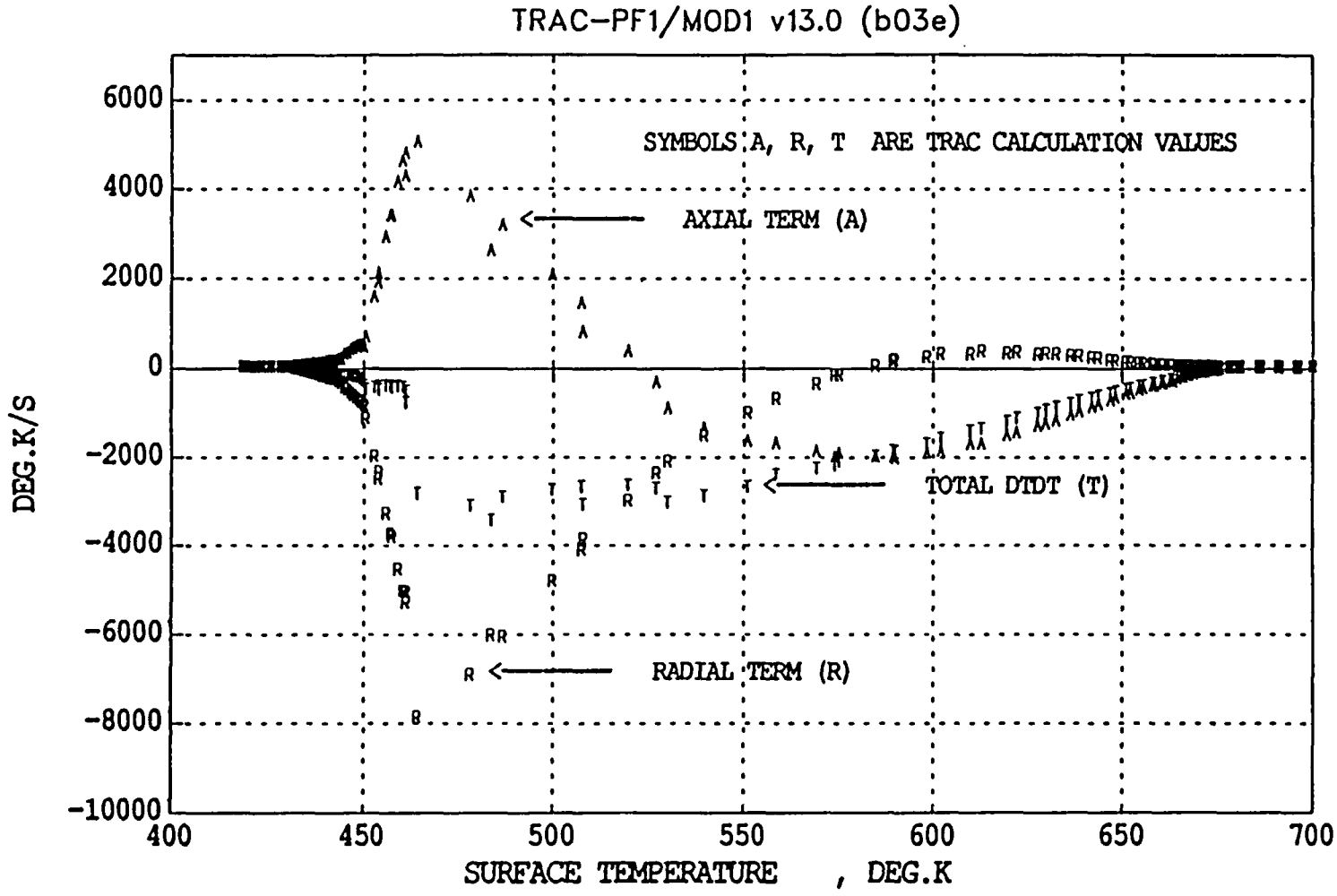

FIGURE 7

HEAT CONDUCTION EQUATION: QUENCH FRONT PROFILE AT 20 SECONDS
TRAC CALCULATION WITH 0.25MM MIN MESH, 0.3MS TIMESTEP

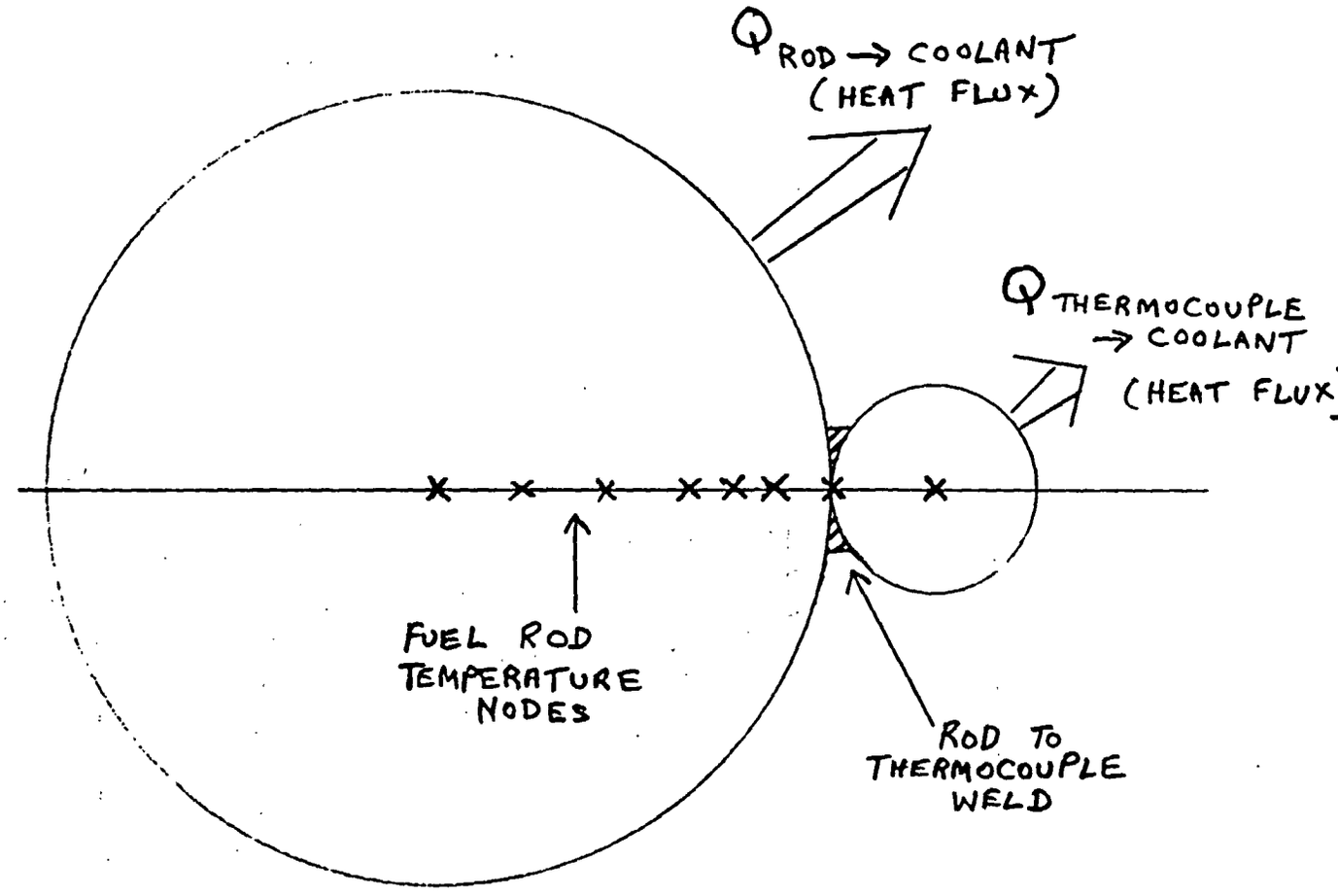

FIG. 8. PLAN VIEW OF TRAC EXTERNAL THERMOCOUPLE MODEL

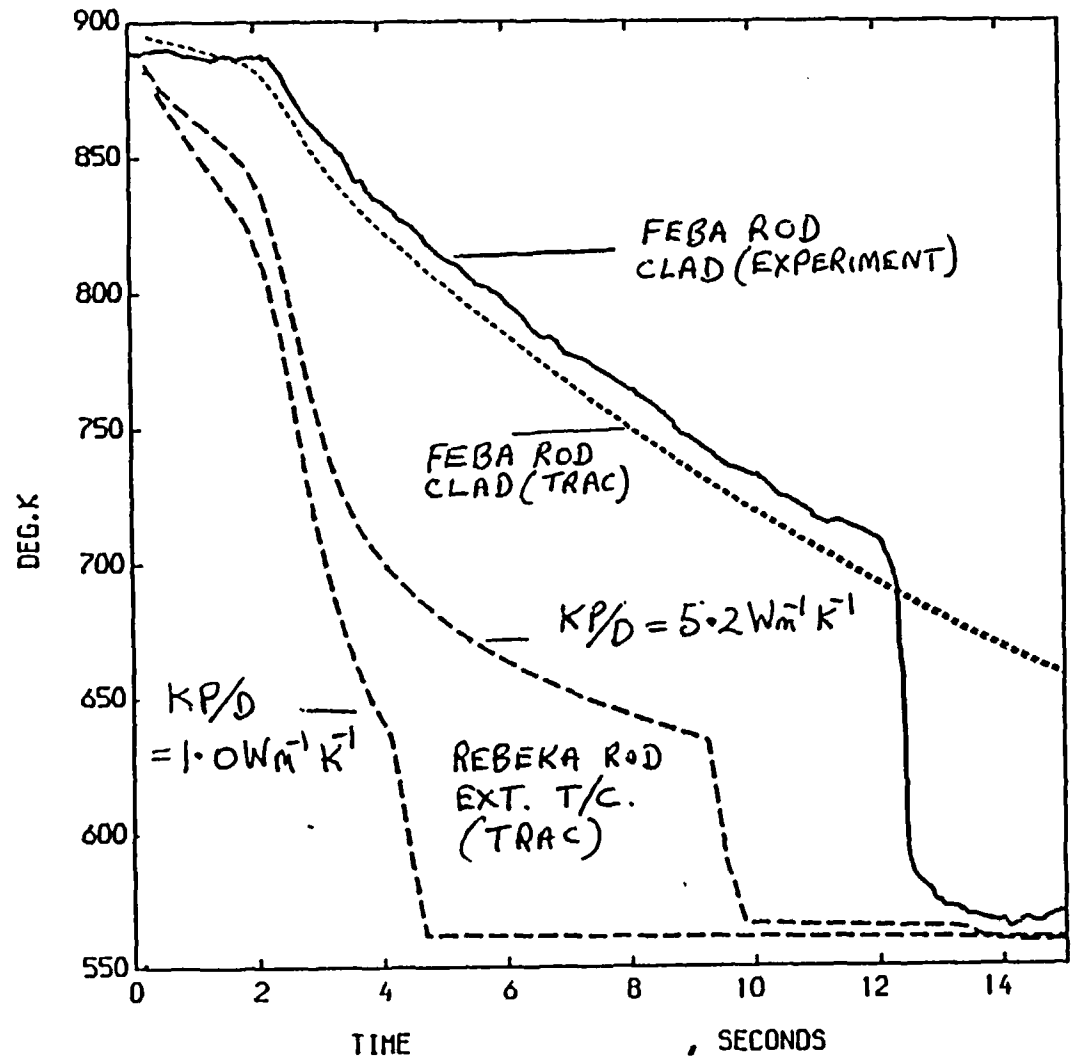

FIG 9. PREDICTIONS OF TRAC EXTERNAL THERMOCOUPLE MODEL FOR LTSF RUN 1: FEBA ROD CLAD TEMPERATURE AND REBEKA ROD EXTERNAL THERMOCOUPLE TEMPERATURES AT AXIAL ELEVATION OF 1.95 m.

Figure 10. Drift Flux Correlations used in New Interfacial Friction Model

	Rod Bundles	Small Pipes $D_h \leq 1.8cm$	Large Pipes $D_h > 1.8cm$
High Upflow Rates $G > 100$ $kg\ m^{-2}\ s^{-1}$	EPRI	EPRI	
Low Up, Down and Counter-Current Flow Rates $G < 50$ $kg\ m^{-2}\ s^{-1}$ $G > -50$ $kg\ m^{-2}\ s^{-1}$	EPRI	Zuber-Findlay Slug Flow	Churn-Turbulent Bubbly Flow + Kataoka-Ishii (1)
High Downflow Rates $G < -100$ $kg\ m^{-2}\ s^{-1}$	EPRI	EPRI	

Interpolation applied between different flow regions in pipes

(1) Churn-turbulent bubbly flow is assumed at low vapour fluxes.

References

EPRI - Chexal and Lellouche (1986)

Zuber-Findlay Slug Flow - Zuber, Staub, Bijwaard and Kroeger (1967)

Churn-Turbulent Bubbly Flow + Kataoka-Ishii - Kataoka and Ishii (1987)

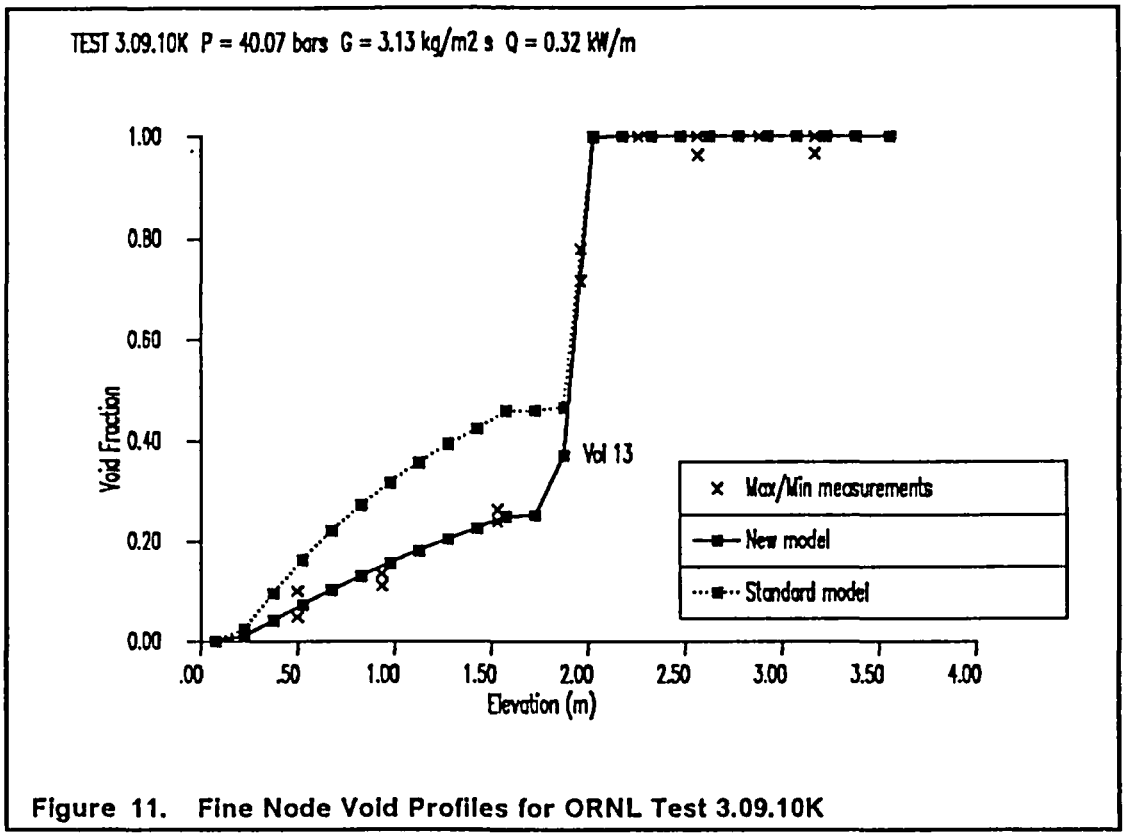

Figure 11. Fine Node Void Profiles for ORNL Test 3.09.10K

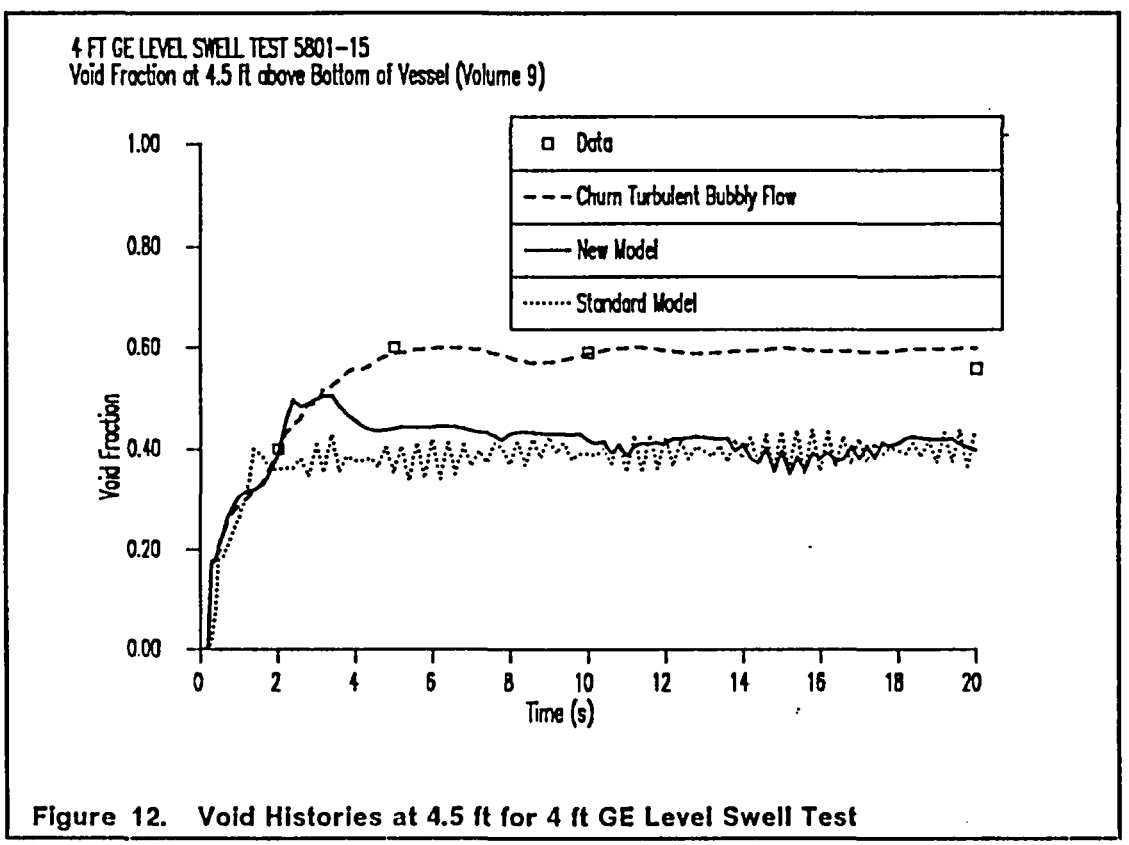

Figure 12. Void Histories at 4.5 ft for 4 ft GE Level Swell Test

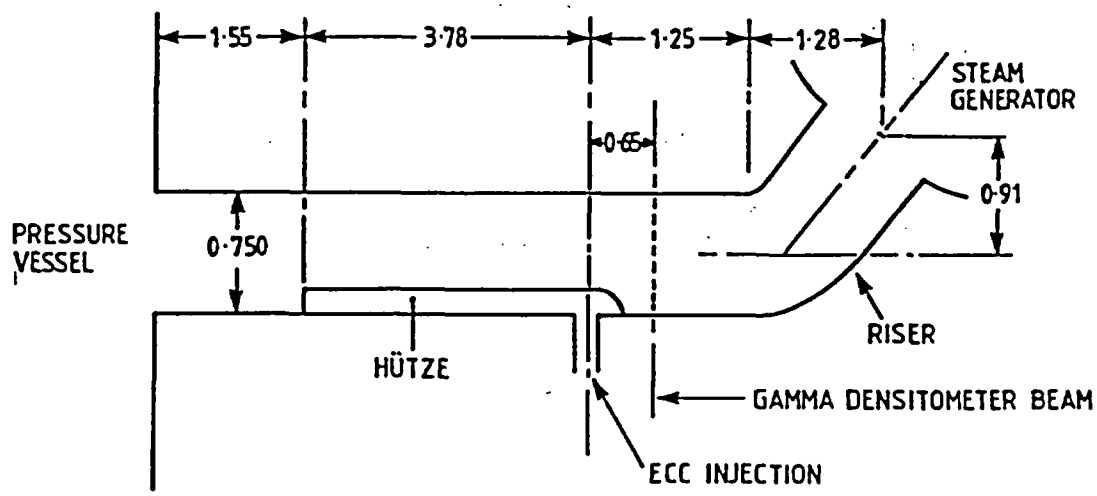

UPTF BROKEN LOOP HOT LEG

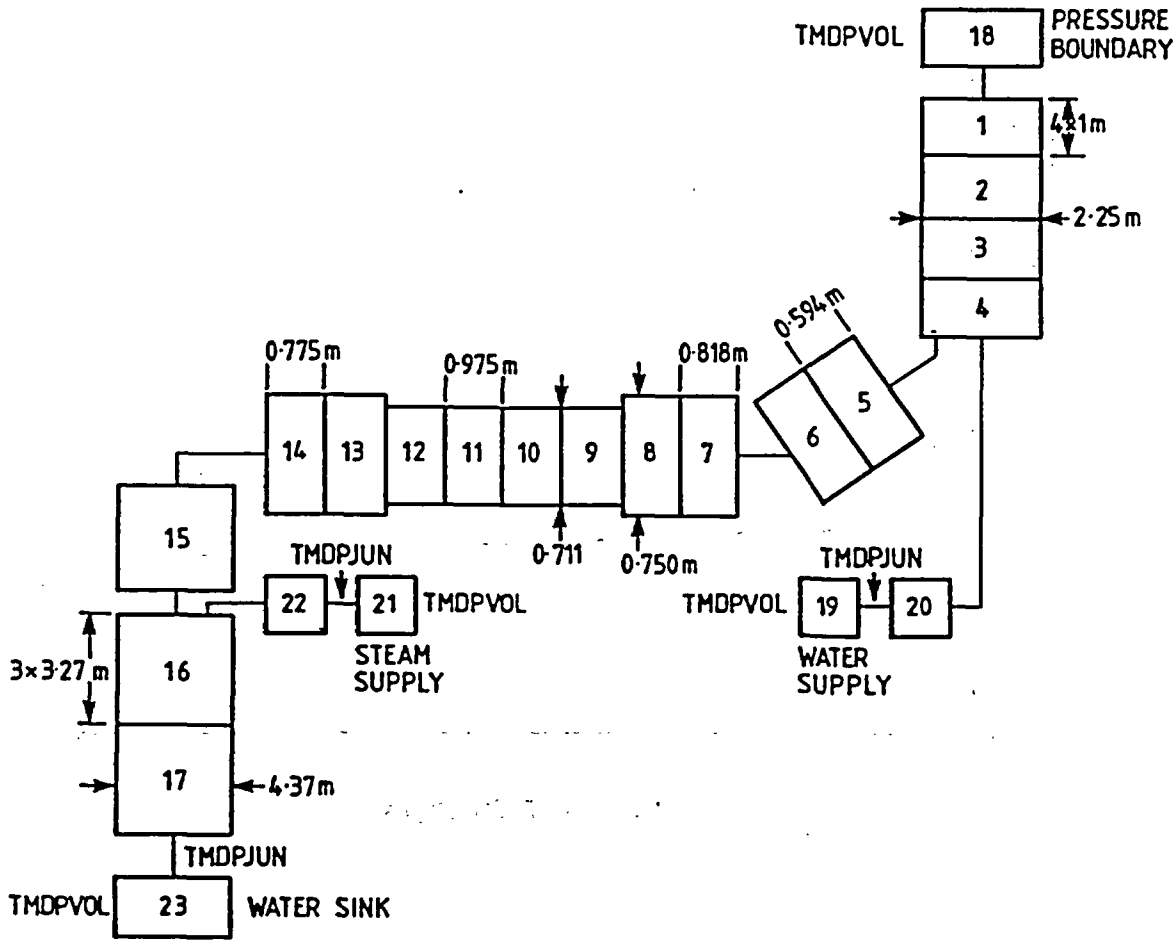

FIG. 13. RELAP5 NODALISATION SCHEME

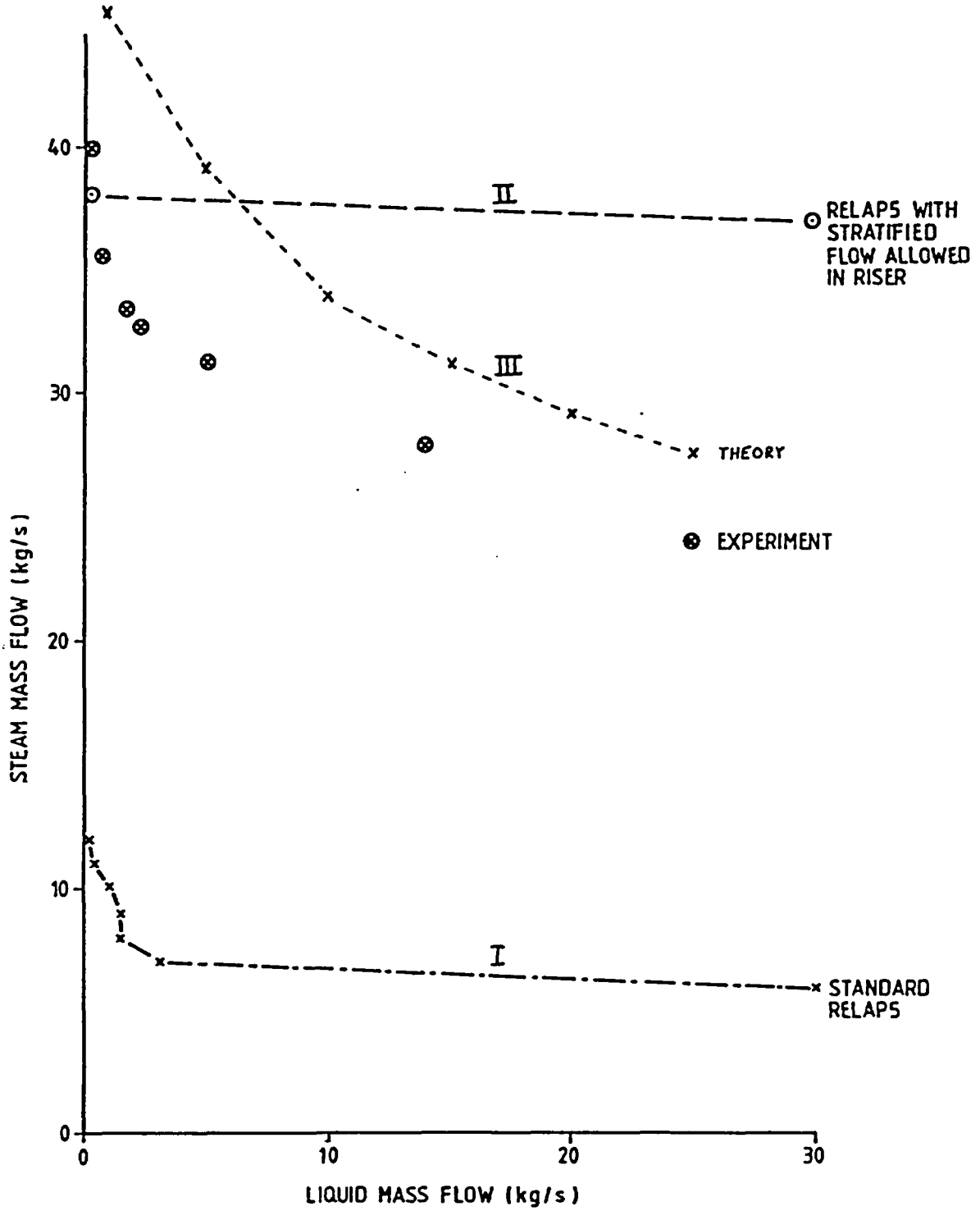

FIG. 14. EXPERIMENTAL AND PREDICTED FLOODING CURVES

Code Improvements Based on Results From the 2D/3D Activities

Yoshio Murao, Hajime Akimoto, Tadashi Iguchi
Akira Ohnuki, Yutaka Abe, Takayuki Suemura

Japan Atomic Energy Research Institute

Abstract

The REFLA core model was developed at Japan Atomic Energy Research Institute(JAERI) and main models were implemented in the TRAC-PF1/MOD1 code. The code, which is called J-TRAC code, was assessed with results of Cylindrical Core Test Facility (CCTF) tests by using measured core boundary conditions and successfully predicted the reflood transients in the core.

In the system calculation, however, it was found that some problems still remain, that is, (1) water accumulation in the upper plenum is not correctly predicted and this caused spiky oscillation of fluid in the system and (2) the accuracy of void fraction prediction in the vertical pipe is not sufficient.

To overcome these problems, it is necessary to develop the water carry-over model from a water pool and improve the shear stress model. JAERI is considering replacement of the TRAC-PF1 shear stress model with the TRAC-BF1 model for further improvement.

Keywords: LOCA; Reflooding, ECCS, Thermal-hydraulic code, Quench, Film boiling, Two-phase flow, Dispersed flow, Liquid slug flow, PWR, Accident analysis

1. Introduction

In the safety analysis on the Loss-of-Coolant Accident (LOCA) of light water reactors, it is very important to evaluate the temperature history of the fuel rod claddings during the reflood phase, which is governing the integrity of the first enclosure of the fission product. For the safety analysis of reflood phase in a PWR-LOCA, JAERI has developed a best estimate code REFLA-1D based on the physical understanding of the phenomena. For analysis of a LOCA, the main model of the REFLA-1D code was installed in the TRAC-PF1/MOD1 code. The code is named the J-TRAC code. This paper describes the models for the REFLA-1D code and the results of assessment of J-TRAC code with the data of the Cylindrical Core Test Facility test. The problems found in the assessment are also described.

2. Description of core thermo-hydrodynamic models of REFLA-1D code

2.1 Flow model [1]

Figure 1 illustrates assumed flow models in the REFLA-1D code. The flow model is classified into two groups, that is, Type 1 and Type 2. Type 1 flow pattern appears when the water is subcooled at the quench front. Type 2 flow pattern appears when the water is saturated at the quench front. The model is developed based on Murao and Sudoh's observation [2],[3], the description of FLECHT report [4],[16], Murao and Iguchi's observation in a small scale

reflood tests [5].

When the water is subcooled in unquenched region, this region can be called the subcooled film boiling region. Sometimes this region is called the inverted annular flow region.

When the water is saturated in unquenched region, a sluggy flow region or a dispersed flow region appears in the region. In the sluggy flow region, the flow pattern is unstable and is like churn-turbulent flow. This region was defined as a transition flow region. In the dispersed flow region, the water is dispersed and entrained in droplet forms by the flow of steam. The droplets are gradually integrated and the integrations are terminated when the diameter of the droplets becomes maximum value (Case 1, this appears at the low flooding rate). Even in this case, the region in a certain distance L from the quench front, the integration of the droplets occurs. The droplets are gradually integrated and finally become large liquid slug of sluggy flow (Case 2, this appears at the high flooding rate). Therefore the final state in Case 2 is the same flow pattern as the transition flow region.

The criterion for initiation of the dispersed flow is that the slip velocity between vapor and liquid phase exceeds a critical velocity, Δu_j.

In the quenched region and the transition flow region, the void fraction can be expressed by the same two-phase flow correlation, Murao-Iguchi correlation, given by,

$$\alpha = \frac{1}{2}\left[1 + \frac{u_{g0}+u_{l0}}{\Delta u} - \sqrt{1 - 2\frac{u_{g0}-u_{l0}}{\Delta u} + \left(\frac{u_{g0}+u_{l0}}{\Delta u}\right)^2}\right], \quad (1)$$

where u_{go} and u_{lo} are superficial velocity of gas phase and liquid phase, respectively, and $\Delta u = u_{g0}/\min(\alpha_{Yeh}, \alpha_{LM})$. α_{Yeh} was derived by slightly modifying Cunningham-Yeh correlation[6]

$$\alpha_{Yeh} = \min\left[0.925\left(\frac{\rho_g}{\rho_l}\right)^{0.239}\left(\frac{u_{go}}{V_{bcr}}\right)^{a}, 1.0\right], \quad (2)$$

where

$$V_{bcr} = 1.53\left(\frac{\sigma g}{\rho_l}\right)^{1/4},$$

$$a = \begin{cases} 0.47 & (u_{go} \geqq V_{bcr}), \\ 0.67 & (u_{go} < V_{bcr}), \end{cases}$$

$$\alpha_{LM}^{-1} = 1 + 3\times 0.28\left(\frac{u_{l0}}{u_{g0}}\right)^{0.64}\left(\frac{\rho_l}{\rho_g}\right)^{0.28}\left(\frac{\mu_l}{\mu_g}\right)^{0.07}.$$

The maximum diameter of droplets can be estimated by a critical Weber number We_c in Case 1,

$$We_c = \frac{\rho_g D_p u_c^2}{\sigma_l}, \quad (3)$$

where u_c is the terminal slip velocity of droplets.

Integration of droplets can be estimated by the following relation: Initial void fraction is expressed as,

$$\alpha_i = f(\Delta u_i) \text{(Function f is the same form as Eq.(1))}. \quad (4)$$

Integration of droplets, that is, decrease of void fraction is expressed as,

$$-\frac{d\alpha}{dt} = \min\left\{\frac{1}{\tau_C}(\alpha-\alpha_t),\ C_1 u_{10}\right\} \quad (5)$$

where τ_C=15.8 s, C_1= 2.0 (if $L_q < L$) or 0.3 (if $L_q > L$), and α_t is the void fraction of flow in the transition flow region. When the estimated void fraction becomes lower than the void fraction of maximum-size droplets α_d, the mixture of the maximum-size droplets and liquid slugs appears. This mixture flow is defined as the droplet-liquid slug mixture flow. The fraction of liquid slugs can be calculated from α, α_d and α_t. The minimum void fraction of the mixture flow is given to be the void fraction of the transition flow.

2.2 Heat transfer model

Transition flow region[7]

Sudo's correlation [8],[9] was slightly modified and used in the subcooled film boiling region. The correlation is

$$h = h_{sat}(1+0.025\Delta T_{sub}) + h_R, \quad (6)$$

where

$$h_{sat} = 0.94\left[\frac{\lambda_g^3 \rho_g \rho_l h_{fg} g}{L_q \mu_g (T_W - T_{sat})}\right]^{1/4},$$
$$h_R = \frac{E\varepsilon (T_W^4 - T_{sat}^4)}{(T_W - T_{sat})}, \quad (7)$$

where L_q is the distance from the quench front. The correlation for saturated film boiling is similar to Ellion's correlation[10] except for the factor 0.94.

For the transition flow region, a new correlation was developed, since Sudo's correlation predicted h_{sat} well for the high flooding rate cases but not for the low flooding rate cases.

An assumed flow model is shown in Fig. 2 and the following assumptions are used:

(1) Vapor film formed on the heated wall is very thin and the steam flow in the film is laminar.
(2) The fraction A of steam generated in the vapor film enters the two-phase mixture column.

Since the gravitational force of the two-phase mixture column of unit length is $\rho_l g(1-\alpha)$, instead of $\rho_l g$ for single phase liquid column of unit length and new correlation should be continuously connected with Eq.(6) at the bulk boiling initiation point, the value A should be 0.893. Finally, the following relation is obtained:

$$h = 0.94 \left[\frac{\lambda_g^3 \rho_g \rho_l h_{fg} g}{L_q \mu_g (T_W - T_{sat})}\right]^{1/4} (1-\alpha)^{1/4}$$

$$+ \frac{E \varepsilon (1-\alpha)^{1/2} (T_W^4 - T_{sat}^4)}{(T_W - T_{sat})}. \qquad (8)$$

This correlation correlates within about 30 % error all data from a series of JAERI small scale test, which was performed with the flooding velocity between 2 and 10 cm/s[7]. To check the applicability of the correlation at a higher flooding rate, Ohnuki, et al. performed a reflood test with the flooding rate between 2 and 30 cm/s[11]. They found that the correlation has a tendency to predict lower heat transfer coefficient than measured results if the core flooding rate is higher than 10 cm/s. They proposed a modified correlation, given by

$$h = 0.94 \left[\frac{\lambda_g^3 \rho_g \rho_l h_{fg} g}{L_q \mu_g (T_W - T_{sat})}\right]^{1/4} (1-\alpha)^{1/4} \times f$$

$$+ \frac{E \varepsilon (1-\alpha)^{1/2} (T_W^4 - T_{sat}^4)}{(T_W - T_{sat})},$$

$$f = \begin{cases} 1.0 & (u_{l0} \leqq 0.016) \\ 3.79 u_{l0} + 0.94 & (0.016 < u_{l0} < 0.28) \\ 2.0 & (0.28 \leqq u_{l0}) \end{cases} \qquad (9)$$

They reported that all data from their reflood test correlated with the modified correlation within about 20 % error.

Dispersed flow region

1) Droplet flow

The following two heat transfer paths are considered for the droplet flow: that is,
(1) Wall to steam,
(2) Steam to droplet.

On the path (1), adopted is the heat transfer correlation for single gas phase flow in a circular pipe. On the path (2), the heat transfer correlation for a solid sphere moving in a gas phase is adopted.

2) Droplet-liquid slug mixture flow[1]

The heat transfer coefficient in this region is calculated as,

$$h = h_t + \frac{\alpha - \alpha_t}{\alpha_d - \alpha_t} (h_d - h_t) \qquad (10)$$

where the void fraction and heat transfer coefficient for the transition flow

are expressed by α_t and h_t, respectively, and for the dispersed flow having maximum-size droplets by α_d and h_d, respectively.

2.3 Quench model[12],[13]

Usually quenching occurs at higher temperature than the so-called liquid maximum superheat, however, sometimes film-boiling-like heat transfer appeared at lower temperature than the liquid maximum superheat. In such a case, an instantaneous quench did not occur even at lower temperature. The axial power distribution in the reactor core is approximated by a chopped cosine and the clad surface temperature is lower in the lower portion of the core than that in the central portion and occasionally lower than the liquid maximum superheat. Considering this situation, the following quench model was derived by Murao:

$$U_q^{-1} = f\,U_H^{-1} + (1-f)\,U_L^{-1} \tag{11}$$

where

$$U_H^{-1} = g\,(T_M) \tag{12}$$

$$U_L^{-1} = g\,(T_{min}) \tag{13}$$

The form of function g(T) was assumed as,

$$g\,(T) = \frac{C_p \rho\,(T_q - T)}{\Phi_0} \tag{14}$$

T_M is expressed by the following equation which was derived by approximating the thermodynamic liquid maximum superheat obtained by Groeneveld[14] using the equation of state for water:

$$T_M = 594.21 + 2.417 \times 10^{-6} p \tag{15}$$

Below the thermodynamic liquid maximum superheat T_M, it is considered that the liquid occasionally contact the heating surface and generated steam hydrodynamically removes the liquid from the surface, that is, hydrodynamically unstable film boiling occurs. The unstable film boiling is terminated when the surface temperature falls down to the minimum film boiling temperature T_{min}, therefore, the film boiling is unstable if the surface temperature is in the range between T_M and T_{min} in the surface temperature. Accordingly the previous quench model cannot be applied to the case where the contact temperature is less than T_M. This case is defined to be a low temperature quench. Sakurai et al.'s data[15] show that T_{min} approaches the thermodynamic liquid maximum superheat T_M line (Eq.(15)) with increase of system pressure as shown in Fig. 3. T_{min} can be approximated by

$$T_{min} = \min(480 + 8 \times 10^{-5} p,\, T_M)\,, \tag{16}$$

where P is system pressure (Pa).

T_q is the apparent quench temperature, at which the wall surface temperature starts to rapidly fall down and the wall is quenched in a short time.

The form of f was assumed as

$$f = \left(\frac{T_q - T_{min}}{T_R - T_{min}} \right)^{\eta} . \qquad (17)$$

In Eq. (17), η is an unknown variable and determined $\eta = 1$ from experimental data.

The wall temperature T_R, whose contact temperature is T_M, can be written as,

$$T_R = T_M + \sqrt{\frac{(C_p \rho k)_l}{(C_p \rho k)_w}} (T_M - T_l) \qquad (18)$$

From the analogy of ϕ and the maximum heat flux on a boiling curve, ϕ was assumed to be a linear function of system pressure and determined from the PWR-FLECHT Group 1 data[16] and the FLECHT low flooding test data[17] taken under the pressures of 0.137, 0.274 and 0.39 MPa, ϕ is written as,

$$\Phi_0 = (6.77p + 3.50 \times 10^5) \ (1 + 2.778 \times 10^{-5} \Delta T_{sub}{}^3) \qquad (19)$$

where ΔT_{sub} is the local coolant subcooling (K).

The equation (11) was assessed with many top-quench data, and demonstrated to be valid in the pressure range between the atmospheric pressure and 7 MPa[11].

2.4 Development of REFLA-1D code[1]

The REFLA-1D code was developed by using above mentioned models. Some unknown variables were determined based on some trial calculations [18] such as JAERI's small scale reflood test and FLECHT tests.

Considering the difference in core water accumulation behavior, Case 1 or Case 2 can be selected in the REFLA-1D code.

The REFLA-1D showed very good predictability for JAERI's small scale reflood tests in Case 2, FLECHT-low flooding test, FLECHT-SEASET[19] in Case 1 and Cylindrical Core Test Facility (CCTF) in Case 2 [20],[21],[22]. The Case 2 appears in test sections with large or cold flow housing. In nuclear reactor, Case 2 is expected to give better simulation.

3. Implementation of JAERI core reflood model into TRAC-PF1 and assessment of J-TRAC code

3.1 Implementation of JAERI core reflood model into TRAC/PF1

Many assessment calculations to check the prediction capability of the TRAC-PF1/MOD1 for reflood phase of a PWR-LOCA were performed at JAERI by using CCTF and SCTF data. These assessment studies showed the poor predictability of the TRAC-PF1/MOD1 code in the core void fraction and the clad temperature transient[23].

At JAERI, JAERI's core reflood models, mentioned above, were introduced into TRAC-PF1/MOD1 code to improve those deficiencies of the TRAC-PF1 code.

That is, for the core hydraulic models, the following models were implemented into the TRAC-PF1 code to improve the interfacial friction factor:
(1) Transition flow model equivalent to the Murao-Iguchi void fraction correlation,
(2) Dispersed flow model equivalent to that of the REFLA-1D code, and
(3) Model for transition from dispersed flow to a transition flow.
And, for the heat transfer models, the following models were implemented into the TRAC-PF1 code to improve the interfacial heat transfer and wall-to-fluid heat transfer:
(1) Film boiling heat transfer correlation by Murao and Sugimoto with a modification for liquid velocity effect proposed by Ohnuki et al.
(2) Quench velocity correlation by Murao,
(3) A dispersed flow model equivalent to that of the REFLA-1D code.

The improved TRAC-PF1 code is named as the J-TRAC code. In order to check the effect of the improvement introduced into the TRAC-PF1 code, assessment calculations with the TRAC-PF1 and J-TRAC codes were conducted with the CCTF test results by using measured core boundary conditions. The following result is an example of assessment results. In the TRAC-PF1 calculation, VESSEL component was used instead of CORE component because the calculation with CORE component was unstable. The core portion is divided into 7 cells due to much CPU time with VESSEL component. On the other hand, in the J-TRAC calculation, CORE component was used and the core was divided into 38 cells. In those calculations, inputted was the core inlet water mass flow rate evaluated from the measured values in the system.

Figure 4 shows the core mass accumulation, integrated core outlet water mass flow and integrated core outlet steam mass flow. In the J-TRAC calculation, the core accumulated water mass is clearly much improved compared with the TRAC-PF1 calculational results, as shown in the figure and the void fraction at each elevation is also qualitatively well predicted as shown in Fig. 5.

Figure 6 shows the comparison of the clad temperatures. Although the both codes gives good comparison in the peak clad temperature, the clad temperature transients are well predicted in the J-TRAC calculation and not in the TRAC-PF1 calculation. And in the TRAC-PF1 calculation, clad temperatures start to rise again at about 300 s which corresponding the core water blow out from the core at about 300 s as seen in Fig. 4.

Figure 7 shows the comparison of heat transfer coefficients at the midplane of the core calculated with the film boiling heat transfer correlations of the TRAC-PF1 and the J-TRAC by using the measured void fraction and the distance from the quench front. In the TRAC-PF1 calculation, the peak clad temperatures were well predicted although the core void fractions were poorly predicted. The reason is thought to be the compensation of the prediction errors in the heat transfer calculation and the core void fraction calculation. The improved models in the J-TRAC code introduced the good predictability in the core thermal-hydraulics. Because of this improvement in the calculational stability of core thermal-hydraulics, total CPU time of J-TRAC calculation is about one-half of the TRAC-PF1 calculation, notwithstanding that the number of the cell for J-TRAC calculation is much larger than that for the TRAC-PF1 calculation.

JAERI successfully finished to install the JAERI reflood models into the TRAC-PF1/MOD2 code as a reflood option at the end of July in Los Alamos National Laboratory (LANL) as one of the JAERI contribution. Other reflood options were scheduled to be implemented into the TRAC-PF1/MOD2 code by United Kingdom and LANL itself as well as JAERI, and after sufficient assessment calculations, a standard reflood option will be determined out of them.

3.2 System calculation with J-TRAC code

As mentioned above, core reflood calculational capability of the J-TRAC code has been greatly improved by introducing the REFLA-1D's model. However, we still have some problems in the system calculation. Here, we describe about instability of upper plenum water accumulation and spiky oscillations of fluid behavior in loop, which were most important problem in CCTF system calculation.

The noding schematics for a calculation of a CCTF test is shown in Fig. 8. The core part is modeled by using a CORE component, and upper plenum is modeled by using a TEE component. This calculation shows a lot of large spikes in pressure and mass flow rates, as shown in Fig. 9. These spikes are caused by sudden evaporation of water entering intermittently into the steam generator from hot leg. And the intermittent water entering is caused by unstable water accumulation in upper plenum of pressure vessel and inlet plenum of steam generators.

Figure 10 shows a void fraction in upper plenum. It oscillates violently, and its lowest value is around the value of 0.75. This value corresponds to the lowest boundary of annular-mist flow region in TRAC-PF1 flow regime map[24]. Once the void fraction becomes less than the value, interfacial shear coefficient rises very rapidly because of interpolation between annular-mist flow and bubbly-slug flow, which is extremely larger than these with other experimental correlations. Because of this extremely rapid jump in interfacial shear around the boundary, void fraction in the upper plenum oscillates violently.

An additional calculation was performed to confirm above mentioned mechanism. In this calculation, Wilson's void fraction correlation[25] was introduced as an interfacial shear model in the upper plenum and steam generator inlet plenum for full range of void fraction. This model forms smooth and gentle slope of interfacial shear against void fraction.

Figure 11 shows the result of this calculation. There is no spike such as found in previous calculation. This means that stable water accumulation model is necessary to stabilize the calculation of system behavior.

Figure 12 is a comparison of the calculated and measured upper plenum water accumulations. While Wilson's void fraction correlation makes water accumulation behavior smooth, there still remains a problem in the amount of water accumulation. According to Iguchi[26], it was known that Wilson's correlation well predicts the void fraction in the water pool of the upper plenum in the CCTF tests. However, present model cannot account the entrainment from the surface of the water pool, so the water level was assumed to be the level of the hot leg, resulting in the overestimation of the water accumulation. Therefore, it is necessary to develop a model for predicting the level of the water pool by considering liquid entrainment from the liquid surface.

4. Comparison of correlations between the TRAC-PF1 and TRAC-BF1 codes

4.1 Review of experimental data base

The accuracy of the calculation is highly dependent on the accuracy of the correlations used in the calculation. It is essential to check the accuracy of the elementary correlations against basic experiments as well as the assessment calculation for the integral tests such as LOFT experiment.

As the first approach of model selection for the phenomena beside the reflooding phenomena, a review was made for correlations of the TRAC-PF1 and the TRAC-BF1 codes for which many assessments have already performed by many researchers against various transients[24],[27].

In the TRAC-PF1 code, simple mechanistic models are used in constitutive packages. For example, in the TRAC-PF1 interfacial friction model, the interfacial friction factor is calculated through the correlations of the bubble diameter based on the critical Weber number, the drag coefficient of solid spherical particle, the fraction of slug bubble in bubbly/slug flow, drop diameter, fraction of drop in liquid phase in annular/dispersed flow, etc. To assess these TRAC-PF1 elementary models, the model requires relatively detailed test data such as the bubble diameter, fraction of slug bubble, drag coefficient for various bubbles, drop diameter, fraction of drop and liquid film at various conditions.

The interfacial friction model of the TRAC-BF1 code is developed based mainly on the drift-flux correlations derived by Ishii,[28] Andersen & Chu,[29] and Andersen, et al.[30] These drift flux correlations were ascertained with data for vertical upward flow, which covers the following range:
(a) Pressure ; 0.7-16.3 MPa,
(b) Mass velocity ; 120-3800 kg/m^{2}s,
(c) Hydraulic diameter; 0.006-0.168 m.
The range covers relatively wide region. The interfacial friction model of the TRAC-BF1 code is expected to be applicable to the region with good accuracy as far as transient effect is not significant.

Figure 13 shows a comparison for the CISE experiment performed at pressure of 4.923 MPa with mass velocity of 388 kg/m^{2}s using a 9.1 mm vertical tube[31]. The CISE experiment was performed at conditions within the range where the basic drift-flux correlations of the TRAC-BF1 interfacial friction model are ascertained. The TRAC-BF1 results show better agreement with measured results than the TRAC-PF1 results although they show a slight overprediction at high quality region.

The TRAC-PF1 code overpredicted the void fraction in the CISE experiment analysis probably due to the overestimation of the interfacial friction. As possible reasons of the overestimation of the interfacial friction, one can list the following items:
In bubbly/slug flow regime,
(a)Too high drag coefficient for bubbles,
(b)Too small fraction of slug bubble in bubbly/slug regime,
(c)Too small bubble diameter,
(d)Missing effect of velocity difference between bubble and slug bubble.
In annular/dispersed flow regime,
(a)Too high drag coefficient for drop and/or liquid film,
(b)Too high fraction of drop in liquid phase,
(c)Too small drop diameter,
(d)Missing the effect of velocity difference between drop and liquid film,
etc.

To identify the reason of the overestimation with the TRAC-PF1 model accurately, detailed experimental data of the two-phase flow are required as listed above. However, enough information is not established at present to identify the reason although we can adjust the void fraction by tuning the coefficients listed above for the CISE experiment. The mechanistic interfacial-friction model of the TRAC-PF1 code is not practical at present because we do not have enough experimental data base to justify elementary correlations. An approach like the TRAC-BF1 code is practical because we can check correlation easily through comparison with wide test data base.

4.2 Assessment of correlations of the TRAC-BF1 code for CCTF tests

In order to check the applicability of the TRAC-BF1 model to the reflood phenomena in PWR, assessment calculations were performed using CCTF test data[32]. The typical flow conditions of the reflood test scatter at pressure of 0.2 through 0.4 MPa with mass velocity of 15 through 100 kg/m^{2}s. These conditions are out of the ascertained range of the drift-flux correlation used to develop the TRAC-BF1 interfacial friction model.

For the assessment calculations, the subroutines of the TRAC-BF1 code for the interfacial friction, interfacial heat transfer, wall friction and wall heat transfer models are picked up and implemented into the J-TRAC code.

Figure 14 shows void fractions at various elevations of the core. The TRAC-BF1 results show good agreement either bottom(below 1.22 m) or top part(above 3.05 m) of the core. The void fraction is overestimated in the center part(between 1.22 and 3.05 m) of the core. Figure 15 shows clad temperatures at various elevations. The TRAC-BF1 results show reasonable agreement at elevations 0.38 and 3.05 m, while the TRAC-BF1 results show an overestimation of the clad temperature at elevation of 1.83 m. The overestimation of the clad temperature in the center part of the core is considered to be caused by the overestimation of the void fraction in that part. These results show that the TRAC-BF1 model is not applicable to the flow condition with low pressure and mass velocity like the reflood in PWR. It is necessary to improve the reflood model of the TRAC-BF1 code.

5. Future plan

(1)Change the interfacial friction model from the TRAC-PF1 type to the TRAC-BF1 type.

For vertical upward flow, the interfacial friction model of the TRAC-BF1 code will be used as the first model, however, the model at low mass velocity will be changed as in the current J-TRAC code. The correlation will be assessed by using the two-phase experiment test data.

For horizontal stratified flow, interfacial friction and wall friction models will be reviewed. The revised model is planned to be assessed for the TPTF test performed at JAERI.

(2)Basic experiment is planned to develop physical models based on physical understanding in the following areas:

(a)Counter-current flow
(b)Annular/dispersed flow
(c)Flow in complicated configuration such as elbow,expansion and contraction

(3)To establish stable system calculation, following models are planned to be revised in the J-TRAC code:

(a)Condensation model
(b)Entrainment model

For the condensation model, the model will be assessed by using the condensation experiment results performed with CCTF.

(4)Assessment of thermal hydraulic models will be continued in cooperation with Japanese academic society using Mini-TRAC code, which can be used in personal computers.

6. Summary

(1)Installation of JAERI's reflood model into the TRAC-PF1/MOD2 code was completed. The model improved predictability of the code for reflood phenomena including both core void fraction and clad temperature transient.

(2)For stable system calculation , following areas are identified as problem areas:

(a)condensation at cold leg,
(b)entrainment from upper plenum to hot leg,

(3)To establish physical models supported by experimental evidences, the mechanistic model of the TRAC-PF1 code is not practical because of scare experimental data base at present. We think that the approach like the TRAC-BF1 code is more practical because of wider experimental data base.

Acknowledgment

The author is deeply indebted to Drs. K. Sato, M. Shiba and Y. Kaneko of Japan Atomic Energy Research Institute for hearty suggestions and encouragement. Part of this work was performed under contract with the Atomic Energy Bureau of Science and Technology Agency of Japan.

Nomenclature

C, C_p	:	Specific heat (J/kgK)
D_d	:	Droplet diameter (m)
E	:	Emmisivity
g	:	Acceleration of gravity (m/s^2)
h_{fg}	:	Latent heat of evaporation (J/kg)
h	:	Heat transfer coefficient (W/m^2K)
L	:	Liquid accumulation length (m)
L_q	:	Distance from quench front (m)
P	:	System pressure (Pa)
T	:	Temperature (K)
T_w	:	Wall temperature (K)
T_q	:	Wall temperature at quench front (K)
U_q	:	Quench velocity (m/s)
u	:	Velocity (m/s)
We_c	:	Critical Weber number
Z	:	Axial distance from quench front (m)
α	:	Void fraction
ΔT_{sub}	:	Subcooling of coolant (K)
ΔT_{sat}	:	Superheat of coolant (K)
Δu	:	Slip velocity (m/s)
ε	:	Stefan Boltzmann constant (W/m^2K^4)
λ	:	Thermal conductivity (W/mK)
μ	:	Dynamic viscosity (Pa s)
ρ	:	Density (kg/m^3)
σ	:	Surface tension (kg/m)

Φ : Heat flux (W/m^2)

(Subscripts)

g : Gas phase
l : Liquid phase
R : Radiative
sat : Saturated
sub : Subcooled

References

(1) Murao, Y. et al.: REFLA-1D/MODE3-A computer code for reflood thermohydrodynamic analysis during PWR-LOCA user's manual, JAERI-M 84-243, Japan Atomic Energy Research Institute, (1984).
(2) Murao, Y.: An analytical study of the thermo-hydrodynamic behavior of the reflood-phase during a LOCA, KFK-2545, (1977).
(3) Murao, Y.: Analytical study of thermo-hydrodynamic behavior of reflood-phase during LOCA, J. Nucl. Sci. Technol, 16[11], 802-817 (1979).
(4) Clement, P., et al.: 5th annual water reactor safety research information meeting, Washington, Nov. 1977.
(5) Murao, Y. and Iguchi, T.: Experimental modeling of core hydrodynamics during reflood phase of LOCA, J. Nucl. Sci. Technol., 19, [8], 613-627, (1982).
(6) Cunningham, J.P. and Yeh, H.C.: Experiments and void correlation for PWR small-break LOCA conditions, Trans, Am. Nucl. Soc., 17, 369-370, (1973).
(7) Murao, Y. and Sugimoto, J.: Correlation of heat transfer coefficient for saturated film boiling during reflood phase prior to quenching, J. Nucl. Sci. Technol., 18 [4], 275-284, (1981).
(8) Sudo, Y.: Film boiling heat transfer during reflood phase in postulated PWR loss-of-coolant accident, J. Nucl. Sci. Technol., 17[7], 516-530, (1980).
(9) Sudo, Y.; Murao, Y.: Film boiling heat transfer during reflood process, JAERI-M-6848, Japan Atomic nergy Research Institute, (1976).
(10) Ellion, M.E.: Jet Propulsion Lab. Memo 20-80 C.I.T., (1954).
(11) Ohnuki,A., et al.: Effect of flooding velocity on core heat transfer during reflood phase, Proceeding of 1987 fall meeting of the Atomic Energy Society of Japan F51, September (1987), (in Japanese).
(12) Murao, Y.: Quench front movement during reflood phase, Presented at 1st Int. Workshop on Fundamental Aspects of Post-dryout Heat Transfer at Salt Lake City (1984), NUREG/CP-006, (1984).
(13) Murao, Y.: Correlation of quench phenomena for bottom flooding during loss-of-coolant accidents, J. Nucl. Sci. Technol., 15[12], 875-885, (1978).
(14) Groeneveld, SD.C.: The thermal behaviour of a heated surface at and beyond dryout, AECL-4309, (1972).
(15) Sakurai, A., et al.: Steady and unsteady film boiling heat transfer at subatmospheric and elevated pressures, presented at the 1980 ICHMT International Seminar, Nuclear Reactor Safety Heat Transfer, Dubrovnik, Yugoslavia, (1980).
(16) Cermak, J.C., et al.: PWR full length emergency cooling heat transfer (FLECHT) Group 1 test report, WCAP-7435, (1970).
(17) Lilly, G.P., et al.: PWR-FLECHT cosine low flooding rate test series evaluation report, WCAP-8838, (1977).
(18) Murao, Y.: Study of the thermo-hydrodynamic phenomena in the nuclear core during reflood phase, JAERI-M 83-032, (in Japanese), Japan Atomic Energy Research Institute, (1983).
(19) Lee, N., et al.: PWR FLECHT SEASET unblocked bundle forced and gravity reflood task. Data evaluation and analysis report.

NUREG/CR-2256, U.S. Nuclear Regulatory Commission, (1981).
(20) Okubo, T., Murao, Y.: Assessment of core thermo-hydrodynamic models of REFLA-1D code with CCTF data for reflood phase of PWR-LOCA, J. Nucl. Sci. Technol., 22 [12], 983-994, (1985).
(21) Murao, Y., et al.: Experimental study of system behavior during reflood phase of PWR-LOCA using CCTF, J. Nucl. Sci. Technol. 19[9], 705-719, (1982).
(22) Murao, Y., et al.: Experimental assessment of evaluation model for safety analysis on reflood phase of PWR-LOCA, J. Nucl. Sci. Technol. 22[11], 890-902, (1985).
(23) Akimoto, H.: Analysis of TRAC-PF1 calculated core heat transfer for a CCTF test, Nucl. Eng. Des., 88 215-227, (1985).
(24) Liles,D.R., et al.: TRAC-PF1/MOD1 correlations and models, NUREG/CR-5069 LA-11208-MS R4, December (1988).
(25) Wilson, J.F., et al.: The velocity of rising steam in a bubbling two-phase mixture, Trans. Am. Nucl. Soc., 5(1) 151-152, (1962).
(26) Iguchi,T.,Murao,Y.: Water accumulation phenomena in upper plenum during reflood phase of a PWR-LOCA by using CCTF data, J. Nucl. Sci. Technol. 20(6) 453-466, (1983).
(27) Rohani,S.Z., et al.: TRAC-BF1 models and correlations, Idaho National Engineering Laboratory, February (1988), (draft copy).
(28) Ishii,M.: One-dimensional drift-flux model and constitutive equations for relative motion between phases in various two-phase regimes, ANL-77-47, October (1977).
(29) Andersen,J.G.M., Chu,K.H.: BWR refill-reflood program Task 4.7-constitutive correlations for shear and heat transfer for the BWR version of TRAC, NUREG/CR-2134 EPRI NP-1582 GEAP-24940, December (1981).
(30) Andersen,J.G.M., et al.: BWR refill-reflood program Task 4.7-model development, basic models for the BWR version of TRAC, NUREG/CR-2573 EPRI NP-2375 GEAP-22051, September (1983).
(31) Agostini,G.,et al.: Density measurement of steam-water mixtures flowing in a turbular channel under adiabatic and heated conditions, CISE-R-291, December (1969).
(32) Okubo,T., et al.: Evaluation report on CCTF Core-II reflood test C2-4 (Run 62), JAERI-M 85-026, March (1985).

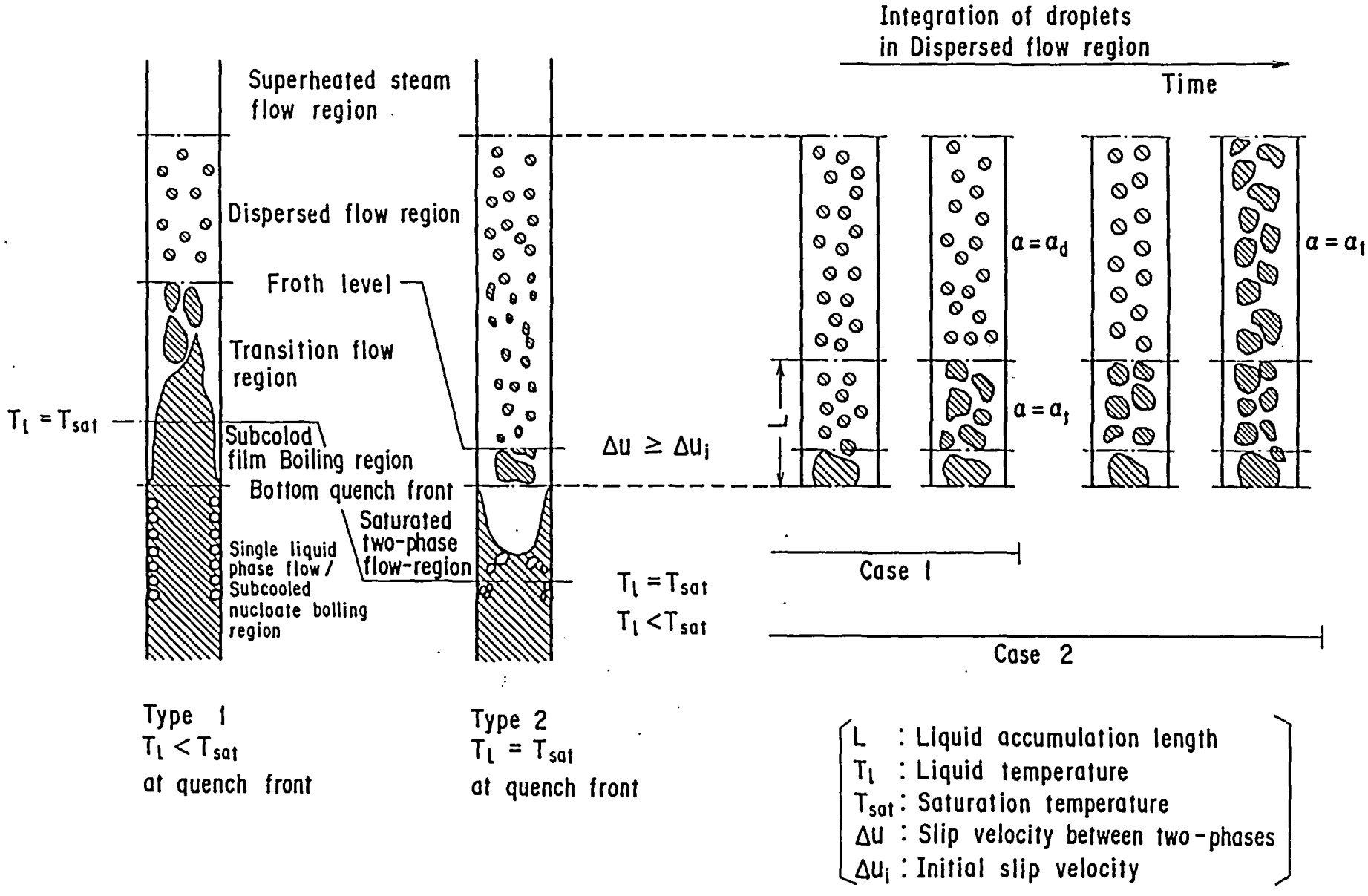

Fig. 1 Reflood flow model

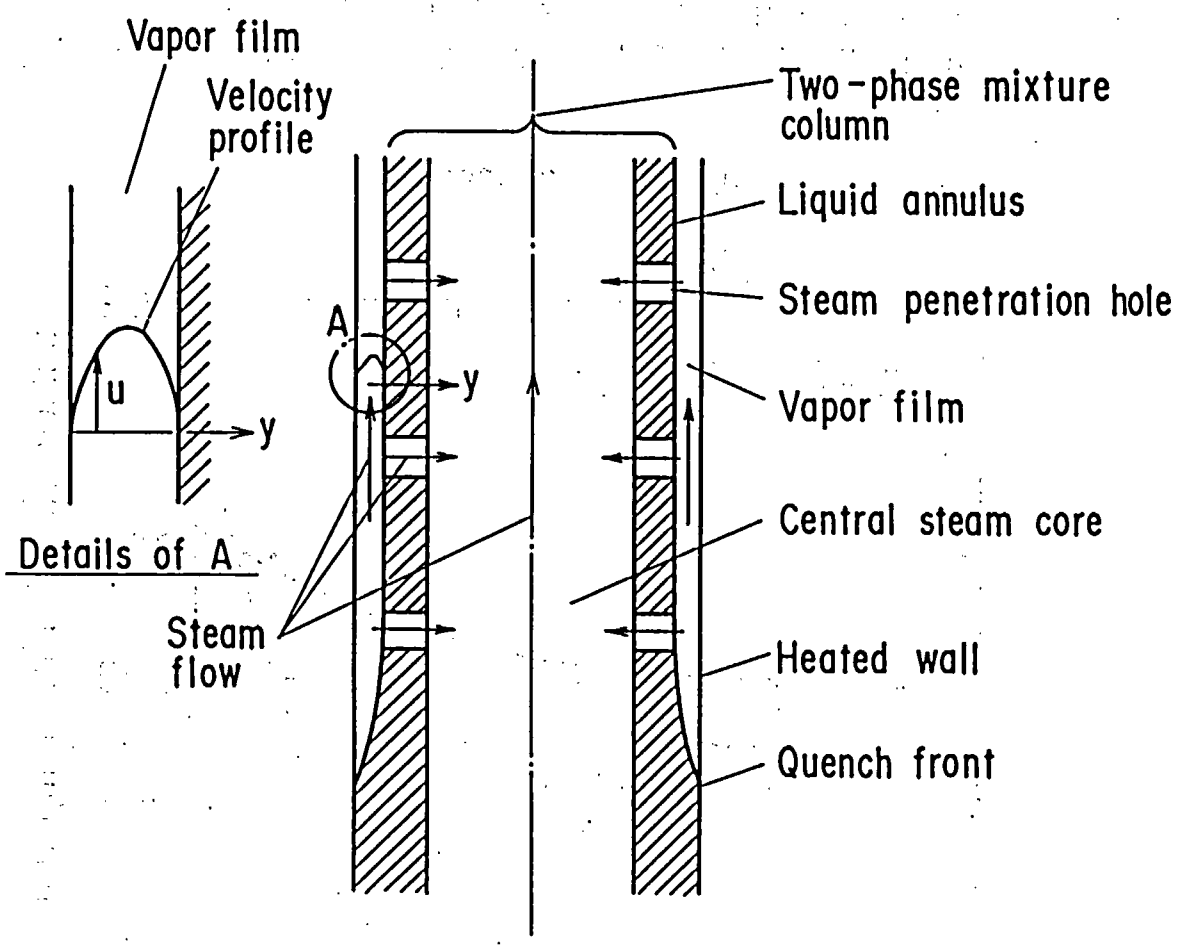

Fig. 2 Flow model of saturated film boiling

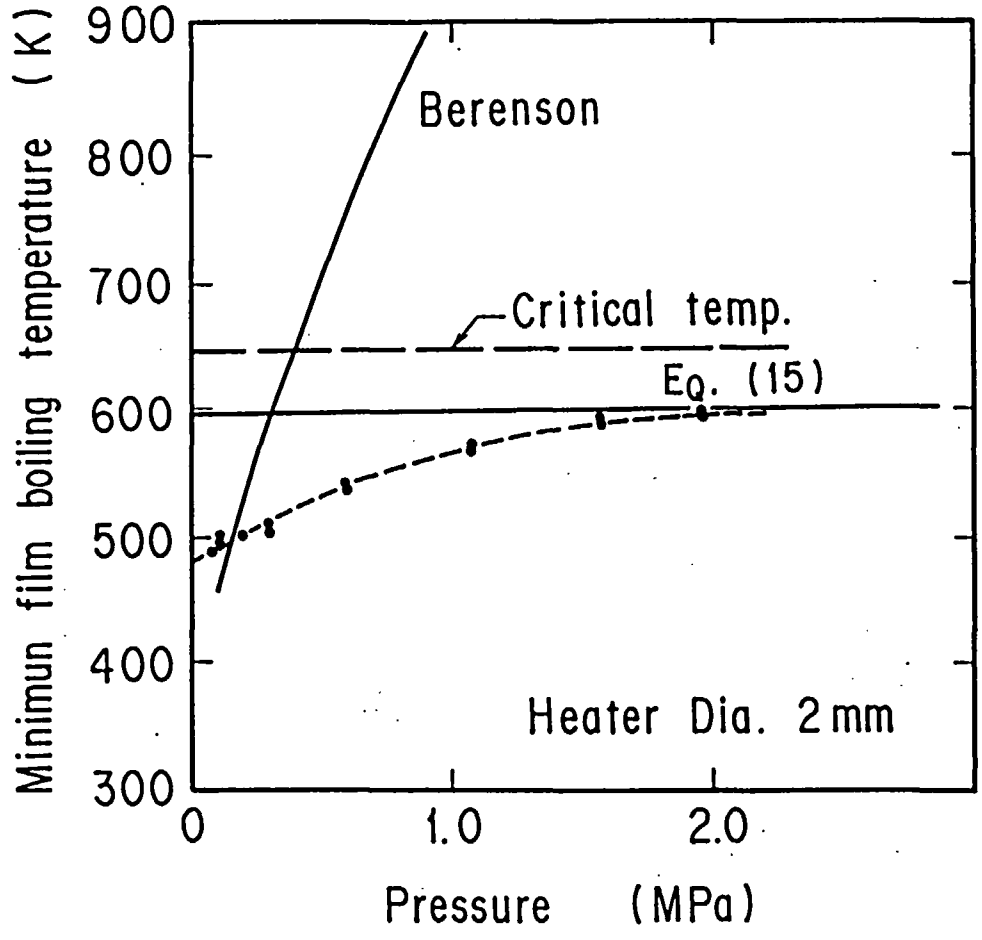

Fig. 3. Effect of system pressure on minimum temperature in saturated film boiling

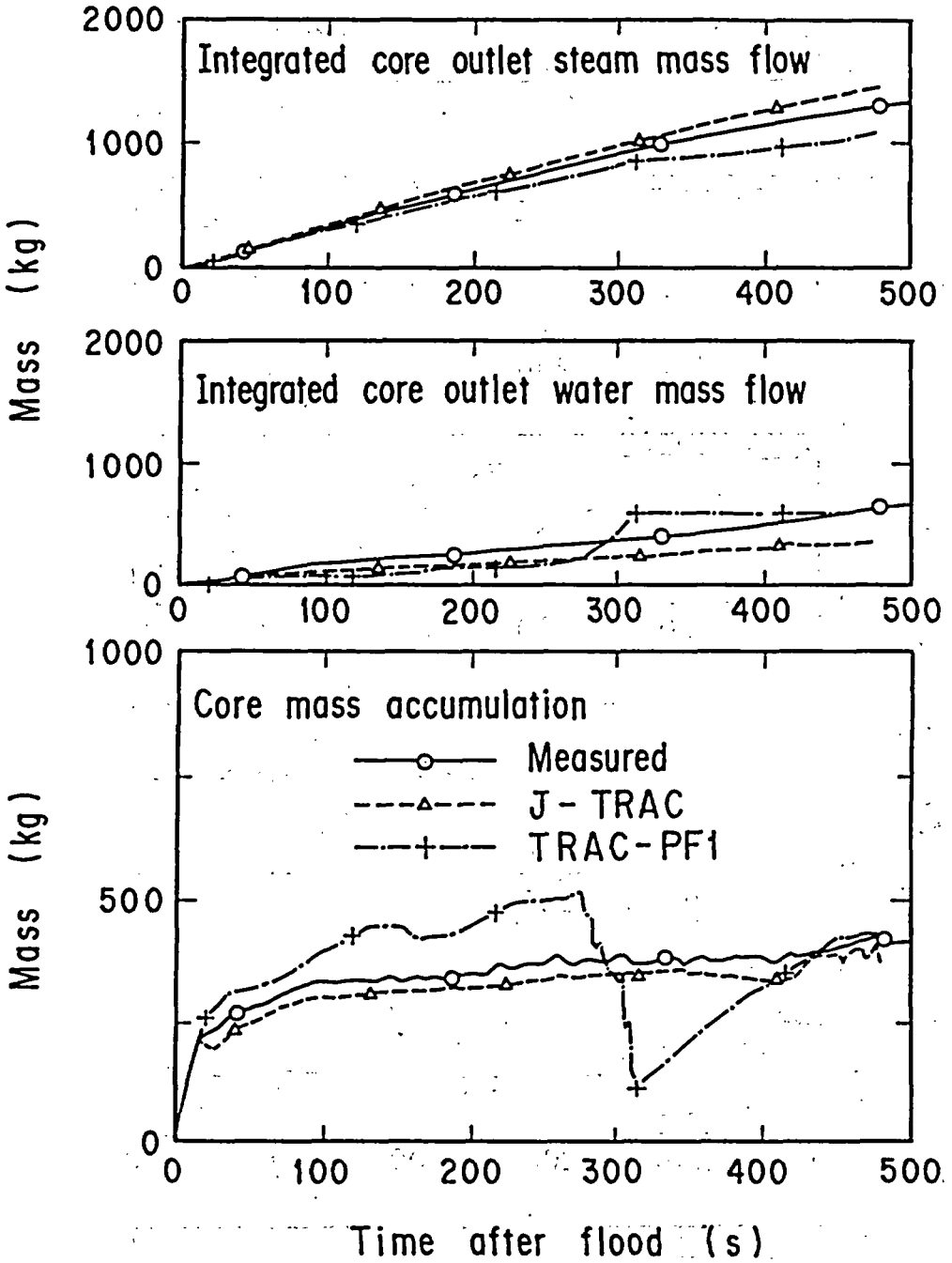

Fig. 4 Overall mass balance at core

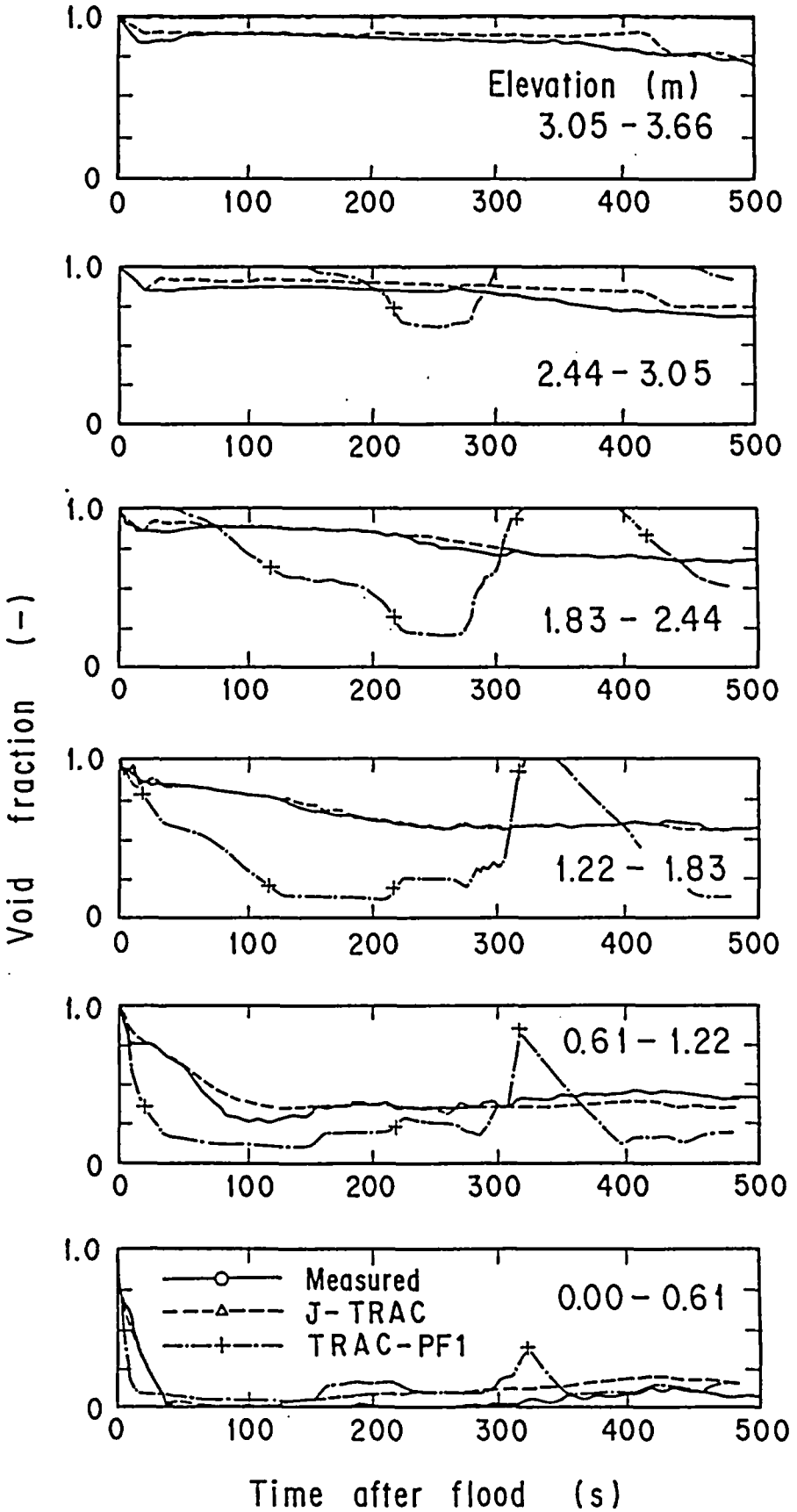

Fig. 5 Void fractions at core

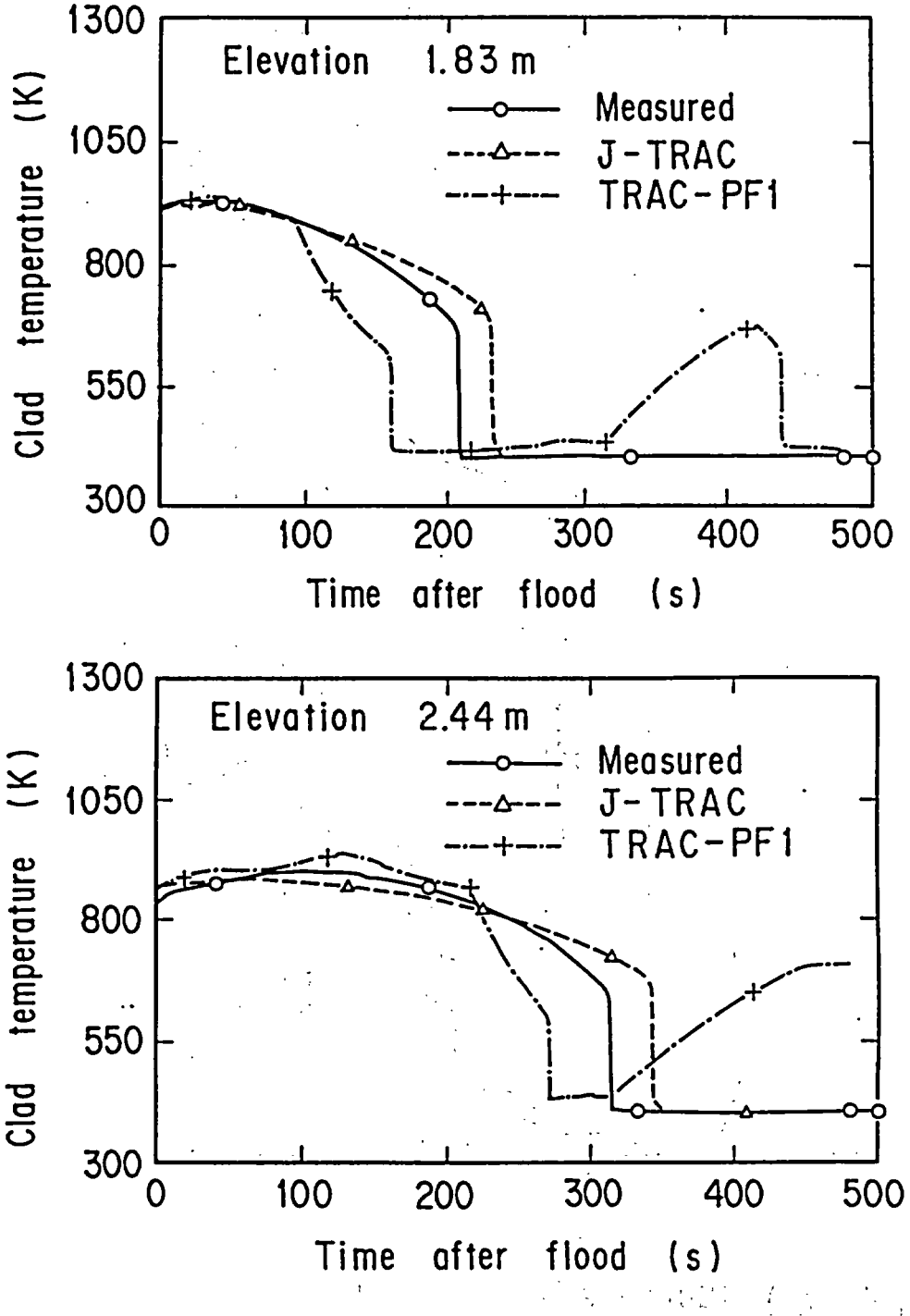

Fig. 6 Clad temperature

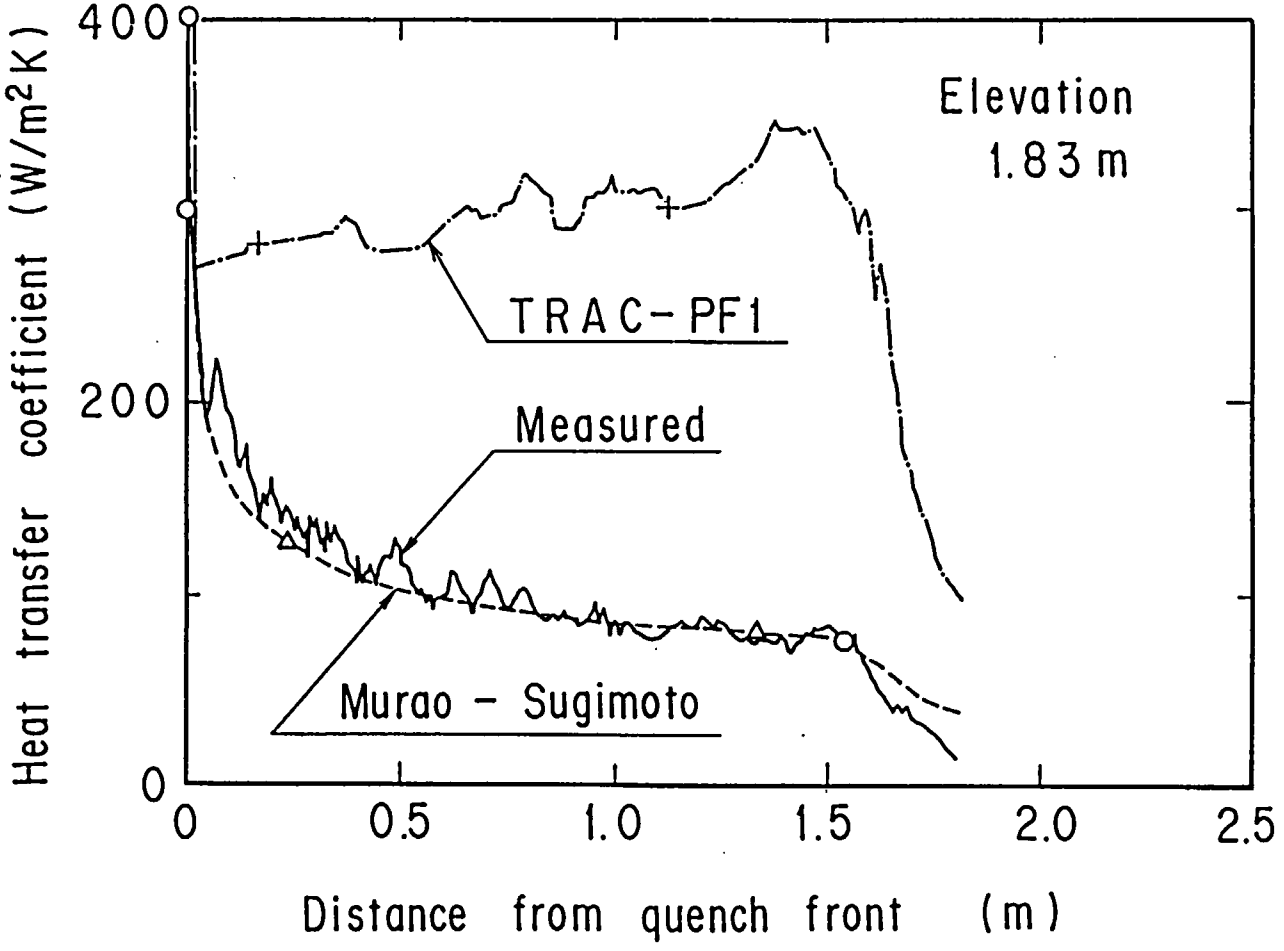

Fig. 7 Heat transfer coefficient

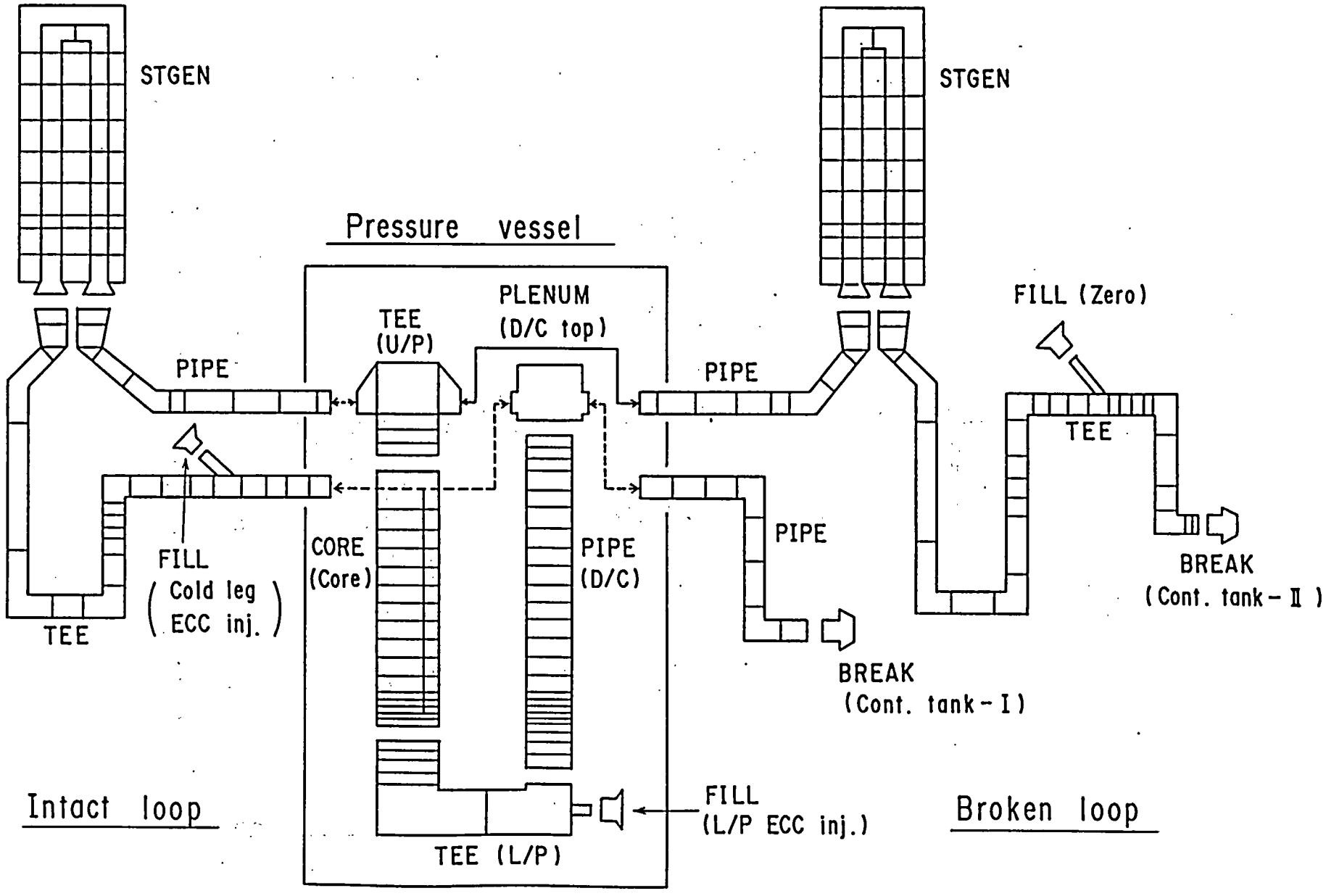

Fig. 8 CCTF noding schematics

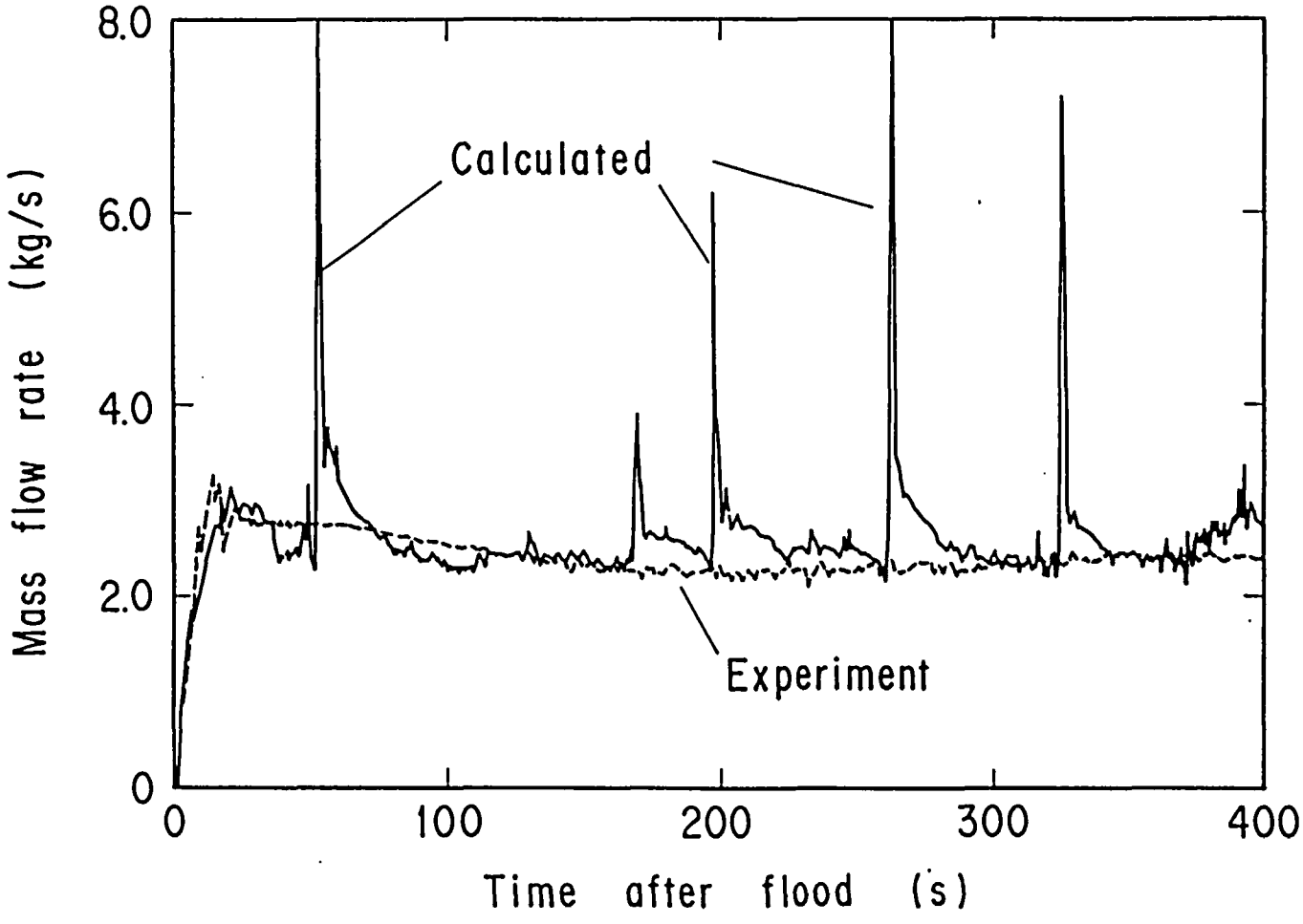

Fig. 9 Mass flow rate at pump simulator of intact loop
(J-TRAC original)

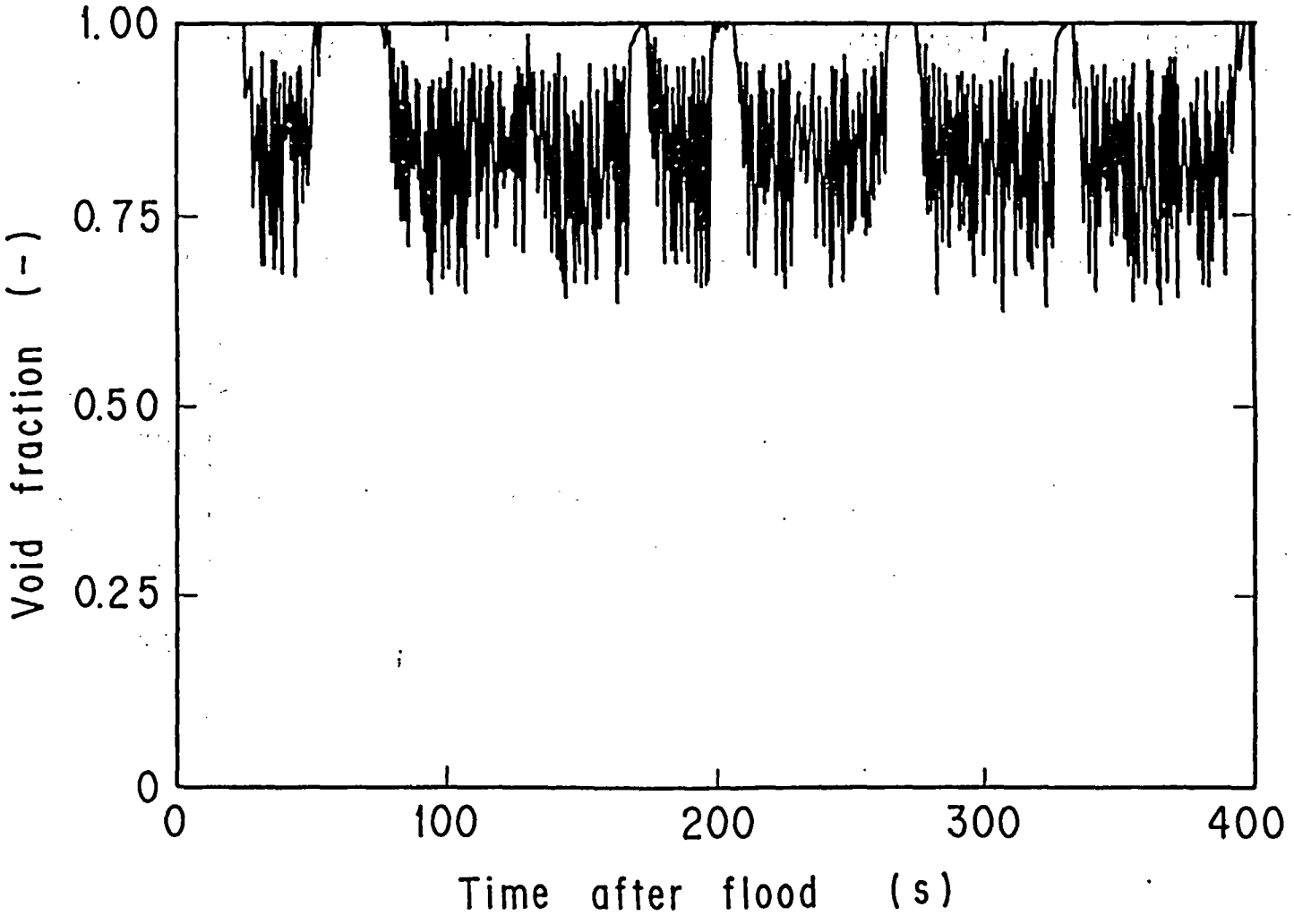

Fig. 10 Void fraction in upper plenum
(J-TRAC original)

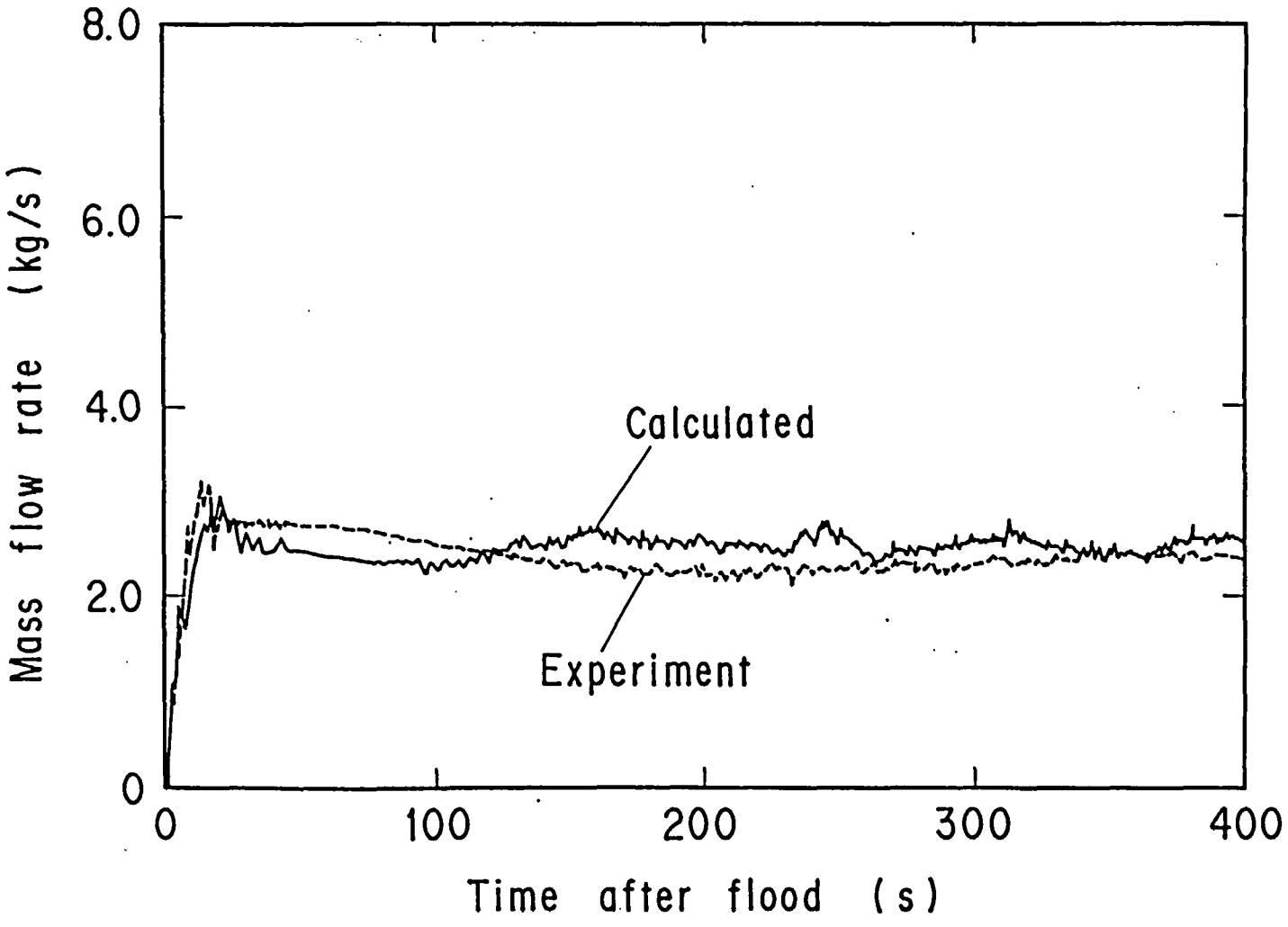

Fig. 11 Mass flow rate at pump simulator of intact loop (J-TRAC with Wilson's correlation)

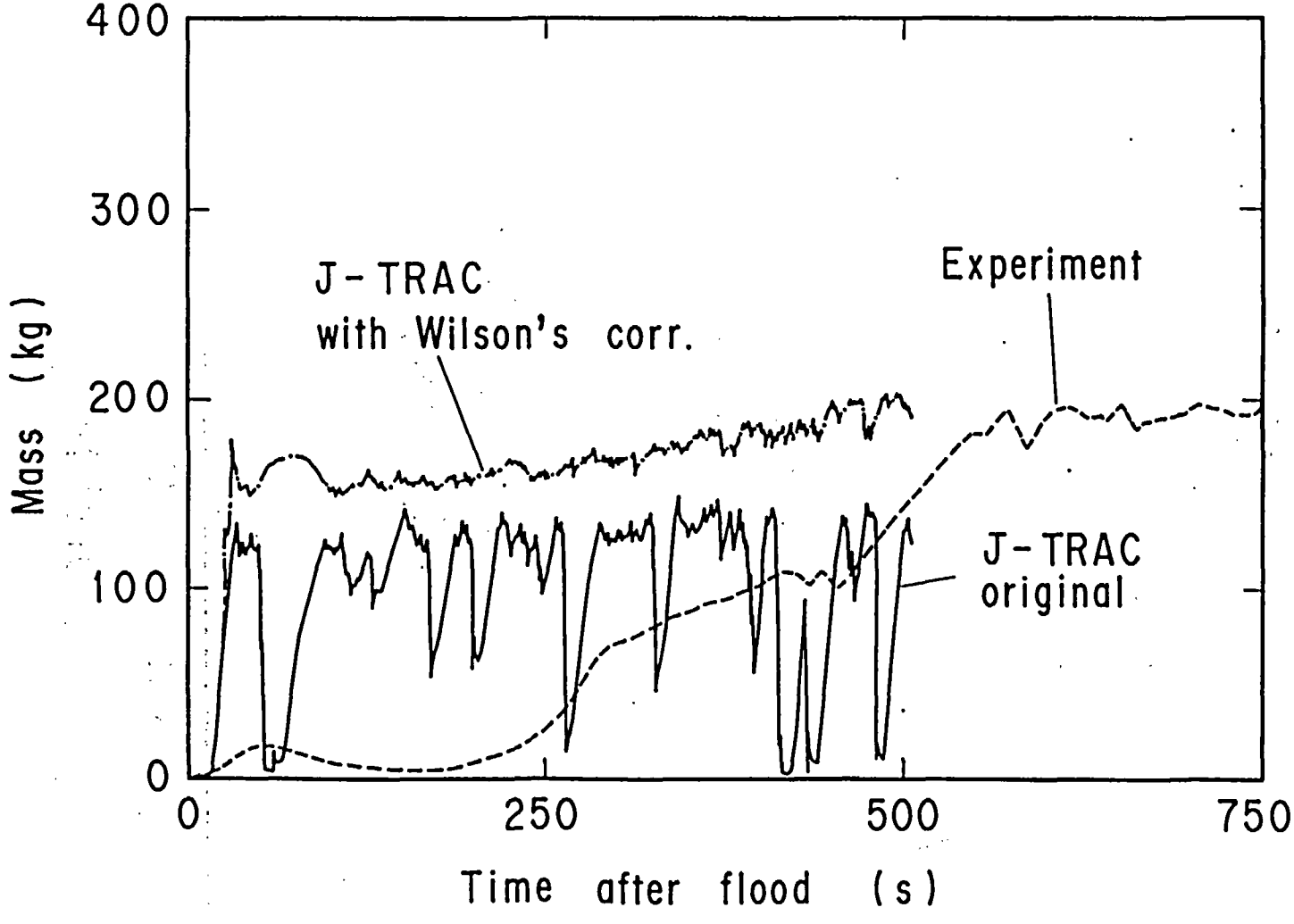

Fig. 12 Water accumulation in upper plenum

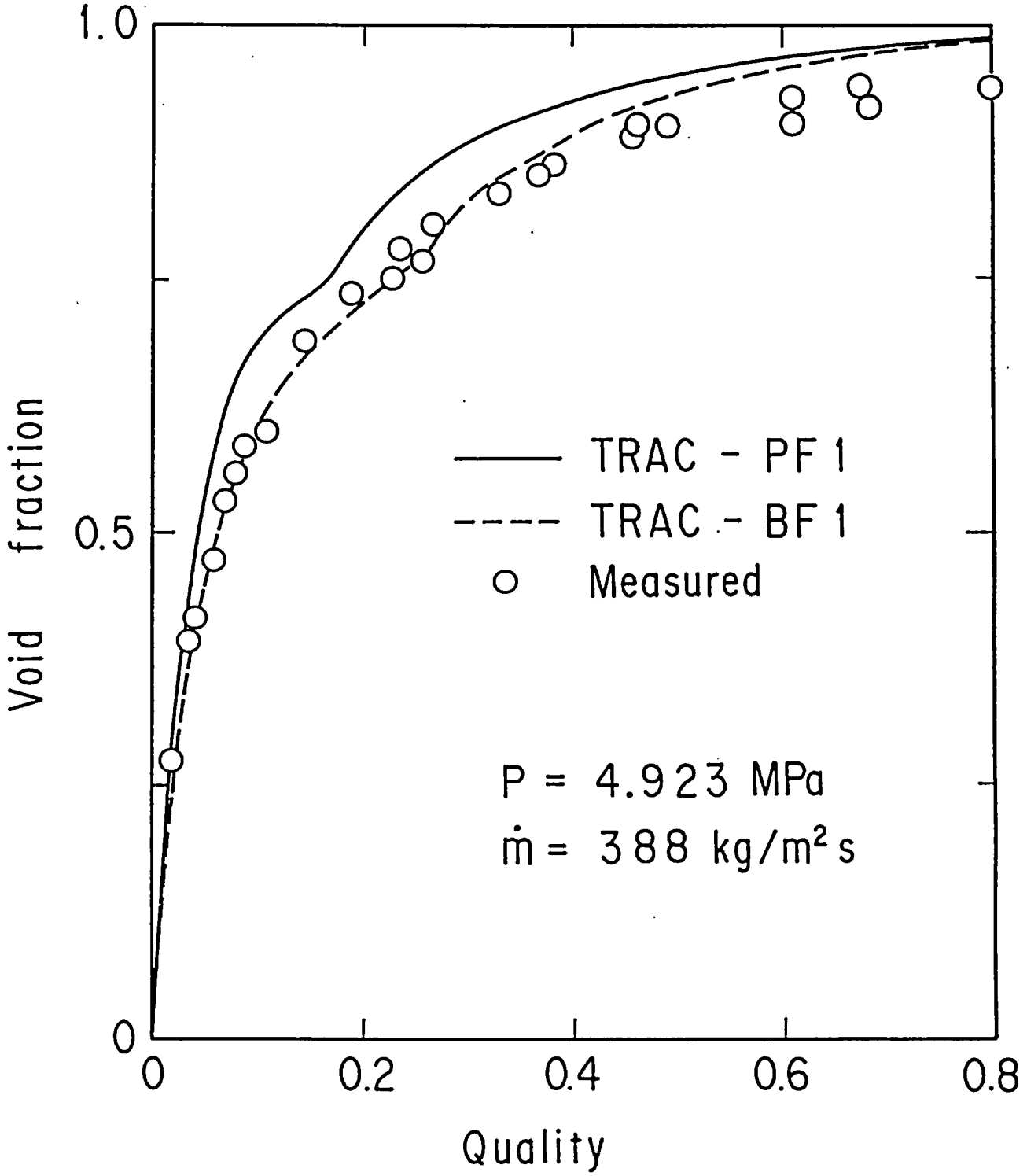

Fig. 13 Void fraction in CISE experiment

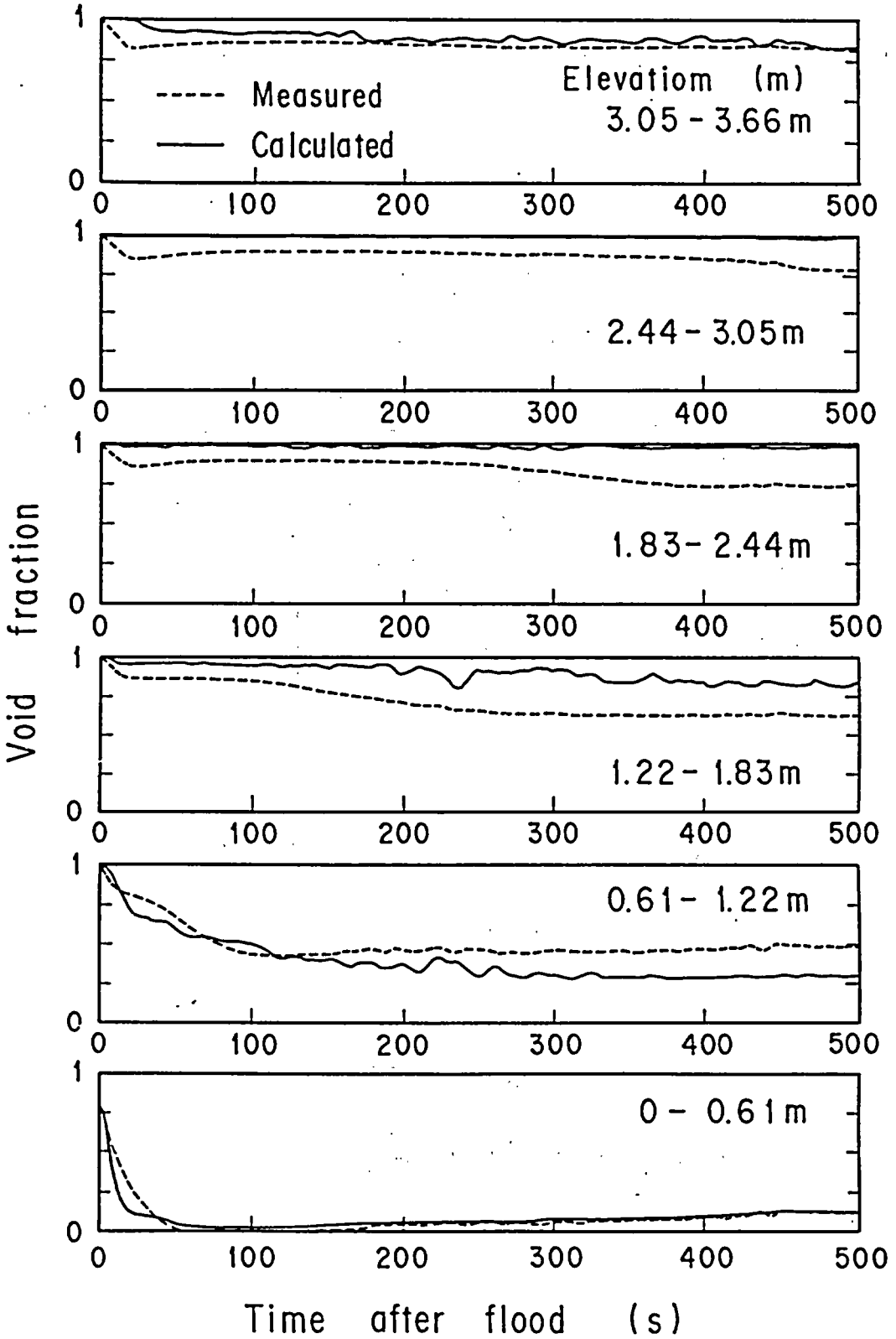

Fig. 14 Void fraction in CCTF base case test (J-TRAC with TRAC-BF1 model)

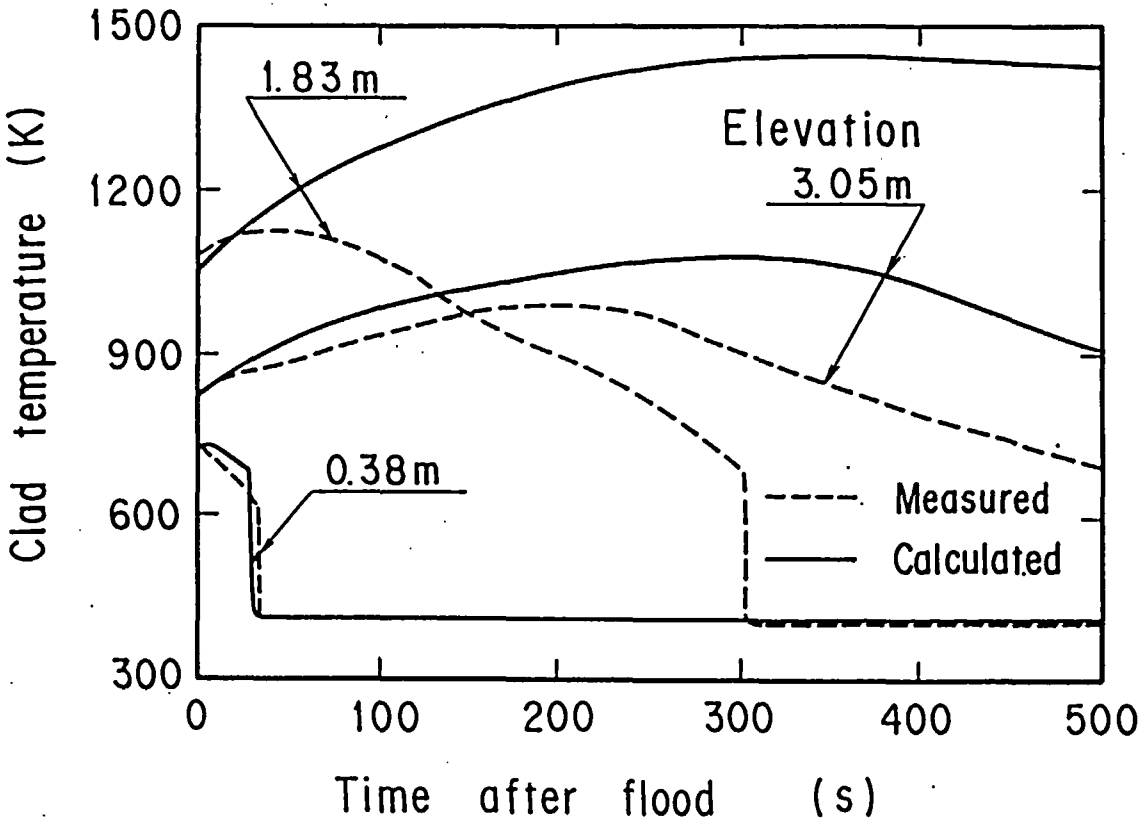

Fig. 15 Clad temperature in CCTF base case test
(J-TRAC with TRAC-BF1 model)

INVESTIGATION OF PWR ACCIDENT TRANSIENTS WITH THE BETHSY FACILITY

R. DERUAZ (CEA-CEN Grenoble)*
G. BAROIS (Framatome)
M. CHAMP (CEA-CEN Fontenay-aux-Roses)
JM. MIRAUCOURT (Electricité de France)

*Mailing address : CEA-CEN Grenoble
SETh/LES
85 X
38041 GRENOBLE - FRANCE

ABSTRACT

BETHSY is a scaled down model of a 900 eMW Framatome PWR which has been designed to allow the study of PWR accident transients with the double purpose of Cathare code and Emergency Operating Procedure verification.

The full operation of the facility was started in 1987. Since then, a fairly large variety of tests have been conducted which include steady state situations (single phase natural circulation -balanced and unbalanced loops- two-phase natural circulation, degraded steam generator mass inventory) as well as accident transients such as 2" and 6" cold leg breaks, steam break at pressurizer, single and multiple steam generator tube ruptures, total loss of feedwater.

In order to illustrate the ongoing Bethsy programme, three different kinds of tests are briefly presented, dealing with two-phase natural circulation, intermediate cold leg breaks and multiple SGTR.

0. INTRODUCTION

Bethsy is an integral test facility which is located at the Nuclear Center of Grenoble and which aims at investigating PWR accident transients. The Bethsy programme is jointly conducted by the Commissariat à l'Energie Atomique, Electricité de France and Framatome and its main objectives are to contribute to the validation of Cathare code and the physical bases of PWR Emergency Operating Procedures.

After a brief review of the Bethsy facility features, the present stage of the programme and the test matrix for the next two years are given, and some results are presented relating to :

- primary coolant system natural circulation patterns under variable mass inventory, core power and steam generator liquid level
- a comparison of the primary coolant system behaviour in case of two 6" cold leg breaks performed in different conditions regarding in particular core power, downcomer-to-upper-head by-pass and safety injection
- a multiple steam generator tube rupture associated with an Emergency Operating Procedure.

1. BETHSY FEATURES

Bethsy is a full pressure (17.2 MPa) scaled down model of a three loop, 900 eMW Framatome PWR. The overall scaling factor, applied to every volume, mass flow rate and power level is close to 1/100, while elevations are 1/1 in order to preserve the gravitational heads. The core power has been limited to 10 % of the nominal value, i.e. 3 MW for the 428 heater rods which make up the core.

As in the reference PWR, Bethsy has three primary coolant loops which are identical and include a main coolant pump capable of delivering up to the nominal flowrate and an active steam generator. The loop piping diameter (118 mm ID) has been defined according to the Froude number criterion applied to hot legs.

Each of the three steam generators is equipped with 34 U-tubes of the same radial dimensions and height stepping as the reference steam generator. U-tubes are so arranged that the secondary side hydraulic diameter is preserved and the tube lane is true to scale.

Every primary and secondary engineered safety system is simulated. This includes HP and LP injection systems, accumulators (one per loop) pressurizer spray and relief circuit, auxiliary feedwater system and steam dumps to the atmosphere or to the condenser.

Special attention has been focussed on the problem of heat losses which may cause undesirable distortions especially in the case of steady state or slow transient tests. The entire primary side as well as steam generators are therefore equipped with trace heaters.

As far as instrumentation is concerned, in order to better understand physical phenomena which are likely to take place on both primary and secondary side, more than 1 200 measuring instruments are used in the Bethsy facility.

Finally a computerized control system, organized according to the principle of distributed microcomputers, enables in particular tests and associated Emergency Operating Procedures to be conducted in the automatic mode.

2. BETHSY PROGRAMME : PRESENT STAGE AND PLANS

The full operation of the Bethsy facility was started in 1987 and since that date a fairly large variety of tests have been carried out which are listed together with our plans for the next two years in Table 1.

After characterization tests regarding pressure drop distribution, heat losses, as well as the behaviour of some components such as the pressurizer or the pressure vessel upper head, and which are essential for a good quality of test analysis and a good understanting of some differences compared to the reference PWR, the performance of both steady state experiments and accident transients has been undertaken :

- steady state tests correspond to situations which are normally encountered during accidents and are of particular interest to carefully investigate related physical phenomena as well as in view of a state oriented approach of Emergency Operating Procedures.
- accident sequences may be initiated either by single or multiple failures. Depending upon the specific objectives which are attached to each test, these transients are either performed without operator actions or together with the associated Emergency Operating Procedure. Although highly improbable, multiple failure accidents are however especially interesting in order to verify the capability of codes to account for combined physical phenomena and to validate the physical basis of state oriented Emergency Operating Procedures and Ultimate Procedures.

Among the tests carried out so far are counterpart tests with the LSTF facility : one (test 4.1a TC) is a two-phase flow natural circulation test and the other (test 6.2 TC) is a 6" cold leg break which will be also probably performed at the Lobi facility. Some results of these two tests are reported in this paper.

The test which will be carried out in December of this year belongs to the category of what is now called Accident Management tests. It consists of a 2" cold leg break without HPS injection and in the course of which a delayed ultimate procedure is conducted. This test is planned to be the next CSNI International Standard Problem.

3. TWO-PHASE FLOW NATURAL CIRCULATION

A good understanding of natural circulation (NC) in the primary coolant system (PCS) is essential since the main coolant pumps are tripped early in the course of a number of accident transients. A series of steady state tests has been carried out in various conditions in order to investigate thermal-hydraulic related phenomena. Two tests have dealt with the study of the effects of a stepwise decrease of PCS mass inventory :

- test 4.1a at a core power of 2 % of nominal power (NP) and standard steam generator liquid level
- test 4.1a TC which was performed at a core power level of 5 % NP and at two steam generator liquid levels (standard value and 1 meter).

In both cases :

- PCS mass inventory was varied from 100 % down to a value leading to a significant core heat up
- PCS pressure was initially set at 15.5 MPa and then behaves freely when decreasing the mass inventory
- the three steam generators were operated at identical and constant conditions (P = 6.8 MPa).

	(1)	(2)
CHARACTERIZATION TESTS		
STEADY STATE tests :		
. Single phase NC		
- Balanced loops (low, high P)	×	
- Unbalanced loops (isolation of 1, 2 SGs)	×	
. Two phase NC		
- Balanced loops		
high P 2% NP, 5% NP	×	
low P		91
- Unbalanced loops		90
- Non condensible gas		90
. Degradation of SG mass inventory		
- Single phase at PCS (NC, FC)	×	
- Two phase NC	×	
. Two-phase flow forced convection		90
. Feed and bleed at PCS		90
SMALL - INTERMEDIATE BREAKS		
Cold leg :		
. 2" : - w HPIS 1 file, EOP	×	
- wo HPIS, delayed ultimate procedure (1)		89
. 3" : - safety injection in intact loops		90
" every loop		91
- pumps on		91
- delayed pump trip		91
. 6" : - UHSN • 3% , conservative power curve	×	
- UHSN 2% , realistic power curve	×	
. 10"		90
Steam break at pressurizer	×	
PV lower plenum		92
RHRS break		91
STEAM GENERATOR TUBE RUPTURE		
. single w HPIS and AFWS - EOP -	×	
. single wo HPIS and AFW		91
. multiple (6 tubes) w HPIS, AFWS - EOP -	×	
LOSS OF FEEDWATER		
. total LOFW - EOP -		89
. 1 HPIS file, 1 relief valve		92
delayed recovery of AFWS		92
BLACK OUT and AFWS failure		92
LARGE BREAKS - reflooding phase -		
. licensing conditions		
- wo non condensible gas		90
- with "		90
. best estimate conditions		91

(1) performed (2) to be performed

Table 1 - BETHSY programme - Status and Plans

We'll restrict here our purpose to present the main results and to stress some particular aspects. More detailed information can be found in [2].

3.1. Primary flow rates

3.1.1. Single and two-phase flow NC

PCS flowrate measurements were performed over a wide range of downcomer liquid velocities by means of a specially designed turboprobe and enabled the effect of primary inventory, core power and steam generator level to be quantified (fig. 1)

Also shown in this figure is the result according to which the flow rate remains unchanged when a given mass inventory is obtained either by draining or charging the PCS.

3.1.2. Reflux condenser mode

The principle of the measurement of the liquid reflux flowrate consists in diverting this liquid flow to a collecting device installed on the hot leg 1 and reinjecting it via a Venturi flowmeter in the upper plenum.
The liquid to vapour flow rate ratio in hot legs has in this way been shown to be close to .5 as long as saturated conditions prevail at the core outlet. In other words up-flow and down-flow sides of steam generator U-tubes equally contribute to steam condensation during reflux condenser mode.
It is worth noting that this result confirms at a quite different scale what has been observed in the Semiscale facility [3]

3.2. Compared behaviour of the three loops

The behaviour of the three loops is found to be very similar till mass inventory is reduced to about 60 %. Below that point the primary flowrate becomes very small and despite the identical feature of the three BETHSY loops, the transition to reflux condenser mode does not occur at the same time in every loop. In particular, complete emptying of the down-flow side of steam generator U-tubes is reached at different primary mass inventories :

	SG1	SG2	SG3
Test 4.1a	40 %	50 %	40 %
Test 4.1a TC	50 %	46 %	41 %

Figure 2 which reports the pressure difference between SG outlet and inlet plena illustrates this point for test 4.1a.

3.3. CCFL during reflux condenser mode

3.3.1. Feed and dump operation of SG U-tubes

At 2 % NP the steam flowrate in hot legs is rather low and no liquid hold-up is observed in hot legs, SG inlet plenum and up-flow side of SG U-tubes.

At 5 % NP, and after the emptying of the third steam generator, a feed and dump operation of the up-flow side of SG U-tubes was observed. This oscillating phenomenon, the period of which is close to 1500 s., is shown in figure 3 for the 37 % mass inventory :

- in a first phase, liquid hold up is built in the ascending part of SG U-tubes (fig. 3a) due to the occurence of countercurrent flow limitation (CCFL). At the same time the liquid level in the pressure vessel is reduced (fig. 3b) and a core uncovery is observed
- this initiates the second phase during which the SG U-tubes are drained and the core collapsed liquid level increases.

Steam generators behave more and more in phase and core uncovery is increased at each new oscillation so that at the third one a significant core heat up occurs and core power is switched off.

All along this oscillating period no liquid hold up is detected either in the hot legs or in the SG inlet plenum.

3.3.2. CCFL at the inlet of SG U-tubes

An estimation of CCFL occurence in SG U-tubes during the reflux condenser mode was made possible, thereby leading to a core power lying within the range 4.6 - 5 % NP. Assuming all U-tubes are behaving in the same way, this corresponds to a value of the Wallis correlation constant ($J_V^{*\frac{1}{2}} + J_L^{*\frac{1}{2}} = C$) such that $.85 \leq C \leq .88$, consistent with values generally accepted for flooding in vertical tubes.

4. 6" COLD LEG BREAKS

4.1. Test conditions

Two 6" cold leg break transients have been carried out :

- test 6.2 under conditions which are representative of the BETHSY reference PWR
- test 6.2 TC which is a BETHSY-LSTF counterpart test.

The major differences between those tests focus on the following points :

	6.2	6.2 TC
Upper head spray nozzles	2 %	.3 %
HPS Injection	in intact loops	no
Auxiliary feedwater	yes	no
Core power decay curve	Figure 4	

Common features are especially :

- break : side oriented nozzle flush with the cold leg ID
- initial conditions : primary and secondary pressures equal to 15.4 MPa and 6.9 MPa respectively, and core power level corresponding to 10 % of nominal power

- scenario :
  - . condenser isolation, main feedwater termination and pump trip all take place at scram (13 MPa)
  - . no Emergency Operating Procedure is conducted
  - . accumulator injection, in intact loops only, is actuated at P = 4 MPa.

4.2. Comparative behaviour

The comparative behaviour of the primary coolant system may be well summarized by the evolution of core collapsed liquid level versus time (fig. 5).

4.2.1. Core liquid level depression

As might be expected, core liquid level depression before loop seal clearance occurs slightly sooner and is significantly larger in test 6.2 TC : the higher core power and the lower upper-head-to-downcomer by-pass bring about a larger hot to cold leg differential pressure mainly through more liquid hold-up in the up-flow side of steam generators -inlet plenum and U-tubes- (fig. 6 and 7).

4.2.2. Core uncovery at boil-off conditions

What is observed concerning core collapsed liquid level at boil-off conditions is certainly more difficult to predict : in spite of HPS injection and larger upper-head-to-downcomer by-pass test 6.2 exhibits at maximum core uncovery (t ≈ 400 s.) a core collapsed liquid level which is reduced by about half a meter in comparison with test 6.2 TC (fig. 5).
This result is not explained by primary mass inventories, which are found to be close together at that time (fig. 8), but lies rather in the fact that liquid distribution is less favourable to the core in test 6.2.
It is seen in figure 9 that loop seals are behaving differently :
- loop seal clearance (LSC) takes place simultaneously in every loop in 6.2 TC
- while the suppression of core liquid level depression is due to LSC of the broken loop only in 6.2, LSC in intact loops being significantly delayed probably because of HPS injection.

Of special concern with regard to core collapsed liquid level at boil-off condition in test 6.2, is that its minimum value, which is classically observed a few seconds after accumulator injection, is reached before LSC in intact loops (fig. 5) ; so liquid remaining in loop seals is lacking in the core and core uncovery is larger.

4.2.3. Third core collapsed liquid level reduction

Finally, figure 5 shows a strong reduction of core mass inventory from t ≈ 1600 s to the end of test 6.2 TC which is not observed in 6.2. This obviously stems from the fact that in 6.2 TC accumulator isolation occurs before primary pressure reaches the LPIS actuation threshold and no HPS injection is made which could compensate the break flowrate.

5. MULTIPLE STEAM GENERATOR TUBE RUPTURE
(test 4.3b)

The main objectives of this test are to verify the physical bases of the Emergency Operating Procedure, notably :
- the behaviour of both the broken SG and the primary side with unbalance between broken and intact loops
- the leak suppression till shutdown conditions.

5.1. Test conditions

5.1.1. Initial conditions

Initial conditions are representative of those of a PWR at 5% NP :

PCS		SCS	
Pressure	15.5 MPa	Pressure	6.6 MPa
Core power	5% NP	SG liquid level	12.5 m
Flowrate	nominal	Auxiliary FW	on

5.1.2. Break characteristics

The break of 6 tubes of the steam generator n° 1 is simulated by an orifice which is located on an external piping linking the SG outlet plenum with the secondary side heat transfer zone (820 mm above tube sheet).

5.1.3. Scenario

The scenario of this test may be divided in 4 phases.

Phase 1 (0 - 650 s) - After break opening, SI signal (P = 11.9 MPa) is followed by :
- immediately : core power decay
  condenser isolation
  main feedwater termination
- after :
  - 10 s : auxiliary feedwater actuation
  - 110 s : HPS injection
  - 300 s : primary pump coastdown

Phase 2 (650 - 4700 s)
This phase deals with leak cancelling by equalizing pressures between the primary side and the rupted steam generator (rSG) :
- the latter is isolated on both sides and its blowdown line is opened to limit the increase of the secondary side level
- PCS depressurization and cooling (recommended max. rate 56°C/h) are conducted by means (respectively) of the auxiliary spray system and the atmospheric dump of the intact steam generators (iSG).

- the HPIS is managed (2 lines - 1 line - charging mode) according to the core outlet subcooling and the pressurizer liquid level.

All along this phase the working point of the PCS is held within the standard states of the Pressure-Temperature diagram while the iSG levels are controlled.

Phase 3 (4700 - 14700 s)

The shift to cold shutdown conditions is now conducted :

- PCS and rSG are simultaneously depressurized (recommended rate 1.5 MPa/hour) by making use of the auxiliary spray and pressurizer heaters together with the rSG blowdown line.
- at the same time PCS is cooled at a maximum rate of 28°C/h by the iSG atmospheric dumps.

Phase 4 (14700 s -> end) :

This last phase has consisted in restarting one intact loop main coolant pump, an action that Plant operators are indeed requested to do before starting phase 3 in French PWR emergency operating procedures.

5.2. First results

At the present stage of the analysis of this test only comments on the overall system behaviour may be made.

Phase 1 is obviously characterized by a sharp drop in PCS pressure while the secondary side pressure increases rapidly up to the opening threshold of atmospheric dumps (fig. 10).

In the course of the leak cancellation phase :

- SG2 and SG3 pressure decrease is such (fig. 10) that PCS is cooled at an average rate of 45°C/h.
  Some oscillations of SG1 pressure are observed which are mainly due to the sensitivity of this parameter to the atmospheric dump opening when the level is very high.
- SG1 collapsed level (fig. 11) indeed escapes the wide range measurement and some liquid is released to atmosphere at that stage of the transient.
  SG2 and SG3 levels are for their part maintained close to 60 % of the narrow range by the control system.

At the end of phase 2, PCS and rSG pressures are equalized (fig. 10) at about 6.4 MPa and the core outlet temperature reaches 240°C.

During phase 3, the average cooling rate of PCS is 25°C/h and PCS to rSG differential pressure is kept close to zero (fig. 10). The depressurization rate of the rSG starts at about .8 MPa/h and rapidly decreases to half this value in spite of the full opening of the blowdown line. From about 8000 to 10 000 s. the rSG depressurization process is stopped, the low value of pressurizer level requiring a shift from PCS depressurization by the auxiliary spray system to the charging mode. A check was then made (ref. 2 in fig. 10) of the method of rSG depressurization which consists in lowering the primary pressure set point and thus reversing the break flow rate ; this attempt was however stopped at t = 11 000 s. because of a fast increase of pressurizer level while the speeding up of depressurisation is not significant. From 11 000 s to the end of phase 3 the blowdown line was used again : the depressurization rate remains rather low (about .4 MPa/h -fig. 10-) and is not increased by the rather large U-tube uncovery which is taking place during this period of time (fig. 11). So, at the end of phase 3

the core outlet temperature reaches 180°C but PCS and rSG pressure remains at about 5 MPa.
The relative slowness of rSG depressurization by the blowdown line is due to the fact that the observed pressure decrease is practically only related to the enthalpy flowrate in this line. Heat transfer at the rSG U-tube surface is small or even zero : with no primary pump in operation no circulation takes place in the U-tubes and fluid temperature in the latter is close to the saturation temperature of the secondary side (fig. 12). A steam bubble is even built up in SG1 U-tubes at t ≈ 10 800 s (fig. 10) and is still present at the end of phase 3.

Also shown in figure 12 is the thermal stratification at the rSG secondary side. Without going into details here, it is not without interest to notice that stratification appears when both the leak flowrate is from primary to secondary side and the HPIS is in operation (safety injection or charging mode). On the other hand this stratification is obviously reduced as soon as a reverse break flowrate takes place.

Finally when the primary pump is restarted at nominal flow rate in the loop 2 at the beginning of phase 4, reverse flow in the U-tubes of the rupted steam generator leads to a partial collapse of the bubble and a fast depressurization of the secondary side (condensation of secondary steam on U-tubes) and of the PCS as well.

6. CONCLUSION

The Bethsy facility, which has been designed to investigate PWR accident transients, is producing useful information for the validation of both Cathare code and Emergency Operating Procedures.

Some results are presented in this paper in a summarized form. They deal with two-phase natural circulation, intermediate cold leg breaks and a multiple SGTR transient.

Flow patterns and related heat transport mechanisms have been studied under variable PCS mass inventory for different core power values and SG liquid levels, when every primary pump is off. Besides more classical results concerning single and two-phase flow natural circulation, some new lessons have been drawn concerning the PCS behaviour when operating in the reflux condenser mode : - the transition from two-phase natural circulation to reflux condenser mode has been found to take place at different mass inventories in each loop - as long as vapour is saturated at the core outlet up-flow and down-flow sides of SG U-tubes equally contribute to condensation - an oscillating PCS behaviour is possible at rather large core powers (≈ 5 % NP) due to CCFL and periodic liquid hold-up in SG U-tubes.

A comparison of core collapsed level evolution in the course of two 6" cold leg breaks performed at different conditions with respect to core power decay, downcomer-to-upper-head by-pass and HPS injection is made. The combination of a small by-pass with a conservative core power decay curve is confirmed as leading to an increase of core liquid level depression before loop seal clearance. While core uncovery at boil-off conditions is shown to be significantly modified whether loop seal clearance takes place at every loop at the same time or not. This point is illustrated here by the fact that a more severe core uncovery is obtained at identical PCS mass inventory in the test with HPS injection

at intact loops (where LSC takes place only at the broken loop before accumulator injection) than in the test where HPIS failure is assumed (where LSC occurs at every loop before accumulator injection).

A multiple steam generator tube rupture (6 tubes) has been conducted together with an Emergency Operating Procedure which mainly consists in :

- cancelling the leak by PCS depressurization (auxiliary spray system) while cooling the PCS by means of the atmospheric dumps of unaffected steam generators

- shifting to cold shutdown conditions by simultaneously depressurizing the rupted SG (blowdown line) while continuing to cool the PCS with the intact SG.

This test confirms the relevance of the physical bases of the EOP. In addition, the restart of a primary pump before depressurizing simultaneously the PCS and the rupted SG is clearly shown to be of great interest : the resulting flow circulation in the U-tubes of the rupted steam generator increases significantly heat transfer between primary and secondary sides and thus greatly improves the efficiency of the rupted SG depressurization by the blowdown line, especially when U-tubes become uncovered (condensation at secondary side).

REFERENCES

[1] B. NOEL, R. DERUAZ - 2" cold leg break at Bethsy facility
NUSCAFE ENS/ANS Meeting - Avignon - Oct. 1988.

[2] P. BAZIN, P. CLEMENT, R. DERUAZ - Natural circulation under variable primary mass inventories at Bethsy facility
NURETH 4 Meeting, Karlsruhe, Oct. 1989.

[3] G.G. LOOMIS, K. SODA - Results of the Semiscale Mod 2A Natural Circulation Experiments.
NUREG/CR 2335, EGG-2200 - Sept. 1982.

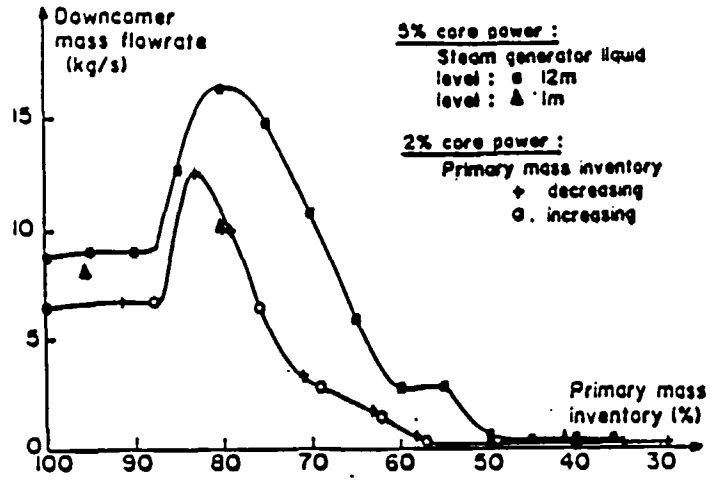

Fig. 1 Test 41a (2 %) and 41a TC (5 %) : downcomer mass flowrate

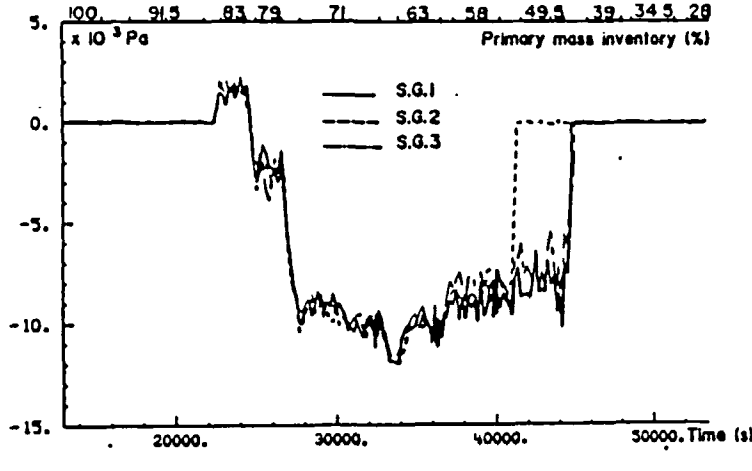

Fig. 2 Test 41a (2 % N.P.) - part 1 : pressure difference between outlet and inlet steam generator channel heads

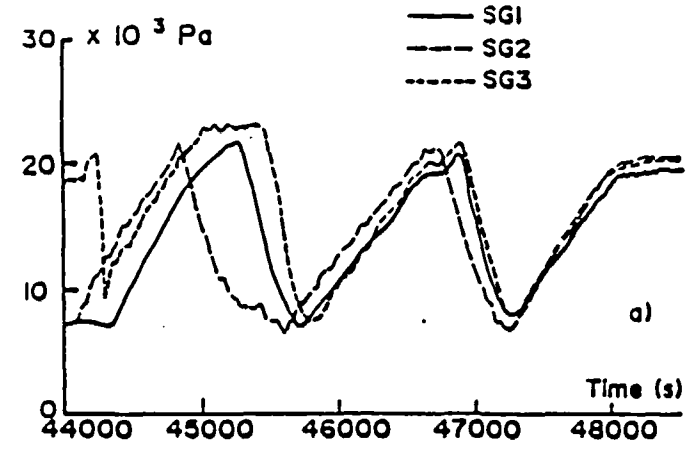

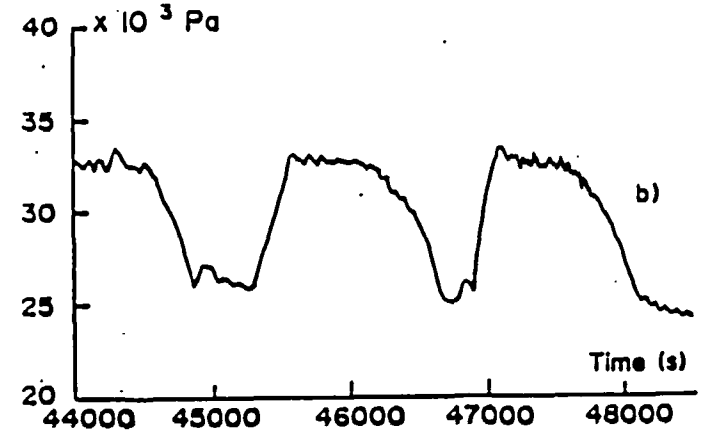

Fig. 3 Test 41a - TC (5 % N.P.) : State at 37 %

a) Up-flow side S.G. U-tubes pressure difference

d) Core inlet - upper plenum differential pressure

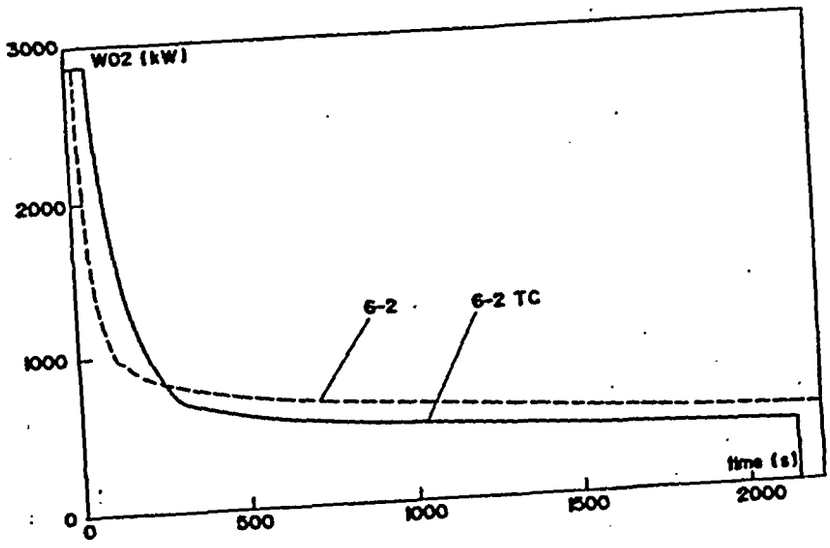

Fig. 4 BETHSY Tests 6-2 and 6-2 TC : Core power

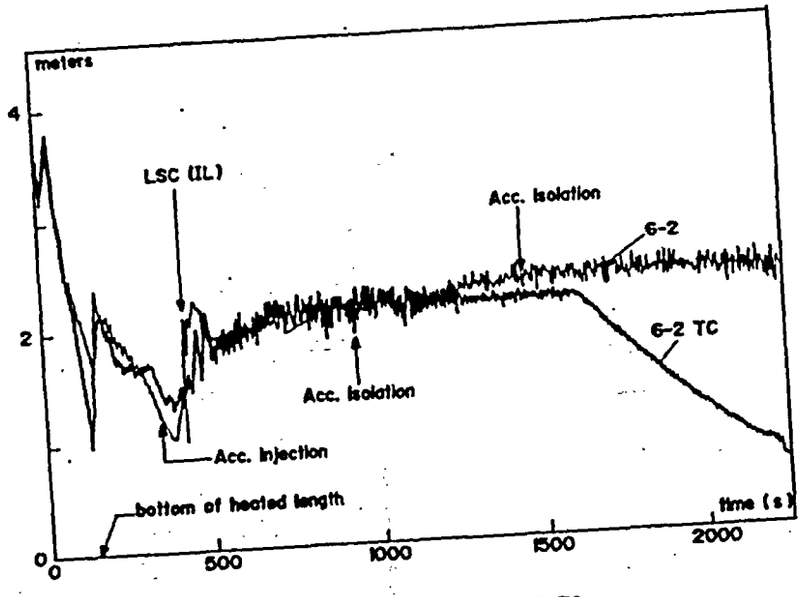

Fig. 5 BETHSY - Tests 6-2 and 6-2 TC
Core collapsed liquid level

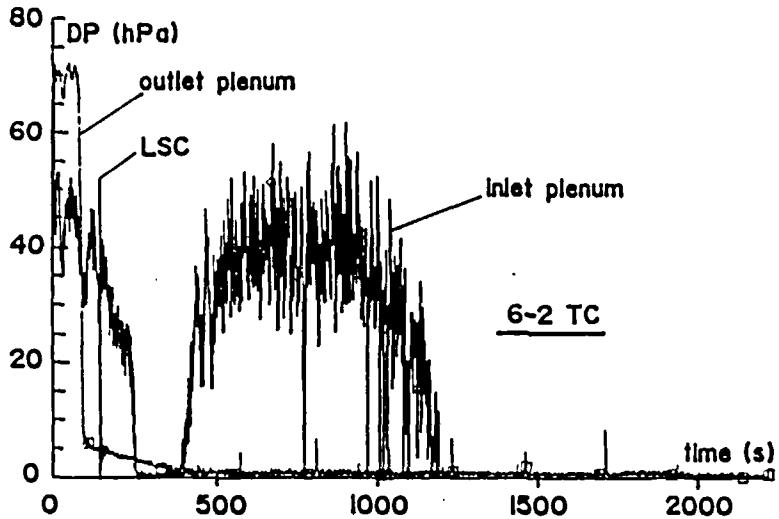

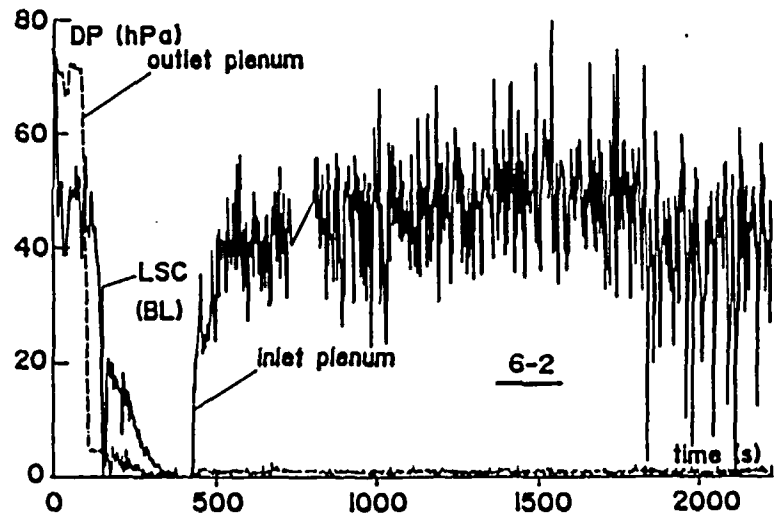

Fig. 6 BETHSY - Tests 6-2 and 6-2 TC
Differential pressure in SG plena

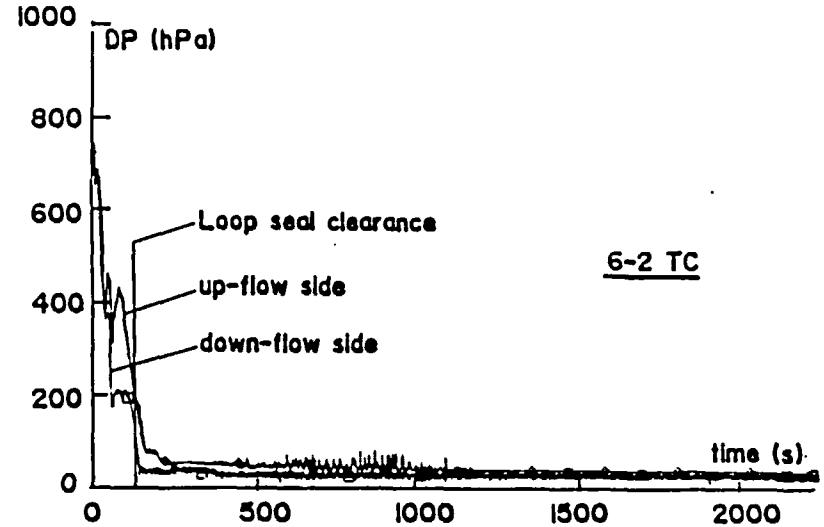

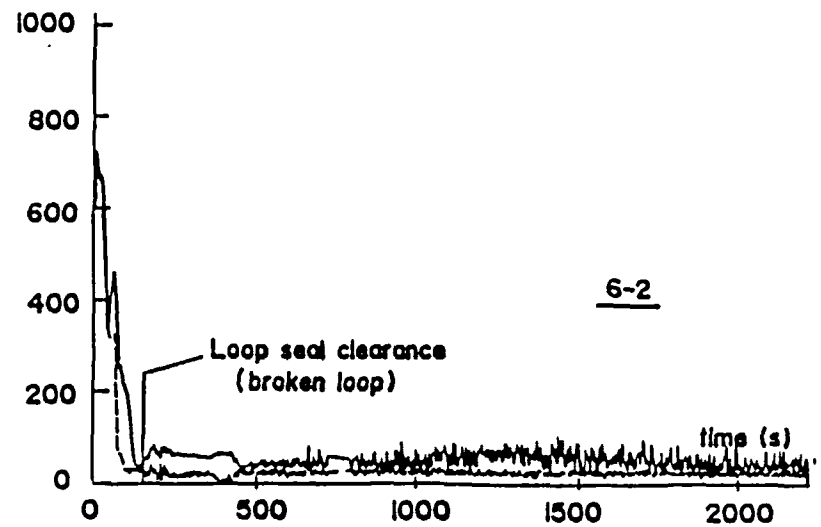

Fig. 7 BETHSY - Tests 6-2 and 6-2 TC
Differential pressure in SGI U-tubes

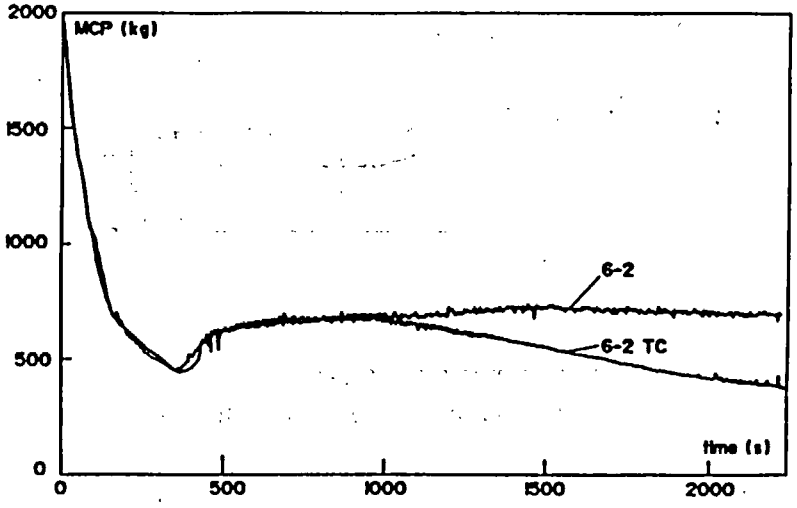

Fig. 8 BETHSY - Tests 6-2 and 6-2 TC
Primary mass inventory

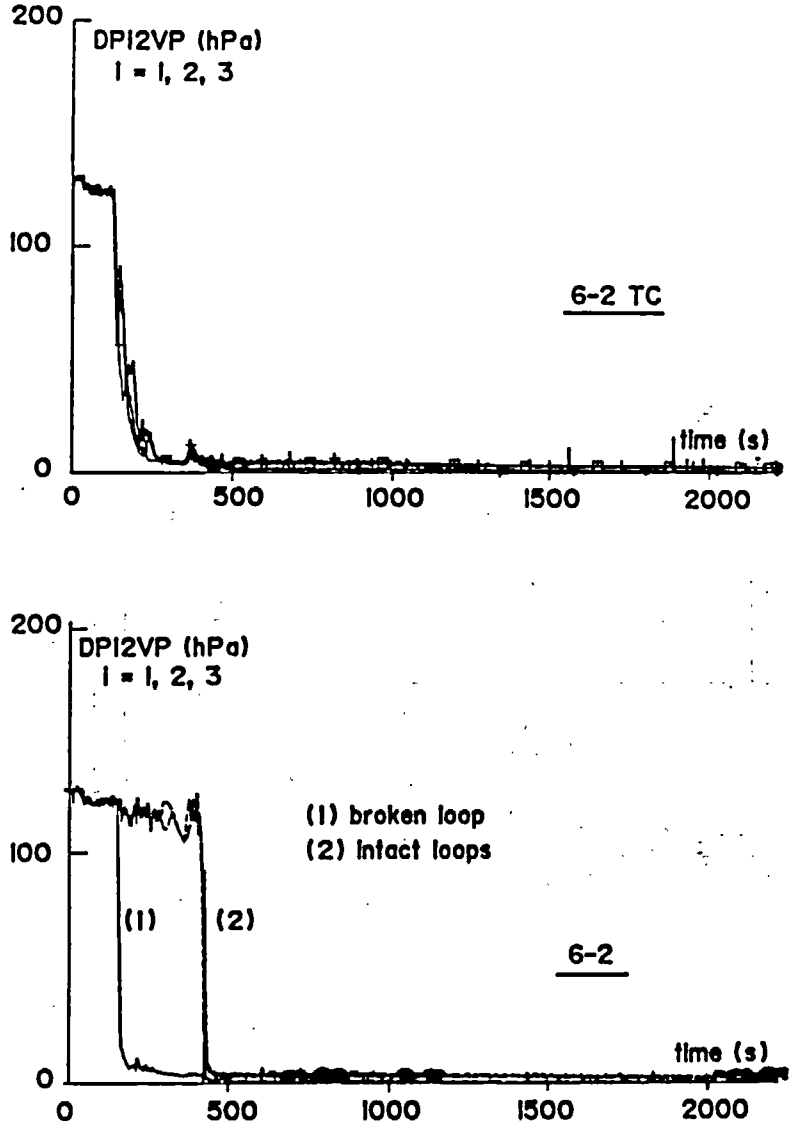

Fig. 9 BETHSY - Tests 6-2 and 6-2 TC
Differential pressure in the
up-flow side of crossover legs

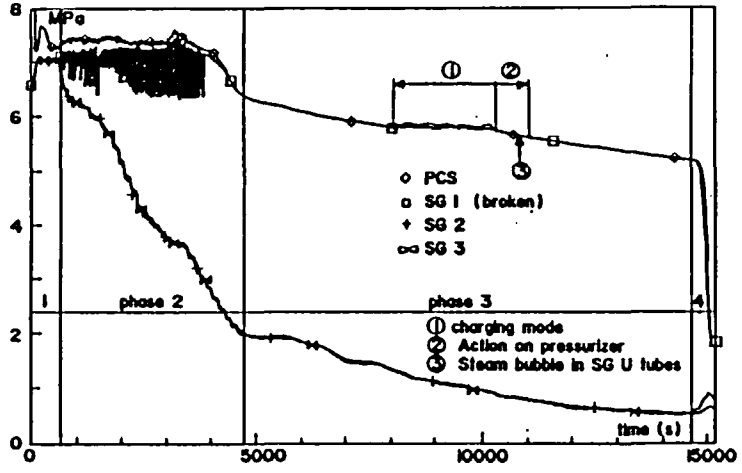

Fig. 10 BETHSY - Test 43b : Multiple SGTR
Primary and secondary Pressure

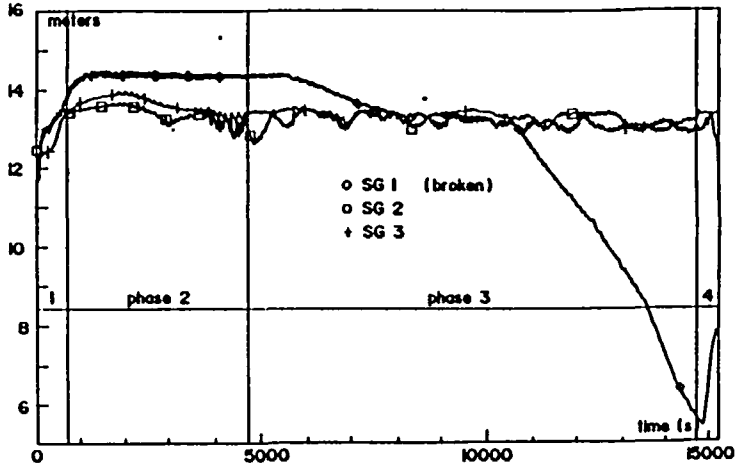

Fig. 11 BETHSY - Test 43b : Multiple SGTR
Steam generator collapsed levels

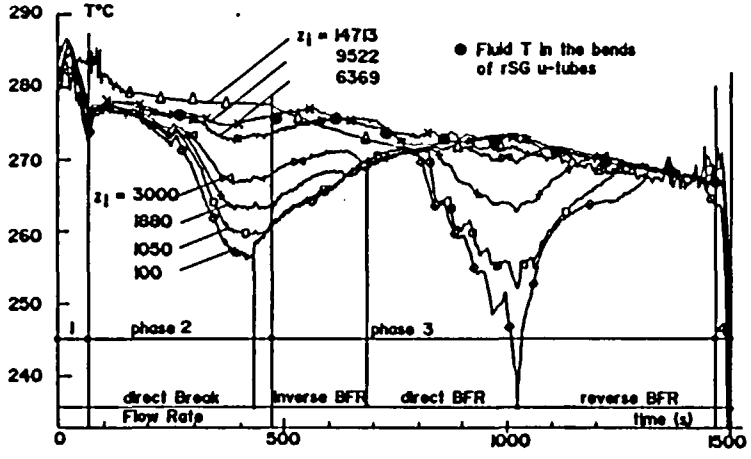

Fig. 12 BETHSY - Test 43b - Multiple SGTR
rSG fluid temperatures

Summary of ROSA-IV LSTF First Phase Test Program and Station Blackout (TMLB') Test Results

K. Tasaka, Y. Kukita and Y. Anoda

Japan Atomic Energy Research Institute
Tokai-mura, Ibaraki-ken 319-11 Japan

1. INTRODUCTION

This paper summarizes major test results obtained at the ROSA-IV Large Scale Test Facility (LSTF) during the first phase of the test program. The results from a station blackout (TMLB') test conducted at the end of the first-phase program are described in some detail.

The LSTF [1-3], shown schematically in Fig. 1, is an integral test facility being operated by the Japan Atomic Energy Research Institute (JAERI) for simulation of PWR thermal-hydraulic responses during small-break loss-of-coolant accidents (SBLOCAs) and operational/abnormal transients. It is a 1/48 volumetrically scaled, full-height, full-pressure simulator of a Westinghouse-type 4-loop (3423 MWt) PWR.

The facility includes two symmetric primary loops each one containing an active inverted-U tube steam generator (SG) and an active reactor coolant pump. The loop horizontal legs are sized to conserve the scaled (1/24) volumes as well as the length to the square root of the diameter ratio in order to simulate the two-phase flow regime transitions [4].

The first phase of the LSTF test program started in May 1985 and ended in August 1988, conducting forty-two test runs. The second phase program started in December 1988 after an outage for replacement of the core fuel-rod assembly. Eight tests have been conducted on the second core assembly by the end of October 1989.

The primary objective of the LSTF first-phase program was to define the fundamental PWR thermal-hydraulic responses during SBLOCAs and transients. Most of the tests were conducted with simulated component/operator failures, including unavailability of the high pressure injection (HPI) system and auxiliary feedwater (AFW) system, as well as operator failure to take corrective actions. These failure assumptions tended to simplify the system responses conveniently for the purpose of the program.

The test matrix for the first phase program is shown in Table 1. The forty-two (42) first phase tests included twenty-nine (29) SBLOCA tests conducted mainly for cold leg breaks, three (3) abnormal transient tests and ten (10) natural circulation tests. Attempts were made in several of the SBLOCA tests to simulate the plant recovery procedures as well as candidate accident management measures for prevention of high-pressure core melt situation. The natural circulation tests simulated the single-phase and

two-phase natural circulation as well as reflux condensation behavior in the primary loops in steady or quasi-steady states.

The most important results from these tests are summarized as follows.

2. SG-LIQUID HOLDUP EFFECTS ON CORE LIQUID LEVEL DEPRESSION DURING LOOP SEAL CLEARING IN COLD LEG BREAK LOCA

The cold-leg break tests [5-15] focused on the steam generator liquid holdup effect on the core liquid level depression during loop seal clearing. The SG liquid holdup enhances the severity of the level depression. This effect, first identified at the Semiscale test facility in 1981 [16], was observed in LSTF tests conducted for break areas greater than 5% (of scaled PWR cold leg cross-sectional area), but not for break areas smaller than 2.5%. For smaller breaks, the transient was slow enough for the liquid in the SG primary side to drain completely before loop seal clearing occurred.

The break flow depended on not only the break area but also the upper pressure-vessel bypass areas which controlled the break flow quality until loop seals were cleared . For the same break area, loop seal clearing occurred later with larger bypass areas, allowing more liquid to drain from SGs before loop seal clearing occurred.

The OECD Nuclear Energy Agency (NEA) Committee on the Safety of Nuclear Installations (CSNI) has chosen one of the LSTF cold-leg SBLOCA tests [17] for the CSNI International Standard Problem No. 26 (ISP-26). This test typically represented the SG liquid holdup effects on core liquid level depression. The primary coolant inventory distribution during this kind of transient is complex, being affected by counter-current flow limiting as well as two-phase mixture level swell. A typical coolant distribution at the time of loop seal clearing during a 5% break test is shown in Fig. 2. Thus, the prediction of the coolant distribution, including the core level depression, and the core heat transfer behavior during level depression, is challenging to ability of computer codes.

3. BREAK LOCATION EFFECT ON BREAK FLOW TRANSIENTS

The LSTF is provided with nineteen (19) nozzles at different locations for simulation of break on the primary and secondary systems.

The twenty-nine (29) SBLOCA tests conducted in the first-phase program encompassed eleven (11) different break locations including: cold leg (leg pipe top, bottom and side), hot leg (top, bottom and side), loop seal, pressurizer top (representing stuck-open power operated relief valves), steam generator U-tube, vessel upper head, and lower head (representing core instrument tube rupture) [9, 18-25].

All these eleven break locations, except the loop seal, were covered by a series of tests conducted for a break area of 0.5% (of the scaled cold leg cross-sectional area) [17-23]. The test results indicated significant break location effects on the break flow rate; the time to the incipient core uncovering was about four times longer for the pressurizer top break

case than for the vessel lower head break case. Figure 3 compares the time-integrated break flow rates measured in these tests. For all of these tests, the primary pressure was held above the secondary pressure (about 8 MPa) since the energy release through the break was smaller than the core decay power. The secondary pressure was kept between the relief valve opening and closing pressures of 8.03 and 7.82 MPa, respectively. The break flow was single-phase liquid for the lower plenum break case until the pressure vessel became almost empty of liquid. For other cases, the break flow quality was affected by phase separation upstream the break. Also, liquid holdup at upper primary regions close to the break was characteristic of the pressurizer and upper head breaks.

For SBLOCA tests with the break located at other locations than cold leg, the core level was depressed temporarily when HPI was initiated after detecting core heatups. This occurred because of condensation-induced depressurization in the cold legs and upper downcomer annulus. These regions had become steam-filled before core uncovering initiated, while the loop seals remained liquid plugged. Thus, the cold-leg depressurization created a differential pressure in the loop seals, until this differential pressure cleared the loop seal of liquid.

4. BREAK AREA EFFECT ON COLD LEG BREAK WITH HPI FAILURE

Most of the cold leg break tests were conducted without injection from HPI. The impact of loss of HPI was dependent on break size. For 5% break tests, core heatups occurred twice during loop seal clearing due to the manometric core liquid level depression, and after loop seal clearing due to boil-off of the vessel coolant inventory. The second heatups were terminated by injection from the accumulators. Steam relief from the break after loop seal clearing depressurized the primary before the maximum heater rod temperature reached to the setpoint temperature for the core protection circuit of 923 K.

For 2.5% break tests, the primary depressurization after loop seal clearing was slower than for 5% break. Thus, the peak heater rod temperature reached the above setpoint before the accumulator restored the core cooling.

For 0.5% (scaled 2 inch) break test, the primary pressure remained higher than the secondary pressure even after loop seal clearing since the steam relief from the break was smaller than the steam production in the core. When no operator action was taken to depressurize the secondaries, the primary pressure remained higher than the accumulator injection pressure of 4.51 MPa.

5. BREAK ORIENTATION EFFECTS ON COLD LEG BREAK

The effect of break orientation was studied for both cold leg and hot leg breaks. The break orientation had only a minor influence for the cold leg break tests [26-27] which were conducted for break areas of 0.5 and 2.5%. The break flow quality was almost independent of the break orientation, since the vapor flow rate to the break was controlled by the steam flow through the upper pressure vessel bypasses. Thus, the time to loop seal

clearing was almost the same for the top, side and bottom break cases as shown in Fig. 4 for the 0.5% break tests. However, the residual coolant inventory after loop seal clearing was different between these three cases since the cold leg liquid level at the time of loop seal clearing was dependent on the break orientation, being lowest for the bottom break and highest for the top break.

6. BREAK ORIENTATION EFFECTS ON HOT LEG BREAK

For 0.5% hot leg break tests [28], the break orientation had a clear influence on break flow quality and thus on break flow rate. The break flow quality was higher for the top break case than for the side or bottom break case. The time to the incipient core uncovering was a factor of about 3 longer for the top break case than that for the side or bottom break case as shown in Fig. 5. Also, it is noteworthy that the time to core uncovering for the 0.5% hot leg top-break case was longer than the 0.43% pressurizer top break case, where the pressurizer surge line was connected to the hot leg at an azimuthal angle of 45^{o} above horizontal. The break orientation had such a clear influence on the break flow since the hot leg level was almost unaffected by the break orientation for this break size.

However, the break orientation effect was less clear for relatively large SBLOCA case (10%) where the hot leg flow was not so clearly stratified as for the 0.5% break cases, and the effect of break orientation on the hot leg liquid level was significant.

Both the cold-leg and hot-leg break orientation effect tests have been post-test analyzed by computer codes CATHARE and RELAP5/MOD2 to assess the break offtake models in these codes.

7. DETECTION OF CORE UNCOVERING AND RECOVERY ACTION SIMULATION

Core heatups were observed in most of the LSTF cold leg break tests which assumed failure of HPI. After continuous core heatups were observed in these tests, attempts were made to restore the core cooling by activating HPI manually or by using other means. HPI was injected into cold leg, or hot legs, or upper plenum to study how the effectiveness of HPI is dependent on the injection location.

For SBLCA tests with the break located not in the cold leg, and with failed HPI, initiating injection into the cold legs generally resulted in a temporary core level depression as has been mentioned.

The parameters which are useful in detecting the core uncovering were discussed [29]. Attempts have been made to simulate the operator-initiated depressurization of the primary and secondary system [30]. Figure 6 shows the primary pressure behavior during a 0.5% hot leg break test, with an assumed failure of HPI, in which the pressurizer power operated relief valves (PORVs) were latched open after detecting core heatups to depressurize the primary to the accumulator injection pressure. The accumulator injection occurred intermittently as core reflooding restored the primary pressure.

8. LOOP SEAL CLEARING AND REFILL DURING COLD LEG BREAK LOCA

The number of loop seals which were cleared of liquid was dependent on the size of cold leg break. Only one out of the two LSTF loops was cleared for break areas smaller than 2.5% whereas both loops were cleared for break areas greater than 5% [32].

For the 0.5% cold leg break tests, with failure of HPI, the loop seal refilled after clearing. The refill occurred as SG condensate dropped into the loop seals [32]. Since this liquid created a differential pressure between the vessel hot leg and cold leg nozzles, the core level, dropping due to the vessel coolant boil-off, was further depressed by this differential pressure. The loop seal was cleared again when HPI was initiated manually, since condensation on the emergency core coolant (ECC) depressurized the cold legs. However, the loop seal was refilled by ECC at 5000 to 6000 s after break.

There is a concern for cold leg break LOCAs that the loop seals may refill with ECC during post-blowdown long-term cooldown where the steam flow through the loop seal may become insufficient, due to the core power decay, to prohibit the ECC in the cold legs to drain into the loop seals [31]. If this occurs, while core boiling persists, the loop seals may be eventually cleared causing a corresponding level drop in the core.

This phenomenon has been studied on the LSTF since December 1987. The test results obtained so far indicate that the loop seal refill is not necessarily controlled by static counter current flow limiting (CCFL) at the reactor coolant pump, but also affected by transient coolant distribution in the primary system [30-31]. The steam flow rate through the loop seal is dependent not only on the core steam production rate but also on the coolant distribution.

It has been also identified that the SG heat transfer alters the net steam production in the system. Since condensation on the U-tube primary side reduces the net steam production, this can result in extremely slow loop seal clearing that may involve quasi-static core level depression leading to core uncovering for an extensive time period. Figure 7 shows the effect of secondary cooling on core temperature behavior during a test in which loop seal clearing and refill occurred cyclically. The secondary cooling slowed the level depression keeping the core uncovered for longer time than without cooling.

Similarly, injecting part of ECC into the hot leg may reduce the net steam production rate because of steam condensation on ECC. This phenomenon has been investigated in a recent experiment.

9. NATURAL CIRCULATION - STEADY-STATE SIMULATION

Natural circulation in the primary system is peculiar to SBLOCAs and related transients. The primary and secondary side flow behavior as well as the SG heat transfer characteristics during natural circulation have been investigated in steady-state and quasi-steady-state experiments [35-

44]. The tests evidenced that the core decay heat can be removed by single-phase and two-phase natural circulation as well as by reflux condensation for a wide range of system variables including core power, coolant inventory and secondary liquid level.

For degraded secondary cooling conditions, the measured overall heat transfer coefficient, defined for the heat transfer area below the secondary collapsed water level, ranged between about 2 and 4 kW/m^2s for all three natural circulation modes observed for a core power range between 2 and 5%.

The tests also indicated that coolant distribution during two-phase natural circulation and reflux condensation modes is controlled by flooding at the hot leg riser section as long as the flooding condition is not reached at the U-tube inlet. The U-tube flooding characteristics can be represented by the Wallis-type flooding correlation as shown in Fig. 8.

One of the advantages of the LSTF over other smaller-scale facilities is that comparatively large number (141) of U-tube per SG is represented. The U-tubes indicated non-uniform parallel-channel behavior during each mode of natural circulation. The mechanism of such behavior has been analyzed.

10. STATION BLACKOUT SIMULATION

A simulation of the station blackout scenario was conducted at the end of the first-phase test program. This test assumed complete unavailability of both onsite and offsite a.c. power, unavailability of turbine-driven auxiliary feedwater, and unavailability of primary and secondary relief valve functions.

The test was initiated from primary pressure and temperatures representative of PWR nominal operating conditions as summarized in Table 2. Since the maximum-available LSTF core power (10 MW) is 14% of the scaled PWR nominal power, the initial steady-state was established for a core flow rate of 14% of the scaled PWR flow rate to obtain prototypical hot leg and cold leg temperatures. The secondary pressure (7.3 MPa) was higher than the PWR secondary pressure during nominal operating conditions, because of requirement to limit the primary-to-secondary heat transfer at 10 MW, i.e., 14% of the scaled value.

The test was initiated by terminating the feedwater to the SG secondaries at time zero. Concurrently, a simulated scram signal was generated. This signal initiated core power decay, closed the steam valves, and initiated pump coastdown. It was assumed that the turbine driven auxiliary feedwater was not available. Thus, the secondary inventory was boiled off through the secondary safety valves which had opening and closing setpoint pressures of 8.68 and 7.69 MPa, respectively.

The primary and secondary pressure responses are shown in Fig. 9. The SG safety valves opened repeatedly until the secondary inventory boiled dry. The last opening occurred at 4500 s for SG-A and 4000 s for SG-B.

This test was characterized by a long-term (more than 7000 s) single-phase

natural circulation which initiated as soon as the pumps stopped as shown in Fig. 10. The core inlet-to-outlet temperature difference decreased with core power decay.

During the single-phase natural circulation, the U-tube primary side temperatures suggested non-uniform flow distribution among the parallel U-tubes as was observed for the steady-state natural circulation tests at the LSTF. In certain U-tubes, the measured fluid temperatures were close to the secondary side temperature indicating a reverse flow. Fluid temperatures in other tubes indicated normal decay along the tube. Reverse flow was observed for five out of the six instrumented U-tubes in Loop-A SG and for all the six instrumented tubes (not at the same time) for the Loop-B SG. Thus, only a part of the SG heat transfer area was active in cooling the primary system. The number of the tubes flowing in the reverse direction changed during the transient. It appears that after 5100 s all the instrumented tubes flowed in the normal direction.

The secondary water level, shown in Fig. 11, became less than 1 m above the tubesheet at 3000 s, causing the SG heat transfer to degrade. The primary pressure started to increase at this time as shown in Fig. 9, lifting eventually the pressurizer safety valve at 4200 s. The safety valve opening and closing setpoint pressures were 17.26 and 17.06 MPa, respectively.

The primary coolant volume was expanding continuously due to the temperature increase (Fig. 12), and thus the pressurizer water level was increasing, as shown in Fig. 13. The level reached to the top of the pressurizer at 4300 s, when the pressurizer safety valve opened for the first time, as the steam relief from the safety valve depressurized the primary system. The pressurizer safety valve opened cyclically thereafter. Then, the fluid in the pressurizer, initially saturated, became subcooled as subcooled fluid in the hot leg penetrated into the pressurizer. The coolant inventory was lost continuously through the safety valve (Fig. 14).

The primary side natural circulation continued as long as the hot leg fluid was subcooled. Once the hot leg became saturated, due to the SG heat transfer degradation as well as subsequent loss of coolant inventory through the pressurizer safety valve, a stationary steam bubble formed at the top of the U-tubes, at 7400 s, blocking the natural circulation.

The fluid in the pressurizer became saturated, with a delay of about 700 s relative to the hot leg saturation. The pressurizer saturation resulted in two-phase discharge which kept the safety valve open after 7800 s, until the pressurizer water level started to drop at 8800 s uncovering the safety valve line inlet. The pressurizer level drop occurred at almost the same time as the uncovering of the surge line inlet at the Loop-A hot leg. The hot legs started emptying at this time, following the complete voiding in the SG primary sides, and became finally empty of liquid at 9300 s.

After the emptying of the hot legs, the water level in the upper plenum and the downcomer dropped concurrently (Fig. 15), due to the continuing coolant boil-off through the pressurizer safety valve. The differential pressure between the upper plenum and the downcomer steam volumes was small (less than 5 kPa) since the steam flow through the upper vessel bypasses equalized the pressures in the two regions.

The core level drop uncovered the core upper regions at 9800 s, resulting in continuous core heatups as shown in Fig. 16. The peak rod surface temperature reached to 880 K at 11500 s when the core electric power was turned off to protect the core. The heater rods were uncovered down to the third temperature measurement elevation from the bottom (28% of the total core heated length) at this time. Steam superheating, up to temperatures of about 740 K, was observed in both hot legs and the pressurizer surge line, but not in the pressurizer where liquid still remained.

The SG secondary-side fluid temperatures are depicted in Fig.17. As the liquid level dropped, the steam region began to be superheated, being heated by the uncovered U-tubes surfaces. The uncovered tube surfaces had considerably higher temperatures than the secondary saturation temperature because of the growing temperature difference between the primary and secondary systems. The superheating resulted in a clear temperature stratification in the steam region.

11. CONCLUDING REMARKS

The LSTF first-phase test program covered a broad spectrum of accidental conditions. The test variables for the SBLOCA tests included break location, break orientation and break area, availability of HPI, upper pressure vessel bypass areas, and post-scram core power decay characteristics.

The core uncovering mechanisms observed in the SBLOCA tests were:

(1) Core level depression during loop seal clearing for cold leg breaks. The loop seal clearing was:

- accompanied by steam generator liquid holdup, which enhanced the level depression, for moderate break sizes, and
- led by loop seal refill with ECC for long-term cooldown following a cold leg break.

(2) Core level depression during loop seal clearing which ocurred subsequent to delayed ECC injection for break locations other than cold leg.

(3) Vessel coolant inventory boil-off, with make-up with ECCS unavailable due to assumed malfunction or due to primary pressure being higher than the ECCS injection pressure.

The primary and secondary side cooling mechanisms were investigated in detail in steady-state natural circulation tests.

Finally, the PWR station blackout (TMLB') scenario was simulated successfully providing experimental data on primary side natural circulation, secondary side boil-off and primary coolant inventory loss through the pressurizer safety valve which eventually led to core uncovering and heatup.

The ongoing second-phase program will further conduct SBLOCA and transient tests to define experimentally the range of accidental conditions which lead to possible core damage, and also to define the time to core uncovering as a function of accidental conditions. Also, study on the effectiveness of operator corrective actions and accident management measures for prevention of core damage will be given more emphasis than in the first-phase program.

REFERENCES

1. ROSA-IV Group, "ROSA-IV Large Scale Test Facility (LSTF) System Description", JAERI-M 84-237 (1984).

2. Koizumi, Y. et al, "ROSA-IV Large Scale Test Facility for PWR SBLOCA Integral Simulation Test," Proc. Specialist Mtg. on Small Break LOCA Analysis in LWRs, Pisa (1985).

3. ROSA-IV Group, "Supplemental Description of ROSA-IV LSTF with No. 1 Simulated Fuel Rod Assembly," JAERI-M 89-113 (1989).

4. Zuber, N., "Problems in Modeling Small break LOCA," NUREG-0724 (1980) U.S. Nuclear Regulatory Commission.

5. Tanaka, M. et al, "A 10% Cold Leg Break Test at ROSA-IV Large Scale Test facility," Proc. Specialist Mtg. on Small Break LOCA Analysis in LWRs, Pisa (1985).

6. Koizumi, Y. et al., "Blind-Blind Prediction by RELAP5/MOD1 for a 0.1% Very Small Cold-Leg Break Experiment at ROSA-IV Large Scale Test Facility", J. Nucl. Technol. (1985).

7. Osakabe, M. et al, "Thermal Hydraulic Mechanism of Core Liquid level Depression and Recovery during Small Break LOCA Experiment," Proc. ANS/ENS Topical Mtg. on Thermal Reactor Safety (1986).

8. Asaka, H. et al., "Analysis of LSTF 10% Cold Leg Break Experiment" Proc. 2nd Intl. Topical Mtg. on Nucl. Power Plant Thermal Hydraulics and Operations, Tokyo (1986).

9. Tasaka, K. et al., "The Results of 5% Small Break LOCA Tests and Natural Circulation Tests at the ROSA-IV LSTF," Proc. 14th Water Reactor Safety Inf. Mtg. (1986), also, Nucl. Engrg. and Des. (1987).

10. Tanaka, M. et al., "A 10% Cold Leg Break Test at ROSA-IV Large Scale Test Facility", Nucl. Engrg. Des. (1986).

11. Osakabe, M. et al, "Core Liquid Level Depression due to Manometric Effect during PWR Small Break LOCA, Effect of Break Area," J. Nucl. Sci. Technol., 24-2 (1987).

12. Osakabe, M. et al, "Core Liquid Level Depression due to Manometric Effect during PWR Small Break LOCA - Effect of Coire Bypass -," J. Nucl. Sci. Technol., 25-3 (1988).

13. Kukita, Y. et al., "Manometric Core Liquid Level Depression during a Small-Break Loss-of-Coolant Accident in a Westinghouse-Type Pressurized Water Reactor", Int. Conf. or Thermal Reactor Safety, ENS/ANS Topical Mtg., Avignon (Oct. 1988).

14. Kukita, Y. et al., "Steam Generator Primary Side Voiding during a Small-Break Loss-of-Coolant Accident in a Westinghuse-Type Pressurized Water Reactor", 1988 ASME Winter Annual Mtg., Chicago (Nov. 1988)

15. Koizumi, Y., Kumamaru, H., Mimura, Y., Kukita, Y. and Tasaka, K., "Temporary Core Liquid Levl Depression during Cold-Leg Small-Break LOCA - Effect of Break Size and Power Level," 4th Int. Topical Mtg. on Nucl. reactor Thermal Hydraulics, Karlsruhe, F.R.G. (Oct. 1989).

16. Leonard, T., "Vessel Coolant Mass Depletion during a Small Break LOCA," EGG-SEMI-6010 (1982).

17. Kumamaru, H. et al., "ROSA-IV/LSTF 5% Cold Leg Break LOCA Experiment Run SB-CL-18 Data Report," JAERI-M 89-027 (1989)

18. Tasaka, K. et al., "The Results of 0.5% Small Break LOCA in ROSA-IV LSTF Break Location Parameter Test Series," 15th Water Reactor Safety Inf. Mtg. (1987).

19. Tasaka, K. et al., "The Effects of Break Location on PWR Small Break LOCA", 3rd Int. Topical Mtg. on Nuclear Power Plant Thermal-Hydraulics and Operations, Seoul, Korea (Nov. 1988), also, Nucl. Engrg. Des. to appear.

20. Renault, C. et al., "CATHARE Analysis of Break Flow Through an Orifice and of Bypass Effects in the Scaled 2-Inch Hot Leg Break LSTF Run SB-HL-03", Int. Conf. or Thermal Reactor Safety, ENS/ANS Topical Mtg., Avignon (Oct. 1988).

21. Schultz, R. et al, "A LSTF Simulation of TMI-2 Scenario in a Westinghouse Type Four Loop PWR," Proc. 5th Intl. Mtg. on Thermal Nucl. Reactor Safety, Karlsruhe, F.R.G. (Sept. 1984).

22. Tasaka, K. et al, "The ROSA-IV Program TMI-2 Type Scenario Experiments: A Multifaceted Investigation," Proc. Specialist Mtg. on Small Break LOCA Analysis in LWRs, Pisa (1985).

23. Suzuki, M. and Tasaka, K., "Simulation Test of PWR Instrument Tube Break LOCA in ROSA-IV Program," J. Nucl. Sci. Technol., 24-12 (1987).

24. Kukita, Y., Asaka, H., Nakamura, H. and Tasaka, K., "Presurized Water Reactor Core Instrument Ruptures: Experimental Simulation at the ROSA-IV LSTF," Nucl. Engrg. Des., to appear.

25. Suzuki, M., "Break Location Effects on PWR SmallBreak LOCA Phenomena," JAERI-M 88-271 (1988)

26. Koizumi Y. et al., "Investigation of Break Orientation Effect during Cold Leg Small Break LOCA at ROSA-IV LSTF", J. Nucl. Sci. Technol. (1988).

27. Asaka, H., Tasaka, K., Koizumi,Y. Kukita,Y. and Yonomoto, T., "Results of 0.5% Cold Leg Break LOCA Experiments at ROSA-IV/LSTF - Effect of Break Orientation -," 4th Int. Topical Mtg. on Nucl. reactor Thermal Hydraulics, Karlsruhe, F.R.G. (Oct. 1989).

28. Clement, P., Serre, F., Kukita, Y. and Tasaka, K., "CATHARE Analysis of ROSA-IV/LSTF Hot-Leg Break Orientation Effects

Experiments," 1989 fall Meeting of Japan Atomic Energy Society (1989).

29. Kawaji, M. et al, "Three Key Indicators Useful for Emergency Operator Action during PWR Small Break LOCA," IAEA Seminar on Operating Procedures for Abnormal Conditions in Nuclear Power Plants, Munich (1986).

30. Kukita, Y. et al., "Intentional Coolant System depressurization: Experimental Studies in the ROSA-III and ROSA-IV Programs," CSNI Specialist Meeting on Intentional Coolant System Depresurization, Garching, F.R.G. (June 1989).

31. Fletcher, C.D. and Callow, R.A., "Long Term Recovery of Westinghouse Pressurized Water Reactors Following a Large Break Loss of Coolant Accident," EGG-TFM-7993 (Feb. 1988) Idaho National Engineering Laboratory.

32. Tasaka, K. et al., "Loop Seal Clearing and Refilling during a PWR Small-Break LOCA," Proc. 16th Water Reactor Safety Inf. Mtg., Gaithersburg (Oct. 1988).

33. Kukita, Y. et al., "Loop Seal Clearing and Refilling during a PWR Small-Break LOCA," submitted for publication in Nucl.Engrg. Des.

34. Katayama, J. Kukita, Y., Nakamura, H. and Tasaka, K., "Loop Seal Reformation during a PWR Cold leg Break LOCA: the Effects of Primary to Secondary Heat Transfer," 1989 Annual Meeting of Japan Atomic Energy Society (1989).

35. Kumamaru, H. et al., "Effect of Steam Generator Secondary Inventory on Reflux Condensation," ASME Paper 86-WA/NE-8 (1986).

36. Koizumi, Y. et al., "Investigation of Natural Circulation Heat Transfer in Primary and Secondary Sides of Pressurized Water Reactor," ASME Winter Annual Mtg. (1987).

37. Kukita, Y. et al., "Flooding at Steam Generator Inlet and Its Impacts on Simulated PWR Natural Circulation," ASME Winter Annual Mtg. (1987).

38. Stumpf, J. et al., "Reversed Primary Side Flow in Steam Generators during Natural Circulation Cooling," ASME Winter Annual Mtg. (1987).

39. Schultz, R. et al., "Single and Two-Phase Natural Circulation in Westinghouse Simulated PWR Natural Circulation," ASME Winter Annual Mtg. (1987).

40. Koizumi, Y. et al., "Heat Transfer and Thermal-Hydraulics of Westinghouse-Type Pressurized Water Reactor Steam Generator -- Assessment of RELAP5/MOD2 Code --", 1988 ASME Winter Annual Mtg., Chicago (Nov. 1988).

41. Kukita, Y. et al., "Non-Uniform Steam Generator U-Tube Flow Distribution during Natural Circulatin Tests in ROSA-IV Large Scale

Test Facility", Nucl. Sci. Engrg. (1988).

42. Chauliac, C. Kukita, Y. and Tasaka, K., "Post-Test Analysis with RELAP5/MOD2 of ROSA-IV/LSTF Natural Circulation Test ST-NC-02," JAERI-M 88-215 (Oct. 1988).

43. Kukita, Y., Nakamura, H., Anoda, Y. and Tasaka, K., "Hot Leg Flow Chracteritics during Two-Phase Natural Circulation in presurized Warter Reactor," 4th Int. Topical Mtg. on Nucl. Reactor Thermal Hydraulics, Karlsruhe, F.R.G. (Oct. 1989).

44. Kukita, Y. and Tasaka, K., "Single-Phase Natural Circulation in Pressurized Water Reactor under Degraded Secondary Cooling Conditions," 1989 ASME Winter Annual Meeting, San Francisco (Dec. 1989).

Table 1 LSTF First Phase Program Test Matrix

TEST MATIX

SBLOCA TESTS		
COLD LEG BREAK	21 RUNS	(0.1-10% IN AREA)
HOT LEG BREAK	4 RUNS	(0.5-10%)
LOOP SEAL BREAK	1 RUN	(5%)
PRESSURIZER TOP BREAK	3 RUNS	(0.43-1.3%)
LOWER PLENUM BREAK	1 RUN	(0.5%)
UPPER HEAD BREAK	1 RUN	(0.5%)
SG TUBE RUPTURE	1 RUN	(0.5%)
TRANSIENT TESTS		
STATION BLACKOUT	3 RUNS	
STEADY-STATE NATURAL CIRCULATION TESTS	10 RUNS	(1-10% POWER)
TOTAL	45 RUNS (INCLUDING 3 SHAKEDOWN RUNS)	

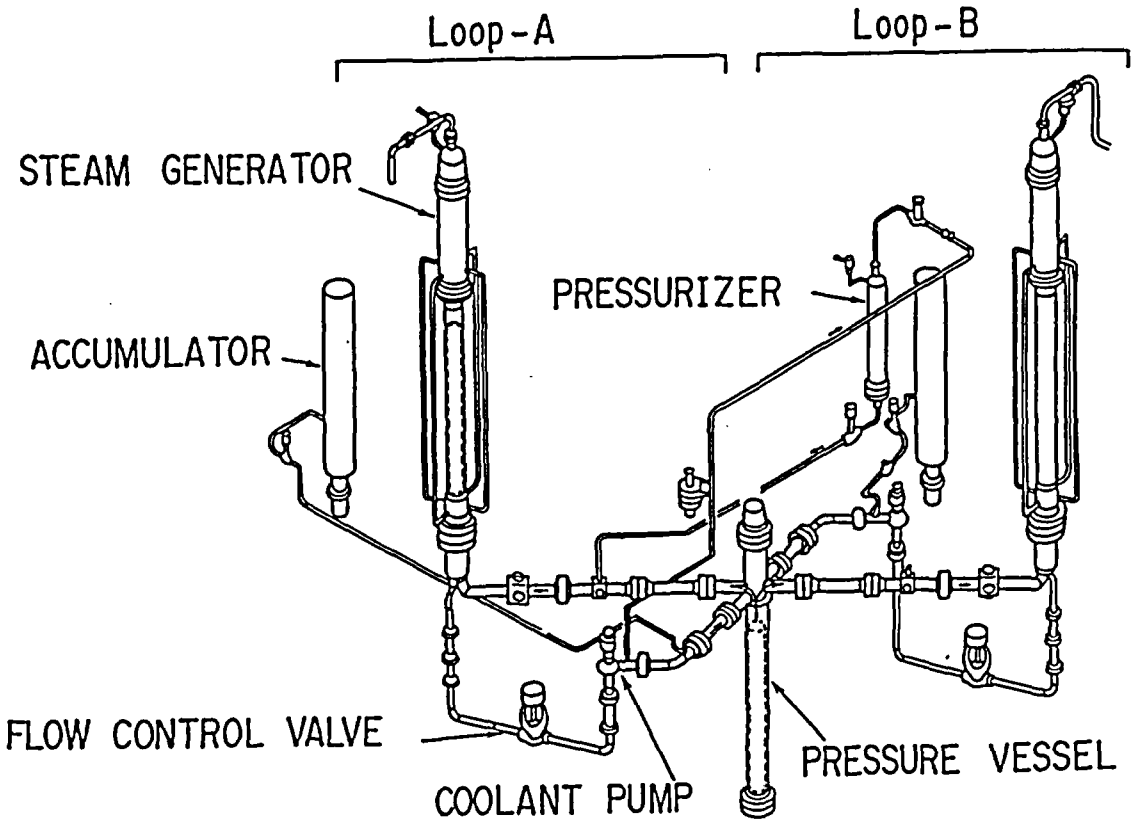

Fig. 1 Schematic of ROSA-IV Large Scale Test Facility (LSTF).

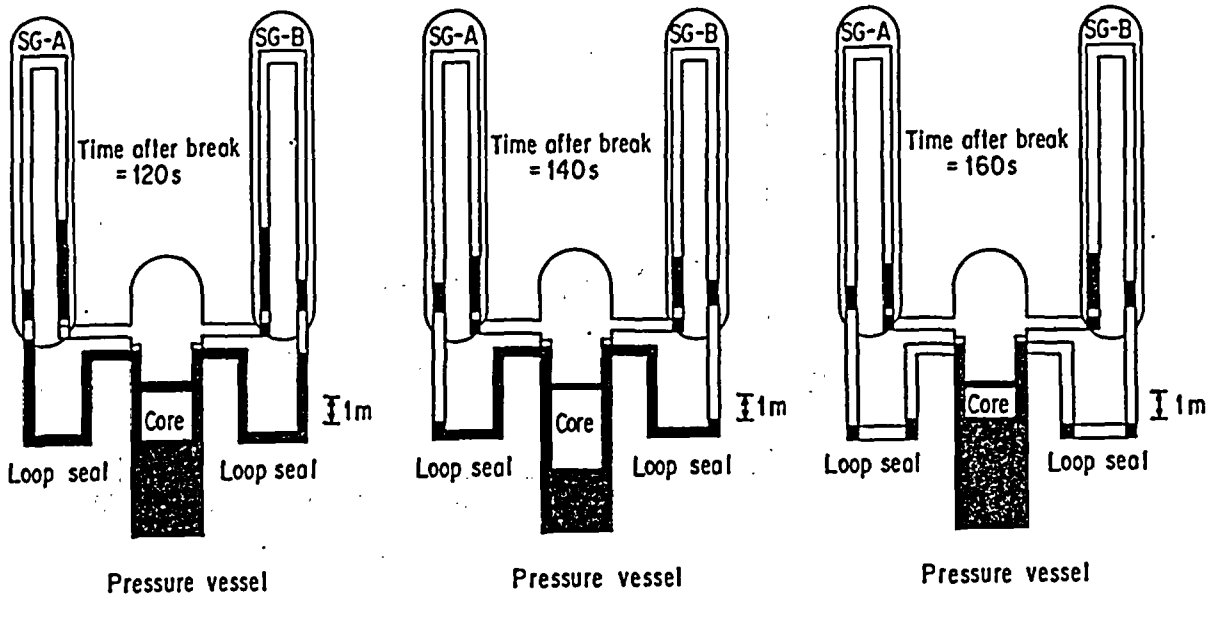

Fig. 2 Coolant Inventory Distribution During 5% Cold Leg Break Test, SB-CL-05.

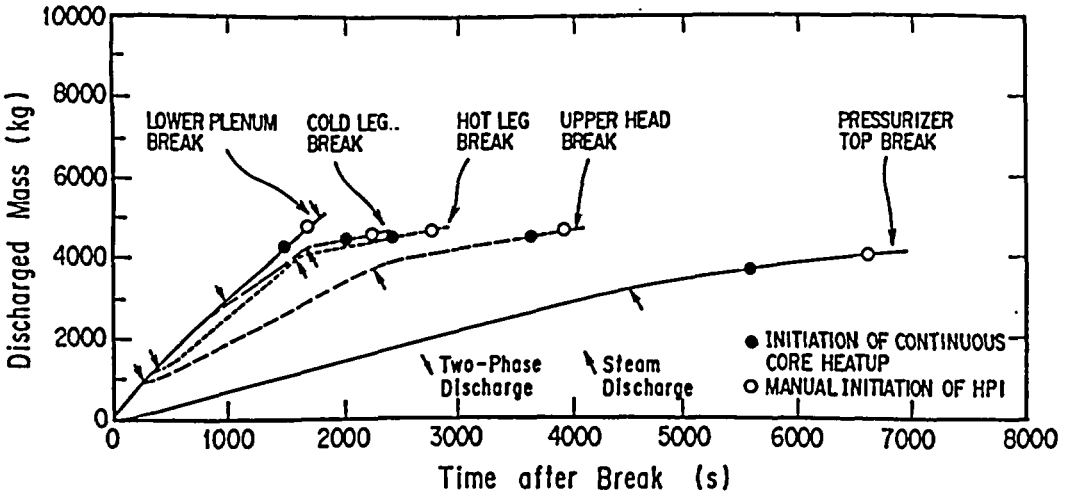

Fig. 3 Break Location Effects on Integrated Break Flow Rate.

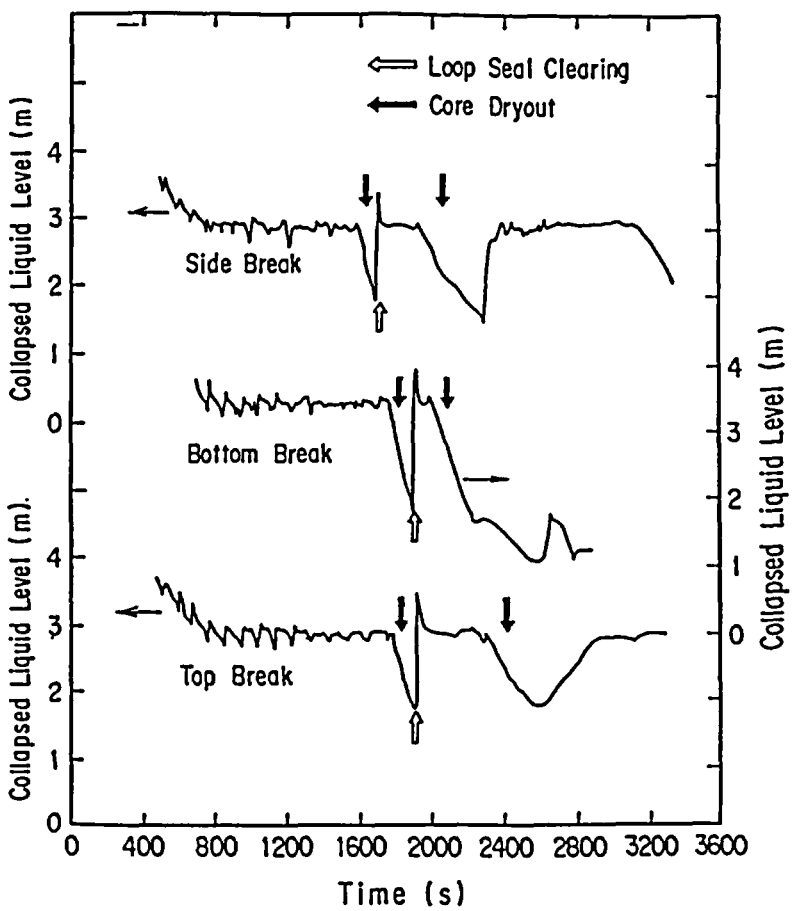

Fig. 4 Break Orientation Effects on Cold Leg Break. Comparison of Core Level Transients for 0.5% Side, Bottom and Top Break Cases.

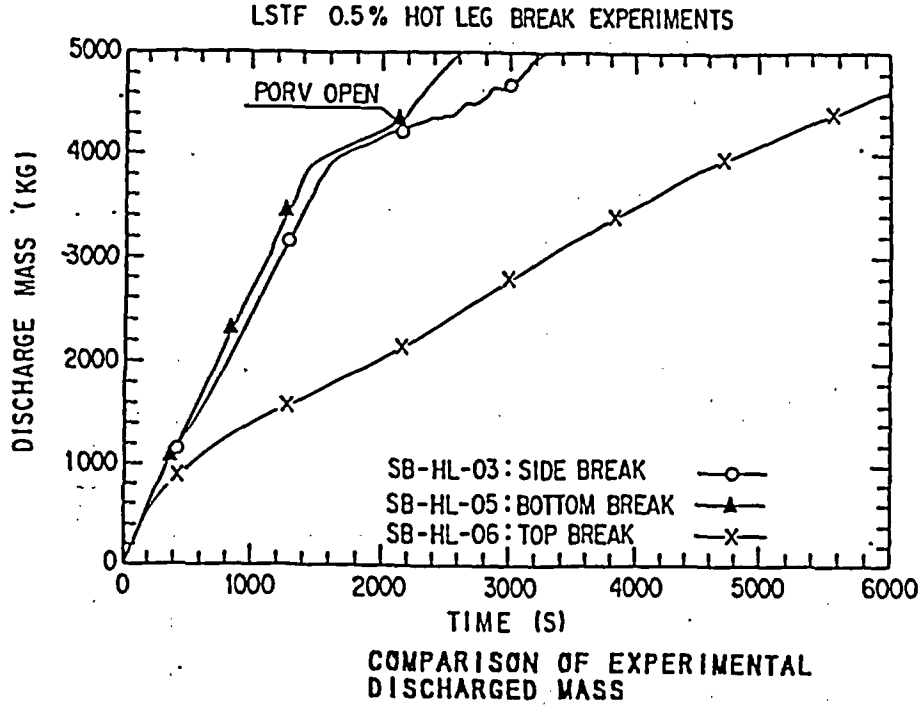

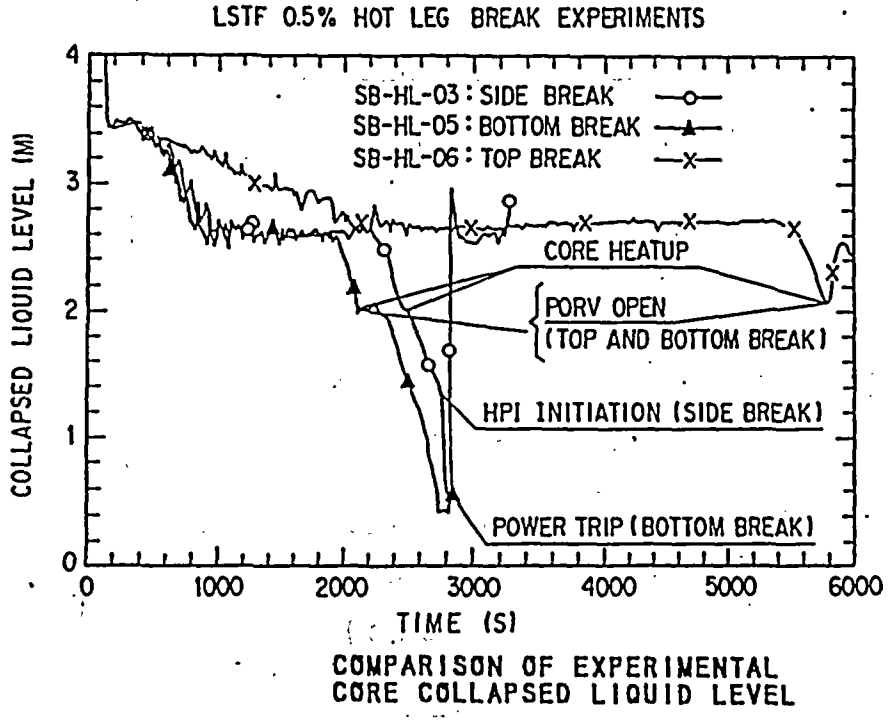

Fig. 5 Break Orientation Effects on Hot Leg Break. Comparison of Integrated Break Flow Rates and Core Levels for 0.5% Side, Bottom and Top Break Cases.

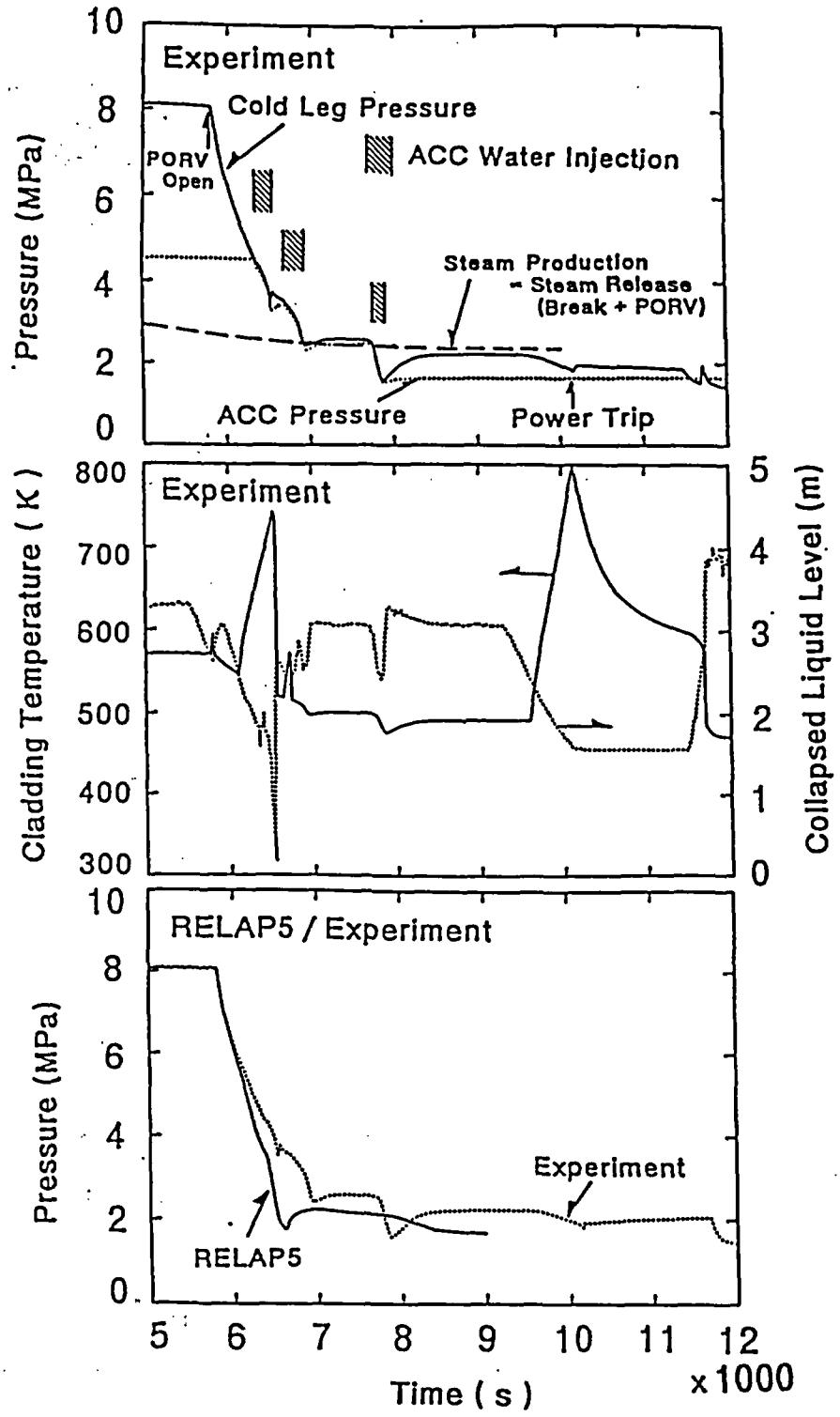

Fig. 6 Primary Pressure and Core Collapsed Level Transients for 0.5% Hot Leg Top Break Test where Pressurizer PORVs Were Latched Open After Initiation of Core Heatup.

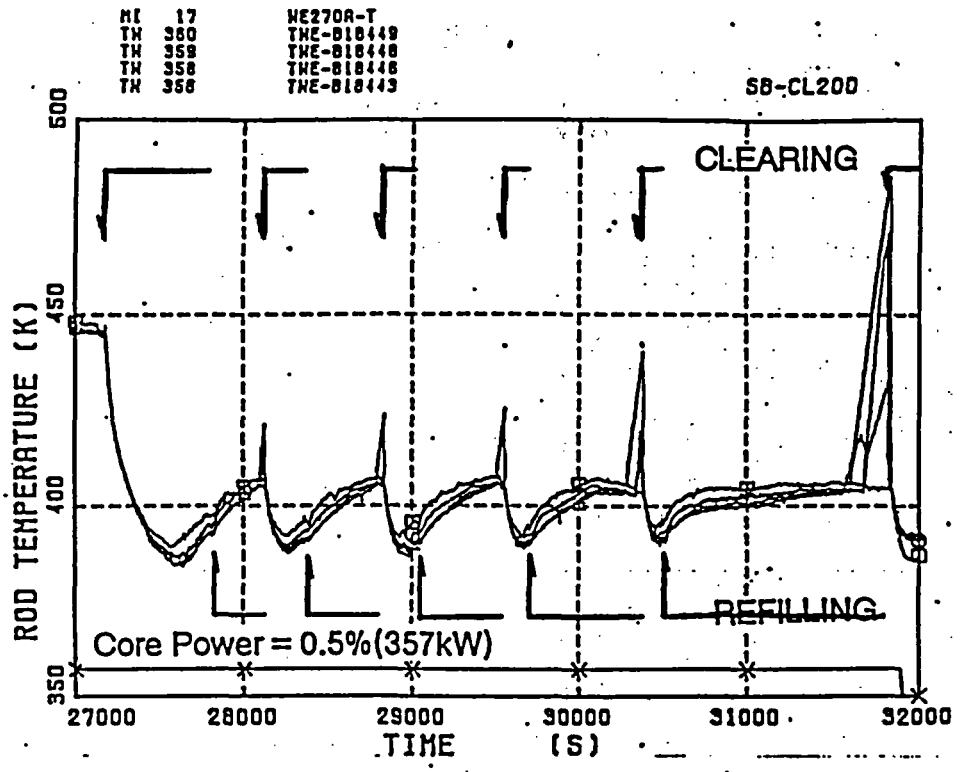

PRIMARY AND SECONDARY SYSTEM FLUID TEMPERATURE

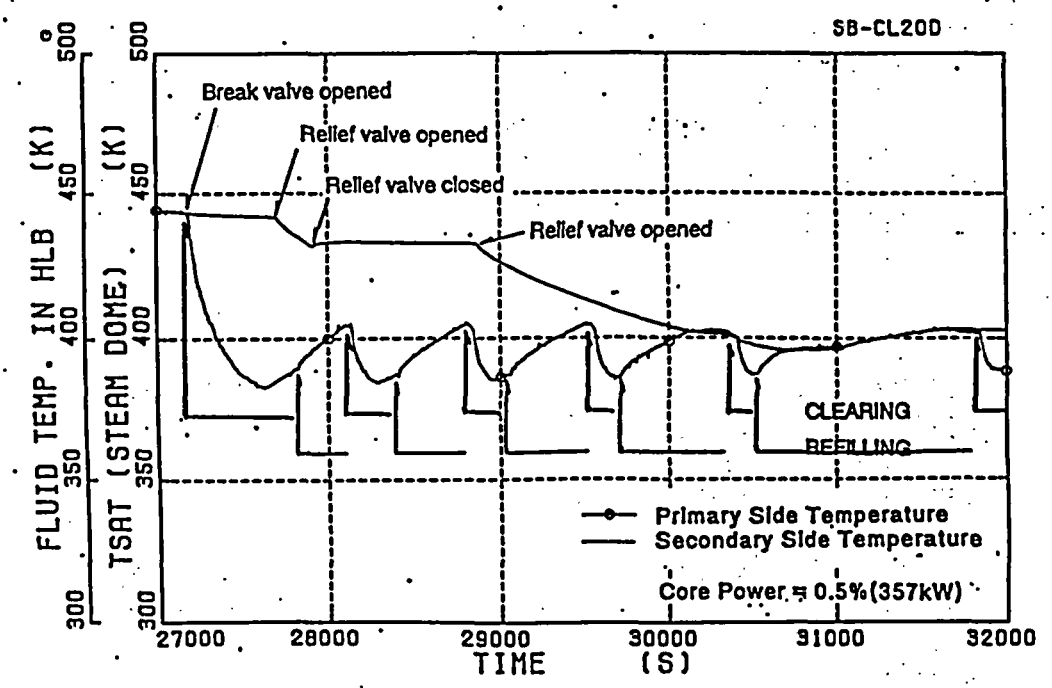

Fig. 7 Primary and Secondary Temperatures and Rod Surface Temperatures During Repeated Loop Seal Clearing and Refilling for a 10% Cold Leg Break Test Which Studied Secondary Cooling Effects on Loop Seal Behavior.

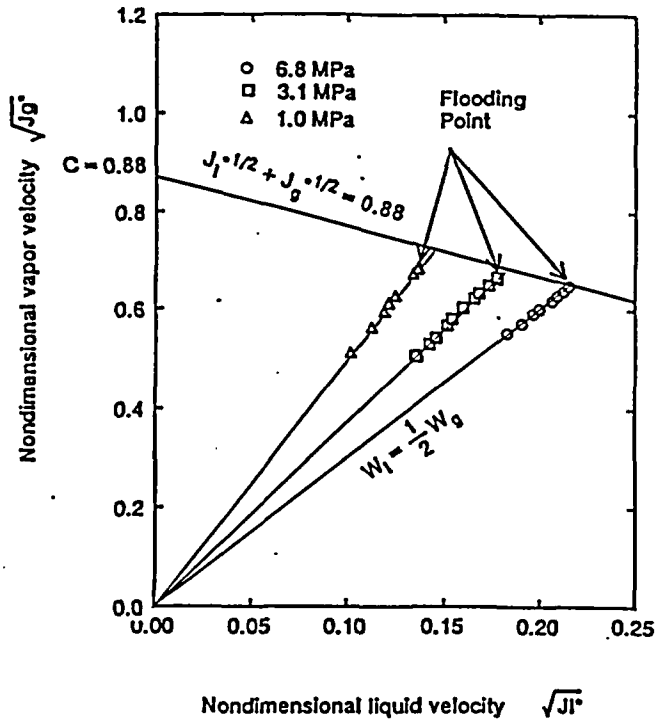

Fig. 8 Steam Generator U-Tube CCFL Characteristics Defined by Steady-State Reflux Condensation Test.

Table 2 Test Conditions for Simulated TMLB' Transient TR-LF-03.

Initial Condition

Primary

pressure	15.6 MPa
hot leg temp.	600 K
cold leg temp.	565 K
core power	10 MW (14%)
mass inventory	5860 kg

Secondary

pressure	7.3 MPa
mass inventory	1800 kg per SG

Test Procedure

1. Steam line valve was closed
2. Feedwater was turned off
3. Heater rod power was controlled to follow the decay power profile (New JAERI curve)
4. Pump coastdown
5. PORVs were unavailable
6. SG safety valve set points,
   8.68 MPa to open
   7.69 MPa to close
7. PR safety valve set points,
   17.26 MPa to open
   17.06 MPa to close
8. External tracing heaters were powered
   49 kW for primary
   36 kW for secondary
9. Core power was augumented (160 kW) to compensate the heat loss
10. Test was finished by power-off when heater rod temperature increased beyond 850.K

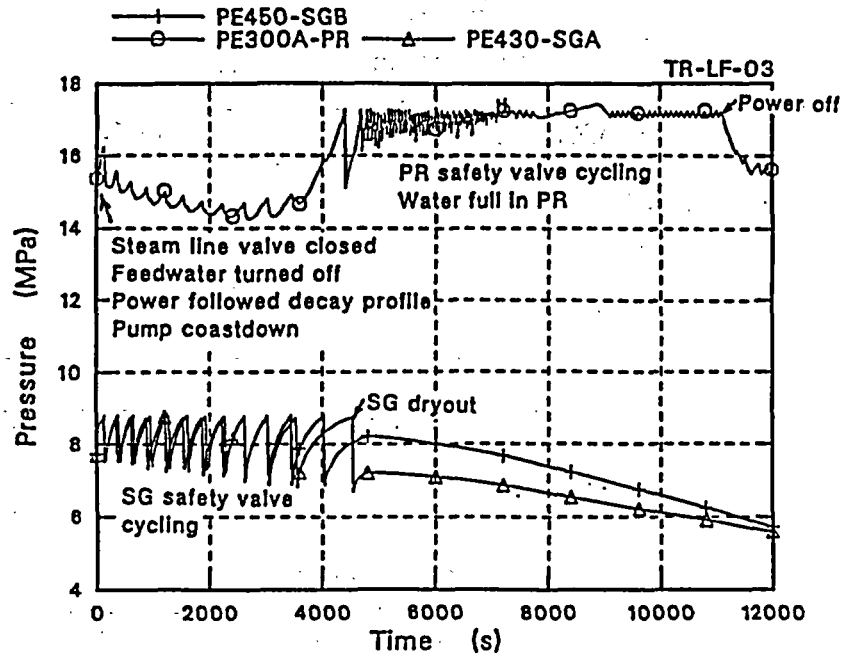

Fig. 9 Primary and Secondary Pressures During Simulated TMLB' Transient.

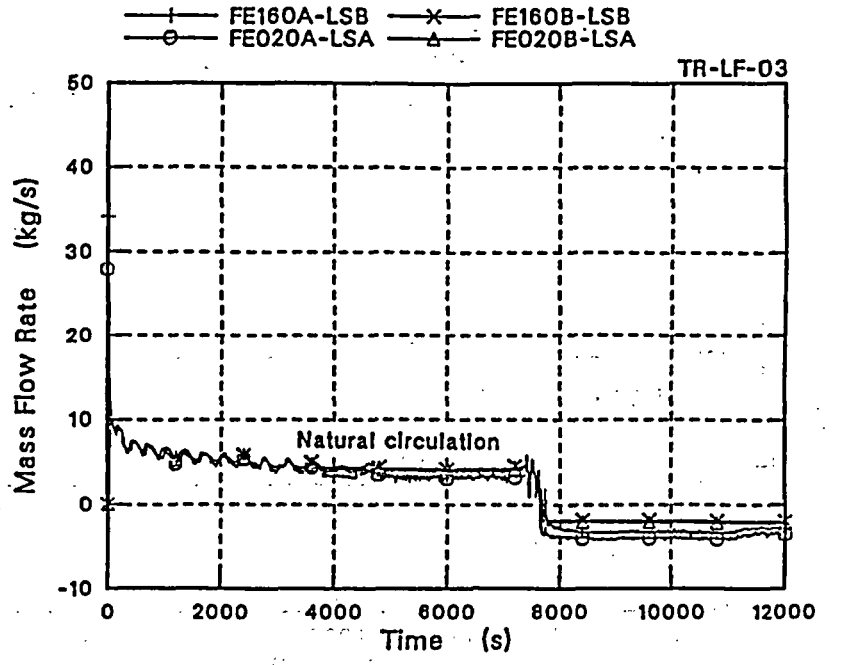

Fig. 10 Loop Flow Rate During Simulated TMLB' Transient.

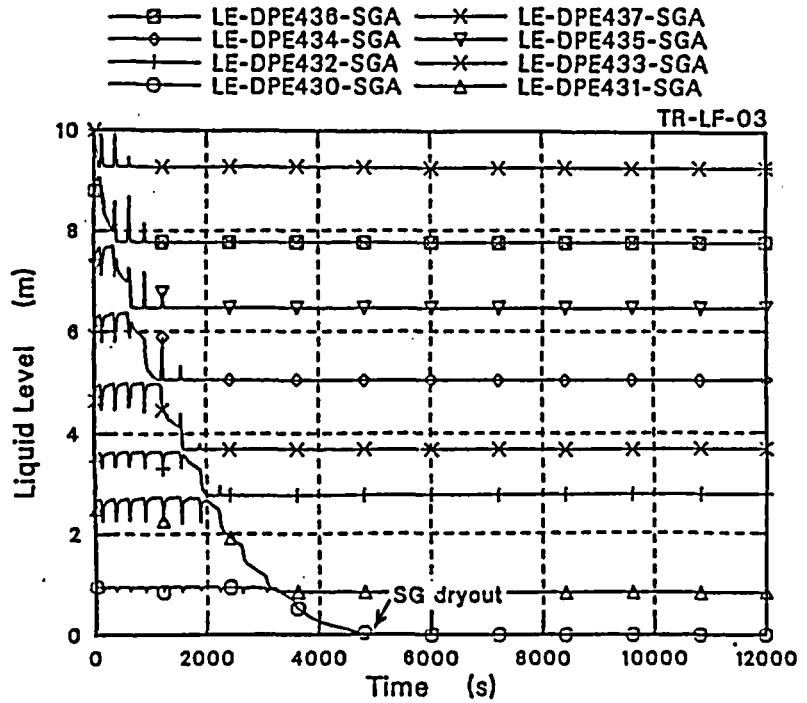

Fig. 11 SG Secondary Side Water Level During Simulated TMLB' Transient.

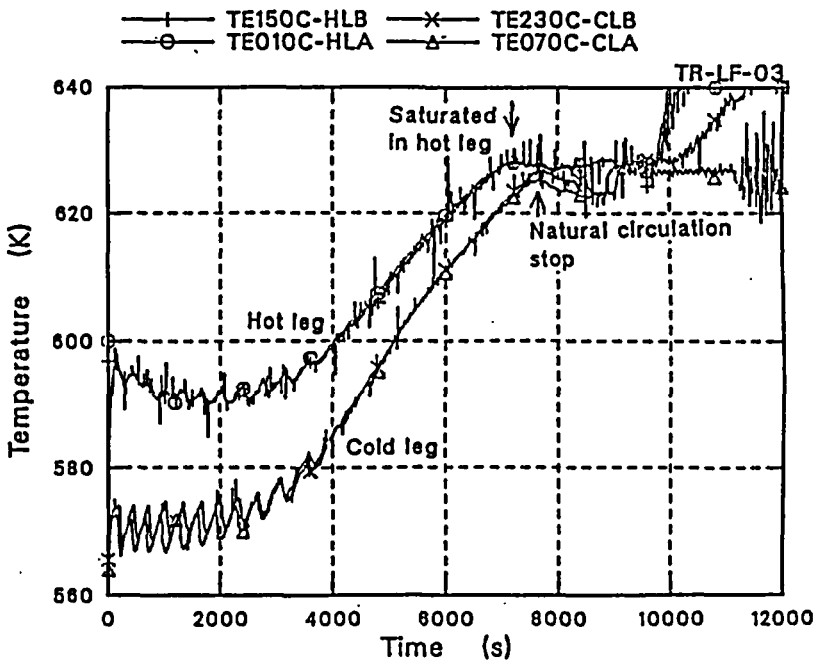

Fig. 12 Primary Loop Fluid Temperatures During Simulated TMLB' Transient.

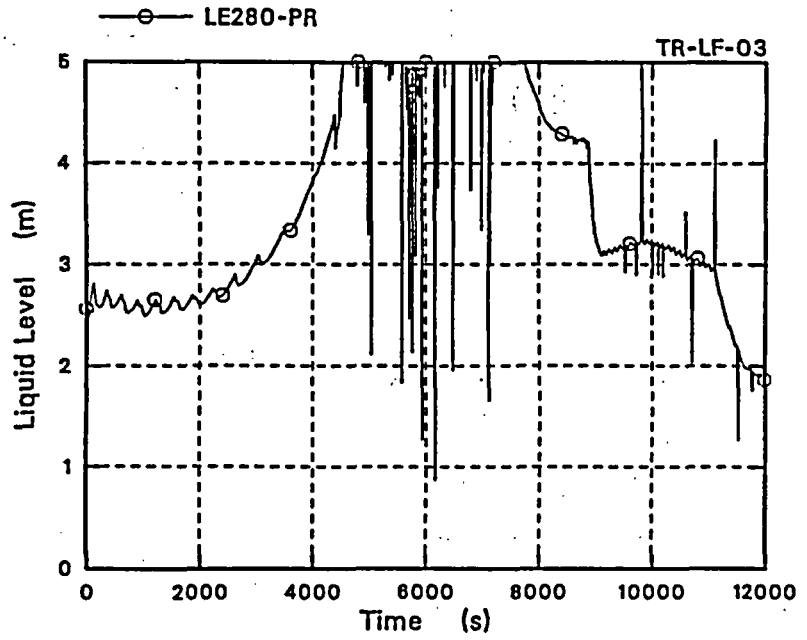

Fig. 13 Pressurizer Collapsed Water Level During Simulated TMLB' Transient.

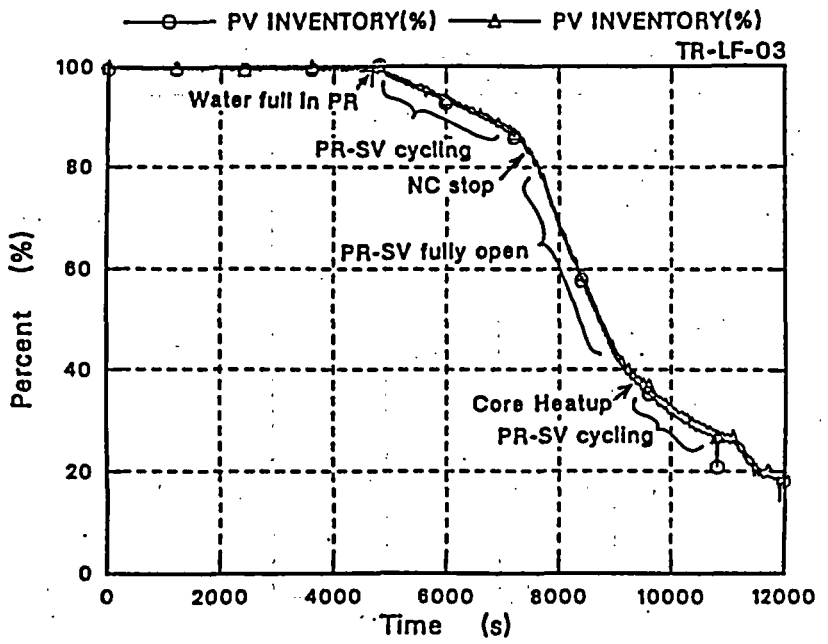

Fig. 14 Primary Coolant Mass Inventory Depletion During Simulated TMLB' Transient.

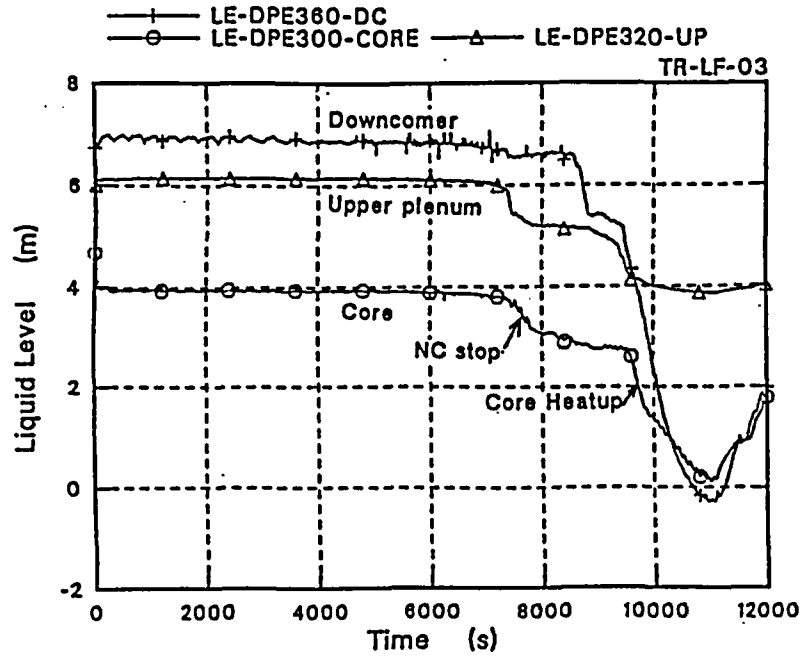

Fig. 15 Pressure Vessel Collapsed Water Levels During Simulated TMLB' Transient.

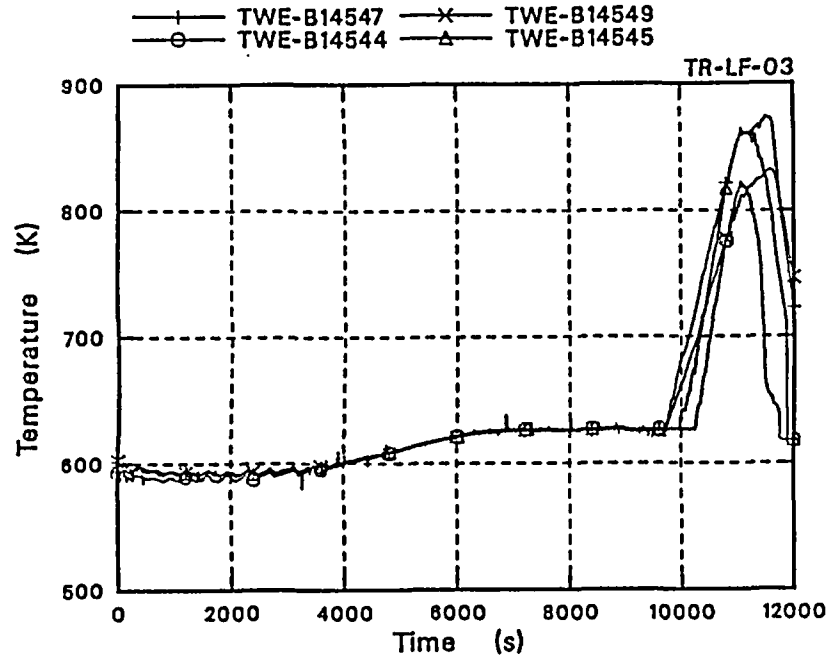

Fig. 16 Core Heater Rod Temperatures During Simulated TMLB' Transient.

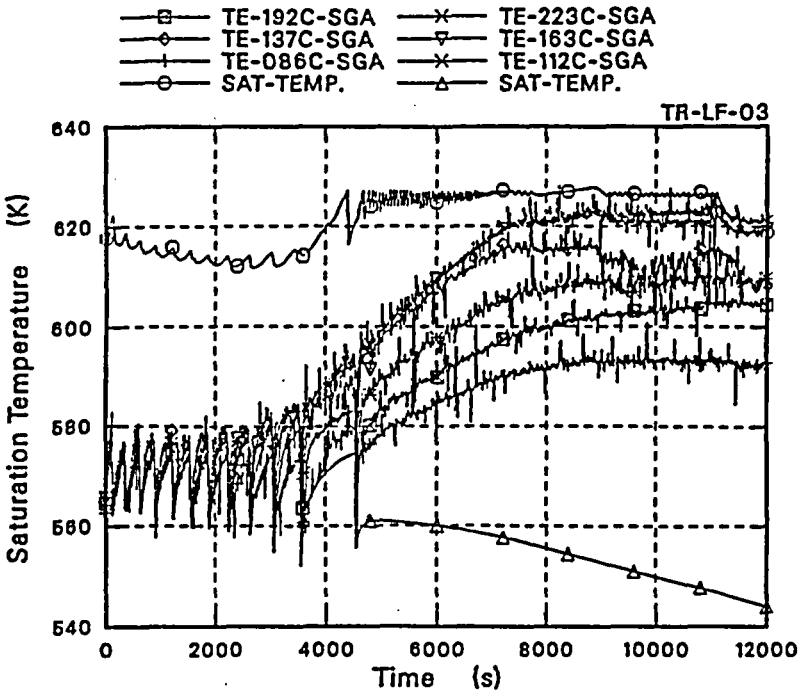

Fig. 17 Secondary Side Fluid Temperatures Compared to Primary and Secondary Side Saturation Temperatures.

UMCP MIST COUNTER-PART TEST

M. di Marzo*, K. Almenas, Y.Y. Hsu, G.A. Pertmer

Chemical and Nuclear Engineering Department
University of Maryland
College Park, MD 20742, USA

* Mechanical Engineering Department

ABSTRACT

Two Small Break LOCA transients are compared to illustrate a scaling methodology for reduced pressure integral facilities. Mapping test 3004 is conducted in the MIST full pressure, full height facility. The counter-part test MIS0317 is scaled and performed in the reduced height, reduced pressure UMCP facility. Inventory is used as the chronological scale and pressure, normalized with the initial and system saturation pressures, is used as characteristic parameter to describe the system behavior. The appropriately normalized results conclusively demonstrate that: a) the same phenomena are observed in the two facilities; b) the sequence of events is analogous and c) the trends described by the normalized pressure versus inventory traces are in good quantitative agreement. Each energy transport mode traversed by the two facilities is compared and the phenomena present are described in detail. The differences between the high and reduced pressure tests are outlined. The findings clearly indicate that pressure and height can be scaled for transient where limited boundary conditions are applied (Auxiliary Feed Water only) and where the break is subcooled. A statement on sensitivity to the initial conditions is also included to define the limitations of the quantitative results.

NOMENCLATURE

A	identifier of components in the loop connected to the pressurizer surge line
B	identifier of components in the loop opposite to the A loop
C_l	specific heat of the liquid
h_{fg}	latent heat of vaporization
I	system liquid inventory
LI	liquid inventory lost
P	pressure
T_{sat}	saturation temperature
v_{fg}	difference between vapor and liquid specific volumes
v_l	liquid specific volume

1. INTRODUCTION

This study addresses the transferability of experimental data obtained in 'reduced' pressure integral facilities to prototypes which operate at high pressure. The term 'reduced' rather than 'low' pressure is used intentionally. It defines facilities that are operating at pressures which can be considerably below the prototypical pressures, but are still sufficiently high so that internal system pressure changes, due to internal friction and elevation, are small compared to the system operating pressure.

The need for the simulation of complex integral system transients prompted the design of a series of integral facilities simulating the transient behavior of OTSG type plants [1,2]. These integral facilities are both at full pressure (MIST) and at reduced pressure (e.i. UMCP). Both UMCP and MIST facilities are constitutes by a reactor vessel, two steam generators, two hot legs, four cold legs and a pressurizer arranged in the raised-loop configuration of a PWR Babcock and Wilcox nuclear power plant. The data used in this study for scaling comparisons are obtained at these two facilities. Data transferability from reduced pressure facilities is desirable because such facilities have installation and operating costs one order of magnitude lower than full pressure facilities.

Past experience has shown that the principal goal of the full pressure test facilities (that is, to eliminate prototype to facility differences due to thermodynamic properties) was only partly realized. During the long term SB-LOCA transients the operating pressure varies significantly with time. Therefore, there is no assurance that property groups used in scaling, which are evaluated at some initial conditions, will maintain their relative magnitudes during the course of the transient. The scaling of thermal hydraulic data generated by integral facilities is a broad and relatively new subject. The terminology that is used is not finalized and is still influenced by the definitions developed in scaling separate effects and single, well defined phenomena. In order to avoid confusion, it is worthwhile to describe, at the outset, what realistic goals can be achieved with a scaling methodology.

It is now recognized that for an integral system it is impossible to provide a set of criteria which would map all of the parameters observed at one geometric scale (or at one set of operating conditions) precisely into a set of operational parameters at another scale (or conditions). An overview of recent studies [3,4,5], shows that a new consensus regarding scaling goals is emerging. Three criteria are identified for a successful simulation of the abnormal behavior of a nuclear power plant: a) the presence of key phenomena is demonstrated; b) the sequence of their occurrence is reproduced; c) their quantitative characteristics are approximated.

The above criteria do not include a requirement for a precise mapping of the time variation of some experimental parameter into a corresponding time response of that parameter in the prototype. Useful information regarding the safety and operational characteristics of a system can be obtained without such an exact correspondence. A necessary corollary of a simulation which is not exact in all respects is that its interpretation has to be based on a

reasonable knowledge of the systems behavior. This implies that the scaling of an abnormal operational transient must start with an understanding of the phenomena which characterize the thermal hydraulic behavior of the system. Fortunately reactor safety related thermal hydraulic studies have advanced sufficiently that this can be achieved with good confidence.

2. PRELIMINARY CONSIDERATIONS

The comparison of tests performed in different facilities is a complex undertaking. The first and most important task is to clearly identify what we are trying to compare. In order to address this crucial question, we must recognize that there are several elements that determine the evolution of the test: initial conditions, system inherent response, and boundary conditions.

The initial conditions are the ensemble of parameter settings that we can control and that are held arbitrarily constant upon reaching steady state conditions prior to the break activation. The degrees of freedom of the system imply that a number of initial conditions must be specified. Other parameters are determined by the system operation and we cannot fix them arbitrarily.

The boundary conditions are those parameters that we can alter during the test. These parameters are altered according to some arbitrary rules which constitute an integral part of the test specifications. We take the approach that the rules might be different in the two systems. However, the imposition of a given boundary condition, during a similar system state, must yield similar effects.

Finally, the system inherent response is the most critical element of a test. A system subjected only to initial conditions will evolve along a trajectory. If no boundary condition is actively imposed, the trajectory will be the result of the inherent system response only. *Comparing two different facilities means comparing the inherent system response to similar initial boundary conditions.*

The issue of scaling is therefore two-fold. First, one must subject the facility to scaled initial and boundary conditions. It is clearly advantageous to select tests for which the influence of boundary conditions is minimal (ideally nonexistent). Second, one must have scaled facilities capable to respond to these applied conditions in similar fashion. This second requirement can be checked only by performing selected tests on both facilities and by comparing the scaled responses of the two systems. These are indeed the objective of this paper.

The representation of the trajectory of a system or of its behavior must be defined. In general we wish to plot a representative parameter against a chronological scale. The temporal scale is the natural scale one would be inclined to select. However, a number of constraints are imposed on such a scale by the pressure at which the facility is operated and by the size of the break under consideration. In an effort to generalize the results of the tests, we proposed a chronological scale based on liquid inventory [6,7,8].

The current practice has identified pressure as the dependent variable which represents the system behavior. The first issue to be addressed is the selection of pressure over some global measure of the system energy transport capabilities (from the reactor vessel to the steam generators) as the representative parameter. The idea of pressure is linked to a local equilibrium of the system and is not related per-se to a global measure. This fact is very important because we are interested in the transient characteristics of the system more than in its quasi-steady state operation. The long term pressure trend is clearly related to the system energy transport characteristics. Therefore, one can argue that pressure incorporates both the instantaneous and the long term system characteristics while a measure of the energy transport capabilities is only relating to the latter.

Once it is decided that pressure is the single most desirable parameter to observe, we still maintain that in order to understand and correctly monitor the test a number of parameters are needed. This means that a simple comparison of the pressure traces is not sufficient to draw meaningful conclusions. However, a similar pressure behavior is a necessary (not sufficient) condition to attempt the comparison of tests performed by different facilities.

The problem of scaling the pressure can be approached considering the initial conditions of the test. The pressure is set by the equilibrium conditions of the pressurizer. This system pressure is clearly marked as the initial value. The procedure to scale this initial pressure will be described later on. It is clear that, since the initial pressure can be one order of magnitude larger in a high pressure facility (such as MIST) compared to a low pressure facility (such as UMCP), some normalization procedure must be devised to compare the two pressure traces.

To normalize the pressure, we need to define a reference value. The inventory is lost through a small break; this means that the flow rate at the break is not a function of the outside conditions (i.e. the break is choked). This is a very important fact because it implies that the reference value for the pressure must be related to the system state not to the atmospheric pressure. Therefore, it is reasonable to resort to information provided by the primary temperatures. At the initial conditions we can identify the maximum system temperature at the core outlet and the minimum temperature at the core inlet. Both these temperatures yield a saturation pressure which could be selected as our reference value.

In the initial portion of the small break LOCA transient the system undergoes a rapid depressurization while the pressurizer empties. Then the pressure drops to a level that can be sustained by an equilibrium condition within the primary loop. This equilibrium condition is related to the maximum system temperature. Therefore, we will use the saturation pressure at the core exit temperature as the base line pressure to normalize the pressure scale. This can be expressed by the following

$$P_{normalized} = \frac{(P - P_{saturation})}{(P_{initial} - P_{saturation})} \qquad (1)$$

It is very important to note that this scaling is arbitrarily set and depends on the initial value of the pressure. The rationale for this selection is grounded in the basic understanding that both facility are operating independently of the outside ambient pressure. This is the conceptual step that one must take in order to float each pressure environment (high pressure and low pressure) within its own references. This is the key which makes it possible to compare so different conditions.

3. SCALING OF THE INITIAL AND BOUNDARY CONDITIONS

Of all the tests performed by the MIST facility, we identified the Mapping Test Series (Group 30) [9] as the ones most desirable for comparison purpose. The reason for this selection is the relative minimal application of imposed boundary conditions during the tests. One of the objectives of these series of tests is to determine the sequence of events subsequent to a small break initiation. In particular, the aim of the various tests is to illustrate the effect of the various imposed boundary conditions on the system. That is, to illustrate the impact of the boundary conditions on the inherent system behavior.

It is very important to realize that the application of a boundary condition provides the experimenter with a number of degrees of freedom during the evolution of the test. By modulating the boundary condition (within the realm of proper scaling), one can affect the system trajectory to conform with an expected or desirable trajectory. The sensitivity of these facilities to initial and boundary conditions is a recognized fact [10]. This means that a minimal variation in timing or magnitude on the application of a given conditions can strongly affect the system trajectory. As an example consider two transients conducted with the same initial conditions (Power of 75 KW, Secondary side elevation at 61%, Initial pressurizer level at 18%, and initial pressure held at 970 KPa). A system maximum pressure of 800 KPa was observed during the complete interruption with a break of 0.16 cm. By reducing the break size to 0.12 cm, in the second test, the maximum peak pressure during the complete interruption was 2080 KPa. Note that the break cross-sectional area was reduced from 2.0 square millimeters to 1.1 square millimeters. Thus a reduction in flow of the order of 60 per cent brought about an increase in normalized peak pressure of 340 per cent.

Among the Mapping tests only one is performed without High Pressure Injection. Therefore, this particular test (3004) is selected because only AFW is activated at one time. The application of this boundary condition will be described in detail and all efforts will be made to duplicate a similar application of this condition for the UMCP facility. The test initiate with a steady state conditions dictated by core power scaled to one per cent of full power and by a secondary side elevation of about 60 per cent of the steam generators height. The pressurizer is connected to the system and its liquid level is at about 19 per cent of its full height while the system pressure is

maintained at about 12 MPa. These are the four degrees of freedom uniquely characterizing this initial conditions.

In the following, the initial and boundary condition of the full pressure MIST test 3004 must be translated to the reduced pressure conditions of the UMCP facility. In general, volume scaling is the typical criteria to transfer information between facilities of different size. We need also to describe novel criteria to translate information concerning the initial pressure and the break size.

Power is scaled by volume which means that the 46.2 KW of MIST correspond to 75.5 KW for UMCP. We have scaled the secondary side by elevation thus having both MIST and UMCP levels at about 60 per cent of the steam generators height. We must scale the pressurizer inventory according to the volume scale. This is achieved by setting the pressurizer level for UMCP at 18 per cent of the total elevation which corresponds to the elevation of 19 per cent for MIST. Note that the pressurizer is not scaled for other initial conditions. That means that only for this inventory level the vapor and liquid volume have an almost identical ratio.

The idea of normalizing the system pressure with the initial pressure and with the saturation pressure corresponding to the initial core outlet temperature has been discussed previously. We noted that the normalization depends on the value that one selects for the initial pressure. This value can be independently fixed by setting the fluid equilibrium temperature in the pressurizer. Proper scaling must be used to obtain the initial value of the pressure. The idea of long term system behavior is based on the relative magnitude of heat sources and sinks in the system. The pressurizer constitute in the initial portion of the transient a source of inventory and a source of energy for the system. We will assume thermal equilibrium in the pressurizer at steady state because one can wait as long as required to achieve such condition. The next step is to look at the rapid depressurization transient. The contribution of the vapor initially in the pressurizer to the total energy of the system is negligible because the vapor expands but does not enter the primary system. Therefore, we should not consider it as a source of energy during the rapid depressurization. The liquid will flow in the hot leg of the primary and will constitute an energy input to the system. We need to consider the system energy prior to the break activation. One can simplify this task by stating that the source (core) and the sinks (steam generators) in the primary are approximated by localized source and sinks which means that a portion of the primary is hot and the remainder is cold. Further, one can refer the energy content of the primary to the cold portion of the system. This means that the energy initially in the pressurizer should be referred to the energy initially in the hot portion of the loop. By assuming that the densities of the liquid in the pressurizer, in the hot and in the cold portion of the primary are comparable and that this is the case for the specific heat of the liquid in these three portion of the system, the criterion for scaling the initial pressure reduces to equating in both facilities the ratio of initial system subcooling and core temperature rise.

MIST initiates its test with pressurizer temperature of 327 °C and core temperatures of 298 °C and 282 °C respectively. This means that the ratio of

subcooling and core temperature rise is about 1.9. The core temperatures for UMCP are independent of the pressurizer conditions and for scaled power and secondary elevations are 126 °C and 105 °C respectively. This means that the pressurizer temperature should be 165 °C which corresponds to a pressure of about 700 KPa for the scaled UMCP initial condition. For identification, the pressurizer surge line is connected to the hot leg of loop A in both facilities.

It can be shown that for various break sizes one obtains various pressure versus inventory behaviors. A more close investigation reveals that the rate of pressure change with time does not depend on the break size. Since the transitions between modes during the transient occurs at similar inventories, one should conclude that the pressure difference spanned during a given mode depends on the length of time that the system takes to traverse that particular mode. In other words the rate of change in pressure with inventory depends on the rate of change of pressure with time (which is not a function of the break) and depends on the rate of change of inventory (which is the break mass flow rate).

The rate of change of pressure with inventory must be equal for both systems (UMCP and MIST). One can calculate the pressure rate of change ratio for the two facilities and infer from the given inventory depletion of the MIST facility the desired inventory depletion for UMCP, thus its scaled break size. To calculate the pressure rate of change ratio we assume to be at the initiation of the complete interruption. At this particular junction the core and the steam generators are decoupled. This means that the heat input (at the core) is used to repressurize the system and to vaporize liquid to replenish the volume of inventory exhausted at the break. Note that the energy of the fluid leaving the system at the break carries no significant enthalpic content.

The heat required by the vaporization process amounts to less than three per cent of the total heat input, hence it will be neglected. Note that this contribution is evaluated as the product of the mass flow rate at the break times the latent heat of vaporization times the ratio of the vapor and liquid densities. Therefore, one can conclude that the heat input is mostly used to repressurize the system. The repressurization process involves the heating up of a portion of the liquid in the system and the heating up of the metal mass. By neglecting the vaporization component, we are allowed to simplify the evaluation of the heating up of liquid and metal mass because the masses of liquid and metal involved are considered scaled. Therefore, we can state that

$$\frac{\left(\frac{dP}{dt}\right)_{UMCP}}{\left(\frac{dP}{dt}\right)_{MIST}} \approx \frac{\left(\frac{C_l\, T_{sat}\, v_{fg}}{h_{fg}\, v_l}\right)_{MIST}}{\left(\frac{C_l\, T_{sat}\, v_{fg}}{h_{fg}\, v_l}\right)_{UMCP}} \qquad (2)$$

The numerical value for the pressure rate of change ratio is found to be equal to 0.17. The rate of inventory depletion for the MIST facility is 0.012 kilograms per second. Recall that we desire equality of the normalized of the pressure rate of change with inventory, thus we evaluate the inventory depletion for the UMCP facility at 0.03 kilograms per second. An orifice of diameter 0.16 centimeters provides an average loss of inventory of 0.033 kilogram per second for the UMCP facility. This is the scaled break size for a single-phase subcooled SB-LOCA. The break location in the MIST facility is at the bottom of the downcomer. In the UMCP facility the break is at the lowest point in one of the two cold legs of loop B which is the loop opposite to the one where the pressurizer surge line is connected.

In summary the scaled initial and boundary conditions for the test are compared in Table 1.

TABLE 1 - Initial and boundary conditions

	MIST	UMCP
Core power	46.2 KW	75.5 KW
Secondary level	61 %	61 %
Initial pressure	12.1 MPa	0.7 MPa
Pressurizer level	19 %	18 %
Break size	0.01 m, scaled	0.0016 m

4. COUNTER-PART TEST

The test data must be normalized in order to be compared. The initial pressure for the MIST test 3004 is 12140 kPa. The saturation pressure corresponding to the core exit temperature is 8200 kPa and the initial inventory is 416 kilograms. Based on this information at the initial condition, we formulate the normalized pressure and inventory according to the following relationships

$$P_{normalized} = \frac{P - 8200}{12140 - 8200} \tag{3}$$

$$I_{normalized} = \frac{I}{416} \tag{4}$$

The test performed on the UMCP facility is also scaled with the same normalization technique. In the initial conditions described in the previous section, the system finds its steady state when the core exit temperature is equal to 126 °C, which corresponds to a saturation pressure of 207 kPa. We also calculated the initial pressure to be about 700 kPa. The test is initiated with a pressure of 711 kPa and the initial inventory is 638 kilograms. The UMCP inventory information is provided as lost inventory (LI). These initial data yield the following relationships for the normalized parameters

$$P_{normalized} = \frac{P - 207}{711 - 207} \tag{5}$$

$$I_{normalized} = \frac{638 - LI}{638} \tag{6}$$

With this scaling for both facilities we are now able to compare the test results. We would like at this time to provide a general overall qualitative comparison of the results. In the following, we will look at the detail of each mode and we will identify the differences and we will also try to correlate the different behavior of the two facilities to their intrinsic characteristics.

First of all, lets look at the two counter-part tests in their original scales. Figure 1 illustrate the pressure versus time trajectory of the two systems (MIST test 3004 and UMCP test MIS0317). Note the semi-logarithmic scale of the pressures and the quite different range of parameters (pressure and time).

Figure 2 shows the same two tests in terms of normalized parameters. The agreement is quite striking. Later in the paper we will also comment on the sensitivity of these result with the initial conditions and we will show that indeed these type of agreement is to be expected. Note that the inventory scale may have fluctuations of the order of five per cent of the total inventory in the two tests. The agreement of the normalized pressure is within some 20 per cent.

4. PHENOMENOLOGICAL SYSTEM BEHAVIOR

The test comparison is by no mean completed at this global level. We must now look at the system behavior during the various modes. In the next section we will analyze each mode separately. We need to explain the various events that take place and we must compare the system responses. When this detailed comparison is completed we will draw our conclusions.

The tests are initiated with a steady state single phase natural

circulation. At the initial time, the break is activated. The pressurizer is the only component where void is present. The pressurizer level drops as inventory is depleted. This initial mode is characterized by a rapid depressurization that lasts until the hot liquid in the pressurizer is able to flash. When the pressurizer is empty and the liquid flashing has subsided, the pressure sharply drops to the saturation pressure corresponding to the initial core exit temperature. At this time void is generated in the core and is accumulating in the vessel upper plenum. When the vessel upper plenum is filling with vapor the liquid level is pushed down. At some time during this transient the upper lip of the hot leg is reached and vapor starts to flow in the hot legs. We then have two phase natural circulation. This mode continues until the system first interrupt the flow at the top of the candy cane. The mechanism of interruption has been described at length in several papers [11,12]. It can be shown that some vapor escapes through the Reactor Vessel Vent Valves (RVVV) into the upper downcomer and into the cold legs where it is suddenly condensed thus causing a sharp collapsing of the vapor space in that region with the consequent interruption of flow at the top of the candy canes. This phenomenon concludes the natural circulation portion of the transient.

Note that the single phase to two phase transition is smooth for both systems and that a slight repressurization is present when the two phase flow natural circulation is about to interrupt. The two systems behave in similar way. Since the pressurizer volume is scaled, both pressurizers are empty at an inventory of 98.4 per cent. However, in the UMCP facility, we observe continued flashing process which is due to the surge line acting as a pressurizer for the system. Here we see an effect of the reduced pressure because the vaporization rate necessary to sustain the pressure is far less for the low pressure facility. The two traces proceed in identical way once the pressure drops to the system saturation pressure. Note that the difference in inventory is in the order of one per cent of the total inventory.

After the first interruption we observe a period of relatively smooth behavior in the pressure which has been identified as the initiation of the Interruption Resumption Mode (IRM). During this period it has been shown that the vapor that escapes in the upper downcomer and in the cold legs through the RVVV is isolated from the cold liquid in those components by a layer of warmer water. Slowly the heat is transferred from the warm liquid layer to the cold water and then vapor is again undergoing a sharp condensation that initiates the propagation period of the IRM. It is very important to note that this mechanism is strongly influenced by the behavior of the RVVV. Thus the different system performance is the direct consequence of the atypical set up of the RVVV in the MIST facility.

Figure 3 provides a detailed comparison of this mode. The IRM in MIST is erratic and quite short while the flapper type RVVV of the UMCP facility generate a well behaved cyclical transient. We use the original pressure versus time data because they provide a more precise trace of the events. If one compares the qualitative phenomena it is easy to detect the initial pull characterized by small oscillations (between 40 and 60 minutes) then the initiation period (up to 70 minutes) and finally some erratic IRM propagation

with a period of about two minutes. For comparison we have inserted a typical IRM trace as observed in the UMCP loop to facilitate the identification of the various phenomena. Note that the period for UMCP is slightly less than two minutes.

The IRM terminates when the system is unable to resume due to the limited liquid inventory available. At this junction the pressure increases rapidly and we characterize the following mode as complete interruption. The complete interruption mode is somehow different for the two facilities. Figure 4 illustrates the various events. In the MIST facility we observe a temporary Boiler Condenser Mode (BCM) that we identify as BCM event. Thereafter, a level control activates AFW and the system responds to this induced recoupling of the secondary side of the steam generator. Then pressure recovers and the system proceeds until full pool BCM is achieved. In the UMCP facility we manually activate the AFW in this particular test and in a similar test which will also be shown in the following section. Then, when the inventory reaches 72 per cent, the UMCP test also exhibits a BCM event. Therefore, we conclude that the sequence of events is reversed. However, the BCM event is generated by the system without external intervention.

We need to describe the details of the BCM event to understand how similar is the system behavior. We know that the BCM event is related to the geometry of the cold legs and its effect on asymmetric behavior. The increased asymmetry between the loops provides a reasonable explanation for the more rapid depletion of the liquid level in loop B which is the cause of the BCM event. This explanation is still tentative because the we were not yet able to confirm it for the MIST facility.

The phenomenology shows a quick depletion of loop B liquid inventory leading to the uncovery of a condensing area in the steam generator when the primary level drops below the secondary level. The vapor condenses, the pressure drops and the liquid is drawn up thus covering the condensing surface. The heat transfer is again interrupt and the pressure recovers. Note that as a consequence of the condensation pull the liquid drops in the steam generator on loop A which causes the level controller to activate AFW in the MIST facility.

In the MIST test there is a level control triggered AFW action during the complete interruption mode that lasts a few minutes. We must now develop a strategy to scale this boundary condition for the UMCP facility. The first concept is the uncoupling of the boundary condition from its activation mechanism. The fact that the operator or a level controller decide that the condition must be applied is irrelevant. What matters is that a boundary condition is applied. Having stated this important concept, we now must look at the generic effects that the boundary conditions has on the system. Once we understand how the system reacts we can apply the boundary condition in the proper way.

The effects of AFW on the system during complete interruption are shown in Fig. 5. One can obtain no effect, temporary depressurization or AFW induced boiler-condenser mode with permanent depressurization. If AFW is applied to a steam generator where the primary level exceeds the AFW injection

elevation, no effect is observed because no heat is transferred from the primary to the secondary. We classify this boundary condition as neutral and we can obtain this behavior by activating AFW on the A loop steam generator. Should we activate AFW on the B loop steam generator, we observed a temporary depressurization due to the condensation of the primary vapor at the AFW injection elevation. However, the sudden contraction of the vapor space pulls the liquid in the steam generator primary upwards and thus flooding the AFW injection. The heat transfer is then minimal and the pressure recovers. The boundary condition is identified as temporary because it bears within itself the mechanism for its neutralization.

When both loops AFW is activated, we observe an AFW induced boiler-condenser mode which persist as long as the AFW is active. This boundary condition is classified as permanent because it alters the system trajectory indefinitely. In the MIST test we recognize the AFW effect as temporary which means that we should apply AFW only to the loop where the primary level has dropped below the AFW injection elevation.

There is also another very important characteristic of the temporary boundary condition. We have observed in the UMCP facility that, after twenty minutes of operation, a significant effect of the AFW temporary boundary condition is present. We identify this long term effect of the temporary boundary condition as a post boiler-condenser plateau. This phenomenon is present both in MIST and UMCP and it is the direct effect of the application of AFW. To demonstrate this relationship between AFW and post BCM plateau we need to compare two tests with and without the application of the AFW. This fact is clearly illustrated in Fig. 6.

To explain this occurrence, let's assume that AFW is initiated in the steam generator B. As a consequence of the condensation of the primary vapor in the steam generator primary, the pressure dips, the secondary level exhibits a spike due to sudden vaporization and the primary level is drawn up toward the AFW injection elevation. Note that liquid is also drawn from loop A steam generator primary and in some occurrence this may even trigger pool BCM in loop A due to the drop of primary level below the secondary level. When the primary level in loop B reaches the AFW injection elevation, condensation subsides and the pressure recovers to its original rate of increase since the core and the steam generators are again uncoupled. The net effect of this action is a strong re-equalization of the two primary levels. This is the cause of the post BCM plateau. In fact, when pool BCM is reached both primary levels are quite close. This creates a competition between the two loops primary level for effective condensing surface. The net result is a slight repressurization that subsides when enough inventory has been lost and the system reaches steady BCM in both loops.

In the UMCP counter-part test, the AFW is applied to the loop that has primary side level in the steam generator below the AFW injection elevation. During the complete interruption, the AFW activation must not cause pool BCM in the other loop because this does not happen in the MIST facility. Therefore, we activate AFW on loop B *shortly* after complete interruption and we interrupt its application when the pressure has recovered its repressurization rate. In the counter-part test (MIS0317), AFW is applied

first on loop B and then on loop A. In other tests we applied the boundary condition as described above. Figure 7 illustrate the comparison in terms of normalized parameters of test 3004 (MIST) and test MIS1005 (UMCP). We selected this test because we must have AFW activation as the last event in order to properly compare the two system behavior. Note the agreement of the pressure peak and the well pronounced post BCM plateau.

In Fig. 2 the comparison of the MIST test with the counter-part test shows a minimal post BCM plateau for the UMCP test because the BCM event subsequent to the AFW activation tends to suppress the long term effect due to the AFW activation.

6. CONCLUSIONS

The sensitivity of the system to initial and boundary conditions is a well recognized fact. Both experiments and code simulation are clearly documenting this issue.

We want to provide at this point a few considerations designed to put the scaling issue into the correct perspective. The ultimate goal of a test facility are clearly outlined in the introduction. We want to repeat them here to focus on the actual requirement of a successful scaled experiments. One wants the experiments or the code simulation to: a) demonstrate the presence of the key phenomena; b) approximate their quantitative characteristics; c) reproduce their sequence of occurrence.

The test comparison presented in the paper is indeed successful according to these three criteria. All the key phenomena are present in both high and reduced pressure data sets. In particular the occurrence of the BCM event is quite remarkable. The magnitude of the normalized pressure fluctuations are indeed comparable within the limitations of the systems sensitivity to initial and boundary conditions. Therefore, the quantitative characteristics of the two systems behaviors is comparable. Finally, all the various transitions between the energy transfer modes do occur at similar inventory ranges for both systems. Except for the inversion between BCM and AFW events during the complete interruption, the sequence of events is identical. This in summary means that it is possible to scale a full pressure transient with a reduced pressure facility without major distortion. This finding constitutes a definite turning point in the scaling strategies proposed up to date and provides a significant input to the future attempts to formulate a set of scaling laws or criteria.

ACKNOWLEDGEMENTS

The authors are indebted to the Computer Science Center of the University of Maryland for the partial support of the computational expenditures. These studies are supported through a grant of the U.S. Nuclear Regulatory Commission.

REFERENCES

[1] M.W. Young and J.P. Sursock eds., Coordination of safety research for the Babcock and Wilcox integral system test program, NUREG/CR-1163 (1987)

[2] T.K. Larson, An investigation of integral facility scaling and data relation methods (Integral System Test program), NUREG/CR-4531 (1987)

[3] Guidelines and procedures for the international code assessment and application program, NUREG/CR-1271 (1987)

[4] N. Zuber, Quantifying reactor safety margins, Proc. of the 16th Water Reactor Safety Research Information Meeting, Gaithersburg, MD (1988)

[5] P.D. Wheatley, Evaluation of operation safety at B&W plants, NUREG/CR-4966 (1987)

[6] Y.Y. Hsu, M. diMarzo, D.W. Sallet, G.A. Pertmer, F.J. Munno, Facility description and scaling principles of the UMCP 2x4 loop, Proc. of Specialist Meeting on Small Break LOCA Analyses in LWR's, Pisa, Italy 1 (1985) pp. 615-635

[7] Y.Y. Hsu, Z. Wang, C. Unal, M. diMarzo, K. Almenas, Scaling for small break LOCA facilities, Proc. 3rd Int. Topical Meeting on Nuclear Power Plant Thermal Hydraulics, Seoul, Korea A10.A-1 (1988)

[8] Z. Wang, C. Unal, M. diMarzo, Y.Y. Hsu, K. Almenas, Use of inventory as a chronological scale of small break LOCA in the IST facilities, Proc. of the 7th UIT National Heat Transfer Conference, Florence, Italy, (1989) pp. 271-279

[9] G.O. Geissler ed., Group report MIST test group 30. Mapping tests, Babcock and Wilcox, BAW-1950 (1987)

[10] K. Almenas, Y.Y. Hsu, M. diMarzo, Z. Wang, G. Pertmer, R. Lee, Reproducability in a multi-loop thermal hydraulic system, Nucl. Tech., 82 (1988) pp. 341-354

[11] M. diMarzo, K. Almenas, Y.Y. Hsu, Z. Wang, The phenomenology of a small break LOCA in a complex thermal hydraulic loop, Nuc. Eng. and Des., 110 (1988) pp. 107-116

[12] Z. Wang, K. Almenas, M. diMarzo, Y.Y. Hsu, C. Unal, Impact of rapid condensations of large vapor spaces on natural circulation in integral systems, Nuc. Eng. and Des. (1989) in press

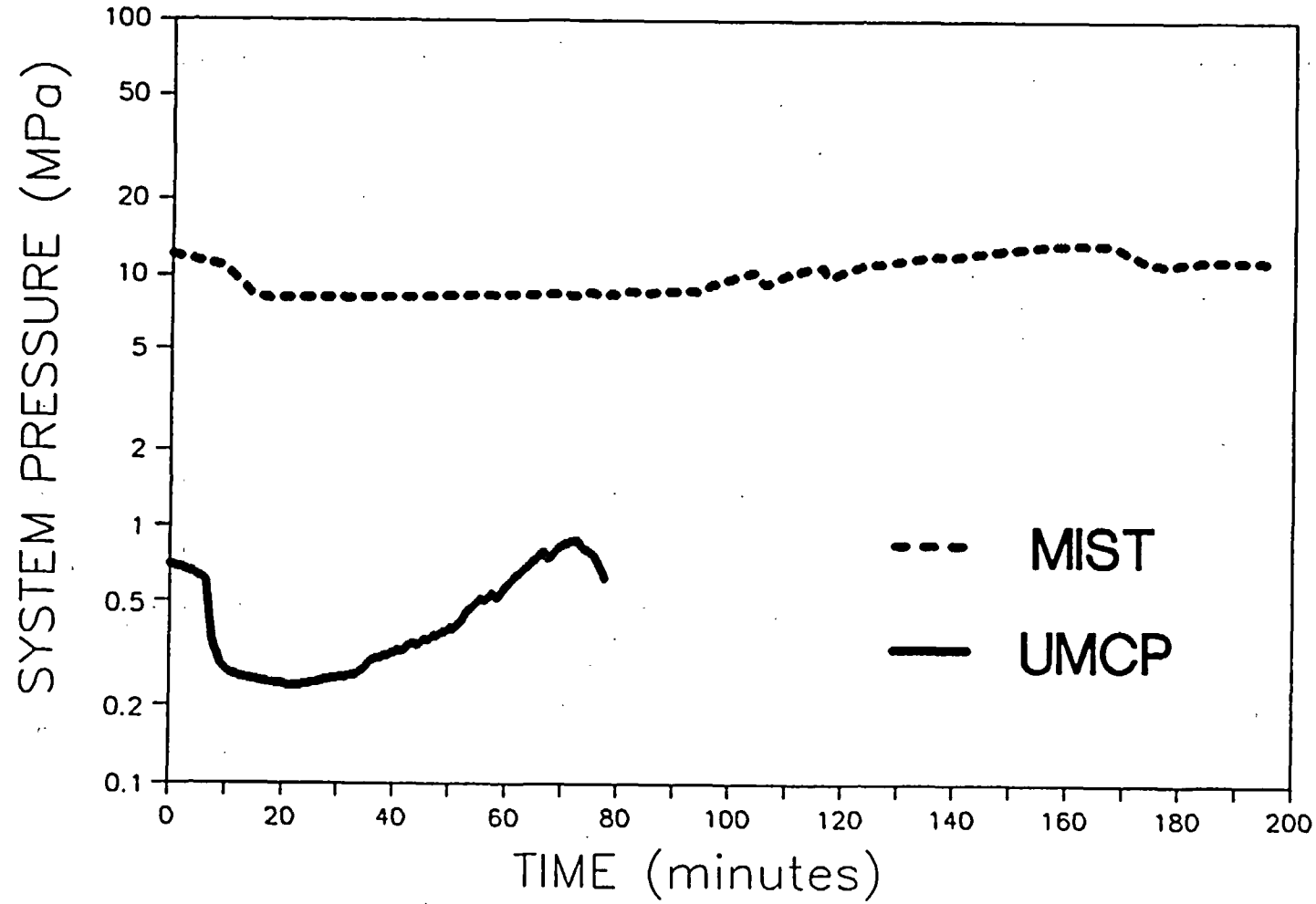

FIGURE 1 - System pressure versus time traces for MIST test 3004 and UMCP test MIS0317

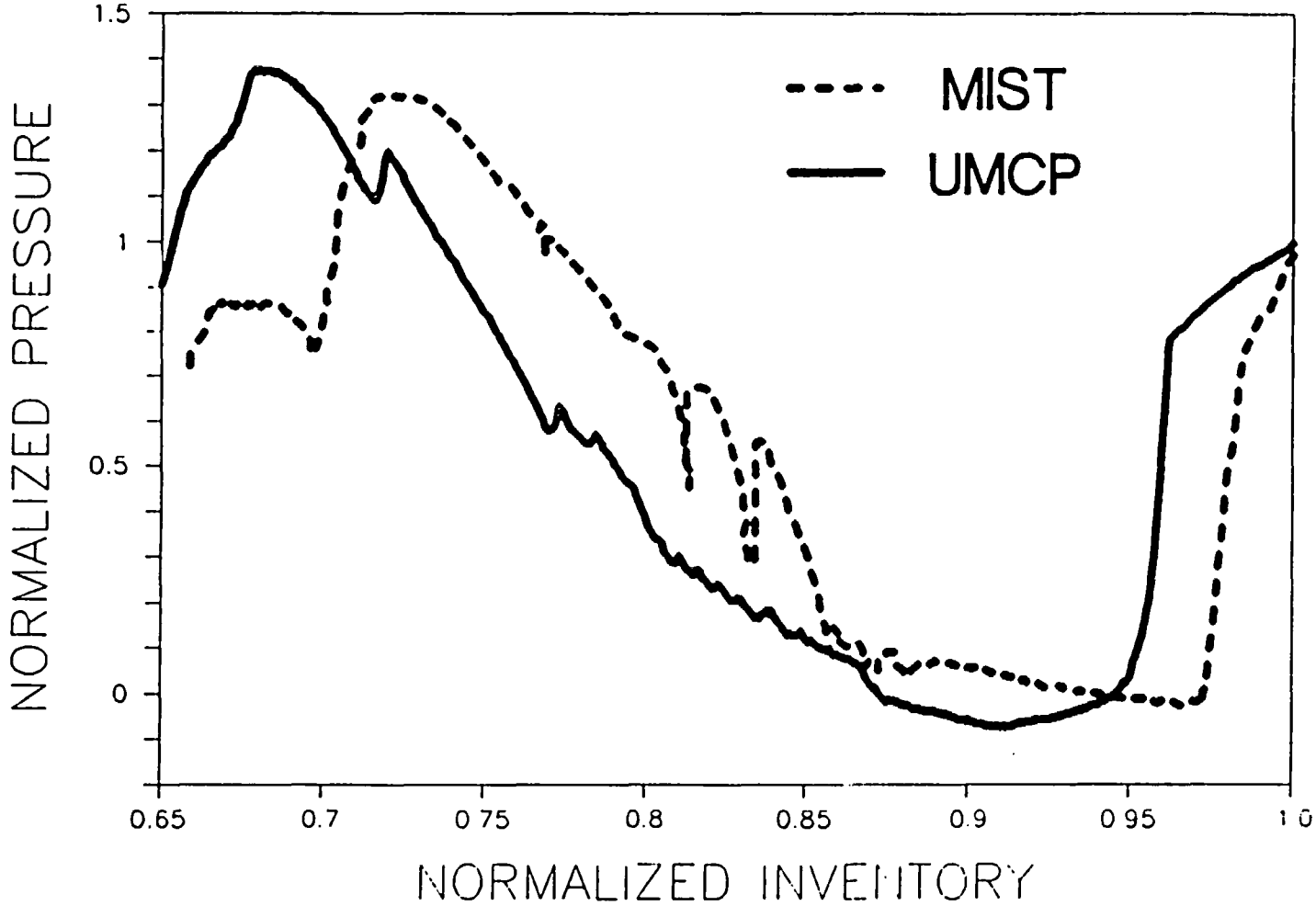

FIGURE 2 - Normalized pressure versus normalized inventory traces for MIST test 3004 and UMCP test MIS0317

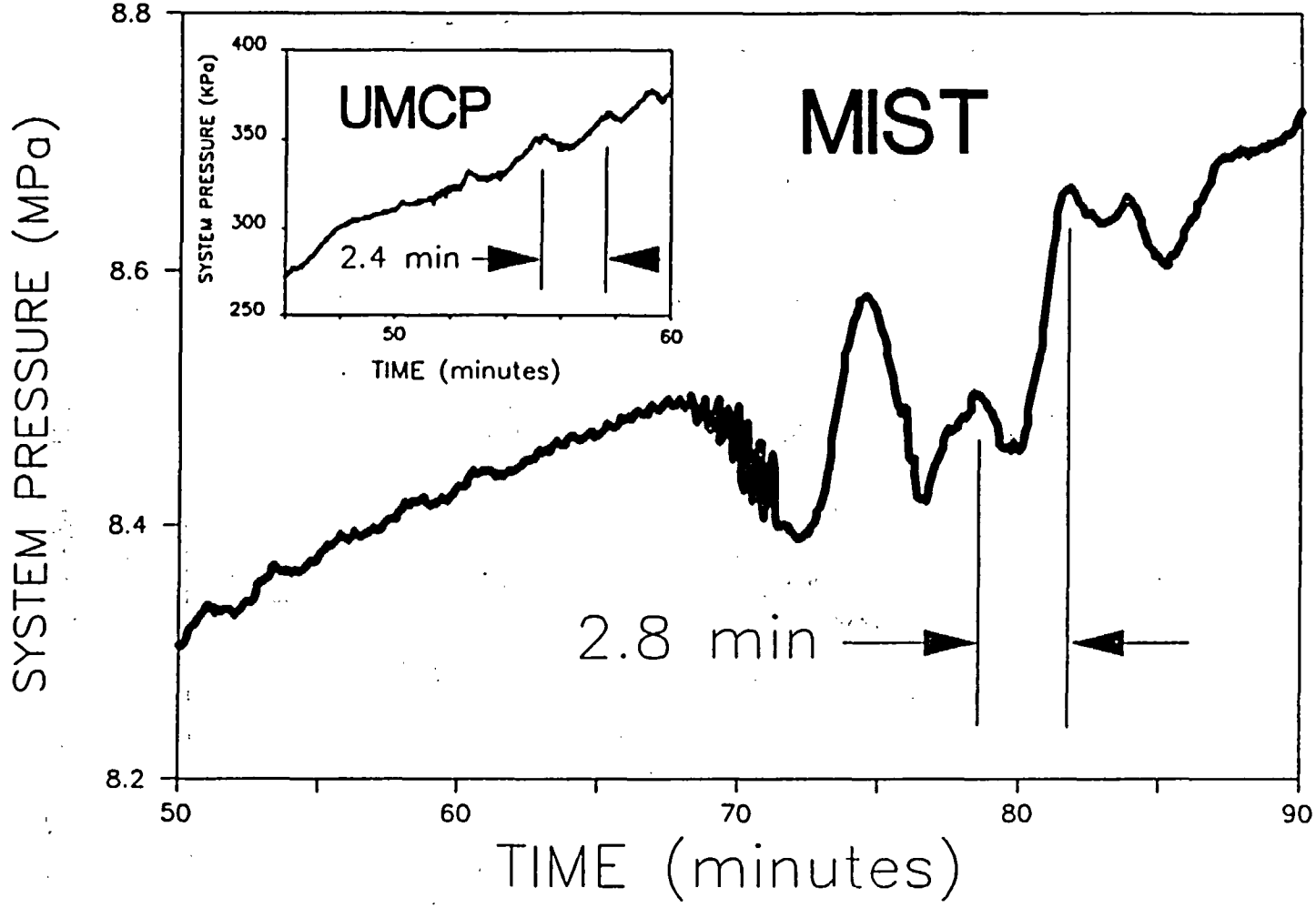

FIGURE 3 - Detail of the IRM initiation for MIST test 3004 and UMCP test BCM0731

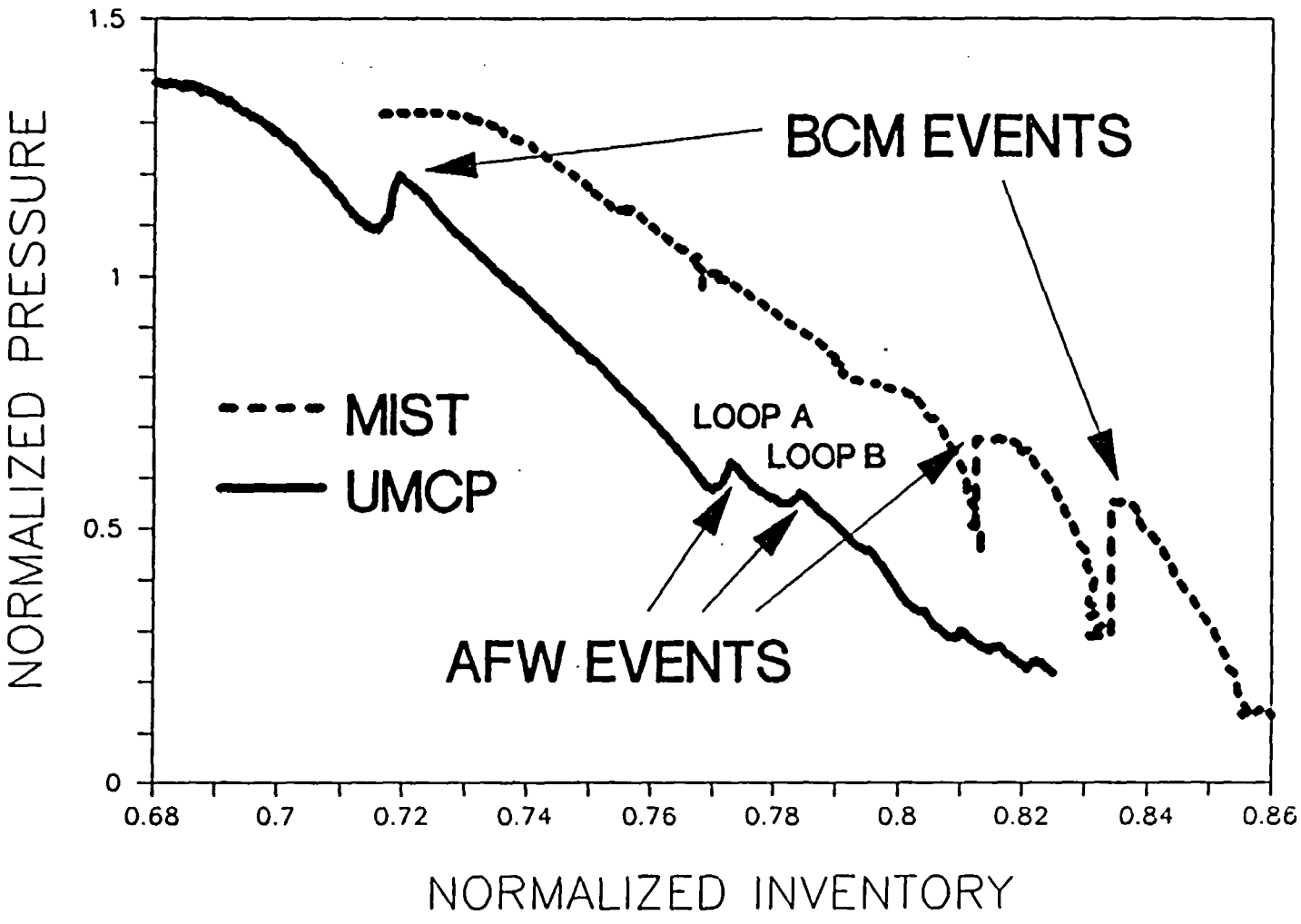

FIGURE 4 - Detail of the complete interruption for MIST test 3004 and UMCP test MIS0317

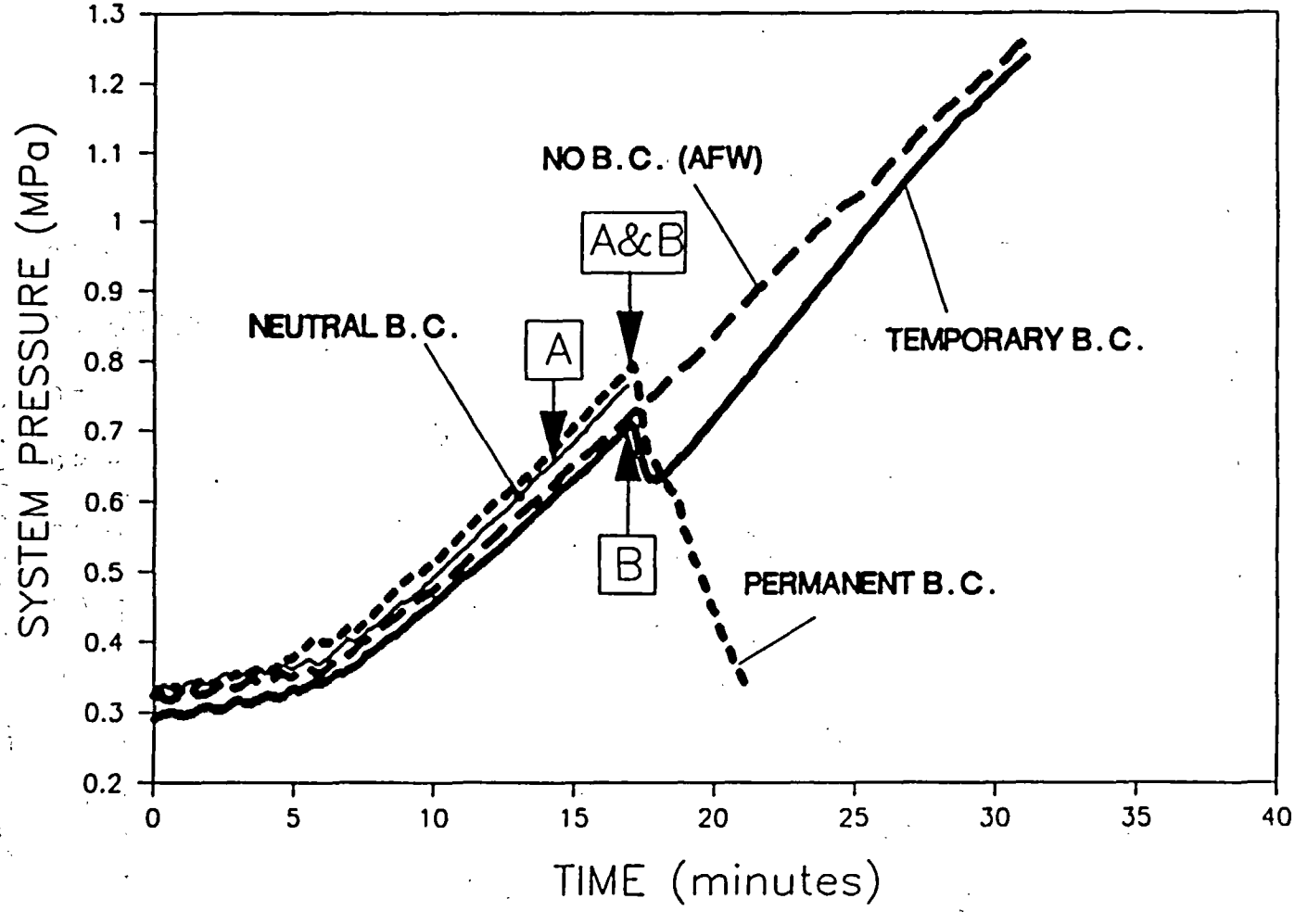

FIGURE 5 - Classification of the AFW boundary condition effects

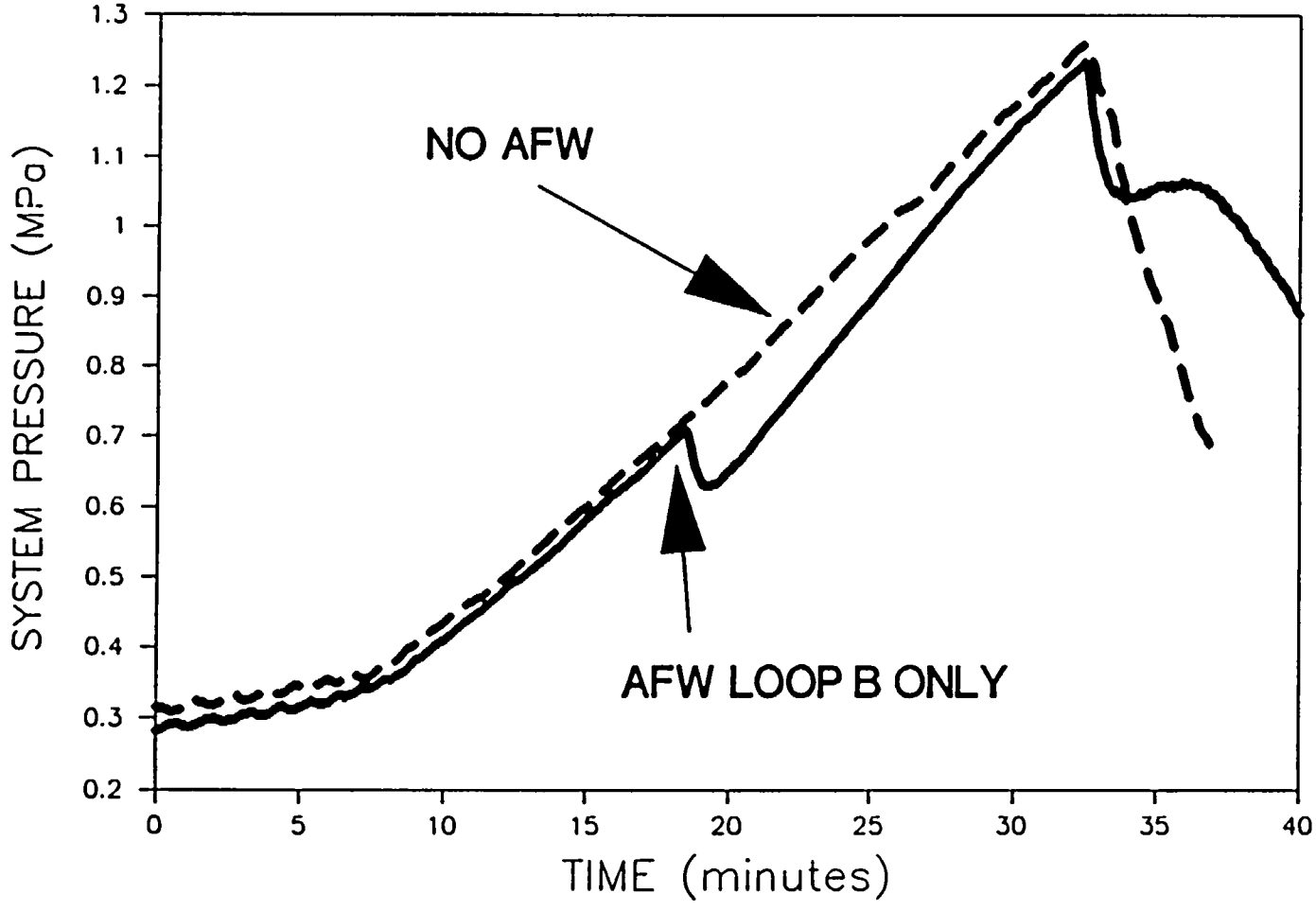

FIGURE 6 - Long term effect of temporary AFW boundary condition

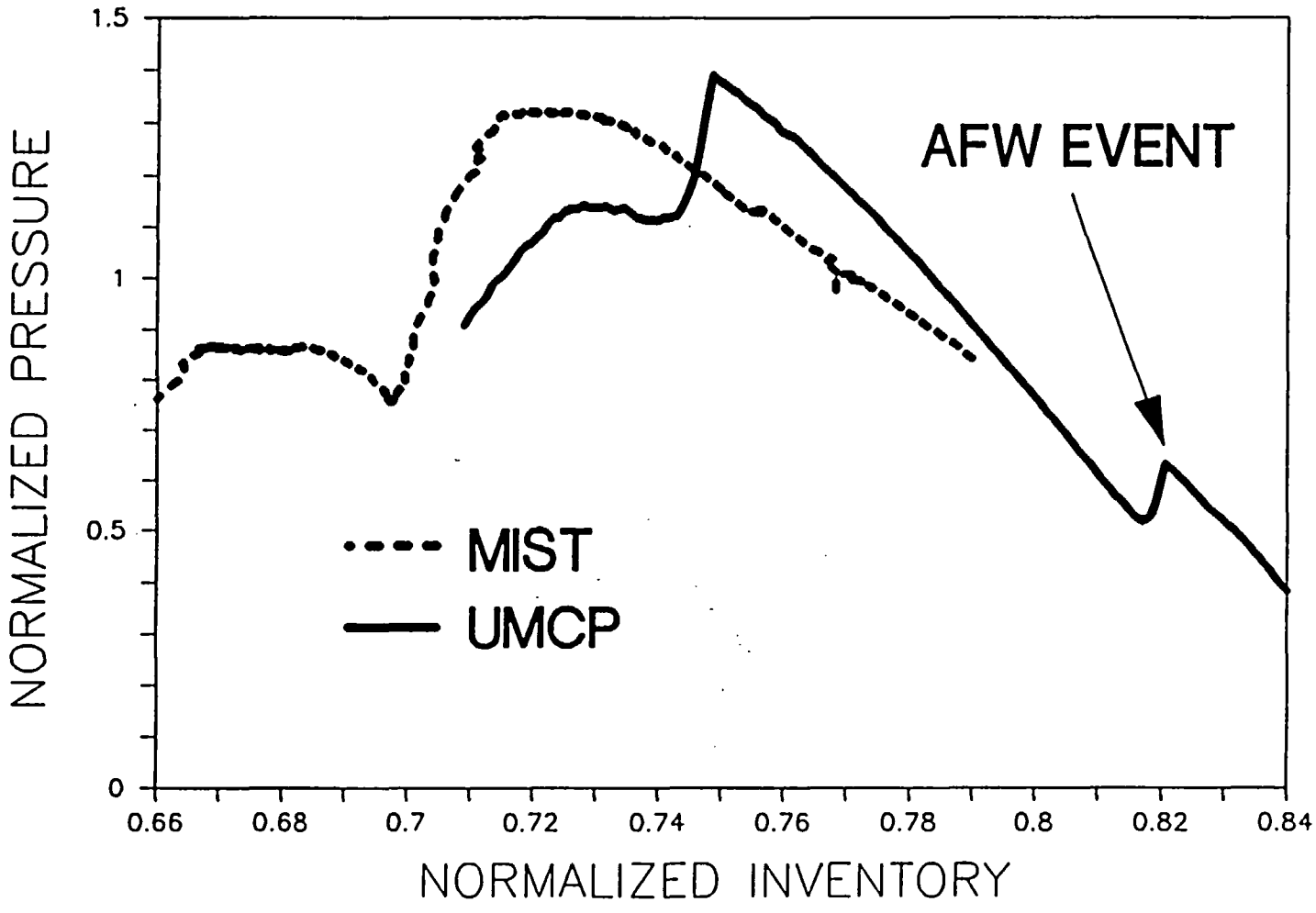

FIGURE 7 - Detail of resumption to BCM and post-BCM plateau for MIST test 3004 and UMCP test MIS1005

MIST Program: Risk Dominant Transient Testing

G. O. Geissler
Babcock & Wilcox, Nuclear Power Division
Lynchburg, Virginia

T. E. Moskal
Babcock & Wilcox, Research and Development Division
Alliance, Ohio

ABSTRACT

The Multiloop Integral System Test (MIST) Facility is a scaled physical model of a Babcock & Wilcox lowered loop, nuclear steam system. MIST was part of a program to address small-break loss-of-coolant accidents (SBLOCAs) specific to the Babcock & Wilcox-designed plants. Data from MIST are used to benchmark the adequacy of system codes, such as RELAP5 and TRAC, for predicting abnormal plant transients.

Toward the end of the test program, a series of tests were performed to explore operating procedures for mitigating various accident conditions and investigate possible alternative strategies. This included tests referred to as Risk Dominant Transients, in which a small-break loss-of-coolant accident was accompanied by the lack of particular auxiliary equipment or control systems that would normally be employed to mitigate the accident condition.

Two of these tests examined SBLOCA transients without the benefit of the high-pressure injection (HPI) system. The first of these utilized standard abnormal transient operating guideline (ATOG) control schemes, and the second employed a more aggressive steam generator pressure control strategy to cool the plant. The results and observations from these tests are summarized in the publication.

INTRODUCTION

The Multiloop Integral System Test (MIST) was part of a multi-phase program to address small-break loss-of-coolant accidents (SBLOCAs) specific to the Babcock & Wilcox-designed nuclear steam system. MIST is sponsored by the U.S. Nuclear Regulatory Commission (NRC), Electric Power Research Institute (EPRI), the Babcock and Wilcox Owners Group, and Babcock & Wilcox (B&W). Test data from the MIST facility have been used to benchmark the predictive capabilities of system codes - RELAP5 and TRAC - for predicting abnormal plant transients.

The MIST Facility is a scaled physical model of a B&W lowered-loop, nuclear steam system. The test loop was designed to operate at typical plant pressures and temperatures with emphasis on leak tightness and minimal heat losses. The MIST model includes all the major components of a plant reactor coolant system, including a full length electrically heated simulated core, two hot legs, two full length once-through steam generators, four cold legs, an external vessel downcomer, simulated reactor vessel vent valves, and pressurizer. The boundary conditions include sealed high-pressure injection, core flood tanks, low-pressure injection, scaled leaks and vents, power-operated relief valve, and scaled feed and steam capabilities for the secondary side of the steam generator. A test facility schematic is shown in Figure 1. A complete description of the MIST facility is contained in Reference 1.

Facility testing was performed under Phases 3 and 4 of the MIST Program. Phase 3 testing included a number of tests to examine the effect of high-pressure injection (HPI) upon the course of a SBLOCA by varying the leak and HPI configuration, HPI capacity, and timing of HPI actuation. High-pressure injection flow was found to have a significant effect by virtue of establishing an equilibrium condition in which primary inventory depletion was halted while the combined effect of leak and HPI flow continued to cool the system. Phase 4 testing was performed in late 1987, and included two tests to explore operating procedures for coping with SBLOCAs in which HPI was not available. These SBLOCA transients accompanied by the lack of a key auxiliary system such as HPI are referred to as Risk Dominant Transients.

TEST PERFORMANCE

The two tests were performed as direct counterparts to a previously performed SBLOCA transient from Phase 3 testing. This reference test had a scaled 10 cm^2 leak in the cold leg B1 discharge piping, and utilized standard abnormal transient operating guideline (ATOG) control schemes. The reference test is referred to as the MIST Nominal Test (in particular, test number 3109AA). The only exceptions were that between Phase 3 and Phase 4 a low-pressure injection system was added and available for these tests, the steam generator pressure control deviated from the standard ATOG control for the second of the two tests, and of course, high-pressure injection flow was unavailable for both tests.

As with the nominal test, the tests were initiated with the loop in steady-state single-phase liquid natural circulation with core power at 3.5% of full (scaled) power, plus 0.57% to offset uncompensated heat losses from the loop. Steam generator pressures were constant at 1010 psia, which corresponds to the plant turbine bypass valve control pressure. The tests were initiated by opening a 10 cm^2 (scaled) leak, and actuating a core power ramp control function to simulate post-trip core power decay. Secondary pressure control was the only control parameter that was different between the two tests being discussed. In the first test, ATOG pressure control was employed. The ATOG control used in MIST approximates control actions called for in plant procedures. The control scheme is automated to obtain readily reproducible and modelable boundary conditions. Generally, this calls for a 100 F/hr cooldown of each steam generator when the difference between the core exit temperature and steam generator saturation temperature is less than 50 F, and constant pressure control when this difference is greater than 50 F. Complete description of the MIST ATOG control is available in Reference 2.

In the second test, ATOG control was employed for the first 30 minutes. Then, each steam generator was depressurized at a rate of 50 psi/min. In prescribing this, it was felt that 30 minutes was a sufficient time for an operator to ascertain that the high-pressure injection system was inoperable and would be for some time. It would be after about 30 minutes that a decision to pursue a more aggressive cooldown strategy would be made.

TEST RESULTS - ATOG COOLDOWN (Test 410AT3)

The primary system depressurized rapidly upon opening the leak (see 1, Figure 2). The initial effect of no HPI was a more rapid depletion of primary system inventory than observed in the nominal test. The depletion was followed by the complete voiding of all four cold leg discharge pipes and primary loop flow interruption. The voiding of the cold legs resulted in voided conditions at the leak site and therefore a decreased leak flow rate. The steam generator secondary pressures responded in a symmetrical manner (decreasing to approximately 750 psia) as the secondary levels were raised by auxiliary feedwater to 31.6 feet as specified (see 2, Figure 2). The steam generator refill to this level is called for as part of the ATOG procedure due to a lack of sufficient subcooling margin in the primary fluid.

When the primary loop flow interrupted, the difference between the core exit temperature and the steam generator secondary saturation temperature was greater than 50 F. Therefore, the control function for the ATOG cooldown did not actuate early (remained at 1010 psia), whereas in the nominal test, the control function became active for one of the steam generators. This activity permitted periods of steam generator heat transfer which, along with HPI, aided primary depressurization in the nominal test. Thus, a significantly different primary system pressure response occurred early in the transient. Test 410AT3 repressurized at this time (see 3, Figure 2) as a result of no HPI and no steam generator heat transfer.

The primary system continued to repressurize, while losing inventory, until the primary level in steam generator A descended to the secondary pool elevation. Steam generator heat transfer was established and resulted in a depressurization of the primary system (see 4, Figure 2). The steam generator B primary level continued to decrease and subsequently heat transfer was also established in steam generator B.

The establishment of steam generator heat transfer resulted in an increase in the secondary pressure (see 5, Figure 2) (therefore increasing the steam generator secondary saturation temperature) and a decrease in the primary pressure (therefore decreasing the core exit temperature that was saturated). Eventually, the difference between the core exit and the steam generator secondary saturation temperature reached 50 F and the ATOG cooldown commenced.

The cooldown resulted in a depressurization of the primary system (see 1, Figure 3), which eventually led to core flood tank and low-pressure injection (LPI) actuation. During this depressurization, all four cold leg discharge pipes remained voided, the cold leg suction pipes began voiding, and little, if any, forward primary loop flow was observed - in fact, indications are that backflow may have existed in each cold leg.

When LPI actuated, a rapid increase of the primary system inventory occurred. All four cold leg discharge and suction pipes refilled completely, the downcomer and the reactor vessel levels increased to near the reactor vessel vent valve elevation, the pressurizer surge line filled, and the hot leg riser and steam generator primary levels also increased but did not refill completely.

The LPI actuation subcooled the core exit temperature and decreased the primary system pressure approximately 25 psi (see 2, Figure 3). The primary system, however, subsequently began to repressurize (see 3, Figure 3) due to stored energy in the system, the decrease in the leak energy as a result of subcooling the leak site, and the decreased steam generator heat transfer that resulted from increasing the primary steam generator levels above the secondary pool level. LPI subsequently terminated due to the increasing primary system pressure. Circulation was not established because of the lack of a sufficient driving head to initiate forward loop flow, despite the substantial addition of inventory provided by LPI.

The core region then began a heatup that resulted in a similar system response to the repressurization that occurred early in the transient. The primary system pressure attained approximately 725 psia during this repressurization phase of the transient (see 4, Figure 3). The primary system continued to lose inventory during the repressurization phase. The steam generator primary levels eventually descended to the secondary pool elevation, steam generator heat transfer was established, and a slight depressurization was observed (see 5, Figure 3). The test was completed at this time.

TEST RESULTS - STEAM GENERATOR BLOWDOWN (Test 410BD1)

This test was also initiated by opening a 10 cm^2 leak in the cold leg B1 discharge pipe, and activating a core power decay ramp. For the first 30 minutes of the test, the same ATOG cooldown procedure was followed. After 30 minutes, a steam generator blowdown of 50 psi/min was activated.

Similar to the first test, the primary system depressurized rapidly upon opening the leak (see 1, Figure 4). The initial effect of no HPI resulted in a rapid depletion of the primary system inventory. Voiding of all four cold leg discharge pipes occurred, partial voiding of the suction pipe in cold legs A1 and B1 also occurred, and primary loop flow interrupted. The steam generator secondary pressures initially responded in a symmetrical manner, however, a slight amount of heat transfer occurred in steam generator B that caused the pressures to diverge slightly (see 2, Figure 4) as the secondary levels were filled by auxiliary feedwater to 31.6 feet. Upon flow interruption, the primary system repressurized (see 3, Figure 4). The repressurization and the phenomena that occurred during the repressurization (e.g. periodic flow pulses in the primary loop) were similar to those observed during the first test. In fact, the primary system pressure responses for the first 37 minutes of the two tests are nearly identical (see 1, Figure 5).

At 30 minutes, the loop operator actuated the 50 psi/min steam generator blowdown control. A hot leg heatup was in progress when the steam generator blowdown began. The blowdown of steam generator B was initiated first and apparently had no effect on the primary system pressure response. The hot leg heatup continued and a flow pulse in loop A caused primary-to-secondary heat transfer (see 7, Figure 4). Primary system flow, however, interrupted again, the primary repressurized, and another hot leg heatup cycle commenced.

During the hot leg heatup, both steam generators continued to blow down and no impact was observed on the primary system pressure response (see 8, Figure 4). The steam generator secondary side levels decreased during this time as more secondary side liquid flashed to steam than was being replenished by auxiliary feedwater flow.

The hot leg heatup eventually resulted in the establishment of sufficient driving head to cause primary system flow. At this time, the auxiliary feedwater flow rate exceeded the steam flow rate in both steam generators and when primary loop flow began, primary-to-secondary heat transfer occurred (see 9, Figure 4) that resulted in a rapid depressurization of the primary system (see 10, Figure 4). The steam valves fully opened; however, the steam generation rates were greater than the flow capacity of the MIST steam lines. Thus, the secondary side pressures increased (see 9, Figure 4) and the 50 psi/min blowdown control could not be achieved (see 11, Figure 4).

When primary-to-secondary heat transfer was established, the auxiliary feedwater flow rate exceeded the scaled head/flow capacity as the control system attempted to maintain a constant level (the MIST facility was designed to perform in this manner). Therefore, had the auxiliary feedwater head/flow characteristic been adhered to, a reduction in secondary side inventory would have occurred. The primary system response may be affected by this method of control because if an inventory reduction had occurred, auxiliary feedwater flow would have to be maintained over an extended period, thus, increasing the potential for heat transfer and depressurization of the primary system.

Subsequent to the rapid depressurization of the primary system, an oscillatory decreasing pressure response occurred (see 11, Figure 4). The oscillatory response resulted from brief periods of heat transfer in steam generator A. During the rapid depressurization and the subsequent depressurizations that occurred in an oscillatory manner, superheated conditions were observed in the downcomer and cold legs. The rapid depressurization quickly decreases the saturation temperature of the primary system. However, the downcomer metal cannot dissipate its stored energy as rapidly, therefore saturated steam discharged through the reactor vessel vent valves becomes superheated in the downcomer. The superheated steam flows backward in the cold leg, impedes, and eventually interrupts flow. The leak discharge also indicated periods of superheated discharge and resulted in reduced leak flow rates. The varying leak fluid conditions appear to have caused the oscillatory primary system pressure response.

The primary system pressure decreased to approximately 290 psia (see 1, Figure 6), all four cold leg discharge pipes had completely voided, and when the loop B cold leg suction pipes began to void, the primary system repressurized (see 2, Figure 6). Since the primary pressure did not decrease to the low-pressure injection system setpoint (200 psia), LPI did not actuate during the initial blowdown of this test.

During the repressurization, the voiding of the cold leg suction pipes resulted in an increased steam generator primary level as the increased pressure displaced the column of liquid. The hot leg riser level also increased (due to a manometric balance within a loop). The cold leg suction voiding alternated between the loops and caused the hot leg riser and steam generator primary levels to (1) increase in the loop whose cold leg suction voided and (2) decrease in the loop whose cold leg suction did not void. This response continued while the loop inventory continued to deplete until the primary levels in both steam generators descended to the secondary pool elevation. The primary system then depressurized (see 3, Figure 6).

When the pressure descended to the LPI setpoint (see 4, Figure 6), LPI flow was initiated. Subsequently, the primary system repressurized in a manner similar to that observed in the first test. The repressurization terminated LPI flow before the loop was refilled. The maximum pressure attained in this repressurization was 625 psia (see 5, Figure 6). The hot leg riser and steam generator primary level response was similar to that observed during the first repressurization. Again, when the loop inventory depleted sufficiently to lower the primary levels to the secondary pool elevation in both steam generators, the primary system depressurized (see 6, Figure 6).

At this time, the facility operator was directed to test two actions intended to enhance loop refill and restore single-phase natural circulation: to open the Power Operated Relief Valve (PORV) (Pressurizer relief valve), and secondly, to bump a reactor coolant pump in one of the cold legs associated with each steam generator.

The PORV was actuated when the pressure was relatively stable after a repressurization cycle (see 7, Figure 6), and was held open for 14 minutes. The primary system depressurized as a result of the open PORV and LPI actuated (see 8, Figure 6). The operator then closed the PORV and the primary system responded in a manner similar to that observed after the first LPI actuation.

The primary system repressurized to approximately 530 psia (see 9, Figure 6) and then depressurized when, as observed in the previous similar depressurizations, the primary level in both steam generators descended to the secondary pool elevation. The reactor coolant pump in cold leg B1 was bumped when the pressure was relatively stable after the repressurization cycle.

The pump bump depressurized the primary pressure (see 10, Figure 6) and LPI actuated for a third time during this transient. The primary system pressure response subsequent to LPI actuation was similar to the previous occurrences. A second reactor coolant pump bump (cold leg A1) was performed (see 11, Figure 6); however, little effect was observed since the test was completed shortly after the second pump bump.

The duration of the second test was 961 minutes. Core power augmentation may have had a significant effect on the repressurizations observed during the transient. At test termination, the core power augmentation was approximately 50% of the total core power. Through reductions in the core power augmentation, the magnitude of the repressurizations may be reduced and the potential for establishing natural circulation cooldown may be enhanced. Consideration should be given to the reduction of the core power augmentation for ambient heat losses. The reduced power may aid the refill process and the potential for establishing natural circulation cooldown may be enhanced.

SUMMARY

The two tests described here, when compared to the MIST nominal test, provide valuable information on the effect of no high-pressure injection during a SBLOCA transient. Subsequent to test initiation, the nominal test exhibited a continuous depressurization trend as a result of having HPI available. The two tests without HPI exhibited repressurization trends and voiding was considerably more extensive around the primary loop, although core temperatures did not exhibit any excursions from saturation temperature. When some form of steam generator heat transfer was established, the primary system pressure also decreased for the tests without HPI.

After the initial depressurization, the nominal test established a leak-HPI equilibrium condition which eventually allowed the loop to refill and establish single-phase natural circulation. Unlike the nominal test, the two tests without HPI eventually depressurized to the low-pressure injection system setpoint, approximately 200 psia. The LPI actuation rapidly increased the primary system inventory, but was unable to refill the primary before being terminated due to a repressurization. After LPI actuation, the lack of a sufficient temperature gradient in the hot leg (to swell the hot leg fluid) and the steam generator primary prevented the establishment of primary loop flow. Thus, natural circulation was not established and the primary system repressurized for both tests where HPI was not available.

The results of these tests indicate that, under the conditions experienced on the MIST Facility, low-pressure injection by itself cannot establish natural circulation and the primary system will experience repressurization cycles.

MIST is necessarily atypical of a plant in certain important aspects. MIST interactions, are therefore, not to be applied directly to a plant. Nevertheless, MIST interactions provide insight into expected plant behavior and therefore are of intrinsic interest. The tests provided useful information on the effects of no HPI, steam generator secondary side blowdown, PORV actuation, and reactor coolant pump bump. The ability to actuate LPI by means of the PORV actuation and the reactor coolant pump bump was also demonstrated.

REFERENCES

1. "Multi-Loop Integral System Test (MIST) Facility Specification", RDD:84:4091-01-01:01, November, 1984. (To be published as an NRC Report in 1990.)

2. "MIST Test Specifications", G. O. Geissler and J. R. Gloudemans, BAW-1894, Babcock & Wilcox, Lynchburg, Virginia, October, 1985.

3. "MIST Final Report (Draft), Volume 11 - MIST Phase IV Final Report", G. O. Geissler, BAW-2067, November, 1988. (To be published as an NRC Report in 1990.)

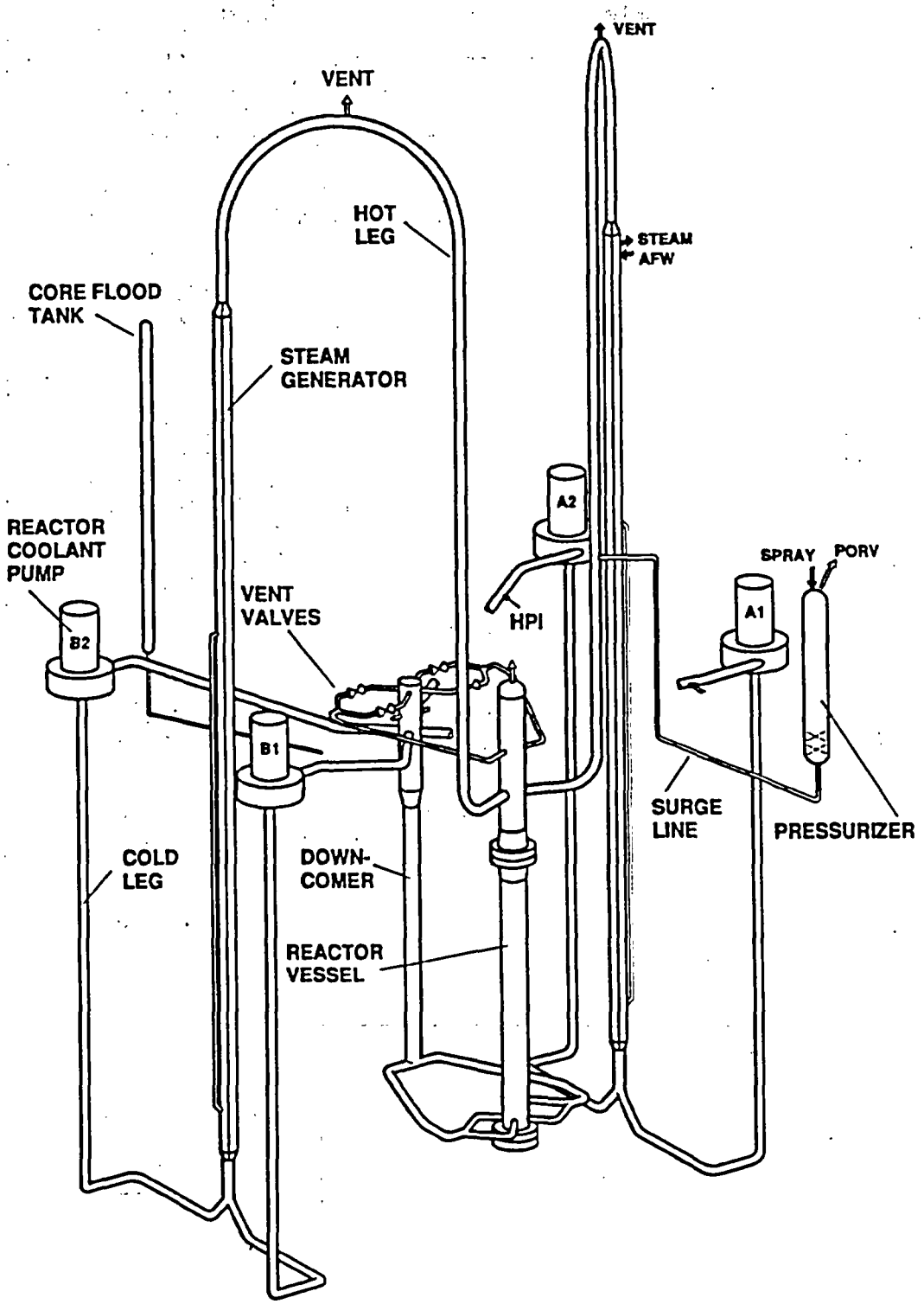

Figure 1. Reactor Coolant System - Multiloop Integral System Test (MIST)

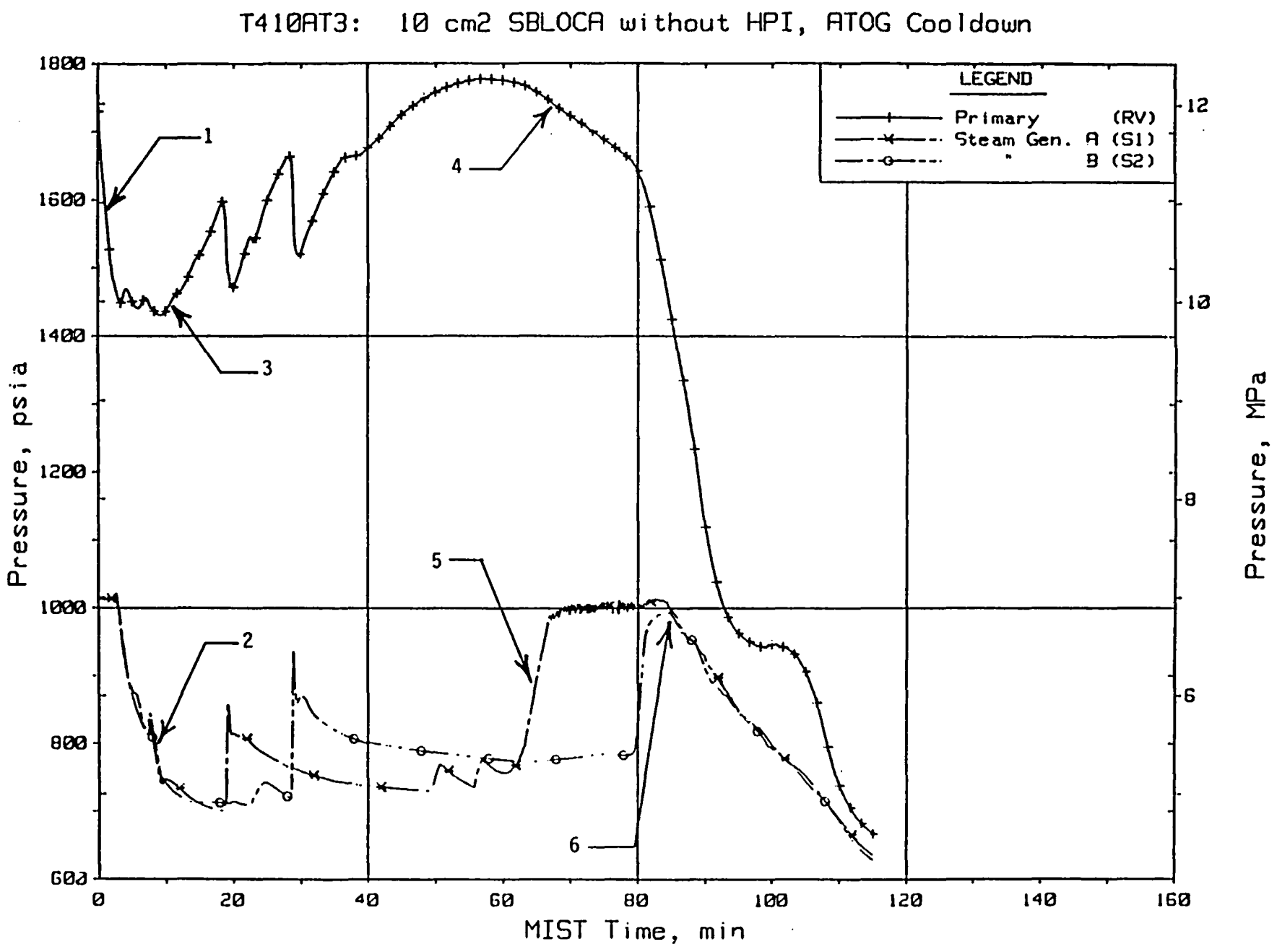

Figure 2. Primary and Secondary System Pressures (first 115 minutes)

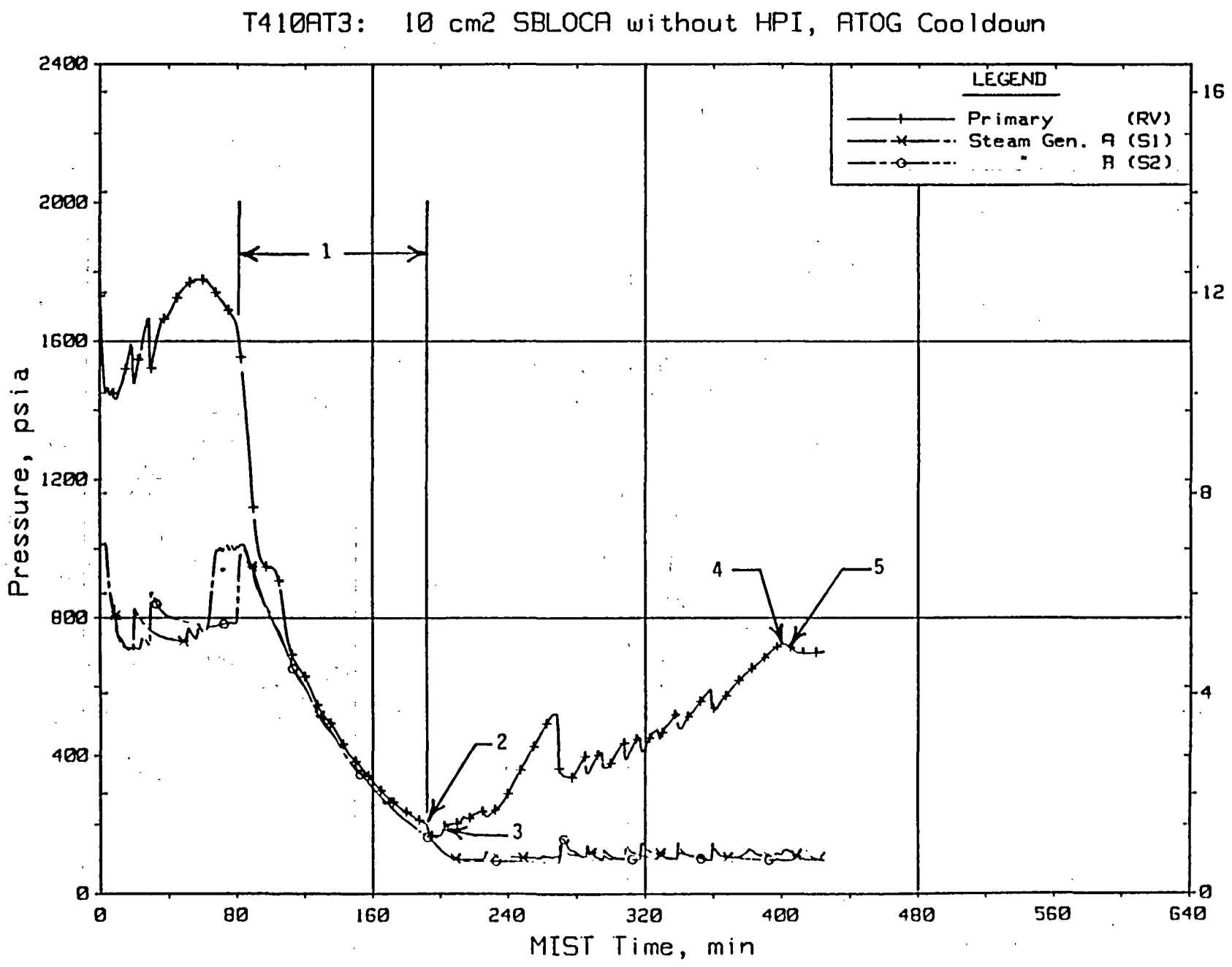

Figure 3. Primary and Secondary System Pressures (Test Duration)

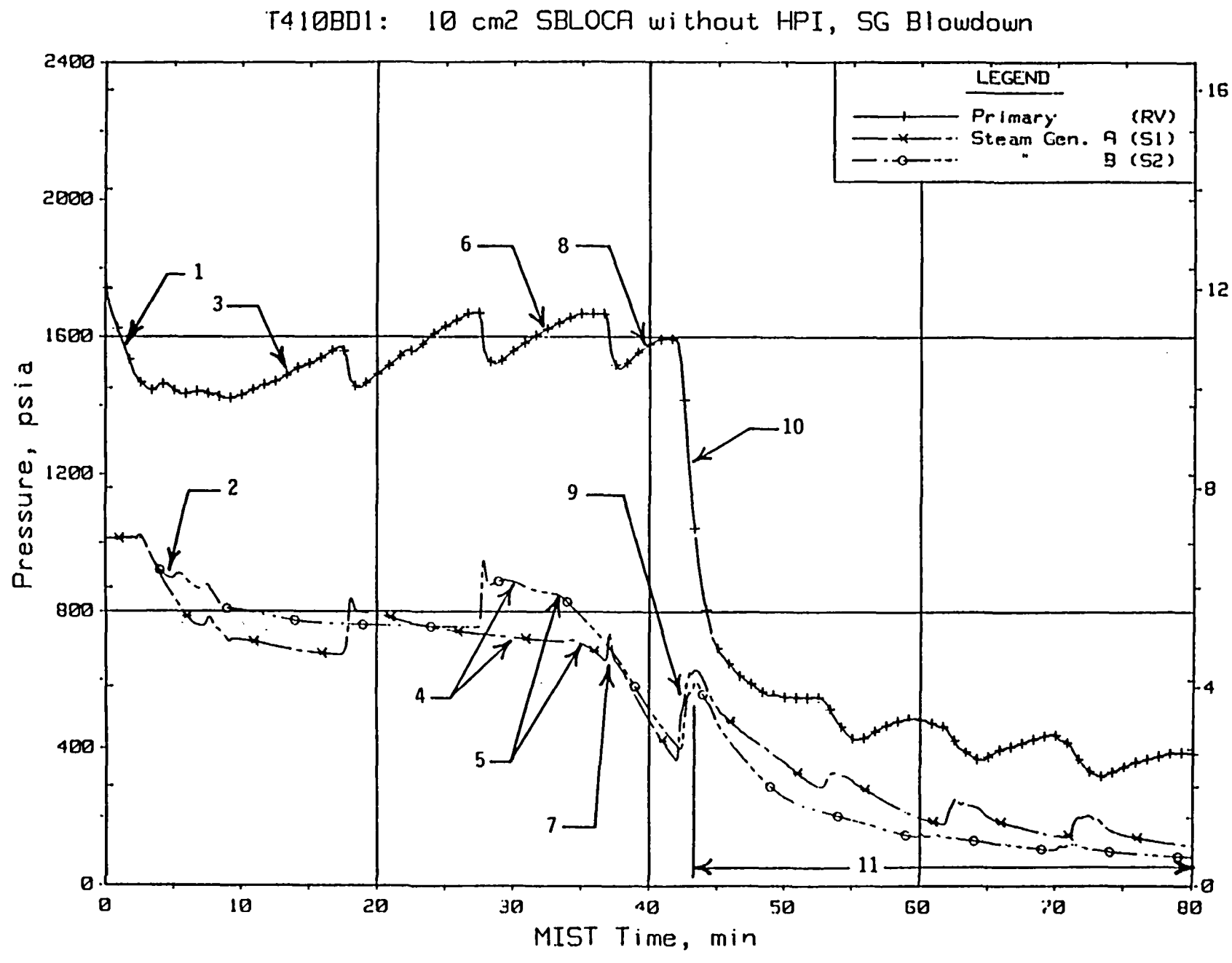

Figure 4. Primary and Secondary System Pressures (first 80 minutes)

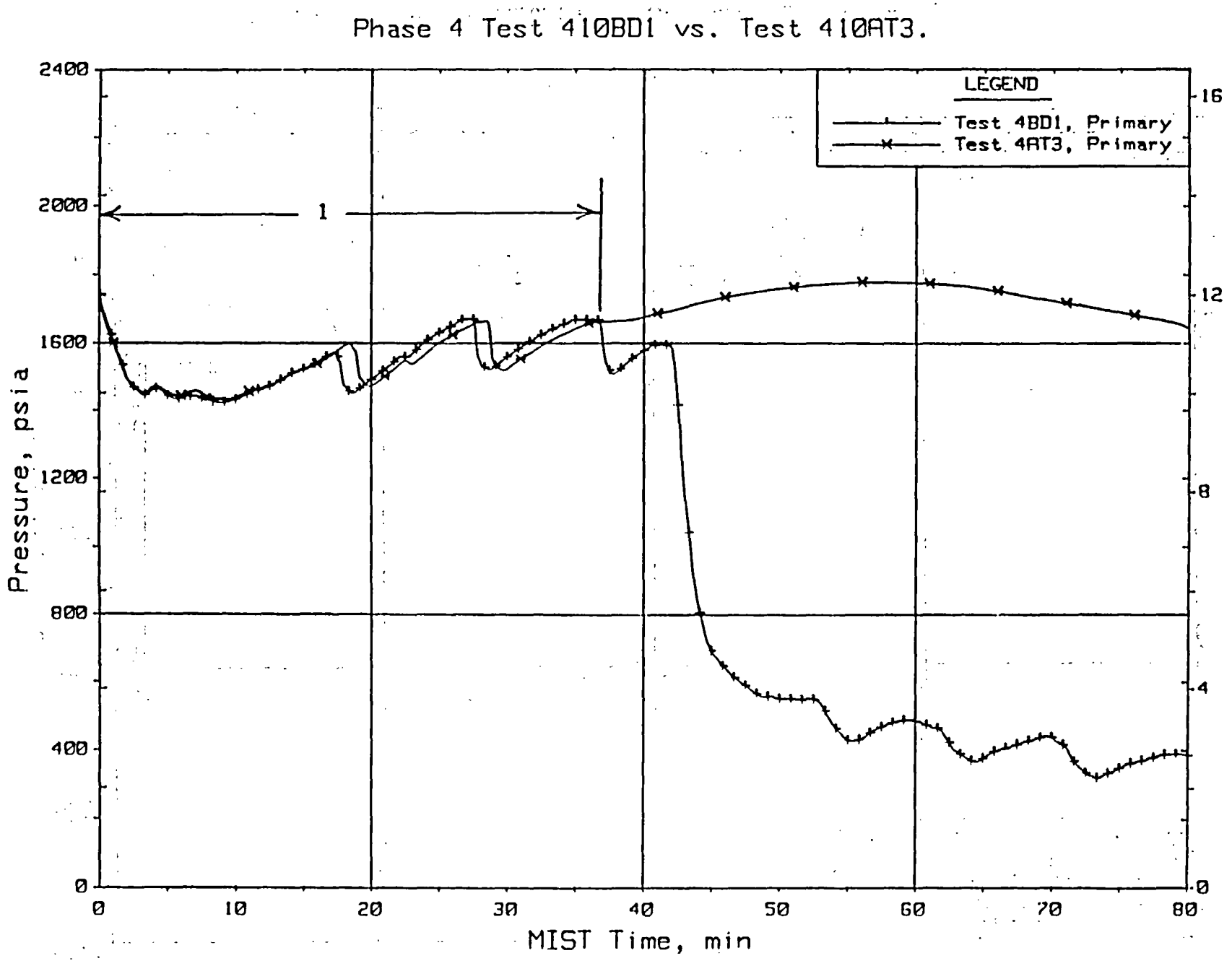

Figure 5. Primary System Pressures

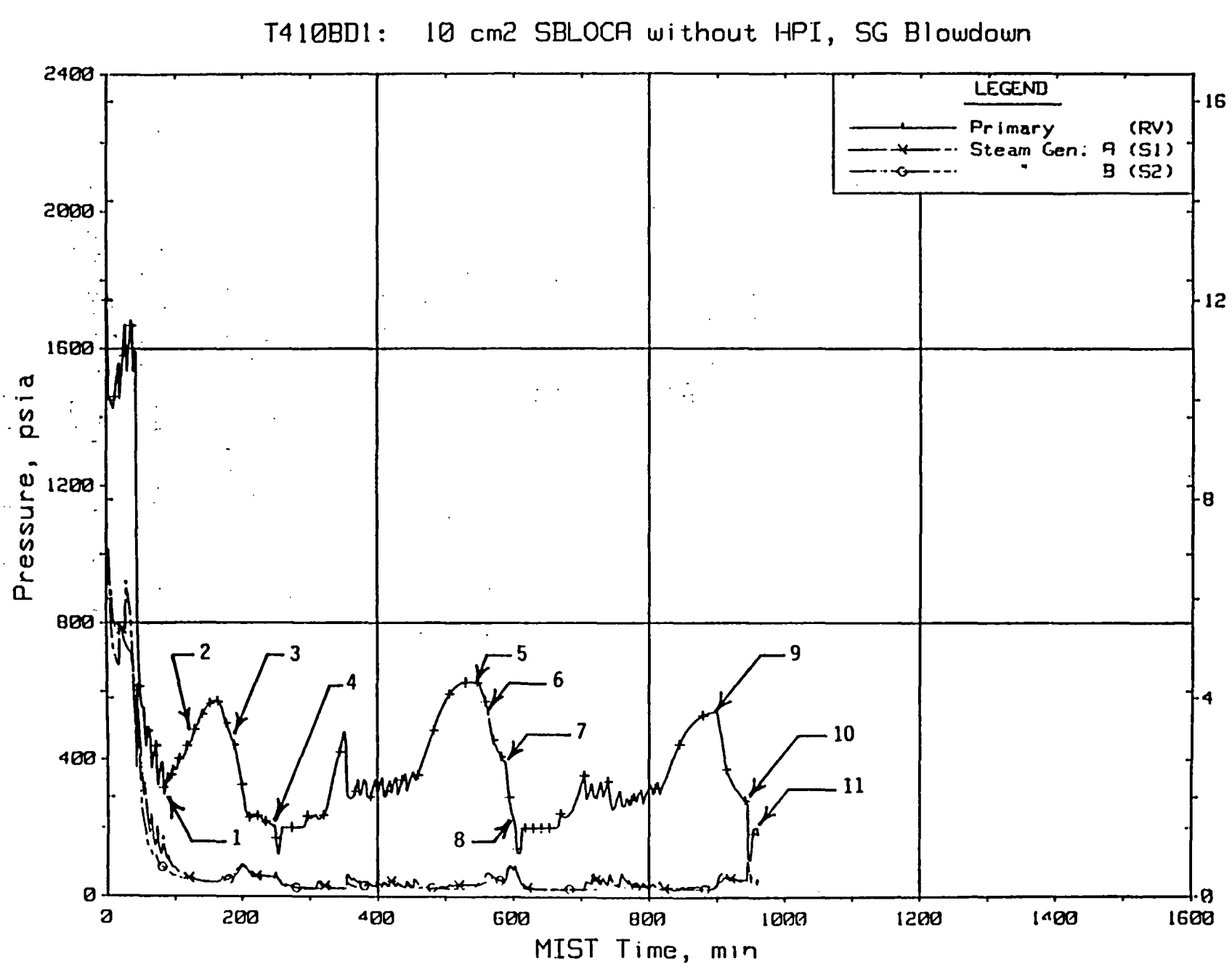

Figure 6. Primary and Secondary System Pressures (Test Duration)

NDE RELIABILITY AND ADVANCED NDE TECHNOLOGY VALIDATION(a)

S. R. Doctor, J. D. Deffenbaugh, M. S. Good, E. R. Green,
P. G. Heasler, P. H. Hutton, L. D. Reid, F. A. Simonen,
J. C. Spanner, T. T. Taylor, T. V. Vo

Pacific Northwest Laboratory
Operated by Battelle Memorial Institute
Richland, Washington 99352

ABSTRACT

This paper is a review of three NRC research programs dealing with the nondestructive examination (NDE) of light water reactors. The focus of work has been assessing the reliability of NDE (with emphasis on computer-based NDE equipment) for finding defects of interest to structural integrity, developing methodology for the ISI plan that overcomes NDE unreliability and provides greater assurance that unacceptable defects will be reliably detected and accurately characterized. There has been extensive work with Section XI and Section V of the ASME Boiler and Pressure Vessel Code.

INTRODUCTION AND HIGHLIGHTS

This paper reports on progress for three programs: (1) Evaluation and Improvement in Nondestructive Examination Reliability for Inservice Inspection of Light Water Reactors (LWR) (NDE Reliability Program), (2) Field Validation, Acceptance, and Training for Advanced NDE Technology, and (3) Evaluation of Computer-based NDE Techniques and Regional Support of Inspection Activities. The objectives and activities for each of the programs is summarized below.

The NDE Reliability Program objectives are to quantify the reliability of inservice inspection techniques for LWR primary system components through independent research and establish means for obtaining improvements in the reliability of inservice inspections. The areas of significant progress will be described concerning ASME Code activities, re-analysis of the PISC-II data, the equipment interaction matrix study, new inspection criteria, and PISC-III.

One of the emphases of the past five years on this program has been the development of requirements for NDE/ISI qualifications for personnel, equipment, and procedures. This work has achieved a major milestone since the requirements in Section XI Appendices VII and VIII have passed the formal

---

(a) Work supported by the U.S. Nuclear Regulatory Commission under Contract DE-AC06-76RLO 1830; Dr. J. Muscara, NRC Program Manager, FIN B2289, B2913, L1100.

acceptance process of ASME Code. Some work remains in that supplements for several inspection applications are still under development.

A re-analysis of the PISC-II round robin test data was made to apply commonly employed statistical analysis procedures to the data and to relate the data to parameters commonly used in the USA. The analysis showed some important trends and confirmed the importance of performing an effective, near surface examination.

The equipment interaction matrix is a study to develop a technical basis for permissible variation in equipment operational parameters for ultrasonic test systems. The work this past year focused on the development of worst case flaws that would cause the maximum adverse variation in equipment response. Once these were found, they were used to perform sensitivity studies to determine the amount of variation they caused in system response for a given variation in this parameter. In general, for bandwidth variations of up to 10%, the output was always limited to less that 10%. For narrow band systems, it was found that for small changes in center frequency, the system response could change radically--up to 40%. New requirements are in preparation for narrow band center frequency requirements.

The new inspection criteria task is developing methodologies and criteria for improved ISI (type, extent, frequency) to meet goals of failure probability, radiation releases, or core melt probabilities. Work on the use of probabilistic risk analysis (PRA) has been conducted on eight nuclear plants, and results have shown a significant trend in the data indicating that PRAs can be used to look generically at the ranking of reactor systems and to set a prioritization for their reliability insofar as they affect the stated goals. This work is occurring in conjunction with participation in an ASME Task Force on Risk-Based Inspection Guidelines.

Work continues in addressing the inspectability of coarse grained materials, and a topical report is being written. A cooperative program in conjunction with the Center for NDE at Iowa State University, under EPRI funding, is being conducted to develop engineering tools for requirements of surface specifications for ASME Code. Currently, Code has no UT surface requirements, and the goal of this work is to develop requirements to insure that the surface conditions do not preclude an effective examination from being conducted.

Participation continues in the PISC-III Program to relate the work of this international program to conditions and practices in the USA.

The objectives of the second program are to develop field procedures for the AE and SAFT-UT techniques, perform field validation testing of these techniques, provide training in the techniques for NRC headquarters and regional staff, and work with the ASME Code for the use of these advanced technologies. The focus of the work has been to use the SAFT technology to undergo blind testing at the EPRI NDE Center. This has involved tests with the technology to detect and characterize defects in thick section plates and

passing the IGSCC sizing performance demonstration test. Plans are in place to conduct further blind tests at the NDE Center and in the PISC-III Program.

The AE technology is undergoing evaluation in an on-reactor test to monitor a recirculation inlet nozzle-to-safe end weld on the Limerick Unit 1 Nuclear Power Station. This is a test to evaluate a condition detected by ultrasonic examination after replacement of the recirculation system piping and is being monitored to assess, in an on-line continuous manner, the condition of the component. Testing is currently in progress, and to date, the results have shown no significant trends. A code case on the AE technology is going through the formal process in Section XI.

The final program's objective is to evaluate the reliability and accuracy of interpretation of results from computer-based ultrasonic inservice inspection systems, and to develop guidelines for NRC staff to monitor and evaluate the effectiveness of inservice inspections conducted on nuclear power reactors. This program started in the last quarter of FY89, and the extent of the program was to prepare a work plan for presentation to and approval from a technical advisory group of NRC staff.

I. NDE RELIABILITY PROGRAM

1.0 CODE ACTIVITIES

Proactive participation in ASME Section XI activities continued toward achieving ASME Code acceptance of NRC-funded PNL research results to improve the reliability of nondestructive examination/inservice inspection (NDE/ISI). The objective of this task is to develop upgraded criteria and requirements for qualifying ultrasonic testing/inservice inspection (UT/ISI) systems.

During the past year, PNL representatives attended four different series of meetings held in conjunction with the ASME Section XI Subcommittee on Inservice Inspection of Nuclear Power Plant Components (SC-XI). PNL staff also attended meetings of the ASME Section V Subcommittee on Nondestructive Examination (SC-V), and its subgroups, to perform essential liaison in conjunction with our efforts to incorporate new Code requirements for acoustic emission testing, eddy current testing, and computerized imaging systems (i.e., SAFT). PNL staff hold memberships on the Working Group on Volumetric Examination and Procedure Qualification, Working Group on Surface Examination and Personnel Qualification, chair a Task Group on Acoustic Emission Monitoring, and serve as Secretary and voting member of the SC-XI Subgroup on Nondestructive Examination (SGNDE). Following each SGNDE meeting, minutes were prepared and distributed to a mailing list of about 75 addressees, along with agenda materials for the next meeting. In addition, PNL staff gave technical presentations to various SC-XI groups on: a) new inspection criteria and b) acoustic emission technology.

A proposed new Appendix VII on Personnel Training and Qualification received final Main Committee (M.C.) approval and was submitted to the Board on Nuclear Codes and Standards (BNCS). Four negatives were received from the initial BNCS letter ballot on Appendix VII, and a technical response letter was prepared to address concerns expressed in these negative ballots. The proposed Appendix VII received final BNCS approval on a second consideration letter ballot, and this document was subsequently published in the Winter 1988 Addenda to ASME Section XI.

A proposed new Appendix VIII on UT/ISI Performance Demonstrations was approved by SC-XI for submittal to the M.C. Both of the Section V representatives submitted negative votes during the initial M.C. consideration of this document. A technical response letter to these negatives was prepared, and selected SGNDE personnel (including a PNL representative) attended the Section V meeting in February in an attempt to resolve these negatives. This liaison effort was successful, and the SC-V representatives withdrew their negative votes during the next M.C. meeting. Upon M.C. approval, the proposed new Appendix VIII was submitted for BNCS consideration. Final BNCS approval occurred in August, and this document is now ready for publication in the 1990 Addenda to ASME Section XI.

Appendix VIII includes essentially all of the provisions of Code Case N-409-2, plus it extends the performance demonstration concept to other Section XI applications such as the clad/base metal interface of pressure vessel shell welds, nozzle inner radius areas, pressure vessel shell welds other than the clad/base metal interface, nozzle-to-shell welds, all piping, dissimilar metal welds, and bolting and studs. Publication of Appendices VII and VIII will represent a significant enhancement in the personnel qualification and performance demonstration requirements for all of the key Section XI ultrasonic testing applications. Furthermore, these documents provide a basis for extending these concepts to the other NDE/ISI methods required by ASME Section XI.

A proposed rewrite of Appendix IV on Eddy Current Examination of Nonferromagnetic Steam Generator/Heat Exchanger Tubing received approval by both the SGNDE and the Section XI Subcommittee during this reporting period. However, ASME approval of this document, which includes an upgrading of requirements for consistency with NRC needs and industry practice regarding multifrequency eddy current testing, has encountered difficulties during the M.C. review.

2.0 PISC II ANALYSIS

2.1 PRESSURE VESSEL INSPECTION

This is an overview of an analysis of ultrasonic inspection performance data that was gathered during an exercise called PISC II (Programme for the Inspection of Steel Components), an international round robin test of ultrasonic inspection capability. Inspection data was gathered on four heavy

section steel components which included two plates and two nozzle configurations. A total of 45 teams, including Europe, Japan, and the United States, produced 429 inspections that are listed in a computer data base that resulted from the PISC-II study.

The objective of this effort is to extract information from the PISC-II data set that is relevant to inservice inspection in the U.S. Specific topics that are relevant to U.S. inspection capability include:

- analysis of U.S. team performance with a comparison to overall performance
- analysis of team performance with respect to requirements of ASME Section XI, Appendix VIII for detection

The inspection data used in this study is a computerized data base available from PISC. Several extensive analyses have already been performed on this data base, and the PISC-II Committee has also summarized the results using simple statistical summaries. In this effort more formal statistical procedures have been applied to the computerized data set than those described in the PISC reports. Formal statistical procedures (i.e., hypothesis tests, log-linear models, and regression models) are used to more properly account for the experimental error in the measurements.

A brief description of the analysis methods and conclusions follow.

2.1.1 Detection Performance

The extent to which flaw detection is affected by the inspection and material variables was evaluated. The evaluation was performed by dividing the chi-squared statistic by its degrees of freedom to rank the variables with respect to importance in influencing POD. The result was that "flaw type" and "procedure" were the most important variables, and "flaw location" (i.e., clad/parent metal) and "country" (U.S./non-U.S.) were still significant but they were relatively of lesser importance. Notably, "flaw type" led all other variables in importance by a significant margin.

The flaws within the clad region were, on average, smaller than those in the base metal regions. This factor, combined with the inherent difficulty of UT inspection of coarse-grained cladding material, suggests that the POD values would tend to be worse for flaws in cladding than in base metal. Not surprisingly, the POD values were consistent with this hypothesis. For example, a manual technique using a 10% DAC (manual-10% DAC) threshold produced a base metal POD that was approximately twice the POD for the clad region. No significant difference between the clad and base metal POD curves were observed for either rough or smooth cracks.

Logistic regression analysis was applied to determine which of three flaw size parameters best correlated with POD. The flaw size parameters examined were: 1) flaw length, 2) flaw depth, and 3) cross-sectional area of

flaw (length times depth). Goodness-of-fit statistics were used to determine if the logistic regression satisfactorily explained the variability in the POD data. On this basis, it was found that flaw length was the most effective in explaining POD, flaw depth was next, and flaw cross-sectional area was least effective. Linear combinations of both depth and length were also examined, but this did not produce an equation that fit the POD data better, or was more reasonable, than either simple length, depth, or cross-sectional area.

2.1.2 Evaluation of PISC-II Inspection Data Using ASME Section XI Performance Demonstration Criteria

The PISC-II detection inspection capability was evaluated using criteria found in the newly adopted ASME Section XI, Appendix VIII entitled "Performance Demonstration for Ultrasonic Examination Systems." These new ASME criteria were applied to the PISC-II "Summary" inspection data from each team. The new Section XI criteria are more stringent for smaller samples sizes, which accounts for experimental error. Some of the Appendix VIII requirements could not be applied to the PISC-II data due to a lack of inner-radius flaws in the PISC-II data base, and the limited amount of blank material present within the PISC-II data. Furthermore, the data received had been cleaned and some non-defect indications were removed from the data base; thus, making it difficult to fully evaluate performance dealing with the false call criteria.

A subset of 25 flaws were selected from within the clad/interface region for evaluation using the ASME performance demonstration criteria. These flaws were all located within 1/4 wall thickness of the cladding for each plate. Of the 55 team/procedure combinations to which this test was applied, only 15% passed the ASME performance demonstration criteria. One reason for such poor performance was that of the 32 teams that examined Plates No. 1 and No. 2, only nine used inspection techniques designed to detect near-surface flaws. But of these nine, seven of them passed the ASME performance demonstration test. Thus, it may be concluded that only inspection techniques designed for detecting near-surface flaws should be used when attempting an ASME performance demonstration test involving near-surface flaws. The manual-20% DAC teams exhibited the best performance (32% of these passed), which is consistent with other situations in which the manual-20% DAC teams also performed well. It was also found that the performance of the clad-side inspections was much better than those performed from the unclad side (i.e., 37% of the clad-side inspections passed the ASME criteria compared with only 3% of the inspections performed from the unclad side). The reason for this is not understood.

The PISC-II results for flaws located within base metal were compared with the ASME Appendix VIII criteria for vessel shell examinations and nozzle-to-vessel welds. Forty-three flaws in PISC-II Plates No. 1 and No. 3 were selected for this portion of the analysis. These results were somewhat more favorable than those from the clad/interface test described above. For the vessel shell data, 34% of the teams met the Appendix VIII criteria; and for the nozzle-to-vessel weld data, only 6% of the teams met the ASME criteria. Again, the best results were achieved by the manual-20% DAC teams who achieved

an impressive 75% pass rate on the vessel shell examination. None of the techniques used were particularly effective for the nozzle-to-vessel weld examination; however, it should be noted that the nozzle geometry in Plate No. 3 was quite complex and presented a difficult inspection problem.

2.1.3 Conclusions

Key conclusions from the analysis are:

- Of all of the test variables examined, there was a significant difference between the performance of U.S. teams and other PISC-II participants, but it was the least of all the variables examined.
- A χ-squared test shows that for PISC-II data the three most important variables influencing flaw detection are flaw physical characteristics (e.g., rough or smooth), inspection procedure, and flaw size.
- Team-to-team variability is a large factor in both detection and sizing performance. This finding illustrates the need for serious study of the human element in ultrasonic inspection.
- The detection performance demonstration requirements proposed by ASME Section XI clearly screen inspection capability well. As an example, only those teams that used special inspection techniques for the clad region successfully passed ASME Code criteria for inspection of that region.

3.2 UT EQUIPMENT INTERACTION MATRIX

The objective of this subtask is to evaluate the effects of frequency domain, UT/ISI equipment interactions, and determine equipment tolerance values for improving inspection reliability. An integrated computer model for the entire inspection system including the pipe section and flaw has been developed to explore the effects of frequency interaction on flaw detection and sizing. This year, the computer model was used to determine the impact of equipment bandwidth and center frequency changes on inspection reliability. The important findings of the computer model calculations were confirmed by experimental measurements.

- Material defects whose inspection should be most sensitive to changes in equipment bandwidth and center frequency changes were identified, and the computer model was used to calculate the acoustic system transfer functions of seven of these postulated worst-case defects for various combinations of material thickness, probe size, and defect orientation. A paper entitled "Worst-Case Defects Affecting Ultrasonic Inspection Reliability" was written and accepted for publication in Materials Evaluation.

- An equipment bandwidth sensitivity study was performed using the computer model and the seven postulated worst-case defects. The results as shown in Figure 1 indicate that the ASME Code bandwidth tolerance of 10% may be sufficient to ensure 2 dB signal amplitude repeatability.

- An equipment center frequency study was conducted using the model and the worst-case defects. The results as shown in Figure 2 indicate that a center frequency change of 10% as allowed by current ASME Code would produce a calibrated echo response change of less than 2 dB for inspection systems with bandwidths greater than 100%. A center frequency tolerance of 5% is required to limit the echo response change of inspection systems with bandwidths between 25% and 100% to less than 2 dB. Further, the study indicated that inspection systems with bandwidths less than 25% may be too sensitive to center frequency changes to allow repeatable detection of worst-case defects.

- An experiment was performed to test the center frequency sensitivity of worst-case defect inspection. The experiment results were in general agreement with the modeling results, but the experiment results do not show as much sensitivity to equipment center frequency changes as the modeling results. The experimental results as shown in Figure 3 indicate that the ASME Code tolerance of 10% is sufficient for inspection systems with bandwidths of approximately 70%. A tolerance of 5% appears to be more appropriate for inspection systems with bandwidths less than 28%. More work needs to be done to determine if the model is over conservative. The results of the bandwidth and center frequency sensitivity studies were presented at the 1989 Review of Progress in Quantitative NDE conference and will appear in the conference proceedings.

It was concluded that the present equipment tolerance for equipment bandwidth is appropriate, but the center frequency tolerance will need to be more tightly controlled for narrow-band inspection systems.

3.0 NEW INSPECTION CRITERIA

Work continued on the assessment of the adequacy of existing ASME Code requirements for ISI and on developing technical bases for improving these requirements to assure safe nuclear power plant operation. Several interrelated activities on this task have been directed to the development of risk-based inspection requirements. Particular attention has been directed to inspection sampling plans and inspection intervals.

3.1 DEVELOPMENT OF RISK-BASED APPROACHES

During this past year, PNL has continued with the development and assessment of approaches for risk-based inspection requirements that utilize probabilistic methods of analysis. This activity has emphasized interactions with NRC staff, ASME groups, other laboratories, and industry efforts as performed by EPRI.

PNL has actively participated in an ASME Task Force on Risk-Based Inspection Guidelines, which is supported by ASME as a society funded research activity. Participation in this group is furthering the goals of the NDE Reliability Program, and will lead to specific recommendations for the introduction of probabilistic methods as a basis for ASME Section XI requirements. While the initial focus is on nuclear power, the group also is collecting insights from applications in other industries such as aircraft, petrochemical, and civil engineering structures. The research task force has met four times during the past year, and has made significant progress towards defining the key elements of a risk-based approach to inspection planning. PNL's probabilistic calculations for ranking inspection priorities has been an important input to the task force effort.

During the next year the ASME Task Force will issue a "white paper" giving general recommendations for risk-based inspection requirements. This particular document will be applicable to any industrial facility or structural system where structural integrity failures have the potential to lead to severe and costly consequences. During the coming year the ASME Task Force will turn its focus to developing a specific approach for the case of nuclear pressure boundary systems and components, and will eventually make recommendations to ASME Section XI for including risk-based methods into code requirements.

3.2 DATA BASE ON PLANT OPERATING HISTORIES

This activity responds to a recommendation from a 1987 workshop with NRC staff, which suggested that data bases and industry records be searched for information on piping failures and repairs, and also for information on findings of in-service inspections. Having selected the Nuclear Power Plant Reliability System (NPRDS) as the most useful source of such data, some 412 individual reports of piping failures were examined for useful trends and insights.

While the data base was known to be an incomplete compilation of all reportable field problems, it was nevertheless believed to contain date on some known problems. Most reports related to conditions of little safety significance, and therefore trends were sought only for cracking and wall thinning modes of degradation within larger diameter piping and components within the most safety significant systems. The data base is very limited in that for the conditions found it was not known if these areas were part of the ISI plan or had ever been inspected. The following trends were noted:

- About 50% of the defects were discovered by ultrasonic inspections performed in accordance either with ASME Section XI or on a supplementary basis. A large number of these reports corresponded to stress corrosion cracking of welds in stainless steel piping.

- Another 15% of the defects were discovered visually during code type inspections, with penetrant methods aiding in most of these detections.

- The remaining 35% of the defects were not discovered during code type inspections, but were found mainly through incidental observations of leakage.

In conclusion it would appear that ISI programs have had a mixed record of success in finding defects by nondestructive examination, and that the data supported a need for continuing efforts to increase the effectiveness of ISI through better sampling plans, more timely inspections and qualification of flaw detection capabilities.

3.3 PRA BASED INSPECTION PRIORITIES FOR EIGHT SELECTED PLANTS

Work continued on a major effort which applies results of existing Probabilistic Risk Assessments (PRA) to establish inspection priorities for pressure boundary systems and components. A pilot application of PRA methods to the Oconee-3 plant had been completed previously. This pilot study demonstrated that PRA methods are a useful tool for identifying those systems, components, piping sections and welds that need to be inspected with the highest priority. The pilot study was therefore expanded to address a larger sample of eight representative plants. The objective was to determine if trends from PRAs can be generalized to establish industry wide generic requirements for inservice inspection.

Table 1 lists the eight plants that have been evaluated. Criteria for selection of plants included:

- cross section of reactor vendors
- cross section of plant designs for each vendor
- A/E considerations
- PRA available for the plant
- exclude plants of unique and/or outdated designs.

The selection includes one or more plants from each for the three PWR vendors (Westinghouse, Combustion Engineering, and Babcock and Wilcox), and two BWR plants (General Electric).

Data from existing probabilistic risk assessments for these eight representative nuclear power plants were used to identify and prioritize the most relevant pressure boundary systems to plant safety. This study demonstrated the feasibility of using risk based methods to develop plant specific inspection plans. Figure 4 shows the rankings of the eight most important systems for the six selected PWR plants. This ranking of inspection priorities considered the consequences of a pipe rupture on plant safety (core melt probability) and also factored in best estimates of the failure probabilities for each of the systems.

TABLE 1. Plants Selected for the Feasibility of Developing Generic Inspection Requirements

Plant Name	Vendor	PRA Source
Surry-1	Westinghouse	NUREG/CR-4550, Vol. 1
Zion-1	Westinghouse	NUREG/CR-4550, Vol. 3
Sequoyah-1	Westinghouse	NUREG/CR-4550, Vol. 5
Oconee-3	Babcock & Wilcox	NSAC/60-SY
Crystal River-3	Babcock & Wilcox	FPC/SAI
Peach Bottom-2	General Electric	NUREG/CR-4550, Vol. 4
Grand Gulf-1	General Electric	NUREG/CR-4550, Vol. 6
Calvert Cliffs-1	Combustion Eng.	NUREG/CR-3511

The results for the eight representative plants generally indicated generic trends for inspection priorities applicable to all PWRs or BWRs. However, the PRA's did show special cases where systems at particular plants may need additional ISI to address special safety concerns for these systems. In certain cases the results suggest improvements in current inspection plans and priorities which are now set by the code in accordance with existing assignments of systems to Class 1,2 and 3 categories.

4.0 PIPING INSPECTION TASK

4.1 INSPECTION OF CAST STAINLESS STEEL

The objective of this task is to evaluate the effectiveness and reliability of ultrasonic inspection of cast materials used within the primary pressure boundary of LWRs. Due to the coarse microstructure of this material, many inspection problems exist and are common to structures such as cladded pipe, inner-surface cladding of pressure vessels, statically cast elbows, statically cast pump bowls, centrifugally cast stainless steel (CCSS) piping, dissimilar metal welds, and weld-overlay-repaired pipe joints. Far-side weld inspection is an inspection technique included in the work scope since the ultrasonic field passes through weld material. Activities included progress in drafting a NUREG/CR topical report on CCSS and procuring a computer-controlled, tone-burst system for evaluation on inspecting CCSS. Advantages of the tone-burst system include high acoustic power, phase measurement of the gated signal, and automated and highly accurate time-of-flight measurements for determining ultrasonic velocity.

4.2 SURFACE ROUGHNESS CONDITIONS

The objective determined for this work was to establish specifications such that an effective and reliable ultrasonic inspection is not prevented by the condition of the exposed surface. Past efforts included an attempt to quantify the effect produced by an outer surface irregularity. This approach was then modified through cooperation between the NRC and EPRI in establishing a mathematical model to be used as an engineering tool to derive guidelines for surface specifications. Activities for the past work period included approval of a coordination plan between EPRI, NRC, the Center for NDE (CNDE) at Ames Laboratory, and PNL; formulation of a matrix of ultrasonic search units, material, geometry, and flaws of interest for future model usage; and discussions concerning development of a research software code for predicting ultrasonic responses in isotropic material.

Both EPRI through the CNDE at Ames Laboratory and the NRC through PNL have developed capabilities that are uniquely suited for establishing a validated model. First, CNDE has extensive experience in the computational modeling of ultrasonic wave propagation fields in solid materials. Second, PNL has extensive experience in mapping ultrasonic fields in solids which is required for providing feedback during model development and for model validation. For this reason, EPRI and the NRC approved a coordination plan in which the two organizations, through the referenced institutes, will cooperate in attempting to determine and validate an ultrasonic computer model.

Experimental measurement of microprobe directivity has been a major concern for the last year. Techniques included use of a half cylindrical block of steel on which an ultrasonic transmitter is circumferentially positioned and a microprobe is positioned at the cylindrical axis as a receiver. The coupling inconsistency, however, of using a piezoelectric, normal incidence, shear-wave transducer has prevented detailed knowledge of the shear-wave directivity of a microprobe. Implementation of a shear-wave electromagnetic acoustic transducer (EMAT) is planned and is expected to solve this problem.

The first major milestone is a research software package which will permit the analysis of surface discontinuities involving isotropic material. Delivery of the software from CNDE to PNL is scheduled for March 1990. After delivery of the software, work is to continue in parallel with expansion of the model to includes anisotropic material for determining guidelines for surface condition when inspecting isotropic material.

4.3 PISC-III

The involvement in the Program for the Inspection of Steel Components Phase 3 (PISC III) is to take advantage of a large international program to support the acquisition of data bases for assessing the reliability of NDE. The PISC program has seven actions devoted to the in-depth study of particular aspects of NDE. Tracking and assessment is occurring for all of these actions, but the discussion here will be on Action 4 for studies on Austenitic Stainless

Steels (AST). PNL, by virtue of this program, is one of the Action 4 co-leaders and has been actively involved with the design, development, and implementation of this action.

The activities this year have focused on finalizing the test design based on the sources of specimens and the supplies of raw material and defects. The program will begin round-robin testing in the spring of 1990 with capability studies on wrought stainless steel. All of the defects exist except for several thermal fatigue cracks and some fabrication-type defects that are being manufactured. Basically, all of the material has been purchased for the CCSS studies, and this represents a major financial investment. These pieces must now be welded together and then defects grown. It is anticipated that the earliest that round-robin testing can begin will be in the middle of 1990 for capabilities studies on CCSS.

The NRC through this program has offered to perform the data analysis for the AST. This involves not only the analysis but writing the report to document the study, results, and conclusions. Several reports will be prepared for the capability, parametric, and reliability studies that are being conducted in this action.

Additional work performed for PISC has included the coordination of the USA teams that examined the PISC Blocks 20, 24, and 25. These were safe-end welds that contained defects, and the studies focused on three different configurations for both BWRs and PWRs. Teams from Commonwealth Edison and Southwest Research Institute were the only ones from the USA for the Action 3 on Nozzles and Dissimilar Metal Welds. We expect other teams to participate in other PISC actions.

II. FIELD VALIDATION, ACCEPTANCE, AND TRAINING FOR ADVANCED NDE SYSTEMS

The program was established to finish up the final steps in the field validation, training, and gaining Code acceptance of the acoustic emission technology and the synthetic aperture focusing technique for ultrasonic testing (SAFT-UT) technology. These two technologies were developed and received extensive laboratory testing but had not received extensive field testing and had not been accepted by the Code bodies. The following contains highlights of these activities and the progress which has been made to complete the work for using these technologies for light water reactor applications.

ACOUSTIC EMISSION

CODE ACTIVITIES

An ASME Code Case version of an earlier Nonmandatory Appendix concerning AE monitoring of reactor components to detect cracking during operation has

been approved by ASME Section XI. The Code Case focuses on monitoring identified flaw indications for growth during reactor operation. The Code Case received three negatives votes at the first consideration by Main Committee. These were resolved but since there were some substantive changes, it returned to Main Committee still on a first consideration basis for the 9/15/89 meeting. It received one negative which must be resolved before the Code Case goes to the Board on Nuclear Codes and Standards.

FIELD VALIDATION

An AE monitoring system has been installed at Limerick Unit 1 Reactor for surveillance of a pipe weld flaw indication detected during a refueling outage in early 1989. Figure 5 shows the installed AE sensors. Instrumentation developed by PNL for NRC under the AE/Flaw Characterization Program is being utilized in this application. Philadelphia Electric Company is supporting this effort as a validation test of AE technology for on-line monitoring of reactor components to detect growth of flaw indications. The AE system has been in operation since May 1989 and appears to be operating satisfactorily. A few AE signals are being detected which locate in the vicinity of the weld. Coolant flow noise has not been a problem. Monitoring is expected to continue for the duration of the current fuel cycle (approximately October 1990).

Plans are still in place to AE monitor Watts Bar Unit 1 reactor when it starts operation. Fueling is currently scheduled for late 1991.

An earlier effort to apply AE technology to surveillance of pipe weld flaws in a Taiwan Power Company reactor did not materialize. Taiwan Power Company funded a visit to the plant in January 1989 and requested a proposal for the application. The proposal was submitted, but it was not funded.

SEMINARS

AE program and SAFT-UT program (including SAFT system demonstration) results and plans were presented at a workshop attended by Region I, II, IV, and NRR personnel in October 1988 at King of Prussia, Pennsylvania.

REPORTS

Hutton, P. H. 1989. "Acoustic Emission for Continuous Monitoring of Light Water Reactor Systems - Current Status" in Proceedings of the 1989 Post-SMiRT Conference No. 14, Monterey, CA, August 23-24, 1989.

SAFT-UT

CODE ACTIVITIES

A draft proposal to add requirements for computerized imaging ultrasonic systems to ASME Section V was prepared and submitted to the SC-V Subgroup on

Ultrasonic Testing. This proposed text would add new requirements under the Article 4 paragraph T-435, plus a Nonmandatory Appendix to provide detailed discussion/requirements for synthetic aperture focusing technique (SAFT) concepts. The proposal provides for the addition of text for other computerized imaging ultrasonic systems.

FIELD VALIDATION

Extensive testing was conducted on the SAFT-UT system at the EPRI NDE Center. This involved a number of tests. The first test was the passing of the IGSCC sizing test for performance demonstration. This test was taken in the form of meeting the intent; but since PNL staff are not certified Level I, II, or III personnel, the test was not taken for PNL personnel to be qualified for field testing. The same performance demonstration test was given to PNL staff that inspectors trying to qualify would have taken. The NDE Center provided a letter that stated that if the PNL staff had taken the performance demonstration test, then they would have achieved the following performance which was a passing grade.

The SAFT-UT system was also tested on four blocks that the NDE Center has which were manufactured from reactor pressure vessel dropouts. These specimens were scanned from the ID using several different inspection probes. These results are being finalized for submission to the NDE Center and will have to await the evaluation of the SAFT performance.

A series of blocks removed from the Midland reactor pressure vessel were examined with the SAFT-UT system. These results are undergoing evaluation and will be provided to Oak Ridge National Laboratory to guide them in cutting specimens from the blocks which contain no defects. The defects will be saved for further NDE studies and evaluation of SAFT-UT performance. This will occur over the next year and, hopefully, will be fully available for disclosure at next year's annual meeting.

III. EVALUATION OF COMPUTER-BASED NDE TECHNIQUES AND REGIONAL SUPPORT OF NDE ACTIVITIES

Ultrasonic inspection systems that use computers to image defects or process data for analysis are rapidly becoming standard for inservice inspection. The reliability of these systems and the proper integration and interpretation of results needs to be established. NRC staff (Regional and Headquarters) who are responsible for reviewing, evaluating, or auditing the field results and use of computer-based ultrasonic systems need additional knowledge to perform these tasks effectively. This project is designed to provide NRC staff the additional knowledge, training, and support for evaluating the reliability and proper use of computer-based ultrasonic systems.

This program has two objectives: the first is to evaluate the reliability and determine the proper usage and interpretation of results from computer-

based ultrasonic inservice inspection systems. The second objective is to develop guidelines for NRC staff to monitor and evaluate the effectiveness of inservice inspections conducted on nuclear power reactors. The objectives will be met by conducting the following activities.

- Review computer-based ultrasonic systems (hardware and software) used in the field to assist ISI functions. Initial efforts will be focused on TEST-Pro and other PC-based systems.

- Develop guidance and provide training for NRC staff to review/audit the use of computer-based UT systems.

- Assess the reliability of computer-based ultrasonic systems according to the requirements of ASME Code Case N 409 Rev. 1 and proposed Appendix VIII. In addition to reviewing existing data, this task will require the conduct of round robin testing.

- Provide ultrasonic test blocks that contain a variety of defects and reflector types and sizes for circulation to NRC staff, especially to the regions.

- Develop a software library of digitized RF ultrasonic signals from a variety of defects and reflectors. The library will have full documentation on all digitized signals and operation of the library and will be compatible for use with NRC equipment.

- Review the feasibility of developing a portable (hand-held) instrument to digitize and record ultrasonic signals on media compatible with PCs for later evaluation. If approved, a prototype model will be developed for use by NRC staff for auditing field inspections.

- Apply acoustic modeling techniques to define UT signal properties which may be used to aid classifying indications as having originated from cracked or noncracked components in various materials and geometries.

This program was initiated in July 1989 and the only work conducted to date was to develop plans for presentation and review by an NRC staff Technical Advisory Group (TAG). The first TAG meeting will be held on October 25, 1989, to focus the program based on priorities established by the NRC staff.

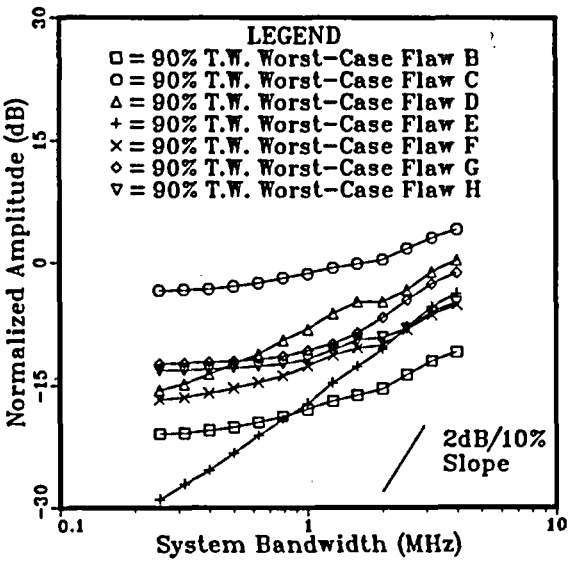

FIGURE 1. Bandwidth Sensitivity Study Results for Seven Postulated Worst-Case Flaws

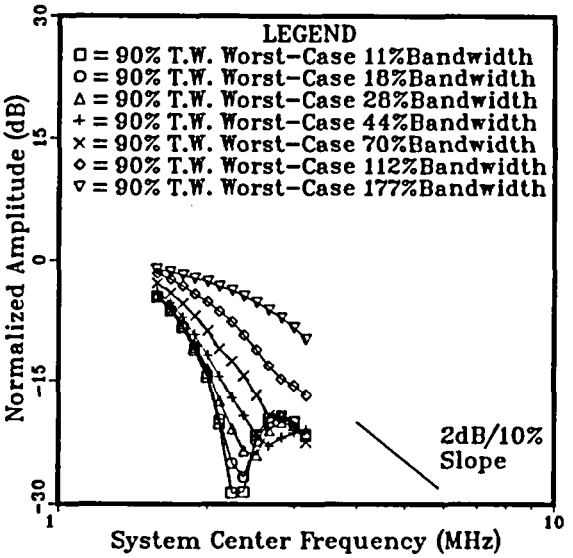

FIGURE 2. Center Frequency Study Results for a Postulated Worst-Case Flaw

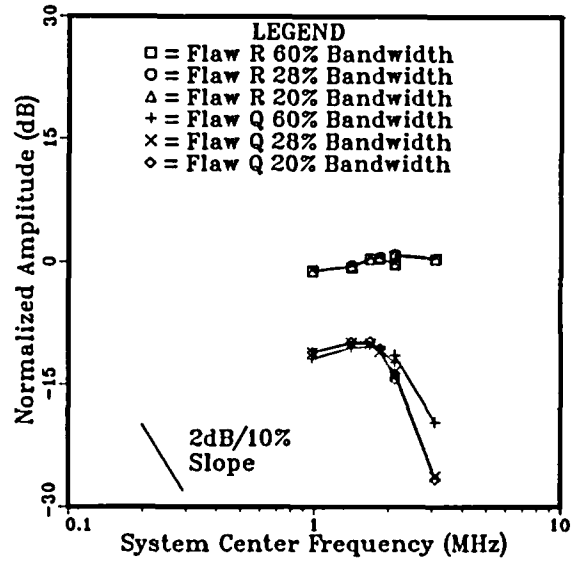

FIGURE 3. Center Frequency Sensitivity Study Results for 50% Through-Wall Flaws

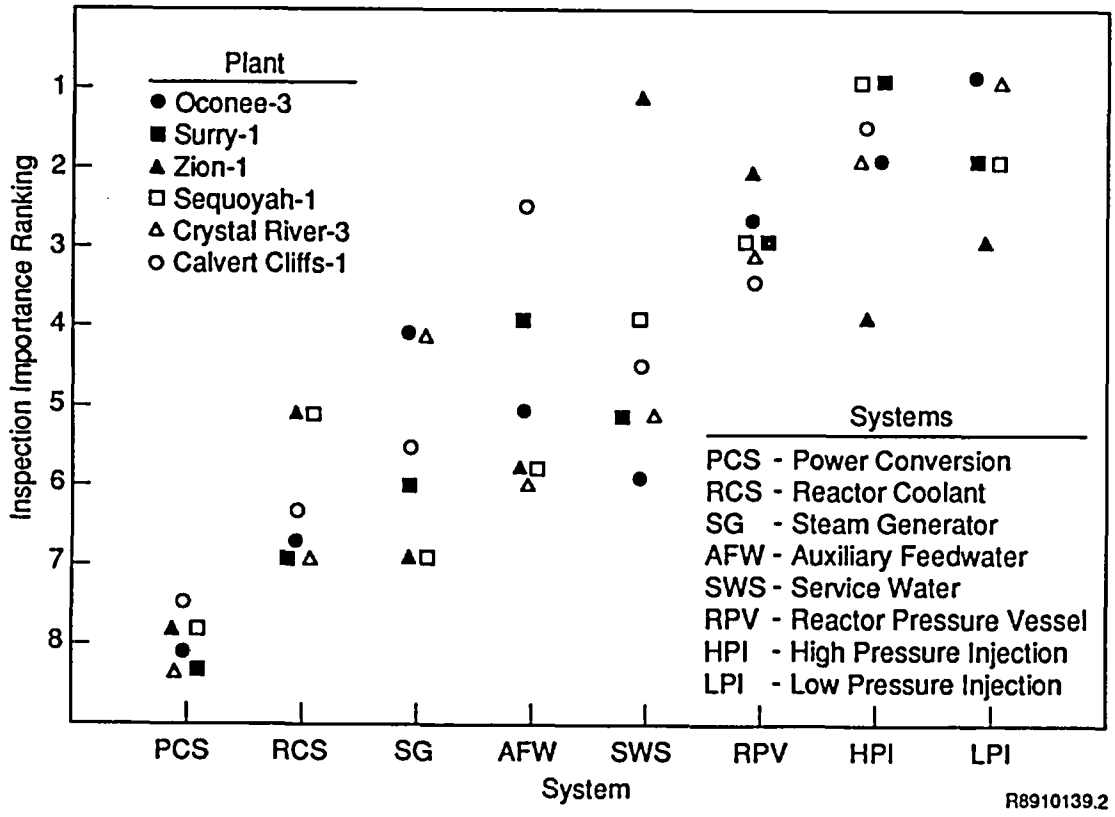

FIGURE 4. Weld Inspection Importance Ranking for Various PWR Systems Based on Core Damage Frequency

AE Monitoring - Limerick Unit 1 Reactor

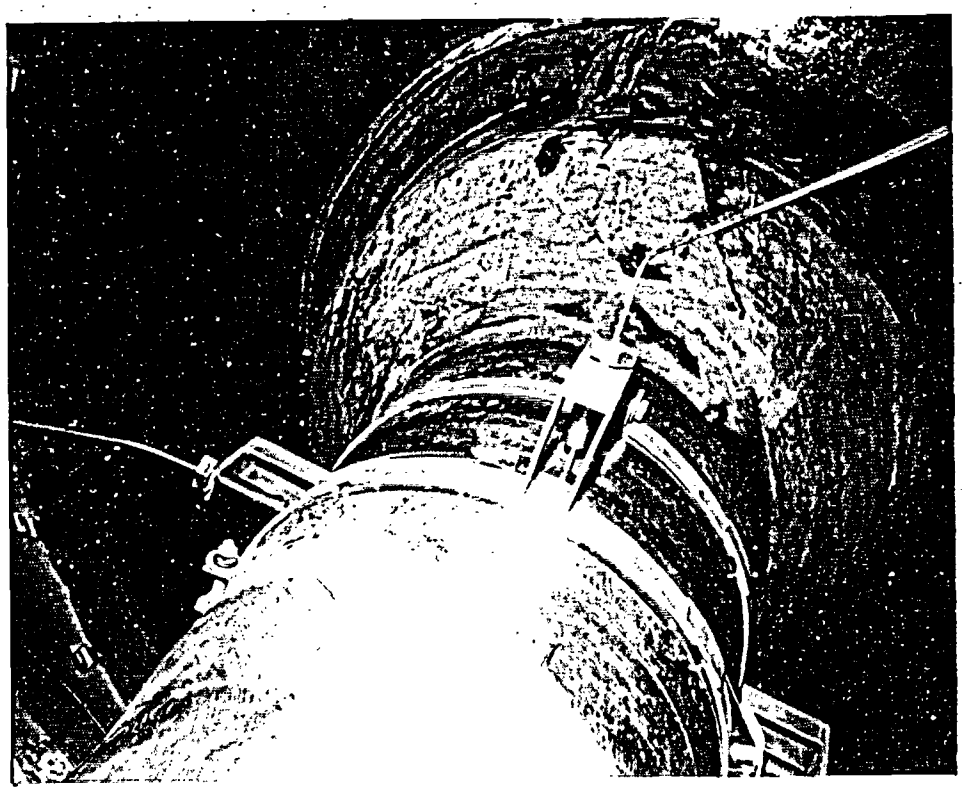

AE Sensor Waveguides Mounted On Pipe

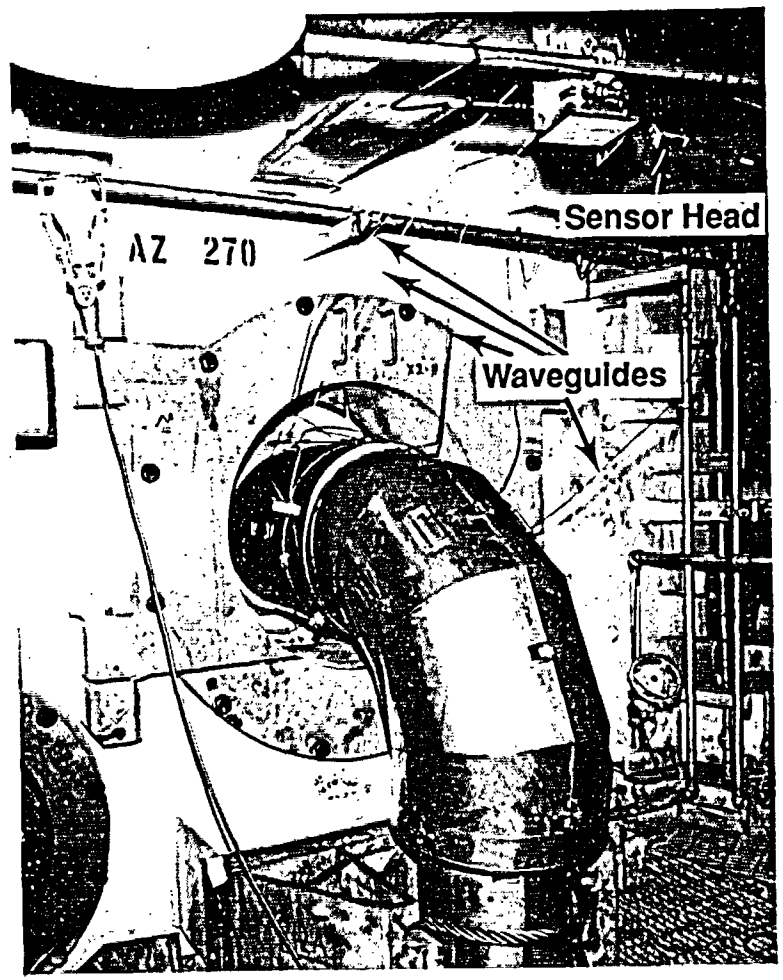

External Arrangement

FIGURE 5. AE Monitoring Pipe Weld at Limerick Unit 1 Reactor

IMPROVED EDDY-CURRENT INSPECTION FOR STEAM GENERATOR TUBING*

C. V. Dodd, J. R. Pate and J. D. Allen, Jr.

Oak Ridge National Laboratory
P.O. Box 2008, Oak Ridge, TN 37831-6158

ABSTRACT

Computer programs have been written to allow the analysis of different types of eddy-current probes and their performance under different steam generator test conditions. The probe types include the differential bobbin probe, the absolute bobbin probe, the pancake probe and the reflection probe. The generator test conditions include tube supports, copper deposits, magnetite deposits, denting, wastage, pitting, cracking and IGA. These studies are based mostly on computed values, with the limited number of test specimens available used to verify the computed results. The instrument readings were computed for a complete matrix of the different test conditions, and then the test conditions determined as a function of the readings by a least-squares technique. A comparison was made of the errors in fit and instrument drift for the different probe types. The computations of the change in instrument reading due to the defects have led to an "inversion" technique in which the defect properties can be computed from the instrument readings. This has been done both experimentally and analytically for each of these probe types.

Measurements and computations were also made of the effect of sampling rate on the accuracy of the defect depth measurement for the bobbin probe. For simple defect signals, a relatively coarse sample rate is sufficient to determine the defect depth. The frequency response of the signal produced as the coil is scanned past the defect determines the desired response of the instrument amplifiers.

Neural networks have been applied to the analysis of eddy-current defect scans in the presence of other signals, such as tube supports, magnetite deposits, and copper deposits. These networks are used on unmixed data and have worked very well for the limited data sets evaluated thus far.

COMPUTER CODE FOR EDDY-CURRENT ANALYSIS

ORNL has written and maintained computer codes for the solution of general eddy-current problems for a number of years. These programs have been updated for use on the PC-AT Clone computers and modified specifically for steam generator-related problems. Many of the new programs have been collected and incorporated

* Research sponsored by the Office Nuclear Regulatory Research, Division of Engineering, U.S. Nuclear Regulatory Commission under Interagency Agreement DOE 1886-8041-7B with the U.S. Department of Energy under Contract DE-AC05-840R21400 with Martin Marietta Energy Systems, Inc.

into a report with instructions for their use and examples of the computer runs.[1] Programs have been written to analyze the probe types shown in Figure 1. These include the differential bobbin probe, which is the most common type of probe used for steam generator tests. The problem of the absolute bobbin probe is very similar, and a second set of programs performs the computations for this problem. The pancake probe, which has many features contributing to a very significant increase in signal-to-noise ratio over the bobbin probe, is also included. The pancake coil inspects a smaller volume of tube than the bobbin coil and exhibits increased sensitivity at the expense of longer inspection times. The reflection coil exhibits still better performance than the pancake coil but is more complex to manufacture and more expensive.

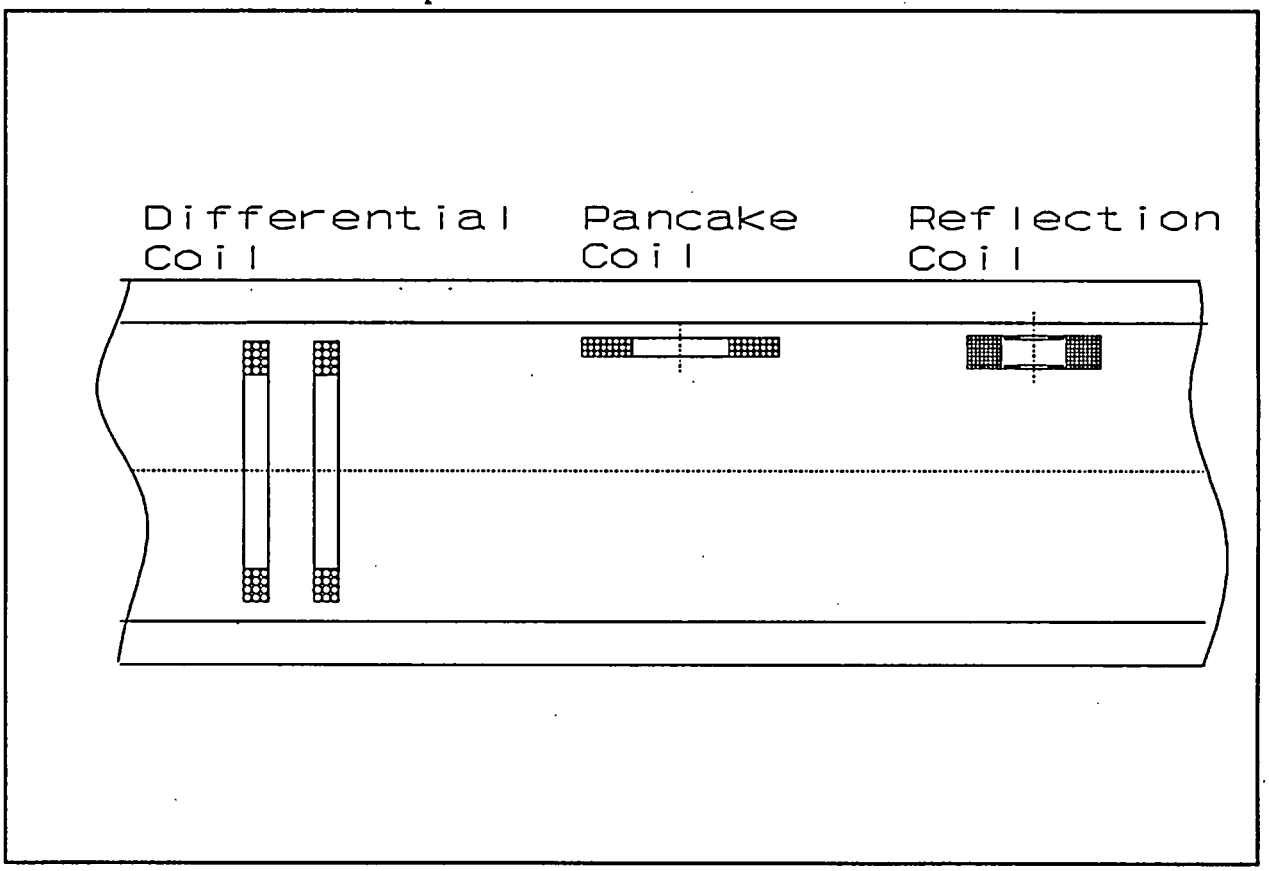

Figure 1 Bobbin probes (absolute and differential), pancake probes and reflection probes are used for eddy-current tests

These probes include most common types used in steam generator inspections. The programs are written to compute the coil impedances or coil voltages and calculate the changes produced as the probe is scanned past a point defect. The point defect can be averaged over depth or volume to approximate a finite sized defect. The response to a defect can be approximated by a defect sensitivity

[1] J. R. Pate and C. V. Dodd, *Computer Programs For Eddy-Current Defect Studies*, ORNL/TM in progress, 1989.

factor multiplied by the volume of the defect. Some of the programs calculate the defect sensitivity factor for an array of defect locations located around the coil and plot contours of the magnitude and phase of the defect sensitivity factor. This is very useful in visualizing the field pattern of a coil system and the response of a defect at various locations throughout the tube wall. Additional programs perform the direct computation of the volume and depth of the defect from the magnitude and phase of the signal as the probe scans across the defect.

DETERMINATION OF DEFECT SENSITIVITY FACTOR FOR PROBES

As an example we have calculated the defect sensitivity factor for a differential bobbin probe. In Figure 2 we show the magnitude of the defect sensitivity factor for the entire probe.

The signal is zero when the defect is far from the probe, increases to a maximum value when the defect is close to the center of the windings of the first coil, and goes to zero again when the defect is located exactly between the two coils. The signal has an anti-symmetrical response as the defect moves past the second coil, reaching a minimum near the center of the windings on the second coil and then increasing to zero as the defect moves far from the probe. One can think of the phase shifting by 180 degrees as the defect passes the probe center, or the amplitude going from positive to negative. The latter convention seems to make the problem easier to explain. The response to the defect is symmetrical with respect to either coil if the coils are far apart, but because the coils are in opposition and the defect signal from each coil is subtracted from the other, the response between the coils is skewed, with the maximum signal shifting toward the outer edge of each coil.

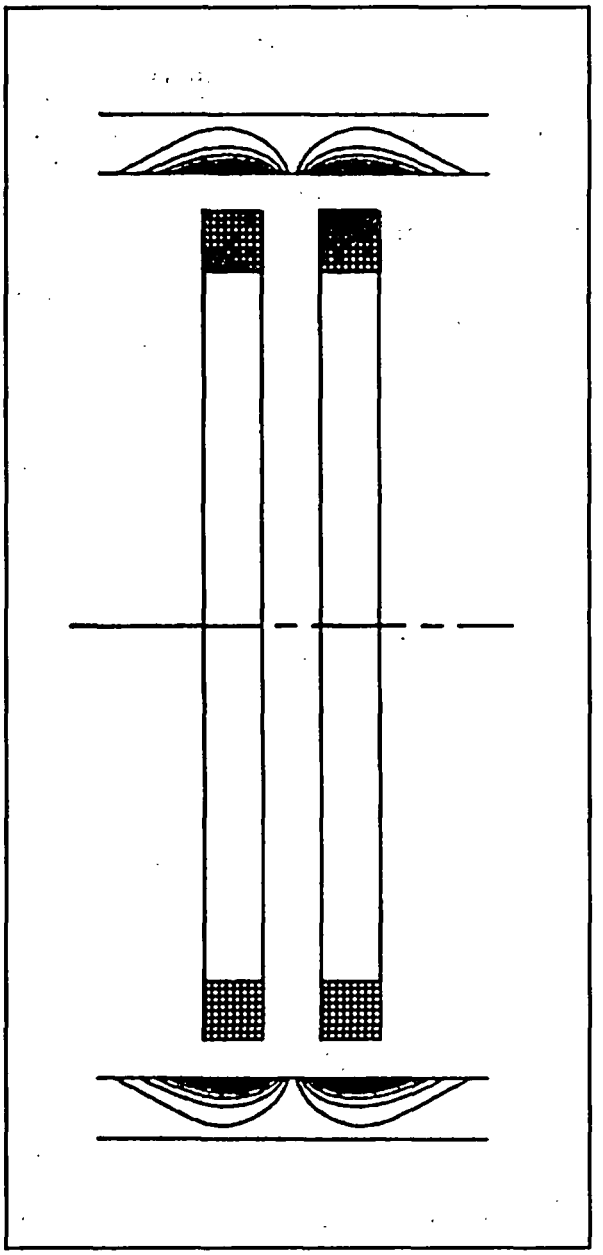

Figure 2 Magnitude contours of the defect sensitivity factor for a differential bobbin probe. These contours represent the magnitude of the impedance change due to a point defect at different locations in the tube wall.

Because of the symmetry of the coil and conductor in Figure 2, the same information is repeated in each of the four quadrants. Thus the behavior can be more clearly represented by a plot of magnitude of the defect sensitivity factor in only the upper left quadrant, as shown in Figure 3. This plot gives more detail than was available in the previous figure. The dotted line represents the probe center where the magnitude has decreased to zero. Since the defect sensitivity factor is a complex quantity with both magnitude and phase, we can also plot the phase as shown in Figure 4. The phase shift increases with distance into the tube and remains relatively constant with distance along the tube. This phase shift increase with distance into the tube is the main contribution to the phase shift with defect depth observed in our eddy-current tests. The phase shift when the magnitude of the signal approaches zero at the probe center is undefined. If we adopt the convention that the amplitude changes sign as the defect passes the center of the probe, the phase has the same value on the opposite side and a smooth transition between. Otherwise, it would vary by 180 degrees as the defect passed the center, giving a discontinuous shift in the phase.

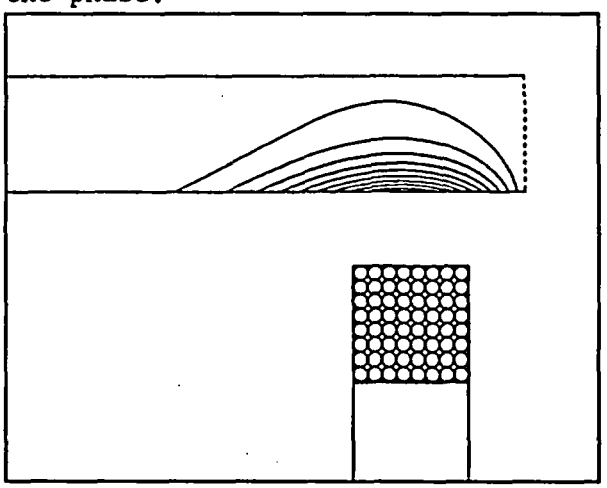

Figure 3 Magnitude contours of the defect sensitivity factor for one quadrant of a differential bobbin probe

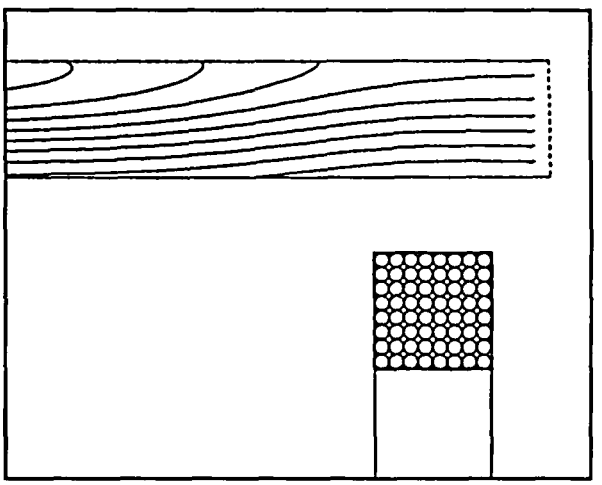

Figure 4 Phase contours of the defect sensitivity factor

From the shape of the defect sensitivity factor curves, we can see how the probe would respond to a small defect anywhere within the metal. These plots show how the sensitivity to a small defect falls off as the defect approaches the tube outer surface and show the volume of metal that is being inspected by the probe. Defect sensitivity factor curves for the pancake and reflection probes fall off much more rapidly with distance into the metal. They are less sensitive to property variations on the outer surface of the conductor, such as copper deposits, magnetite deposits, or tube supports. They also are sensing a smaller volume of material at one time and so are still sensitive to small defects on the outer surface. On the other hand, due to their relatively small size, they are more sensitive to spacing variations between the coil and metal. Therefore their liftoff must be controlled by mechanical means or by electronic compensation. For best results, a combination of the two is necessary.

MINIMIZATION OF SYSTEM ERRORS

Various probe systems can be compared for different conditions and property variations using ORNL-developed multiple property techniques. If we have a set of property variations for a given eddy-current test, we can either measure or calculate the response of our eddy-current instrument for each possible combination of the test properties. In general, the calculations are performed first since they can be made quickly and cheaply, particularly compared to the cost of constructing accurate standards and making experimental measurements. Later, when a good system design is achieved, we can construct the probe, standards, and instrument and make the measurements experimentally, since we are not generally able to construct the probe to the accuracy needed to use the same calibration coefficients. Then, since we know both the instrument readings and the initial test properties, we can calculate a set of least-squares coefficients to relate the properties to the readings. Due to the nonlinearity of eddy currents, it is generally better to use a polynomial function of the readings rather than the readings directly. This does not affect the least-squares process and yields a much better fit between the readings and the properties.

The properties can then be recomputed using the coefficients and compared to the original set of properties with which we started. The difference between these two sets is called the fit error. In addition to the fit error, there is a second error known a drift error. Since all instrument measurements have some error, we vary each individual reading by the maximum amount that the instrument can drift, and compute the change in the property. The absolute sum of the individual errors is called the drift error. An rms sum of the drift error and the fit error gives us a good measure of how accurately we can perform a given inspection. We can also vary the coil design, operating frequency, instrument design, the degree and type of instrument reading polynomial, and in some cases, the sets of property variations that we will allow. Comparisons can be made of the error present in the various tests, and the best compromises can be chosen. In general, the best system design will have fit and drift errors of about the same size. In Figure 5 we show how the error in calculation of the defect size varies with coil mean radius for pancake and reflection probes.

We can see that the reflection probe gives a more accurate measurement of the defect depth for this particular set of properties. We can also see that the measurement error is relatively constant with probe size. The error due to liftoff variation decreases as the probe size is increased but is offset by an increase in errors due to property variations on the outside of the tube. The pancake coil error reaches a minimum at a mean radius of 0.040 in., while the reflection probe error reaches a minimum at a smaller mean radius. Usually a second factor, such as the amount or coverage of the tube, will force a compromise to be made. In order to achieve adequate coverage of a tube with 0.875 in. diameter with an array of sixteen coils, the probe mean radius needs to be about 0.040 in. The sensitivity increases very little for smaller sized reflection probes. A set of coefficients is obtained for each property we wish to calculate, and that set of coefficients multiplied by the readings extract that particular property, even in the presence of the variation of all of the other properties. This overall technique is very general and will work for any type of instrument readings and set of properties. It has been applied

successfully to a number of complex eddy-current test problems in addition to the steam generator problems. The instrument readings that have been used were both multiple frequency and pulsed. Data from other types of NDE tests can also be used as the instrument readings, although this technique has not been widely applied outside of eddy-current tests as of this date.

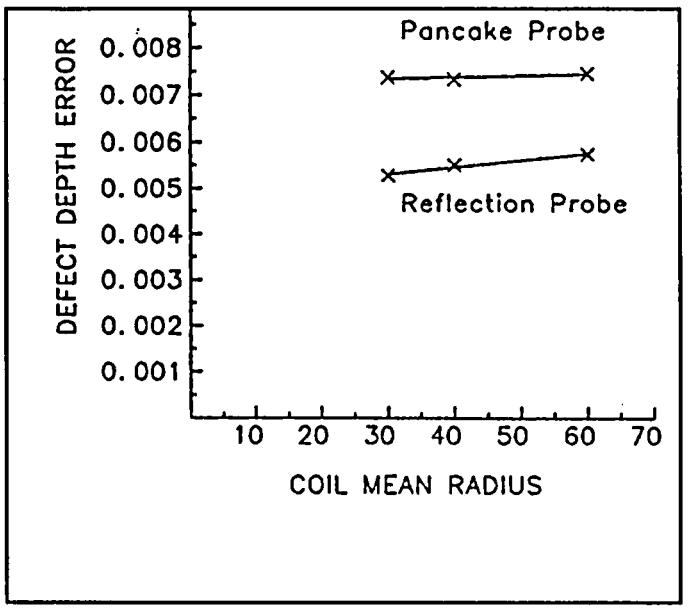

Figure 5 Defect depth measurement error for a reflection probe and a pancake probe plotted against probe mean radius

As an example of the polynomial fit optimization process for a given system, defect depth error data were determined for 780 different combinations of properties with a second order reading polynomial for the magnitude and phase and a cross term between the magnitude and phase. Thus, there were as many as five reading terms for each frequency. In general, the defect accuracy increases for higher order polynomial fits and decreases as more properties are added to the set. For an increase to a third degree polynomial, the fit error decreased by about 20%. Since, for this problem, the fit error was considerably larger than the drift error, the rms error also decreased by about 20%. On the other hand, the number of possible combinations of polynomials and the time required to calculate all of them is increased by a factor of 27. A computer program is used to find the best polynomial fit for each simultaneous combination of three operating frequencies. The frequencies are selected from a set of six frequencies, and only the best fit and the lowest rms error are printed out for each three-frequency combination. Most of the preliminary design is done with second order polynomial approximations and for a relatively small number of property sets until we approach a final design. Then the longer running studies with higher degree polynomials and larger sets of properties can be performed.

SAMPLE RATE STUDY

Another application of the use of our computer codes has been for a sample rate study.[2] The study was initiated to resolve questions about a proposed modification of the inspection code. In the study, both the rate of sampling as the tube was scanned and the instrument frequency response were investigated. The study consisted of both experimental measurements made on ASME Section XI standard defects using a Zetec MIZ17 and the computed effects of a point defect.

---

[2] C. V. Dodd, *Effects of Sampling Rate on Eddy-Current Measurements*, Oral Presentation at ASME meeting, Salt Lake City, January 16, 1989.

The ASME defects are much longer than a point defect so that the latter represents the limiting case for both the sample rate and frequency response studies. In Figure 6 we show the magnitude of the defect signal as we scan across both a point defect and the ASME Section XI 40% defect. Note that the point defect response is concentrated in a smaller distance along the tube than the experimental defect. The convention of the magnitude changing signs has been followed in Figure 6 so that the phase shift is relatively constant with distance along the tube.

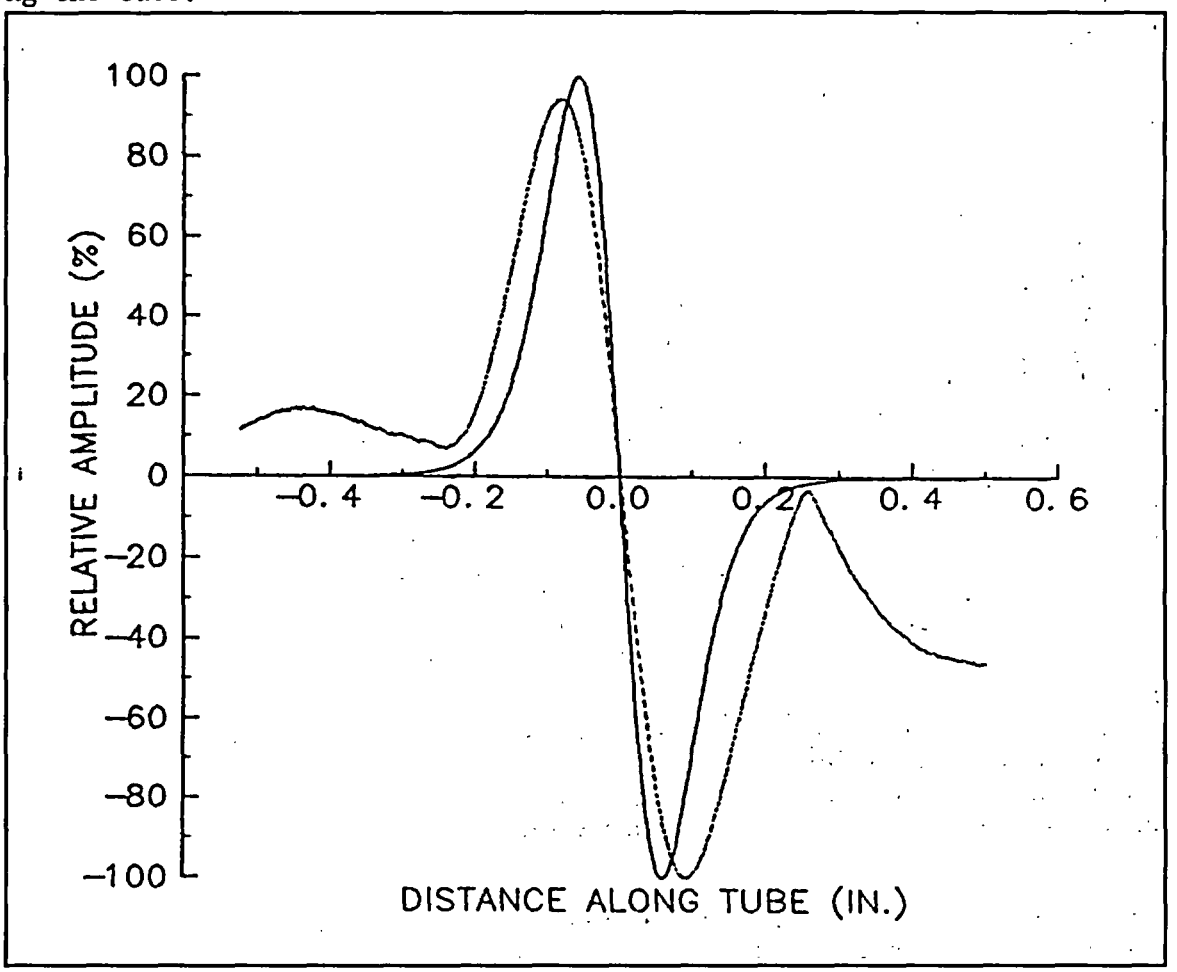

Figure 6 Magnitude of defect signal as a function of distance along tube. The calculated value for a point defect is solid, the measured value for a 40% defect is dashed.

If we assume a constant probe speed, the defect signal has a given frequency response. For purposes of this plot, we have assumed a constant inspection speed of one foot per second. This is the standard inspection speed used in most generator inspections in the US with a differential bobbin probe.

In Figure 7 we show the frequency response of two defect signals. We have taken the Fourier transform of the complex defect signal, so that any phase variations in the defect signal are included in the frequency response. Note that the point

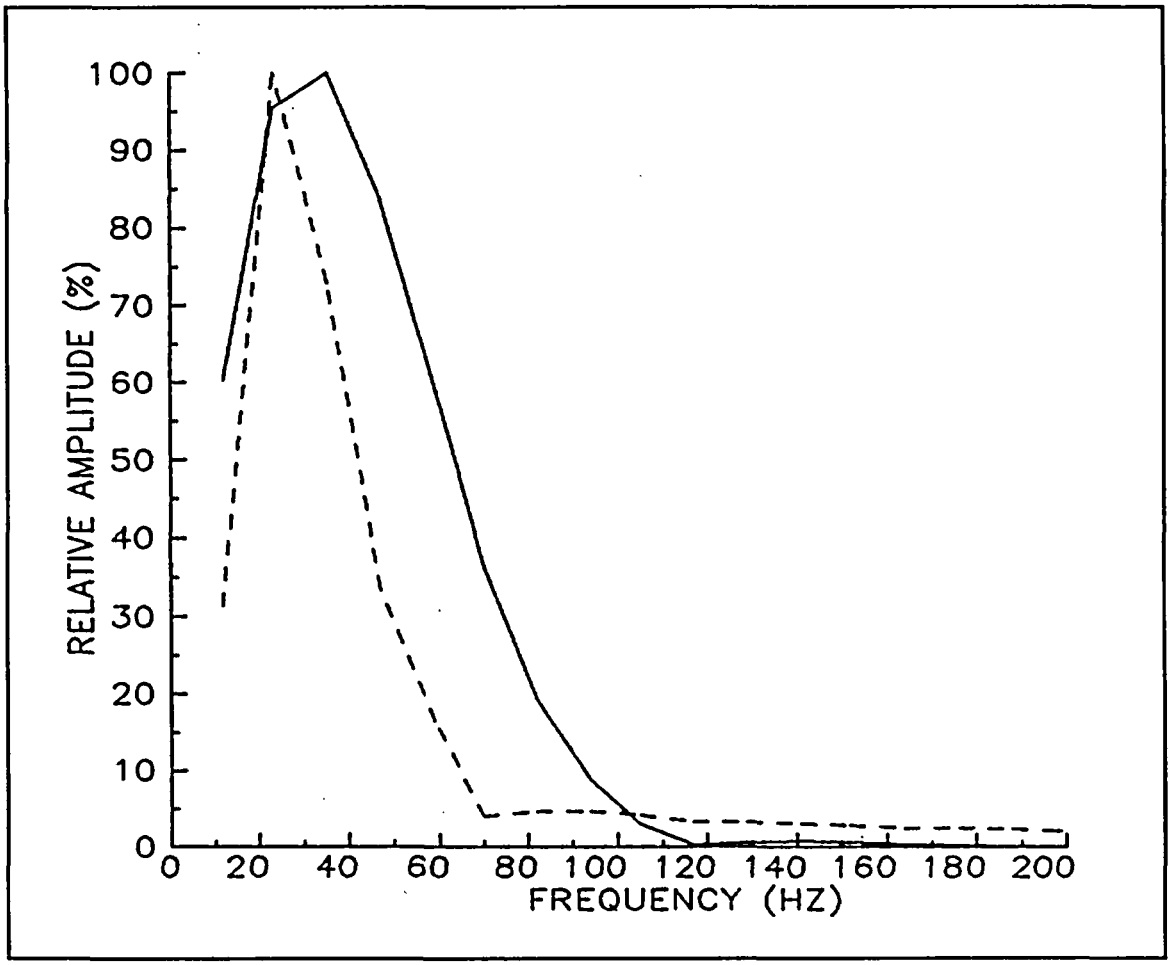

Figure 7 Frequency response of the defect signal as the probe is pulled at a constant speed of a foot per second. The solid curve is calculated for a point defect and represents the maximum frequency response. The dashed curve is for a measured 40% defect.

defect has a higher frequency response than the experimental defect and represents the upper limit of the defect response. The experimental defect also has a long tail that continues on up in frequency, rather than going to zero as the calculated defect does. This is caused by noise, such as probe wobble, instrument noise and digitizing noise, in the experimental measurements. For the best measurements, this high frequency tail should be attenuated by a low-pass filter. All of the defect signal information will be captured with a cut-off frequency of 120 Hz for the 1 ft per second inspection speed. The noise signals above the 120 Hz cut-off will be attenuated. For faster scanning speeds, the cut-off frequency of the low-pass filter should be raised in proportion to the inspection speeds.

An additional consideration is the number of readings taken per inch of tube scanned. In general, this will depend on the shape and size of the probe relative to the tube. An additional consideration is the tube wall thickness

which influences the coil-to-coil spacing in the probe. The following studies were performed for a 7/8 in. od tube with a 0.050 in. wall thickness, inspected with a standard Zetec 720 differential bobbin probe. Figure 8 shows the pattern produced as a 40% defect is scanned at a resolution of 100 samples per inch. The resolution is quite good in this case. If, however, the defect is scanned at a resolution of 25 samples per inch, as shown in Figure 9, the resolution is much poorer and the error in sizing the defect increases, depending to some extent on which technique is used to size the defect.

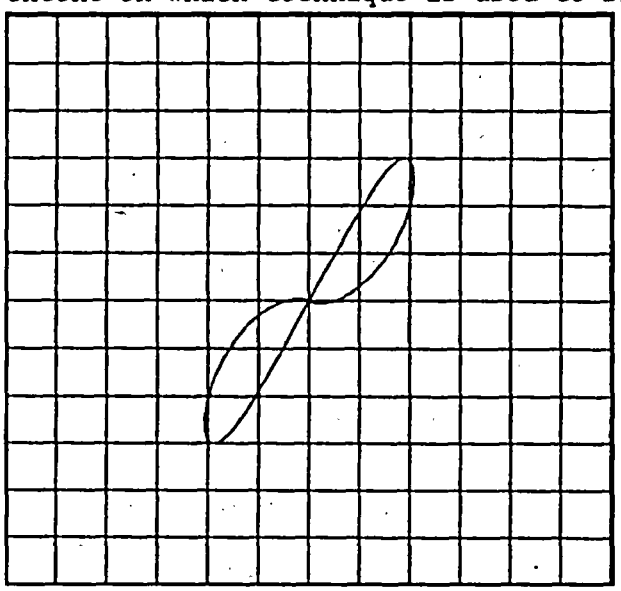

Figure 8 The Lissajous plot is made up of 100 discrete readings per inch. For the plots made up of 25 readings per inch, we can take every fourth reading from this plot.

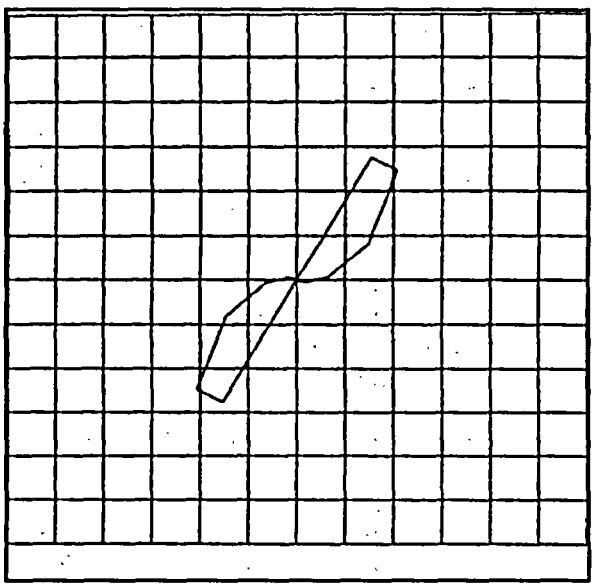

Figure 9 Lissajous plot of a 40% deep defect using 25 readings per inch.

The defect size can be determined using either the maximum slope of the phase or by measuring the phase shift at maximum amplitude. The former method is more accurate for sparse data samples. The sample rate is generally specified as a number of samples per second for a given instrument. This must be converted to the number of samples per inch of tube scanned by dividing by the scan speed used for the test.

In addition, other tube sizes can be approximated from the data shown here by scaling techniques. In general, if we halve the diameter of the tube, tube wall thickness and the probe dimensions, the scan rate in samples per inch would have to be doubled to achieve the same level of sensitivity. The amount of error depends on the depth of the defect and on the number of samples per inch. In Table I we show the variation in the error as a function of these two parameters. Note that the error calculated for the 40% point defect is somewhat greater than that for the experimental defects. This is due to the spread of the signal from the experimental defects along the tube. The point defect represents the worst case error. The defects in this table are sized using the phase at maximum amplitude, which, as noted above, increases the error. Thus, this table

represents the maximum error that may occur for the ASME Section XI defects in bare tubing. Additional studies are underway to determine the error caused by sample rate for defect depth measurements with more complex and mixed signals when other factors such as tube sheets, copper deposits and magnetite deposits are present.

Table I Possible errors in percent of wall thickness for different sample rates.

DEFECT SIZE (%) SAMPLES PER INCH	100	80	60	40	40Cal
1000	0.00	0.00	0.00	0.00	0.00
500	0.03	0.14	0.19	0.16	0.23
250	0.16	0.21	0.28	0.28	0.46
200	0.18	0.24	0.38	0.25	0.59
100	0.36	0.49	0.83	0.81	1.16
50	0.70	0.91	1.59	1.61	2.31
40	0.92	1.16	2.12	1.98	2.93
25	1.51	1.93	3.11	3.41	6.25
20	1.74	2.26	3.97	3.93	6.47

NEURAL NET STUDY

The application of artificial neural networks to the evaluation of eddy-current signals from steam-generator tubes is being investigated under separate funding. The following remarks are intended as a brief introduction to the general nature and present status of this effort.

The term "neural network" has come to have nearly as many meanings as there are students of the field. Nevertheless, the following may be taken as generally representative of the intent. An artificial neural network is a modifiably interconnected set of active, generally non-linear, elements which, in some fashion, accept input signals from the environment, and which both return to the environment some indication of their collective response to these signals and adjust their response to them in a manner which tends to increase the network's capacity for giving unique responses to stimuli with which it has become familiar. The input signals may comprise a pixel by pixel representation of an image, a parametric description of a physical object, a relational description of the time dependent behavior of some system, or the like. For properly prepared networks, the network response will, in the first case, be expressed by the recall, or reconstitution, of one or more of the images the network has previously "learned" and which it finds sufficiently analogous to the presented stimulus. Similarly, the response to a set of parameters will be one of the responses already known for objects described by the same, or nearly the same, set of parameters. The response can be an image, a string of characters or words, an ordered set of control signals, etc. The response to a relational description of some system behavior can be thought of as a path along which the system can be carried, perhaps from one set of operating conditions to a second, while satisfying some set of boundary conditions. These examples only hint at the range of problem types to which neural networks have already been applied. Whatever the application, most artificial networks are designed to capture in their "neural" elements some of the characteristics of the biological neurons which form the building blocks of natural intelligent systems. The more important of these characteristics are noted below.

Reduced to elemental form, the biological neuron may be described in terms of

four components. The NERVE BODY (or SOMA) itself is a roughly globular region of 10-80 microns diameter. For our purposes, the nerve body may be considered the source of the nerve impulses via which neurons communicate among one another. These impulses (spikes of millisecond duration) leave the soma along the AXON and, as a result of dense branching of the axon, arrive at receptor sites on as many as 150,000 other neurons. These receptor sites, called SYNAPTIC JUNCTIONS (or simply SYNAPSES), are usually formed, not on the receiving neuron bodies themselves, but on densely branched filamentary extensions of the soma called DENDRITES. The synaptic junctions can be of two general types. An activating junction is one which, upon the arrival of a neuron impulse, leads to an increase in the probability that the receiving neuron will itself emit an impulse (or fire). An inhibiting junction has the opposite effect. Associated with each of the junction types is a property generally referred to as the Connection Strength, or Weight. The overall effect of an impinging neuron impulse is mediated by this weight. It is because the weights associated with each of the two junction types can, under certain conditions, exhibit a capacity for stimulus-driven alteration that learning can take place.

The artificial neural systems on which our NDE studies are based are derived from the LILARTI schemes of Allen and Schell and represent the most recent in a series of synthetic neural net systems intended from their conception primarily for the purpose of exploring cognition and the degree to which artificial systems can be made to develop and exhibit it. Thus, these systems bear little relation to the products of more conventional work in the area whose structures reflect far more the influence of mathematical rigor than biological reality. Although initially the name of the program which both translated a quasi-biological network definition into a functional network and managed the processing defined by that network, LILARTI has come to refer to that network which, at a given moment, exhibits the most interesting behavior. Although capable of incorporating any combination of members of a nearly limitless spectrum of connectivity classes (most of which are characterized by pseudo-random connectivity within the bounds of their class definitions), the more recent LILARTI systems have shared some characteristic elements. Those associated with the (so far always present) visual system have generally been a small (usually in the range of 31x31 to 101x101 pixel square) "retina", several scene decomposition regions (edge detectors, etc.), outline- or contour map-forming regions, "interesting site" locators, a scene reconstruction region (not altogether inaccurately referred to as a visual cortex), several trainable regions for a learned hierarchy of scene abstractions, and regions whose neurons function very much like the often damned (and, indeed, biologically unlikely) "grandmother cells". A second input sense (referred to, whatever the data source, as the keyboard) serves a broadly analogous set of neural regions. It is the trainable interaction between and among the higher level elements of two (or, in general, several) sensory subsystems which is principally responsible for the more interesting characteristics of a LILARTI wiring. Of the several unusual features of the LILARTI systems, three are of particular importance here. First, and earliest to be incorporated, is the capacity for interaction and contextual learning among the various senses, an attribute which, it is hoped, will ultimately justify the rather grand and early assigned term, "cognitive complementarity". Arising naturally from the concept of cognitive complementarity are the linked notions of the formation of generalized

abstractions of features neurally derived from input data and the formation of a related grammar therefrom. Even for the relatively simple neural systems so far explored, these properties have emerged in a natural manner and lend themselves effectively to those applications for which some sort of interface between a system's representation of its actions and a human's representation of his is required.

For our present purposes, this interaction exhibits itself as a capacity for describing to a user the characteristics of the eddy-current signals with which it is presented. These signals are Lissajous patterns obtained at two frequencies, each presented at two different scales to the "retina" of the neural system so that, in effect, the neural system "sees" four representations of flaw signals simultaneously. This simultaneity of presentation leads naturally to a learning mechanism by which the system discovers what portions of the separate signals can usefully be related in order to produce the most nearly singular description of the presented flaw and to discriminate flaw signals from signals produced by such perturbing influences as tube supports, magnetite deposits, and the like.

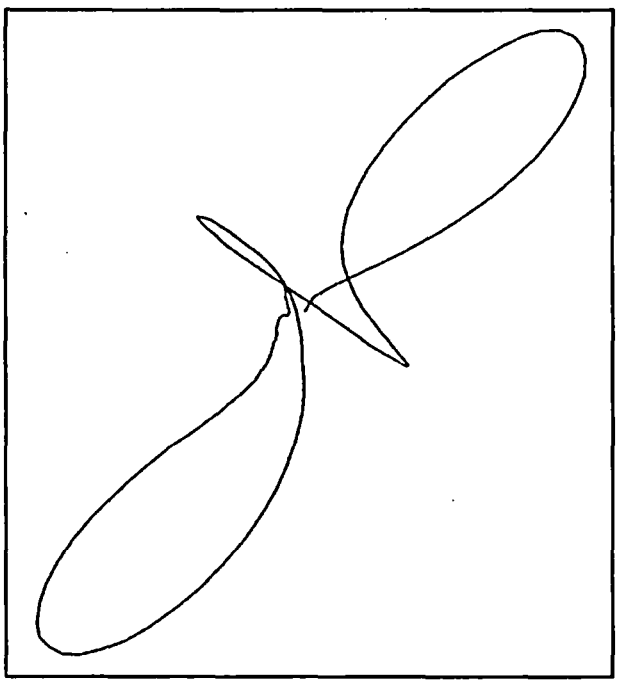

Figure 10 Scan of a 40% OD defect located 0.1 in from center of tube support, made at 500 KHz, 1350 X 1350 resolution.

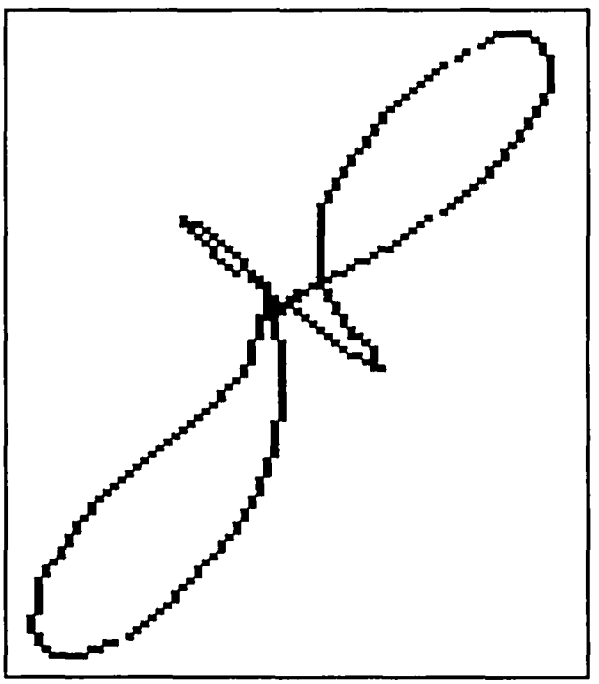

Figure 11 Scan of a 40% OD defect located 0.1 in from center of tube support, made at 500 KHz, 101 X 101 resolution.

Figure 10 illustrates a typical single frequency signal produced when a defect is near the tube support. The defect is the small signal Lissajous pattern with the large tube support signal superimposed. As the relative position of the defect is moved with respect to the tube support, the tube support signal can mask the much smaller defect signal. Magnetite and copper signals can be considerably larger than the tube support signal. In Figure 11 we see the same

signal at a much lower resolution. While the complex image is visible in this particular scan, this is not always the case. The resolution of 101 X 101 is slightly above the practical limit of the size of the neural network with the available memory in our computer.

Since the data at one frequency do not contain enough information to give an unambiguous measure of the defect in the presence of other property variations, we have to use multiple frequency data. We therefore used both the 100Khz and 500Khz signals for our analysis. In Figure 12, we show the data at both frequencies. Since we did not have the resolution to show the fine detail near the center of the plot, we magnified these pixels and showed them to the right of the whole plot.

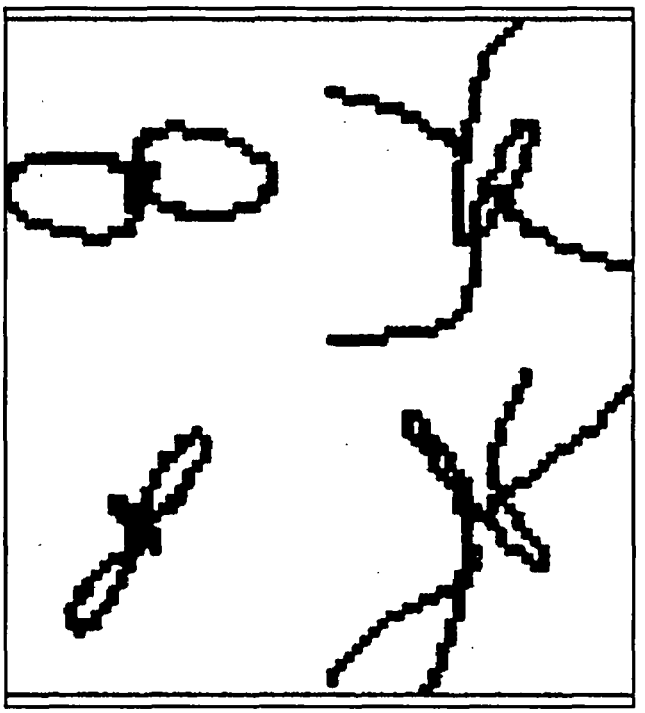

Figure 12 Scan patterns produced by a 40% defect located near a tube sheet at 500KHz and 100KHz. Each part of the image has a resolution of 39 X 39, with an overall resolution of 81 X 81 for the whole picture.

The neural network is presented these pictures for different depth defects that are located at different distances from the tube support, with no mixing to reduce the effects of the tube support. These data were obtained by scans of the ASME Section XI defects, using a MIZ17. To date, results with a still small LILARTI type network comprising about 30,000 neurons and 325,000 connections are promising indeed. The better "tuned" wirings (a representative example of which appears as Figure 13) have yielded overall error rates below 5% when trained with no more than 40 composite signals, or "quartets", over training times which, given that the system runs on a PC clone, are not excessive (of the order of 12 hours). Although our present studies involve flaw evaluation in the presence of only one variable perturbation (distance from the tube support), it is feasible, within the context of the present computing environment, to extend the neural system sufficiently to permit flaw evaluation in the presence of two additional perturbing influences (probably copper and magnetite deposits on the outer surface of the tube). If this extension can indeed be fit into the confines of the present 16 Megabytes of PC memory, and if the processing time is not unduly compromised thereby, we shall attempt to train the system to the degree required to perform flaw size determinations in the presence of any combination of the three perturbing influences. If this effort succeeds, we will retrain the system on the "raw" data signals from the EPRI Level II Data Evaluator training tapes and determine if the network can pass the Level II Inspector's test and thus be qualified for data evaluation.

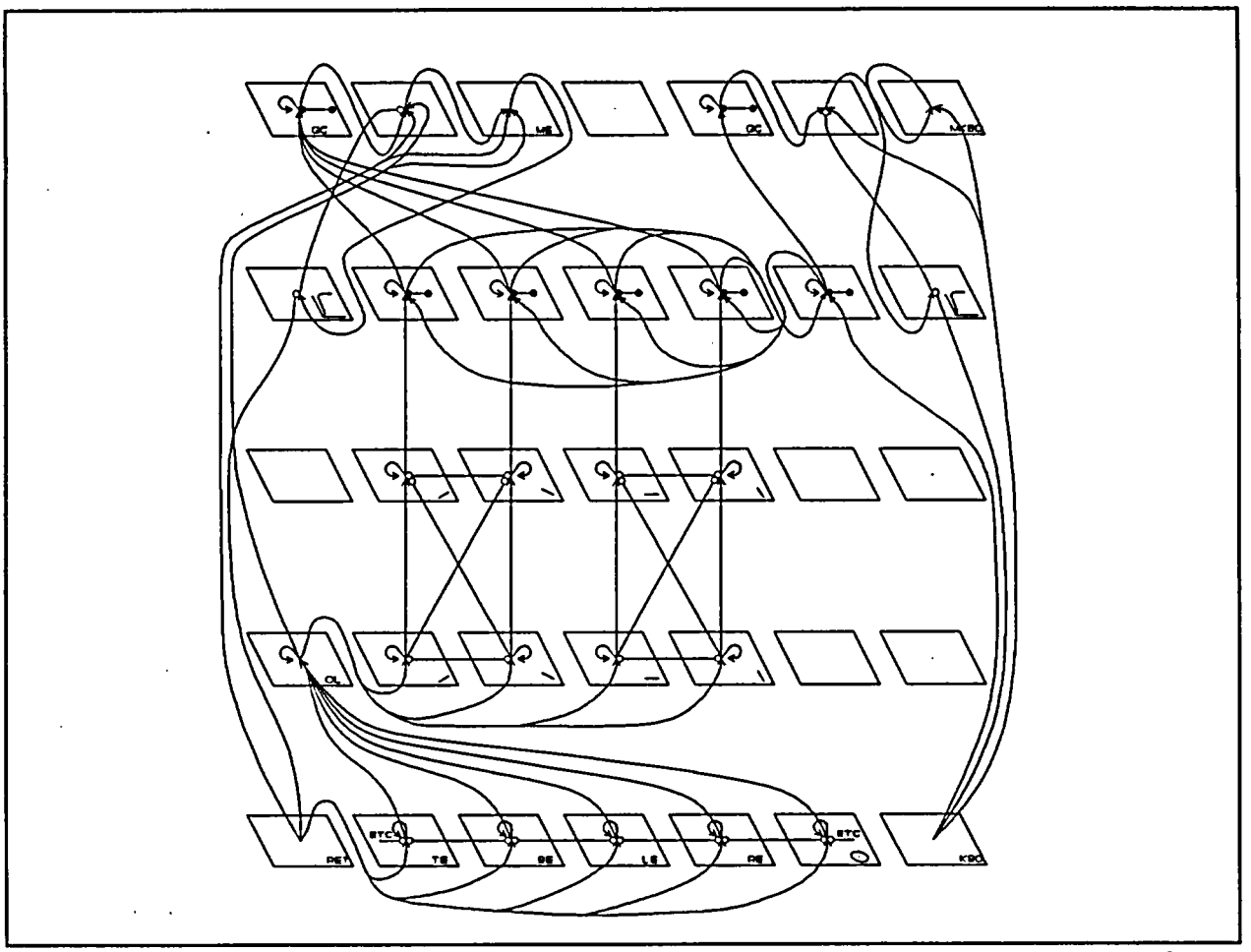

Figure 13 The Lilarti Neural Network for Evaluation of Eddy-Current Signals

Extensions much beyond those just noted will inevitably require considerably more computing speed and more memory. One of the most important of these extensions is the increasing of system resolution so that the rescaling aspect of the "quartet" presentation of data can be avoided. We would, of course, maintain the capacity for simultaneous examination of data obtained at two or more frequencies as is it clear from other studies that single frequency measurements cannot lead to unambiguous flaw descriptions in the presence of numerous perturbations (many of which produce, in any case, signals larger than those due to the flaw whose detection and evaluation is desired). This first extension, and one or two less demanding ones as well, would require no more than an order of magnitude increase in processing speed and a factor of four increase in memory and can almost certainly be evaluated in the generation of personal computers just now beginning to appear. Longer term goals include extensions of the developing techniques into such NDE areas as Ultrasonic Testing and Two-Dimensional X-ray imaging and could most effectively be explored in the

context of dedicated architectures not unlike those with which we already have some considerable experience.[3,4,5,6]

We conclude this section with two observations. First, present eddy-current data evaluation practice requires that two independent analyses be performed on the data. If we succeed in meeting our near-term goals, it would not be unreasonable to suggest that one of these independent analyses be performed by the multiple-property technique already well explored and that the other be performed by a well trained neural network system. Certainly, the two approaches should be seen as complementary, not competitive. Finally, it is worth noting that the resolution problem associated with the neural network studies is somewhat analogous to the sample rate problem discussed earlier, an analogy not unrelated to the similarity between the data of Figures 9 and 12. Although we cannot translate the results of one study directly into the domain of the other, the data we have obtained (and continue to obtain) for the neural network studies can be applied directly in the study of sample rate effects in the presence of complex properties.

SUMMARY AND CONCLUSIONS

The power of computerized analysis and synthesis routines for investigation and optimization of complex physical considerations in eddy-current inspection problems for steam generator tubing has been illustrated with several examples. Development of computer codes and applications is ongoing, and a collection of proven codes has been published.[1] Computed aided system design and data analysis can be expected to play a much greater role in steam generator inspection as the process becomes more complex and new degradation modes demand more definitive data. Best and most cost-effective solutions to inspection problems are expected to require significant ongoing efforts based on the work that has already been done.

---

[3] Philip L. Butler, *Design and Implementation of a Parallel Processing Machine for Artificial Intelligence Applications*, Philip L. Butler, Master's Thesis, University of Tennessee, December 1987.

[4] P. L. Butler, J. D. Allen, Jr., et al., *Parallel Architecture for OPS5*, pp. 452-57 in 15th Annual International Symposium of Computer Architecture, Honolulu, Hawaii, May 30-June 2, 1988, IEEE.

[5] P. L. Butler, J. D. Allen, Jr., *Design and Implementation of a Parallel Computer for Expert System Applications*, pp 638-45 in Applications of Artificial Intelligence VI, ed. Mohan M. Trivedi, SPIE.

[6] Winner R&D-100 Award, 1988.

HYDROGEN WATER CHEMISTRY FOR BWRS: A STATUS REPORT ON THE EPRI DEVELOPMENT PROGRAM

Robin L. Jones and J. Lawrence Nelson
Electric Power Research Institute
Palo Alto, California, USA

ABSTRACT

Many boiling water reactors (BWRs) have experienced extensive intergranular stress corrosion cracking (IGSCC) in their austenitic stainless steel reactor coolant system piping, resulting in serious adverse impacts on plant capacity factors, O&M costs, and personnel radiation exposures. A major research program to provide remedies for BWR pipe cracking was cofunded by EPRI, GE, and the BWR Owners Group for IGSCC Research between 1979 and 1988. Results from this program show that the likelihood of IGSCC depends on reactor water chemistry (particularly on the concentrations of ionic impurities and oxidizing radiolysis products) as well as on material condition and the level of tensile stress. Tests have demonstrated that the concentration of oxidizing radiolysis products in the recirculating reactor water of a BWR can be reduced substantially by injecting hydrogen into the feedwater. Recent plant data show that the use of hydrogen injection can reduce the rate of IGSCC to insignificant levels if the concentration of ionic impurities in the reactor water is kept sufficiently low. This approach to the control of BWR pipe cracking is called hydrogen water chemistry (HWC). This paper presents a review of the results of EPRI's HWC development program from 1980 to the present. In addition, plans for additional work to investigate the feasibility of adapting HWC to protect the BWR vessel and major internal components from potential stress corrosion cracking problems are summarized.

INTRODUCTION

Intergranular stress corrosion cracking (IGSCC) of sensitized material adjacent to welds in Type 304 and Type 316 stainless steel piping systems has been responsible for more than 1000 cases of pipe cracking in BWRs in the United States since 1974. These cracks have had serious adverse impacts on plant capacity factors, O&M costs, and personnel radiation exposure and have cost U.S. utilities several billion dollars during the past decade. To provide remedies for BWR pipe cracking, a major R&D program was cofunded by EPRI, GE and the BWR Owners Group for IGSCC research between 1979 and 1988. Results from this program show that the likelihood of IGSCC depends on reactor water chemistry as well as on the metallurgical condition of the stainless steel and the level of tensile stress. The two key aspects with respect to the contribution of water chemistry to IGSCC are the oxidizing power of the water (as reflected by the electrochemical potential (ECP) of stainless steel immersed in the water) and the concentrations of ionic impurities, particularly sulfate and chloride. Plant data indicate that by injecting hydrogen

into the feedwater, the oxidizing power of the reactor water can be reduced to a point at which IGSCC cannot be detected if, at the same time, the concentrations of ionic impurities in the coolant are maintained at the very small levels normally recommended for BWR power operation.[1] This approach to BWR chemistry control is called hydrogen water chemistry (HWC).

This paper presents a review of the results of EPRI's HWC development program from 1980 to the present. Because progress through 1985 has been reviewed in detail elsewhere[2], emphasis is placed on recent and current activities. In addition, plans for further work to investigate the feasibility of adapting HWC to protect the reactor vessel and internals from corrosion damage are outlined.

DEFINITION OF HWC REQUIREMENTS FOR PIPING PROTECTION AND VERIFICATION OF FEASIBILITY

Laboratory Tests

An extensive laboratory test program was begun in 1980 to systematically study and document the effects of BWR water chemistry variables on corrosion and corrosion cracking of structural materials. The materials studied included stainless steels, Inconels, carbon steels and low alloy steels, and the chemistry variables were ionic impurity concentration, dissolved oxygen content, and temperature. Corrosion phenomena investigated were general corrosion, crevice corrosion, corrosion fatigue, hydrogen embrittlement, and stress corrosion cracking.

The results[2-4] showed that IGSCC damage to BWR pipes most likely occurs mainly during power operation, when the coolant is at a temperature of about 288°C and contains about 200-ppb dissolved oxygen. At this temperature, ionic impurities and dissolved oxygen were found to independently influence IGSCC of sensitized austenitic stainless steels. It was shown that at ionic impurity levels typical of those found in BWR reactor water under power operation (i.e., conductivity <0.3μS/cm), IGSCC was effectively suppressed at dissolved oxygen contents below 20 ppb, which resulted in stainless steel ECPs below about -230 mV on the standard hydrogen electrode (SHE) scale. Some of the constant extension rate test (CERT) results are shown in Figure 1. Other test results showed that under the low-oxygen/ low-conductivity conditions where IGSCC of sensitized stainless steel was not observed, the corrosion performance of other structural materials was generally either unchanged or improved compared with the behavior observed when the dissolved oxygen concentration was raised to 200 ppb. The only exceptions were the initial rates of general corrosion for carbon and low-alloy steels, which were found to be faster at the lower oxygen level.

In-Plant Program at Dresden-2

By 1982, the laboratory test data indicated clearly that reducing the oxygen content of the BWR coolant during power operation would result in a more benign service environment for structural materials. An earlier study[5] cosponsored by GE, Commonwealth Edison Company (CECo) and the Department of

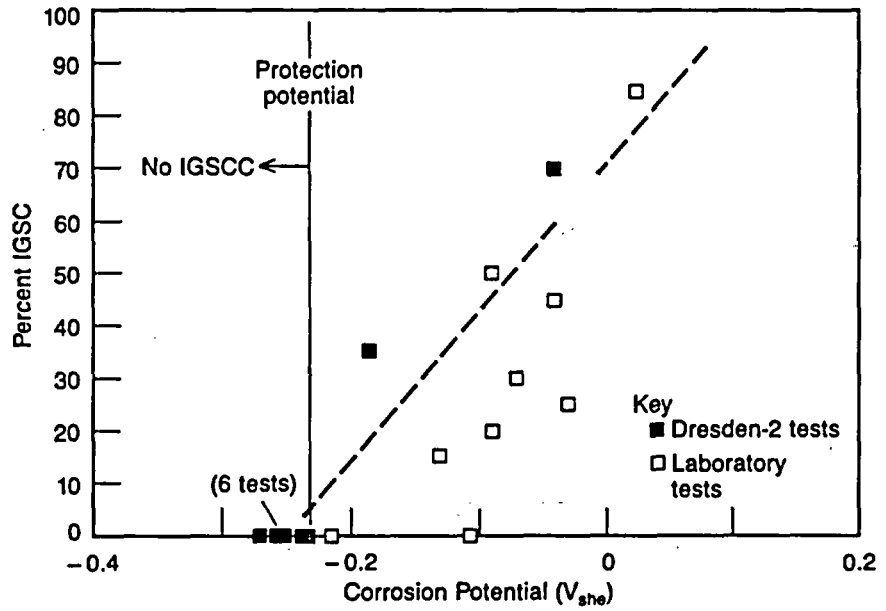

Figure 1. Variation of IGSCC fraction of Type 304 CERT specimen fracture surface with ECP.[2]

Energy (DOE) had suggested that the addition of hydrogen to the feedwater was a promising approach to reducing the oxygen concentration of the recirculating coolant, and a short-term Swedish in-plant test had demonstrated the feasibility of this approach. Accordingly, a one-month test was performed during 1982 at CECo's Dresden-2 plant with sponsorship from DOE, GE, EPRI, and CECo to assess the feasibility of implementing HWC as long-term remedy for IGSCC in the plant's recirculation system piping. The results[2] showed that:

- The oxygen concentration in the recirculation system could be reduced into the desired range by hydrogen injection (Figure 2).
- The in-reactor IGSCC behavior of sensitized Type 304 stainless steel was similar to the in-laboratory behavior (Figure 1).
- Hydrogen injection increased the steam line radiation fields (Figure 3) and the environs dose rates (Figure 4) because N-16, which is always found in the core, partitioned into the steam under the more reducing conditions created by hydrogen injection instead of remaining in the recirculating water.

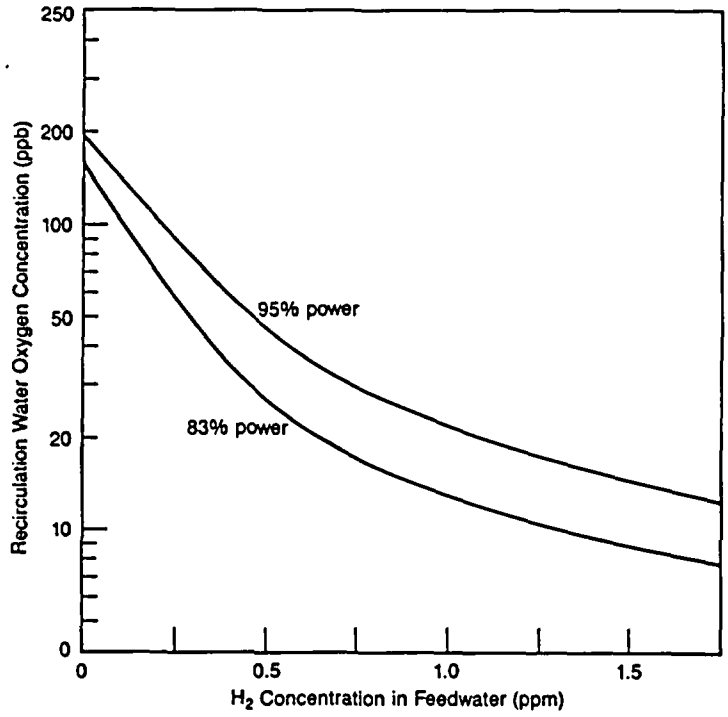

Figure 2. Effect of hydrogen addition on the oxygen content of the recirculating water at Dresden-2.(2)

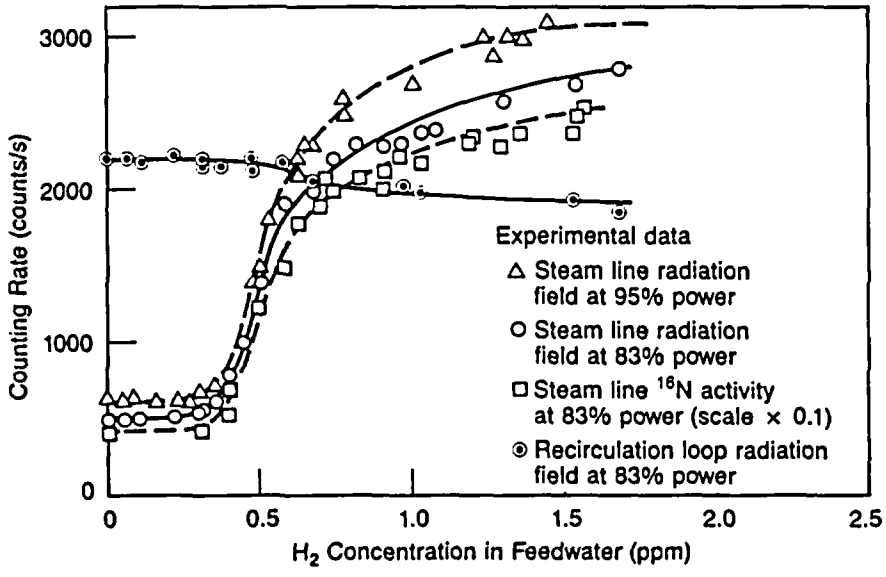

Figure 3. Variation of operating radiation fields at Dresden-2 with hydrogen addition rate.(2)

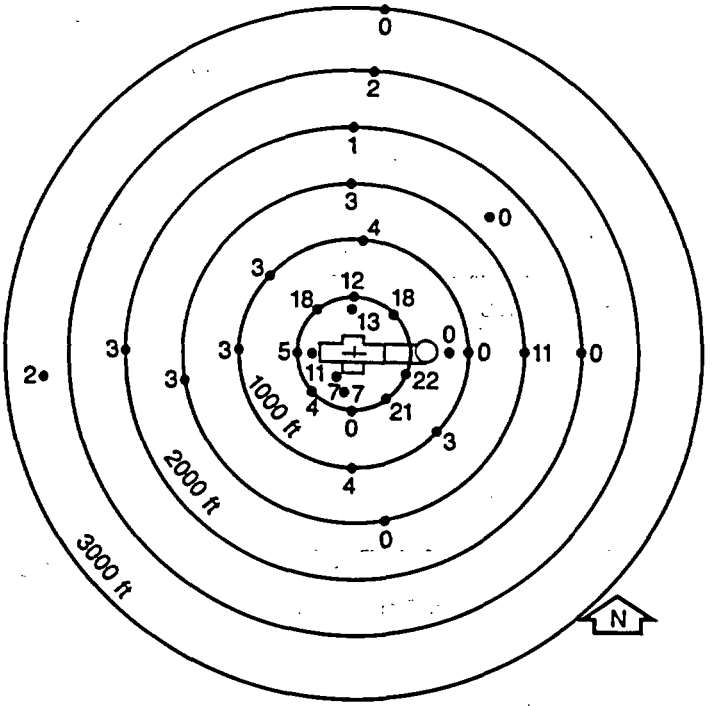

Figure 4. Net contribution of HWC to Dresden environs dose rates. Units are μR/h.[2]

Following the successful completion of the one-month test, EPRI, CECo, and GE cosponsored a long-term project at Dresden-2 to confirm the feasibility of full-time HWC operation. This project currently has completed three 18-month operating cycles and has verified that operation of the plant in the IGSCC-suppression regime is possible for >90% of the time at power and that the rate of IGSCC in sensitized stainless steel is thereby reduced to low levels (Figure 5). Moreover, it has been shown that the steamline radiation field increase is manageable at Dresden-2 and has a negligible impact on personnel radiation exposures. Further, adverse effects studies have revealed no major effects of hydrogen injection on plant operations, fuel performance, or shutdown radiation fields.[2]

Short-Term Tests at Other U.S. BWRs

By 1986, short-term tests of hydrogen injection had been conducted at six GE-type BWRs. The results of these tests showed that the response to hydrogen injection was plant-specific. For example, Figure 6 shows the different relationships observed between the stainless steel ECP in the recirculation system and the feedwater hydrogen concentration. However, stainless steel ECPs <-230 mV (SHE) were found to be attainable in the recirculation system in all plants tested, and when this ECP was established in conjunction with low ionic impurity concentrations, IGSCC was found to be suppressed (Figure 7).

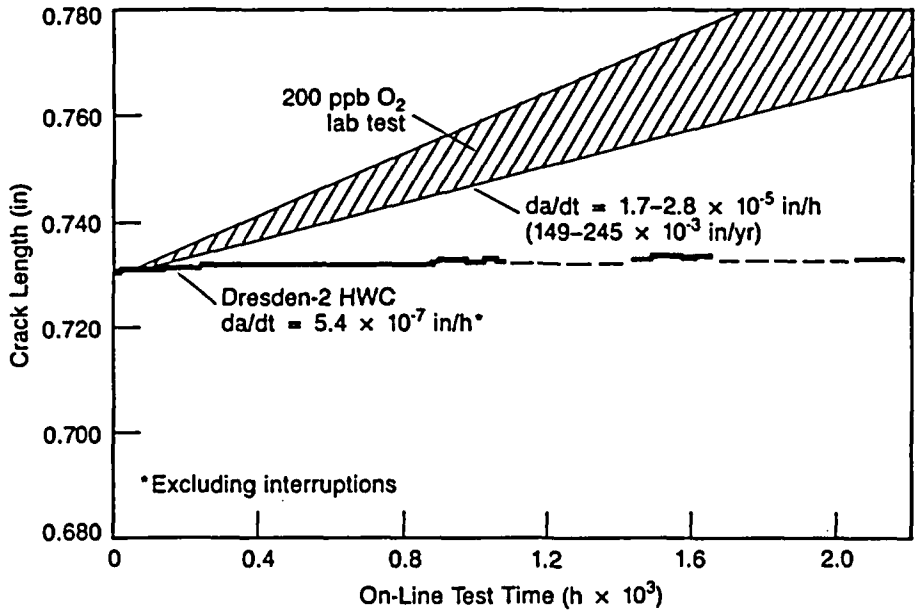

Figure 5. Crack length vs. time curves for sensitized Type 304 specimens tested at Dresden-2 and in the laboratory.(2)

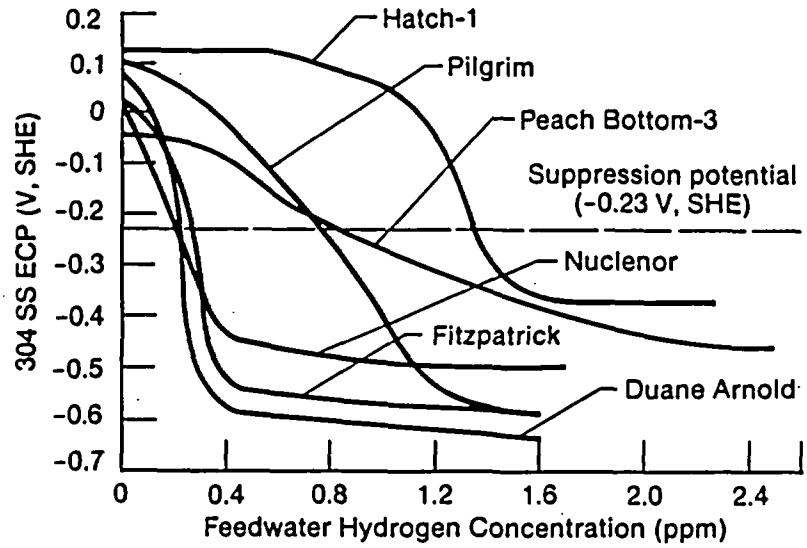

Figure 6. Relationships between stainless steel ECPs in recirculating water and hydrogen addition rate for 6 BWRs.(7)

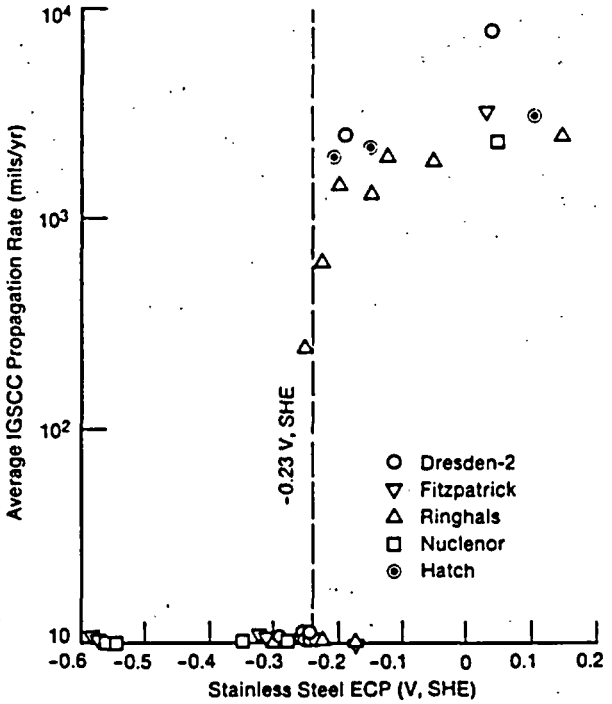

Figure 7. Results of in-plant CERTS showing the relationship between the rate of IGSCC for sensitized Type 304 stainless steel and the stainless steel ECP.[7]

It was not until recently that it was possible to explain the plant-to-plant variability of the feedwater hydrogen concentration required to achieve a particular oxygen concentration in the recirculation system. However, modeling studies[6] revealed that the hydrogen concentration requirement could be correlated with variations in the radiation dose rate in the downcomer region. For example, Figure 8 shows that the feedwater hydrogen concentration required to attain an oxygen concentration of 2 ppb in the recirculation system correlates strongly with downcomer dose rate for all but two of the plants tested to date. The two exceptions are believed to be attributable to the presence of significant levels of soluble copper in the reactor water.[6]

DEVELOPMENT OF INDUSTRY CONSENSUS GUIDELINES

HWC operating guidelines were developed during 1987 by an industry committee that included representatives of utilities, NSSS vendors, consultant companies, and EPRI. Independent review of the draft document generated by the committee was provided by a technical review team consisting of one representative of each U.S. BWR utility (usually a plant or corporate chemistry manager). Additional review and approval was provided by the utility committees of the BWR Owners Group for IGSCC research.

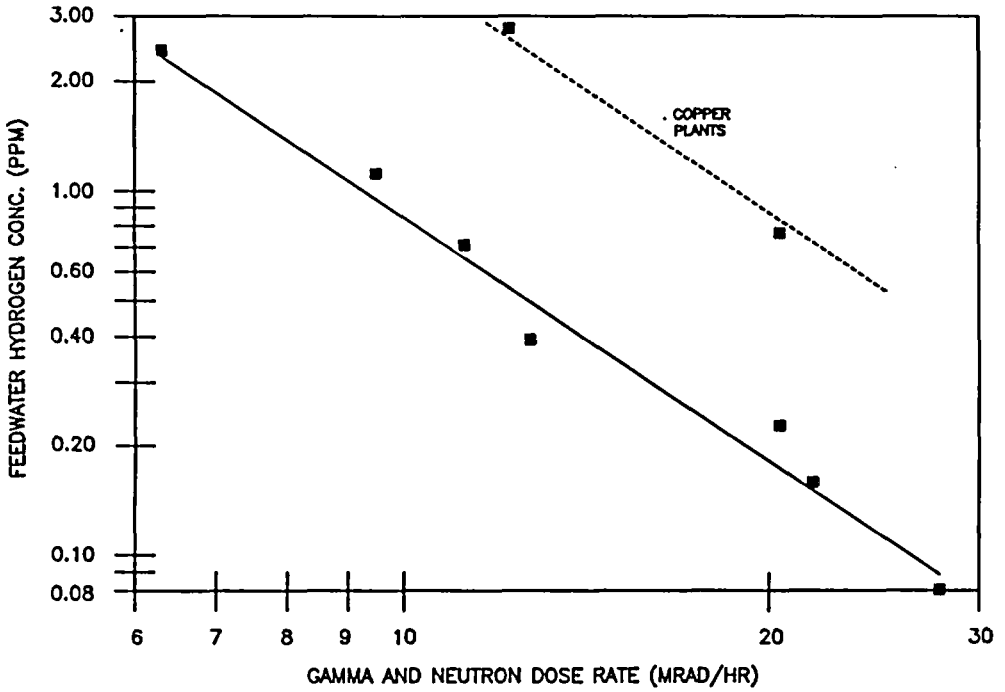

Figure 8. Relationship between feedwater H_2 concentrations required to attain 2-ppb O_2 concentration in the recirculation system and downcomer dose rate.[6]

The goal of the Guidelines Committee was to define a practical BWR water chemistry specification that would reduce rates of IGSCC in Type 304 stainless steel recirculation system piping to insignificant levels during power operation while maintaining acceptable fuel performance and radiation field buildup behavior. Protection of reactor internals was not considered by the committee. It was felt to be important that the HWC guidelines be as consistent as possible with the normal water chemistry guidelines[1] so that no major perturbations in the chemistry control program would be required to respond to an interruption of hydrogen injection. The committee undertook an extensive review of laboratory and in-plant test results and found that to achieve its goal, it was necessary only to add stainless steel ECP (measured in an autoclave connected to the recirculation system) to the control parameters specified for power operation; all other control parameters and values remained the same as those in the normal water chemistry guidelines. Figure 9 illustrates the resultant relationship between the two chemistry specifications. The oxygen content of the recirculating coolant was considered as an alternative to ECP as the key HWC control parameter, but it was found to be impossible to specify a single oxygen concentration that would provide IGSCC protection on a generic basis. A variety of diagnostic and confirmatory measurements (including IGSCC measurements in autoclaves connected to the recirculation system) were also recommended by the committee in the final version of the HWC operating guidelines, which was published by EPRI in December 1988.[7]

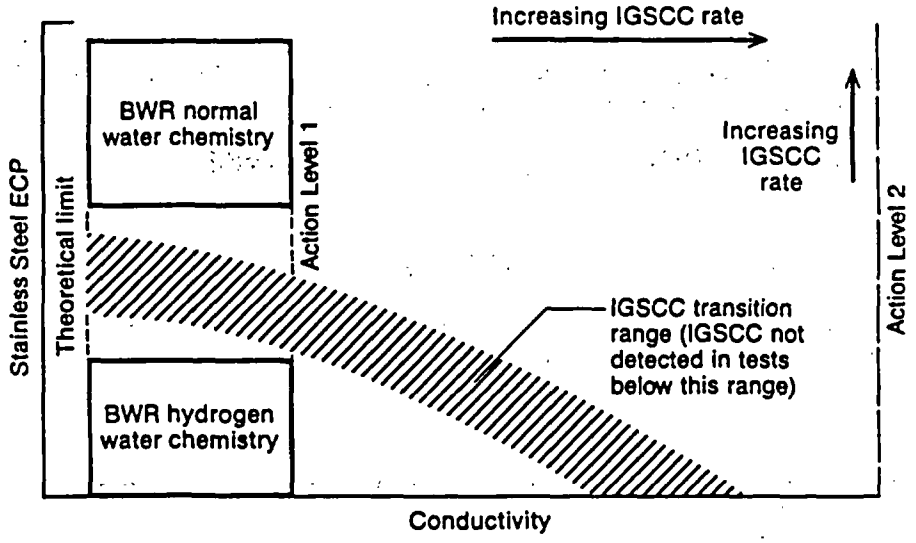

Figure 9. Relationship between the BWR chemistry regimes defined by the normal water chemistry[1] and HWC[7] guidelines and the regions where IGSCC of sensitized stainless steel is observed in tests.

A companion document to the HWC operating guideline, providing consensus guidance on HWC implementation, was published by EPRI in September 1987.[8] The goal in this case was to develop generic NRC-accepted guidelines for the design, construction and operation of HWC installations at BWRs. This objective was achieve by assembling an industry committee to prepare a draft document, submitting the draft to the NRC for review, and reconvening the committee to revise the document to respond to the NRC comments. A letter indicating NRC approval is bound into the published document.[8]

Together, the HWC operating and implementation guidelines provide U.S. utilities with a recommended HWC operating specification and an NRC-acceptable approach for implementing hydrogen injection. Most U.S. utilities recognize that HWC is a more benign BWR operating environment than normal water chemistry, and near-term adoption of HWC is planned at many plants in addition to the five BWRs currently using the technology.

ONGOING WORK AND PLANS FOR FURTHER DEVELOPMENT

In the course of its work, the HWC Guidelines Committee identified several areas of uncertainty with regard to HWC operation:

1. The degree of corrosion protection achieved elsewhere in the coolant circuit during HWC operation when the current, piping-oriented guidelines are used;

2. The relationship of measurements made in autoclaves to the conditions actually experienced by the recirculation system piping;

3. The rate of damage accumulation during periods when the ECP or ionic impurity concentrations exceed the guideline values;

4. The effects of copper and zinc on ECP, crack growth and fuel performance;

5. The fuel performance under HWC beyond three cycles.

Ongoing and planned EPRI research addressing these uncertainties will be discussed in the remainder of this paper.

SCC of Reactor Internals

Several BWR reactor internal components, including major structural components such as the top guide and core support plate, are potentially susceptible to SCC. Access limitations make inspection of many of these components difficult and, in some cases, practically impossible. Regulatory concern over potential safety implications is increasing. Prior field experience plus current data and models support the existence of a significant concern. Numerous components have already cracked and are listed in Table 1. Many of these components are fairly easily replaceable and cracking is chiefly a reliability issue. Safety concerns are mainly confined to core support structures, such as the core support plate, core shroud and top guide, and to attachment welds.

Although mandatory inspections are unlikely in the short term, it is, however, quite likely that regulatory bodies will mandate inspection of many of these components in the longer term. The potential cost impact on utilities is likely to be large since it is very probable that inspections will reveal some damage to some internals at some plants. Since repair of some components, as mentioned previously, may be very difficult, operation with HWC is an attractive possibility for SCC mitigation, especially if HWC can be adapted to prevent crack initiation and growth for some of the less accessible components, such as those located below the core.

The goals of future EPRI HWC development work are to resolve by 1992 the issues which were identified by the HWC Guidelines Committee and to provide a technical basis for revised BWR water chemistry guidelines that will prevent, or substantially mitigate, SCC problems in BWR pressure boundary and reactor internals while maintaining satisfactory fuel performance and minimizing radiation field buildup. Attainment of these objectives requires a chemistry model that can account for plant-to-plant differences and predict chemistry throughout the coolant system, together with in-plant and test reactor data to benchmark the model.

BWR Chemistry Model Development

A first generation chemistry model is already available and is shown schematically in Figure 10. The model divides the primary circuit into ten zones and uses chemical kinetics equations to calculate local concentrations of hydrogen, oxygen and hydrogen peroxide within each zone. An example of the output from this model is shown in Figure 11.

Table 1. Service-Induced Cracking In BWR Vessels and Internals

The following is a partial list of BWR internal components and vessel attachments that have exhibited service-induced cracking. These problems were attributed to stress corrosion cracking except where noted.

Shroud head bolts

Shroud support at access cover weld

Recirculation inlet nozzle

- Safe ends
- Thermal sleeves
- Nozzle at attachment weld

Recirculation outlet nozzle safe end

Core spray nozzle

- Safe end
- Thermal sleeve

Core spray piping

Core spray spargers

Feedwater nozzles

- Cladding (thermal fatigue)
- Nozzle bore (corrosion-assisted cracking)

Feedwater spargers (vibration and thermal fatigue)

Control blade sheaths

In-core instrumentation tubes

Steam dryer support ring

Steam dryer bracket (fatigue)

Jet pump hold down beams

Jet pump instrumentation lines (fatigue)

BWR-1 steam generator shell

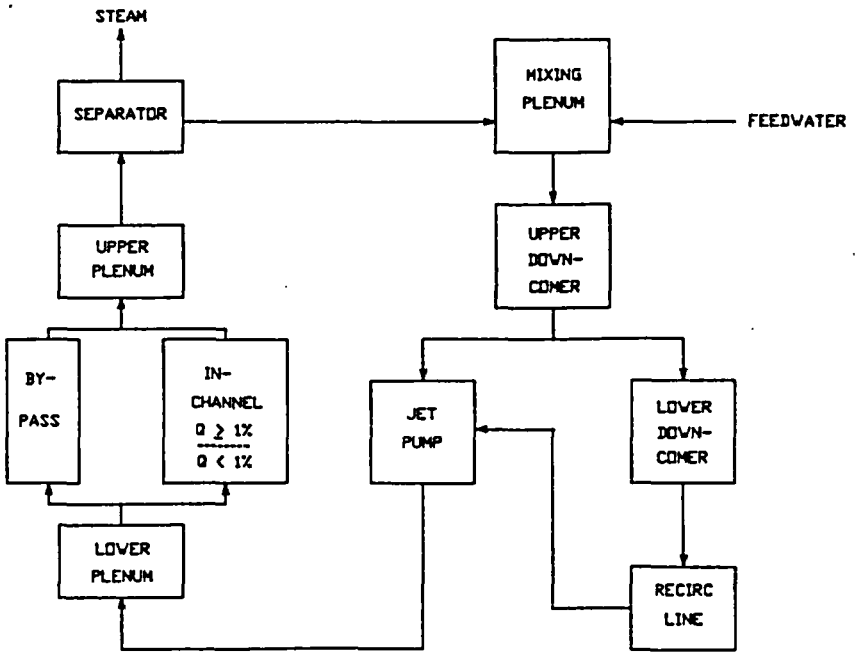

Figure 10. Schematic illustrating the various input/output elements in the water chemistry model of the BWR primary circuit.(6)

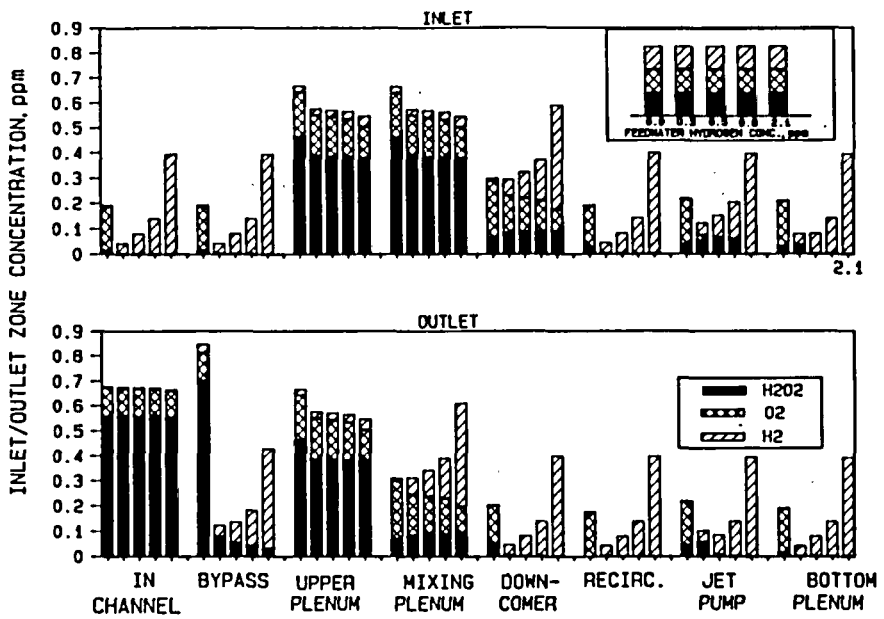

Figure 11. Calculated inlet and outlet concentrations of dissolved O_2, H_2O_2, and H_2 for several feedwater H_2 concentrations at various locations within a BWR-4.(6)

The inlet and outlet concentrations for eight regions of the primary circuit of a particular BWR are shown as a function of feedwater hydrogen concentration. It should be noted that, according to the calculations, injection of hydrogen has little effect in areas such as the upper plenum and in the channel regions. However, areas such as the by-pass, downcomer and lower plenum respond quite markedly to increases in hydrogen concentration in the feedwater. The model indicates that hydrogen injection should be able to protect several internal regions of the reactor, including most of the regions where access for inspection is limited.

In its present form, the model does a reasonable job of accounting for plant-to-plant differences in response to hydrogen injection and indicates that a major source of these differences is a result of the recombination rate of H_2 and O_2 in the downcomer. Predictions of the model are more accurate for some plants than for others, as noted in Figure 12. For example, the model predicts well the response of FitzPatrick to hydrogen injection. However, the model predicts a similar response for Hatch-1 which is in conflict with the experimental data, as shown in Figure 12. As mentioned earlier, it has been speculated that this difference is primarily due to the high concentration of copper in the water at the Hatch-1 plant.[6]

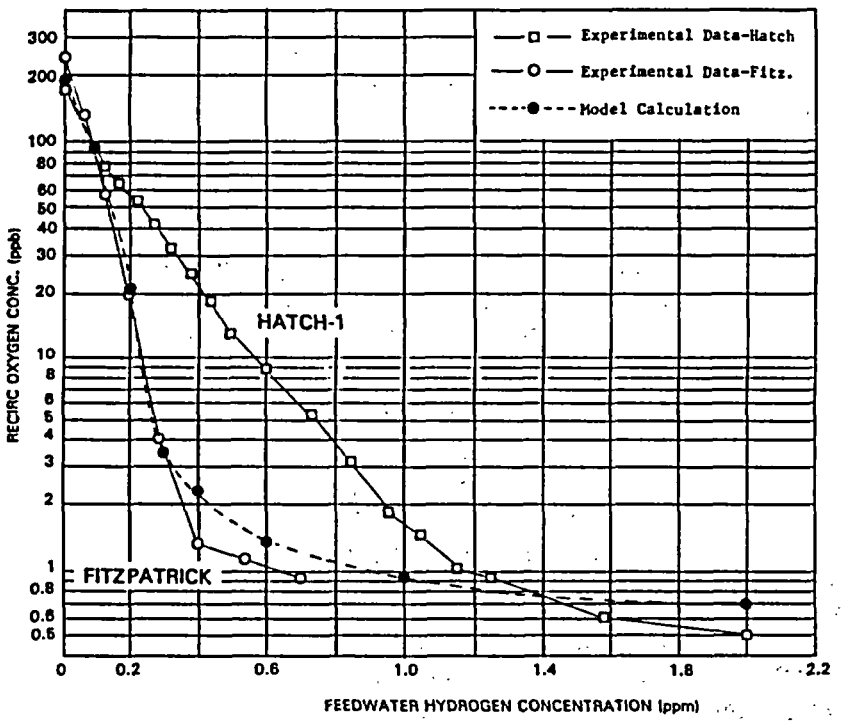

Figure 12. Comparison of calculated and measured reactor recirculation water O_2 concentrations at various feedwater H_2 concentrations for Fitzpatrick and Hatch-1. These plants are nearly identical except for the presence of copper at Hatch-1.[6]

Further development of the predictive capabilities of the model are necessary and are planned in the future. These planned improvements to the model should account for the effects on recombination rate of specific chemistry impurities such as copper and also benchmark the model with data from additional in-plant tests. At the present time the model predicts only concentrations of various chemical species. The intention is to continue development of the model so as to be able to calculate ECP throughout the coolant circuit as a function of hydrogen injection rate.

In-Plant Measurements

Several in-plant measurement campaigns are planned to resolve current HWC issues and to provide benchmarking data for further model development. These programs are summarized in Table 2 along with the various host plants. Host plants are selected to cover three major variables: power density; copper concentration in the water; and jet pumps vs. no jet pumps.

The program at Duane Arnold Energy Center (DAEC) is currently underway and is addressing several key issues such as: (1) in-vessel ECP as a function of location and hydrogen injection rate; (2) the relationship between crack growth rate and ECP for relevant in-vessel conditions; and (3) the relationship between chemistry in the recirculation pipe and that in a test autoclave. The specific objectives of this program are: to determine to what extent HWC will protect reactor internals at DAEC; to qualify ECP and crack growth rate as measured in an autoclave as being representative of actual material behavior in a recirculation pipe; and to benchmark the chemistry model.

The approach was to make ECP, crack growth and chemistry measurements as a function of hydrogen injection rate at several locations in the coolant circuit. ECP measurements were taken near the core-plate and top guide, in the recirculation piping, and in an autoclave the influent of which came from the recirculation system sample point. Crack growth measurements were taken at the same locations except for near the core plate, where crack growth tests were not possible due to space limitations. The physical arrangement of the various ECP and crack growth sensors is shown schematically in Figure 13. The locations of the water chemistry measurements are shown in Figure 14. The in-core sensors are located in two low-power range monitor (LPRM) assemblies. The first LPRM assembly consists of ECP sensors slightly below the top guide and above the core plate. Ag/AgCl and platinum are used as reference electrodes and Type 316SS as the measurement electrode. The second LPRM assembly contains two precracked double cantilever beam (DCB) specimens below the top guide. Both DCB sensors are made of Type 304SS; one is solution-annealed and the other sensitized. The in-pipe and in-autoclave sensors each consist of two precracked DCB specimens of sensitized Type 304SS. Measurement and reference electrodes are located at both locations.

Favorable ECP response was observed in the in-core portion of the reactor during a recent hydrogen injection test at Duane Arnold. The ECP in the bottom portion of the core was lowered to <-230 mV SHE at a hydrogen injection rate into the feedwater of ~25 scfm. At an injection rate of 45 scfm, the highest injection rate performed, an ECP of <-350 mV SHE was measured at the

Table 2. Planned and Potential HWC In-Plant Programs

Issue	Planned Action	Host Plant		
		In Progress	Planned	Potential
Fuel performance	Extend current surveillance program to 4 cycles	Dresden-2		
Effects of copper	In-autoclave crack growth and ECP vs H_2 and Cu		Hatch-1	
	Fuel surveillance			Hatch-1 Peach Bottom-2
IGSCC during excursions	In-autoclave crack growth and ECP during controlled excursions in O_2 and conductivity		Peach Bottom-2	
Effects of zinc injection	In-autoclave crack growth and ECP vs H_2 and Zn injection			Hope Creek Fitzpatrick
	Fuel surveillance			Hope Creek
In-vessel ECP	Direct ECP measurements with in-core sensors	DAEC	Pilgrim	NMP-1 Fitzpatrick Monticello
In-vessel crack growth	Direct measurements with in-core sensors	DAEC		NMP-1 Fitzpatrick Monticello
In-pipe vs in-autoclave	Comparison of ECP and crack growth in-pipe and in-autoclave using same measurement methods	DAEC		Dresden-2

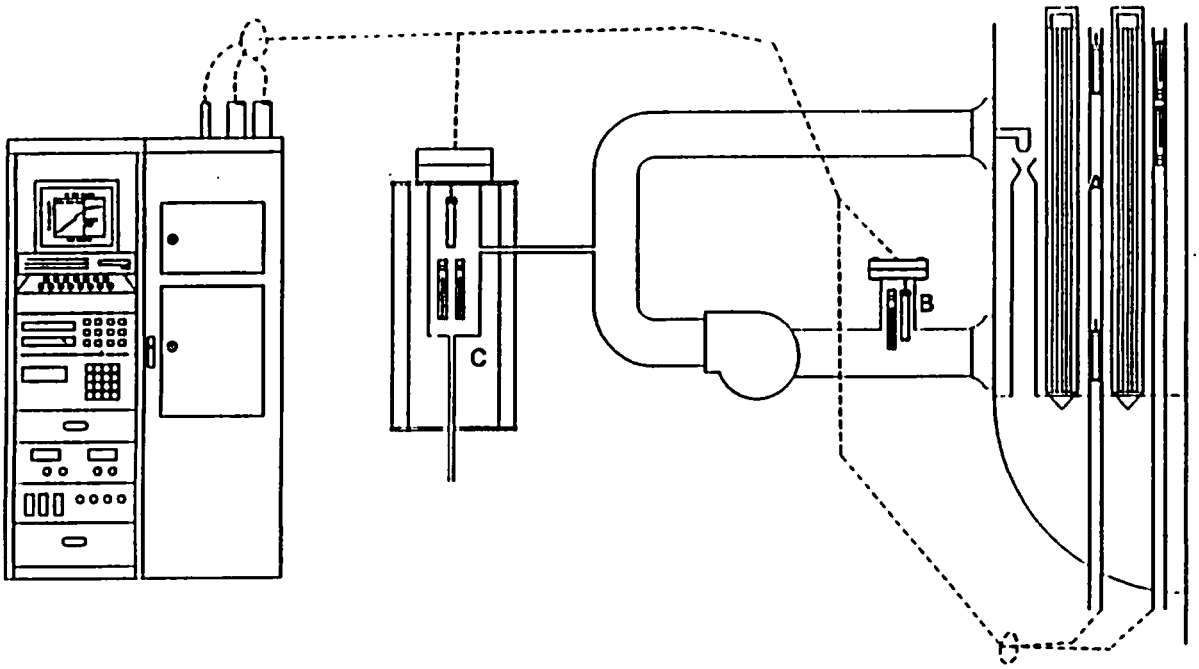

Figure 13. Schematic illustrating the locations of ECP and crack growth sensors at Duane Arnold. A. Reactor core. B. Recirculation flange. C. Test autoclave.

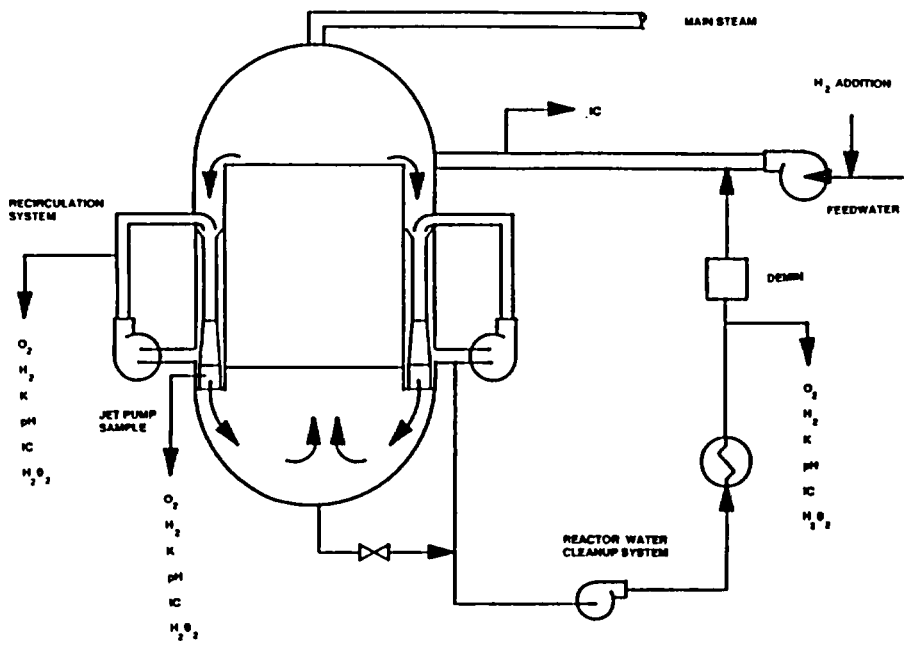

Figure 14. Schematic illustrating the sampling locations and chemical analyses being made at Duane Arnold.

bottom of the core. In addition, good agreement was measured between the ECP values of the in-pipe and in-autoclave sensors during hydrogen injection; both locations measured <-500 mV SHE at injection rates greater than 6 scfm.

No cracking was observed in any of the in-core crack growth sensors even during normal water chemistry operation. It was expected that the furnace-sensitized DCB sensor would initiate cracking shortly after plant startup. However, this was not the case and, after 2000 hours of exposure, cracking has still not been observed in either this sensor or in the solution-annealed sensor. This result was unexpected and is not understood at this time.

In spite of the unexpected behavior of the crack growth sensors, the main objectives of the program at DAEC have been met. The results confirm the reliability of the autoclave ECP measurements specified in the HWC guidelines[7] and demonstrate that reactor internals in the downcomer and lower head at DAEC can be protected by hydrogen injection, in accordance with model predictions for this plant.

SUMMARY

Hydrogen water chemistry for BWRs, which was conceived as a remedy for BWR pipe cracking problems, has been under development in the United States for more than a decade. The results of laboratory tests have shown that IGSCC of sensitized stainless steel is suppressed at low ECP levels in water of similar purity to that of the reactor water in an operating BWR. Field trials have demonstrated that the ECP of stainless steel in the recirculation systems of operating BWRs can be reduced to low values by injecting hydrogen into the feedwater, without adversely affecting fuel performance or shutdown radiation fields. Hydrogen injection does, however, increase radiation fields (especially in the turbine building) during operation. Guidelines have been prepared that define both the chemistry conditions that are required to prevent significant IGSCC in recirculation system piping during power operation, and NRC-acceptable methods of designing, constructing and operating hydrogen storage and injection facilities.

The development of HWC as a BWR pipe-crack remedy is essentially complete. Current and future development activities are mainly aimed at the adaptation of HWC for the protection of BWR reactor vessels and internals from corrosion cracking damage. This adaptation activity involves efforts to build improved BWR chemistry data for model benchmarking. Results to date are encouraging and suggest that within a few years, it will be possible to define revised HWC operating guidelines that will substantially reduce the likelihood of IGSCC damage to most of the potentially susceptible components in BWR plants.

ACKNOWLEDGMENTS

The list of contributors to EPRI's HWC program is now much too long to enumerate in detail. However, the authors wish to thank their many colleagues at EPRI, General Electric Company, Commonwealth Edison Company, and Iowa Electric Light and Power Company without whose efforts this paper would certainly not have been possible.

REFERENCES

1. "BWR Normal Water Chemistry Guidelines: 1986 Revision", EPRI NP-4946-SR, Electric Power Research Institute, September 1988.

2. "Hydrogen Water Chemistry for BWRs" A Status Report", EPRI NP-4592-SR, Electric Power Research Institute, June 1986.

3. "Plant Materials Program: Progress June 1981 to May 1982", EPRI NP-2879-SR, Electric Power Research Institute, February 1983.

4. B. M. Gordon et al., "Hydrogen Water Chemistry for BWRs: Materials Behavior", EPRI NP-5080, Electric Power Research Institute, March 1987.

5. E. L. Burley, "Oxygen Suppression in BWRs--Phase I Final Report", DOE/ET/34203-44 (NEDC-23856-4), U.S. Department of Energy, July 1981.

6. C. P. Ruiz et al., "Modeling HWC for BWR Applications", EPRI NP-6386, Electric Power Research Institute, June 1989.

7. "BWR Hydrogen Water Chemistry Guidelines: 1987 Revision", EPRI NP-4947-SR, Electric Power Research Institute, December 1988.

8. "Guidelines for Permanent BWR HWC Installations--1987 Revision", EPRI NP-5283-SR-A, Electric Power Research Institute, September 1987.

CAST STAINLESS STEEL AGING: MECHANISMS AND PREDICTIONS*

O. K. Chopra and H. M. Chung

Materials and Components Technology Division
Argonne National Laboratory
9700 South Cass Avenue
Argonne, IL 60439 USA

Abstract

Charpy-impact and J-R curve data are presented for several experimental and commercial heats, as well as for reactor-aged material of CF-3, CF-8, and CF-8M cast stainless steels. The effects of material variables on the embrittlement of cast stainless steels are evaluated. In general, the low-carbon CF-3 cast stainless steels are the most resistant and the Mo-containing, high-carbon CF-8M steels are the most susceptible to low-temperature embrittlement. The ferrite morphology strongly affects the extent or degree of embrittlement, whereas material composition influences the kinetics of embrittlement. The kinetics of embrittlement can vary significantly with small changes in the constituent elements of the cast material. The mechanisms of embrittlement are also established. Mechanical-property data are analyzed to develop the procedure and correlations for predicting the kinetics and extent of embrittlement of reactor components from known material parameters. The method and examples of estimating the impact strength and fracture toughness of cast components during reactor service are described. The lower-bound values of impact strength and fracture toughness for cast stainless steels at LWR operating temperatures are defined.

1. Introduction

A program is being conducted to investigate the significance of low-temperature embrittlement of cast duplex stainless steels under LWR operating conditions and to evaluate possible remedies to the embrittlement problem in existing and future plants. The scope of the investigation includes the following goals: (1) establish the aging mechanism and validate the simulation of in-reactor degradation by accelerated aging, (2) establish the effects of key compositional and metallurgical variables on the kinetics and extent of embrittlement, and (3) obtain fracture toughness data on long-term-aged materials for extrapolation to predict the degree of toughness loss suffered by cast stainless steel components during normal and extended service life of reactors.

Microstructural and mechanical-properties data are being obtained on 19 experimental (static-cast keel blocks) and six commercial heats (centrifugally cast pipes and a static-cast pump impeller and pump casing ring), as well as reactor-aged material of CF-3, CF-8, and CF-8M grades of cast stainless steel. Six of the experimental heats are also in the form of 76-mm-thick slabs. The reactor-aged material is from the recirculating cover plate assembly of the KRB reactor, which was in service in Gundremmingen, Federal Republic of Germany, for ~12 yrs (~8 yr at service temperature of 284°C). Fractured impact test bars from five heats of aged cast stainless steel were obtained from Georg Fischer Co. (GF), Switzerland, for microstructural characterization. All the materials are from a previous study of long-term aging behavior of cast stainless steel.[1] The data on chemical composition, ferrite content, hardness, ferrite morphology, and grain structure of the

* RSR FIN Budget No. A2243; RSR Contact: J. Muscara.

experimental and commercial heats have been reported elsewhere.[2-6] The ferrite content of the cast materials ranges from 3 to 30%. The chemical composition, hardness, and ferrite content and distribution of some of the cast materials are given in Table 1. Specimen blanks for Charpy-impact, tensile, and J-R curve tests are being aged at 290, 320, 350, 400, and 450°C for up to 50,000 h.

The mechanical-property data for several heats of cast stainless steel aged up to 30,000 h have been presented earlier.[7-9] A preliminary assessment of the processes and significance of the thermal aging in cast stainless steels was also presented.[9] The results indicate that thermal aging at temperatures below 500°C increases the tensile strength and decreases the impact energy and fracture toughness of the steels. The Charpy transition curve shifts to higher temperatures. Different heats exhibit different degrees of embrittlement. For cast stainless steel of all grades, the extent of embrittlement increases with an increase in ferrite content. The low-carbon CF-3 steels are the most resistant, and the Mo-containing, high-carbon CF-8M steels are the least resistant to embrittlement.

Embrittlement of cast stainless steels results in a brittle fracture associated with either cleavage of the ferrite or separation of the ferrite/austenite phase boundary. The latter generally occurs in the high-carbon steels because of the presence of large $M_{23}C_6$ carbides at the phase boundaries. For CF-8 steels, the phase-boundary carbides form during production heat treatment of the casting. Consequently, the unaged CF-8 steels exhibit low lower-shelf energy and high mid-shelf Charpy transition temperature (CTT) relative to the CF-3 steels. The fracture mode for CF-8 steels in the lower-shelf or transition-temperature regime is predominantly phase-boundary separation (Fig. 1).[7,8] In contrast, the CF-3 steels show a dimpled ductile failure. Fracture by phase-boundary separation is observed in only a few heats of unaged CF-8M steels and is dependent on whether the material contains phase-boundary carbides. The metallographic data indicate that additional precipitation of phase-boundary carbides and/or growth of existing carbides occurs in the high-carbon steels during thermal aging, particularly after aging at 400 or 450°C.[8]

The mechanical-property data also indicate that the kinetics and extent of embrittlement are controlled by several mechanisms that depend on material parameters and aging temperature. Materials aged at 450°C show significant precipitation of phase-boundary carbides (also nitrides in high-nitrogen steels) and a large decrease in ferrite content of the material.[9] Furthermore, the decrease in ferrite is significantly greater for CF-8M steels than for the other grades. Such processes either do not occur or their kinetics are extremely slow at reactor temperatures. Consequently, data obtained at 450°C aging do not reflect reactor operating conditions, and extrapolation of the 450°C data to predict the extent of embrittlement at reactor temperatures is not valid.

This paper summarizes of the mechanical-property data for several heats of cast stainless steel aged up to 30,000 h at 290, 320, 350, and 400°C. The results are analyzed to develop the procedure and correlations for predicting the kinetics and extent of embrittlement of reactor components from known material parameters. The mechanisms of thermal embrittlement of cast stainless steels are also discussed.

2. Room-Temperature Impact Energy

The results from room-temperature Charpy-impact tests on the various experimental and commercial heats, aged up to 30,000 h at 290, 320, 350, and 400°C, were analyzed to determine the kinetics and extent of embrittlement. The variation of the Charpy-impact energy (KCV) with time can be expressed as

Table 1. Product Form, Chemical Analysis, Hardness, and Ferrite Morphology of Various Heats of Cast Stainless Steel

Heat	Grade	Product Form	Dimensions (mm)	Composition (wt.%)							Hardness (R_B)	Ferrite Content (%)		Ferrite Intercept (μm)
				C	N	Mn	Si	Ni	Cr	Mo		Calc.	Meas.	
56	CF-8	Keel B.	180 x 120 x 30-90	0.066	0.030	0.57	1.05	9.28	19.65	0.34	82.5	7.3	10.1	84
59	CF-8			0.062	0.045	0.60	1.08	9.34	20.33	0.32	83.2	8.8	13.5	75
61	CF-8			0.054	0.080	0.65	1.01	8.86	20.65	0.32	85.2	10.0	13.1	82
60	CF-8			0.064	0.058	0.67	0.95	8.34	21.05	0.31	86.7	15.1	21.1	63
47	CF-3			0.018	0.028	0.60	1.06	10.63	19.81	0.59	79.6	8.4	16.3	68
52	CF-3			0.009	0.052	0.57	0.92	9.40	19.49	0.35	81.6	10.3	13.5	69
51	CF-3			0.010	0.058	0.63	0.86	9.06	20.13	0.32	83.8	14.2	18.0	52
63	CF-8M			0.055	0.031	0.61	0.58	11.85	19.37	2.57	81.5	6.4	10.4	81
65	CF-8M			0.049	0.064	0.50	0.48	9.63	20.78	2.57	89.9	20.9	23.4	43
64	CF-8M			0.038	0.038	0.60	0.63	9.40	20.76	2.46	89.7	28.9	28.4	41
P1	CF-8	Pipe	890 OD 63 wall	0.036	0.056	0.59	1.12	8.10	20.49	0.04	84.9	17.7	24.1	90
P2	CF-3	Pipe	930 OD 73 wall	0.019	0.040	0.74	0.94	9.38	20.20	0.16	83.8	12.4	15.6	69
I	CF-3	Impeller	NA	0.019	0.032	0.47	0.83	8.65	20.14	0.45	81.0	20.9	17.1	65
P4	CF-8M	Pipe	580 OD 32 wall	0.040	0.151	1.07	1.02	10.00	19.64	2.05	83.1	5.9	10.4	182
68	CF-8	Slab	610 x 610 x 76	0.063	0.062	0.64	1.07	8.08	20.64	0.31	84.6	14.9	23.4	87
69	CF-3	Slab	610 x 610 x 76	0.023	0.028	0.63	1.13	8.59	20.18	0.34	83.7	21.0	23.6	35
74	CF-8M	Slab	610 x 610 x 76	0.064	0.048	0.54	0.73	9.03	19.11	2.51	85.8	15.5	18.4	90
75	CF-8M	Slab	610 x 610 x 76	0.065	0.052	0.53	0.67	9.12	20.86	2.58	89.5	24.8	27.8	73
KRB	CF-8	Pump Cover Plate		0.062	0.038	0.31	1.17	8.03	21.99	0.17	–	27.7	34.0	173

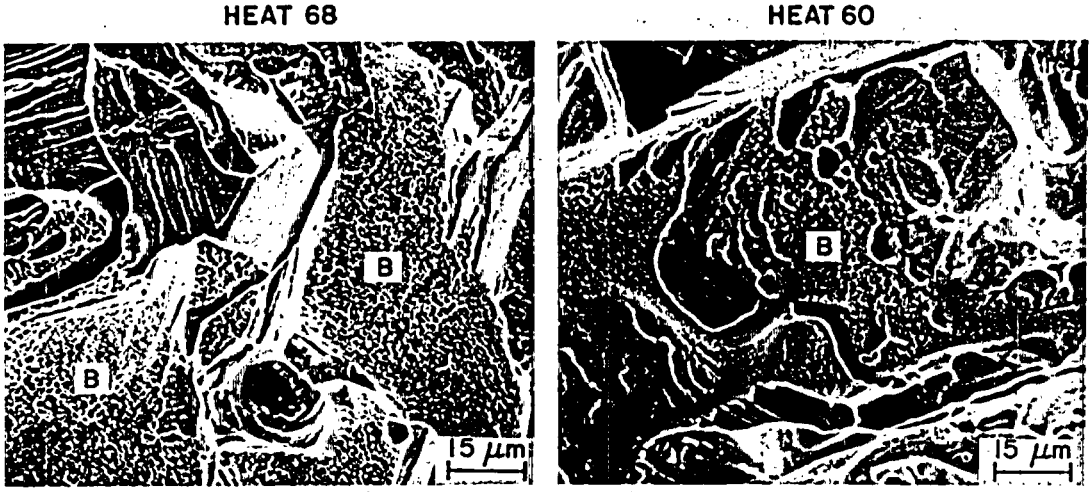

Fig. 1. Fracture Surface of Charpy-Impact Specimens of Unaged CF-8 Steel Tested at -196°C. Fracture mode B = phase-boundary separation.

$$KCV = K_m + \beta\{1 - \tanh [(P - \theta)/\alpha]\}, \quad (1)$$

where P is the aging parameter, K_m is the minimum impact energy reached after long-term aging, β is half the maximum decrease in impact energy, θ is the log of the time to achieve β reduction in impact energy, and α is a shape factor. The aging parameter represents the time to achieve a specific degree of aging at 400°C. The aging time to reach a given degree of embrittlement at different temperatures is determined from the equation

$$t = 10^P \exp\left[\frac{Q}{R}\left(\frac{1}{T} - \frac{1}{673}\right)\right], \quad (2)$$

where Q is the activation energy, R the gas constant, T the absolute temperature, and P the aging parameter that represents the degree of aging reached after 10^P h at 400°C.

The values of the constants in Eqs. (1) and (2) were obtained from the best fit of the Charpy data for various heats of cast stainless steel aged up to 30,000 h at 290, 320, 350, and 400°C. The activation energies and 95% confidence limits are given in Table 2. Charpy-impact data for three of the heats are plotted as a function of aging time in Fig. 2, along with the fitted curves of the form given by Eqs. (1) and (2). The confidence limits are large for some heats because of the relatively small decrease in impact energy and significant scatter in the data. The Charpy data obtained from 290°C aging showed no reduction in impact energy even after aging for 30,000 h; instead, a slight increase in impact energy was observed relative to the unaged values. This increase in impact energy is real and was observed for most heats aged at low temperatures, i.e., 30,000 h at 290°C or 3,000 to 10,000 h at 320°C. The low-temperature-aging data tends to bias the analyses to yield higher values for activation energies; therefore, the results from the 290°C aging were excluded from the analysis to obtain the activation energies for some of the heats. Data from long-term aging are needed to establish the kinetics of embrittlement between 320 and 290°C.

Table 2. Activation Energies for the Kinetics of Embrittlement for Various Heats of Cast Stainless Steels

Heat	Ferrite (%) Meas.	Ferrite (%) Calc.[a]	Material Parameter Φ[b]	Activation Energy, kJ/mole (kcal/mole) Average	95% Confidence Limit	From Ref. 9
47	16.3	8.4	11.3	134 (32.1)	53–216 (12.6–51.6)[c]	92 (21.9)
51	18.0	14.3	11.9	218 (52.1)	116–320 27.7–76.5)[c]	184 (44.1)
69	23.6	21.0	14.4	170 (40.6)	113–226 (27.0–54.1)[c]	–
56	10.1	7.3	14.1	–	–	234 (56.0)
59	13.5	8.8	23.8	–	–	196 (46.9)
60	21.1	15.4	54.6	240 (57.3)	194–285 (46.4–68.2)	199 (47.5)
68	23.4	14.9	92.1	166 (39.6)	133–199 (31.7–47.6)	–
P1	24.1	17.7	66.1	239 (57.1)	203–274 (48.5–65.6)	–
63	10.4	6.4	13.3	–	–	102 (24.3)
64	28.4	29.0	42.0	141 (33.8)	111–172 (26.5–41.0)	143 (34.1)
65	23.4	20.9	41.9	177 (42.2)	140–214 (33.4–51.1)	152 (36.4)
66	19.8	19.6	21.0	171 (40.9)	96–246 (23.0–58.7)[c]	126 (30.2)
75	27.8	24.8	116.7	159 (38.0)	138–180 (32.9–43.0)	–
P4	10.0	5.9	41.5	152 (36.3)	123–181 (29.5–43.2)	–

[a]Calculated from chemical composition with Hull's equivalent factor.

[b]$\Phi = \delta_m^2 (C + 0.4N) (Cr + Mo + Si)\ 1/1000$, where δ is the measured ferrite content in %, 1 is the mean ferrite spacing in μ, and the concentrations of C, N, Cr, Mo, and Si in the cast stainless steel are in wt.%.

[c]Standard deviation is large because of the relatively small decrease in impact energy and large scatter in the data.

The activation energies reported earlier in Ref. 9 are also listed in Table 2. Charpy data for long-term aging (i.e., 30,000 h) at 320 and 290°C were not included in the analyses in Ref. 9. Thus, the calculated activation energies primarily represent the kinetics of embrittlement at temperatures of 350 to 400°C. These values are 15 to 20% lower than those determined from aging data at temperatures of 320 to 400°C. The results suggest that the activation energy of embrittlement is not constant in the temperature range of 290-400°C, but increases with a decrease in temperature. A similar behavior has been reported for several heats of CF-8M steels aged at temperatures of 300 to 400°C.[10] Consequently, the extrapolation of the 400°C aging data to reactor temperatures may not be valid and would yield conservative estimates of embrittlement for some of the heats of cast stainless steel.

3. Extent of Embrittlement

The Charpy-impact data obtained at room temperature were analyzed to develop a correlation between material variables and the extent or degree of embrittlement, i.e., minimum room-temperature impact energy [K_m in Eq. (1)] that would ever be achieved after long-term aging. It is well established that the extent of embrittlement increases with

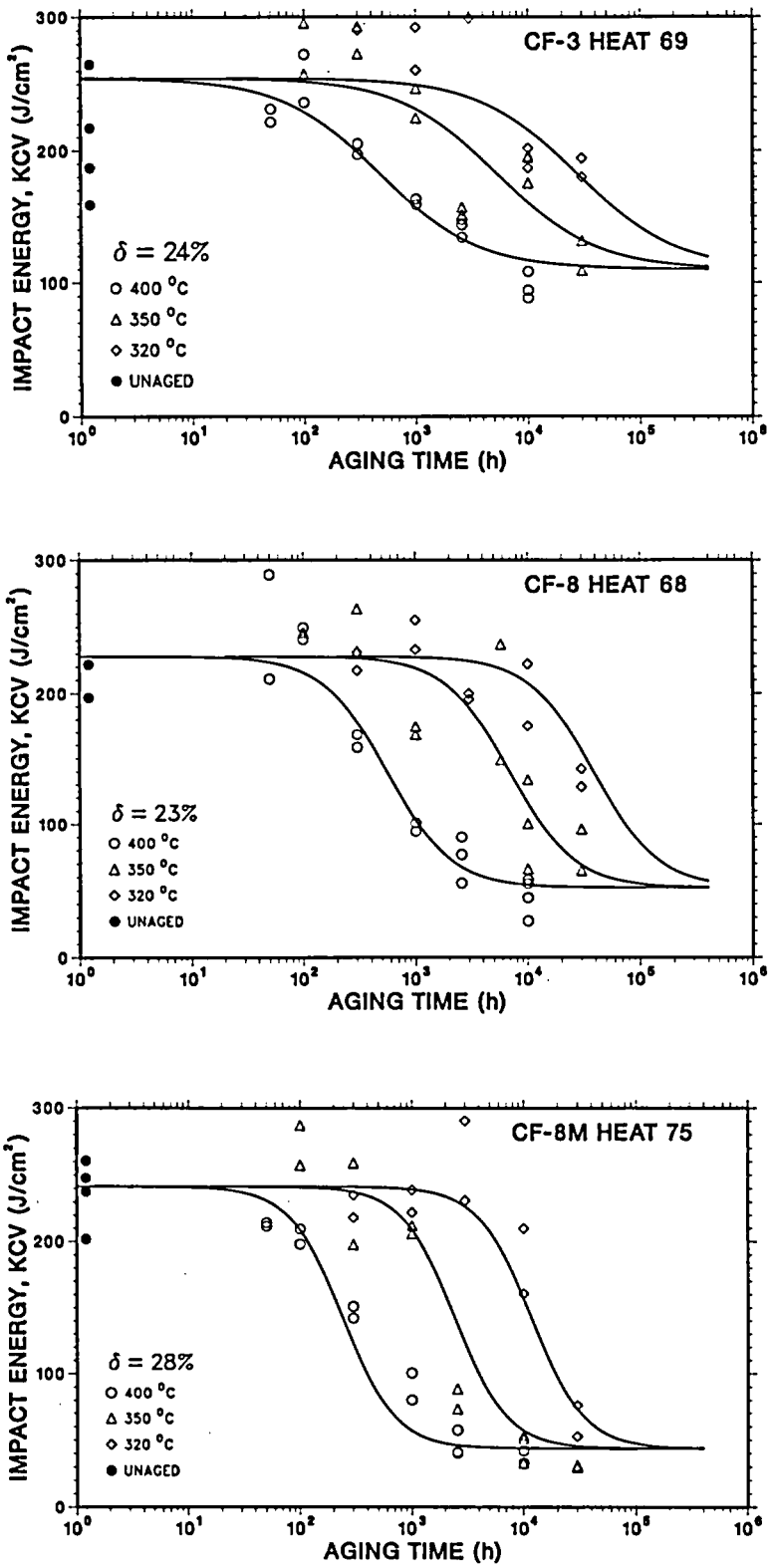

Fig. 2. Effect of Thermal Aging on Room-Temperature Impact Energy of CF-3, CF-8, and CF-8M Cast Stainless Steels.

an increase in the ferrite content of the cast stainless steel. Furthermore, Charpy-impact data for several heats of CF-8 and CF-8M steels, aged for 10,000 h at 350 or 400°C, indicate that the impact energy decreases with an increase in the Cr content, irrespective of the ferrite content of the steel.[10] A better correlation was obtained when the total concentration of ferrite formers (i.e., Cr, Mo, and Si) is considered.[10] A sharp decrease in impact energy occurs when either the Cr content exceeds 18 wt.% or the concentration of Cr + Mo + Si exceeds 23.5 wt.%. The concentrations of C and N in the steel also increase the extent of embrittlement because of their contribution to phase-boundary carbides or nitrides and the subsequent fracture by phase-boundary separation. Consequently, an exponential function of the various material variables was used to analyze the data on the minimum room-temperature impact energy. Best-fit curves of the data were obtained with a material parameter Φ given by

$$\Phi = \delta_m^2 \, (C + 0.4\, N)\, (Cr + Mo + Si)\, l \; (\times 10^{-3}), \qquad (3)$$

where the measured ferrite content δ_m is in %, the Cr, Mo, Si, C, and N contents are in wt.%, and the mean ferrite spacing l is in μm. The results indicate that both the amount and spacing of ferrite influence the extent of embrittlement. A similar correlation, but without the effect of ferrite spacing, has been proposed earlier by investigators at Electricité de France (EdF).*

The minimum impact energy is plotted in Fig. 3 as a function of the material parameter Φ. Results from the studies at Framatome (FRA),[11,12] Central Electricity Generating Board (CEGB),[13] and Electric Power Research Institute (EPRI)[14] are also presented in the figure. The data show a good correlation with the material parameter. However, the impact energy for FRA Heat 4331[12] is significantly lower than that predicted from Fig. 3. This heat contains 0.2% Nb. The fracture surface of the impact test specimen (Fig. 4) shows that the phase boundaries are decorated with very large Nb carbides that crack easily. The large phase-boundary carbides alter the deformation and fracture behavior of the material, i.e., initiation of cleavage by carbide cracking. A difference in fracture mode is reflected in the values of the yield and maximum loads for the instrumented Charpy tests, shown in Fig. 5 for FRA Heat 4331 and Argonne National Laboratory (ANL) Heat 74. The corresponding Charpy transition curves are shown in Fig. 6. Both heats are CF-8M and contain ~20% ferrite, yet the transition curves are significantly different. The 65-J (~50 ft·lb) transition temperature is 220°C for Heat 4331 (aged for 700 h at 400°C) and 20°C for Heat 74 (aged for 10,000 h at 400°C). The yield loads are comparable for both heats, indicating similar degree of strengthening in the two heats. However, Fig. 5 shows that failure occurs at ~14 kN load in Heat 4331 and at ~18 kN load in Heat 74. The difference in the maximum load at failure suggests a difference in fracture mechanism. The present correlation does not consider the effects of Nb on embrittlement.

The correlation in Fig. 3 indicates that the impact energy will be less than 50 J/cm^2 (30 ft·lb) for those cast stainless steels for which the material parameter is greater than ~60. For cast stainless steels containing >10% ferrite, the mean ferrite spacing is in the range of 40 to 200 μm; Cr + Mo + Si concentration is ~22% for CF-8 or CF-3, and ~24% for CF-8M; N content is typically 0.04%. Thus, for cast materials with 0.06% C and 100 μm ferrite spacing, the impact energy will be below 50 J/cm^2 when the ferrite content is above 20%. However, cast materials with 10 or 15% ferrite can also reach very low impact strength when ferrite spacing or N content is high.

* M. Guttmann, EdF, private communications, October 1987.

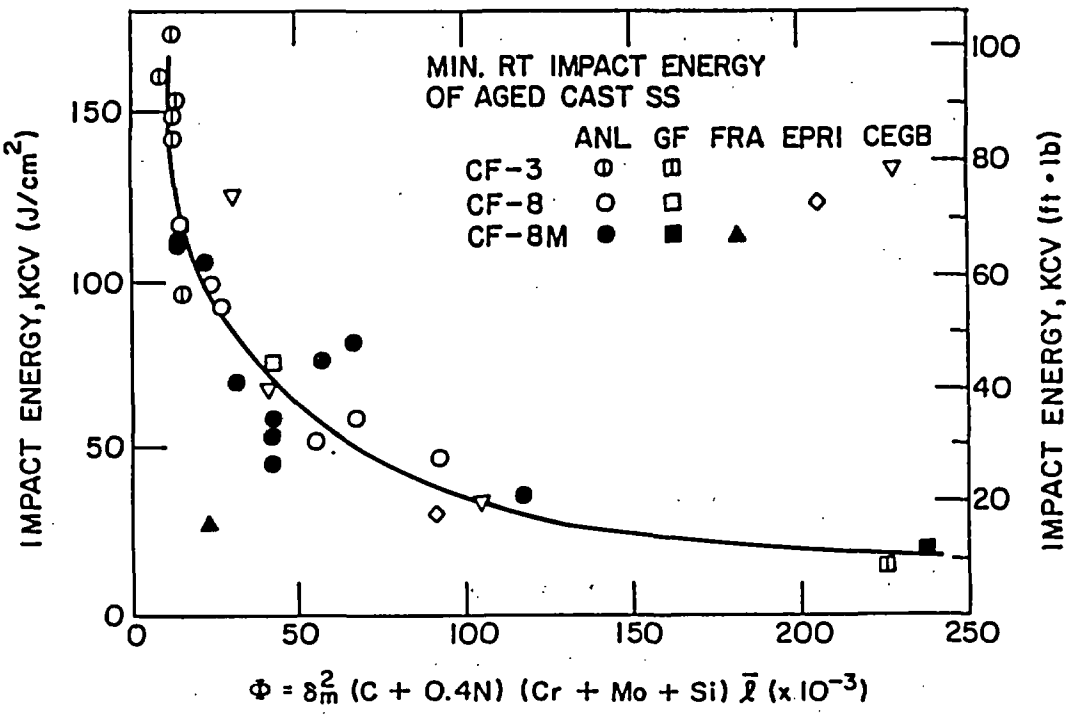

Fig. 3. Correlation between Minimum Room-Temperature Impact Energy and Material Parameter Φ for Aged Cast Stainless Steels.

Fig. 4. Fracture Surface of Charpy-Impact Specimen of FRA Heat 4331 Aged for 700 h at 400°C and Tested at Room Temperature.

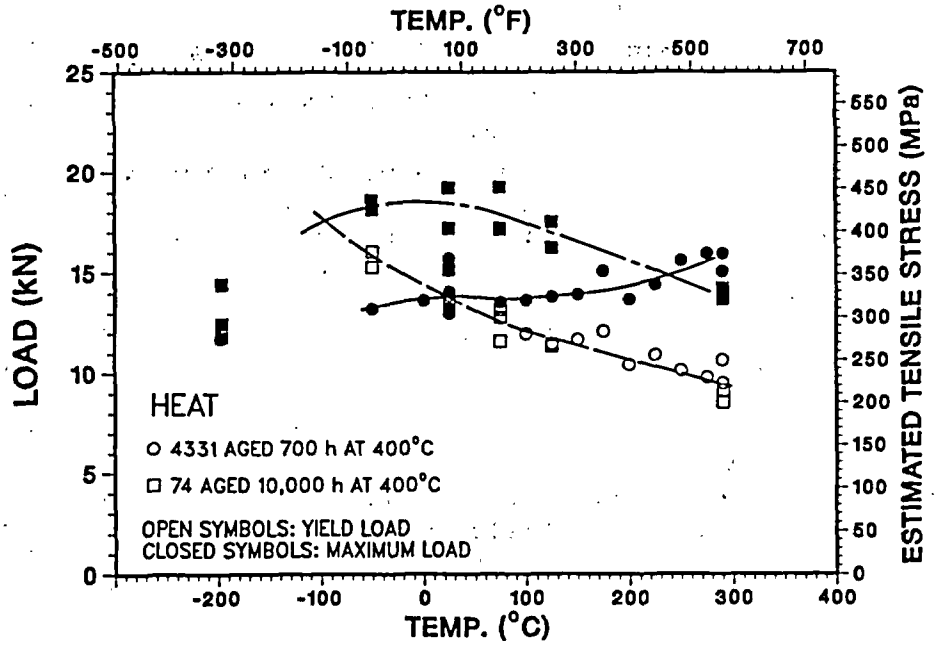

Fig. 5. Yield and Maximum Loads from Charpy-Impact Data for FRA Heat 4331 Aged for 700 h at 400°C and ANL Heat 74 Aged for 10,000 h at 400°C.

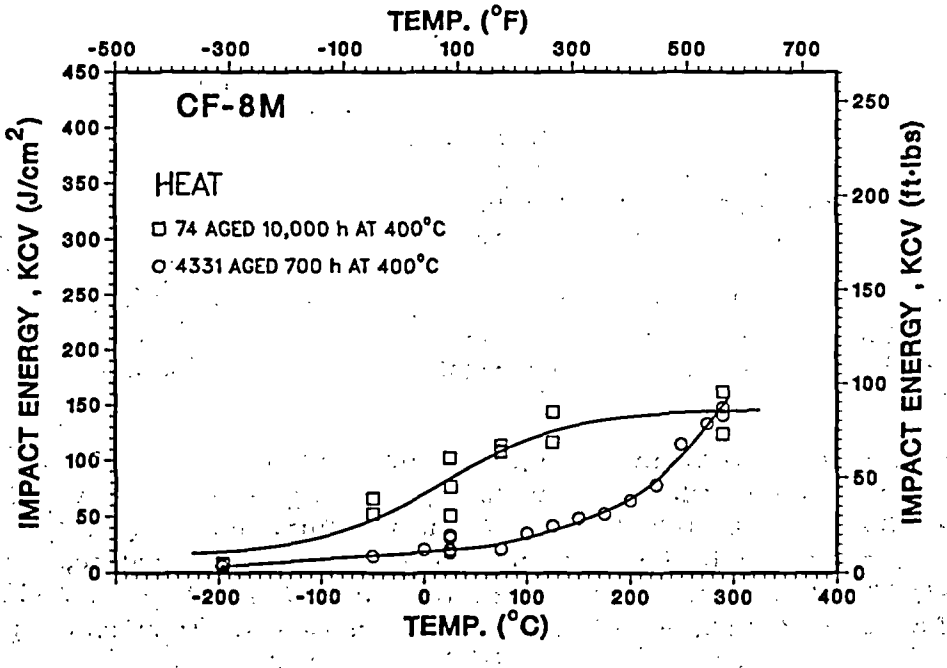

Fig. 6. Charpy Transition Curves for Heats 4331 and 74 Aged at 400°C.

Figure 3 can be used to estimate the extent of embrittlement (expressed as room-temperature impact energy) of a specific cast stainless steel component. The variables in the material parameter can be determined nondestructively. The compositions are generally known, and ferrite content can be calculated from the composition or measured with a ferrite scope. Ferrite spacing is the variable that is least readily available, but it can be determined by surface replica techniques. However, a conservative estimate of the possible extent of embrittlement can be obtained by assuming the highest value observed in the material data base, i.e., ferrite spacing of ~180 μm.

The effect of material parameter Φ on the extent of embrittlement is seen clearly in Fig. 7, where the impact energies of several heats with comparable values of Φ are plotted as a function of the aging parameter P. The different temperatures and times of aging are normalized in terms of P by Eq. (2). The results show that the extent of embrittlement increases with an increase in Φ. For each range of Φ, there is a saturation value of minimum impact energy. This behavior is independent of the kinetics of embrittlement, e.g., the extent of embrittlement is comparable for Heats 60, P1, 64, 65, and P4, whereas the activation energies range between 140 and 240 kJ/mole (34 and 57 kcal/mole). The ferrite content also varies significantly for these heats; 10% for Heat P4 and 28% for Heat 64.

4. Charpy Transition Curves

Assessment of the extent of embrittlement at reactor operating temperatures requires an evaluation of the effects of aging on the Charpy transition curves. The Charpy data were fitted with a hyperbolic tangent function of the form

$$KCV = K_0 + B\{1 + \tanh [(T-C)/D]\}, \quad (4)$$

where K_0 is the lower-shelf energy, T is the test temperature, B is half the difference between upper- and lower-shelf energy, C is the mid-shelf CTT in °C, and D is the half-width of the transition region. The best-fit curves for the three grades of cast stainless steel aged at 350°C for times up to 30,000 h are shown in Fig. 8. Thermal aging decreases the impact energy and shifts the transition curves to higher temperatures. The results suggest a "saturation effect" for upper-shelf energy (USE) after aging. The values of USE decrease significantly after aging for ~2600 h at 350°C and do not change for longer aging times. After saturation of USE, the decrease in impact energy is due to an increase in CTT, i.e., the value of B in Eq. (4) remains constant and only C and D increase with longer aging times. This behavior is observed at all aging temperatures and for all heats. The three heats in Fig. 8 have similar amounts of ferrite, and the "saturation" values of USE are comparable. However, the shift in CTT is significantly different; the CF-8M steel exhibits the largest shift.

The room-temperature Charpy data (Fig. 7) indicate that for a specific range of material parameter Φ, a saturation value of minimum impact energy is reached when P is ~3.5, i.e., ~3,000 h at 400°C or ~30,000 h at 350°C. A similar saturation effect on the Charpy transition curves cannot be established with any acceptable degree of confidence from the existing data. The transition curves for the three grades of cast stainless steel aged to P values of 3.4 to 4.0 are shown in Fig. 9. For Heat 69 (Φ ~14), the minimum room-temperature impact energy is close to the USE. The transition curves for the three aging conditions are comparable and suggest a saturation effect, i.e., the curves represent the maximum CTT that would ever be achieved after long-term aging. An increase in CTT would mean a further decrease in room-temperature impact energy for Heat 69. The

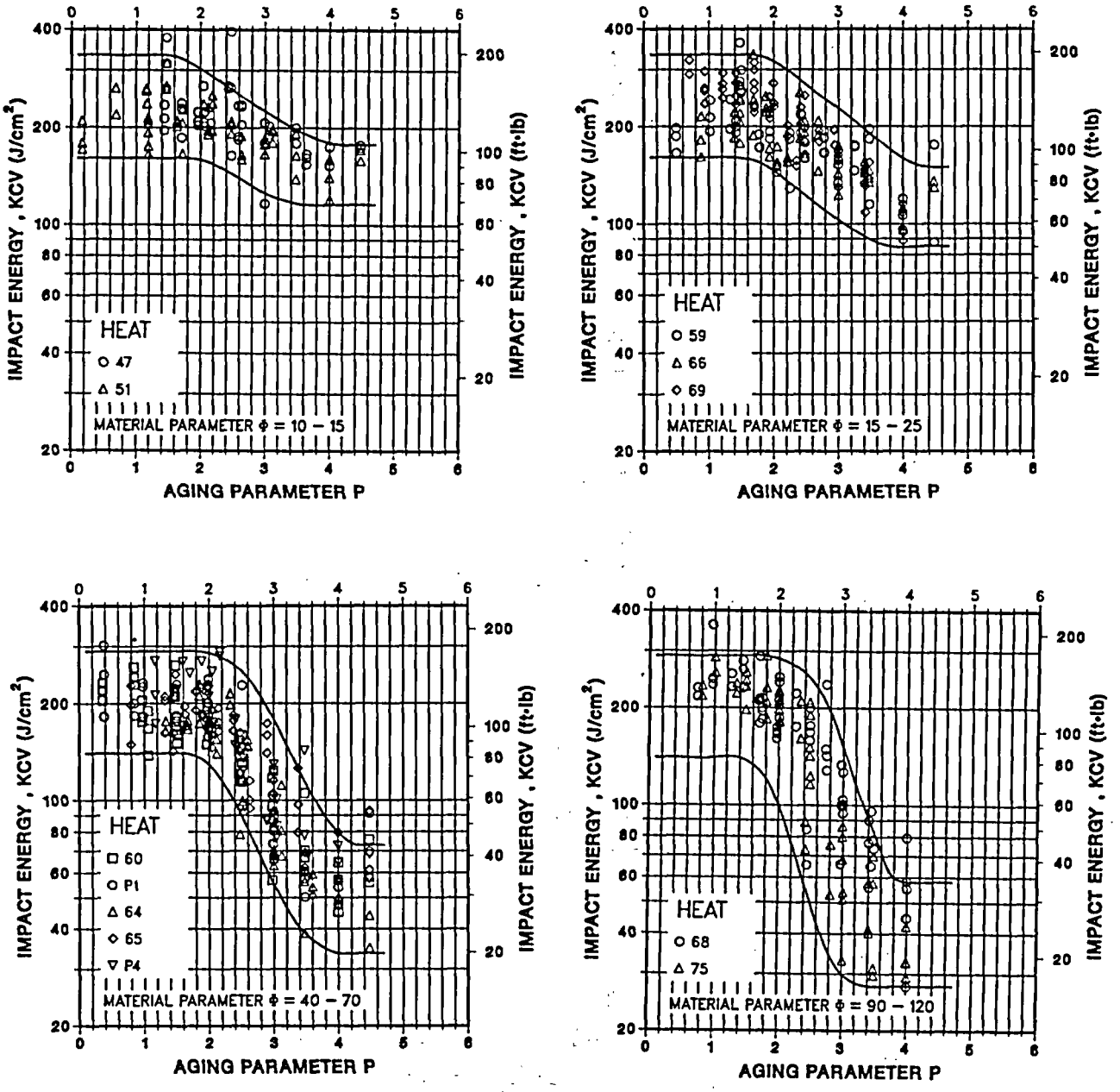

Fig. 7. Effect of Thermal Aging on Room-Temperature Impact Energy of CF-3, CF-8, and CF-8M Steels with Different Ranges of Material Parameters Φ.

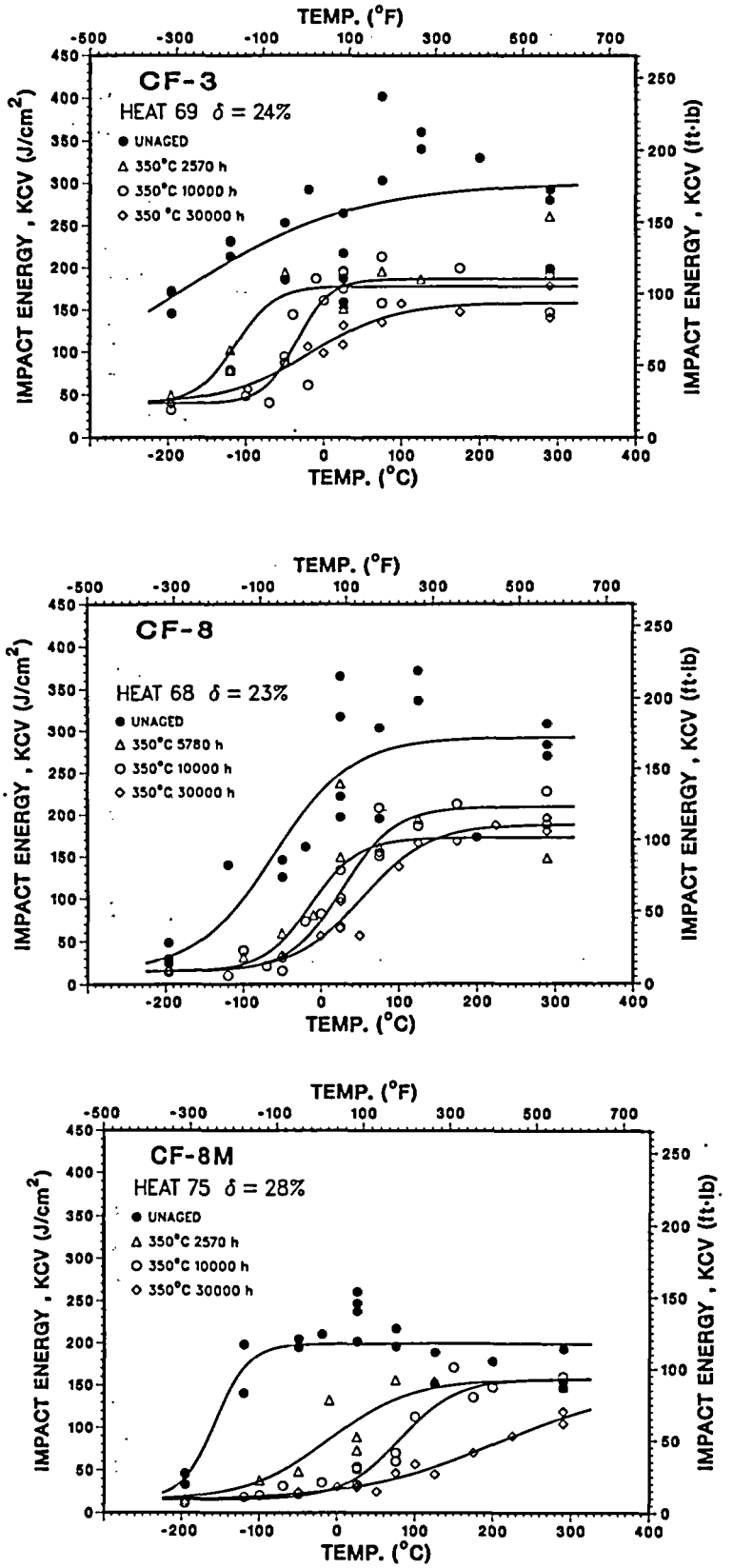

Fig. 8. Effect of Aging Time on Charpy Transition Curves of CF-3, CF-8, and CF-8M Steels Aged at 350°C.

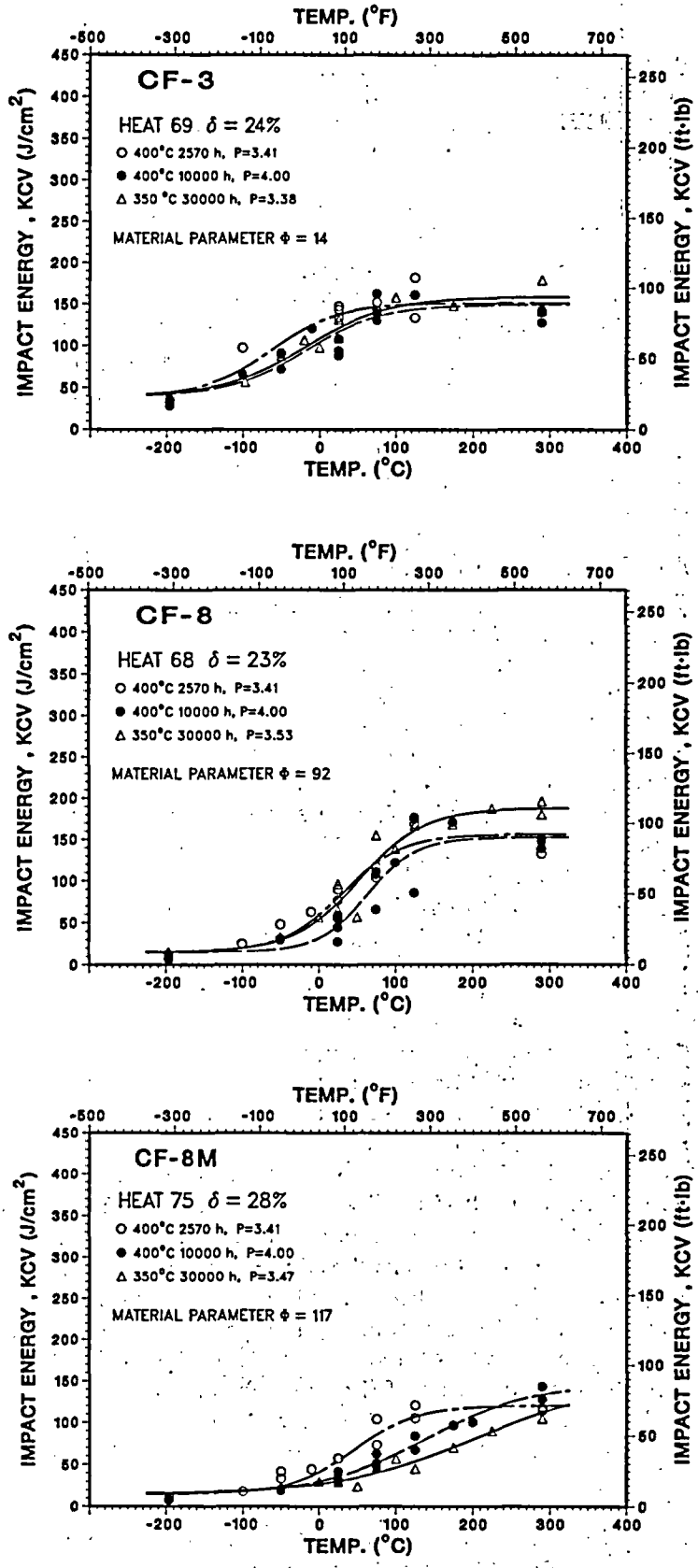

Fig. 9. Charpy Transition Curves for CF-3, CF-8, and CF-8M Steels Aged to P Values of 3.4 to 4.0.

transition curves for Heat 68 (Φ ~92) are also comparable but may not represent a saturation condition. The minimum room-temperature impact energy is close to the lower-shelf energy; an increase in CTT would not significantly change the room-temperature impact energy.

Transition curves for Heat 75 (Φ ~117) do not exhibit a saturation effect. The results indicate that, although the room-temperature impact energy does not change for P values >3.5, the impact energy at reactor temperatures can continue to decrease with time. This behavior is not unique to CF-8M steels and has been observed in the EPRI study on CF-3 steel (Φ ~90).[14] Long-term-aging data are needed to establish the impact energies at reactor temperatures and to determine whether a saturation effect in transition curves is achieved for some of the heats, e.g., heats with low values of material parameter Φ.

The transition curves for Heats 69, 68, and 75 also indicate that the transition curves for 350°C aging are lower than those after aging for an equivalent time at 400°C, particularly for the CF-8M steel. The mid-shelf CTT for the three grades of cast stainless steel aged up to 30,000 h at 320, 350, and 400°C are plotted as a function of the aging parameter P in Fig. 10. For 350 or 320°C aging, the change in CTT with P, i.e., slope of the lines in Fig. 10, is approximately the same for the three heats. However, the values of the CTT for 400°C aging are lower than those for aging at 350°C.

These results raise an important issue: the kinetics of embrittlement established from the room-temperature Charpy data are not representative of the kinetics of embrittlement at reactor temperatures. The aging parameters P in Fig. 10 were calculated with activation energies obtained from room-temperature data. These values of P may not be valid for the high-temperature results. The kinetics of embrittlement cannot be obtained with any reasonable confidence from the high-temperature data. The results often yield negative values for activation energy. Figures 8 and 9 show that the impact energy at 290°C decreases rapidly during the initial 3000 h of aging and does not change significantly with longer aging times, particularly for heats with low values of Φ.

5. Fracture Toughness

The J-R tests were conducted at Materials Engineering Associates, Inc.,[15] and ANL on eight heats of cast stainless steel. The tests were performed on 1-T compact tension specimens according to ASTM specifications E813-85 and E1152. However, the values of J_{IC} were determined from the intersection of the power-law curve with the 0.15-offset line rather than the 0.2-offset line. The J-R curve tests on cast stainless steels[12] indicate that a slope of four times the flow stress for the blunting line expresses the J-vs-Δa data better than does the slope of two times the flow stress defined in E813-85. The values of J_{IC} reported in this paper were determined by using a slope of two times the flow stress for the blunting line. Consequently, the J_{IC} values are slightly higher relative to the data from the FRA study.[12] An average value of tearing modulus was determined from the power-law curve between the exclusion lines. The results indicate that thermal aging decreases the fracture toughness J_{IC} and tearing modulus of the material at room temperature and at 290°C. The fracture toughness results are consistent with the Charpy-impact data, i.e., unaged and aged materials that show low impact strength also exhibit lower fracture toughness.

The fracture toughness J_{IC} values and Charpy V-notch impact energies obtained at room temperature are plotted in Fig. 11. Results from the studies at Westinghouse (WH),[16] FRA,[11,12] and EPRI[14] are also shown. For low values of toughness (i.e., J_{IC} <500 kJ/m^2), J_{IC} decreases linearly with impact energy. The dashed lines represent the lower-bound

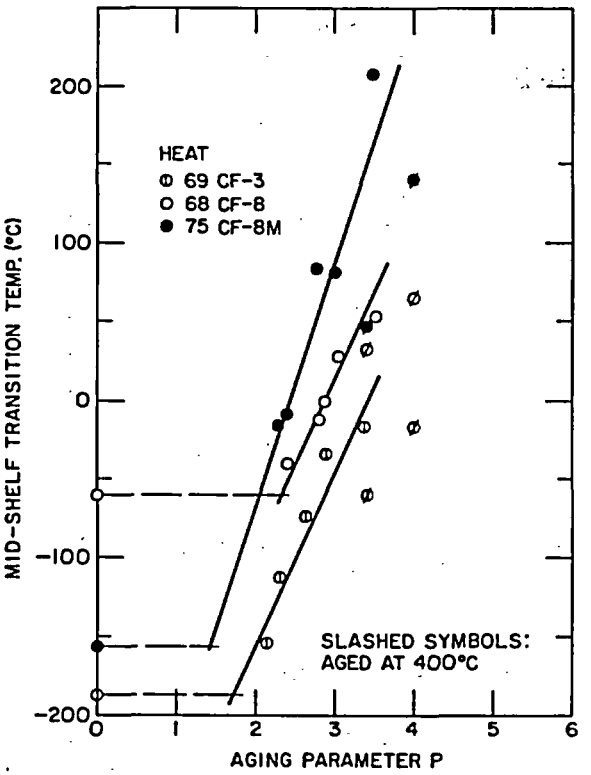

Fig. 10. Change in Mid-Shelf Charpy Transition Temperature with Thermal Aging.

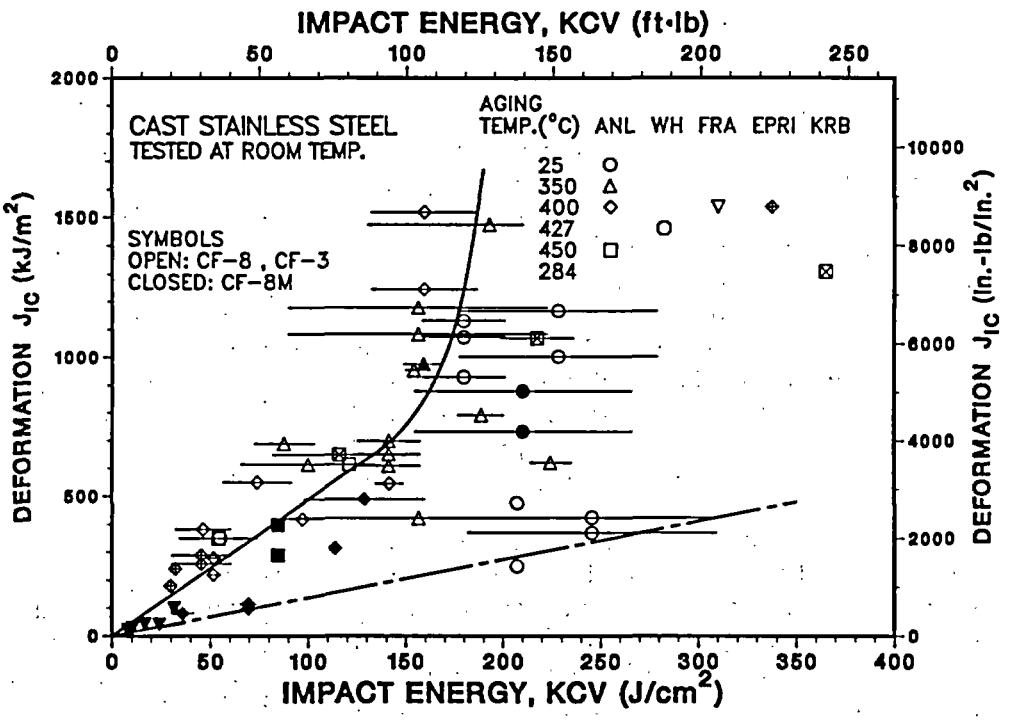

Fig. 11. Correlation between Room-Temperature Fracture Toughness (J_{IC}) and Impact Energy for Cast Stainless Steels.

values. The slope of the lower-bound curve is 0.143, which agrees well with the correlation between J and KCV proposed for flaw evaluation procedures for ferritic steel piping.[17] The tearing modulus also decreases with thermal aging. Figure 12 shows the room-temperature values of tearing modulus and J_{IC} for various heats and aging conditions. The dashed lines represent the lower-bound values.

Figures 3, 11, and 12 can be used to estimate the minimum room-temperature fracture toughness of any specific cast stainless steel aged for long times. The minimum room-temperature impact energy is determined from Fig. 3 and the fracture toughness J_{IC} and tearing modulus are estimated from Figs. 11 and 12. For the various heats investigated, the maximum value of material parameter Φ was ~120. This would correspond to minimum room-temperature impact energy of ~30 J/cm^2 (~18 ft·lb) and J_{IC} and tearing modulus values of 40 kJ/m^2 and 30, respectively. The impact energy, J_{IC}, and tearing modulus of heats that are very sensitive to thermal aging (i.e., Φ >150) could be as low as 15 J/cm^2, 20 kJ/m^2, and 15, respectively.

The influence of thermal aging on fracture toughness at reactor temperatures is difficult to estimate accurately from the present data. As discussed in Section 4, although the room-temperature impact energy reaches a minimum saturation value, the high-temperature impact energy can continue to decrease. For some heats, the extent and kinetics of embrittlement determined from room-temperature data are not representative of embrittlement at reactor temperatures. Figure 13 shows a plot of J_{IC} values at 290°C as a function of room-temperature impact energies for various heats and aging conditions. The results indicate that the room-temperature lower-bound curve, i.e., dashed line in Fig. 13, would yield a conservative estimate of J_{IC} at 290°C. Fracture toughness data from long-term-aged material will be helpful in establishing the lower-bound curve for J_{IC} at reactor temperature. The correlation between tearing modulus and J_{IC} values at 290°C is shown in Fig. 14.

6. Mechanisms of Embrittlement

Embrittlement of cast duplex stainless steel results in a brittle fracture associated with either cleavage of the ferrite phase or separation of the ferrite/austenite phase boundary. The degree of embrittlement is controlled by the amount of brittle fracture. Cast stainless steels with poor impact strength exhibit >80% brittle fracture. For some cast steels, although a fraction of the material may fail in a brittle fashion, the surrounding austenite provides ductility and toughness. Such steels have adequate impact strength even after long-term aging. A predominantly brittle failure occurs when either the ferrite phase is continuous, e.g., in cast material with a large ferrite content, or the ferrite/austenite phase boundary provides an easy path for crack propagation, e.g., in high-carbon cast steels with large phase-boundary carbides. Consequently, the amount, size, and distribution of the ferrite phase in the duplex structure and the presence of phase-boundary carbides are important parameters in controlling the degree or extent of embrittlement.

Thermal aging of cast stainless steels at temperatures of 300 to 450°C leads to the precipitation of additional phases in the ferrite matrix, e.g., formation of a Cr-rich α' phase by spinodal decomposition, nucleation and growth of α', precipitation of a Ni- and Si-rich G phase, γ_2 (austenite), and $M_{23}C_6$ carbide.[18-20] The additional phases provide the strengthening mechanism and strain hardening to increase the local tensile stress. Consequently, the critical stress level for brittle fracture is achieved at higher temperatures. Microstructural data indicate that formation of α' by spinodal decomposition is the

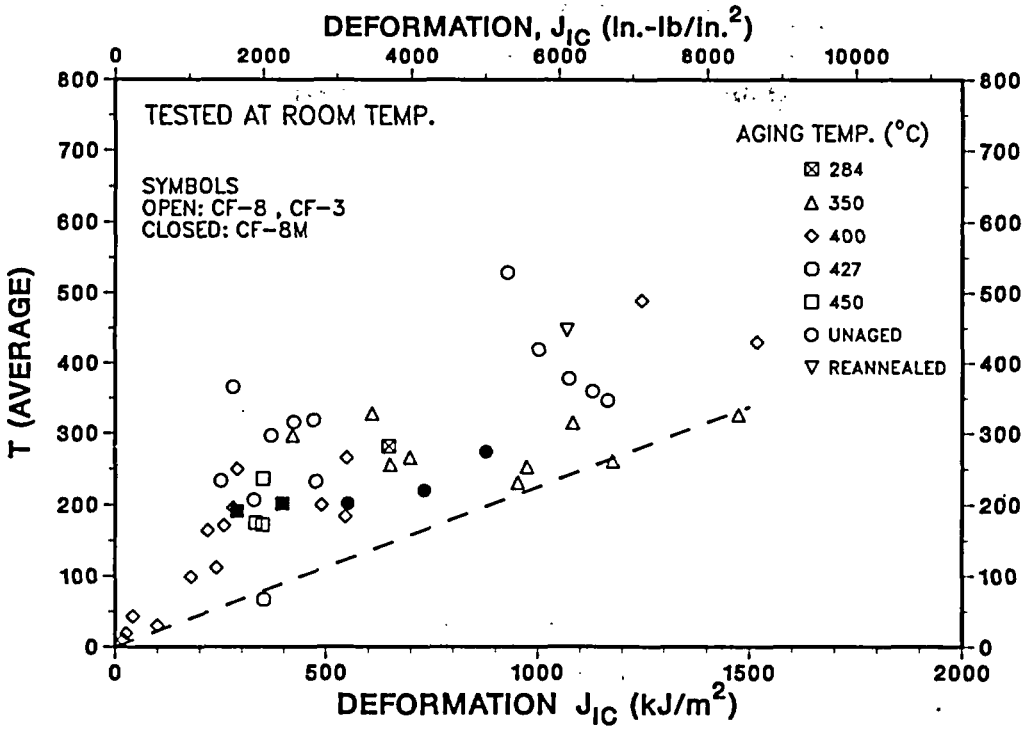

Fig. 12. Correlation between Room-Temperature Tearing Modulus (T) and Fracture Toughness (J_{IC}) for Cast Stainless Steels.

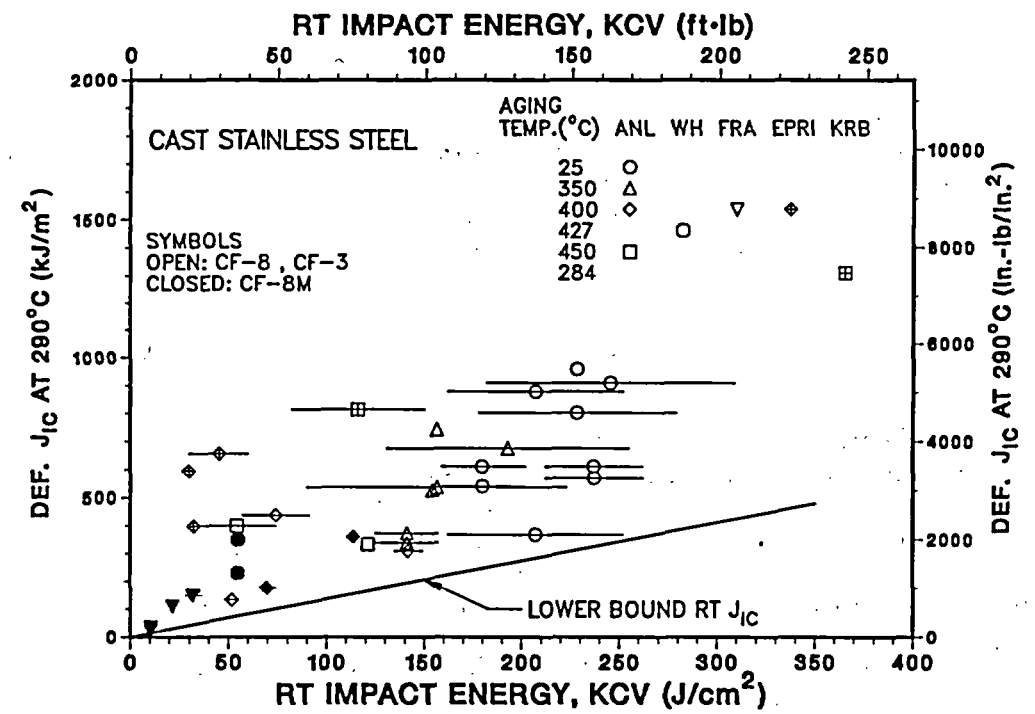

Fig. 13. Correlation between Fracture Toughness (J_{IC}) and Room-Temperature Impact Energy for Cast Stainless Steels.

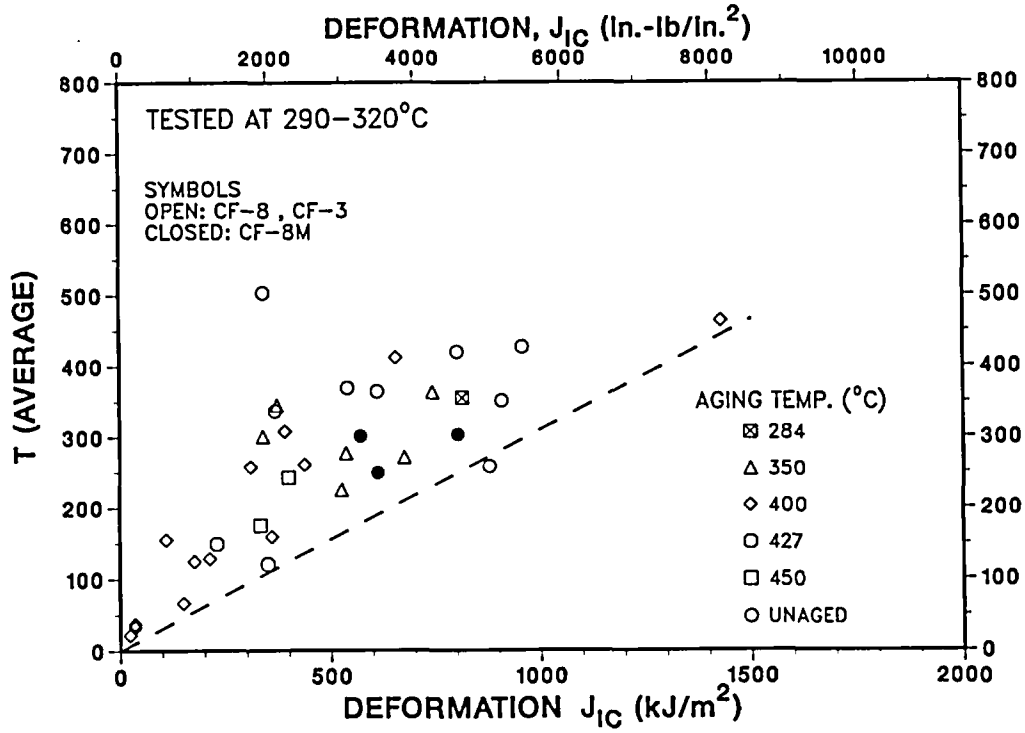

Fig. 14. Correlation between the 290°C Tearing Modulus (T) and Fracture Toughness (J_{IC}) for Cast Stainless Steels.

primary strengthening mechanism.[8,18-20] Consequently, the kinetics of spinodal decomposition primarily control the overall rate of low-temperature embrittlement of cast stainless steel. Other precipitate phases have secondary effects on embrittlement.

Spinodal decomposition and G-phase precipitation in low-temperature-aged cast stainless steel have been investigated by transmission electron microscopy (TEM), atom-probe field-ion microscopy (APFIM), small-angle neutron scattering (SANS), and extraction replica techniques.[18-24] The temperature dependence of the spinodal reaction in CF-3 stainless steel yields an activation energy of 250 ± 30 kJ/mole (59 ± 7 kcal/mole).[24] This value is comparable to that for Cr diffusion in Fe-Cr alloys and is significantly higher than the activation energy for low-temperature embrittlement obtained from mechanical-property data [i.e., in the range of 65 to 230 kJ/mole (15 to 55 kcal/mole)]. The low values of the activation energy of embrittlement are most likely due to the synergistic effects of other precipitate phases on embrittlement.

Precipitation of carbides or nitrides at the phase boundaries causes fracture by phase-boundary separation and facilitates cleavage of ferrite by particle cracking. Consequently, a lower degree of spinodal decomposition is needed for a given change in mechanical properties. Precipitation of carbides or nitrides, which occurs primarily at 400 or 450°C, is extremely slow at lower temperatures. The influence of phase-boundary carbides, thus, would tend to increase the apparent activation energy of embrittlement.

The other factor that can influence the overall kinetics of embrittlement is precipitation of the G phase, a multicomponent phase consisting of Ni, Si, Mo, Cr, Fe, and some Mn, and C.[21,22] Cast stainless steels that show precipitation of G phase after aging generally exhibit faster kinetics of embrittlement. Also, the activation energy of embrittlement decreases with an increase in the volume fraction of G phase. The aging conditions in

which G phase has been detected by TEM or SANS, in various aged cast stainless steels, are shown in Fig. 15. The kinetics for the decrease in the Charpy-impact energy of aged cast stainless steel are also plotted in the figure. The solid lines represent the average time for 50 and 80% reduction in impact energy for the various ANL heats. Actual aging time for a given decrease in impact energy varied significantly for the various heats and is shown by the horizontal scatter bars. The aging times for the CF-8M steels were generally lower than those for the CF-3 or CF-8 steels. The results indicate that, at 400°C, the reduction in impact energy is largely complete before G phase is detected in any of the heats. However, G-phase precipitation and the decrease in impact energy occur simultaneously at temperatures <350°C. These results suggest that the influence of G-phase precipitation on embrittlement would be greater at low temperatures. At 400°C, the kinetics of spinodal decomposition are much faster than G-phase precipitation, which follows nucleation and growth.

The exact nature of the effects of G phase on embrittlement are not well understood. A possible effect is the depletion of Ni and Mo from the ferrite matrix. The ferrite matrix typically contains ~5% Ni. The presence of Ni in single-phase Fe-Cr alloys is known to promote spinodal decomposition,[25] but alloys with >4% Ni take longer to embrittle than do alloys with <4% Ni.[26] The aging times at 400 or 425°C required for an 80% reduction in impact energy are a factor of ~3 slower for an Fe-26Cr-6Ni alloy than for the Fe-26Cr alloy.[26] Furthermore, at temperatures of 400 to 475°C, embrittlement of ferritic steels is faster than that of cast duplex stainless steels.[27] The seemingly opposite effects of Ni on spinodal decomposition and embrittlement in Fe-Cr alloys are attributed to promotion of twinning as a mode of deformation in alloys containing >4% Ni.[26,28-30] Addition of Mo to Fe-Cr alloys also promotes twinning.[28,30] Although spinodal decomposition is faster in Ni-containing alloys, it is less effective as a strengthening mechanism because of twinning as a mode of deformation. Consequently, a greater degree of spinodal decomposition would be needed for the same degree of embrittlement.

The precipitation of G phase can change the composition of ferrite, thus, alter the deformation behavior and fracture mode of aged cast stainless steels. Deformation twins in ferrite are observed in aged cast stainless steels at all test temperatures. Figure 16 shows twins in fractured Charpy specimens of Heat P1 aged for 30,000 h at 350°C and tested at room temperature and 290°C. At high temperatures, the phase boundaries have a jagged appearance and have moved to accommodate the deformation due to twinning. Such adjustments in the phase boundaries are difficult at lower temperatures and cracks can form at twin/phase boundaries or twin/twin intersections. Twin boundary cracks are observed in aged cast steels. Heat P1 has a high activation energy, e.g., 239 kJ/mole (Table 2); thus, the contribution of G phase is expected to be negligible. The twinning behavior of heats with low activation energies is being investigated to establish the role of G phase in deformation and fracture mode of aged cast stainless steels.

7. Kinetics of Embrittlement

Results from the present study, together with data from FRA[11,12] and GF[1] studies, were analyzed to develop a correlation between the activation energy of embrittlement and the chemical composition, in wt.%, of the cast material. The results have been presented earlier.[9] The analyses yielded two separate correlations: one for the ANL and FRA data, given by

$$Q(\text{kJ/mole}) = 90.54 + 9.62\,\text{Cr} - 8.12\,\text{Ni} - 7.53\,\text{Mo} + 20.59\,\text{Si} - 123.0\,\text{Mn} + 317.7\,\text{N}, \quad (5)$$

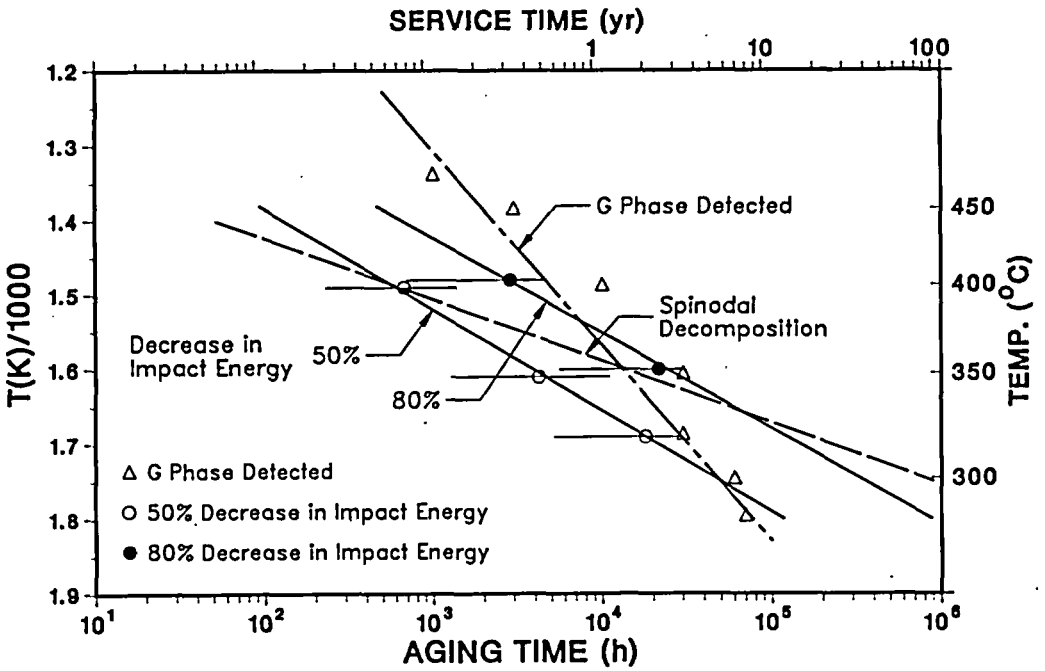

Fig. 15. Arrhenius Plots for Precipitation of G Phase and Reduction in Charpy-Impact Energy for Aged Cast Stainless Steel.

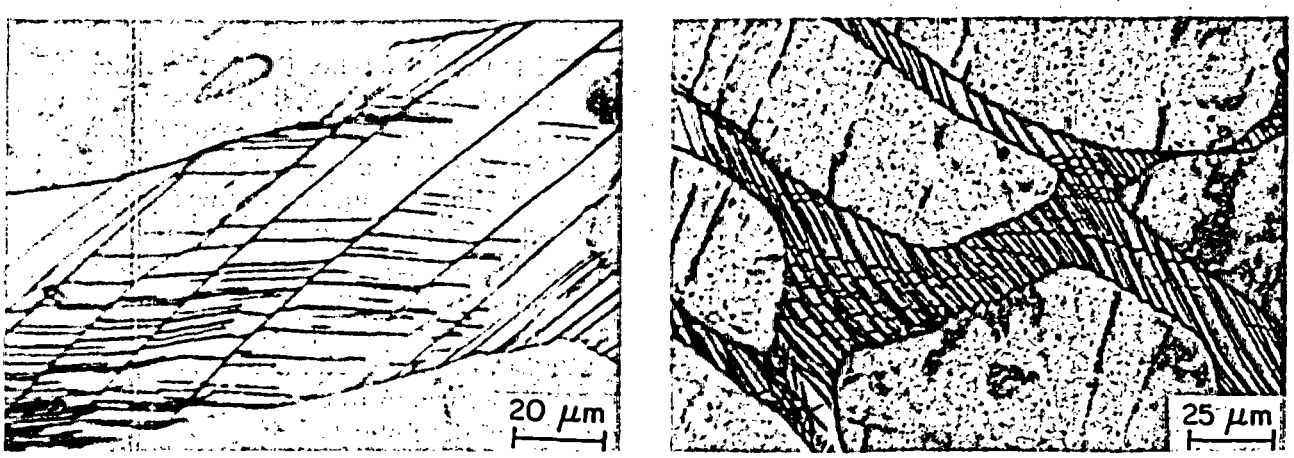

Tested at Room Temp. Tested at 290°C

Fig. 16. Deformation Twins in Charpy-Impact Specimens of CF-8 Steel Aged for 30,000 h at 350°C and Tested at Room Temperature and 290°C.

and the other for the GF data, given by

$$Q(\text{kJ/mole}) = -66.65 + 6.90\,Cr - 5.44\,Ni + 8.08\,Mo + 17.15\,Si + 44.1\,Mn + 297.1\,N. \quad (6)$$

The activation energy values reported in Ref. 9 were used in the analyses. The activation energies for Heats 68, 69, 75, and P4 were not included in the analyses. For these heats, the activation energies predicted from Eq. (5) are in good agreement with the experimental values, Table 2. Equation (5) also accurately predicts the kinetics of embrittlement observed in the CEGB study on three heats of CF-3 steel.[13]

The reasons why a unified expression could not be obtained for the two data sets and for the different effects of constituent elements in the two expressions are not clearly understood. As discussed in Section 6, the precipitation or growth of phase-boundary carbides or nitrides during aging would increase the activation energy of embrittlement. An increase in C or N in the steel promotes carbide or nitride precipitation and, thus, increases the activation energy. The positive sign of the coefficient for N agrees with this behavior; the correlation for the C content in the steel was poor.

The contribution of other elements, i.e., Ni, Si, Mo, and Mn, is expected on the basis of their effects on G-phase precipitation. These elements should promote G-phase precipitation; hence, the coefficients for these elements should have a negative sign, because G-phase precipitation decreases the activation energy of embrittlement. The Si coefficient has a positive sign in both expressions, and the Mo and Mn coefficients are positive in Eq. (6). These results indicate that other factors, not included in the analysis, influence the kinetics of embrittlement. A possible factor may be the dislocation density in the ferrite matrix. The G phase preferentially precipitates at dislocations.[18-20] Consequently, the defect structure in the as-cast material will strongly affect G-phase precipitation. A mechanistic understanding of the variations in activation energy is desirable to avoid "surprises" in material composition. Information on the role of G phase on embrittlement could provide a unified correlation for all compositions.

8. Preliminary Assessment of Embrittlement

Embrittlement of any cast stainless steel component during reactor service can be estimated from the data obtained in the present study. Realistic estimates of impact strength and fracture toughness for a specific heat of cast stainless steel, as a function of time and temperature of reactor service, can be obtained in two steps. First, it is necessary to establish the extent or degree of embrittlement, i.e., the minimum toughness that would ever be achieved by the material after long-term aging; then, the rate of decrease or the kinetics of embrittlement can be determined.

The material information required to estimate the degree of embrittlement is the chemical composition and the ferrite content and spacing. The minimum impact energy, K_m, is determined from the correlation between the material parameter Φ and impact energy (Fig. 3). Fracture toughness, i.e., J_{IC} and tearing modulus, is estimated from the correlations between J_{IC} and impact energy and between tearing modulus and J_{IC} (Figs. 11-14).

Figure 3 also indicates that the minimum room-temperature impact energy for the worst heat of cast stainless steel (i.e., a material parameter of >200) can be as low as 15 J/cm^2. This corresponds to a lower-bound J_{IC} of 20 kJ/m^2 and a tearing modulus of 15. The correlations for realistic estimates of fracture toughness at reactor temperatures have not yet been established. Available data indicate that the room temperature values are also applicable at reactor temperatures, however, the values may be too conservative for some compositions of cast stainless steel.

The rate of decrease of toughness, i.e., the kinetics of embrittlement, can be estimated from Eqs. (1), (2), and (5) when chemical composition and initial impact strength of the cast material are known. The constant β in Eq. (2) is obtained from the difference between initial strength and minimum impact energy K_m. The activation energy Q is determined from Eq. (5). The average value of the constant α in Eq. (2) is 1.0; the average value of θ is 3.0 for CF-3 and CF-8 steels and 2.6 for CF-8M steel. The decrease in impact energy, as a function of time and temperature of reactor service, is determined from Eqs. (1) and (2).

Figure 17 shows examples of the predicted embrittlement behavior of heats susceptible to embrittlement (A and C) and typical heats of CF-8M and CF-8 cast stainless steel (B and D). The corresponding fracture toughness J_{IC} and tearing modulus can be determined from Figs. 11-14. Table 3 provides the theoretical chemical composition and ferrite content and spacing of the heats. All compositions are within ASTM specification A351. The compositions of Heats A and C give high ferrite content and fast kinetics of embrittlement, i.e., low activation energy. The mean ferrite spacing for most cast stainless steels with >10% ferrite ranges from 40 to 200 μm; the average value for thick castings (e.g., GF heats or the KRB pump cover in Table 1) is ~175 μm. A large value of the ferrite spacing was selected for Heats A and C to obtain a conservative estimate of the extent of embrittlement.

The results show that the impact energies of Heats A and C will decrease to below 40 J/cm^2 after four or five years of service at 320°C. Heats B and D, with lower ferrite content (15%), exhibit much less embrittlement, i.e., the impact energy will not decrease below 90 J/cm^2 even after long service. The kinetics of embrittlement are also slower for Heats B and D. The results also show that the minimum impact energy is important in estimating the embrittlement behavior. Slow kinetics of embrittlement, i.e., a high activation energy, delay the decrease in impact strength, but the material would reach the lowest value of impact strength after long reactor service. This behavior is seen for Heat E, which has the same material parameters as Heat C, but an arbitrarily assumed activation energy of 188 kJ/mole, rather than the calculated value of 75 kJ/mole, to illustrate the effect of slower kinetics. Even with very slow kinetics, impact energy decreases to ~40 J/cm^2 after ~40 yr of service.

9. Conclusions

Charpy-impact and J-R curve data for several experimental and commercial heats of cast stainless steel are presented. The materials were thermally aged up to 30,000 h at temperatures of 290 to 450°C. The results indicate that aging at these temperatures leads to an increase in tensile strength and a decrease in impact energy, fracture toughness (J_{IC}), and tearing modulus of the material. The Charpy transition curve shifts to higher temperatures. The J_{IC} values are consistent with the Charpy-impact data, i.e., the relative reduction in impact energy is similar to the relative decrease in J_{IC} values. In general, the low-carbon CF-3 cast stainless steels are the most resistant, and the Mo-containing, high-carbon CF-8M steels are the most susceptible to low-temperature embrittlement.

The effects of material variables on the embrittlement of cast stainless steels have been evaluated. The chemical composition of the steel and the ferrite content and spacing are important parameters in controlling the extent and kinetics of embrittlement. Ferrite morphology strongly affects the extent of embrittlement, whereas material composition influences the kinetics of embrittlement. Small changes in the constituent elements of the cast material can cause the kinetics of embrittlement to vary significantly.

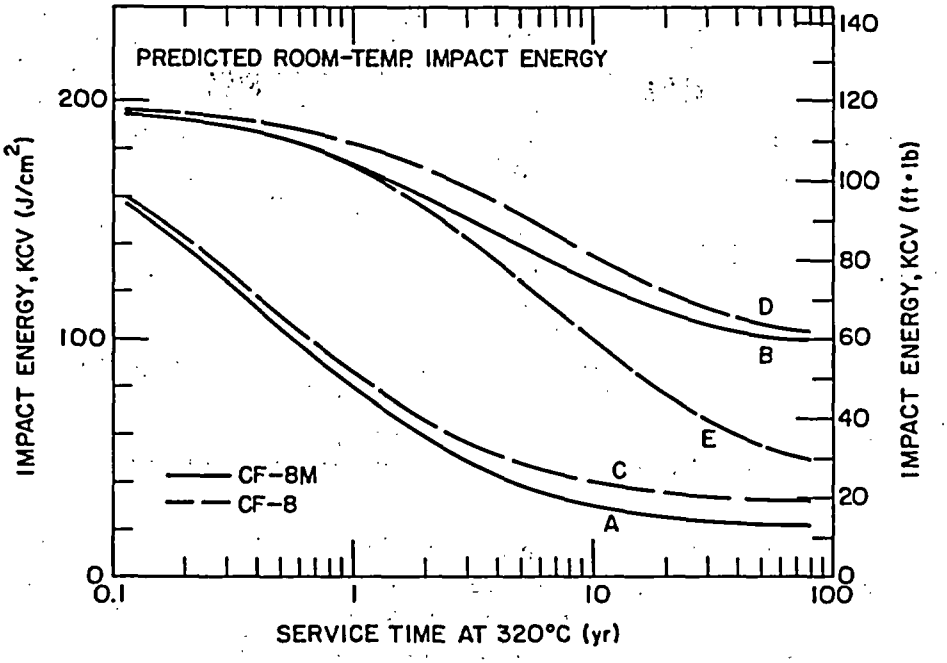

Fig. 17. Predicted Embrittlement Behavior of CF-8M and CF-8 Cast Stainless Steels.

Table 3. Theoretical Chemical Composition and Ferrite Morphology of Cast Stainless Steel used for Predicting Embrittlement under LWR Conditions

		Composition (wt.%)							Ferrite			
Heat	Grade	C	N	Mn	Si	Ni	Cr	Mo	Content[a] (%)	Intercept[b] (μm)	ϱ^a (kcal/mole)	K_m[d] (J/cm²)
A	CF-8M	0.05	0.02	1.2	1.2	10.0	21.0	2.6	28	180	18	20
B	CF-8M	0.05	0.05	0.5	1.0	9.0	19.5	2.0	15	80	40	90
C	CF-8	0.04	0.02	1.3	0.5	8.4	21.0	0.4	24	200	18	30
D	CF-8	0.05	0.05	0.5	1.0	8.5	20.5	0.4	15	80	45	90
E	CF-8	0.04	0.02	1.3	0.5	8.4	21.0	0.4	24	200	45	30

[a]Calculated from chemical composition with Hull's equivalent factor.
[b]Assumed values.
[c]Calculated from Eq. (5), value for heat E was arbitrarily assumed.
[d]Determined from Fig. 3.

The mechanisms of embrittlement of cast duplex stainless steel have been discussed. Embrittlement is caused by brittle fracture associated with either cleavage of ferrite or separation of ferrite/austenite phase boundaries. The formation of the α' phase by spinodal decomposition of the ferrite provides the strengthening mechanism to raise the local tensile stress above the critical value for cleavage and thus promotes brittle fracture. Precipitation and/or growth of phase-boundary carbides or nitrides leads to brittle failure by phase-boundary separation and also facilitates cleavage of the ferrite by particle cracking. Therefore, the degree of brittle fracture, hence, the degree of embrittlement of a specific heat of cast stainless steel, depends strongly on the amount and spacing of the ferrite in the duplex structure.

The kinetics of embrittlement are controlled by spinodal decomposition, precipitation and growth of phase-boundary carbides, and precipitation of the G phase in ferrite. The rate of embrittlement for a specific cast stainless steel depends on the relative contributions of carbide and G-phase precipitation; activation energies can range from 65 to 230 kJ/mole.

Mechanical-property results from the present study and data from other investigations have been analyzed to develop the procedure and correlations for predicting the kinetics and extent of embrittlement of reactor components from known material parameters. The method and examples of estimating the impact strength and fracture toughness of cast components during reactor service are described. Results indicate that the lower-bound values of impact energy, fracture toughness J_{IC}, and tearing modulus at room temperature could be as low as 15 J/cm^2, 20 kJ/m^2, and 15, respectively. Available data indicate that the lower-bound values at room temperature may also be applicable at reactor temperatures. These values are probably very conservative for most materials. The range of material parameters representative of reactor components should be defined for realistic estimates of the lower-bound fracture toughness of cast components.

Acknowledgments

This work was supported by the Office of the Nuclear Regulatory Research in the U. S. Nuclear Regulatory Commission. The authors are grateful to A. Sather, W. K. Soppet, G. M. Dragel, and L. Bush for their contribution to the experimental effort. The authors also thank J. Muscara, W. J. Shack, and T. F. Kassner for their helpful discussions.

References

1. A. Trautwein and W. Gysel, "Influence of Long Time Aging of CF-8 and CF-8M Cast Steel at Temperatures Between 300 and 500°C on the Impact Toughness and the Structure Properties", *Stainless Steel Castings*, eds. V. G. Behal and A. S. Melilli, ASTM STP 756, Philadelphia, p. 165 (1982).

2. O. K. Chopra and H. M. Chung, *Long-Term Embrittlement of Cast Duplex Stainless Steels in LWR Systems: Annual Report, October 1983-September 1984*, NUREG/CR-4204, ANL-85-20 (March 1985); Nucl. Eng. Des., 89, p. 305 (1985).

3. O. K. Chopra and H. M. Chung, *Long-Term Embrittlement of Cast Duplex Stainless Steels in LWR Systems: Annual Report, October 1984, September 1985*, NUREG/CR-4503, ANL-86-3 (January 1986).

4. O. K. Chopra and H. M. Chung, *Long-Term Embrittlement of Cast Duplex Stainless Steels in LWR Systems: Semiannual Report, October 1985-March 1986*, NUREG/CR-4744 Vol. I, No. 1, ANL-86-54 (September 1986).

5. O. K. Chopra and G. Ayrault, in *Materials Science and Technology Division Light-Water-Reactor Safety Research Program: Quarterly Progress Report*, October-December 1983, NUREG/CR-3689 Vol. IV, ANL-83-85 Vol. IV, p. 129 (August 1984).

6. O. K. Chopra and H. M. Chung, in *Materials Science and Technology Division Light-Water-Reactor Safety Materials Engineering Research Programs: Quarterly Progress Report*, January-March 1984, NUREG/CR-3998 Vol. I, ANL-84-60 Vol. I, p. 52 (September 1984).

7. O. K. Chopra and H. M. Chung, "Aging Degradation of Cast Stainless Steels: Effects on Mechanical Properties," in *Environmental Degradation of Materials in Nuclear Power Systems-Water Reactors*, eds. G. J. Theus and J. R. Weeks, The Metallurgical Society, Warrendale, PA p. 737 (1988).

8. O. K. Chopra and H. M. Chung, "Effect of Low-Temperature Aging on the Mechanical Properties of Cast Stainless Steels," in *Properties of Stainless Steels in Elevated Temperature Service*, ed. M. Prager, MPC-Vol. 26/PVP-Vol. 132, ASME, New York, p. 79 (1988).

9. O. K. Chopra and H. M. Chung, "Initial Assessment of the Processes and Significance of Thermal Aging in Cast Stainless Steels," in *Proc. 16th Water Reactor Safety Information Meeting*, U. S. Nuclear Regulatory Commission, NUREG/CP-0097 Vol.3, p. 519 (March 1989).

10. S. Bonnet, J. Bourgoin, J. Champredonde, D. Guttmann, and M. Guttmann, "Evolution of Mechanical Properties of Various Cast Duplex Stainless Steels in Relation to Metallurgical and Aging Parameters: An Outline of Current EDF Programmes," presented at *Intl. Workshop: Intermediate Temperature Embrittlement Processes in Duplex Stainless Steels*, August 1-2, 1989, Oxford, U.K.

11. G. Slama, P. Petrequin, and T. Magep, "Effect of Aging on Mechanical Properties of Austenitic Stainless Steel Castings and Welds," presented at *SMIRT Post-Conference Seminar 6, Assuring Structural Integrity of Steel Reactor Pressure Boundary Components*, August 29-30, 1983, Monterey, CA.

12. Y. Meyzaud, P. Ould, P. Balladon, M. Bethmont, and P. Soulat, "Tearing Resistance of Aged Cast Austenitic Stainless Steel," presented at *Intl. Conf. on Thermal Reactor Safety (NUCSAFE 88)*, October 1988, Avignon, France.

13. P. H. Pumphrey and K. N. Akhurst, "The Aging Kinetics of CF-3 Cast Stainless Steel in the Temperature Range 300°C to 400°C," presented at *Intl. Workshop: Intermediate Temperature Embrittlement Processes in Duplex Stainless Steels*, August 1-2, 1989, Oxford, U.K.

14. P. McConnell and J. W. Sheckherd, *Fracture Toughness Characterization of Thermally Embrittled Cast Duplex Stainless Steel*, Electric Power Research Institute Report NP-5439 (September 1987).

15. A. L. Hiser, *Tensile and J-R Curve Characterization of Thermally Aged Cast Stainless Steels*, Materials Engineering Associates, Inc., NUREG/CR-5024, MEA-2229 (September 1988).

16. E. I. Landerman and W. H. Bamford, "Fracture Toughness and Fatigue Characteristics of Centrifugally Cast Type 316 Stainless Steel Pipe after Simulated Thermal Service

Conditions," in *Ductility and Toughness Considerations in Elevated Temperature Service*, MPC-8, ASME, NY, p. 99 (1978).

17. A. Zahoor, R. M. Gamble, H. S. Mehta, S. Yukawa, and S. Ranganath, *Evaluation of Flaws in Carbon Steel Piping*, Electric Power Research Institute Report NP-4824M (October 1986).

18. H. M. Chung and O. K. Chopra, "Microstructure of Cast Duplex Stainless Steel after Long-Term Aging," in *Proc. Second Intl. Symp. on Environmental Degradation of Materials in Nuclear Power Systems - Water Reactors*, American Nuclear Society, LaGrange Park, IL, p. 287 (1986).

19. H. M. Chung and O. K. Chopra, "Kinetics and Mechanism of Thermal Aging Embrittlement of Duplex Stainless Steels," in *Environmental Degradation of Materials in Nuclear Power Systems - Water Reactors*, eds,. G. J. Theus and J. R. Weeks, The Metallurgical Society, Warrendale, PA, p. 359 (1988).

20. H. M. Chung and O. K. Chopra, "Long-Term-Aging Embrittlement of Cast Austenitic Stainless Steels - Mechanism and Kinetics," in *Properties of Stainless Steels in Elevated Temperature Service*, ed., M. Prager, MPC-Vol. 26/PVP-Vol. 132, ASME, New York, p. 17 (1988).

21. J. Bentley, M. K. Miller, S. S. Brenner, and J. A. Spitznagel, "Identification of G-Phase in Aged Cast CF-8 Type Stainless Steel," in *Proc. 43rd. Electron Microscopy Society of America*, ed., G. W. Bailey, San Francisco Press, p. 328 (1985).

22. M. Vrinat, R. Cozar, and Y. Meyzaud, "Precipitated Phases in the Ferrite of Aged Cast Duplex Stainless Steel," *Scr. Metall.* **20**, p. 1101 (1986).

23. T. J. Godfrey and G. D. W. Smith, "The Atom Probe Analysis of a Cast Duplex Stainless Steel," *J. Phys. Paris Colloq.* C7, Vol. 47, suppl. to No. 11, p. 217 (1986).

24. J. M. Sassen et al., "Kinetics of Spinodal Reaction in the Ferrite Phase of a Duplex Stainless Steel," in *Properties of Stainless Steels in Elevated Temperature Service*, ed., M. Prager, MPC-Vol. 26/PVP-Vol. 132, ASME, New York, p. 65 (1988).

25. H. D. Solomon and L. M. Levinson, "Mössbauer Effect Study of 475°C Embrittlement of Duplex and Ferritic Stainless Steels," *Acta Metall.* **26**, p. 429 (1978).

26. K. Nakano, M. Kanao, and A. Hoshino, "Effect of Nickel Content and the Austenite Phase on Low Temperature Toughness and Embrittlement Behavior of Fe-26%Cr Alloys," *Trans. Nat. Res. Inst. Met.* **20**, p. 1 (1978).

27. P. J. Grobner, "The 885°F (475°C) Embrittlement of Ferritic Stainless Steels," *Metal. Trans.* **4**, p. 251 (1973).

28. T. Magnin and F. Moret, "Mechanical Twinning in Ferritic Stainless Steels," *Scr. Metall.* **16**, p. 1225 (1982).

29. T. Magnin, J. LeCoze, and A. Desestret, "Twinning and Stress Corrosion Cracking of Ferritic Phase of Duplex Stainless Steels," in *Duplex Stainless Steels*, ed., R. A. Lula, American Society for Metals, Metals Park, Ohio, p. 535 (1983).

30. M. Anglada. M. Nasarre, and J. A. Planell, "High Temperature Mechanical Twinning of Two Fe-Cr-Mo-Ni Ferritic Stainless Steels," *Scr. Metall.* **21**, p. 931 (1987).

Environmentally Assisted Cracking in Light Water Reactors*

T. F. Kassner, J. Y. Park, W. E. Ruther, and W. J. Shack

Materials and Components Technology Division
Argonne National Laboratory
Argonne, Illinois 60439

Abstract

Topics that have been considered during this year include (1) stress corrosion cracking (SCC) of austenitic stainless steels (SS), (2) fatigue of Type 316NG SS, and (3) SCC of ferritic steels used in reactor piping, pressure vessels, and steam generators. Constant-extension-rate-tests (CERTs) and crack-growth-rate (CGR) tests on 1TCT specimens were performed to quantify the effects of chromate, sulfate, chloride, and low levels of organic impurities on SCC of sensitized Type 304 and Type 316NG SS. Some organic substances were found to actually inhibit SCC of sensitized Type 304 SS. Fatigue tests on Type 316NG SS showed that even at 0.5 Hz the fatigue life in the environment is about half of that in air, and the reduction in life increases at lower frequencies. CGR tests on A533-Gr B pressure vessel steel are in progress on conventional specimens and composite specimens of A533-Gr B/Inconel-182/Inconel-600. Some of the specimens have been plated with either nickel or gold to reduce contact between the surface of low-alloy steel and the environment. Comparison of the results from the bare and plated specimens will provide insight into whether electron transfer through the oxide film on the bulk surface of the ferritic steel is important in the overall SCC process.

1. Objective

Piping in light-water-reactor (LWR) power systems has been affected by several types of environmental degradation. Intergranular stress corrosion cracking (IGSCC) of austenitic stainless steel (SS) piping in boiling-water reactors (BWRs) has required research, inspection, and mitigation programs that have cost several billion dollars. As extended lifetimes are envisaged, other potential environmental degradation problems such as corrosion fatigue must be considered. The objective of this program is to develop an independent capability for the assessment of environmentally assisted degradation in LWR systems.

2. Scope

Research during the past year focused on (1) stress corrosion cracking (SCC) of austenitic SS, (2) fatigue of Type 316NG SS, and (3) SCC of ferritic steels used in reactor piping, pressure vessels, and steam generators.

Significant decreases in the impurity levels in reactor coolant systems of BWRs in the U.S. have been achieved. In many plants the remaining impurities are soluble corrosion products such as chromate that are difficult to eliminate from the coolant system, since only a small fraction of the recirculation system water passes through the reactor water cleanup system (RWCS), and organic species, which are also difficult to eliminate from coolant systems, since resin beds primarily remove ionic impurities. Water chemistry

*RSR FIN Budget No. A2212; RSR Contact: J. Muscara.

studies during this year have focussed on the effects of chromate, low levels of sulfate, and organic impurities on SCC to further quantify the benefits of this improved water chemistry.

The effects of operating temperature and environment on the fatigue behavior of Type 316NG SS have been studied. The latter data are needed to assess the degree of conservatism inherent in the ASME Code Section III Fatigue Design Curves for this material. The environmental and material conditions that can produce SCC susceptibility in the ferritic steels used for vessels and piping are also being studied. Although it is known that these materials become susceptible to transgranular SCC (TGSCC) in high-temperature water, the ranges of dissolved oxygen and impurity concentrations in coolant water that can lead to SCC in these materials remain inadequately defined.

3. Summary of Research Progress

3.1 Influence of Water Chemistry on SCC of Austenitic SS

Effect of Chromate in Water with ~5 and 200 ppb Dissolved Oxygen

Soluble corrosion products from system materials are the major species present in the BWR water when ingress of ionic impurities into the coolant system from leaks in condenser tubes and from the ion-exchange resins in the RWCS, including resin fines, is maintained at very low levels. Examples include Cu^+ and Cu^{2+} in plants with either copper alloy condenser tubes and/or feedwater heaters and $HCrO_4^-$ from corrosion of stainless steel piping, weld cladding on the interior of the reactor vessel, and internal components fabricated from this material. Although chromate (K_2CrO_4) is used as a corrosion inhibitor in component cooling water systems (CCWS) in BWRs and pressurized-water reactors (PWRs),[1] these systems operate at relatively low temperatures (~170°C) and pressures (~150 psig), and direct ingress of chromate from the CCWS into the reactor coolant water is unlikely under normal operating conditions. Nevertheless, because only a small fraction of the recirculation water in BWRs passes through the RWCS (3–6%), the concentration of corrosion-product ions in the reactor water can be considerably greater than in the feedwater (e.g., ~30–40 ppb versus <1 ppb, respectively). The effect of copper ions on SCC of sensitized Type 304 SS in low-oxygen (<5 ppb) water has been reported.[2,3]

The effect of chromate on SCC of the steel was investigated by CERTs in water with ~0.2 and <0.005 ppm dissolved oxygen. Chromate was added to the feedwater as either H_2CrO_4 or K_2CrO_4 over the concentration range of ~0.05 to 90 ppm. Analogous to our previous results on the effect of dissolved oxygen and various oxyanions on SCC of the steel,[4,5] if cathodic reduction of the chromate ion to chromite or Cr_2O_3 is the rate controlling step in the overall SCC process and occurs according to the reactions

$$CrO_4^{2-} + 2H_2O + 3e^- = CrO_2^- + 4OH^- \quad (1)$$

$$HCrO_4^- + H_2O + 3e^- = CrO_2^- + 3OH^- \quad (2)$$

$$2HCrO_4^- + 3H_2O + 6e^- = Cr_2O_3 + 8OH^-, \quad (3)$$

the corresponding chemical equilibria can be written as

$$K_{eq} = [OH^-]^4 [CrO_2^-] / [e^-]^3 [CrO_4^{2-}] \quad (4)$$

$$K_{eq} = [OH^-]^3 [CrO_2^-] / [e^-]^3 [HCrO_4^-] \quad (5)$$

$$K_{eq} = [OH^-]^8 [Cr_2O_3] / [e^-]^6 [HCrO_4^-]^2, \quad (6)$$

and the reciprocal of the electron concentration would depend on the concentration of chromate as given by the following equations

$$1/[e^-] = k_1 [CrO_4^{2-}]^{1/3} / [OH^-]^{4/3} [CrO_2^-]^{1/3} \quad (7)$$

$$1/[e^-] = k_2 [HCrO_4^-]^{1/3} / [OH^-] [CrO_2^-]^{1/3} \quad (8)$$

$$1/[e^-] = k_3 [HCrO_4^-]^{1/3} / [OH^-]^{4/3} [Cr_2O_3]^{1/6}. \quad (9)$$

Since the CGR is proportional to $1/[e^-]$ for many impurity species that undergo cathodic reduction,[2-5] Eqs. (7)-(9) indicate that the CGR should depend on the 1/3-power of the chromate concentration in low-oxygen water for the electrochemical potential-pH regime corresponding to Eqs. (1)-(3), if cathodic reduction of the chromate ion is the rate controlling step.

The experimental results in Table 1 and Fig. 1 indicate that the CGRs indeed exhibit this dependence over a wide range of chromate concentration and conductivity of the feedwater, irrespective of the $pH_{25°C}$. Although $pH_{25°C}$ or $pH_{289°C}$ in itself is not an important factor in SCC under these conditions, the dependence of the CGR on $pH_{25°C}$ in Fig. 2 is consistent with the relationship between the chromate concentration and $pH_{25°C}$ for both acidic and basic solutions.

The dependence of electrochemical potential (ECP) of the steel on chromate concentration and conductivity of the feedwater in the CERTs is shown in Fig. 3. The ECP values for Type 304 SS in acidic solutions (H_2CrO_4) increase from ~-350 to +500 mV(SHE) over the concentration range of ~0.1 to 50 ppm chromate. In near-neutral and basic solutions (K_2CrO_4), the ECP values increase from ~-350 to ~0 mV (SHE) over the range of ~0.03 to 0.3 ppm and then decrease to <-100 mV (SHE) as the chromate concentration increases to 90 ppm. As indicated by the filled symbols in Fig. 3, IGSCC occurs at ECP values >-100 mV (SHE), whereas TGSCC is observed at lower values. The dependence of the CGR on the 1/3-power of the chromate concentration and conductivity in Fig. 1 is primarily applicable to the IGSCC regime, since the CGRs for TGSCC, which occurred at low chromate concentrations (<0.1 ppm) and ECP values (< -150 mV [SHE]), tend to fall below the trend line.

The effect of chromate in water containing ~0.2 ppm dissolved oxygen on the SCC behavior of sensitized Type 304 SS was also investigated. The results, which are given in Table 2 and Fig. 4, indicate that chromate additions to the oxygenated water increase the CGRs. However, the dependence on concentration is weaker at the higher oxygen level. For example, the CGR in oxygenated water with 0.1 ppm chromate is higher by a factor of ~2.5 than in low-oxygen water at the same chromate concentration, but the CGRs are the same ($\sim 1.0 \times 10^{-8}$ m·s^{-1}) in the high- and low-oxygen environments at chromate concentration of ~1.0 ppm. In comparison with other species at the 0.1 ppm level in simulated BWR water (~0.2 ppm dissolved oxygen),[7] chromate is less deleterious than sulfate and arsenate, and more deleterious than nitrate, borate, carbonate, and chloride in CERTs at 289°C and a strain rate of 1×10^{-6} s^{-1}.

The effect of chromate on the ECP of Type 304 SS in oxygenated water is shown in Fig. 5. When chromate is present in acid form, the ECP values of increase from ~50 mV(SHE) at a concentration of ~0.1 ppm to +350 mV(SHE) at the 10 ppm level. When chromate is added to the feedwater as K_2CrO_4, the ECP values of Type 304 SS decrease from ~50 to -100 mV(SHE) over this concentration range.

The CERT results indicate that chromate acts in a similar manner to other oxyanions regarding its effect on SCC of sensitized Type 304 SS. These species undergo cathodic reduction and contribute to crack growth by scavenging electrons produced by anodic

Table 1. Influence of H_2CrO_4 and K_2CrO_4 at Low Dissolved-Oxygen Concentration (<5 ppb) on the SCC Susceptibility of Sensitized Type 304 SS Specimens[a] in 289°C Water

	Feedwater Chemistry			CERT Parameters						Potentials	
Test No.	Anion Conc., ppm	Cond. at 25°C, µS/cm	pH at 25°C	Failure Time, h	Maximum Stress, MPa	Total Elong., %	Reduction in Area, %	SCC Growth Rate,[b] $m \cdot s^{-1}$	Fracture Morphology[c]	304 SS, mv(SHE)	Pt, mv(SHE)
A170	0.1	0.50	5.93	123	509	44	49	4.3×10^{-9}	0.42D, 0.58T	-540	-498
A187	0.2	0.83	5.85	97	497	35	42	4.7×10^{-9}	0.65D, 0.35G_3	12	31
A186	0.3	1.08	5.74	98	480	35	41	6.2×10^{-9}	0.57D, 0.43G_3	9	-5
A171	1.0	3.50	5.17	77	423	28	40	7.2×10^{-9}	0.39D, 0.61G_3	80	86
A174	5.0	18.1	4.43	56	366	20	34	1.4×10^{-8}	0.20D, 0.80I	284	278
A172	10.0	34.0	4.14	54	358	20	28	2.0×10^{-8}	0.14D, 0.86I	341	337
A173	50.0	175.0	3.42	44	367	16	22	2.0×10^{-8}	0.30D, 0.70I	487	483
A177[d]	0.05	0.35	6.71	128	513	46	49	2.2×10^{-9}	0.68D, 0.32T	-333	-312
A188[d]	0.1	0.46	6.33	140	519	50	52	1.1×10^{-9}	0.81D, 0.19T	-167	-191
A176[d]	0.5	1.46	7.07	100	487	36	52	8.0×10^{-9}	0.39D, 0.61G_3	-9	-16
A179[d]	1.0	2.56	7.48	95	479	34	52	1.0×10^{-8}	0.22D, 0.78G_3	-1	-10
A175[d]	5.0	14.1	7.44	72	426	26	38	1.1×10^{-8}	0.52D, 0.48I	-25	-23
A178[d]	90.0	230.0	8.54	56	376	20	32	2.9×10^{-8}	0.05D, 0.95I	-140	-138

[a]Lightly sensitized (EPR = 2 $C \cdot cm^{-2}$) specimens (Heat No. 30956) were exposed to the environments for ~20 h before being strained at a rate of 1×10^{-6} s^{-1}.

[b]SCC growth rates are based on measurement of the depth of the longest crack in an enlarged micrograph of the fracture surface and the time period from the onset of yield to the point of maximum load on the tensile curve.

[c]Ductile (D), transgranular (T), granulated (G), and intergranular (I), in terms of the fraction of the cross-sectional area. Characterization of the fracture surface morphologies is in accordance with the illustrations and definitions in Reference 6.

[d]Chromate added as K_2CrO_4.

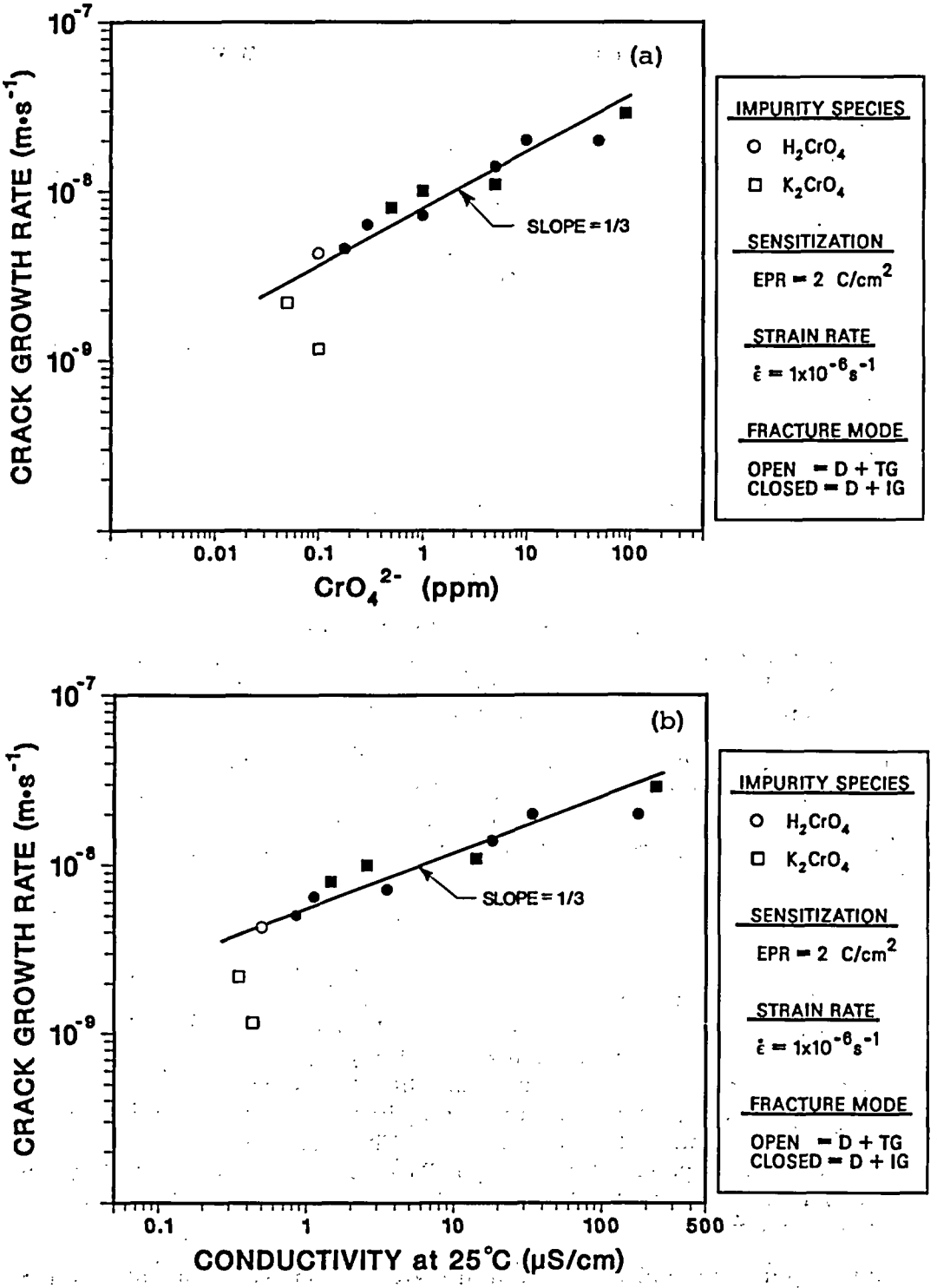

Figure 1. Dependence of the Crack Growth Rate of Sensitized Type 304 SS CERT Specimens at 289°C on (a) Concentration of Chromate and (b) Conductivity of the Low-Oxygen (<5 ppb) Feedwater. Open and closed symbols denote ductile plus transgranular and ductile plus intergranular fracture morphologies, respectively.

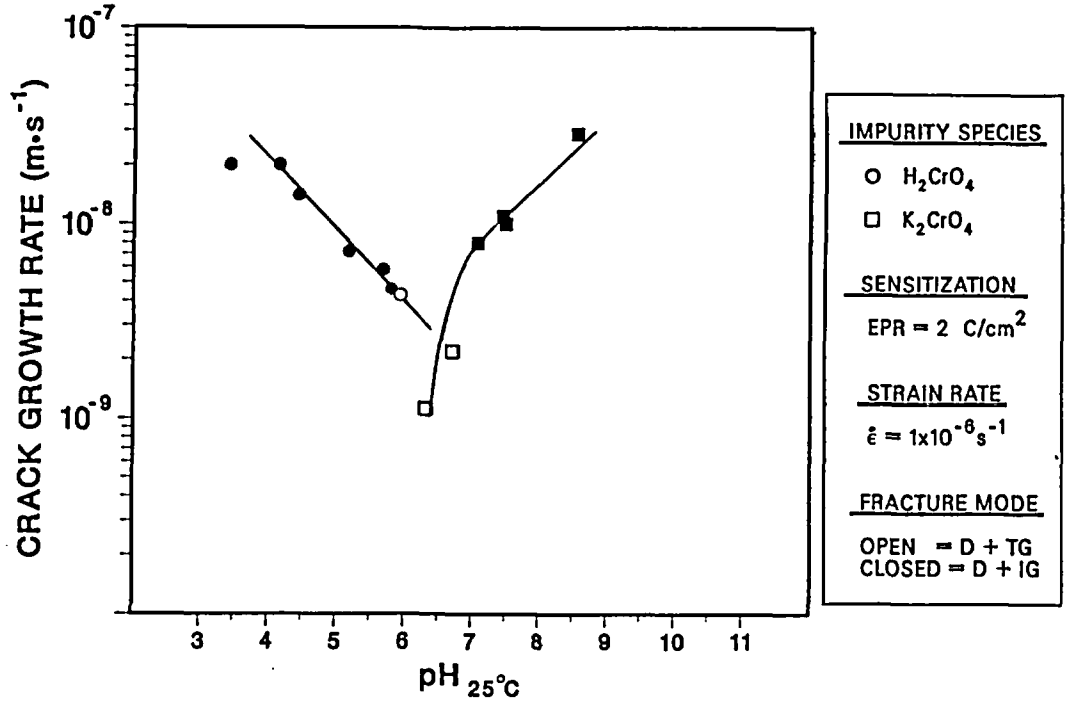

Figure 2. Dependence of the Crack Growth Rate of Sensitized Type 304 SS CERT Specimens at 289°C on $pH_{25°C}$ of the Low-Oxygen (<5 ppb) Feedwater. Open and closed symbols denote ductile plus transgranular and ductile plus intergranular fracture morphologies, respectively.

dissolution of metal at the crack tip in a slip-dissolution mechanism[8,9] of crack advance. IGSCC occurs at chromate concentrations >0.1 ppm in the absence or presence of dissolved oxygen; however, the rates are somewhat higher in the latter environment since both oxygen and chromate undergo cathodic reduction and contribute to the overall cathodic partial process.

Effect of Organic Acids in Oxygenated (~200 ppb) Water

Typical chemicals at power plants include paint products, glycol, hydraulic fluids, lubricants, detergents, chemical cleaners, laundry chemicals, freons, diesel fuel, and ion-exchange resin regeneration chemicals. Potential chemical contaminants[10] and possible pathways[11] for entry of various substances into BWR coolant systems have been evaluated. Some of the long-lived products that may exist in BWR water due to organic intrusions are carboxylic acids, alcohols, phenolics, aromatic hydrocarbons, hydrogen halides, sulfuric and sulfonic acids, amines, and other substances.[10] These organic impurities and their decomposition products are a potential concern in BWR water and PWR secondary-system water in terms of increased susceptibility to localized corrosion and SCC of piping and heat-exchanger tube materials.

Organic impurities are also a concern in PWR secondary-coolant water systems because organic acids increase cation conductivity, which complicates secondary water monitoring and control. A recent survey of organic acids, total organic carbon, and inorganic anions in the secondary water cycles of 13 PWRs indicated that organic acids were responsible for a major fraction of the cation conductivity in many of the plants.[12] Acetic and formic were the most common acids; however, lactic, propionic, and butyric acids were also present in

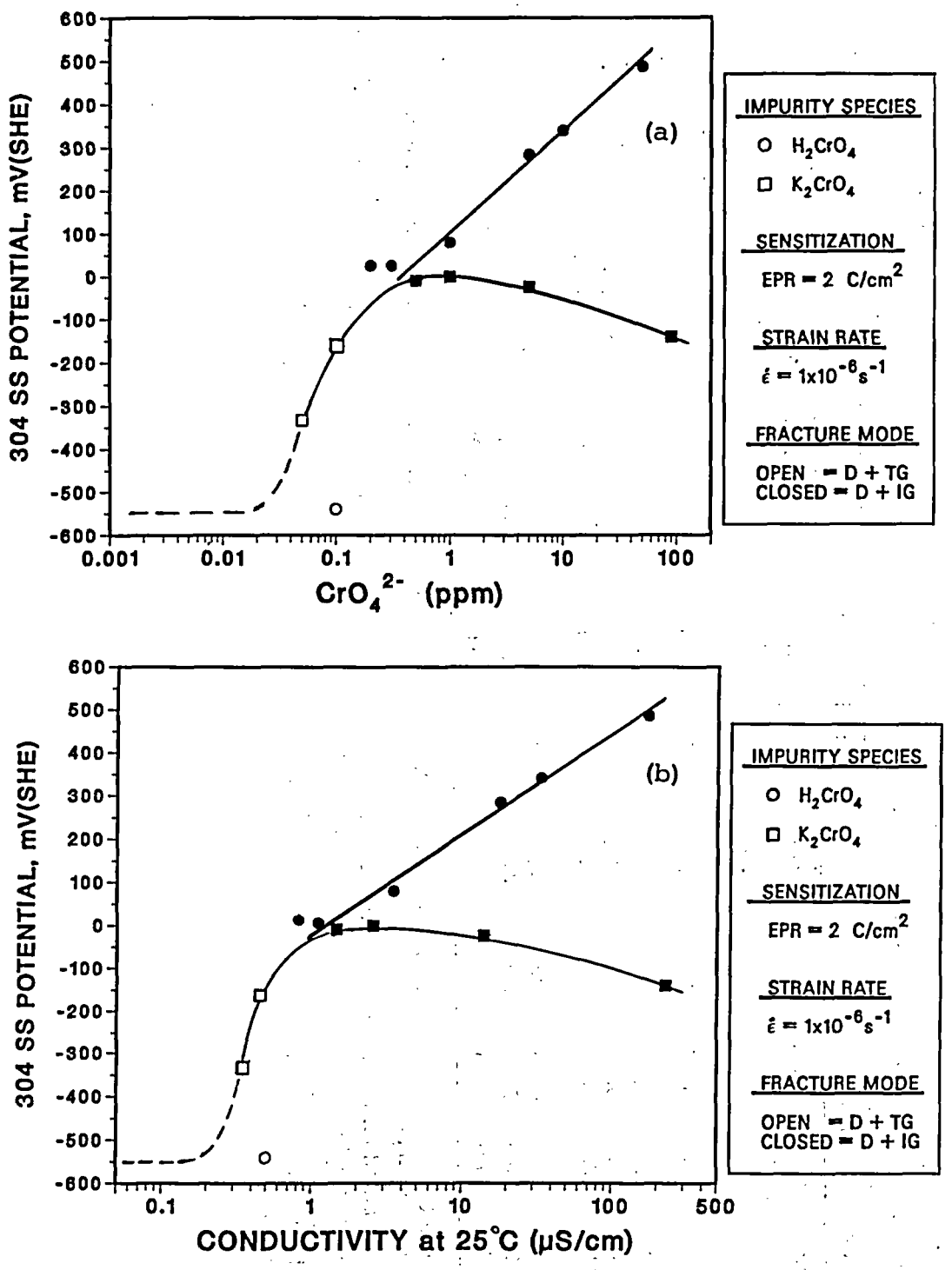

Figure 3. Dependence of the Steady-State Electrochemical Potential of Type 304 SS on (a) Concentration of Chromate and (b) Conductivity of the Low-Oxygen (<5 ppb) Feedwater during CERTs on Sensitized Type 304 SS Specimens at 289°C. Open and closed symbols denote ductile plus transgranular and ductile plus intergranular fracture morphologies, respectively.

Table 2. Influence of H_2CrO_4 and K_2CrO_4 on the SCC Susceptibility of Sensitized Type 304 SS Specimens[a] in Water Containing ~0.2 ppm Dissolved Oxygen at 289°C

	Feedwater Chemistry				CERT Parameters						Potentials	
Test No.	Oxygen, ppm	Anion Conc., ppm	Cond. at 25°C, μS/cm	pH at 25°C	Failure Time, h	Maximum Stress, MPa	Total Elong., %	Reduction in Area, %	SCC Growth Rate,[b] $m \cdot s^{-1}$	Fracture Morphology[c] mv(SHE)	304 SS, mv(SHE)	Pt, mv(SHE)
A2	0.24	-	0.14	6.12	166	493	60	66	4.0×10^{-9}	0.80D, 0.20T	44	60
A183	0.23	0.1	0.61	6.02	76	442	27	40	6.5×10^{-9}	0.66D, 0.34G_3	54	66
A184	0.23	1.0	3.40	5.17	72	422	26	36	9.1×10^{-9}	0.41D, 0.59I	155	173
A185	0.22	10.0	34.0	4.14	47	337	17	30	1.8×10^{-8}	0.12D, 0.88I	348	337
A180[d]	0.22	0.1	0.48	6.68	95	479	34	43	6.8×10^{-9}	0.49D, 0.51I	50	59
A181[d]	0.24	1.0	2.70	7.02	82	442	29	41	9.8×10^{-9}	0.53D. 0.47G_3	6	27
A182[d]	0.25	5.0	9.80	7.75	75	411	27	51	9.4×10^{-9}	0.38D. 0.62I	-30	52

[a]Lightly sensitized (EPR = 2 $C \cdot cm^{-2}$) specimens (Heat No. 30956) were exposed to the environments for ~20 h before being strained at a rate of 1×10^{-6} s^{-1}.

[b]SCC growth rates are based on measurement of the depth of the longest crack in an enlarged micrograph of the fracture surface and the time period from the onset of yield to the point of maximum load on the tensile curve.

[c]Ductile (D), transgranular (T), granulated (G), and intergranular (I), in terms of the fraction of the cross-sectional area. Characterization of the fracture surface morphologies is in accordance with the illustrations and definitions in Reference 6.

[d]Chromate added as K_2CrO_4.

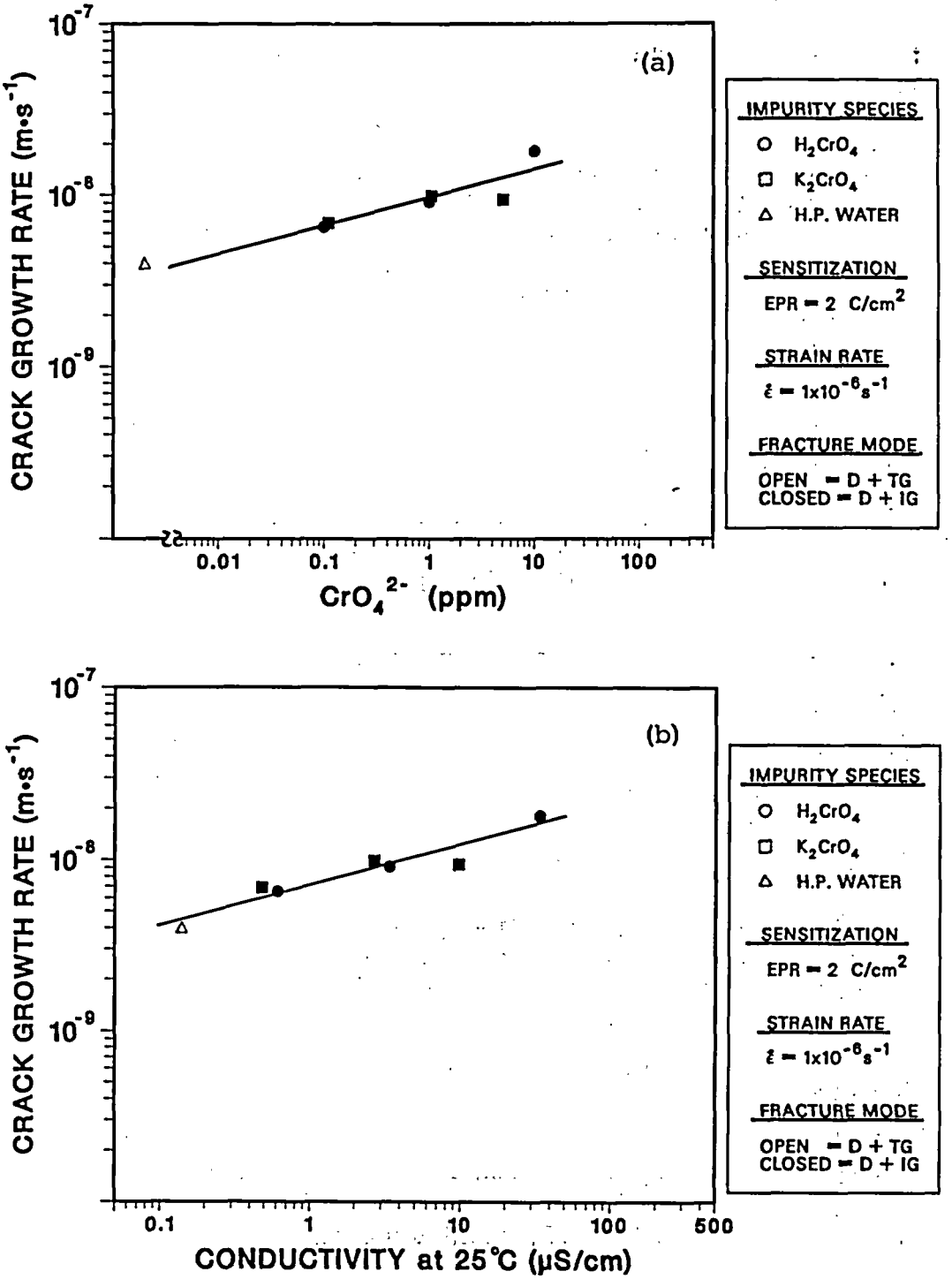

Figure 4. Dependence of the Crack Growth Rate of Sensitized Type 304 SS CERT Specimens at 289°C on (a) Concentration of Chromate and (b) Conductivity of Oxygenated (~0.2 ppm) Feedwater. Open and closed symbols denote ductile plus transgranular and ductile plus intergranular fracture morphologies, respectively.

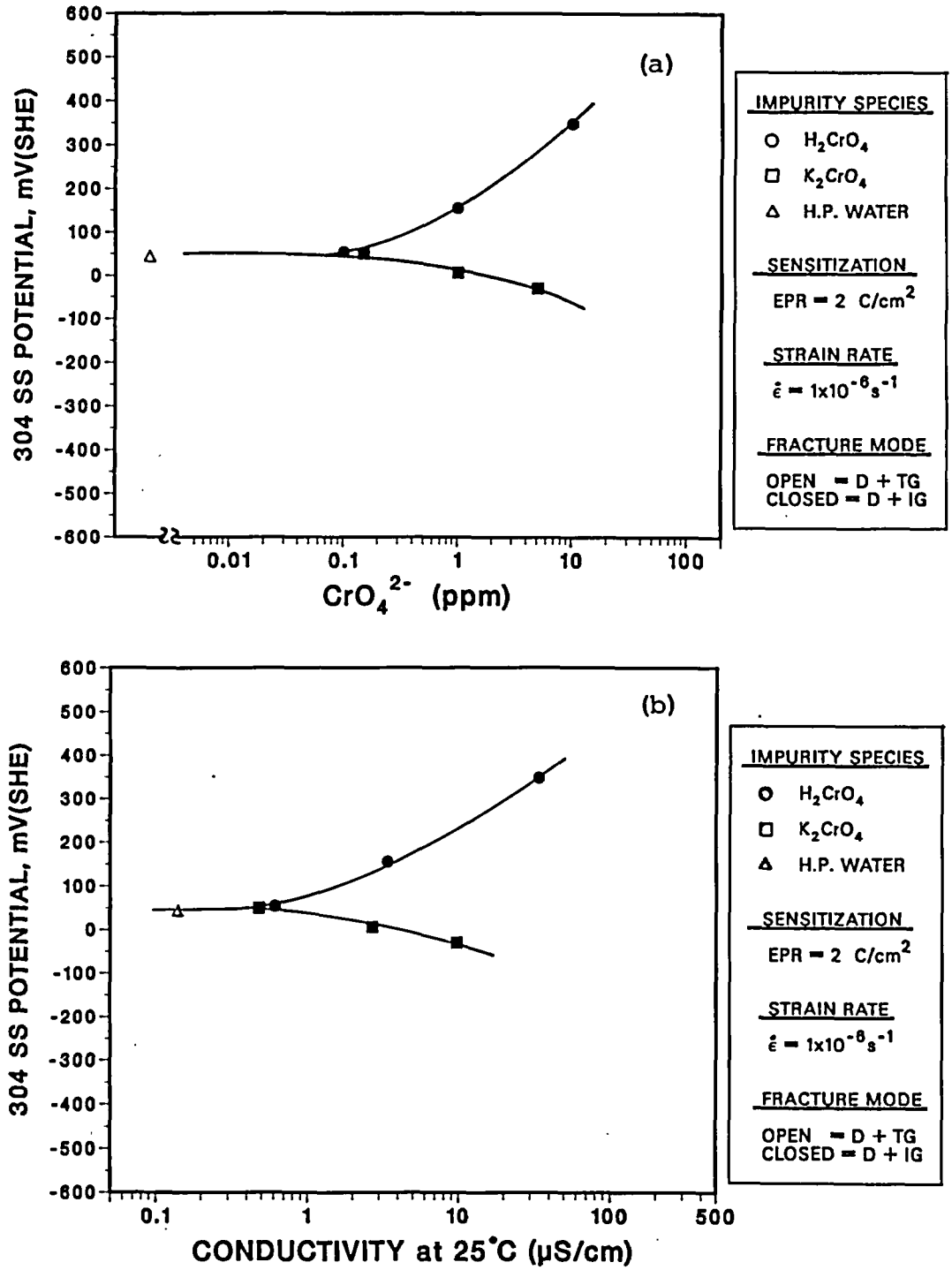

Figure 5. Dependence of the Steady-State Electrochemical Potential of Type 304 SS on (a) Concentration of Chromate and (b) Conductivity of Oxygenated (~0.2 ppm) Feedwater during CERTs on Sensitized Type 304 SS Specimens at 289°C. Open and closed symbols denote ductile plus transgranular and ductile plus intergranular fracture morphologies, respectively.

some of the systems. Make-up water was the major source of the organic impurities, some of which were in colloidal, nonionic form.[12]

To distinguish between the role of organic oxygen scavengers, which react with dissolved oxygen in the water, and that of other organic species, which conceivably adsorb on the material surface and influence cathodic reduction of oxygen, the effect of both types of organic substances on SCC susceptibility of sensitized Type 304 SS was investigated. Subsequently, the influence of several carboxylic acids on the SCC behavior of the steel was determined in cyclic loading tests on fracture-mechanics-type specimens in oxygenated water.

The organic substances that were investigated are listed in Table 3. The oxygen scavengers are commonly used to control corrosion of carbon-steel boiler and copper-alloy condenser tubing in fossil-fired steam-generating systems,[13] whereas the organic acids are among those species found in BWR and PWR coolant systems at low concentrations due to ingress and decomposition of organic substances used in the plants. Although chemical oxygen scavengers are not typically used in reactor coolant systems (in contrast to hydrazine and hydrogen, which are added to the feedwater in PWR steam generators[14] and in BWRs,[15] respectively), their beneficial effect can be rationalized in terms of the well-known influence of low-oxygen concentration on the ECP and SCC susceptibility of austenitic stainless steels.[2-5, 16-18] Although the organic acids could act in a similar manner, i.e., scavenge oxygen, other mechanisms can, in principle, account for their effect on SCC of sensitized Type 304 SS in high-temperature water.

The influence of several chemical oxygen scavengers at a concentration of 1.0 ppm in feedwater containing 0.2 ppm dissolved oxygen on the CERT parameters of lightly sensitized Type 304 SS at 289°C is shown in Table 4. Failure times increase and the crack growth rates decrease markedly when these species are added to the feedwater. The low effluent values (<10 ppb) and the large decrease in the ECP values for Type 304 SS and the platinum electrode (i.e., to <-180 mV [SHE] from ~+90 and ~+180 mV, respectively) demonstrate that these species react with dissolved oxygen in the water. In the case of N,N diethyl-hydroxylamine and 2-butanoneoxime, which has minimal effects on feedwater conductivity and pH, the fracture mode was 100% ductile and the time-to-failure increased by a factor of 3 compared to that in high-purity water. These two species were particularly effective in mitigating SCC.

The effect of several carboxylic acids (acetic, formic, lactic, oxalic, propionic, butyric, and valeric) at a concentration of 1.0 ppm on the SCC susceptibility of sensitized Type 304 SS in oxygenated water is shown in Table 5. In contrast to the previous results, these species increase the time-to-failure by at most a factor of ~2, and with a few exceptions, the ECP of the steel decreases by ~30 mV relative to that in high-purity water. For the most part, the ECP values of the platinum electrode decreased to values below ~-100 mV [SHE], although the effluent dissolved oxygen concentration was >0.15 ppm by colorimetric analyses. The fracture mode of the specimens was intergranular in all instances except in the test with 1.0 ppm propionic acid, where TGSCC occurred. Results from a test with 1.0 ppm of carbonic acid are also included in Table 5, since this species is a likely decomposition product of the various acids at high temperatures in reactor coolant systems where a gamma radiation field also may be present. Carbonic acid does not appear to have a deleterious effect on SCC.

Table 6 presents results from a series of fracture-mechanics crack growth tests on sensitized Type 304 SS in deionized water containing 0.2-0.3 ppm dissolved oxygen, in oxygenated water with 0.1 and 1.0 ppm propionic or butyric acid, and in water with 1.0 ppm butyric acid and either 0.1 ppm sulfate or chloride. The crack length as a function

Table 3. Organic Substances for SCC Tests on Sensitized Type 304 SS

Oxygen Scavengers	Formula
Ascorbic acid	$C_6H_8O_6$
Hydroquinone	$C_6H_4(OH)_2$
Carbohydrazide	$(N_2H_3)_2CO$
2-Butanoneoxime	$CH_3CH_2C(=NOH)CH_3$
N,N Diethylhydroxylamine	$(C_2H_5)_2NOH$
Organic Acids	**Formula**
Formic	$HCOOH$
Acetic	CH_3COOH
Lactic	$CH_3CH(OH)COOH$
Oxalic	$(COOH)_2$
Propionic	CH_3CH_2COOH
Butyric	$CH_3(CH_2)_2COOH$
Valeric	$CH_3(CH_2)_3COOH$
Benzoic	C_6H_5COOH
Carbonic	H_2CO_3

of time is plotted in Figs. 6 and 7 for 10 tests conducted over ~10,500 h. A baseline CGR of 2.9×10^{-10} m·s^{-1} was obtained in deionized water in Test No. 1. The addition of 0.1 ppm propionic acid in Test No. 2 had no effect on the CGR, as can be seen in Table 6 and Fig. 6; however, an increase in concentration to 1.0 ppm (Test No. 3) caused a decrease in the CGR by an order of magnitude. When propionic acid was no longer added to the feedwater (Test No. 4), the CGR returned to the initial baseline value.

In Test No. 5, 1.0 ppm butyric acid was added to the oxygenated feedwater and no crack growth was observed over a time interval of ~1150 h under low-frequency, high-R loading at a K_{max} value of ~34 MPa·m$^{1/2}$. A decrease in the butyric acid concentration from 1.0 to 0.1 ppm eventually caused the CGR to increase to a value of 1.9×10^{-10} m·s^{-1} after ~500 h. The lower concentration of the acid was not sufficient to inhibit crack growth, as was the case in Test No. 2 with 0.1 ppm propionic acid in the feedwater.

In Test No. 7, the butyric acid concentration in the oxygenated feedwater was increased to 1.0 ppm, and 0.1 ppm sulfate (as H_2SO_4) was also added. As can be seen in Table 6 and Fig. 7, the CGR increased significantly to a value of 7.4×10^{-10} m·s^{-1}. When sulfate was removed from the feedwater in Test No. 8, the CGR once again decreased to zero over a period of ~600 h. In Test No. 9, 0.1 ppm chloride (as NaCl) was added to the oxygenated feedwater containing 1.0 ppm butyric acid. The CGR of the steel increased to a value of ~1.5×10^{-10} m·s^{-1} over an interval of ~1150 h. In the last experiment (No. 10), chloride was not added to the feedwater and the CGR again decreased to zero, even at the relatively high stress intensity factor of ~40 MPa·m$^{1/2}$. The results in Tests 7–10 clearly indicate that the organic acid was not effective in inhibiting crack growth in the material when either sulfate or chloride was present in the oxygenated water at relatively low concentrations.

The ECPs of the Type 304 SS and the platinum electrode were monitored throughout the tests. The results in Table 6 indicate that the ECP of the Type 304 SS and platinum did

Table 4. Influence of Several Organic Oxygen Scavengers on the SCC Susceptibility of Sensitized Type 304 SS Specimens[a] in 289°C Water at a Feedwater Dissolved-Oxygen Concentration of ~0.2 ppm

	Feedwater Chemistry					CERT Parameters						Potentials	
Test No.	O_2 Conc., ppm	Organic O_2 Scavenger	Conc., ppm	Cond., µS/cm	pH at 25°C	Failure Time, h	Maximum Stress, MPa	Total Elong., %	Reduction in Area, %	Fracture Morphology[b] m·s^{-1}	SCC Growth Rate,[c]	304 SS, mV(SHE)	Pt, mV(SHE)
A144	0.25	–	–	0.26	6.43	73	297	14	15	0.16D, 0.84I	1.5×10^{-8}	98	158
A143	0.18	–	–	0.16	6.21	101	350	19	12	0.16D, 0.84I	9.6×10^{-9}	86	196
A196	0.24	l-Ascorbic	1.0	1.8	5.44	237	523	44	31	0.49D, 0.51T	1.3×10^{-9}	-578[d]	-497[d]
A198	0.20	Iso-Ascorbic	1.0	1.8	5.29	210	–	39	28	0.42D, 0.58G_3	2.1×10^{-9}	-184[d]	-395[d]
A197	0.22	Hydroquinone	1.0	0.11	6.23	272	527	51	46	0.36D, 0.64G_3	1.1×10^{-9}	-395[d]	-275[d]
A199	0.23	Carbohydrazide	1.0	0.34	6.54	219	494	45	31	0.59D, 0.41T	1.6×10^{-9}	-607[d]	-531[d]
A200	0.25	2-Butanoneoxime	1.0	0.09	6.57	304	531	57	70	1.00D	0	-188[d]	-192[d]
A201	0.25	N,N Diethyl-hydroxylamine	1.0	0.12	6.53	305	525	57	73	1.00D	0	-359[d]	-361[d]

[a]Lightly sensitized (EPR = 2 C·cm^{-2}) specimens (Heat No. 30956) were exposed to the environments for ~20 h before straining at a rate of 5.2×10^{-7} s^{-1}.

[b]Ductile (D), transgranular (T), granulated (G), and intergranular (I), in terms of the fraction of the cross-sectional area. Characterization of the fracture surface morphologies is in accordance with the illustrations and definitions in Reference 6.

[c]SCC growth rates are based on measurement of the depth of the longest crack in an enlarged micrograph of the fracture surface and the time period from the onset of yield to the point of maximum load on the tensile curve.

[d]Effluent dissolved oxygen concentration was <10 ppb by CHEMetrics colorimetric analyses.

Table 5. Influence of Several Organic Acids on the SCC Susceptibility of Sensitized Type 304 SS Specimens[a] in 289°C Water at a Feedwater Dissolved-Oxygen Concentration of ~0.2 ppm

	Feedwater Chemistry					CERT Parameters						Potentials	
Test No.	Oxygen Conc., ppm	Impurity Acids	Anion Conc., ppm	Cond., μS/cm	pH at 25°C	Failure Time, h	Maximum Stress, MPa	Total Elong., %	Reduction in Area, %	Fracture Morphology[b]	SCC Growth Rate,[c] $m \cdot s^{-1}$	304 SS, mV(SHE)	Pt, mV(SHE)
A144	0.25	-	-	0.26	6.43	73	297	14	15	0.16D, 0.84I	1.5×10^{-8}	98	158
A143	0.18	-	-	0.16	6.21	101	350	19	12	0.16D, 0.84I	9.6×10^{-9}	86	196
A146	0.21	Acetic	1.0	3.9	5.07	104	390	19	26	0.29D, 0.71I	7.0×10^{-9}	103	111
A147	0.23	Formic	1.0	7.2	4.81	118	393	22	28	0.33D, 0.67I	6.4×10^{-9}	9	-333
A148	0.23	Lactic	1.0	3.7	5.09	161	442	30	36	$0.18D, 0.82G_3$	4.3×10^{-9}	-206	-406
A151	0.24	Oxalic	1.0	7.4	4.80	208	513	39	44	$0.48D, 0.52G_2$	3.5×10^{-9}	-2	-255
A149	0.25	Propionic	1.0	3.1	5.16	201	513	38	41	0.61D, 0.39T	2.9×10^{-9}	26	-134
A150	0.24	n-Butyric	1.0	2.7	5.27	189	485	35	59	$0.83D, 0.17G_3$	2.3×10^{-9}	55	-228
A190	0.25	n-Butyric	1.0	2.8	5.20	190	485	35	31	$0.23D, 0.77G_3$	2.7×10^{-9}	54	0
A191	0.26	iso-Butyric	1.0	2.8	5.21	147	450	28	39	$0.50D, 0.50G_3$	3.5×10^{-9}	53	-
A192	0.26	n-Valeric	1.0	2.5	5.27	163	469	31	37	$0.43D, 0.57G_3$	3.2×10^{-9}	36	-102
A193	0.25	iso-Valeric	1.0	2.7	5.27	167	452	31	60	$0.62D, 0.38G_3$	3.0×10^{-9}	61	-125
A194	0.22	Benzoic	1.0	2.7	5.22	185	482	35	60	$0.29D, 0.71G_3$	2.6×10^{-9}	49	-274
A195	0.24	Na Benzoate	1.0	0.75	6.57	162	467	30	47	$0.28D, 0.72G_3$	3.2×10^{-9}	-2	-313
A152	0.22	Carbonic	1.0	0.60	5.90	207	505	39	58	$0.79D, 0.21G_3$	2.0×10^{-9}	18	-165

[a]Lightly sensitized (EPR = 2 $C \cdot cm^{-2}$) specimens (Heat No. 30956) were exposed to the environments for ~20 h before straining at a rate of 5.2×10^{-7} s^{-1}.

[b]Ductile (D), transgranular (T), granulated (G), and intergranular (I), in terms of the fraction of the cross-sectional area. Characterization of the fracture surface morphologies is in accordance with the illustrations and definitions in Reference 6.

[c]SCC growth rates are based on measurement of the depth of the longest crack in an enlarged micrograph of the fracture surface and the time period from the onset of yield to the point of maximum load on the tensile curve.

Table 6. Crack Growth Results for a Sensitized Type 304 SS Specimen[a] during Experiments[b] at 289°C in Water Containing 0.2–0.3 ppm Dissolved Oxygen[c], Carboxylic Acids, and Impurity Anions

Test No.	Test Time, h	Water Chemistry						Electrode Potentials		Type 304 SS	
		Organic Acid	Conc., ppm	Impurity Anion[e]	Conc., ppm	pH at 25°C	Cond., μS/cm	304 SS, mV(SHE)	Pt, mV(SHE)	K_{max}[d] MPa·m$^{1/2}$	Growth Rate, m·s^{-1}
1	141 1458	–	–	–	–	6.50	0.13	195	200	30.4	2.9×10^{-10}
2	1458 2465	Propionic	0.1	–	–	5.95	0.48	190	190	31.4	2.9×10^{-10}
3	2465 3452	Propionic	1.0	–	–	5.17	3.0	206	220	31.6	0.2×10^{-10}
4	3452 4680	–	–	–	–	6.53	0.12	190	200	33.6	2.9×10^{-10}
5	4680 5836	Butyric	1.0	–	–	5.27	2.5	170	180	33.6	~0
6	5836 7182	Butyric	0.1	–	–	6.18	0.38	180	190	34.8	1.9×10^{-10}
7	7182 7566	Butyric	1.0	Sulfate	0.1	5.18	3.7	190	190	37.0	7.4×10^{-10}
8	7566 8188	Butyric	1.0	–	–	5.23	3.0	190	230	37.0	~0
9	8188 9341	Butyric	1.0	Chloride	0.1	5.21	3.2	200	210	39.8	1.5×10^{-10}
10	9341 10490	Butyric	1.0	–	–	5.16	3.1	175	220	39.8	~0

[a]Compact tension specimen (1TCT). AISI 304 SS (Heat No. 30956) received the following heat treatment: solution anneal at 1050°C for 0.5 h plus 700°C for 0.25 h plus 500°C for 24 h (EPR = 2 C·cm^{-2}).

[b]Frequency and load ratio, R, for the positive sawtooth waveform were 8×10^{-2} Hz and 0.95, respectively.

[c]Effluent dissolved-oxygen concentration; feedwater oxygen concentration was 0.4–1.0 ppm.

[d]Stress intensity, K_{max}, values at the end of the test condition.

[e]Sulfate and chloride added as H_2SO_4 and NaCl.

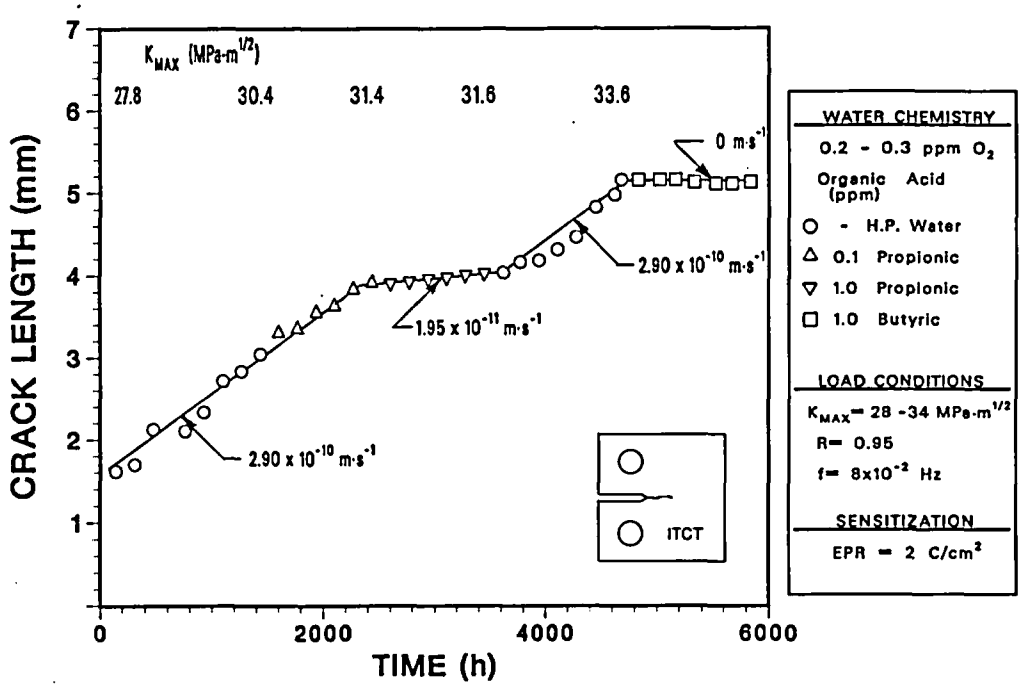

Figure 6. Crack Length versus Time for a 1TCT Specimen of Sensitized (EPR = 2 C·cm^{-2}) Type 304 SS in Oxygenated Water (0.2–0.3 ppm) without and with 0.1 and 1.0 ppm *Propionic and Butyric Acid at 289°C.*

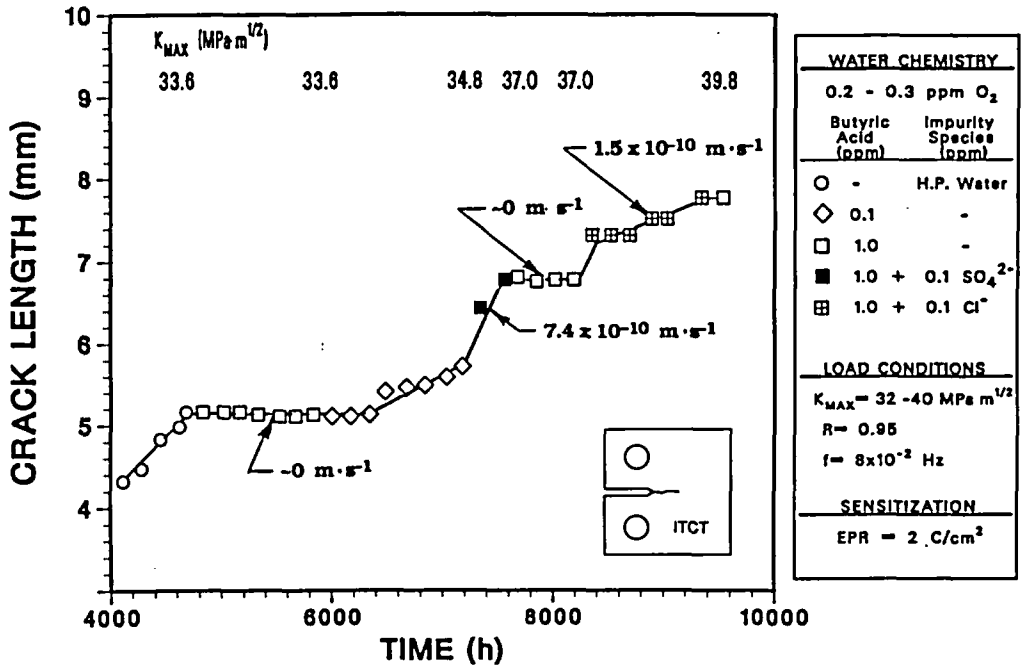

Figure 7. Crack Length versus Time for a Continuation of the Test on a 1TCT Specimen of Sensitized (EPR = 2 C·cm^{-2}) Type 304 SS in Oxygenated Water (0.2–0.3 ppm) with 0.1 Butyric Acid, and 1.0 ppm Butyric Acid without and with 0.1 ppm of Sulfate or Chloride at 289°C.

not decrease when the organic acids were present in the water, in contrast to the CERT experiments in Table 5 where the ECP values of the platinum electrode were lower by ~400 mV than the values obtained in high-purity oxygenated water. This can be attributed to the higher oxygen concentrations in the feedwater (0.4–1.0 ppm) used to maintain the effluent values in the range of 0.2–0.3 ppm in the large autoclave system.

A mechanism whereby the organic acids could inhibit SCC in oxygenated water even though the ECP regime of the steel is conducive to cracking (>–250 mV [SHE] at 289°C) is as follows. It is known that many organic substances such as aliphatic alcohols and acids, carboxylic acids, and others adsorb on metal and oxide electrodes at very high potentials associated with oxygen evolution at ambient temperature.[19-23] The rate constant for oxygen evolution is independent of the presence of the inhibitor, i.e., the effect of the inhibitor was mainly to block active reaction sites.[19] The adsorbability of the various substances increases as the molecular weight increases,[20,21] and the adsorption follows a logarithmic isotherm at concentrations $\geq 10^{-5}$ M (≥ 1 ppm).[21-23] It is plausible that carboxylic acids, at a similar concentration in the water, adsorb on the oxide surface of Type 304 SS and inhibit oxygen reduction, which is the cathodic partial process that couples with anodic dissolution at the crack tip in a slip–dissolution mechanism[8,9] of crack growth.

The pronounced effect of these substances on crack growth can be rationalized from the mechanism of oxygen reduction on electrode surfaces. Cathodic reduction of oxygen is a complex electrochemical process that can proceed along two reaction paths according to the nature of the electrode material, the electrolyte, and the reaction conditions, i.e., a direct $4e^-$ path described by the equation

$$O_2 + 2H_2O + 4e^- = 4OH^- \qquad (10)$$

or by two consecutive $2e^-$ steps that are represented by the equations

$$O_2 + H_2O + 2e^- = HO_2^- + OH^- \qquad (11)$$
$$HO_2^- + H_2O + 2e^- = 3OH^-. \qquad (12)$$

Both the direct $4e^-$ and sequential $2e^-$ paths have been reported for various electrode-electrolyte systems.[24-30] If oxygen reduction occurs through a $4e^-$ path, adsorption occurs through a bridged configuration in which each adsorbed molecule requires two adjacent vacant sites[29,30] as depicted by the equation

$$2M + O_2 = M \begin{array}{c} O \\ / \quad \backslash \\ O \quad\quad O \end{array} M \quad (O_2 \text{ ads}). \qquad (13)$$

From reaction rate theory, the rate of reduction is first-order in the concentration of dissolved oxygen, C_{O_2}, but second-order in fractional coverage of empty sites; i.e.,

$$\Theta_o = K_{eq} [C_{O_2}] [\Theta_m]^2, \qquad (14)$$

where Θ_o and Θ_m are fractional surface coverage of O_2 and empty sites, respectively. For a $2e^-$ path, oxygen adsorption occurs via an end-on configuration[29,30] depicted by the equation

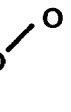

$$M + O_2 = M \qquad (O_2 \text{ ads}) \tag{15}$$

where the rate of reduction is first-order with respect to O_2 concentration and the vacant sites, i.e.,

$$\Theta_o = K_{eq} [C_{O_2}] \Theta_m. \tag{16}$$

Equations (14) and (16) suggest that a decrease in available sites, Θ_m, by adsorption of organic species would have a more significant effect on the available sites for oxygen reduction, Θ_o, for a $4e^-$ reduction path than on a $2e^-$ path for the same dissolved-oxygen concentration.

Previous results[4,5] indicated that the CGR of the steel follows a 1/4-power dependence over several orders of magnitude of the oxygen concentration, i.e., a $4e^-$ process according to Eq. (10), in contrast to a $2e^-$ path (Eqs. [11] or [12]) where a 1/2-power dependence would be expected, as is observed in the case of the reduction of sulfate to sulfite, which is a $2e^-$ process.

With cathodic reduction of oxygen as the rate-controlling process for SCC at a fixed strain rate, and the relationship between the fractional surface coverage of oxygen available for this reaction (Eq. [14]), one can rationalize the strong mitigating effect of the various organic species on the CGR of the steel in oxygenated water. For example, a decrease in the value of Θ_m from 1.0 (high-purity water) to ~0.3 or 0.1 by blockage of ~70 or 90% of the available sites would decrease Θ_o by a factors of ~10 or 100, respectively. For comparison, the CGRs of the steel in the CERT experiments in Table 5 decreased by factors of ~4 to 5 relative to high-purity water, which suggests that <70% of the sites were blocked by the higher molecular weight carboxylic acids at a concentration of 1.0 ppm. However, at this concentration the results of the fracture-mechanics tests in Table 6 and Figs. 6 and 7 indicate at least an order of magnitude decrease in the CGRs (i.e., $< 2 \times 10^{-11}$ m·s^{-1}) relative to high-purity water.

The inability of the organic species (i.e., butyric acid) to mitigate SCC when sulfate is present in the water is consistent with the site blockage mechanism, since site blockage is not as effective for $2e^-$ reduction process, e.g., Eq. (16). Because the chloride ion does not undergo cathodic reduction, its deleterious effect on SCC in oxygenated water containing the organic acid must be attributed to other mechanisms. These include: (a) adsorption of chloride ions may decrease surface coverage by the inhibitor,[31,32] (b) chloride could act as an "anion bridge" for electron transfer across the oxide/electrolyte interface that accelerates redox reactions,[33-36] and (c) chloride may be incorporated into the oxide film and alter the passivity and transport properties.[37,38]

Effect of Sulfate in Oxygenated (0.2–0.3 ppm) Water

Fracture-mechanics CGR tests on Types 316NG and 304 SS were performed to help quantify the beneficial effects of improved water purity. The tests were performed on sensitized (EPR = 2 C·cm^{-2}) Type 304 SS and a Type 316NG SS specimens at 289°C in water with 0.2–0.3 ppm dissolved oxygen at a load ratio, R, of 0.95, a frequency of 0.08 Hz, and a K_{max} of ~28 MPa·m$^{1/2}$. The tests were initiated in oxygenated water with 0.1 ppm sulfate (as H_2SO_4) at a conductivity of 0.9 μS·cm^{-1} and the impurity level was varied during the

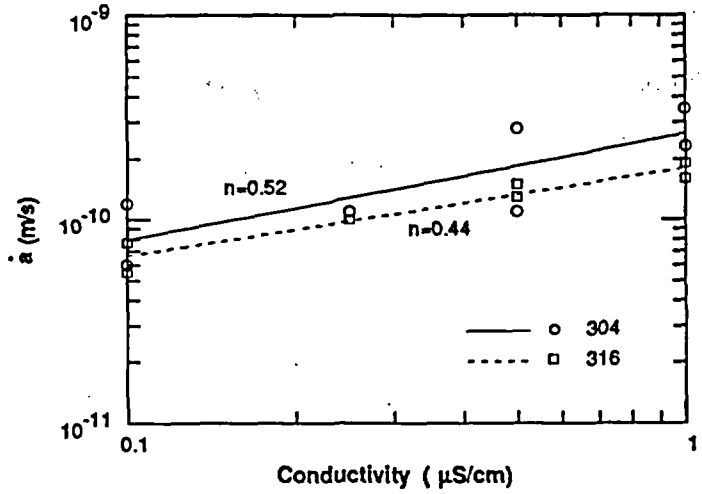

Figure 8. Crack Growth Rates from Fracture Mechanics Specimens of Sensitized Type 304 and Type 316NG SS as a Function of Conductivity. The conductivites are associated with sulfate levels from ~0 to 100 ppb.

tests to obtain conductivity values between 0.1 and 0.9 $\mu S \cdot cm^{-1}$. The CGRs as a function of the conductivity are shown in Fig. 8.

As expected, the CGRs of sensitized Type 304 SS decrease with improvement of the water quality. Data from earlier work[39] suggest that a "threshold" effect marked by a sharp decrease in crack growth rate ȧ may exist at a very low conductivity level, but for the range of conductivities in these tests the dependence of ȧ on conductivity is fairly weak. An empirical fit to the data gives a power-law dependence on conductivity of ~0.5. This is consistent with the results of a statistical analysis of a much larger number of tests (85) on Types 304 and 316NG SS in which ȧ was also found to depend on the conductivity to the power ~0.5. The results are also consistent with the behavior observed in CERTs at a low dissolved oxygen concentration with sulfate additions in the range of 0.1–10 ppm.[39]

The model for SCC growth rates developed by Ford et al.[40] predicts a stronger dependence on impurity level than is observed in these tests. The dependence on conductivity is not given explicitly in the model, but parametric calculations show that over the range of conductivities of interest, e.g., 0.1–1.0 $\mu S \cdot cm^{-1}$, the effective power-law dependence on conductivity is typically 1.0–1.5. The predicted behavior of sensitized Type 304 SS (EPR=15 $C \cdot cm^{-2}$) at an electrochemical potential of 100 mV(SHE) is shown in Fig. 9. The effective power-law dependence in this case is 1.4.

Although the model[40] appears to over predict the effect of conductivity on the crack growth rate, in general predictions from the model are reasonably good. In Fig. 10, model predictions are compared with experimental results from 85 CGR tests on Types 304 and 316NG SS at sulfate levels from 0–100 ppb, R values from 0.8–1.0, and stress intensity values from 18–64 $MPa \cdot m^{1/2}$. In almost all cases the predicted results were within a factor of 10 of the experimental values.

3.2 Fatigue of Type 316NG SS

Residual-life assessment reviews for LWRs indicate that low-cycle fatigue is a potentially significant degradation mechanism in LWR primary piping. This degradation mechanism must be considered when justifying extended operation of an LWR plant.[41] Current fatigue design for austenitic SS piping is based on the ASME Section III Fatigue Design

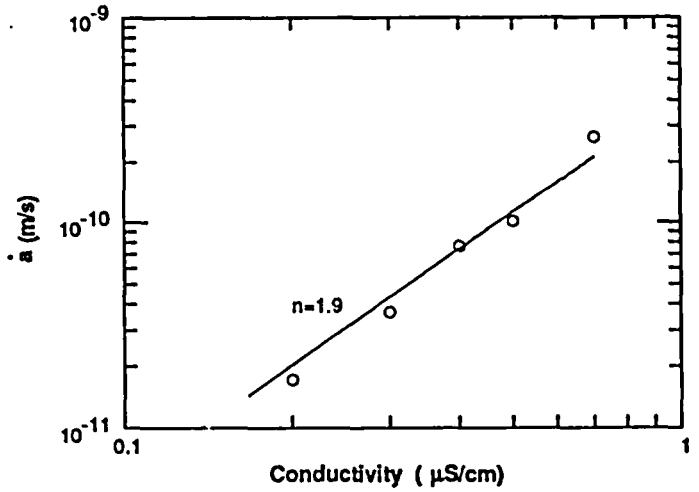

Figure 9. Predicted Dependence of CGR on Conductivity for Sensitized (EPR=15 C·cm^{-2}) Type 304 SS at an ECP of 100 mV(SHE) According to the Model of Ford et al.[40]

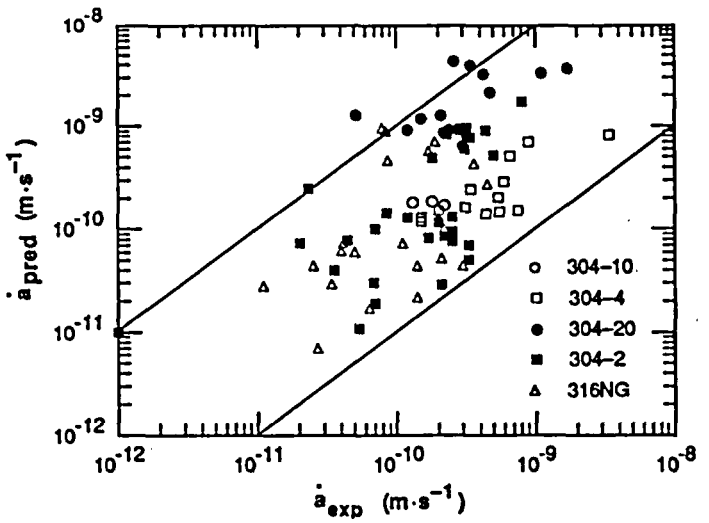

Figure 10. Comparison of Predicted and Measured CGRs for 85 Tests on Types 304 and 316NG SS at Sulfate Levels from 0–100 ppb, R Values from 0.8–1.0, and Stress Intensity Values K from 18–64 MPa·m$^{1/2}$.

Curves. Environmental effects are not explicitly considered in these curves. Instead, the design curves are obtained by introducing a factor of 2 on the strain range or 20 on the cycles from the mean life curve, whichever is more conservative. Several studies[42,43] have shown that the effect of the standard BWR environment on the fatigue life of A106-Gr B and A333-Gr 6 steel can completely erode the "2 or 20" margin in the Code Design Curve.

The objective of the current work is to provide additional information on the effects of operating temperature and environment on the fatigue behavior of Type 316NG SS. The data are needed to assess the degree of conservatism inherent in the ASME Code Section

III Fatigue Design Curves for this material. They may also be needed for decisions on life extension beyond the current 40-year design life.

Baseline in-air tests were performed with the same specimen design and loading systems that were used for the tests in simulated BWR water. The tests in air were performed under strain-control where the strain in the specimen was measured with an axial extensometer. The specimen stroke was monitored during these tests. Because it is difficult to actually monitor the specimen strain in tests in an autoclave, these tests were run in stroke-control. The stroke values in the autoclave tests were selected to match those measured in the corresponding strain-control test in air. Rather than match the stroke values in the two tests on a cycle-by-cycle basis, average values over a range of cycles were selected as shown in Fig. 11. Benchmark tests were performed to show that the lives obtained under the variable amplitude stroke control were consistent with those obtained under strain control. These results are summarized in Table 7. Variations in life between the strain- and stroke-control tests are small and are within the scatter expected for tests in strain control at this strain range.

The tests in the simulated BWR environment were performed in high-purity water at 288°C with ~0.2 ppm dissolved oxygen in the effluent water. The lives at a given strain range in the environment are dependent on frequency. The results of the tests to date are summarized in Table 8.

The normalized fatigue life N_{env}/N_{air} is relatively independent of strain range, at least over the strain ranges examined to date, and depends primarily on the strain rate as shown in Fig. 12. The data show that at the lowest strain rates the life in the environment is about a third of that in air. The data are too limited at this point to assess whether the strain-rate effect has reached saturation, i.e., whether further decreases in the strain rate would not lead to a corresponding decrease in fatigue life.

These results may be compared with similar data obtained by Iida et al.[44] for an A333-Gr 6 steel in water with 8 ppm dissolved oxygen shown in Fig. 13. The A333 steel shows a stronger strain rate dependence and a more severe reduction in fatigue life. In this case, the relative fatigue life is also almost independent of strain range for values from ~0.2 to 1%.

3.3 Stress Corrosion Cracking of Ferritic Steels

Plain carbon and low-alloy steels are used extensively as piping and pressure vessel materials in PWRs and BWRs. The steels include A106-Gr B and A333-Gr 6 for seamless pipe and A302-Gr B, A508-2, and A533-Gr B plate for pressure vessels. Although operating experience with ferritic steel components in reactor pressure boundaries is considerably better than with weld-sensitized austenitic SS, instances of cracking of these steels have occurred in the U.S. and abroad. The objective of the current work is to better define the environmental and material conditions that can produce SCC susceptibility in these steels.

The results of CERTs on several types of ferritic steel (A333, A106, A155, A516, and A533B) are summarized in Table 9. The tests were performed in deoxygenated water (~5-25 ppb) at 289°C with 0.1 ppm sulfate (as H_2SO_4) at strain rates of 1.0×10^{-6}, 5.0×10^{-7}, and 2.5×10^{-7} s^{-1}. All materials showed transgranular cracking on the fracture surfaces, except for A533B. However, A533B also showed TGSCC when the strain rate was decreased to 2.5×10^{-7} s^{-1}. The average crack growth rates varied from 1×10^{-9} to 9×10^{-9} $m \cdot s^{-1}$. The results of the current tests can be compared with previous CERT results[45] in water with 0.2-0.5 ppm oxygen. Although there is substantial scatter in the data, overall the

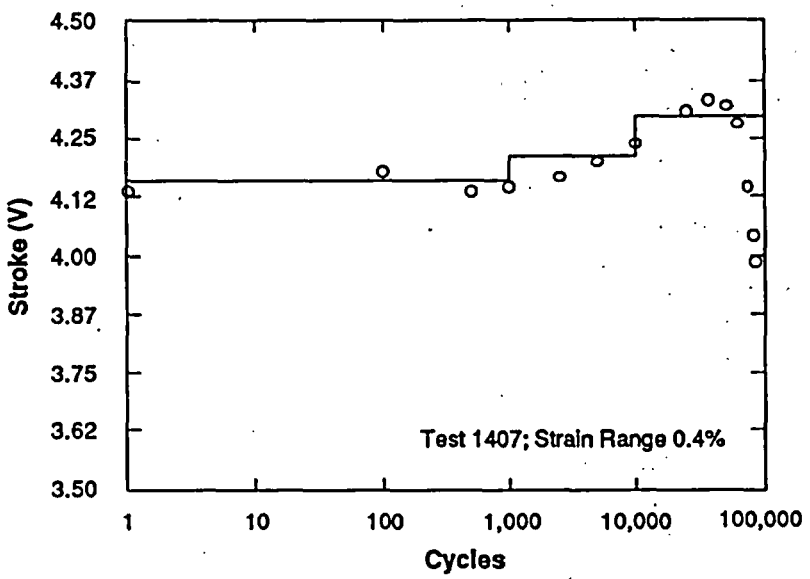

Figure 11. Variable Amplitude Stroke History Used to Simulate Strain Control.

Table 7. Comparison of Fatigue Lives of Type 316NG SS in Strain and Stroke Control

Test No.	Control Type	Strain Range, %	Temp., °C	Cycles to Failure
1392	Strain	0.5	~22	60,741
1420	Stroke[a]	0.5	~22	54,249
1409	Strain	0.5	288	53,144
1410	Stroke	0.5	288	51,194

[a]Test performed with autoclave.

CGRs are lower in the low-oxygen environment, and the A533B steel appears to be less susceptible to cracking.

As expected from related work on the fatigue crack growth of ferritic steels in reactor environments,[46,47] there appears to be a strong correlation between the sulfur content of the steel (particularly the presence of sulfide inclusions) and susceptibility to SCC. There are far fewer inclusions in the less susceptible A533B steel than in the more susceptible materials. Fractographic evidence also indicates that SCC initiates at inclusion sites. Fracture surfaces of A516 and A533B ferritic steel specimens (Heat Nos. DP2-F34 and XE5-M) after tests in water with 5-25 ppb and 0.2-0.3 ppm oxygen, respectively, plus 0.1 ppm sulfate are shown in Figs. 14 and 15. In both cases the transgranular cracks initiate at inclusions.

Fracture-mechanics CGR tests are being performed on specimens from a plate of A533-Gr B pressure vessel steel (Heat No. 02, containing 0.018% sulfur and 0.012% phosphorus) in deionized water with 0.2 -0.3 ppm dissolved oxygen at 289°C. One test involves a composite 1TCT specimen of the ferritic steel/Inconel-182/Inconel-600, which was fabricated by overlaying the ferritic steel with In-182 weld metal and then electron-beam

Table 8. Comparison of Fatigue Lives of Type 316NG SS in Air and Simulated BWR Water

Test No.	Environment	Strain Range, %	Frequency, Hz	Cycles to Failure
1409	Air[a]	0.5	0.5	53,194
1410	Air[b]	0.5	0.5	51,194
1420	Air[c]	0.5	0.5	54,249
1414	Water[d]	0.5	0.5	26,230
1418	Water[d]	0.5	0.5	25,714
1423	Water[d]	0.5	0.05	17,812
1425	Water[d]	0.5	0.005	13,684
1408	Air[a]	0.75	0.33	21,548
1426	Water[d]	0.75	0.5	12,069
1427	Water[d]	0.75	0.05	6,679
1428	Water[d]	0.75	0.005	5,897
1430	Air[a]	0.30	0.33	168,852
1431	Water[d]	0.30	0.5	116,754
1434	Water[4]	0.30	0.05	40,643

[a]Baseline test in air at 288°C under strain control.
[b]Baseline test in air at 288°C under stroke control.
[c]Baseline test in air at ~22°C under stroke control in the autoclave.
[d]High-purity water with 0.2 ppm dissolved oxygen at 288°C.

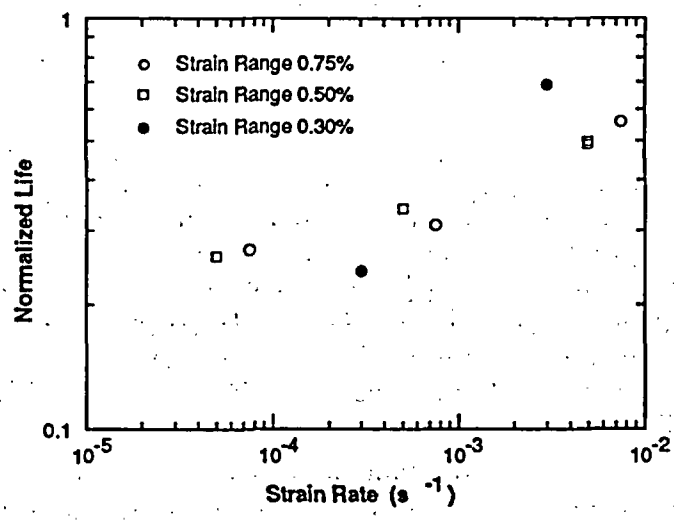

Figure 12. Normalized Fatigue Life as a Function of Strain Rate.

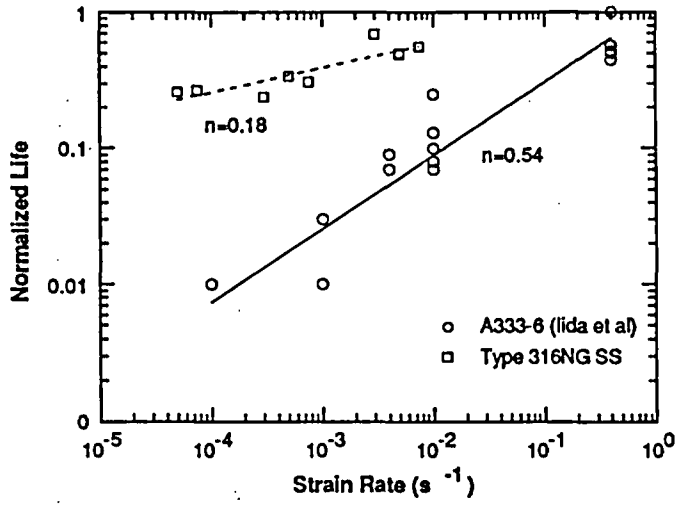

Figure 13. Comparison of the Effect of Strain Rate on Normalized Fatigue Life of A333 Gr 6 Steel and Type 316NG Stainless Steel.

welding In-600 to the In-182. The specimen is designed so that the crack will proceed from the In-182 into the ferritic steel. The specimen was nickel plated to prevent contact of the large surface of low-alloy steel with the environment in order to simulate a crack in a clad low-alloy steel vessel.

In another test system a conventional 1TCT ferritic specimen, a nickel plated specimen, and a gold plated specimen are being tested. The plated specimens are included in order to determine whether electron transfer through the oxide film on the bulk surface of the ferritic steel is important in the overall SCC process, and hence, to assess the validity of using data obtained from specimens without cladding to analyze the behavior of a clad ferritic vessel, where only the crack surface is exposed to the environment. The composite specimen, mentioned previously, is intended to address the question of whether the K_{ISCC} value determined from conventional fatigue precracked specimens is applicable to the more prototypical case when a crack in the ferritic steel initiates from a stress corrosion crack in the In-182 weld metal.

The composite specimen fatigue was precracked in the environment and the SCC test was initiated at a load ratio of 0.95, a frequency of 0.08 Hz, and a K_{max} of 28 MPa·m$^{1/2}$. Crack growth in the In-182 weld metal of the composite specimen occurred at a rate of 2.5×10^{-10} m·s^{-1} for the first 1800 h, i.e., a rate typical of austenitic SS under similar loading conditions. Crack length measurements indicate that the crack tip reached the interface between the In-182 weld metal and the low-alloy steel, but did not enter the ferritic material. The K_{max} value was then increased to 35 MPa·m$^{1/2}$ to determine if cracking would resume at the higher stress intensity. Since no sustained crack growth was observed at this stress intensity level, the K_{max} value was then increased to 40 MPa·m$^{1/2}$, and again no sustained crack growth was observed. The tests are still ongoing and the stress intensity levels will be increased until sustained crack growth is observed.

In the other system, the conventional and the nickel- and gold-plated specimens were precracked under a cyclic load (a sawtooth wave shape with 12-s loading and 1-s unloading time) of R=0.25 at 0.08 Hz and a maximum initial stress intensity of 20 MPa·m$^{1/2}$. During this precracking phase the crack growth rates were 4×10^{-9} m·s^{-1} for the bare and

Table 9. CERT Data on Ferritic Steels in Water with 0.1 ppm Sulfate and 5-25 ppb Oxygen at 289°C

Materal Heat No.	Specimen No.	Strain Rate, s^{-1}	Max Load, MPa	T_f, h	RA, %	Elong., %	Crack Growth, $m \cdot s^{-1}$	ECP, mV(SHE)
A106-Gr B DP2-F29	29B-8	1.0×10^{-6}	557	54.8	32.7	19.3	5.9×10^{-9}	-147
"	29B-9	"	554	66.1	35.4	24.7	5.0×10^{-9}	-136
A106-Gr B DP2-F30	30C-9	2.5×10^{-7}	604	200.1	22.2	18.7	4.8×10^{-9}	-131
A155-CK70 DP20F26	26-5	5.0×10^{-7}	525	131.2	31.6	22.8	2.0×10^{-9}	-144
"	26-6	2.5×10^{-7}	527	280.5	63.7	26.0	1.1×10^{-9}	-47
"	26-8	"	523	249.0	32.6	22.6	1.3×10^{-9}	+19
SA333-Gr6	F9-6	5.0×10^{-7}	539	134.1	37.7	23.3	3.1×10^{-9}	-137
A533-Gr B A5401	W7-6	1.0×10^{-6}	653	61.2	73.7	21.9	Ductile	-146
"	W7-8	"	650	61.6	73.1	22.6	Ductile	-197
"	W7-10	5.0×10^{-7}	654	124.5	73.1	23.3	Ductile	-126
"	W7-11	2.5×10^{-7}	658	168.9	46.9	13.5	3.1×10^{-9}	-153
"	W7-12	"	659	207.7	46.3	18.1	2.3×10^{-9}	-172
A533-Gr B XE5-M	5M-8	1.0×10^{-6}	605	70.1	71.4	25.4	Ductile	-140
"	5M-10	"	602	64.8	69.2	24.3	Ductile	-157
"	5M-11	5.0×10^{-7}	609	122.0	68.0	21.6	Ductile	-192
"	5M-13	2.5×10^{-7}	606	241.4	52.7	21.5	1.9×10^{-9}	-141
"	5M-14	"	608	227.5	53.2	20.1	2.1×10^{-9}	-47
A516-Gr70 DP2-F34	34-6A	1.0×10^{-6}	500	85.2	35.4	31.3	5.8×10^{-9}	-157
"	34-7B	"	499	69.1	47.2	27.2	8.9×10^{-9}	-130

nickel-plated specimens and 2×10^{-8} $m \cdot s^{-1}$ for the gold-plated specimen, i.e., the gold-plated specimen had a crack growth rate a factor of 5 larger than the other specimens. The crack length, determined by the d.c. potential method, is plotted versus test time in Fig. 16. After fatigue precracking, the load ratio was changed to R=0.95 and the crack growth tests were continued in the same environment. No crack growth was observed in any of the specimens for stress intensity values up to 30 $MPa \cdot m^{1/2}$.

4. Conclusions

Conclusions and major findings from work on environmentally assisted cracking of LWR materials over the past year are as follows.

Water Chemistry Influence on SCC of Austenitic SS

- Chromate acts in a similar manner to other oxyanions regarding its effect on SCC of sensitized Type 304 SS. This species undergoes cathodic reduction and contributes to crack growth by scavenging electrons produced by anodic dissolution of metal at the crack tip in a slip-dissolution mechanism[8,9] of crack advance.

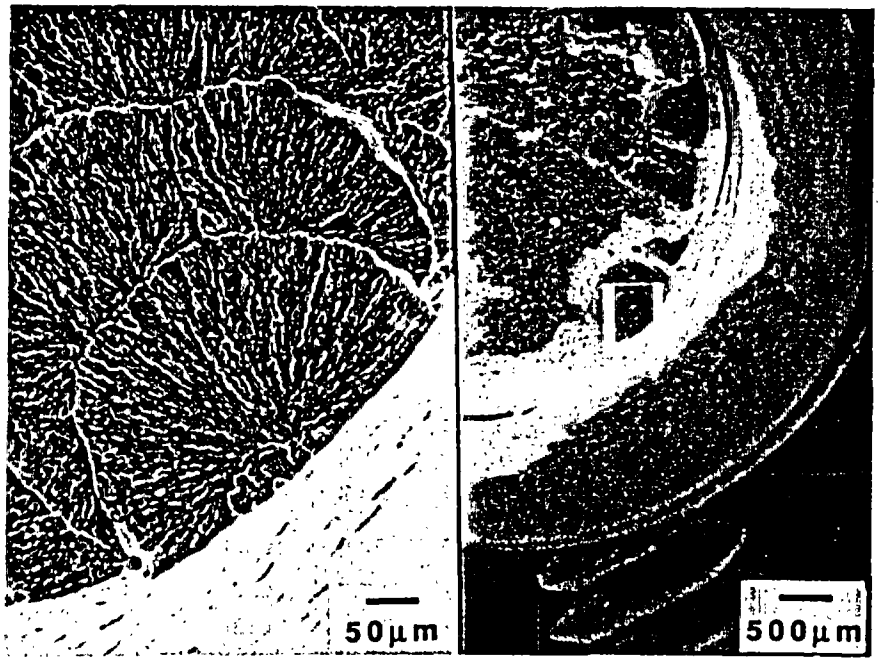

Figure 14. Fracture Surface of A516-Gr 7 Ferritic Steel CERT Specimen (Heat No. DP2-F34 Specimen No. 34-6A) after a Test in Water with 0.1 ppm Sulfate and 5-25 ppb Oxygen at 289°C. Initiation of transgranular cracking at inclusion sites is evident.

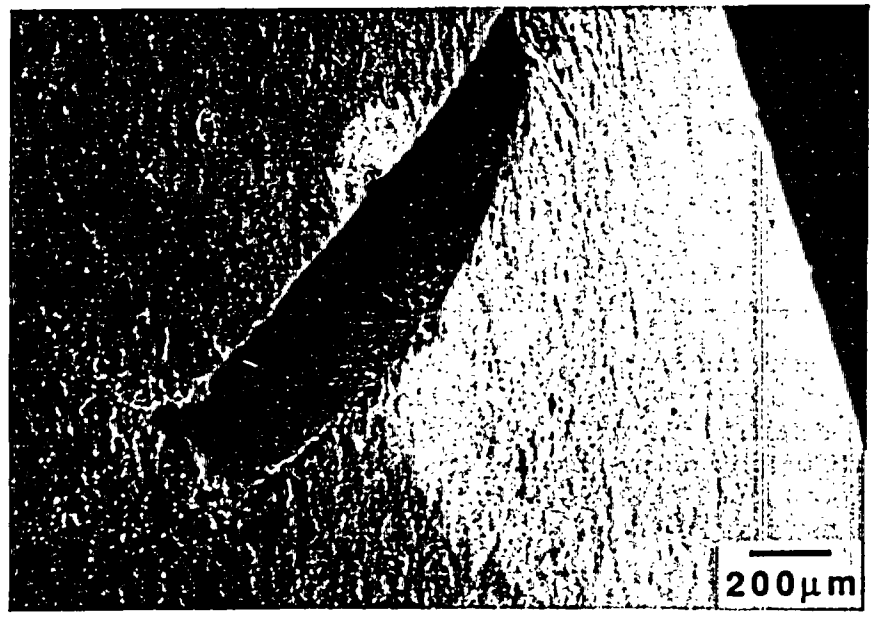

Figure 15. Surface of A533-Gr B Ferritic Steel CERT Specimen (Heat No. XE5-M Specimen No. 5M-3) after a Test in Water with 0.1 ppm Sulfate and 0.2-0.3 ppm Oxygen at 289°C. Crack initiation at an inclusion site is evident.

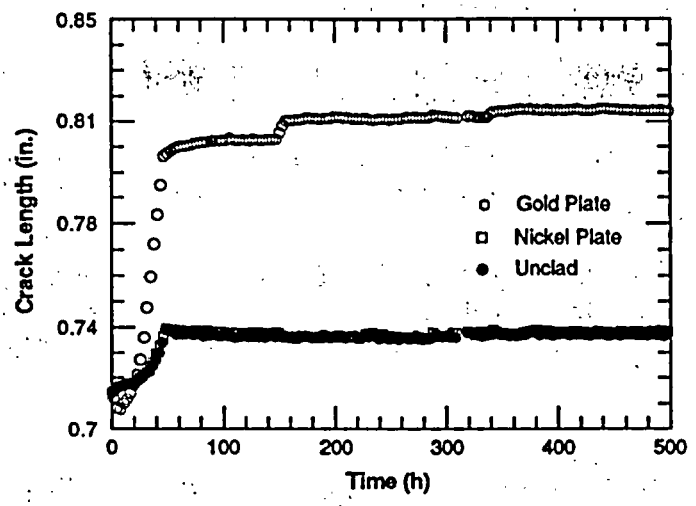

Figure 16. Crack Length versus Time for Au- and Ni-Plated and Non-Plated (Bare) 1TCT Specimens of A533-Gr B Carbon Steel in Deionized, Oxygenated Water at 289°C.

- In comparison with other species at the 0.1 ppm level in simulated BWR water, chromate is less deleterious than sulfur species, and more deleterious than nitrate, borate, carbonate, and chloride in CERTs at 289°C and a strain rate of 1×10^{-6} s^{-1}.
- Results of this and other investigations[48,49] indicate that carbonic and carboxylic (acetic, formic, lactic, oxalic, propionic, and butyric) acids at low concentrations (~1 ppm) do not have a deleterious effect on IGSCC of sensitized Type 304 SS under simulated normal BWR water chemistry.
- Short-chain carboxylic acids mitigate IGSCC of the steel under high-R, low-frequency loading at stress intensity values of <40 MPa·$m^{1/2}$.
- The role of the organic acids at low concentrations in oxygenated water in mitigating SCC of sensitized Type 304 SS primarily involves adsorption on and blockage of active sites for the cathodic reduction of oxygen, in contrast to that of commonly used chemical organic oxygen scavengers, which decrease both the dissolved oxygen concentration and the ECP of steel (and platinum) to very low values.
- Site blockage by carboxylic acids (butyric) was not effective in mitigating IGSCC when other ionic species (sulfate or chloride) were present in the oxygenated water at low concentrations (~0.1 ppm).
- Surface reactions involving organic substances, dissolved oxygen, and various ionic species in high-temperature water contribute to the complex nature of IGSCC of sensitized Type 304 SS, and under certain conditions can predominate over concomitant mechanical and electrochemical processes at the crack tip.
- A SCC model developed by Ford et al.[40] tends to over predict the effect of conductivity on the CGR of sensitized Type 304 SS on the basis of our experimental data; however, overall predictions from the model are reasonably good.

Fatigue of Type 316NG SS in Simulated BWR Water

- The normalized fatigue life N_{env}/N_{air} of Type 316NG SS depends primarily on the strain rate and is relatively independent of strain range.
- At the lowest strain rates, the fatigue life in the environment is about a third of that in air, but the data are too limited to assess whether the strain-rate effect has reached saturation.
- A comparison of the results on Type 316NG SS with similar data obtained by Iida et al.[44] for an A333-Gr 6 steel indicates that the A333 steel shows a stronger strain-rate dependence and a more severe reduction in fatigue life in oxygenated water.

SCC of Ferritic Steels

- A comparison of current results in deoxygenated water (~5–25 ppb) with previous CERT results[45] in the water with 0.2–0.5 ppm oxygen, with and without sulfate addition to the feedwater, indicates that the overall the CGRs are lower in the low-oxygen environment, and the A533B steel appears to be less susceptible to cracking than other ferritic steels.
- As expected from related work on the fatigue crack growth of ferritic steels in reactor environments,[46,47] there appears to be a strong correlation between the sulfur content of the steel (particularly the presence of sulfide inclusions) and susceptibility to SCC. Inclusions are far fewer in the less susceptible A533B steel than in the more susceptible materials.
- Fracture-mechanics CGR tests are being performed on A533-Gr B steel and on a composite specimen that was fabricated by overlaying the ferritic steel with In-182 weld metal to address the question of whether the K_{ISCC} value determined from conventional fatigue precracked specimens is applicable to the more prototypical case when a crack in the ferritic steel initiates from a stress corrosion crack in the In-182 weld metal. No sustained crack growth has been observed in the ferritic steel at a stress intensity level of 40 $MPa \cdot m^{1/2}$.

References

1. G. E. Brobst, "Chromate Substitutes for Corrosion Inhibitors in Cooling Systems," EPRI NP-5569 (December 1987).
2. W. E. Ruther, W. K. Soppet, and T. F. Kassner, in *Environmentally Assisted Cracking in Light Water Reactors: Semiannual Report, April – September 1987*, NUREG/CR-4667 Vol. V, ANL-88-32 (February 1989), pp. 24–37.
3. W. E. Ruther, W. K. Soppet, and T. F. Kassner, in *Environmentally Assisted Cracking in Light Water Reactors: Semiannual Report, October 1987 – March 1988*, NUREG/CR-4667 Vol. 6, ANL-89/10 (August 1989), pp. 27–42.
4. W. E. Ruther, W. K. Soppet, and T. F. Kassner, in *Light-Water-Reactor Safety Research Programs: Quarterly Progress Report, January – March 1985*, NUREG/CR-4490 Vol.I, ANL-85-75 Vol. I (March 1986), pp. 25–42.

5. W. E. Ruther, W. K. Soppet, and T. F. Kassner, in *Environmentally Assisted Cracking in Light Water Reactors: Semiannual Report, April – September 1985*, NUREG/CR-4667 Vol. I, ANL-86-31 (June 1986), pp. 27–41.

6. H. D. Solomon, Corrosion (Houston) **40**, 493–506 (1984).

7. W. E. Ruther, W. K. Soppet, and T. F. Kassner, Corrosion (Houston) **44**, 791–799 (1988).

8. F. P. Ford, "Stress Corrosion Cracking," in *Corrosion Processes*, R. N. Parkins, ed., Applied Science Publishers, New York, (1982), pp. 271–309.

9. D. A. Vermilyea, in *Proc. Intl. Conf. on Stress Corrosion Cracking and Hydrogen Embrittlement of Iron Base Alloys*, R. W. Staehle, J. Hochmann, R. D. McCright, and J. E. Slater, eds., NACE, Houston (1983), p. 208.

10. B. H. Dillman, R. A. Reed, and C. C. Lin, "BWR Coolant Impurity Identification Study, Final Report," EPRI NP-4156 (August 1985).

11. B. H. Dillman, J. C. Elliot, R. A. Head, J. E. Osterle, and R. S. Tunder, "Monitoring of Chemical Contaminants in BWRs," Final Report, EPRI NP-4134 (July 1985).

12. J. E. Richards and W. A. Byers, "Industry-wide Survey of PWR Organics, Final Report," EPRI NP-4698 (July 1986).

13. S. D. Strauss, "Advances in Chemical Water Treatment Improve Reliability of Steam-Generating Systems," Power, (October 1986), pp. 15–20.

14. PWR Secondary Water Chemistry Guidelines, Revision 1, EPRI NP-5056-SR, Electric Power Research Institute, Palo Alto, CA (March 1987).

15. BWR Hydrogen Water Chemistry Guidelines: 1987 Revision, EPRI NP-4947-SR, Electric Power Research Institute, Palo Alto, CA (October 1988).

16. J. N. Kass and R. L. Cowan, "Hydrogen Water Chemistry for BWRs," in Environmental Degradation of Materials in Nuclear Power Systems-Water Reactors, Proc. of the 2nd Int. Symp., Monterey, CA, September 9–12, 1985, ANS, La Grange Park, IL (1986), pp. 211–218.

17. M. E. Indig, B. M. Gordon, R. B. Davis, and J. E. Weber, "Evaluation of In-reactor Stress Corrosion Cracking via Electrochemical Measurements," ibid., pp. 411–418.

18. D. D. Macdonald and G. Cragnolino, "The Critical Potential for IGSCC of Sensitized Type 304 SS in High Temperature Aqueous Systems," ibid., pp. 426–434.

19. Yu. M. Tyurin, G. F. Volodin, and V. S. Paducheva, Elektrokhimiya **7**, 1309–1312 (1971).

20. V. I. Naumov, L. A. Smirnova, G. N. Afon'shin, and Yu. M. Tyurin, Elektrokhimiya **7**, 1872–1876 (1971).

21. Yu. M. Tyurin, V. I. Naumov, Vyach. N. Flerov, and Yu. V. Battalova, Elektrokhimiya **10**, 1119–1123 (1974).

22. V. I. Naumov and Yu. M. Tyurin, Elektrokhimiya **8**, 1220–1223 (1972).

23. Yu. M. Tyurin, G. F. Volodin, L. A. Smirnova, and Yu. V. Battalova, Elektrokhimiya **9**, 532–536 (1973).

24. P. K. Adanuvor and R. E. White, J. Electrochem. Soc. **134**, 1093–1098 (1987).

25. P. K. Adanuvor and R. E. White, J. Electrochem. Soc. **135**, 2509–2516 (1988).

26. V. Jovancicevic and J. O'M. Bockris, J. Electrochem. Soc. **133**, 1797–1807 (1986).

27. Lj. M. Vracar and D. B. Sepa, J. Electrochem. Soc. **133**, 1835–1839 (1986).

28. E. J. Taylor, N. R. K. Vilambi, and A. Gelb, J. Electrochem. Soc. **136**, 1939–1944 (1989).

29. J. C. Huang, R. K. Sen, and E. Yeager, J. Electrochem. Soc. **126**, 786–792 (1979).

30. S. M. Kaska, S. Sarangapani, and Jose Giner, J. Electrochem. Soc. **136**, 79–83 (1989).

31. T. Murakawa and N. Hackerman, Corros. Sci. **4**, 387–396 (1964).

32. K. Aramaki, T. Mochizuki, and H. Nishihara, J. Electrochem. Soc. **135**, 2427–2432 (1988).

33. J. P. Cushing and A.T. Hubbard, J. Electroanal. Chem. **23**, 183–203 (1969).

34. R. de Levie and L. Pospisil, J. Electroanal. Chem. **25**, 340–341 (1970).

35. R. R. Dogonadze, J. Ulstrup, and Yu. I. Kharkats, J. Electroanal. Chem. **39**, 47–61 (1972).

36. N. C. Hung and Z. Nagy, J. Electrochem. Soc. **134**, 2215–2220 (1987).

37. T. Okada, J. Electrochem. Soc. **131**, 241–247 (1984).

38. J. R. Galvele, "Present State of Understanding of the Breakdown of Passivity and Repassivation," in *Passivity of Metals*, R. P. Frankenthal and J. Kruger, eds., The Electrochemical Soc., Inc., Princeton, NJ, (1978), pp. 285–327.

39. W. E. Ruther, W. K. Soppet, and T. F. Kassner, in *Environmentally Assisted Cracking in Light Water Reactors: Semiannual Report, April–September 1985*, NUREG/CR–4667 Vol. 1, ANL–86–31, pp. 27–52 (June 1986).

40. F. P. Ford, D. F. Taylor, P. L. Andresen, R. Ballinger, "Corrosion–Assisted Cracking of Stainless and Low–Alloy Steels," EPRI NP–5064S (February 1987).

41. V. N. Shah and P. E. MacDonald, "Residual Life Assessment of Major Light Water Reactor Components–Overview Volume 1," NUREG/CR–4731 EGG–2469 Vol. 1 (June 1987).

42. H. S. Mehta, S. Ranganath, and D. Weinstein, "Application of Environmental Fatigue Stress Rules to Carbon Steel Reactor Piping," EPRI NP–4644M Vols. 1 and 2 (July 1986).

43. D. A. Hale, S. A. Wilson, E. Kiss, and A. J. Gianuzzi, "Low–Cycle Fatigue Evaluation of Primary Piping Materials in a BWR Environment," GEAP–20244 (September 1977).

44. K. Iida, H. Kobayashi, and M. Higuchi, "Predictive Method of Low Cycle Fatigue Life of Carbon and Low Alloy Steels in High Temperature Water Environments," in Proc. of the 2nd Int. Atomic Energy Agency Specialists' Meeting on Subcritical Crack Growth, NUREG/CP-0067, Vol 2, April 1986.

45. J. Y. Park, in *Environmentally Assisted Cracking in Light Water Reactors: Semiannual Report, October 1987-March 1988*, NUREG/CR-4667 Vol. 6, ANL-89-10, pp. 43-47 (August 1989).

46. J. H. Bulloch, "The Effect of Sulfide Distribution and Morphology on Environmentally Assisted Cracking Behavior of Ferritic Reactor Pressure Vessel Materials," in *Proc. of the 3rd Int. Symp. on Environmental Degradation of Materials in Nuclear Power Systems-Water Reactors*, G. J. Theus and J. R. Weeks, eds., American Nuclear Society, LaGrange Park, IL, 1988.

47. P. M. Scott, A. E. Truswell, and S. G. Bruce, Corrosion (Houston) **40**, 350-357 (1984).

48. T. Christman and G. Cragnolino, Corrosion (Houston) **44**, 345-353 (1988).

49. L. Ljungberg, D. Cubicciotti, and M. Trolle, Corrosion (Houston) **45**, 215-222 (1989).

Acknowledgments

W. F. Burke, D. J. Dorman, D. R. Perkins, D. L. Rink, and J. C. Tezak contributed to the experimental effort in this program.

AGING RISK ASSESSMENT METHODOLOGY: DEMONSTRATION STUDY ON A PWR AFWS[a]

A. J. Wolford
C. L. Atwood
W. S. Roesener

Idaho National Engineering Laboratory, EG&G Idaho, Inc.
Idaho Falls, ID 83415

ABSTRACT

The problem of analyzing age-dependent plant risk necessitates rethinking a basic principle of PRA; the assumption that all equipment failure probabilities are constant. This paper presents a methodology to detect and quantify increasing failure rates. The methodology is applied to a 16 year old PWR auxiliary feedwater system. Based upon plant-specific maintenance data and the accompanying PRA, this study concludes that age-dependent behavior can be inferred from the data sources, and that the implied core damage frequency can be computed from these data. The primary purpose of such an aging analysis is not for extrapolation of risk into the distant future, but to help determine near-future contributors to risk and add insight to decisions for corrective actions. This use of aging risk analysis is therefore consistent with the NRCs use of PRA in general. A useful product of this work is the development of a step-by-step procedure for aging risk assessment.

1. INTRODUCTION

The risk associated with the operation of many individual nuclear power plants has been calculated using Probabilistic Risk Assessment (PRA) techniques. To date, PRA calculations have used time-averaged unreliabilities and unavailabilities as inputs such that the calculated risks are a time-average and say nothing of the risk trends. This lack of knowledge of the age-dependent risk and trends has become a source of concern with the recognition of the potential for operation of plants for years beyond the original 40 year license period. The calculation of an age-dependent risk, at least when considering active standby safety components, is a fairly simple matter given the age-dependent inputs. The development of valid, and noncontrived age-dependent inputs is not such a simple matter. It involves the reduction of large amounts of raw data, which were not recorded for the purposes of PRA, into failure time-histories, and the characterization of these time-histories by a mathematical model. Working hypotheses related to the development of a model must then be tested

---

[a]Work supported by the U.S. Nuclear Regulatory Commission, Office of Research, under DOE Contract No. DE-AC07-76ID01570

The specific methodology and procedure developed for the reduction of the information and the application and testing of the model is outlined in a stepwise fashion in following sections of this paper. Results of the application of the methodology to the Maintenance Records from the Auxiliary Feedwater (AFW) System of an older Pressurized Water Reactor (PWR) are used throughout the paper to demonstrate the methodology. In addition, a very brief discussion of the AFW system is presented to allow better understanding of the application.

2. AUXILIARY FEEDWATER SYSTEM: A BRIEF DESCRIPTION

The basic function of the Auxiliary Feedwater (AFW) System is to remove heat from a nuclear power plant core through heat exchange in the steam generators which are the interface between the primary (nuclear) water system and the secondary (steam) water system. The system function is performed during normal plant start-ups and shutdowns and during emergencies following loss of the main feedwater system. The system operates an average of 100 hours each year. The AFW systems in use generally consist of two motor driven pumps, one steam-turbine driven pump, and piping and valves. These components pump, carry and control water to the steam generators. See Figure 1 for a schematic representation of the AFW System, including relevant nomenclature.

3. STEP-BY-STEP PROCEDURE FOR AGING RISK ANALYSIS

The following steps refer to the flow diagram shown in Figure 2.

Step 1 - Obtain Component Time-Histories

The first step is to obtain the information required to develop time-histories for the systems/components to be analyzed. Possible sources of information include: maintenance records, material histories, operating records and plant process computer data. Comparison of data from numerous sources will aid in the development of the most reliable component time-histories. Although very little attention is given to this step in this paper, it should not be construed that the development is trivial or unimportant. To the contrary, the component time-histories are the backbone of the analysis and may be extremely difficult to develop. Poorly developed time-histories can result in either the false identification of aging where none is occurring or the false conclusion that aging is not occurring when it actually is. Of course, the latter case will result in the underestimation of risk. An overview for data base development which could be applied to the development of component time-histories was prepared by the Yankee Atomic Electric Company[1].

Step 2 - Define Relevant Component Failure Modes

Step two consists of the identification of the failure modes that will contribute to an increase in plant risk. These failures modes should be obtained from a plant-specific PRA. Caution should be taken not to ignore

FIGURE 1 SCHEMATIC DIAGRAM OF A PRESSURIZED WATER REACTOR AUXILIARY FEEDWATER SYSTEM.

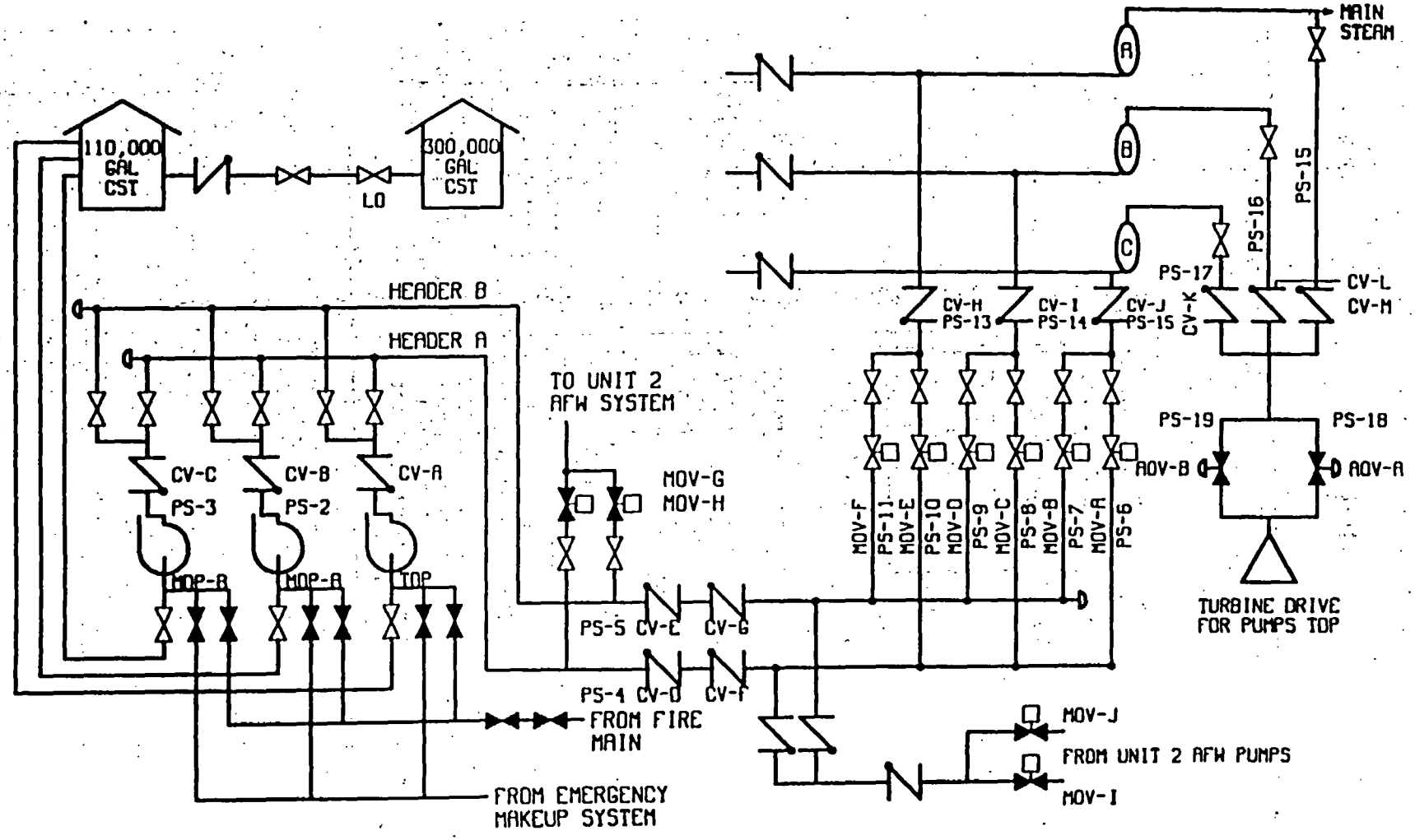

S91 WSR-1089-01

FIGURE 2 STEP-BY-STEP PROCEDURE FOR AGE-DEPENDENT RISK QUANTIFICATION.

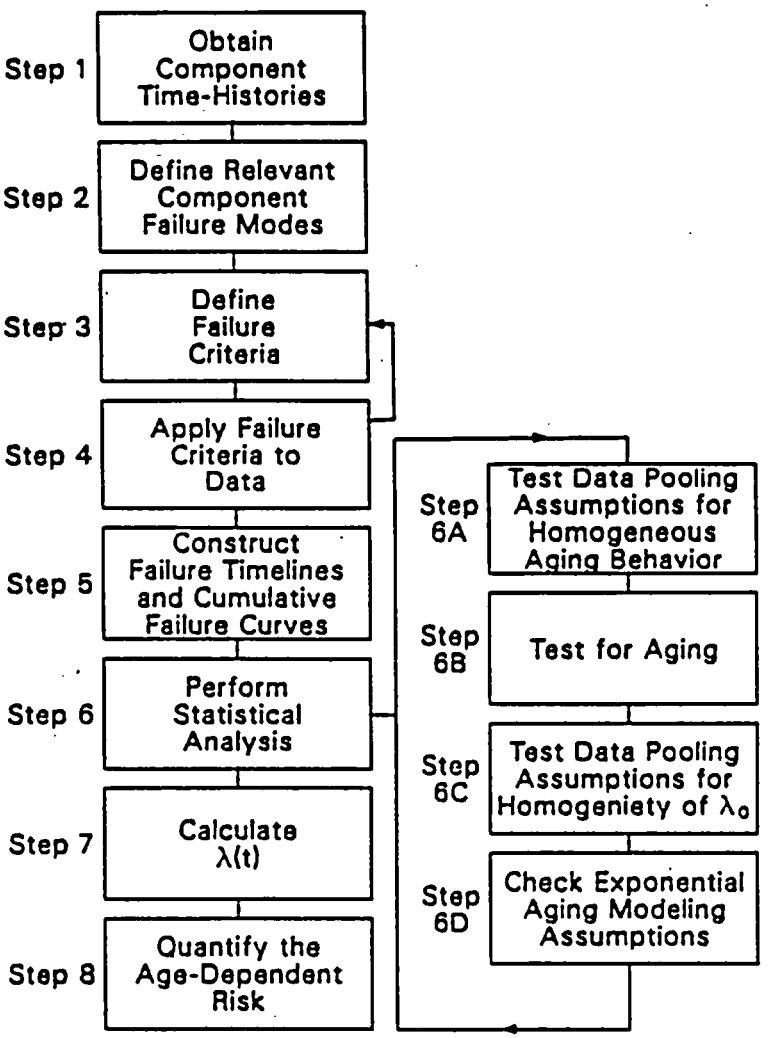

failure modes that were removed from consideration in a PRA at an early stage due to their low contribution to risk (e.g. removed from the cut sets by truncation). These failure modes may become more important, potentially even controlling, later in system life. A list of the seventeen failure modes obtained from a NUREG 1150 PRA study for a PWR[2] and adapted to the system from which the maintenance records were obtained is shown in Table 1. Adequate data to support development of component time-histories for the two testing and maintenance failure modes was not available from the maintenance records, therefore these two modes were not quantified even though they may be an important contributor to the age-dependent risk increase associated with the operation of the AFW system.

Step 3 - Define Failure Criteria

The determination of whether a particular record from the information gathered in step one describes the occurrence of one of the failure modes listed in step two is often subjective. This is because the information in the records was not designed for the development of failure tracking, therefore the information is imprecise as to the exact condition of the component. In order to reduce this subjectivity and to facilitate a more repeatable development of failure time-histories, two sets of failure criteria for each failure mode are developed.

The first set of criteria are developed for what is called a BROAD definition of failure. The criteria consist of a list of those conditions which are considered to possibly describe a failure, but which may only describe a problem which was fixed before it was actually necessary to remove the component from service. An example would be as follows:

> Steam Driven Pumps - A failure record is considered to describe a BROAD failure if it states one of the following:
> 1. That conditions existed that led to a bearing repair or replacement,
> 2. That conditions existed that led to the repair of the trip/governor valve,
> 3. That conditions existed that led to the repair of the pump for some unspecified reason.

This last case is very broad, and is a catchall for those records that state that repairs have occurred, but that give no clue as to why the repairs took place. Records that are removed from consideration as failures by the broad definition include those due to preventive maintenance programs, design changes, functionally unimportant boundary leaks, gauge replacements, and minor deficiency repair.

The second set of criteria are developed for what is called a NARROW definition of failure. The criteria consist of a list of those conditions which are considered to describe the actual occurrence of a failure. These failures either resulted in an automatic loss of component function or the immediate manual removal of the component from service to avoid damage. An example would be as follows:

TABLE 1 AUXILIARY FEEDWATER SYSTEM COMPONENT FAILURE MODES, DESCRIPTIONS AND RELEVANT FIGURE 1 COMPONENT NUMBERS

Failure Mode	Description
AFW-ACT-FA-PMP*	No actuation signal to pump. * MDP-A,B
AFW-ACT-FA-*	No actuation signal to steam supply valve. * AOV-A,B
AFW-AOV-LF-*	Loss of flow through steam supply valve. * AOV-A,B
AFW-CKV-FT-CV*	Check valve fails to open. * 3" - CV-H,I,J 4" - CV-B,C 6" - CV-A,D,E,F,G Main Steam: 3" - CV-K,L,M
AFW-CKV-OO-CV*	Backflow through pump discharge check valve.* CV-A,B,C
AFW-MOV-PG-*	Motor operated valve plugged. * MOV-A,B,C,D,E,F
AFW-PMP-LK-STMBD-*	UNDETECTED, simultaneous leakage through one of the following combinations of check valves: At least one of CV-H,I,J PLUS Either CV-D & F or CV-E & G PLUS CV-A for *TDP or CB-B FOR *MDP-A CV-B or CV-C for *MDP-B.
AFW-PMP-FR-*	Pump fails to run. * TDP, MDP-A,B
AFW-PMP-FS-*	Pump fails to start. * TDP, MDP-A,B
AFW-PMP-TM-*	Pump unavailable due to testing or maintenance. * TDP, MDP-A,B
AFW-PSF-FC-XCONN	Flow diversion to opposite unit through motor operated valves. * MOV-G,H,I,J
AFW-PSF-LF-*	Faults in pipe segments. * Various pipe segments.
AFW-TNK-VF-CST	Insufficient water available from 110,000 gallon condensate storage tank.
AFW-XVM-PG-XV*	Manual valve plugged. * Various manual valves.
AFW-*-TM-*	Component unavailable due to testing or maintenance. * Any AFW component in testing or maintenance when it is required to be in service.
ACP-TAC-LP-BUS*	AC power not available. * 1A,1B
DCP-TAC-LP-BUS*	DC power not available. * 1A,1B

Steam Driven Pumps - A failure record is considered to describe a NARROW failure if it states one of the following:

1. That a pump trip occurred,
2. That a gross loss of lubrication occurred,
3. That erratic control by the trip/governor valve occurred.

The narrow failures are a subset of the broad failures. The use of the broad and narrow definitions of failure enables a risk quantification to be done using data describing failures which certainly took place, without the masking effect caused by information in which less confidence is placed. At the same time, the quantification of a combination of the actual and possible failures enables the identification of risk trends which should be further investigated to check their validity. The setting of these criteria is not simple and may involve some iteration with their application as described in step four.

Step 4 - Apply the Failure Criteria to the Component Time-Histories

The component time-histories are reviewed in step four to identify all potential and actual failures. Update of the failure criteria defined in step three is performed, as necessary, to incorporate knowledge gained by the in-depth review of the data.

Table 2 shows an example of the application of the failure criteria listed in step three to a portion of the Maintenance Records for the Turbine Driven Pumps. Only the descriptive fields that were useful in determining whether a failure had occurred are shown: "Problem Description" and "History Summary."

Step 5 - Construct Failure Timelines

It is useful to construct graphical representations of the data at this point, before continuing with any statistical analysis. This provides a "feel" for the data and some simple trends can be immediately identified. However, it is difficult to determine without statistical analysis of the data whether the apparent trends are statistically significant. An example of a failure timeline is shown in Figure 3.

Step 6 - Perform Statistical Analysis

The next step is to model the age-dependent behavior of the components for which time-histories have been developed and to estimate model parameters from the data. The model chosen to describe the data is of an exponential form which is referred to in this paper as the exponential failure rate.

$$\lambda(t) = \lambda_0 e^{\beta t}$$

Having chosen the model, statistical techniques are applied to make inference about the aging rate β, the initial failure rate λ_0, and the rate of failure $\lambda(t)$. The method follows work of Cox an Lewis[3]. Some of the details of the development of the equations are presented in a Technical Report on a survey of various data sources to develop failure rates[4]. The full details will be presented in two reports now in preparation[5,6]. In this paper, the general concepts are stated, but the specific equations are not presented.

TABLE 2 EXAMPLE OF MAINTENANCE RECORDS BEFORE SCREENING

PROBLEM DESCRIPTION	HISTORY SUMMARY	FAILURE CLASSIFICATION
GROSS OIL-LOW DISCHARGE PRESSURE	RENEWED THRUST BEARING LININGS	NARROW
EXCESSIVE DISCHARGE PREE-PT15	REDUCED SPEED OF PUMP AT GOVERNOR	BROAD
BODY TO BONNET LEAK	RENEWED BONNET GASKET	------
GOV VALVE WILL NOT CONTROL PUMP SPEED	FIXED SATISFACTORY	NARROW
REFUEL BUMS	DID BUMS CHECKS	------
VARIOUS REPAIRS	REPAIRED AND TESTED GOV TRIP VALVE	BROAD
DRAIN, CLEAN, INSPECT SUMP REFILL	DRAINED OIL, CLEANED SUMP	------
SIGHT GLASS HAS OIL LEAK	TIGHTENED SIGHT GLASS	------
REPLACE GAUGE AND REPAIR LEAK	REPLACED GAUGE	------
OIL LEAK ON PUMP	REPAIRED PUMP AND HELD PM CHECK	BROAD
BUMS AS PER MMP-P-FW-004	VOID	------
OUTBOARD PUMP BEARING THROWING OIL	RENEWED THRUST BEARING	BROAD
OIL SEAL PACKING LEAK	RENEWED THRUST SHOE	BROAD
OVERSPEED TRIP VALVE TRIPS	STRAIGHTENED LINKAGE	NARROW

FIGURE 3 FAILURE TIMELINE FOR THE TURBINE DRIVEN PUMPS.

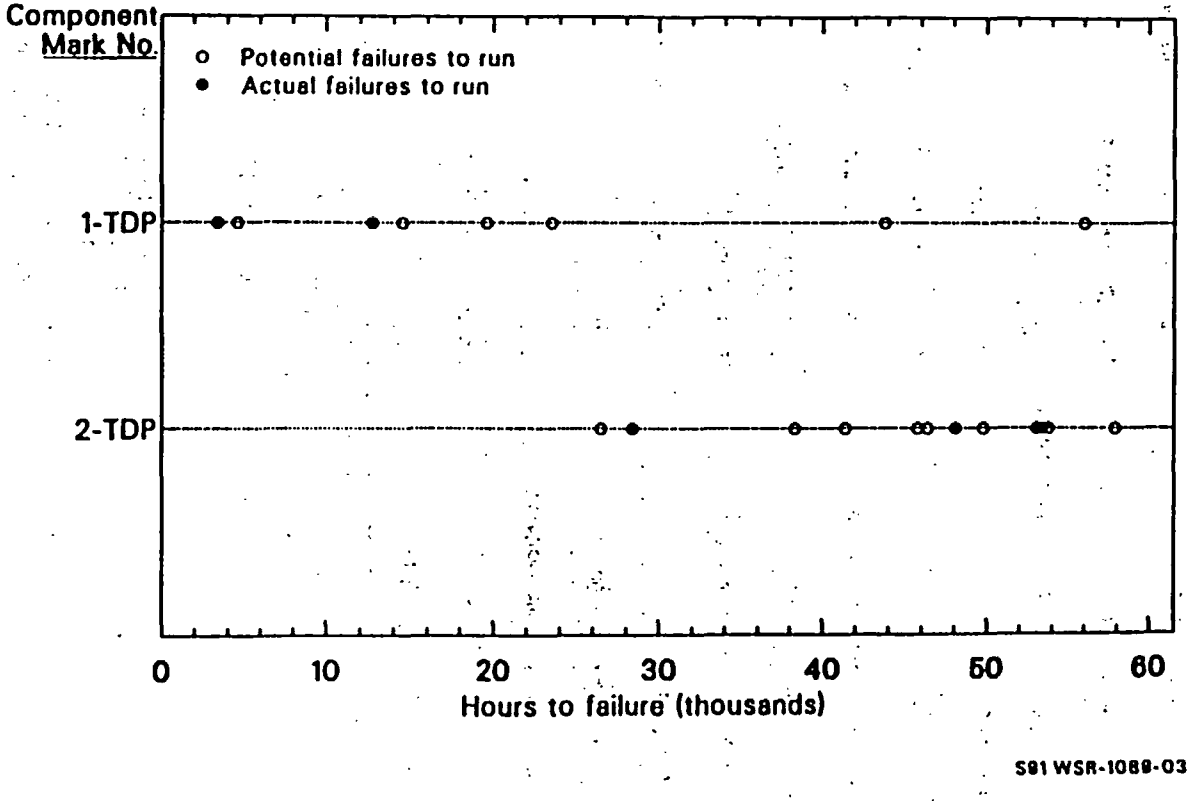

1-FW-P-3A

The input for the broad and narrow definitions of failure are placed in an appropriate format for computer code manipulation and then the following assumptions are checked:

Similar components have a common aging rate and therefore can be pooled for analysis (β is the same for all members of the group),

The aging rate associated with a group of components is zero ($\beta = 0$),

Similar components, having a common aging rates, also have a common initial failure rate and therefore can be pooled for analysis (λ_0 is the same for all members of the group),

And finally, the aging model chosen (exponential) adequately describes the data.

Step 6A - Test Data Pooling Assumptions for Homogeneous Aging Behavior

The assumption that similar components have the same aging rate, β, is the first to be checked. The null hypothesis can be stated as: For a group of N components, $\beta_1 = \beta_2 = \ldots = \beta_N$. The test statistic is based on the difference between the maximum likelihood estimator of β for an individual component and the maximum likelihood estimator for the rest of the components taken as a group. The overall significance level is based on the Bonferroni inequality and rejected at 0.05 or less. If the pooling assumption is rejected, outliers are identified. A decision to delete an outlier should be based on an understanding of the physical process which resulted in the observed anomalous behavior.

A graphical presentation of the results of the evaluation is made to allow for a visual understanding of the test. The example graph in Figure 4 shows the maximum likelihood estimator for the aging rate β, and the associated 95% confidence interval for each component that indicated failure. Qualitative analysis can be made by checking the estimators and intervals to see if they overlap in a reasonable fashion. Also plotted for each component is the maximum likelihood estimator of the value of β for all the OTHER components taken as a group. The spread between the individual and group estimators is used to develop the statistic for checking the assumption of homogeneous value of β.

Figure 4 represents a case where the hypothesis was accepted. Visually, the graph demonstrates that the confidence intervals all overlap and in this case all individual estimates of β lie within the individual confidence intervals of all the other components. Qualitatively, the pooling of the data for analysis appears acceptable. The quantitative test indicates a significance level of 1.00. This statistically supports the conclusion that the grouping is reasonable.

The results of this statistical test are shown in Tables 3 and 4 for each of the 14 groups of data developed from the AFW System Maintenance Records. Only one of the fourteen groups, the narrow Turbine Driven Pump fails to run, resulted in rejection of the constant failure rate hypothesis. In the absence of further data on the Turbine Driven Pump, the record was split for further analysis, thus a total of 15 groups of data were formed.

FIGURE 4 COMPONENT COMPARISONS FOR β FOR PUMP DISCHARGE CHECK VALVES. HYPOTHESIS OF SIMILAR β ACCEPTED: COMPONENT DATA CAN BE POOLED.

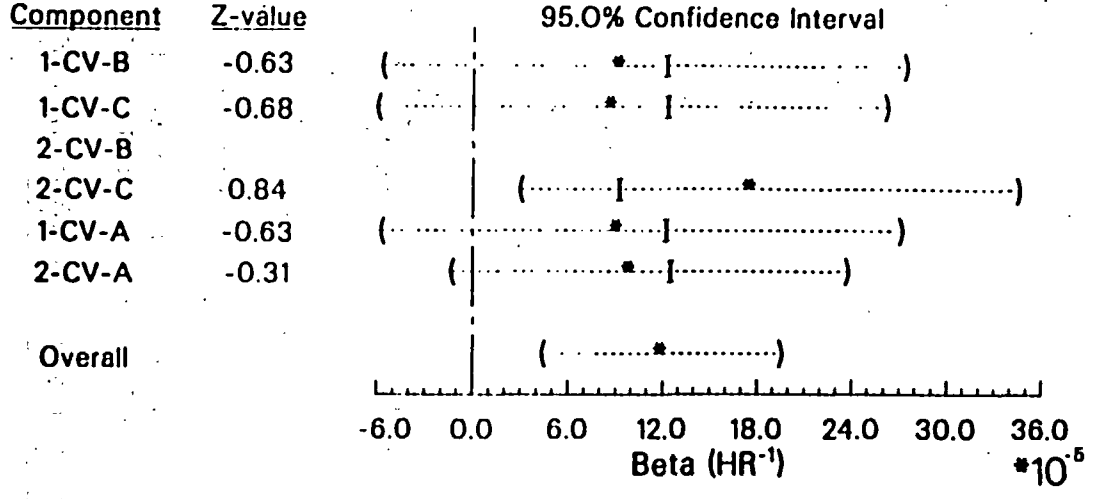

Significance level for testing equality of betas = 1.00

(- Lower bound
) - Upper bound
• - Maximum likelihood estimate for only the associated component
I - Maximum likelihood estimate for all but the associated component

S91 WSR-1089-05

TABLE 3 RESULTS OF STATISTICAL ANALYSIS FOR THE BROAD FAILURE CASES

FAILURE MODE	SIGNIFICANCE LEVEL FOR TESTING EQUALITY OF β[a]	SIGNIFICANCE LEVEL FOR TESTING $\beta = 0$[b]	SIGNIFICANCE LEVEL FOR TESTING EQUALITY OF λ_0[a]	CONCLUSION
AFW-PMP-FR-TDP	0.006	0.09[d]	----[e]	NOT HOMOGENEOUS
AFW-PMP-FR-TDP (unit 1 only)	N/A[c]	0.91	----[e]	NOT AGING, SINGLE COMPONENT
AFW-PMP-FR-TDP (unit 2 only)	N/A[c]	0.002	N/A[c]	AGING, SINGLE COMPONENT
AFW-PMP-FS-MDP	0.67	0.46	----[e]	NOT AGING, HOMOGENEOUS
AFW-PMP-FR-MDP	0.31	0.13	----[e]	NOT AGING, HOMOGENEOUS
AFW-MOV-PG	1.00	0.06	----[e]	NOT AGING, HOMOGENEOUS
AFW-MOV-FC	1.00	0.60	----[e]	NOT AGING, HOMOGENEOUS
AFW-PMP-STMBD	0.71	0.03	1.00	AGING, HOMOGENEOUS
AFW-CKV-00	1.00	0.0001	0.66	AGING, HOMOGENEOUS

a. A value of 0.05 or less indicates strong evidence that the components do not have the same aging rate, β, or the same initial failure rate, λ_0.

b. A value of 0.05 or less indicates strong evidence that the components failures were not generated by a constant failure rate process.

c. Equality comparisons can not be made for a single component.

d. Without separation of components based on rejection of test for homogeneous β, the Turbine Driven Pumps would show no statistically significant aging trend.

e. Not checked, because aging was not statistically significant.

TABLE 4 RESULTS OF STATISTICAL ANALYSIS FOR THE NARROW FAILURE CASES

FAILURE MODE	SIGNIFICANCE LEVEL FOR TESTING EQUALITY OF β[a]	SIGNIFICANCE LEVEL FOR TESTING $\beta = 0$[b]	SIGNIFICANCE LEVEL FOR TESTING EQUALITY OF λ_0[a]	CONCLUSION
AFW-PMP-FR-TDP	0.13	0.80	----[c]	NOT AGING, HOMOGENEOUS
AFW-PMP-FS-MDP	0.11	0.10	----[c]	NOT AGING, HOMOGENEOUS
AFW-PMP-FR-MDP	0.69	0.30	----[c]	NOT AGING, HOMOGENEOUS
AFW-MOV-PG	1.00	0.23	----[c]	NOT AGING, HOMOGENEOUS
AFW-MOV-FC	0.32	0.68	----[c]	NOT AGING, HOMOGENEOUS
AFW-PMP-STMBD	0.71	0.03	1.00	AGING, HOMOGENEOUS
AFW-CKV-00	----[d]	----	----[c]	NO DATA

a. A value of 0.05 or less indicates strong evidence that the components to not have the same aging rate, β, or the same initial failure rate, λ_0.

b. A value of 0.05 or less indicates strong evidence that the components failures were not generated by a constant failure rate process.

c. Not checked, because aging was not statistically significant.

d. No actual failures for this mode.

Step 6B - Test For Statistically Significant Aging

The next assumption checked is that the data were actually created by an age-independent process, i.e., the failure rate is constant and the aging rate is zero. The null hypothesis can be stated as: For a group of N components, $\beta_1 = \beta_2 = \ldots = \beta_N = 0$. The test statistic is applicable regardless of the form of the age-dependent failure rate and is a measure of the variation between the average of the failure times and the center of the observation period. This concept is represented in Figure 5. The top case represents a component that exhibits increasing time between failures, the middle a noncommittal component, and the bottom an aging component. For the purposes of this study, if the significance level was less than 0.05, and therefore the hypothesis of constant failure rate must be rejected, then the component shows statistically significant aging. The test is one-sided, testing $\beta = 0$ against the alternative $\beta > 0$.

In the application of this test to the 15 groups of data developed from the AFW System Maintenance Records, only four were found to show statistically significant aging. The results are displayed in Tables 3 and 4. It is interesting to note that if the first assumption had not been checked and therefore the turbine driven pumps had remained grouped, then the pump group would have demonstrated no aging. With the separation of the two pumps, based on the rejection of the homogeneous beta assumption, one of the pumps is found to be aging and the other not.

Step 6C - Test Data Pooling Assumptions for Homogeneity of λ_0

The adequacy of the assumption that the initial failure rate, λ_0, for similar components is equal is checked for all component groupings showing significant aging. The null hypothesis can be stated as: For a group of N components, $\lambda_{01} = \lambda_{02} = \ldots = \lambda_{0N}$. The test statistic is developed in an analogous fashion to that for the testing of homogeneity of β. The graphical presentation is also analogous and an example is not given. The hypothesis was accepted for the four component groupings considered to be aging as indicated in Tables 3 and 4.

Step 6D - Check the Exponential Aging Modeling Assumption

Most age-dependent failure rate models have one common feature: when the time becomes large, the models predict physical large failure rates. The exponential form used in this methodology is certainly prone to this problem. However, this is not serious if the data are adequately described over the time period of collection and if the results are not extrapolated far into the future. The problem of extrapolation is avoided by only predicting risk a few years past the date of data collection. The problem of adequate description of the data by the model is checked in this step by development of a statistic which measures the spread between the time when the various failures actually occurred and the time when they would be expected to occur based on the model and estimated parameters. The Kolmogorov-Smirnov test is used to test the hypothesis: The failure times were generated by a Poisson process with an exponential failure rate and the parameter values as estimated.

FIGURE 5 TESTING THE PROCESS FOR STATISTICALLY SIGNIFICANT AGING.

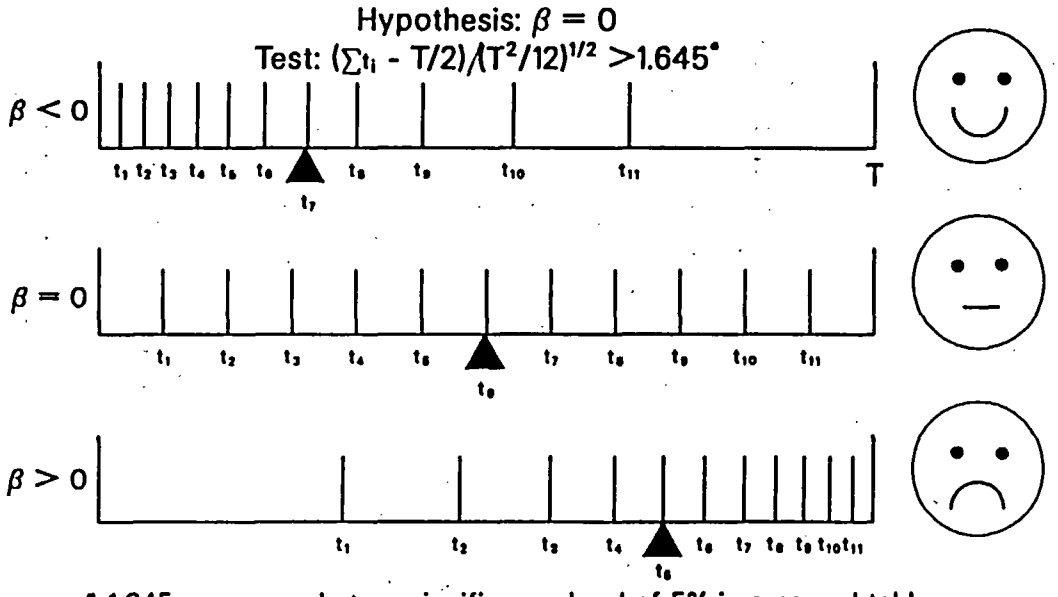

* 1.645 corresponds to a significance level of 5% in a normal table

S152 AJW-0190-08

Once again, a graphical presentation is made to allow for qualitative understanding of the statistical test results. The presentation is known as a Quantile-Quantile (QQ) plot (Figure 6). Plotted on the X-axis are the actual failure occurrence times and plotted on the Y-axis are the calculated expected occurrence times. Since the axis scales are identical, the intersection of the first failure, the second failure, etc., should show no marked divergence from the 45 degree line if the model is adequate. If the overall plot shows a marked divergence from the 45 degree line, such as a large "S" shape so that the intersections are much lower in one half of the plot and much higher in another, then the exponential aging model would be considered inadequate to describe the data. A fairly good fit is shown in Figure 6. The results of the statistical test for the four groups of data considered to be aging indicated acceptance of the hypothesis that the exponential model adequately described the data.

Step 7 - Calculate $\lambda(t)$

For all sets of components that survive the screening of step six, the estimated value of $\lambda(t)$ and its associated confidence interval are calculated as a function of time. The maximum likelihood estimator of the failure rate is calculated at any desired time using the maximum likelihood estimators of aging rate and initial failure rate. Standard statistical analysis techniques are used to make joint inference to develop the confidence interval at each time.

Step 8 - Quantify the Age-Dependent Risk

The final step of the methodology is to calculate the risk incurred by the plant as a function of time, using the results from above as age-dependent basic-event input to a PRA. The methods for use of PRAs are somewhat plant specific and the details of the quantification are not presented here. The basic approach is to convert the $\lambda(t)$ and confidence interval for each component into the necessary parameters which describe the distribution for each associated basic event. This will be very simple for risk analysis tools which use failure rate and distribution as the basic event input. It is somewhat more complicated for risk analysis tools which use unreliability and unavailability for the basic event input, but methodology for conversion of distributions can be developed. In this study,

- Only AFW system data are used to develop time-dependent inputs to the PRA. Inputs for all other systems remained at the original time-averaged values used in the PRA, and

- Only those AFW system components showing statistically significant trends were used as time-dependent inputs. All other AFW inputs remained at the original time-averaged values used in the PRA.

FIGURE 6 QUANTILE-QUANTILE PLOT FOR THE TURBINE DRIVEN PUMP EXHIBITING STATISTICALLY SIGNIFICANT AGING.

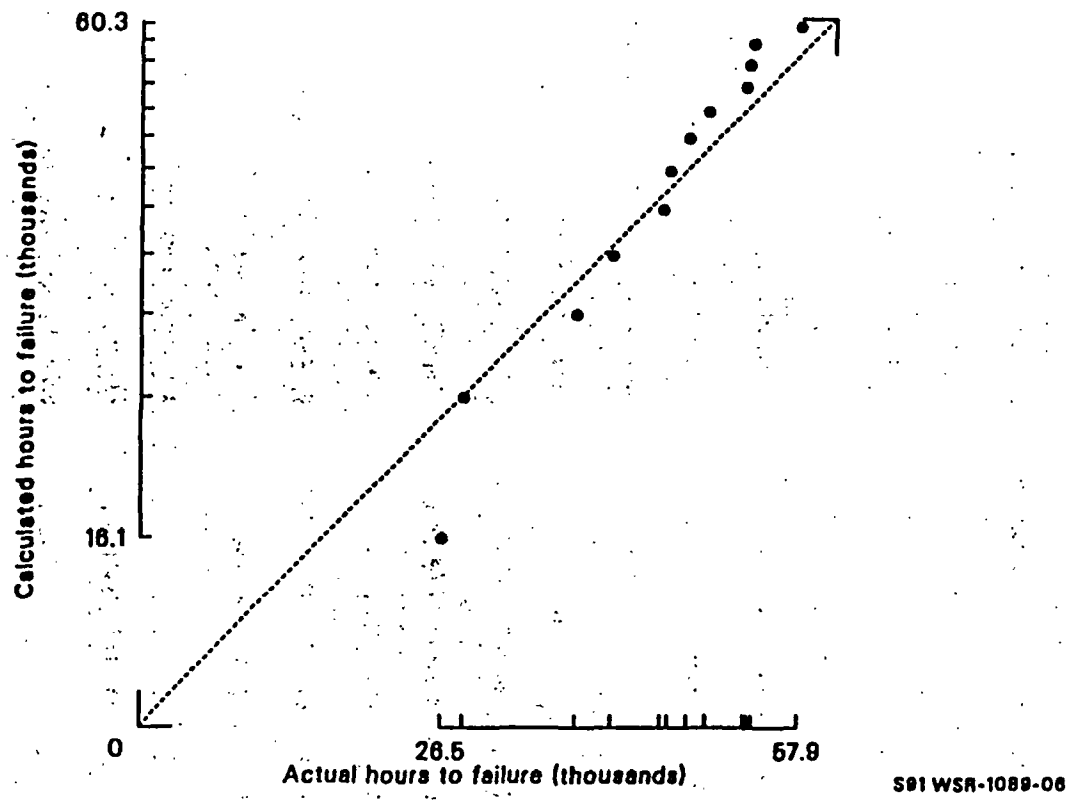

The results for the single time dependent event for the narrow failure case and for the three age-dependent events for the broad failure case are shown in Figures 7 and 8, respectively. A NUREG 1150 PRA was used with necessary modifications to reflect the source of the component failure rate information. The resulting risk is represented as core damage frequency plotted as a function of time. The first time plotted is representative of the end of the data collection period and is the twelfth year of plant operation. The data is extrapolated to fifteen years, and while the risk at fifteen years is not expected to equal the value shown, the indicated trends are useful for making decisions. The base line in each figure represents the risk calculated at time zero, using the initial failure rate for the components which are showing time dependent aging and the time-averaged failure rates for the balance. The initial risk is slightly less in the broad failure case because the initial age-dependent failure rates are less than the time-averaged failure rates. This is as would be expected if the time averages are correct.

In the narrow case (Figure 7), the risk has not increased at the "present" time (year 12). The trend for the future indicates that the maintenance program continues to be successful with only a slight risk increase due to steam binding of the pumps. Based on this information, an engineer might recommend that no action be taken at present to change the plants maintenance procedures and that another risk calculation to check the steam binding trend and to look for developing trends be performed in a year.

In the broad failure case (Figure 8), the risk has tripled at the "present" time and the trends are for rapid increase in the near future. Once again a rather minor effect is seen at the end of the period for the steam binding failure mode, however, two new failure modes are seen in the broad case, and they have a noticeable effect on risk. The dominant mode is that of pump discharge check valves failing to shut. This failure, in combination with the failure of the associated pump results in the recirculation of all flow backwards through the idle pump, and therefore a complete failure of the system if no recovery action is taken by the operator. (Note that the risk values calculated DO NOT include recovery). The trend is for near term increases in this effect. The other failure mode seen is the failure of the Turbine Driven Pump to run. This mode has caused a doubling of the initial failure rate at the "present" time. The trend for this mode is fairly flat, indicating that the turbine-driven pump failure to run is so high that the unreliability is nearly one, i.e., the pump is sure to fail sometime during its mission. Note that this is not an artifact of the model, it is a reflection of the high unreliability of the pump at the "present" time.

Since the second plot of risk is based on a broad definition of failure, it is also one in which an engineer would have less confidence. As opposed to immediately taking action to adjust the maintenance and testing programs associated with the pump discharge check valves and the Turbine Driven Pump, the engineer might recommend a more thorough evaluation of the failure data for these two components to develop higher confidence in a set of data on which to repeat the statistical analysis. The results would then be combined

FIGURE 7 NEAR TERM PREDICTION: CORE DAMAGE FREQUENCY SHOWING CONTRIBUTION OF AGE-DEPENDENT EVENTS, NARROW DEFINITION OF FAILURE.

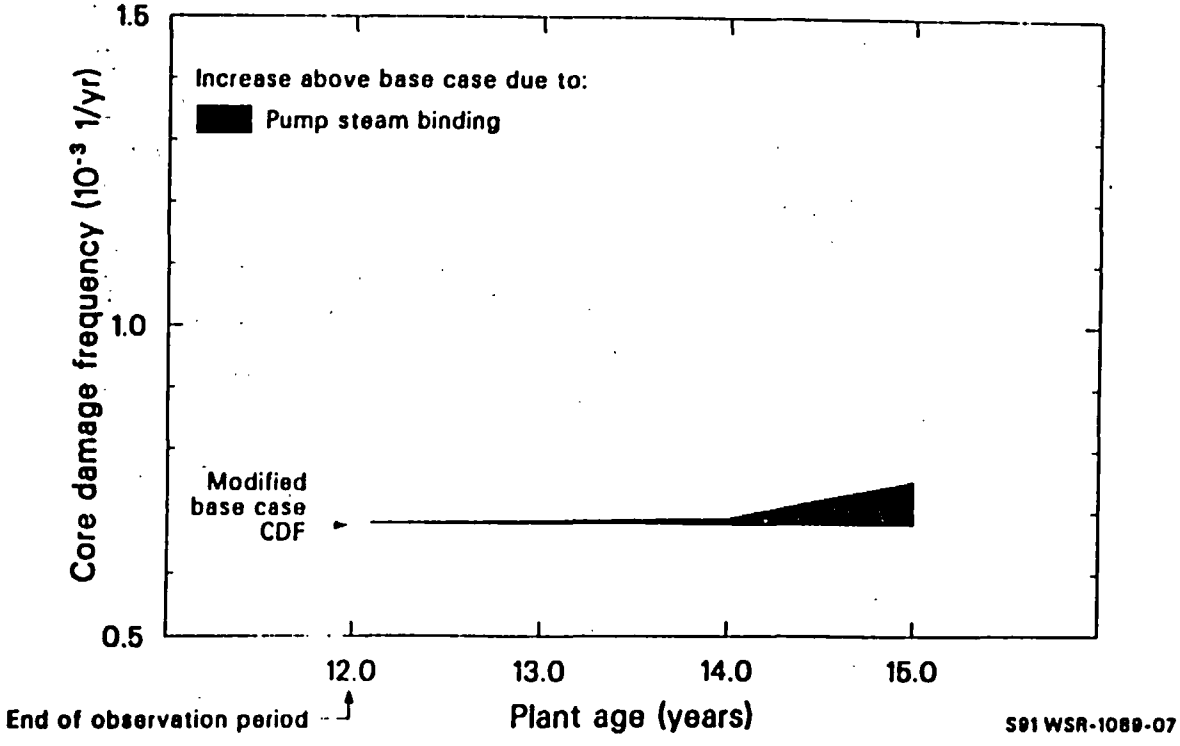

FIGURE 8 NEAR TERM PREDICTION: CORE DAMAGE FREQUENCY SHOWING CONTRIBUTION OF AGE-DEPENDENT EVENTS, BROAD DEFINITION OF FAILURE.

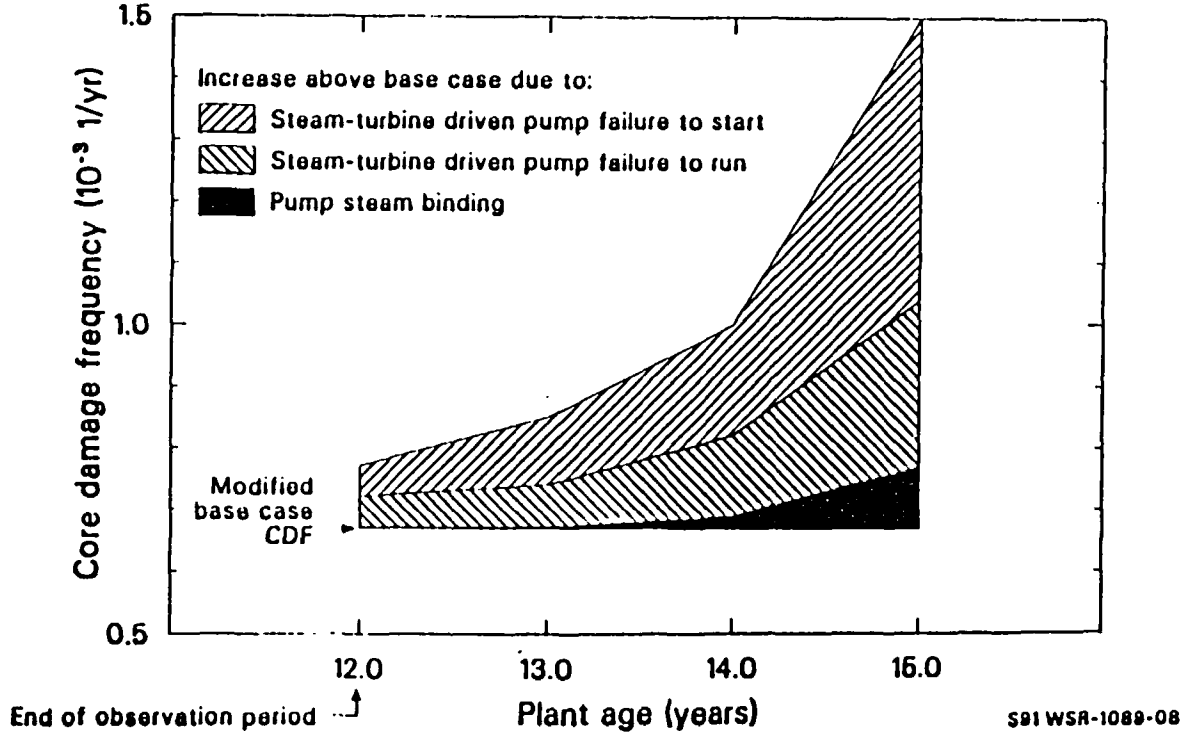

with the age-dependent components identified by the narrow definition of failure, in this case the pump steam binding, and the risk recalculated. The engineer's search for more information might result in identification of only one or two failures out of the original ten potential failures being considered as actual, with the others defined as non-failures. The resulting analysis might well show no aging trend. On the other hand, the failures may be found to be a safety concern and action would then be warranted to arrest the trend. In this case, another analysis might be performed in six months to check the results of the actions taken to control the risk.

CONCLUSIONS

The following conclusions can be made based on the development and application of the methodology:

The methodology for the age-dependent quantification of risk provides current age-dependent risk and near-term trends that can be used to check the ability of plant maintenance and testing programs to control risk at an acceptable level. The results cannot be used to predict far future risk because of the great difficulty in accounting for possible human intervention and corrective action.

The data must be developed carefully to avoid inclusion of events that are not actually failures. Such inclusions may either mask actual risk trends of concern or identify trends that are not of concern.

The former is clearly a safety concern, while the latter may result in a safety concern due to the inappropriate use of limited resources. Additionally, the data must be developed carefully to avoid exclusion of events that might be failures. Such exclusion can result in the failure to identify trends. A narrow and broad set of failure time-histories may be developed to accomplish these two tasks simultaneously.

The assumptions made in pooling components and applying models must be statistically checked to avoid problems similar to those which arise from poor data development.

The methodology described provides features for both the careful development and statistical analysis of data used to quantify age-dependent risk.

REFERENCES

1. Ghahramani, 1989 "PRA Data Base Development: An Integrated Approach," Proceedings of the International Topical Meeting on Probability, Reliability and Safety Assessment, Volume 2, April 2-7, Pittsburgh, Pennsylvania. p. 882.

2. R. C. Bertucio et al., 1988, Analysis of Core Damage Frequency from Internal Events: Surry Unit 1, Draft, NUREG/CR-4550 Rev. 1, Vol. 3, Part 1.

3. D. R. Cox and P. A. W. Lewis, 1966, The Statistical Analysis of Series of Events, London: Chapman and Hall (US distributor: Halsted Press).

4. A. J. Wolford et al., 1989, A Survey of the Nuclear Plant Reliability Data System and Licensee Event Reports to Determine Linear Failure Rates, EGG-SSRE-8603.

5. A. J. Wolford et al., in preparation, Aging Risk Assessment Methodology: Demonstration Study on a PWR Auxiliary Feedwater System, NUREG/CR-5378.

6. C. L. Atwood, in preparation, Estimating Hazard Functions for Repairable Components.

SAND89-1755C[1]

Loss-of-Coolant Accident (LOCA) Testing of Aged Cables for Nuclear Plant Life Extension

Mark J. Jacobus
Sandia National Laboratories
P. O. Box 5800
Albuquerque, NM 87185

ABSTRACT

Sandia National Laboratories is conducting long-term aging research on representative samples of nuclear power plant Class 1E cables. The objectives of this program are to determine the suitability of these cables for extended life (beyond 40-year design basis) and to assess various cable condition monitoring (CM) techniques for predicting remaining cable life. Twelve different cable products have been aged for long times at relatively mild exposure conditions in three test chambers to nominal equivalent lifetimes of 20, 40, and 60 years. Following the aging process, the cables in each chamber were exposed to a sequential accident profile consisting of 110 Mrad of high dose rate gamma irradiation followed by a simulated design basis loss-of-coolant accident (LOCA) steam exposure (except the 20-year chamber, which has not yet been LOCA tested). This paper discusses the results of the LOCA testing on the cables aged to 60 years. Although some of the cables experienced electrical failures, the results of these tests indicate a good life extension potential for a number of popular cable products.

1.0 INTRODUCTION AND OBJECTIVES

The primary purposes of this test program are to assess the effectiveness of various cable CM techniques for predicting how cables will perform in an accident environment and to gain an indication of whether cable life extension beyond 40 years is practical. To accomplish these objectives, we have conducted simultaneous radiation and thermal aging on three test chambers to equivalent nominal lifetimes of 20, 40, and 60 years. After aging, a sequential accident exposure consisting of high dose rate radiation followed by a steam exposure has been completed on the 40- and 60-year test chambers. Data obtained from CM techniques employed during aging will be correlated with observed performance of cables during the LOCA. This paper only discusses the results of the LOCA testing on the cables aged to 60 years.

---

1 The Long-Term Cable Aging Program is supported by the United States Nuclear Regulatory Commission and performed at Sandia National Laboratories, which is operated for the U.S. Department of Energy under contract number DE-AC04-76DP00789.

2.0 EXPERIMENTAL ARRANGEMENT

The testing is being performed in two phases: a long-term simultaneous thermal and radiation aging phase followed by a sequential accident exposure consisting of high dose rate radiation followed by steam exposure. Twelve cable products, representative of nuclear plant usage, are included in our study.[1] Cable insulation materials include cross-linked polyethylene (XLPE), ethylene propylene rubber (EPR), polyimide, and silicone rubber (SR). Cable jacket materials include neoprene, chlorosulfonated polyethylene, and fiber glass braid. Three different sets of cable specimens are being tested: one set aged to a nominal lifetime of 20 years, a second to 40 years, and a third to 60 years. Actual simulated lifetimes will vary because of the different activation energies of the specimens. We chose artificial aging times of 3, 6, and 9 months. The aging temperature selected was based on an assumed plant ambient temperature of 55°C with no conductor heat rise. Based on the Arrhenius equation and an assumed activation energy of 1.15, the resulting aging temperature is 95°C. A nominal aging temperature of 100°C was selected for the aging exposure. The planned radiation aging dose was 1 Mrad/year of simulated life. The resulting (accelerated) dose rate for our test is 9 krads/hr. The actual exposure rate is about 10 krads/hr, substantially less than typically employed in industry qualifiaction tests. Additional details of the test program and the CM measurements employed may be found in Reference 1.

The accident tests consisted of irradiation followed by a simulated design basis LOCA steam exposure. The accident dose was 110 Mrads at a dose rate of 600 krad/hr. The accident profile was similar to that in IEEE 323-1974,[2] Appendix A for "generic" qualification, except that the accident exposure was accelerated to 10 days and no chemical spray was included. The accident profile included superheated steam conditions during the first 11 hours of the test, followed by saturated steam for the rest of the test. The actual temperature and pressure profiles from the accident test are shown in Figure 1 for the first 24 hours. The temperature and pressure remained constant from 24 hours until 245 hours, when they were gradually reduced to ambient conditions.

During the LOCA test, most of the conductors were energized to a nominal voltage of 110 Vdc through a 1 A fuse. All shields, as well as the few conductors that were not energized to 110 V, were connected to ground. Insulation resistances (IRs) of the powered cables were monitored automatically throughout the LOCA test at varying scan intervals. These intervals ranged from 10 seconds during the transient portions of the tests to 5 minutes during long steady portions. Measurements on every cable were also performed periodically at 50, 100, and 250 Vdc with an IR test apparatus that uses a Keithley electrometer. The IR test apparatus was designed and used for CM during aging.[1] In the figures that follow, the periodic measurements are shown along with the "continuous" measurements. Prior to testing, both measurement methods were verified using resistors of known value. Because of the design of the "continuous" system, its absolute upper range was 10^9 Ω. However, its accuracy degrades rapidly above about 3×10^8 Ω. By contrast, the electrometer measurements are accurate in the 10^{12} Ω region.

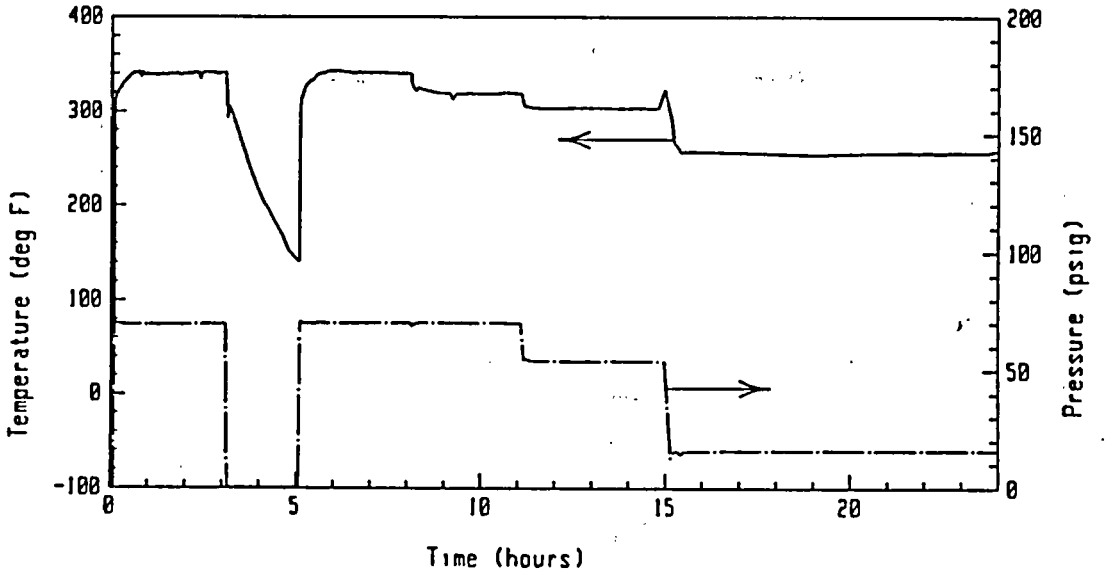

Figure 1 Accident Test Temperature and Pressure Profiles

3.0 EXPERIMENTAL DATA

This section presents some of the IR data from the LOCA tests on cables aged to 60 years. It should be remembered that the actual simulated lifetimes of the tested cables varies depending on the assumed plant ambient conditions and the actual activation energies of the materials of each cable product. All of the tested cables had an exposed cable length of about 15 feet in the test chamber.

3.1 Cross-Linked Polyethylene Insulated Cables

Figure 2 shows the results from Rockbestos 3-conductor irradiation XLPE cables. The figure shows the average of 3 samples (of 4 that were energized) whose fuses did not open throughout the 10 day test. Only the first 24 hours of the test are shown in Figure 2--the remainder of the plot would be above 10^7 Ω. Figure 3 shows the IR behavior of the remaining energized conductor. The fuse for this conductor opened at about 84 hours into the test. The IR degraded rapidly, going from greater than 10^7 ohms (consistent with the IRs for the other conductors) down to fuse opening within one hour. Based on the discrete IR measurements, the 2 Rockbestos conductors that were not energized continuously showed no evidence of failure. The reason for the one conductor failing has not yet been determined.

Figure 4 shows the average IR behavior of 2 conductors of a Brand Rex 3-conductor cable. The IR remained well above 10^6 Ω throughout the test and was above 10^8 Ω for the part of the test that is not shown. The only other XLPE cable included in the test program, Raychem Flamtrol single conductors, maintained IRs above 10^7 Ω throughout the test.

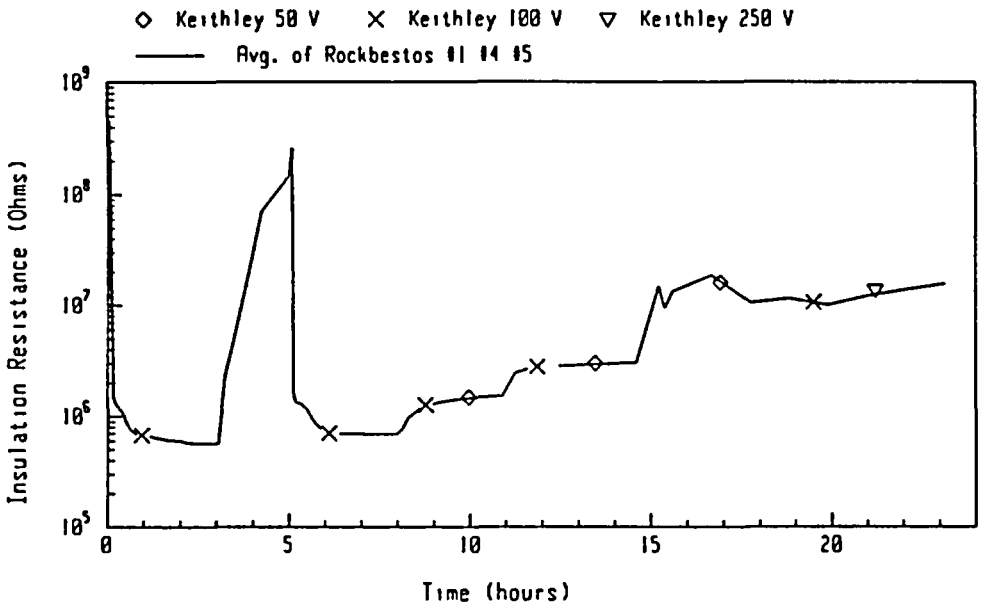

Figure 2 Performance of 3 Rockbestos XLPE Multiconductors

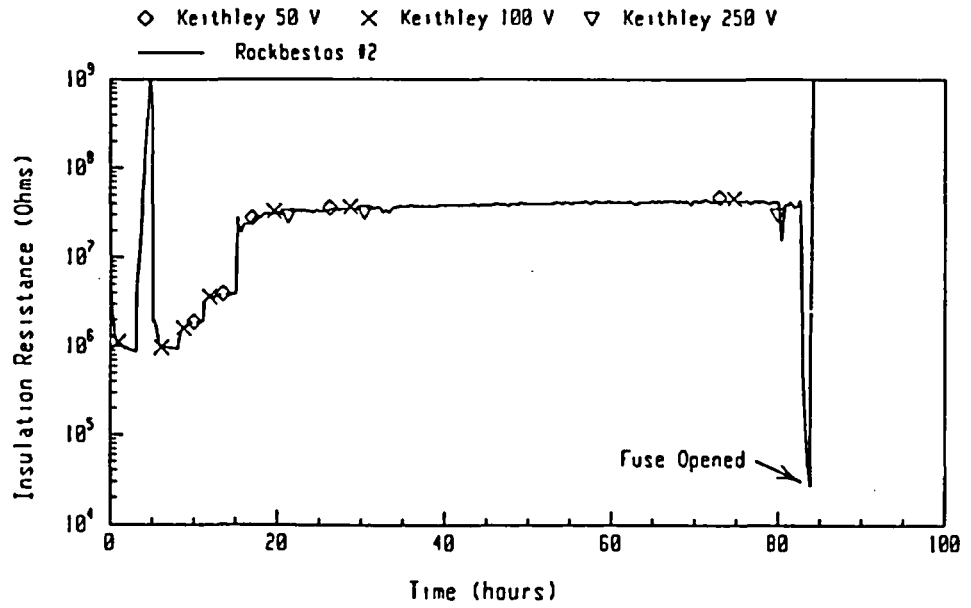

Figure 3 Performance of 1 Rockbestos XLPE Multiconductor That Failed

3.2 Ethylene Propylene Rubber Insulated Cables

Figure 5 shows the behavior of Anaconda FR-EP single (from disassembly of a multiconductor cable) and multiconductor cables during the first 24 hours of the accident test. The IRs were well above 10^5 Ω throughout the test. The single conductor had consistently higher IR than the multiconductors, typically by a factor of 4-10.

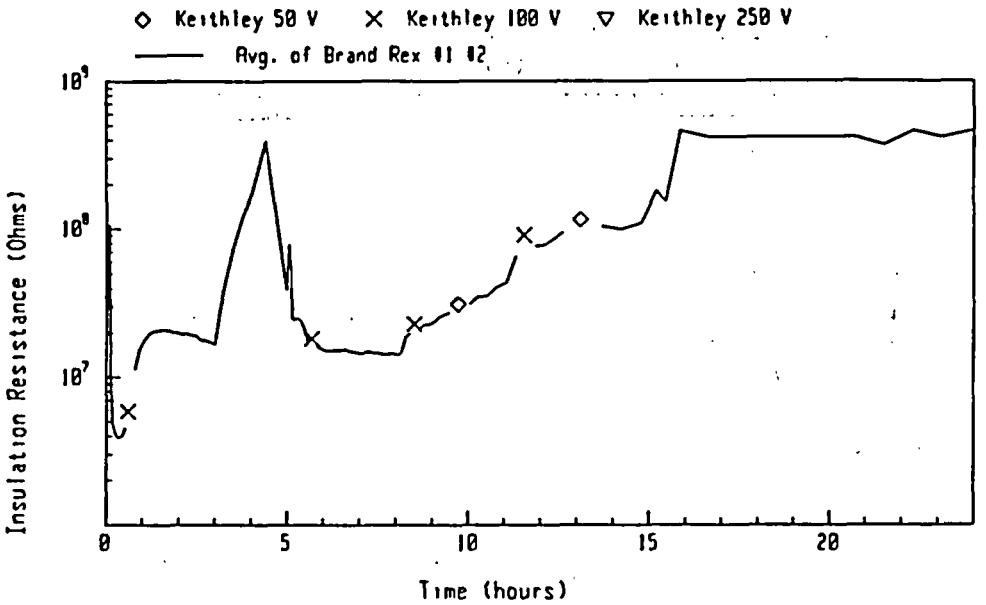

Figure 4 Performance of 2 Brand Rex XLPE Multiconductors

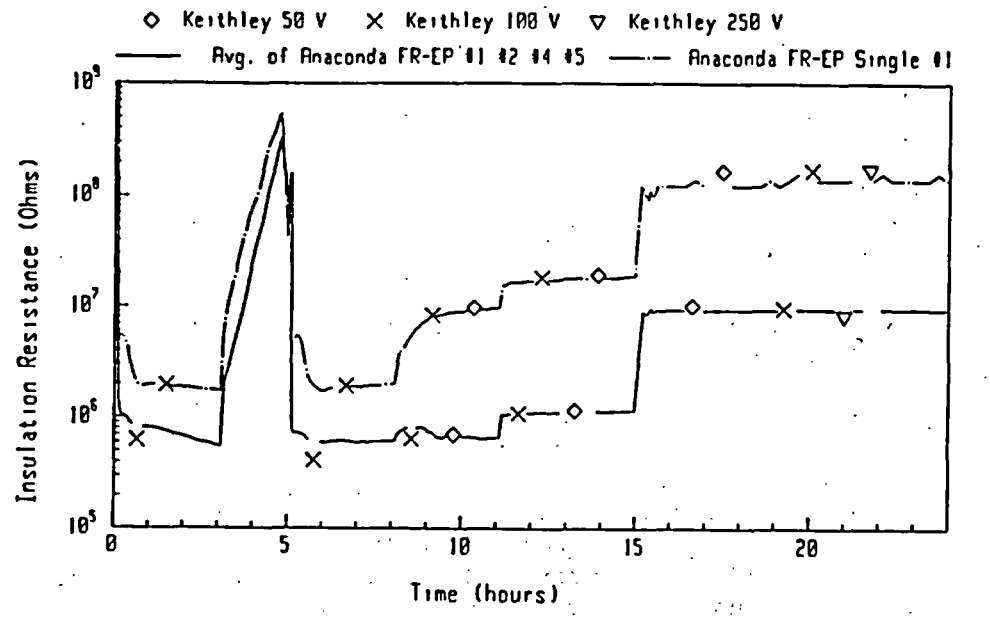

Figure 5 Performance of Anaconda FR-EP Single and Multiconductors

Figure 6 compares the behavior of BIW Bostrad 7E single conductors (removed from multiconductor cables) with multiconductor cables during the first 24 hours of the accident test. The IR of the multiconductors fell as low as 3.6×10^4 Ω during the most severe part of the accident exposure, while the single conductors remained above 10^5 Ω. The single conductors had IRs 2-6 times higher than the multiconductors. The minimum IRs of the multiconductors are in the range where the accuracy of certain sensitive instrumentation circuits could be affected.

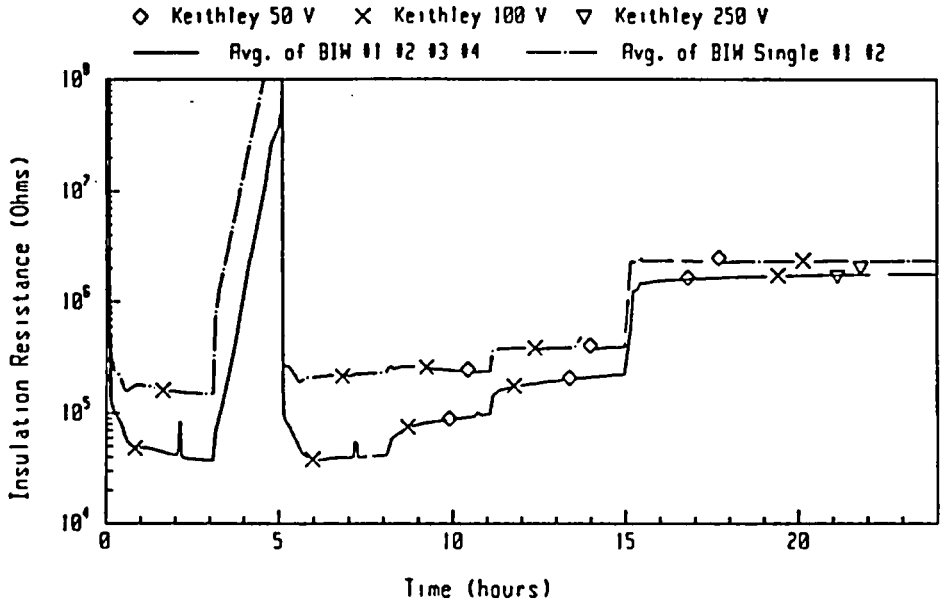

Figure 6 Performance of BIW Bostrad 7E Single and Multiconductors

Of 4 Okonite Okolon single conductors that were tested, 3 of them maintained IRs well above 10^6 Ω throughout the accident test. The behavior of the other conductor is shown in Figure 7. The fuse for this conductor opened at 172 hours. The cable experienced an initial rapid decrease in IR of several orders of magnitude at 133 hours, followed by a gradual decrease over the next 40 hours. The reason for this failure is still being investigated. Prior to the 133 hour point, there was no indication that this cable was behaving differently than the other Okolon conductors.

Figure 8 compares the IR of 2 Dekoron Dekorad ethylene propylene diene monomer (EPDM, a category of EPRs) single conductors (removed from a multiconductor cable) with the 2 conductors of a multiconductor cable. In all cases, the IRs remained above 10^6 Ω, but the difference between single conductors and multiconductors was only evident during the 340°F exposure and was only about a factor of 2. The fuses for two additional conductors from a second multiconductor cable both opened (Figure 9), one at 178 hours and one at 181 hours. For the first 140 hours of the test, the IRs for these cables were very close to the IRs of the cables that successfully completed the entire test. At 140 hours, conductor #1 began a gradual degradation that lasted 40 hours before its fuse opened. Conductor #2 began losing IR at 158 hours into the test, but its fuse did not open until 20 hours later. A significant decrease in IR occurred soon after a 250 V IR was completed at 173 hours. The higher voltage stress may have accelerated the IR degradation. At the time of the 250 V measurement, the IR of conductor #1 had already degraded much more than the IR of conductor #2. When the chamber was opened after the accident test, the failed multiconductor was found severely degraded. The jacket was split open with bare conductors visible along the cable.

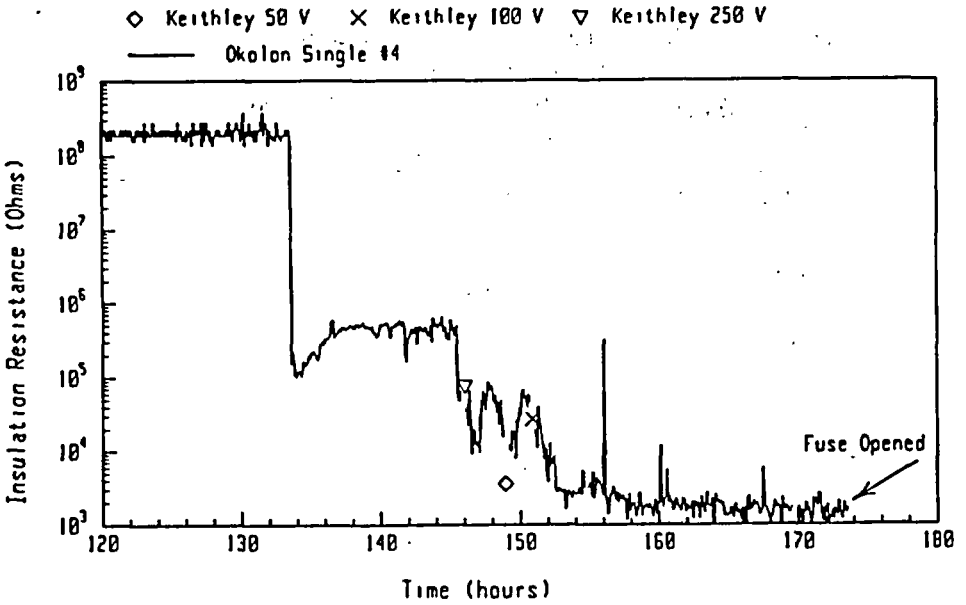

Figure 7 Performance of Okonite Okolon Single Conductor That Failed

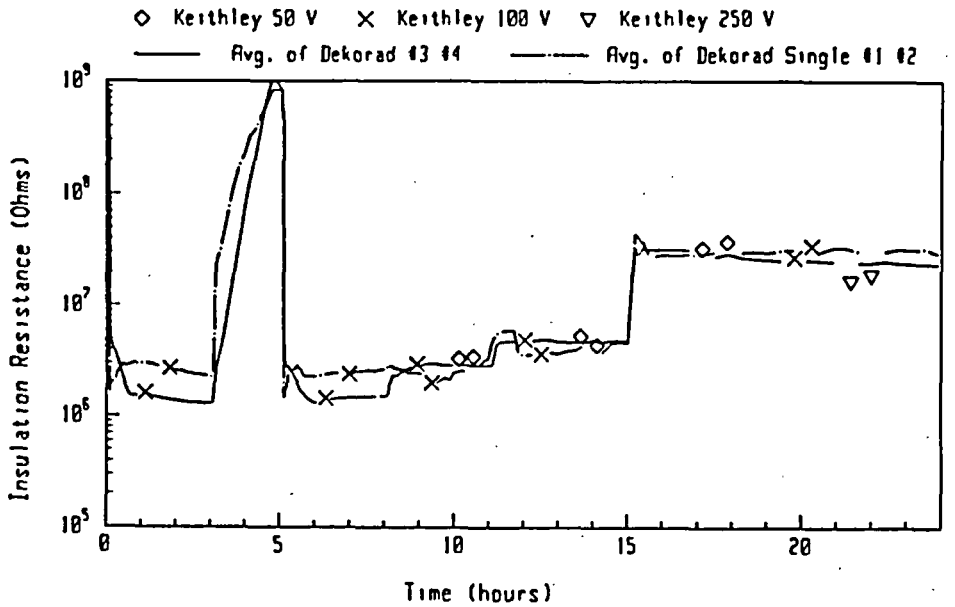

Figure 8 Performance of Dekoron Dekorad Single and Multiconductors

3.3 Other Cable Insulations

Figure 10 shows the behavior of Kerite FR/FR single conductors during the first 24 hours of the test. The IR dipped as low as 6000 Ω during the second transient to 340°F, but then it recovered by an order of magnitude. The superheated steam conditions may have contributed to the

recovery by drying out the cable. As the temperature was lowered to 320°F and to 300°F, the IR did not recover as it typically did for most cables. Rather, the IR decreased to about 10000 Ω. When the temperature was lowered to 250°F, the IRs increased, but they never exceeded 10^5 Ω until the cooldown to ambient temperature began. The ambient temperature IRs after cooldown were about 10^6 Ω.

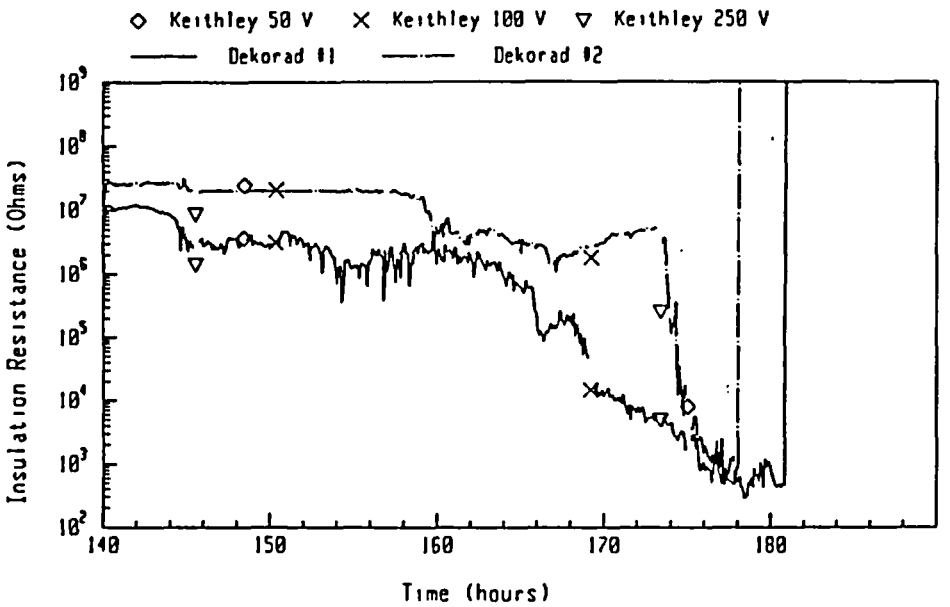

Figure 9 Performance of Dekoron Dekorad Multiconductors That Failed

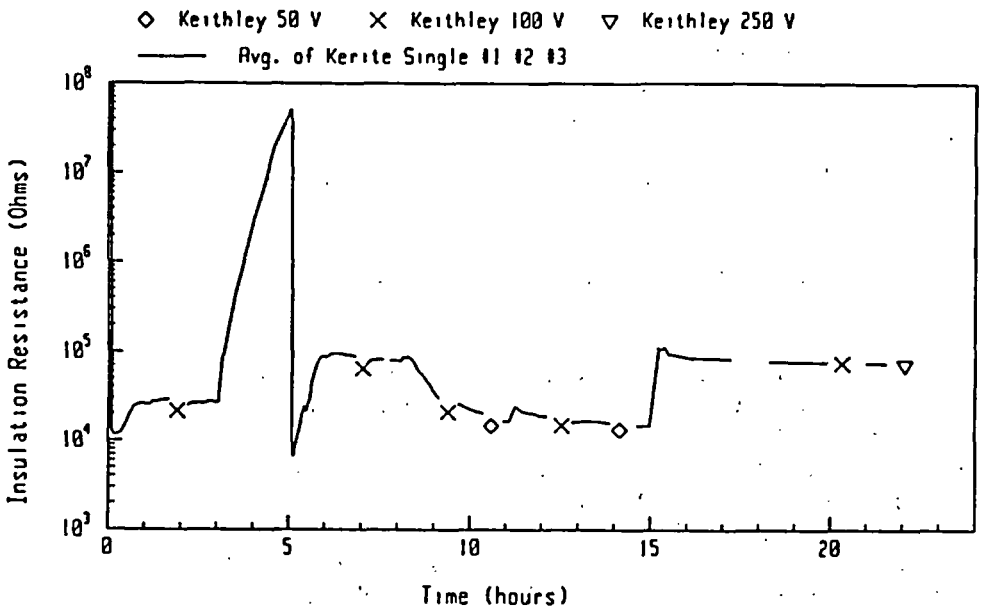

Figure 10 Performance of Kerite FR/FR Single Conductors

Two Rockbestos SR single conductor silicone cables were tested. Both of these cables had IRs that were well above 10^7 Ω throughout the test. Two cables with polyimide (Kapton) insualtion were also tested. One of them was damaged during test setup and its fuse opened very early into the test. The IR behavior of the second conductor is shown in Figure 11. Although the IR was normally above 10^7 Ω, a very substantial thermal transient behavior is indicated by the Figure, with the IR dipping down to about 10^5 Ω during the first transient, then recovering by more than 2 orders of magnitude.

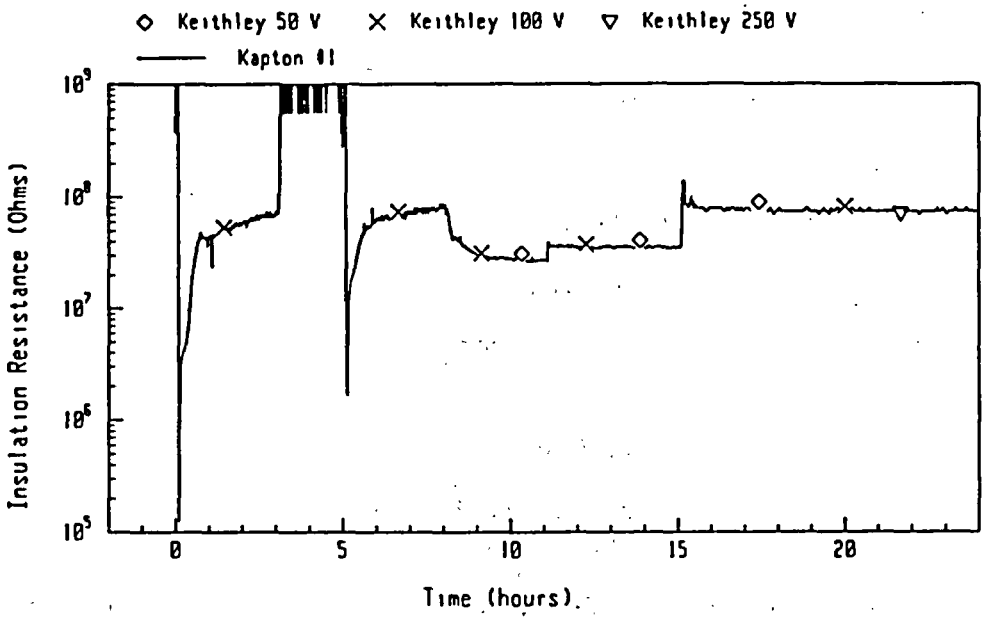

Figure 11 Performance of Polyimide (Kapton) Single Conductor

The final cable type tested was Rockbestos RSS-6-104/LE coaxial cable. The IR behavior of one of these cables is shown in Figure 12. The other one performed very similarly. The IRs remained above $5x10^7$ Ω throughout the test. Note that the on-line measurement setup was unable to accurately measure the high IR this cable had throughout much of the exposure.

3.4 Single Versus Multiconductor Performance

Three EPR cable products were represented in both single and multiconductor configurations. In all cases, the single conductors had higher IRs than the multiconductors during the 340°F peaks. As the temperature was reduced, the differences became more significant for Anaconda FR-EP cables, less significant for the BIW Bostrad cable, and disappeared altogether for the Dekoron Dekorad cables. A typical test strategy following IEEE 383-1973[3] might include only single conductors, which is non-conservative for some cable types. Whether this difference is significant would depend on the application of the cable as well as the absolute value of the cable IR during the test.

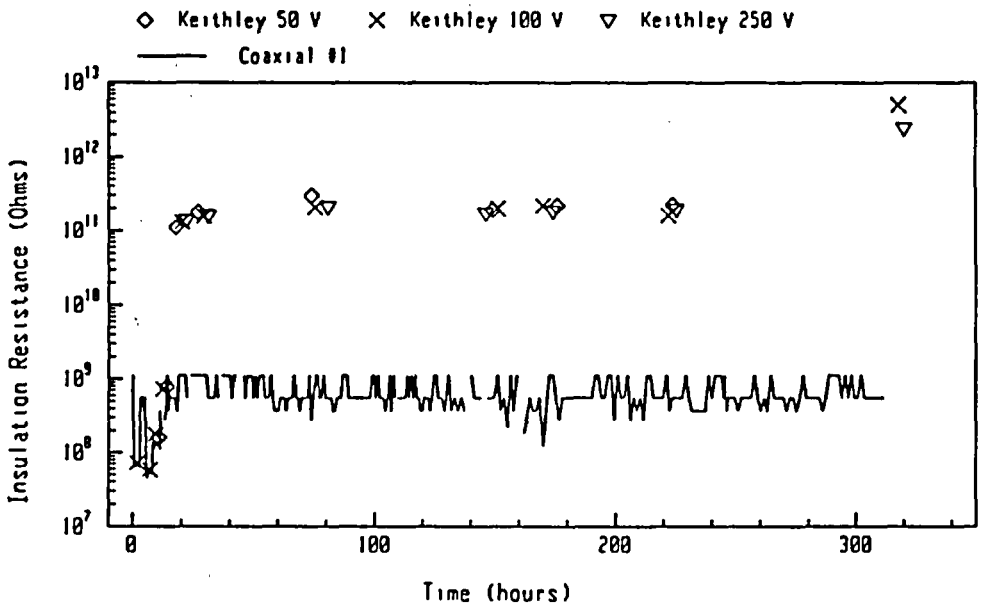

Figure 12 Performance of Rockbestos RSS-6-104/LE Coaxial Cable

3.5 Cable Performance During Transients

Although the previous figures are not scaled to examine the transient behavior of the cables, they do give some indications. Since data was acquired every 10 seconds during the transient, we have expanded plots to provide more detail during the first hour of the test. Although the plots will not be shown here, an indication of the cable behavior will be given. Most of the multiconductor cables exhibited a thermal lag characteristic similar to what would be expected. A steady value of IR for the multiconductors was attained in about 3 minutes. This lag time was fairly consistent for all of the multiconductors. The Brand Rex cable showed a significant recovery effect, with the IR increasing by a factor of 5 between several minutes and an hour into the transient.

As expected, single conductors had much less thermal lag. The time lag was typically 30 seconds to reach a steady IR. The polyimide cable had the most interesting transient behavior after the initial lag period--it recovered more than two orders of magnitude during the next 30 minutes.

During the second transient, the cable behavior was generally the same. However, the Brand Rex IR went directly to its steady state value with no overshoot/recovery; the Kerite had more overshoot, followed by more recovery (to a net higher steady state IR after the second transient); and the initial IR decrease for the polyimide was an order of magnitude less than in the first transient.

3.6 Cable Behavior Versus Applied Voltage

The discrete data that was acquired with the electrometer apparatus at 50 V, 100 V, and 250 V provides some insight into cable IR behavior at different voltages. Although IR should theoretically be constant with applied voltage, it has been argued that IR actually decreases as applied voltage is increased. The data in Figures 2-12 indicates that IR is largely independent of voltage over the range of 50-250 V for the cables tested.

3.7 Discrete Versus Continuous Insulation Resistance Measurements

In this test program, both discrete and (almost) continuous IR measurements were performed. The agreement between the two independent methods is excellent for IRs in the range of the on-line measurement system. The data indicates that discrete IR measurements are generally adequate for IR monitoring. However, a number of cables showed significant effects during the transient portions of the test that would not be seen with only the discrete measurements. For example, the polyimide IR measured after it reached steady state was well above 10^7 Ω at 340°F, while the minimum IR during the exposure was down near 10^5 Ω.

4.0 CONCLUSIONS

The conclusions that may be drawn from the data presented above are as follows:

a) Many cables successfully passed the accident exposure following artificial aging to a nominal lifetime of 60 years using an aging acceleration factor of about 80.

b) Several cable samples opened 1 A fuses during the accident exposure, with the earliest failure (other than the damaged polyimide cable) at 80 hours. Other samples had IRs early in the accident exposure that might be marginal for some applications.

c) Although one of the cables using polyimide insulation was inadvertently damaged when tightening a test chamber flange, the other one did well during the LOCA tests (it did exhibit a strange thermal shock effect).

d) Single conductor EPR cables had IRs ranging as much as a factor of 10 above comparable multiconductors. During the 340°F part of the test, the single conductors IRs were at least a factor of two higher than the multiconductors. Tests using only single conductors can therefore be non-conservative in estimating accident IRs.

e) Total thermal lag time was typically 3 minutes for multiconductor cables and 30 seconds for single conductors.

Some cables exhibited IR recovery following the initial thermal lag. This indicates that discrete time IR measurements may not capture worst case IR values. Otherwise, discrete measurements appear suitable for performance monitoring.

f) Over the range of 50-250 Vdc, cable insulation resistance was essentially independent of applied voltage.

5.0 REFERENCES

1. M. J. Jacobus, G. L. Zigler, and L. D. Bustard, "Cable Condition Monitoring Research Activities at Sandia National Laboratories," SAND88-0293C, *Proceedings: Workshop on Power Plant Cable Condition Monitoring*, Electric Power Research Institute EPRI EL/NP/CS-5914-SR, July 1988.

2. "IEEE Standard for Qualifying Class 1E Equipment for Nuclear Power Generating Stations," IEEE Std. 323-1974, The Institute of Electrical and Electronic Engineers, Inc., 1974.

3. "IEEE Standard for Type Test of Class 1E Electric Cables, Field Splices, and Connections for Nuclear Power Generating Stations," IEEE Std 383-1974, The Institute of Electrical and Electronic Engineers, 1974.

Assessment of PWSCC Damage in PWR Steam Generator Tubes[a]

V. N. Shah, Idaho National Engineering Laboratory
D. B. Lowenstein, A. P. L. Turner, S. R. Ward, J. A. Gorman
Dominion Engineering, Inc.
P. E. MacDonald, Idaho National Engineering Laboratory
G. H. Weidenhamer, United States Nuclear Regulatory Commission

ABSTRACT

This paper presents a model for assessing primary water stress corrosion cracking (PWSCC) damage to pressurized water reactor (PWR) steam generator tubes. PWSCC damage has been detected at three locations in the recirculating steam generator: roll transition regions, U-bends, and tube dents. The model accounts for residual stresses, microstructure, and primary coolant temperatures. High residual tensile stresses and low mill-annealing temperatures contribute significantly to PWSCC. PWSCC is a thermally activated process; small increases in operating temperature accelerate damage. The model employs a Weibull distribution to estimate the times to failure of steam generator tubes for failures caused by PWSCC. The model uses tube degradation results obtained from inservice inspections and from destructive examinations. This paper also describes a life assessment procedure for steam generator tubes.

1. INTRODUCTION

The Aging Assessment and Mitigation Project is a part of the Nuclear Plant Aging Research Program being sponsored by the United States Nuclear Regulatory Commission (NRC). The main objective of the project is to develop an understanding of the aging degradation of the major light water reactor (LWR) structures and components and to develop procedures for predicting the useful life of these components so that the impact of aging on the safe operation of nuclear power plants can be evaluated and addressed.

The major effort of the project consists of integrating, evaluating, and updating the technical information relevant to aging and license renewal from current or completed NRC and industry research programs. The project has been divided into five steps: (1) identify and prioritize the major reactor components, (2) identify degradation sites, mechanisms, stressors, and potential failure modes of each component and then evaluate the current inservice inspection methods, (3) assess advanced inspection, surveillance, monitoring, and mitigating methods, (4) develop residual life assessment models and procedures, and (5) support the development of technical criteria for license renewal. The first two steps have been completed, including the qualitative aging assessment of twenty major components.[1] A thorough assessment of emerging fatigue monitoring methods and advanced material evaluation methods is being conducted as part of Step 3.

---

a. Work sponsored by the United States Nuclear Regulatory Commission, Office of Nuclear Regulatory Research, under DOE Contract No. DE-AC07-76ID01570.

Life assessment procedures are being developed for five major components as part of Step 4: reactor pressure vessels, metal containments, reinforced concrete containments, cast stainless steel components, and steam generator tubes. A general life assessment procedure for many of the major components is as follows: (a) evaluate the damage state of the component at the beginning of the operating period, (b) estimate the additional damage expected during the operating period, (c) evaluate component integrity at the end of the operating period to ensure that acceptable safety margins exist, and (d) establish an inservice inspection program. In Step 5, the project results are being used to develop technical guidelines for making license renewal decisions.

The integrity of the pressurized water reactor (PWR) steam generator tubes is important to plant safety. The tubes constitute more than one-half of the primary system pressure boundary and are the life-limiting components of a PWR steam generator. Sudden rupture of several degraded tubes at one time might lead to a major plant temperature and pressure transient and result in uncovering of the core. A failed tube or plug might cause mechanical damage to other tubes, resulting in multiple failures. Sudden depressurization of the secondary side may cause simultaneous failure of several degraded tubes. Leakage of primary coolant through a ruptured tube may cause radiological release directly into the environment, bypassing the containment. Such leakage would also cause radioactive contamination of the secondary side, making maintenance and waste disposal tasks more difficult.

Steam generator tubes at many PWR plants have experienced significant aging degradation. The three most widespread types of degradation mechanisms affecting U.S. PWR plants are primary water stress corrosion cracking (PWSCC) on the primary side, intergranular attack (IGA) and intergranular stress corrosion cracking (IGSCC) on the secondary side, and fretting wear and thinning.[2] Other corrosion mechanisms, such as wastage, pitting, and denting, have occurred in many older steam generators but have been avoided in most newer generators by changes in operating procedures. However, pitting damage continues to be significant at some plants. Erosion-corrosion, corrosion fatigue, and fatigue at U-bends have affected relatively few tubes. However, a sudden fatigue failure of a U-bend has occurred at one plant, and the failure is considered significant because of its location and nature.

This paper discusses PWSCC damage to PWR steam generator tubes. The current status of the PWSCC damage in operating PWR plants and the factors causing the damage are discussed first. Then the residual stresses introduced by design, fabrication, and operation of the tubes are evaluated. The use of a Weibull distribution to estimate the PWSCC failure times for the tubes is presented next. Then the remedial measures for PWSCC damage are briefly discussed. Finally, a life assessment procedure for steam generator tubes is outlined.

2. CURRENT STATUS OF PWSCC IN OPERATING POWER PLANTS

PWSCC was first observed in 1971 in the hot leg roll transition region at Obrigheim. Increasingly, tubes have been removed from service as a result of significant PWSCC damage at high stress locations such as roll transitions, tight radius U-bends, (in rows 1 and 2), and tube dents at tube support plate intersections. High residual stresses, low amounts of intergranular carbides, and high operating temperatures contribute to PWSCC damage.

Currently, at least 35 plants worldwide have experienced some degree of roll transition PWSCC. At least 25 plants have reported cracking due to U-bend PWSCC, and five plants have noted PWSCC at dents. Three plants have reported PWSCC in the cold leg roll transition of tubes pulled from steam generators and examined destructively.[3,4,5] In some plants the cracking has been limited to only a few tubes, while in other plants it has been extensive, affecting thousands of tubes. In some plants the cracking has occurred within the first fuel cycle, while in some other plants, those operated at lower temperatures, it has occurred after as long as 14 years of operation. Field experience indicates that PWSCC has been limited to Westinghouse type recirculating steam generators.

Most of the PWSCC cracks in the roll transition region are axial, but at a few plants the cracks are circumferential. Circumferential cracks are of special concern because they pose a risk of sudden tube rupture without the warning generally provided by low level leakage through the axial cracks. The field data indicate that the roll transition cracks are generally found in the areas of most severe geometry, where high tensile stresses are likely to be present. In one plant, recent eddy current test results show axial indications in 90% of the hot leg tubes of one steam generator and 60% in the other.[4] In contrast, circumferential cracks do not represent a generic problem. Circumferential cracks of significant size have been found in few steam generators; a 75 to 90% through-wall crack in one tube has been reported at one plant. The main remedial measures for the tubes with defects in the roll transition region are sleeving and plugging, which are discussed in Reference 2.

Most of the PWSCC cracks in the U-bend are between the tube flank and extrados in the irregular transition region of row 1 tubes (see Figure 1). The irregular roll transition region represents the abrupt change in geometry between the straight portion of the tube and the U-bend. The cracks in the irregular transition region are parallel to the tube axis, and the resulting leakage increases slowly. In one plant, the leakage rate at shutdown was 12 to 24 L/h (3 to 6 gph) and increasing slowly. To date, no sudden rupture of the tube because of cracks in the irregular transition region has been reported. However, PWSCC cracks oriented parallel to the tube axis have been reported in the hot leg side of the apex region in two plants, and at one of those plants such a crack led to sudden rupture of the tube.[4] The resulting leak rate was about 570 L/min (150 gpm). The crack was attributed to high residual stresses resulting from denting of the tubes near the top support plate. Tube denting caused the flow slots to close, which forced the legs of the row 1 U-bends to bend inward, increasing the ovality of the tube and resulting in high tensile stresses in the apex region.[6] However, cracks in the apex region do not represent a widespread problem.[4] The main remedial measure for defects in the U-bend region is plugging. In several plants, all tubes in the first one or two rows have been plugged as a preventive measure. This may not be a practical preventive measure for the newer plants that have only a small margin of excess tubes.

PWSCC cracks at dents can be either axial or circumferential, but some cracks with significant axial components are usually present. Damage due to denting near the support plates was significant during the late 1970s; however, it is no longer an important cause of tube failures.[3] This is largely because of more stringent control of secondary-side chemistry in

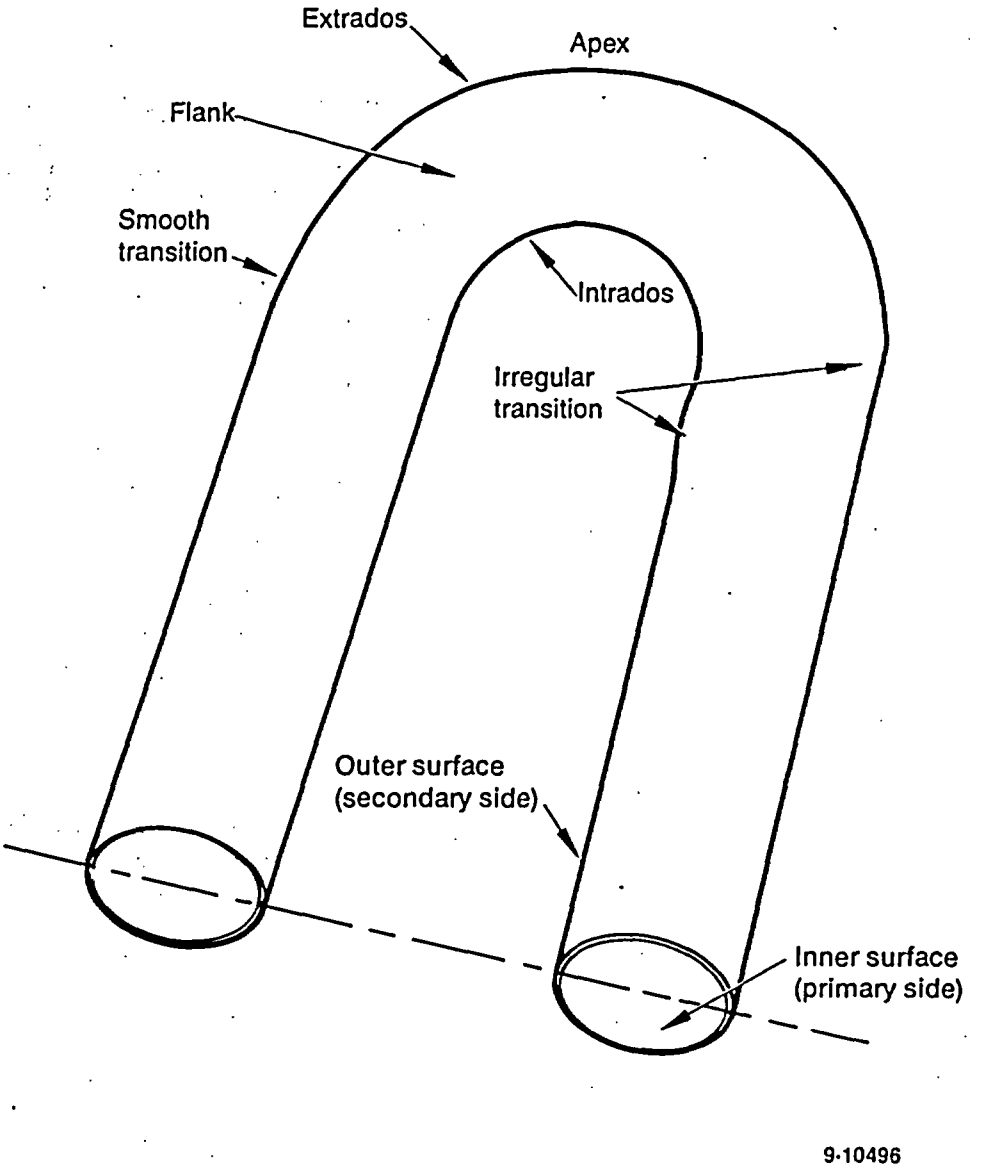

Figure 1. Identification of locations on the U-bend tubes, including the intrados, extrados, and flanks.

older plants, such as eliminating copper alloys from the feed train, minimizing condenser leaks, and adding boric acid. Newer steam generators use corrosion-resistant tube support plates and good secondary water chemistry to control denting. However, a widespread denting problem in the newer steam generators in EDF (Electricite de France) plants recently has been reported whose cause is not yet well understood.[7] Oxidation-induced metallic sludge around the tubes next to the tubesheet had apparently caused constriction (denting) on the hot leg tubes in the middle part of the tube bundle and resulted in cracks that leaked at a rate of about 3.1 L/h (0.82 gph). It is very likely that the residual stresses introduced by denting caused PWSCC. About eight plants have been off the line because of this problem. EDF is considering plugging the affected tubes as a temporary solution. EDF is also developing a sleeving technique and planning to apply a new chemical cleaning process as a long-term solution.

3. CONDITIONS NECESSARY FOR PWSCC DAMAGE TO OCCUR

PWSCC is a thermally activated, intergranular cracking mechanism that occurs when the following three conditions are present: susceptible tubing material, high tensile stresses, and high operating temperature. PWSCC has been reported in Alloy 600 tubes with low mill-annealing temperatures and with tensile stresses of yield stress magnitude. PWSCC is more likely to be found on hot leg tubes because of higher operating temperatures as compared to cold leg tubes.

3.1 Susceptible tubing material

Tubes with increased quantities of intergranular carbides are more resistant to PWSCC. Heat treatment applied to the tubing material after cold working to final tube size controls the formation of intergranular carbides. Before the final heat treatment, intergranular carbides are present in the cold worked tube as a result of previous heat treating. The final heat treatment includes mill annealing of the tube, during which cold worked material recrystalizes and new grain boundaries are formed. If the mill-annealing temperature is low, that is 980°C (1800°F) or less, the carbides do not dissolve, so they remain (at the old grain boundaries) as intragranular carbides. At a higher mill-annealing temperature of about 1065°C (1950°F), most of the carbides dissolve in the solid solution. During cooling from the higher mill-annealing temperature, carbides precipitate at the new grain boundaries. In contrast, during cooling from the low mill-annealing temperature, no carbides can form at the new grain boundaries because no dissolved carbon is present in the solid solution. Thus, the higher mill-annealing temperature results in larger quantities of intergranular carbides and makes the tubing material more resistant to PWSCC. However, if the final cooling rate is such that significant chromium depletion takes place, then the material will be sensitized and becomes susceptible to secondary side intergranular stress corrosion cracking (IGSCC).

Before the early 1970s, tubes in the Westinghouse type plants were subjected to high mill-annealing temperatures [980 to 1065°C (1800 to 1950°F)]. Those tubes were resistant to PWSCC. Later, during the 1970s, the mill-annealing temperature was reduced to 955°C (1750°F), and the tubes in the Westinghouse type plants became less resistant to PWSCC. During the late 1970s, a special thermal treatment for

the tubes was adopted. The special thermal treatment included high mill-annealing temperatures [1065°C (1950°F)] followed by holding the tubing at a lower temperature [705°C (1300°F)] for a long period of time (15 hours). This special treatment provides the desired amount of intergranular carbides without any chromium depletion, and thus makes the tube resistant to both PWSCC and secondary side IGSCC.

Tubes in Combustion Engineering steam generators are resistant to PWSCC because higher mill-annealing temperatures are used during final heat treatment.

A different heat treatment is used on once-through steam generators. The entire steam generator is held at 620°C (1150°F) for 10 hours after the final assembly. This heat treatment results in large quantities of intergranular carbides and relief of the residual stresses in the tubing. As a result, the tubing in the once through steam generator is resistant to PWSCC. However, the heat treatment causes depletion of chromium at the grain boundary, and both the primary and secondary sides of the tubing become susceptible to attack by sulphur species. Such attack has occurred at two Babcock & Wilcox plants.[8,9]

Large grain size and lower yield stress are associated with the high mill-annealing temperature. Tubing material with grain size larger than ASTM 6 is less susceptible to PWSCC. Similarly, tubing material with yield stress less than 379 MPa (55 ksi) is less susceptible to PWSCC.

3.2 High tensile stresses

Tubes with high tensile stresses on the inside surface are susceptible to PWSCC. Total stresses in the tube are the algebraic sum of the residual stresses (introduced by the various fabrication processes and by tube bending and installation methods) and the applied stresses (caused by operating environments). Denting of the tube introduces additional residual stresses that are included in the total stresses. This section discusses stresses in the recirculating steam generator tubes; as mentioned earlier, the tubes in the once-through steam generator are not susceptible to PWSCC.

Residual stresses. Fabrication of straight tubes includes forming of the tube by piercing or extrusion processes, cold drawing, straightening, and polishing. The diameter and wall thickness of a finished recirculating steam generator tube are in the range of 17.475 to 22.225 mm (0.688 to 0.875 in.) and 1.067 to 1.397 mm (0.042 to 0.055 in.), respectively. Residual stresses in the finished tube are introduced mainly by the straightening operation; these stresses are seldom measured. Berge et al. have reported hoop (circumferential) stresses ranging from -103 to -172 MPa (-15 to -25 ksi) on the inner surface (the minus sign indicates compressive stress) and 93 to 145 MPa (13.5 to 21 ksi) on the outer surface of the tube.[10] The measured axial stresses were very low. Some other measurements on a few tubes show that the magnitude of the residual hoop stress on the outside surface is highly variable and frequently equals or exceeds 240 MPa (35 ksi).[2]

Bending introduces high residual stresses in the U-bends of the row 1 and row 2 tubes of recirculating steam generators. A typical bend radius of a row 1 U-bend is 55.4 mm (2.18 in.). Bending reduces the distance between the extrados and intrados and increases the distance between the flanks. The percentage change in the distance is called ovality. For steam generators constructed by Westinghouse Electric Corporation, the U-bending machine uses a ball mandrel during bending of rows 1 and 2 tubes to prevent excessive ovalization and collapse of the tube (see Figure 2). An outer roller bends the tube by forcing it to conform to the outer surface of a stationary die. The ball mandrel moves inside the tube as the outer roller revolves around the die, such that the mandrel is always located where the tube is being bent. The machine operates without an internal mandrel while bending tubes for rows 3 and above. A different method is used for Westinghouse type steam generators constructed in France; the U-bending machine operates without an internal mandrel while bending the row 1 U-tubes (see Figure 3).[10] The bending process introduces an abrupt change in the ovality at the extrados near the transition between the end of the bend and the straight portion of the tube. The magnitude of the abrupt change is larger if a ball mandrel is used.[11] The region that includes this abrupt change in ovality is called the irregular transition zone. In the irregular transition zone, the wall thickness changes significantly (~20%) along the extrados. Maximum ovality along the extrados/intrados is ~5%, and is ~2% near the irregular transition zone.[12]

Tensile residual stresses are highest at the inside surface of the irregular transition zone, higher in the tubes bent by a bending machine using a ball mandrel, and vary significantly along the U-bend. Different magnitudes of the stresses are reported in the literature, and the differences may be due to different methods used to measure residual stresses. (Strain gages may be used to measure the strain released during sectioning of the tube. Residual stresses in the tube are estimated from the measured released strain. The estimated residual stresses are generally smaller than those measured with the X-ray diffraction method.[13]) Some researchers have reported axial and hoop stresses of 690 MPa (100 ksi) at the inside surface of row 1 tubes and 462 MPa (67 ksi) for row 2 tubes.[14,15] In contrast, Rudd has reported high residual stresses in the axial direction 620 MPa (90 ksi)] and low residual stresses in the hoop direction [276 MPa (40 ksi)], measured with the X-ray diffraction method.[12] However, the hypothesis that the residual stresses in the axial direction are significantly higher than those in the hoop direction is not substantiated by the presence of only axial cracks in the irregular transition region in the operating plants. Further research is being conducted to resolve this issue. Rudd also reported axial residual stresses of 900 and 760 MPa (130 and 110 ksi) measured below the surface at 0.076 and 0.152 mm (0.003 and 0.006 in.), respectively. These stresses, measured after electropolishing, were higher than stresses measured at the surface.

Residual stresses much higher than yield stress [380 MPa (55 ksi)] of the annealed material are possible because the tube material has been strain hardened. [The yield strength of cold drawn Inconel 600 tubing has been reported as 937 MPa (133 ksi).][6]

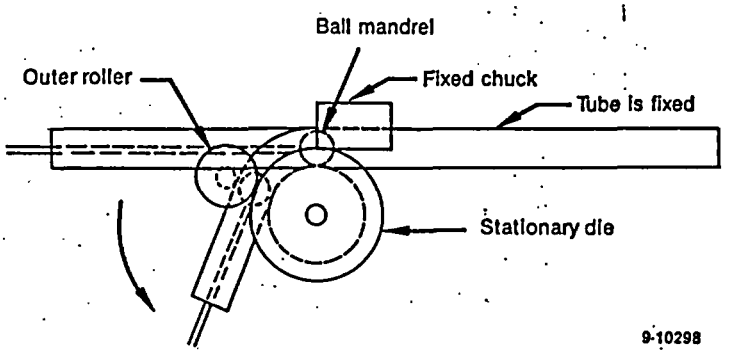

Figure 2. Tube bending process using a ball mandrel for steam generators constructed by Westinghouse Electric Corporation.

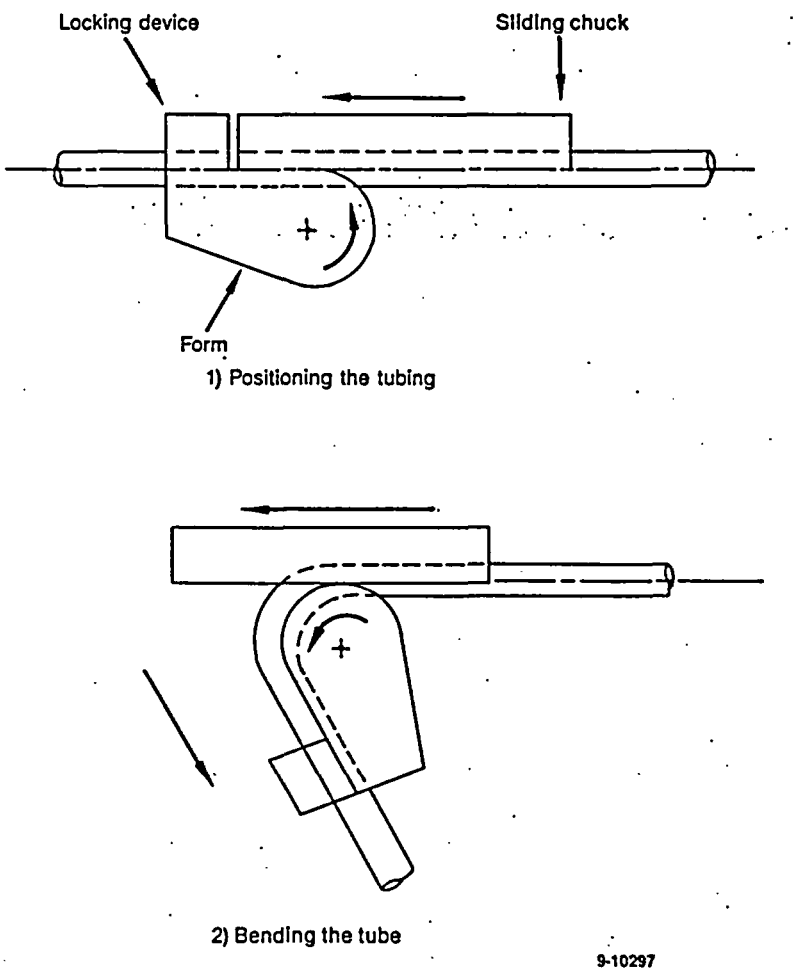

Figure 3. Tube bending process for Westinghouse type steam generators constructed in France.

The bent tubes, also called U-tubes, are installed in a thick [~530- to 560-mm (21- to 22-in.)] tubesheet. Ends of the U-tubes are expanded at the bottom portion [~51 to 64 mm (2 to 2.5 in.)] in some steam generators and the full depth of the tubesheet in others. Nominal radial clearance (crevice size) between the unexpanded tube and tubesheet hole is 0.20 to 0.25 mm (8 to 10 mil). Of the three expansion techniques (rolling, explosive forming, and hydraulic forming) available for tube expansion, rolling is the most commonly used. Numerous residual stress measurements have been made on tubes expanded by this technique. Little is known about the residual stresses introduced by the other two techniques. Typical roll expansion may cause about 4 to 6% reduction in tube wall thickness. The transition from the expanded portion of the tube to the unexpanded portion is called the roll transition region. On the inside surface, both hoop and axial residual stresses are compressive on either side of the transition, but in the transition region itself, both stresses are tensile and equal to 448 MPa (65 ksi) in the axial direction and 517 MPa (75 ksi) in the hoop direction.[14,15] If the tubesheet holes are oversized, then the magnitudes of the residual stresses would be higher.

Applied stresses. Operating pressures and temperatures introduce biaxial stresses in the steam generator tube wall. Pressure induced hoop stresses are calculated for the primary to secondary pressure differential of 9.2 MPa (1,330 psi) using the thick wall formula. The magnitude of the hoop stresses on the inside surface is 76 MPa (11 ksi) for the hot leg and cold leg roll transition and U-bend. The corresponding axial stresses are 34 MPa (5 ksi). Temperature differences between primary and secondary coolants introduce thermal stresses. Typical values for hot leg inlet, average cold leg outlet, and secondary water temperatures are 325, 290, and 280°C (615, 555, and 535°F), respectively, and the corresponding thermal stresses on the tube inside surface are compressive, with hoop and axial stresses being approximately equal. The magnitudes of the thermal stresses at the hot leg and cold leg roll transitions are -48 and -14 MPa (-7 and -2 ksi), respectively, if sludge is absent, and are zero if sludge is present. The magnitude of thermal stresses at the U-bend are -28 MPa (-4 ksi). U-bends of both row 1 and row 2 have the same pressure and thermal stresses. Several simplifying assumptions were made in calculating the applied stresses listed here. Local bending stresses caused by pressure and overall thermal expansion are not included. In addition, the eccentricity of tube bore, variation in wall thickness, and U-bend flexibility modify calculations of applied stresses but are not accounted for in the values presented here.

Corrosion of support plates has caused denting of the adjacent tubes and introduced tensile residual stresses on the inside surface. The typical magnitude of the tensile stresses is 415 MPa (60 ksi), and the stresses are the same in both axial and circumferential directions. Residual stresses caused by denting near the sludge pile are not yet known.

Typical residual and applied stresses on the inside surface of the roll transitions, U-bends, and straight portion of the tube are summarized in Table 1. Stresses caused by denting are also listed.

Table 1. Estimated stress levels for various locations on the inside surface of steam generator tubing

Location	Pressure Axial/Hoop	Thermal Axial/Hoop	Residual Axial/Hoop	Total Axial/Hoop	Max Tensile Stress
Estimated stresses[a] (ksi)					
Hot leg roll transition, no sludge	5/11	-7/-7	65/75	63/79	79
Hot leg roll transition, with sludge	5/11	0/0	65/75	70/86	86
At tube support plate, no denting	5/11	0/0	-1/-25	4/-14	4
At tube support plate, with denting	0/0	0/0	60/60	60/60	60
Row 1 U-bend	5/11	-4/-4	100/100	101/107	107
Row 2 U-bend	5/11	-4/-4	67/67	68/74	74
Cold leg roll transition, no sludge	5/11	-2/-2	65/75	68/84	84
Cold leg roll transition, with sludge	5/11	0/0	65/75	70/86	86

a. Negative sign indicates compressive stress.

4. QUANTITATIVE ASSESSMENT OF PWSCC DAMAGE

Numerous investigations by vendors, universities, national laboratories, and other organizations have confirmed the PWSCC phenomenon and agreed upon the dependence of PWSCC on temperature, stress, and heat treatment. The PWSCC data from operating plants correlate well with the data from the laboratories. This information is used to develop parametric relationships between PWSCC damage and the factors of temperature, stress, and heat treatment. The damage model described in this paper is based on these parametric relationships. PWSCC has occurred extensively in the field (see Section 2), so a large and statistically valid database of inspection and destructive evaluation of PWSCC damage exists. Statistical distribution of these results has been used to predict the fraction of tubes failed (defined as tube removal from service or renewal by sleeving) as a result of PWSCC damage. In this paper a Weibull distribution is used to characterize failure times. (Use of the log normal distribution is also reported in the technical literature.) The model is described first. Then the application of the Weibull distribution is discussed.

4.1 Model for Assessing PWSCC Damage

PWSCC is a thermally activated, stress dependent process. The PWSCC damage rate increases in proportion to stress, σ, to the fourth power; i.e.,

$$\text{rate} \propto \sigma^4 \quad . \tag{1}$$

This is a well established correlation that has been used by a number of investigators in Alloy 600 stress corrosion cracking research.[16] The exponent of four on the damage rate is typical of stress exponents for creep, and thus is consistent with modern models for PWSCC, which say that slow straining at the crack tip is an essential part of the cracking process.

The PWSCC damage rate increases with temperature according to the following exponential relation:

$$\text{rate} \propto \exp(-Q/RT) \tag{2}$$

where Q is the activation energy, T is the absolute temperature in Rankine, and R is the gas constant. This is the standard form for thermally activated processes, and is supported by several recent studies. The activation energy Q is estimated from field data to be 168 kJ/mol (40 kcal/mol).[17] The rate of damage decreases with decreasing temperatures. For an 11°C (20°F) decrease in temperature from the operating temperature of 327°C (620°F), the rate of damage will decrease by a factor of 1.89. For smaller values of Q, the rate of damage will decrease by a smaller factor for the same decrease in temperature.

Based on these stress and temperature dependencies, the characteristic failure time t_r for PWSCC of Alloy 600 tubes can be described by an equation of the form:

$$\frac{1}{t_r} = \text{rate} = A\,\sigma^4 \exp(-Q/RT) \quad . \tag{3}$$

The constant A includes plant to plant variations such as in material and chemical environment.

4.2 Weibull Distribution for PWSCC Failure Times

Most failure processes are statistical in nature in that all samples do not fail at exactly the same time, even in well controlled laboratory tests. The behavior expected for steam generator tube failures is for the tubes to have a mean life expectancy, with the actual times to failure scattered around the mean. The mean life should be determined by the average material and environmental conditions. The scatter in lifetimes will be a function of variability in the materials and environment as well as the basic statistical nature of the process. This type of behavior can be described by a Weibull distribution, which is the most widely used probability distribution for lifetimes. It has been used with good success to correlate fatigue and stress corrosion cracking data for metals, glasses, ceramics, and fibers.[18-20] Preliminary analysis of PWSCC of Alloy 600 (Inconel) steam generator tubes using a Weibull distribution function shows excellent correlation with field results. For these reasons, the Weibull function is being used for extrapolating steam generator tube failure data to obtain residual life predictions.

The two-parameter equation of the cumulative Weibull distribution is:[21]

$$F(t) = 1 - \exp\left[-(t/tr)^b\right] \qquad (4)$$

where:

$F(t)$ = cumulative fraction of tubes failed

t = time of operation in equivalent full power years (EFPY)

t_r = characteristic time of the Weibull probability distribution (63.2% of a population has failed by the completion of a period of service equal to the characteristic time)

b = the slope of the distribution when plotted on a Weibull probability graph.

The value of the exponent b determines how much scatter there is in times to failure in a given population. Statistical variations in residual stresses and material properties between different tubes in one steam generator are assumed to be accounted for by the parameter b. As b increases, the distribution becomes narrower. As b becomes very large, the Weibull distribution approaches a deterministic equation in which all samples fail simultaneously when the service time equals the characteristic time t_r. When b = 1, the Weibull distribution is the same as an exponential distribution. When b = 3.25, the Weibull distribution approaches a normal distribution. A two parameter Weibull distribution model has been found adequate to represent PWSCC failure at U-bends and roll transitions. However, a three parameter model may be needed to predict PWSCC failure at the dented tubes; the third parameter represents the incubation time, that is, the time to cause denting damage.[2]

The use of equivalent full power years (EFPY) as the measure of time is a means of roughly accounting for the effects of changes in operating temperature. When reactor power is reduced, the hot leg inlet temperature decreases. As discussed earlier, relatively small changes in temperature cause a large change in the rate of degradation. This is accounted for by measuring time in EFPY because, at reduced power, operating time in EFPY increases at only a fraction of the rate of passage of actual time.

Analysis of data using the Weibull distribution is frequently done graphically using Weibull probability graph paper. Weibull probability paper is scaled such that Weibull distributions are represented by straight lines. By simple mathematical manipulations, the Weibull distribution shown in Equation (4) can be transformed to the following form:

$$\ln\left\{\ln\left[\frac{1}{1 - F(t)}\right]\right\} = b\,\ln(t) - b\,\ln(tr) \tag{5}$$

This equation is in the form of the equation for a straight line

$$Y = b\,X + C \tag{6}$$

where

$$Y = \ln\left\{\ln\left[\frac{1}{1 - F(t)}\right]\right\} \tag{7}$$

$$X = \ln\,(t) \tag{8}$$

$$C = -b\,\ln\,(t_r) \quad . \tag{9}$$

Weibull probability paper is scaled in the variables X and Y. Thus, Weibull probability paper has as its abscissa a logarithmic scale for time, and as its ordinate ln (ln {1/[1 - F(t)]}). Hence, when plotted on Weibull probability paper, failure data for cumulative fraction of a population failed F(t) vs time should fall on a straight line if the process is described by a Weibull distribution.

A linear least square method is applied to plot the PWSCC failure data on the Weibull probability paper. The error in the Y coordinate is minimized by minimizing the error norm E_r given by

$$E_r = \sum_i (Y_i - bX_i - C)^2 \tag{10}$$

where the sum is taken over all data pairs X_i, Y_i. As the failure data included in the Weibull plot increase, the uncertainty decreases, and the magnitude of parameter b (namely, the slope of the Weibull plot) tends to increase. However, only a small change in the slope of the Weibull plot for PWSCC failures has been found with the increase in data.

4.3 Application of Weibull Model

The Weibull probability distribution considers as its basis all tubes in a given population. However, certain degradation mechanisms pose a degradation risk to only a subset of the entire tube population. In these cases, an estimate of the reduced population must be made before performing any statistical analyses of the plant inspection data. This population estimate is used as a new basis for the Weibull probability distribution. In the case of PWSCC, the entire tube population is at risk with regard to roll transition PWSCC, and tube support plate PWSCC caused by denting. Alternatively, PWSCC in the U-bend region will progress at different rates in different rows because of different stress levels in the tube. Therefore, each row of the tubes must be analyzed separately. In practice, only the inner two rows of tubes will contribute significantly to tube failure probabilities. PWSCC at dents is limited to those tubes where denting has occurred. Denting is detected by eddy current testing (ECT) inspections. Therefore, the population at risk can be defined from inspection data. If denting occurs generally throughout the steam generator, it may be possible to treat PWSCC at dents as a global mechanism using the mean time to denting as an incubation time. If only a fraction of the tubes experience denting, PWSCC at dents should be analyzed on a reduced population basis using an appropriate incubation time to account for the time required for denting to occur. (Analysis of the denting mechanism itself is presented in Reference 2.)

Plants for which a particular type of PWSCC has been seen in three or more inspections, and in which at least 1% of the total tubes (of the corresponding population) have failed from this PWSCC type by the most recent inspection, can usually be evaluated using only the plant's own data. This involves the use of a least squares fit of a Weibull equation to existing plant data as described earlier. This method is considered to provide the greatest degree of certainty in predicting future degradation. The accuracy of the projections will increase as the amount of available data increases. It should be possible to make accurate predictions of the rate of degradation (characteristic time t_r and Weibull slope b) long before a sufficient number of tubes has failed to threaten the life of the steam generator. However, early inspection results may not accurately reflect the true rate of degradation because PWSCC damage is difficult to detect when cracks are still small.

If a particular type of PWSCC has been seen at a given plant in fewer than three inspections, or if less than 1% of the total tubes have failed from this PWSCC type, the inspection results from the plant are used to establish the time that significant failures are first observed (this establishes one data point for the Weibull plot). Data for the same type of PWSCC failure from other plants are used to establish an average slope for the Weibull plot. This allows the analyst to make estimates of future tube failures from PWSCC for cases where plant-specific data are insufficient to reliably define the slope of the Weibull plot. However, the predictions are less accurate.

Plant inspection data from several plants for PWSCC failure in the hot leg roll transitions and U-bends and at the tube support plates have been compiled and plotted using a Weibull distribution (see Figure 4). These plants have Westinghouse-type recirculating steam generators with

low-temperature mill-annealed tubing. Data from only those plants with greater than 1.0% cumulative failure by the final reported inspection and more than three inspection events exhibiting degradation were used. These examples are illustrative of the scatter that is to be expected in plant inspection data for PWSCC degradation. The data for each plant lie approximately on straight lines. The slopes of these lines (each representing the PWSCC failure history at a specific location, and for a specific plant) were compared. While the intercepts of these lines vary considerably (representing differences in the characteristic time for the failure process), all the slopes, regardless of plant or PWSCC type, are similar. As a result, all sets of data can be approximately represented by lines with slopes of b = 2.66. This value was determined by a least squares fit to the data from the plant for which the most reliable information was available. As shown in Figure 4, the points for the other sets of data are sufficiently close to being parallel to the characteristic line with the slope b = 2.66 that this slope can be used to make short extrapolations to predict the future rate of degradation at these plants. Because of the uncertainty in the slope of the Weibull distribution for each individual plant, projections over longer times have greater uncertainty.

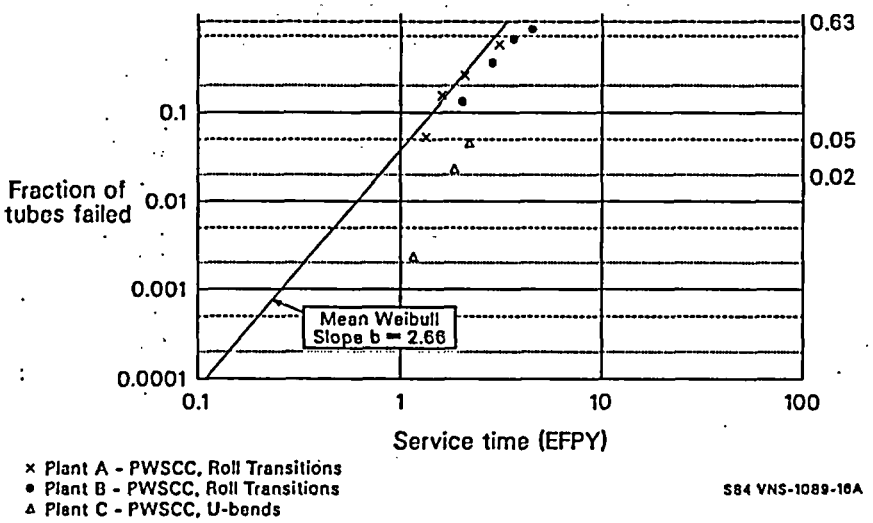

Figure 4. Weibull plot of PWSCC failures.

The data shown in Figure 4 are for PWSCC at a number of steam generator locations. They are believed to be for plants that have similar tubing material and primary water chemistry so that the plants are all within the same PWSCC population. However, this has not been verified by any detailed review of material and operating specifications. In order to obtain maximum accuracy for predicted failure rates, it would be preferable to compile more extensive data for individual steam generator locations susceptible to PWSCC, from plants as similar as possible to the plant to be analyzed. This is the recommended procedure where sufficient data from comparable plants are available. For purposes of illustration, the mean slope given in Figure 4 can be used for approximate analysis of the anticipated rate of steam generator degradation by PWSCC, for any PWSCC type, at plants in the same PWSCC population if at least one inspection data point for PWSCC is available.

5. REMEDIAL MEASURES FOR PWSCC DAMAGE

Remedial measures applied to prevent or slow the initiation of PWSCC depend on eliminating high tensile stress or reducing hot leg temperature. Specific examples of remedial measures are as follows.

5.1 Roll Transition PWSCC

Two remedial techniques have been field-demonstrated and tested as being effective at retarding the initiation of PWSCC in the roll transition region. Both Rotopeening and shot peening employ a technique whereby hard spheres impact the inside of the tube and impart a compressive stress on the tube inside surface. Because PWSCC requires a tensile stress for crack initiation, the peening techniques prevent crack initiation by this redistribution of tube residual stresses, thus reducing the future failure rates for this type of PWSCC. Figure 5 shows the hypothetical effect of shot peening on a Weibull distribution of PWSCC at the roll transition region. Shot peening is considered appropriate for implementation on operating plants, while both Rotopeening and shot peening are acceptable for implementation on preoperational units. Peening is not considered effective for preventing growth of existing cracks in operating steam generators, but it is effective in preventing formation of additional cracks.[4]

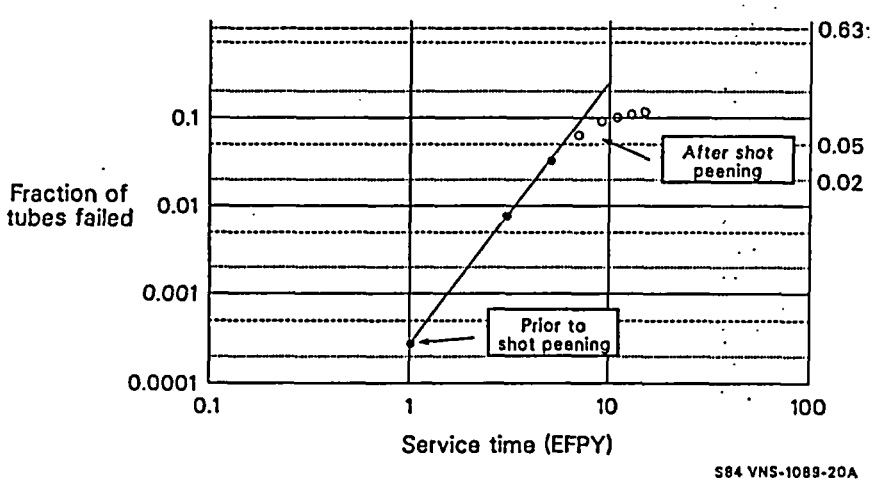

Figure 5. Weibull plot showing reduced rate of PWSCC failures at roll transitions after shot peening.

5.2 U-Bend PWSCC

One field-demonstrated remedial technique has been tested as being effective in retarding the initiation of U-bend PWSCC: an in situ stress relief performed on the row 1 and row 2 U-bends either before plant startup or after a limited period of operation. This method employs a short time, high temperature heat treatment to reduce residual stresses due to forming of these tight-radius U-bends.[4]

5.3 PWSCC at Dents

Local stress relief of tube/tube support plate intersections has been used on a trial basis at one U.S. plant in order to prevent further PWSCC at dents at these locations. Global stress relief of the entire steam generator may also be effective, although no field testing of this method has been conducted. Treatments of this type will be effective only if further denting is prevented. When denting is progressing even very slowly (and dents are still small) the tubing will have stresses equal to the material yield stress. This stress level is sufficient to cause rapid PWSCC.

Reduction in hot leg temperatures may significantly reduce the PWSCC damage rate at all three susceptible sites. The only measures that have been developed to remediate existing PWSCC are sleeving and electroplating. Sleeving has been used to repair tubes that have experienced degradation by other mechanisms. Electroplating with nickel has been used on a trial basis at a plant in Belgium. Details of these measures are presented in References 1 and 2.

6. LIFE ASSESSMENT PROCEDURE FOR STEAM GENERATORS

This section briefly summarizes an overall procedure for life assessment of steam generator tubes based on the PWSCC model presented in this paper. Although this paper discusses only the PWSCC mechanism, the procedure presented here is general enough that it can be applied to other degradation mechanisms active in steam generator tubes. The procedure consists of the following five steps.

Step 1--Characterization of Steam Generator Construction. In order to make the most accurate possible projections of steam generator reliability and remaining life, it is necessary to establish as much information about the construction and operating conditions for the steam generator as can be obtained. This information allows the experience of the steam generator being analyzed to be compared with that of other similar units. The information includes a general description of the steam generator, including manufacturer, model number, and date of commercial power operation. The information also includes the data on tubing and tube support design, material, and fabrication specifications. For example, important tube data consist of number of tubes, tube dimensions, mill-annealing temperatures, grain size, yield strength, expansion method and depth, and tube bending method.

Special procedures for improving the performance of steam generator tubing or for mitigating the consequences of failures have been applied to a number of plants, particularly those that were not put into service until the 1980s. Examples of such modifications are peening of hot leg transitions, and preventive plugging of row 1 U-bends. These modifications can have a profound influence on the anticipated tubing failure rates for a given steam generator. Expected steam generator performance and the method of analysis to be used depend on when such measures were applied.

Step 2--Characterization of Operating Conditions. The operating conditions that are most important to the determination of steam generator tubing performance are temperature and water chemistry. Normal operating temperatures are slightly different from plant to plant. Because of the

high activation energies of some degradation mechanisms, even relatively small changes in temperature can have significant effects on tube life. Therefore, hot and cold leg temperatures during normal operation for each plant should be determined as closely as possible. Characterization of the secondary water chemistry should include normal quality in terms of pH, concentration of treatment chemicals, average concentrations of impurities, and any history of significant upsets, such as condenser leaks, during which water quality deviated significantly from normal.

Step 3--Probable Degradation Mechanisms. Characterization of steam generator construction and operating conditions will allow a given plant or steam generator to be classified with other plants with similar characteristics. This will allow projections to be made of the most probable degradation mechanisms that will occur in the generator. Identification of the most likely degradation mechanisms will assist in the interpretation of tube inspections so that the most accurate determination of present steam generator condition can be made. Early projections of steam generator life limits can also be guided by the experience from similar plants with longer service histories.

Step 4--Review of Tube Inspection Results. The basic source of data for determination of current steam generator condition and tube failure experience is the results of periodic inservice inspections. Such data are available for all operating steam generators. However, the number of tubes inspected and the reliability of the identification of degradation mechanisms detected will be quite variable from plant to plant. For plants that have experienced few tube failures, only a small percentage of the tubes are inspected at each outage. Classification of defects observed during inspections is difficult until enough failures of a given type have been observed to establish a pattern to guide the analyst. Thus, as discussed in previous sections, the reliability of data when only a small fraction of one percent of the tubes have failed is often questionable. For these reasons, analysis of tube inspection data should include comparison of trends with those expected based on the experience of similar older plants, and review of raw data as well as compilations of numbers of tubes failed. Such reviews will help to ensure the reliability of statistical projections for PWSCC failures using the Weibull distribution method presented in Section 4. Methods for projection of tube failures caused by other degradation mechanisms are presented in Reference 2.

Step 5--Potential Life-Limiting Degradation Mechanisms. For each degradation mechanism observed in a steam generator, an analysis should be carried out as prescribed in Reference 2 to project the future rate of tube failures. The overall condition of the generator and the future progression of its degradation as a result of all active degradation mechanisms can be calculated from the predicted failure distributions for the individual mechanisms using probability theory for dependent processes as described in Reference 2. In most cases, the life of the generator will be determined primarily by one or two degradation mechanisms. When these have been identified, particular attention should be paid to the analysis of these mechanisms because the accuracy of the overall life projection will be almost exclusively determined by the accuracy of the projections of degradation from these mechanisms.

In addition to analyzing degradation mechanisms that have been observed in a given generator, the analyst should use the results from similar plants

to predict what additional types of degradation will be observed in the future. Frequently, the first mechanism of degradation observed will not determine the overall life of the generator. Degradation mechanisms observed early in the life of the generator may be limited to a small percentage of the tubes, may be amenable to remedial measures, or may progress more slowly than degradation mechanisms first observed at a later time. Therefore, overall life assessment must always be at least qualitatively based on overall industry experience.

7. CONCLUSIONS AND RECOMMENDATIONS

Tensile stress, mill-annealing temperature, and operating temperature are the main parameters determining the rate of PWSCC damage. Roll transitions, irregular transitions at U-bends, and dented tubes are the most susceptible sites for PWSCC damage. The model presented in this paper can be used to accurately estimate the rate of PWSCC damage. However, improved information on the stress and temperature dependence of the PWSCC rate is needed for more accurate prediction of PWSCC at locations with lower tensile stresses and temperatures. Improved information on the effects of primary water chemistry on the PWSCC rate is also needed for more accurate prediction.

A Weibull distribution may be successfully used to predict future PWSCC failures if inspection results are documented with sufficient details regarding the degradation mechanisms causing the failures. However, in many cases, degradation mechanisms are not identified in inservice inspection reports. This makes it difficult to perform meaningful statistical analysis of tube failure data using the method presented in this paper. This is also true for methods for analyzing other degradation mechanisms as discussed in Reference 2. It is recommended that the inspection report identify the probable degradation mechanism for each plugged tube and each reportable indication. It is also recommended that the inspection report include a brief history of steam generator operation.

The procedure presented in this paper can be used to predict the time and site of cracking and to identify the possible degradation mechanism responsible for cracking. This information can be used to optimize inservice inspection methods and schedules. The procedure can also be used to interpret service performance. Use of the procedure will assist in identification and evaluation of potential remedial measures, and can ultimately improve the reliability and the safety of steam generators.

REFERENCES

1. V. N. Shah and P. E. MacDonald, editors, Residual Life Assessment of Major LWR Components - Overview, Volumes 1 and 2, NUREG/CR-4731, EGG-2469, Volume 1 - June 1987, Volume 2 - November 1989.

2. D. B. Lowenstein, A. P. L. Turner, S. R. Ward, and J. A. Gorman, Life Assessment Procedures for Major LWR Components, Volume 4: PWR Steam Generator Tubes (Draft), NUREG/CR-5314, EGG-2562, Volume 4 (Draft), November 1989.

3. O. S. Tatone and R. S. Pathania, "Steam Generator Tube Performance: Experience with Water-Cooled Nuclear Power Reactors During 1982," Nuclear Safety, 26, 5, September-October, 1985, pp. 623-639.

4. E. S. Hunt and J. A. Gorman, Status and Suggested Course of Action for Nondenting-Related Primary-Side IGSCC of Westinghouse-Type Steam Generators, EPRI NP-4594-LD, May 1986.

5. "Preventing Tube Degradation in Japan," Nuclear Engineering International, 30, 365, February 1985, pp. 43-44.

6. E. P. Morgan, "Review of U-bend Cracking as a Result of Tube Denting," in Workshop Proceedings: U-Bend Tube Cracking in Steam Generators, EPRI WS-80-136, June 1981.

7. "EDF Mystified by Widespread Tube Denting in Newer Steam Generators," Nucleonics Week, Nov. 9, 1989, p.1.

8. Licensee Event Report, Three Mile Island, Unit 1, Defective OTSG Tubes, 5-31-85, LER No. 7-1.

9. S. L. Harper et al., "The Role of Sulfur in the Corrosion of NSG," Proceedings of the Third International Symposium on Environmental Degradation of Materials in Nuclear Power Systems - Water Reactors, The Metallurgical Society, 1988, pp. 457-463.

10. P. H. Berge, H. D. Bui, J. R. Donati, and D. Villard, "Residual Stresses in Bent Tubes for Nuclear Steam Generators," Corrosion-NACE, Vol. 32, No. 9, September 1976, pp. 357-364.

11. S. Yashima et al., "Stresses of Steam Generator U-tubes Affecting Stress Corrosion Cracking," ASME, Paper No. 82-NE-5.

12. C. O. Rudd, Residual and Applied Stress Analysis of an Alloy 600 Row 1 U-Bend, EPRI-NP-5282, September 1987.

13. C. O. Rudd, "A Review of Nondestructive Methods for Residual Stress Measurement," Journal of Metals, July 1981, pp. 35-40.

14. Dominion Engineering, Proceedings: 1987 EPRI Workshop on Mechanisms of Primary Water Intergranular Stress Corrosion Cracking, EPRI NP-5987M, September 1988.

15. EPRI/SGOG Workshop on Primary Side Cracking, St. Petersburg Beach, Florida, December 1985.

16. R. Bandy and D. Van Rooyen, "Initiation and Propagation of Stress Corrosion Cracking of Alloy 600 in High Temperature Water," in Proceedings of the International Symposium on Environmental Degradation of Materials in Nuclear Power Systems - Water Reactors, p. 763, The National Association of Corrosion Engineers, Houston, Texas, 1984.

17. A. A. Stein and A. R. McIlree, "Relationship of Annealing Temperature and Microstructure to Primary Side Cracking of Alloy 600 Steam Generator Tubing and the Prediction of Stress Corrosion Cracking in Primary Water," in Proceedings of the Second International Symposium on Environmental Degradation of Materials in Nuclear Power Systems - Water Reactors, p. 47, American Nuclear Society, La Grange Park, Illinois, 1986.

18. W. Weibull, "A Statistical Function of Wide Applicability," J. Appl. Mech., 18, 1951, pp. 293-297.

19. W. Weibull, "A Statistical Representation of Fatigue Failures in Solids," Acta Polytech., Mech. Eng. Ser., 1 1949.

20. J. N. Berrettoni, "Practical Applications of the Weibull Distribution," American Society for Quality Control Convention Transactions, 1962, pp. 271-285.

21. C. Lipson and N. J. Sheth, Statistical Design and Analysis of Engineering Experiments, New York: McGraw-Hill, 1973.

COMPREHENSIVE AGING ASSESSMENT OF CIRCUIT BREAKERS AND RELAYS FOR NUCLEAR PLANT AGING RESEARCH (NPAR) PROGRAM PHASE II

J.F. Gleason

Wyle Laboratories
Huntsville, Al 35807

ABSTRACT

This paper discusses the research being sponsored by the Office of Regulatory Research, Nuclear Regulatory Commission as part of the Nuclear Plant Aging Research (NPAR) Program. It reports on the Phase II tasks which are to resolve resolve technical safety issues related to the aging degradation of circuit breakers and relays. The objectives of Phase II are to: (1) identify and characterize aging and service wear effects of circuit breakers and relays which, if unchecked, could impair plant safety; (2) identify and develop methods of inspection, surveillance, and condition monitoring, and of evaluating residual life of circuit breakers and relays, which will assure timely detection of significant aging effects prior to loss of safety function; (3) evaluate the effectiveness of storage, maintenance, repair and replacement practices in mitigating the rate and extent of degradation in circuit breakers and relays caused by aging and service wear.

INTRODUCTION

Relays and circuit breakers are important nuclear power plant safety related equipment which are susceptible to degradation with time. Methods are available to detect and mitigate aging degradation and thereby minimize its impact. This paper describes the background of the research strategy, describes the objectives of the research and defines the testing being performed on naturally aged and degraded equipment in order to determine the methods most effective for detection of age degradation.

BACKGROUND

The Nuclear Plant Aging Research (NPAR) Program is intended to resolve technical safety issues related to the aging

degradation of electrical and mechanical components, safety systems, support systems, and civil structures used in commercial nuclear power plants. The NPAR Program is based on a phased approach to research.

The Phase I study- NUREG/CR-4715,BNL-NUREG-52017 AN,RV, "AN AGING ASSESSMENT OF RELAYS AND CIRCUIT BREAKERS AND SYSTEM INTERACTIONS," identified relays and circuit breakers used in nuclear plants, failure mechanisms of these relays and circuit breakers, that some failure mechanisms are age related, and that failure of safety systems is possible from relays and circuit breaker failures if adequate maintenance and testing are not performed. It also proposed some potential inspection, surveillance and condition monitoring methods to detect significant aging methods prior to loss of safety function. In the Phase I evaluation, it was decided that a Phase II assessment is warranted.

OBJECTIVES

The objectives of Phase II are to: (1) identify and characterize aging and service wear effects of circuit breakers and relays which, if unchecked, could impair plant safety; (2) identify and develop methods of inspection, surveillance, and condition monitoring, and of evaluating residual life of circuit breakers and relays, which will assure timely detection of significant aging effects prior to loss of safety function; (3) evaluate the effectiveness of storage, maintenance, repair and replacement practices in mitigating the rate and extent of degradation in circuit breakers and relays caused by aging and service wear.

The relays and circuit breakers which are being reviewed are:

- **Protective Relays** - they protect plant power systems from effects of electrical overloads, faults and transients
- **Auxiliary Relays** - actuated by protective relays for high current applications
- **Control Relays** - used in nuclear protective system logic
- **Timing Relays** - delays operating function until initiating condition has existed for a selected time
- **Electronic Relays** - solid state device used in protective or control relay applications
- **Molded Case Circuit Breakers** - 480 volt and below; they are the most prevalent, used to supply individual circuits and feeders for low voltage AC and DC distribution
- **Metal Clad 480 volt Circuit Breakers** - used in the power supply to 480 volt distribution buss as well as to feed individual circuits for major safety related equipment such as medium sized motors

o **Metal Clad 4KV Circuit Breakers** - these are housed in large metal cabinets and are used for main circuit breakers for large safety related equipment and the emergency power busses

TECHNICAL ISSUES

Within the last ten years, many examples of safety significant events involving circuit breakers and relays have been reported. Some examples are:

- o Failure of circuit breakers and relays can lead to loss of mitigating capacity and inadvertent actuation of safety related systems(reported in IE Notice 85-82).
- o Age related failure of circuit breakers has resulted in an Anticipated Transient without SCRAM (ATWS) event (reported in IE Bulletin 83-01).
- o Failure of circuit breakers to isolate faults can cause significant damage to associated equipment, increase the chance of fires and lead to loss of multiple systems.
- o Failure of protective relays to detect abnormal voltage conditions can allow reduced voltage conditions to exist thus affecting equipment operability and prevent diesel generator loading.
- o Counterfeit and refurbished molded case circuit breakers may exist in safety related applications (reported in NRC Bulletin 88-10 and IE Notice 88-46).
- o Commercial grade circuit breakers have been mistakenly used as seismically qualified (reported in NRC Bulletin 88-10 and IE Notices 83-19, 87-66, 88-14).
- o Service life of relays has been shorter than expected (reported in IE Bulletin 84-02 and IE Notices 81-01, 82-04, 82-13, 84-20).
- o Relays used in low current applications have degraded due to contact oxidation and resulted in a reactor SCRAM (reported in NRC IN 88-98).
- o Older plants may contain older vintages of relays which were more seismically vulnerable than newer models (reported in NRC IN 88-14).

The recent Santa Cruz/ San Francisco Earthquake of October 17, 1989 has vividly shown the consequences of strong seismic motion on seismically vulnerable structures and equipment. The importance of successful seismic performance of all safety

related structures and equipment of nuclear power plants, including the circuit breakers and relays, is obviously an industry and public concern. The successful operation of the nuclear plants near this recent earthquake was reported with great relief by many news sources. The continued vigilance on assuring the operability status, seismic performance and other Design Basis Event performance of circuit breakers and relays are the main issues of Phase II.

INSPECTION, SURVEILLANCE and CONDITION MONITORING

The research effort has reviewed and is verifying improved inspection, surveillance and condition monitoring (ISM) methods. Testing of naturally aged and degraded circuit breakers and relays is being performed. Eighteen ISM methods are being evaluated. They include: Vibration/Acoustics, Surge Current Comparison, Pick-up/Drop-out voltage, Inrush/Holding current, Current Signature Analysis, Operability, Set point Drift, Timing tests, Magnetic Flux Monitoring, Contact/coil Resistance, High Potential Test, Insulation Resistance, Infrared Thermal Scanning, Infrared Pyrometry, On-contact Temperature measurement, Ion Detection, Lubrication, Visual inspection and Root cause Failure Analysis.

Some techniques are intrusive, requiring disturbing of leads, etc.; the following are the most encouraging in that they are non-intrusive, can be used with all types of circuit breakers and relays, data can be obtained rapidly, trended and computer analyzed:

o **Vibration/Acoustics** - preliminary tests have shown that circuit breakers and relays have distinct and repeatable vibration signatures, and aged and refurbished devices experience differences in amplitude and frequency. Many variables for vibration signature monitoring are being investigated in order to evaluate the practicability of the method. Some of the variables are:

- o Changes in frequency pattern caused by aging, using specimens with different aging
- o Changes in acceleration pattern caused by degradation, using purposely degraded as well as naturally degraded specimens
- o Location where vibration signature is measured
- o Method of attachment of vibration signature accelerometers

o **Infrared Thermal Scanning** - this technique has shown differences in thermal signatures in aged devices. Two methods of

making infrared temperature measurements are being evaluated. they are scanners and pyrometers. Many variables of these temperature monitoring methods are being investigated in order to evaluate practicability of each method. Some of the variables are:

- o Temperature changes caused by aging, using specimens with different aging
- o Temperature changes caused by degradation, using purposely degraded as well as naturally degraded specimens
- o Effect of the infrared emissivity of the specimen to cause differences in temperature measurements
- o Effect of covers on obtaining significant temperature information
- o Effect of viewing angles since views normal to equipment may not always be available
- o Effect of distance to the target
- o Instrument sophistication
- o Accuracy of measurement

Additional tasks being performed in this Phase II research include (1) in-situ testing at plants to confirm analyses and laboratory results and to provide estimates of cost effectiveness and practicability of application; (2) evaluation of the role of maintenance in mitigating age effects and (3) application and /or development of methodology which will provide a service life prediction and define surveillance and inspection intervals.

CONCLUSION

The research results will be utilized to identify inspection, surveillance and condition monitoring needs of circuit breakers and relays to assure safety of aged nuclear power plants. Inspection and surveillance intervals will be defined. Service life parameter limits and service life prediction methodology are to be provided. Recommendations will be made to modify or develop regulatory guides and may provide additional information to supplement existing NRC bulletins on counterfeit and refurbished circuit breakers.

AGING ASSESSMENT OF AUXILIARY FEEDWATER SYSTEMS[1]

D. A. Casada

Oak Ridge National Laboratory
Oak Ridge, Tennessee

Abstract

A study of Pressurized Water Reactor Auxiliary Feedwater (AFW) Systems has been conducted by Oak Ridge National Laboratory (ORNL) under the auspices of the Nuclear Regulatory Commission's Nuclear Plant Aging Research Program. The study has reviewed historical failure experience and current monitoring practices for the AFW System. This paper provides an overview of the study approach and results.

I. Introduction

The Phase I aging study of the AFW System has focused on a) a review of historical failure data for AFW System components and b) a detailed review of the AFW System design and operating practices at a plant owned by a cooperating utility. These two aspects of the study provide indication of the historical sources of problems for AFW Systems and the extent to which the problem areas are being covered by current monitoring/maintenance programs.

II. AFW System Design and Functions

Due to variations resulting from a number of factors, including numbers of steam generators and their design, evolving regulatory requirements, design changes made in response to identified problems, and designer preferences, there is not a standard system design. As a result, even two plants with similar Nuclear Steam Supply Systems which are constructed during the same time frame may have significant differences in AFW System design. While there is no standard design, the three loop system depicted in Figure 1 can be used as a basis for

[1] Research sponsored by the Office of Nuclear Regulatory Research, U.S. Nuclear Regulatory Commission under Interagency Agreement 1886-8082-8B with the U.S. Department of Energy under contract DE-AC05-84OR21400 with the Martin Marietta Energy Systems, Inc.

identifying certain features which are representative of those normally included in the AFW System design.

The AFW System's principal role is to support removal of stored and decay heat from the Reactor Coolant System (RCS). The Steam Generators act as a heat sink during both normal operation and following reactor trips. During normal operation, the Main Feedwater system provides feedwater to the SGs, where it is converted to steam and then used to drive the main turbine and provide process steam for various plant equipment. During normal power operation, the AFW System is in standby (except when in test). Following an operating transient or accident, as well as during routine startups and shutdowns, the AFW System is used to provide a safety related source of water to the Steam Generators. The water delivered by the AFW System is heated and vaporized in the Steam Generators. Steam thus generated can be released to atmosphere through the safety related Main Steam Safety Valves or Atmospheric Dump Valves, or to the atmosphere and/or condenser through non-safety related Steam Dump Valves.

The AFW System must not only support the heat removal, but also allow the heat removal to take place in a controlled manner, even under design basis accident conditions. There are four general functional requirements of the AFW System:

- Provide flow to intact SGs following design basis transients/accidents
- Isolate flow to faulted or ruptured SGs
- Maintain a liquid barrier between the Reactor Coolant System and the environment following design basis accidents to ensure that any primary to secondary tube leakage is "scrubbed" before release
- Support normal startup and shutdown evolutions

As noted, the AFW System is used, at most plants, in support of normal plant startup and shutdown. However, this is not the primary basis for its design. Rather, it is specifically designed for the mitigation of the consequences of design basis transients and accidents, including Loss of Main Feedwater, Main Feed Line Break, Main Steam Line Break, Small and Large Break Loss of Coolant Accidents, Steam Generator Tube Rupture, and others. In addition, proper functioning of the AFW System is critical to the ability of a plant to deal with an important accident condition, Station Blackout, which has not been historically treated as a design basis accident.

Pump Suction Sources

Most plants have a dedicated storage tank, commonly designated as the Condensate Storage Tank (CST), that is used to maintain a reserve inventory of high quality water for the AFW pumps. The inventory available for the AFW pumps may actually come from multiple sources, depending upon plant design. For purposes of this discussion, the normal source(s) of water will be referred to as the CST. Plants which are under Standard Technical Specifications have a designated inventory that must be maintained in the CST during Modes 1-3. The CST

is safety grade, seismically qualified at some plants, but not at others. Normal system alignment would have the suction flow path from the CST to the AFW pumps open, and in fact, manual valves in the suction flow path may be required to be locked open.

The majority of plants also include a backup source of water, normally from the plant's ultimate heat sink system which is commonly called the Emergency Service Water (ESW) System. Depending upon plant design, the ESW may be the only safety grade source of water (for example, if the CST is non-safety grade). Switchover from the CST or other normal supply sources to the ESW may be either automatic or manual. Low suction pressure is the normal switchover condition monitored for plants including automatic switchover. Some plants use suction pressure transmitters to provide AFW pump tripping under low suction pressure conditions (it should be noted that this trip function has been removed at several plants, and replaced with an alarm only to avoid spurious tripping). Even for plants which do not use automatic switchover, low suction pressure instrumentation may furnish main control board indication and annunciation to provide the operator with an indication of the need for suction transfer. CST or other normal water source level instrumentation also provides the operator with suction status. For plants with manual switchover only, some provide totally remote switchover capability, while others require local valve realignment.

Check valves are usually included in the normal suction supply lines. These valves are depended upon to prevent flow reversal into the CST in the event that ESW must be used as the suction source. In some cases, where the normal suction sources are non-safety grade, the suction check valve forms the boundary between safety and non-safety grade portions of the AFW System.

Pumps

The Figure 1 flow diagram indicates two motor driven and one turbine driven pump. This is the most typical configuration; however, there are a number of pump combinations at operating plants. In addition to variations in the number of pumps per unit, the types of drivers vary. There are various combinations of motor, turbine, and diesel driven pumps in the AFW pump population.

The motor driven pumps receive their power from emergency busses. Pump breaker closure not only starts the associated pump, but auxiliary contacts for the breaker are often used to provide control signals to other AFW System features.

Steam for the turbine driven pumps is supplied by one or more (typically two) SGs. There are a number of steam supply control arrangements. Some plants start the turbine by opening a normally closed Trip & Throttle (T&T) valve, located immediately adjacent to the turbine. Other plants leave the T&T valve normally open and start the turbine by opening one or more upstream isolation valves. Some plants have pressure control valves in the steam supply line which limit steam pressure available to the turbine, while at other plants, full steam pressure is available to the turbine (less line and governor losses). Turbine speed, and therefore pump flow, is controlled by turbine governor valve position, which in turn receives control signals which are typically based on turbine speed

and, for some controllers, a flow or other differential pressure sensor (such as steam supply to pump discharge differential pressure).

Some plants include non-safety related pumps that are similar in function to the AFW pumps. Where available, these pumps are used in support of normal startup/shutdown (in some cases, they are referred to as Startup Feed Pumps). While these pumps have not been considered in this study, their availability can have a substantial impact upon the service wear of AFW pumps and other AFW equipment, since the AFW pumps would not be routinely used for startup/shutdown purposes. The non-safety related pumps can also substantially enhance the availability of post-accident secondary cooling. As an example, following the June 1985, Davis-Besse loss of feedwater and AFW, feed flow to the SGs was ultimately restored by use of a startup feed pump.

Pump Discharge and Flow Distribution

Pump discharge lines include flow paths to the SGs and minimum recirculation flow paths. The recirculation flow may be controlled by orifices, line size, control valves, or a combination of these means. Some plants include both a minimum recirculation flow path and a full flow test loop, both of which recirculate flow to the CST or other suction source. Other plants use a common flow path for both, while yet others do not have a full flow test loop, but only a mini-flow recirculation path.

Recirculation flow paths, both of the full flow and the mini-flow variety, may include valves which automatically isolate under certain conditions. For instance, plants with full flow recirculation test loops typically include automatic isolation valves which close in the event that an automatic start signal occurs. Other plants provide for automatic isolation of the mini-flow path in the event that the associated pump is the only available pump or if delivered flow to the SGs is sufficient to provide what has been determined to be adequate for pump protection.

Valving between the pumps and the SGs provides for control of individual pump flow, flow to specific SGs, and a means of preventing backleakage from the SGs or from Main Feedwater. The arrangements of valves between the pump discharge and the SGs vary considerably in terms of numbers, operator types, layout configuration, control signal sources, and normal standby position.

Some plants use automatic discharge pressure control valves for motor driven pumps to provide pump runout protection. These valves may be either normally closed or open, and receive a control signal following pump start. The valve control signal is normally geared toward maintaining discharge pressure or flow at a designated setpoint. The control setting may or may not be adjustable from the main control room. Other plants do not use automatic valve positioning to regulate individual pump flow/discharge pressure; rather, nonadjustable, fixed means, such as cavitating venturis, flow restricting orifices, or valves locked in a throttled position are utilized. For yet other plants, it is not clear, from Final Safety Analysis Report descriptions and other information available, what pump runout protection (other than operator action) is available.

Pump discharge line configurations normally allow more than one SG to be fed by each pump (although some two loop plants are arranged such that only one pump normally feeds one SG). All three loop plants are configured such that all three SGs are fed by all pumps, while most four loop plants are designed and normally aligned to allow feeding of all four SGs by a turbine driven pump and feeding of two SGs by each motor driven pump. Control of flow to individual SGs is provided by a variety of combinations. Motor, air, electrohydraulic, and solenoid operated valves are used as flow control devices. There are diverse control designs for the valves. Control valves at some plants are normally closed while corresponding valves are normally open at other plants. Those that are normally closed typically receive an open signal on associated pump start or AFW actuation signal. At some plants, the flow distribution valves automatically modulate to maintain a preset flow or SG level, while at other plants, the valves go to a full open or other fixed position and remain there unless repositioned by an operator.

The flow distribution valves may be used as a part of a faulted SG isolation system, a system which automatically detects and isolates any SG which is depressurized. This system supports the functions of both assuring that intact SGs can receive AFW flow as well as minimizing the adverse impact of feed or steam line breaks on the RCS and Containment. Other plants rely upon flow limiting devices, such as cavitating venturis, on a temporary basis following a faulted SG event, and ultimately upon operator action to detect and then to isolate flow to the faulted SG. Yet other plants depend solely upon operator recognition and isolation of the faulted SG, with no automatic break detection and isolation or fixed flow limiting devices available. It is important to note that the valves used in the AFW System to isolate flow are not normally seat leak tested, even if they are classified as containment isolation valves.

Some plants have dedicated AFW SG nozzles, while the AFW discharge lines at other plants connect with Main Feedwater piping upstream of the SGs. Various combinations of check valves and isolation valves are used to avoid backleakage of hot feedwater or steam into the AFW System. There are typically several check valves, and in some cases, closed isolation valves in series between the pumps and the SGs.

III. Failure Data Analysis Results

In order to gain some insights into the importance of various AFW System components from an historical failure perspective, reviews of failure data through 1986 for Westinghouse and Babcock & Wilcox plants from INPO's Nuclear Plant Reliability Data System (NPRDS)[2], the Nuclear Operations Analysis Center's Licensee Event Report (LER), and S. M. Stoller's Nuclear Power Experience (NPE) databases were conducted. Each record from the three databases was reviewed and combined to form a single ORNL database, thereby avoiding redundant entries while establishing a more thorough set of failure records. It should be recognized that even though the ORNL database is more comprehensive than any of the three sources individually, there is no doubt that there are still a considerable number of

[2]Plant specific information from the NPRDS database is proprietary. The results of the study are presented without identification of individual plants.

failures of AFW System components which are not included. Therefore, use of the data for certain purposes (such as absolute failure rate determination) would yield deceptive results. On the other hand, the failure data can be more useful for other purposes, such as relative comparisons of the failure rates of various component types.

Components were classified into five groups for this study: Pump Drivers, Valve Operators, Valves, Pumps, and Other. Information available from the three databases was reviewed for each failure record and the component group was assigned. Other parameters, such as the method of detection, the subsystem affected, and the extent to which the system was degraded as a result of the failure, were also assigned for each failure record. The data was then analyzed for trends and comparative evaluation. Examples and highlights of the results follow.

It was determined that the component group which contributed the most heavily to system degradation was Pump Drivers. Although there were more failures reported for both the Valve and Valve Operator groups, the system degradation associated with those groups was somewhat less due to the fact that the average impact of a valve or valve operator failure was less than that for a pump or pump driver. Figure 2 provides the numbers of failures and the system degradation associated with the different component groups. The Relative System Degradation indicated in Figure 2 is a measure of the overall impact of the associated failures, taking into account both the number of failures as well as the effect of each individual failure upon the system.

While most AFW System failures reported were detected by either programmatic monitoring (such as surveillance tests) or by routine observation (for example, noting valve stem leakage during an area walkdown), it was found that about 18% of the system degradation was detected during demand events (such as failure of a pump to start automatically in response to a valid start signal following a reactor trip). Figure 3 indicates the distribution of failure counts and system degradation associated with the three methods of detection.

Each failure record was reviewed to determine which subsystem was affected by the failure. The subsystems designated were: Turbine Driven Pump (TDP), Motor Driven Pump (MDP), Diesel Driven Pump (DDP), and Common (primarily includes common flow distribution components which affect more than one subsystem). The failure counts and system degradation associated with each subsystem type are summarized in Figure 4. The TDP subsystem was found to be responsible for half of the failure counts and more than half of the overall system degradation, in spite of the fact that there were fewer TDPs than MDPs in service at the plants included in the ORNL database (51 TDPs with 604 pump-years of service vs. 77 MDPs with 808 pump-years of service).

From Figure 2, it can be seen that Pump Drivers were responsible for about 37% of overall AFW System degradation. Further review of the Pump Driver failure records indicated that 73% of the Pump Driver related degradation (constituting 27% of overall system degradation) was associated with turbine drives. Figure 5 indicates the comparison of system degradation contributions from the different types of pump drivers. It is interesting to note that the two diesel drives in

the failure database which had a total of only 13 pump-years of service (less than 1% of the service life of all AFW pump drives in the failure database) caused 9% of the Pump Driver related degradation. This can be compared to motor drives, which had about 56% of the service life of all AFW pump drives in the failure database, but caused less than 20% of the Pump Driver related degradation.

Failures of turbine drives (including the turbine and its control system) were evaluated in detail to determine the specific sources of the failures. Figure 6 provides a summary of the failure sources. Note that over half of the turbine drive failures originated with the Instrumentation and Control and Governor Control aspects of the turbines. Furthermore, as indicated by Figure 7, almost one-third of the I&C/Governor Control failure related degradation was detected during demand events.

IV. Plant Monitoring Practices Review Results

A detailed review of the operating, maintenance, and surveillance procedures in use at a plant owned by a cooperating utility (Reference Plant) was conducted. The focus of this review was to determine how well potential sources of system degradation and failure were being monitored programmatically. As a part of this effort, the system design, physical layout, and controls were also reviewed in detail.

A number of areas were found in which failures could exist at the Reference Plant without being detected by the programmatic monitoring practices. The non-detectable failure sources covered a variety of areas, including mechanical, hydraulic, and electrical. The types of non-detectable failure sources found to be most prevalent were I&C related, including contacts, relays, limit switches, coincidence circuits, etc. It was also noted that several sources of degradation which would affect the ability of the system to perform under design basis conditions were not monitored periodically. Examples of non-detectable failures follow.

- Suction valves from Emergency Service Water (ESW) to the motor driven pumps are designed to automatically open if a low suction pressure condition exists. There are three suction pressure switches in the normal suction line. A low suction pressure condition, as detected by any two out of the three switches will, by design, cause the automatic transfer to occur. There are, therefore, three possible coincidences than can cause the transfer: A+B, A+C, and B+C. Only one of the three coincidences is periodically verified to cause the transfer. There are four sets of contacts that are not checked.

- The AFW System is needed to support cooldown and depressurization of the Reactor Coolant System to the point where the Residual Heat Removal (RHR) System can be placed into service. The steam generator pressure corresponding to the point where RHR can be placed into service is about 120 psig.

The turbine driven pump, which is driven from steam from one of two steam generators, is only tested when steam pressure is greater than 842 psig. It should be noted that this is consistent with the plant's Tech Specs.

- Steam Generator Blowdown Isolation Valves are designed to close automatically on AFW pump starting. There is no testing which verifies that the automatic closure occurs.

In the review of the Reference Plant procedures, it was found that the testing frequencies for system components varied substantially. For example, the trip & throttle (T&T) valve for the AFW turbine was found to be stroked over 40 times a year in conjunction with AFW System testing, while the AFW turbine's I&C /Governor Control system is checked once every 18 months, at best. It should be noted that the testing frequencies are largely dictated by the plant's Technical Specifications.

V. Findings and Recommendations

The results of the failure database and the Reference Plant reviews provided complementary indicators. There were indications from both reviews that I&C related areas were being the least well monitored. Historically, a significant fraction of AFW System failures that were detected during demand circumstances were I&C related. A large number of the failure or degradation sources that would not be detectable at the Reference Plant were also I&C related.

It was also found that the turbine driven pump subsystem, and more specifically, the turbine and its controls, were a significant source of system degradation historically. For the turbine, I&C/Governor Control failures were dominant.

When current testing practices are considered in conjunction with the historical failure data, it becomes apparent that the current monitoring programs are not optimized. The example of the imbalance in testing frequencies for the trip and throttle valve actuation and the turbine I&C/Governor Control system noted above becomes even more significant when the historical failure data is considered. Per Figure 6, over half of the turbine drive problems have been I&C /Governor Control related, while about 20% have been associated with the T&T valve. It should be noted that many of the T&T valve failures were attributed to wear in the valve linkage, which may be indicative of excessive testing.

Phase II of the AFW System study will focus on improved testing patterns. It is anticipated that restructuring of testing requirements to reduce testing that provides little or no confidence in the ability of the system to perform as required will be recommended. Recommendations related to the comprehensiveness of testing, both from the standpoint of ensuring that all necessary components and controls are checked, as well as from the standpoint of demonstrating design basis capability, are also expected.

In light of the significance of AFW turbine failures found in the review of the AFW System, a Phase I study of turbine drives (to include safety related

turbines at BWR plants as well as AFW turbines) will be undertaken. It is anticipated that this study will focus on the governor and control related areas.

Figure 1. AFW SYSTEM FOR A THREE LOOP PLANT

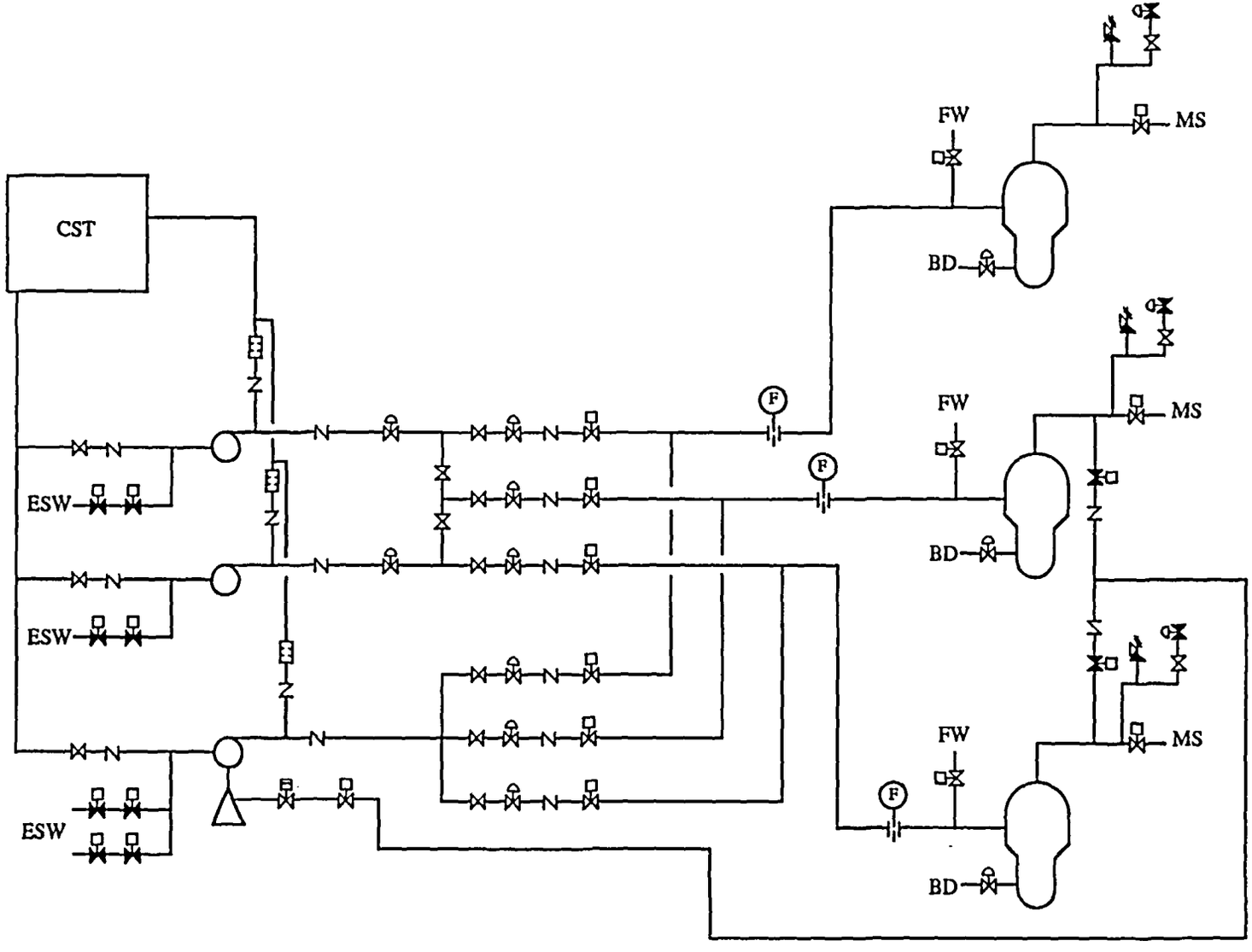

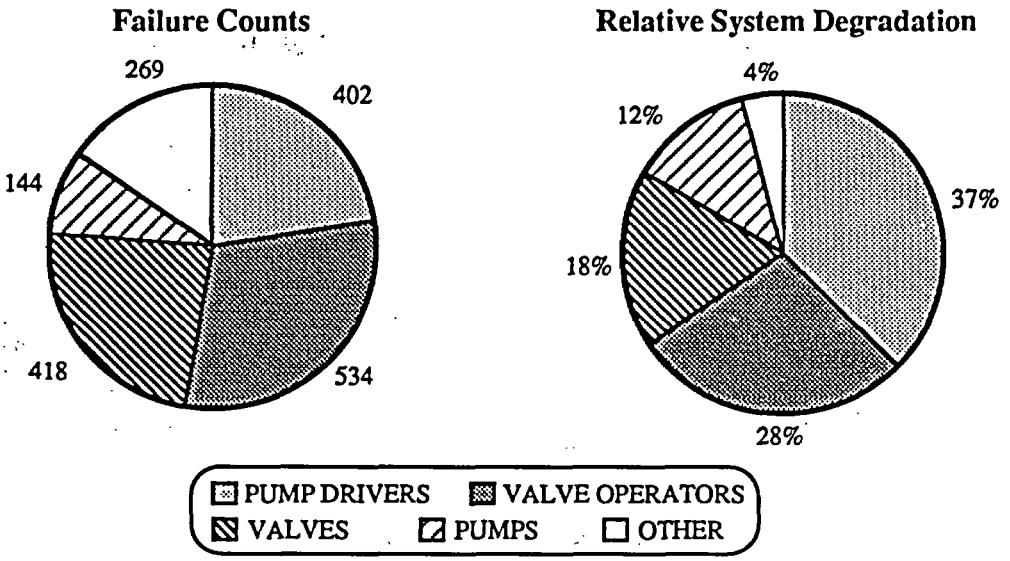

FIGURE 2. Failure Count and Relative System Degradation Distributions for AFW System Component Groups

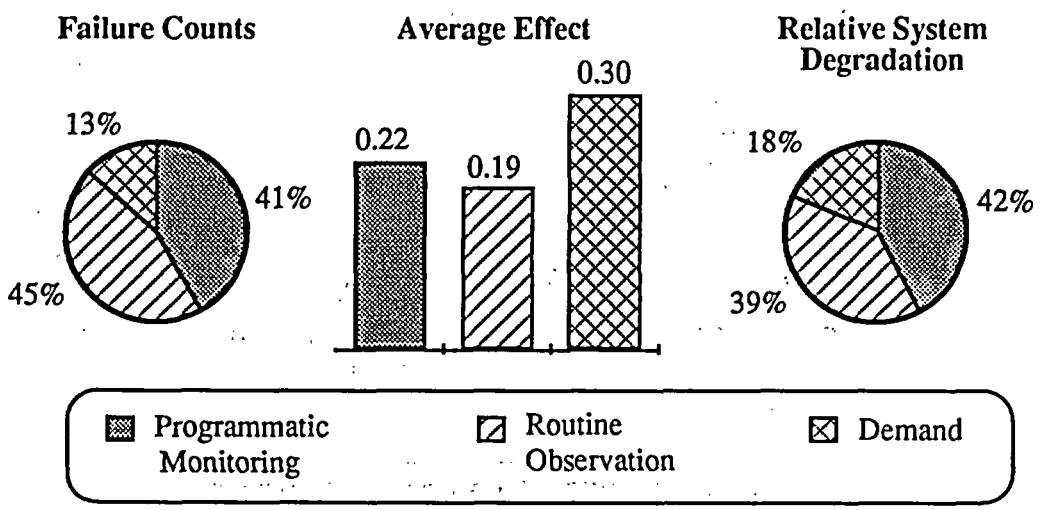

Figure 3. Method of Detection Summary - All Failures

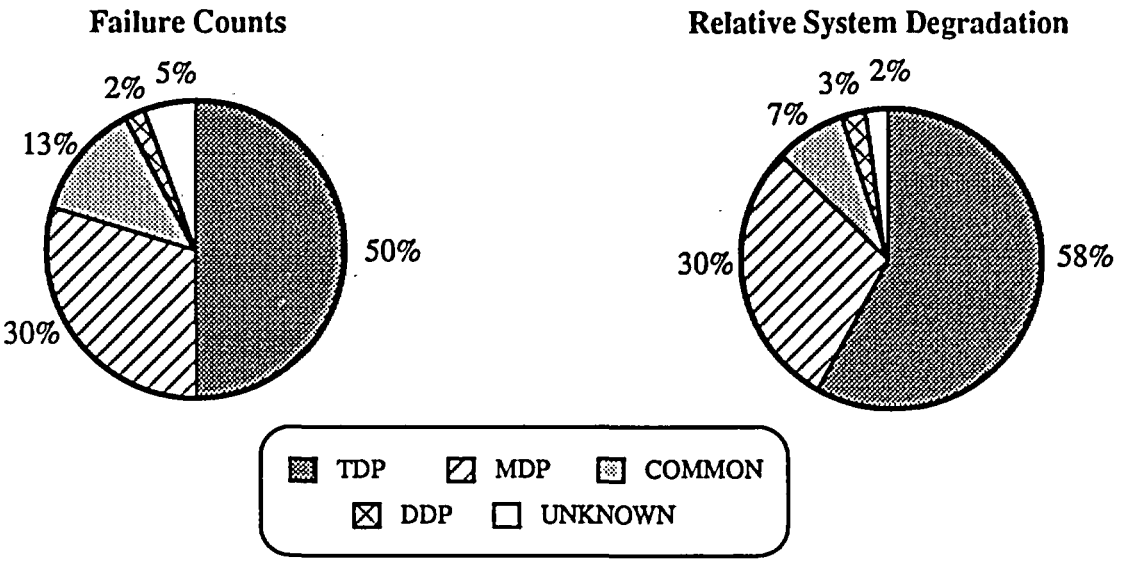

Figure 4. Failure by Subsystem Summary

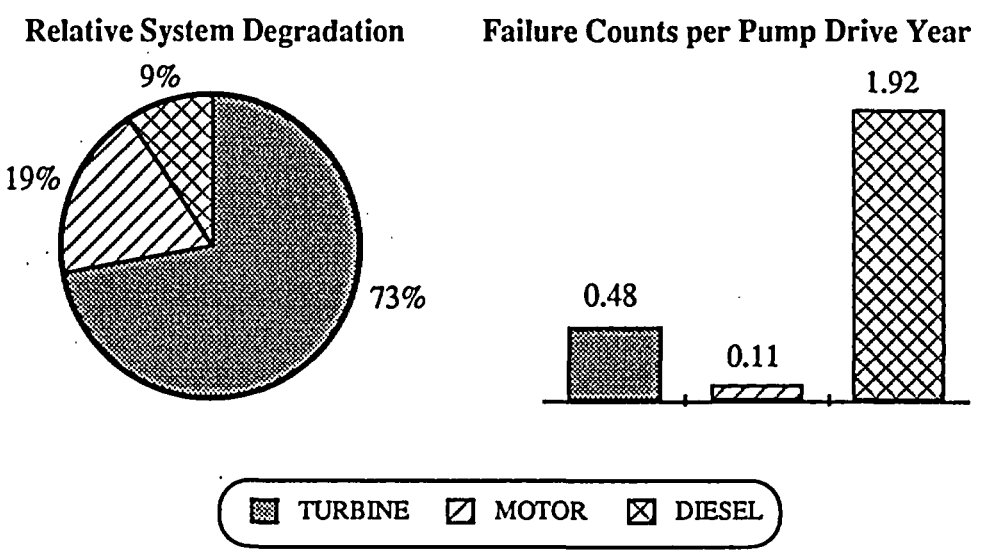

Figure 5. Pump Driver Summary

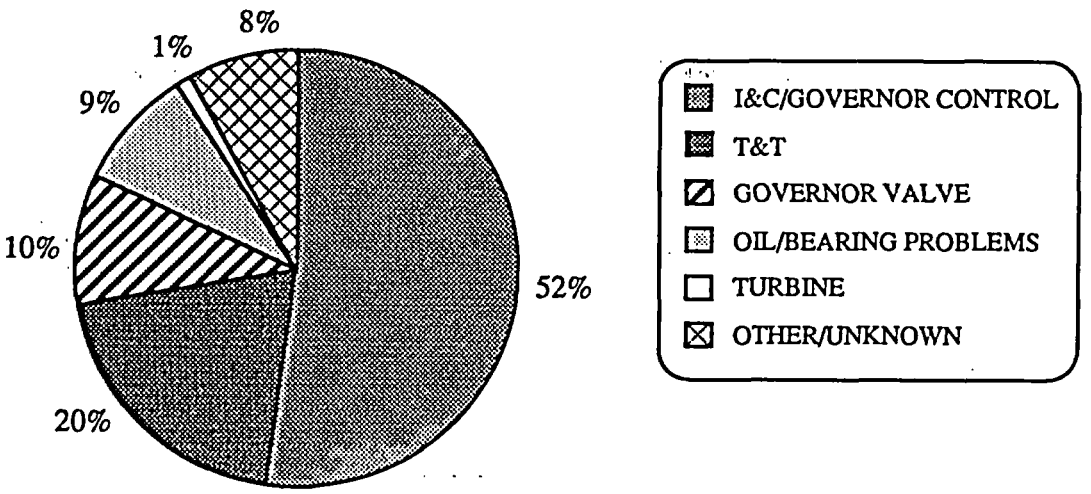

Figure 6. Sources of Turbine Drive Failures - Relative System Degradation

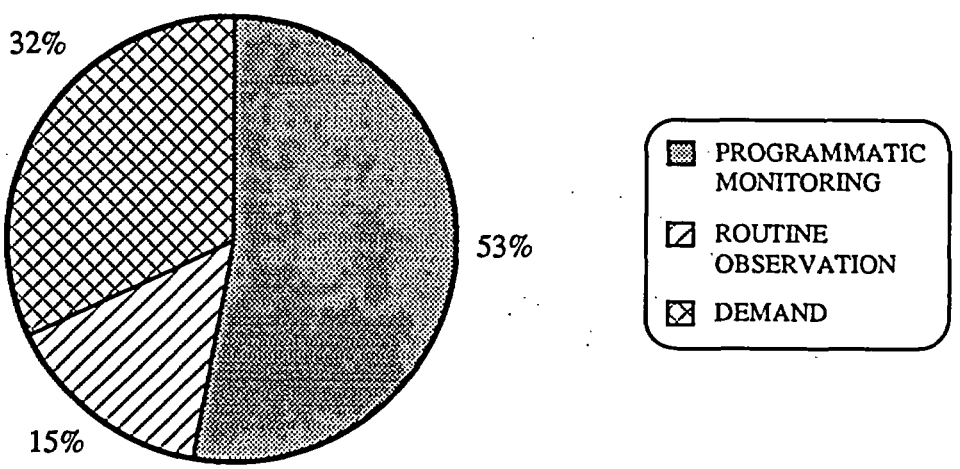

Figure 7. Turbine I&C/Governor Failure Summary by Detection Method - Relative System Degradation

INSTRUMENT AIR SYSTEM - AGING IMPACT ON SYSTEM AVAILABILITY[1]

M. Villaran, M. Subudhi and R. Fullwood
Brookhaven National Laboratory
Upton, New York 11973

ABSTRACT

The effects of aging on Instrument Air (IA) systems in Nuclear Power Stations have been studied as part of the Nuclear Plant Aging Research (NPAR) Program. The aging phenomena has been characterized by analyzing operating experience from actual plant maintenance records. In addition, various national data bases were utilized to obtain instrument air system data to supplement and validate the plant data base findings.

Time-dependent failure rates were calculated for several components to identify aging trends. A computer program was developed and implemented to model a typical IA system and perform time-dependent Probabilistic Risk Assessment calculations. Using the time-dependent failure rates calculated from the data, the effects of aging on system unavailability and component importance were investigated.

INTRODUCTION

The Nuclear Plant Aging Research (NPAR) program was established by the Nuclear Regulatory Commission to address concerns related to aging effects on the safety and reliability of nuclear power plants. The goals of the program are to characterize aging and service wear effects, and to identify methods of detecting and mitigating them. Initial work under the NPAR program focused on specific components[1-8], whereas more recent work has addressed complete systems[9,10].

This paper presents preliminary technical results from the phase I evaluation of the effects of aging on Instrument Air (IA) systems in nuclear power stations. The goal of the phase I work is to characterize the aging phenomena by identifying predominant failure causes, modes, and mechanisms, as well as time-dependent aging trends.

IA SYSTEM DESIGN AND OPERATION

Nuclear power stations utilize compressed air systems to provide air for all pneumatic instrumentation and controls, and for station service and maintenance usage. This is usually accomplished by two or more discrete systems distinguished from each other by the quality of the air which they supply. The instrument air (IA), or control air (CA), system is designed to provide compressed air of high quality for the operation of pneumatic instrumentation and controls. The instrument air specifications require the supply of clean, filtered, dry, oil-free air, at a specified minimum pressure dew oil-free air,

[1] Work done under the auspices of the U.S. Nuclear Regulatory Commission.

at a specified minimum pressure dew point. The service air (SA), or plant air (PA), system is designed to supply clean, oil-free air usually at the same pressure as the instrument air system.

Compressed air systems found at nuclear power stations can be grouped under two generic configurations. The Type I configuration shown in Figure 1 will consist of at least two 100 percent capacity instrument air compressors taking suction from the atmosphere through an intake filter/silencer and discharging through an aftercooler, a moisture separator, and into an air receiver tank.

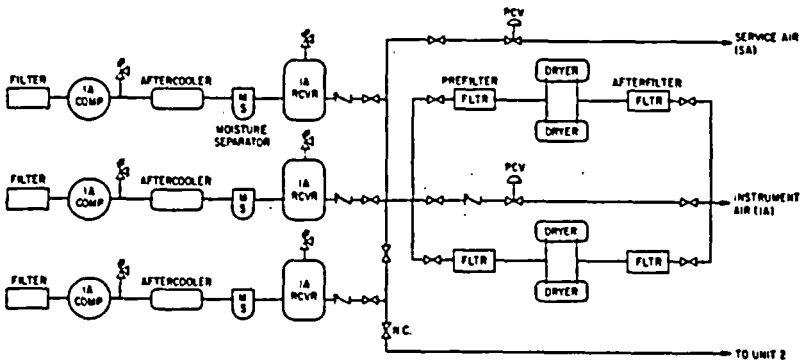

Figure 1 Simplified Schematic of a Type I Compressed Air System: Multiple IA Compressors with Tap Off to Service Air System

From the discharge header of the air receivers one branch will pass through a filter/dryer train (or one of several parallel filter/dryer trains) to remove moisture, oil, and particulates from the compressed air thereby providing the high quality required by the instrument air system. The other branch will usually pass through a filter and then directly to the service air supply system of the plant via a pressure control valve which is set to isolate the service air system when instrument air system pressure drops below a design setpoint.

The second general configuration consists of one or more instrument air compressors supplying a stand-alone instrument air system together with one or more service air compressors feeding a distinct service air system. Such an arrangement for a Type II compressed air system is illustrated in Figure 2.

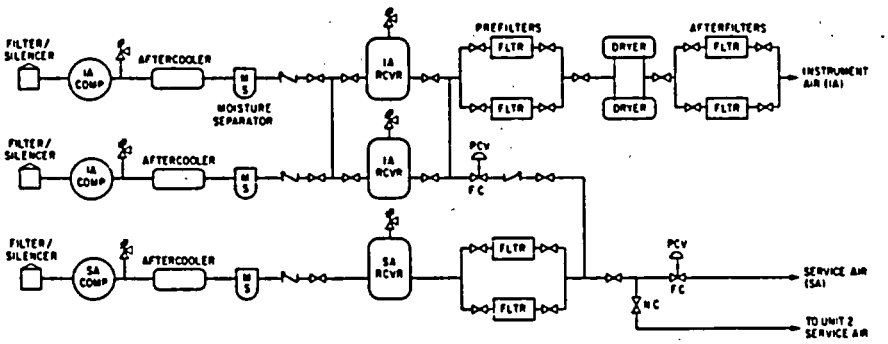

Figure 2 Simplified Schematic of a Type II Compressed Air System: Separate IA Compressors and Service Air Compressors

The discharge from the instrument air receivers will pass through a filter/dryer train before feeding out into the instrument air distribution system. The service air receivers may supply the service air distribution system either directly, or as shown by way of a filter prior to distribution to remove particulate and moisture/oil contaminants.

In the Type I configuration, the service air system is supplied from the instrument air compressors. The instrument air loads are more critical to plant operation and safety than the service air loads. Therefore, when compressor failures, leakage of instrument air, high demand, or other excessive use cause the instrument air header pressure to drop below a critical design setpoint pressure, the isolation valve feeding the service air supply system will close automatically. This will conserve the supply of compressed air available to feed the pneumatic controls and instrumentation essential to plant operation.

In the Type II configuration, the service air system and the instrument air system have their own dedicated compressors as their sources of compressed air, as illustrated in Figure 2. In this compressed air system, the service air compressors serve as a backup source for the instrument air system. The piping is arranged so that upon low instrument air header pressure, the crossconnect valve between the service and instrument air systems will automatically open. Service air will then be supplied via a checkvalve to the instrument air header upstream from the filter/dryer train.

Compressor Air Systems at Multiple Nuclear Sites

Most multiple unit nuclear plants have compressed air systems made up from the basic configuration types discussed in the previous section. Two approaches to providing compressed air to multiple reactor nuclear stations were encountered in a survey of 38 plants performed as part of this study. The first design utilizes a separate compressed air system for each unit independent from the other units at the site save for a crossconnect valve (usually a locked-closed manual valve) between the service air systems in most cases. The second approach provides one large, multiple redundant component compressed air system shared among all the reactor units at a site.

In the first method, with independent air systems, each individual unit's compressors and associated equipment are usually provided with sufficient capacity to handle the compressed air demand for normal shutdown of both units. The crossconnect valve between the service air systems of each unit air would only be opened in circumstances where one unit's compressed air system was out of service or otherwise unable to meet its pneumatic demand. The instrument air systems in the units reviewed very rarely provided any direct cross-unit interties in their design. The instrument air supply to essential pneumatic controls and instrumentation is too critical to risk jeopardizing adequate capacity to both units should an intertie be erroneously opened. Examples of independent systems with service air crossconnect valves to other units are shown in Figures 1 and 2.

Multiple reactor plants with shared compressed air systems typically employed multiple redundant compressors and supply trains, and multiple redundant filter/dryer trains to assure high availability. The distribution arrangements are normally designed to allow individual sections to be isolated for maintenance without affecting the supply of air to other portions of the system. Ring header arrangements are frequently used to provide better availability of the compressed air supply. The multiple compressors are usually powered from the electrical systems of different units to provide greater assurance that one compressor source will remain operating at all times.

AGING ANALYSIS

To evaluate the effects of aging on compressed air system performance in nuclear stations, failure data and operating experience information were collected from several sources for analysis. Among these were plant specific data, the Nuclear Plant Reliability Data System (NPRDS), and Licensee Event Reports (LER's).

Among the data sources available, the plant specific operating and maintenance records for compressed air systems proved to be the most useful for the purposes of this study. Each event was reviewed to assure consistency in aging determinations and interpretations of failure characteristics. In addition, data from NPRDS and the LER data bases were obtained and analyzed to supplement and validate the plant data findings.

The NPAR definition of aging[10] was applied to each of the failures to determine if the failure was aging related. The fraction of failures that could be attributed to aging was then determined for each of the data sources. Large aging fractions were found from the analysis of the actual plant data and LER's indicating that aging degradation is present in compressed air systems and is a significant contributor to failures.

For example, Figures 3 and 4 illustrate the aging fraction found in an older plant, "A", and a new plant, "C", respectively. The plant "A" failures reviewed occurred in the plant air systems during the fourteenth through the eighteenth years of system operation, whereas, the plant "C" plot depicts air system failures from initial service through the first eight years of operation.

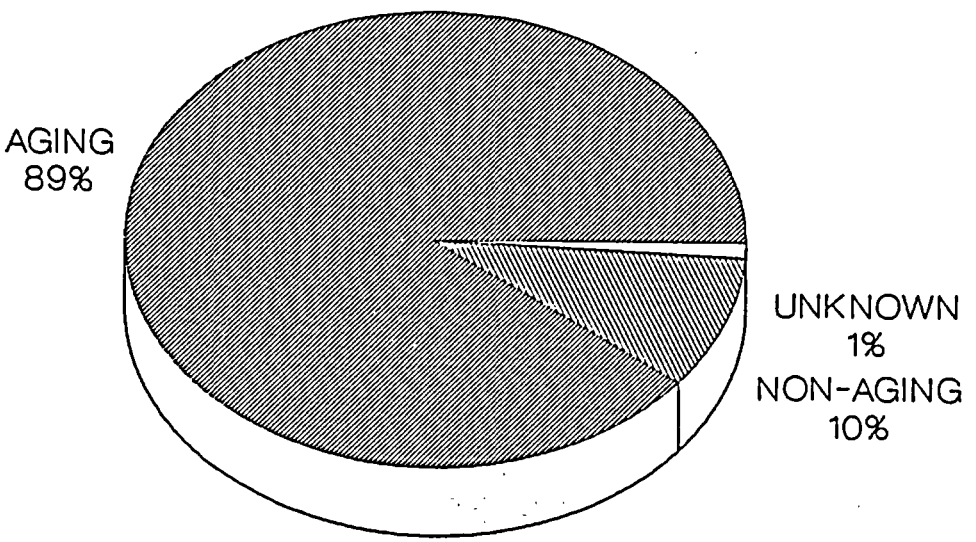

Figure 3 Aging Fraction - Plant "A"

The aging fractions determined for these plants indicated that aging-related degradation appears to be playing a significant role in compressed air system failures. As would be expected, the older plant, Plant "A", shows a proportionately higher percentage of aging related failures than the new plant. In the new plant, the equipment is operating in the early stage of operating life prior to the period when wearout and aging effects predominate. Operation and maintenance problems contribute a higher percentage early in system life, due to the "learning process" experienced by plant personnel; also, preventative maintenance procedures have not yet been optimized, further contributing to this category. Equipment "break-in" failures and design/installation problems are more common early in the system's life, thereby, additionally reducing the relative proportion of aging-related failures in a newer air system such as the one in Plant "C".

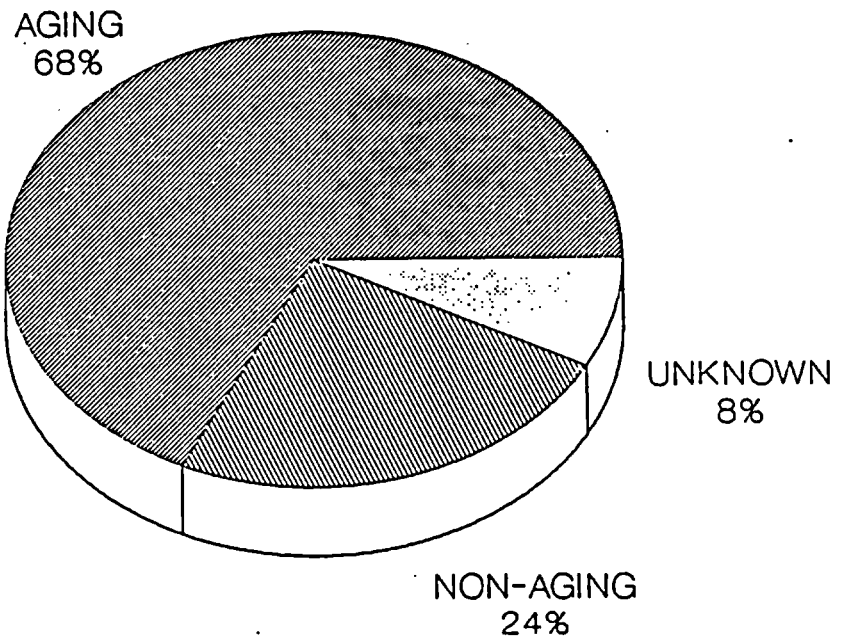

Figure 4 Aging Fraction - Plant "C"

By comparison, the aging fraction exhibited by the LER data base from the OSRR study[5] indicated that slightly more than half of the compressed air system LER's are aging-related. Due to the reporting requirements associated with 10CFR50.73 for Licensee Event Reports, the LER data base is a less representative distribution of the entire set of the IA failures that are occurring. Only those incidents that result in a reportable event are included. This results in a larger proportion of events caused by operational/administrative/maintenance type errors.

In a nuclear power station, as at all power plants, the instrument air system and the service air system are continuously operating systems, whether the plant is at power or shutdown. Although the system is in continuous operation, the actual pneumatic demand will vary widely, therefore, the quantity of compressors required to meet the pneumatic loads of the plant will also vary. At least one compressor will always be operating under normal circumstances, modulating the unloader valve to maintain the system at nominal pressure.

Since the compressed air systems are not typically classified as safety-related, there are fewer alarms and surveillance tests associated with them. Consequently, the methods of failure detection are typically visual inspection during operator walkdowns, abnormalities noted during daily or weekly parameter

logging, problems noted by plant personnel using compressed air or working in the area of the air compressing equipment and auxiliary equipment, and problems revealed during periodic preventative maintenance testing and inspections.

For component level analyses, plant data were obtained for six nuclear units. The data for each plant were sorted to determine the distribution of air system failures among the various components. The ranges of the failure percentages for each major component at the six plants in the study is illustrated in Figure 5. Compressors, air system valves (within the study boundary), dryers, filters, and instrumentation, in that order, account for the majority of failures, followed by piping, air receivers and aftercooler/moisture separator units. This would be a good basic starting point for the allocation of maintenance resources for the instrument air system, modified depending upon the individual contributions of each component to the overall system availability.

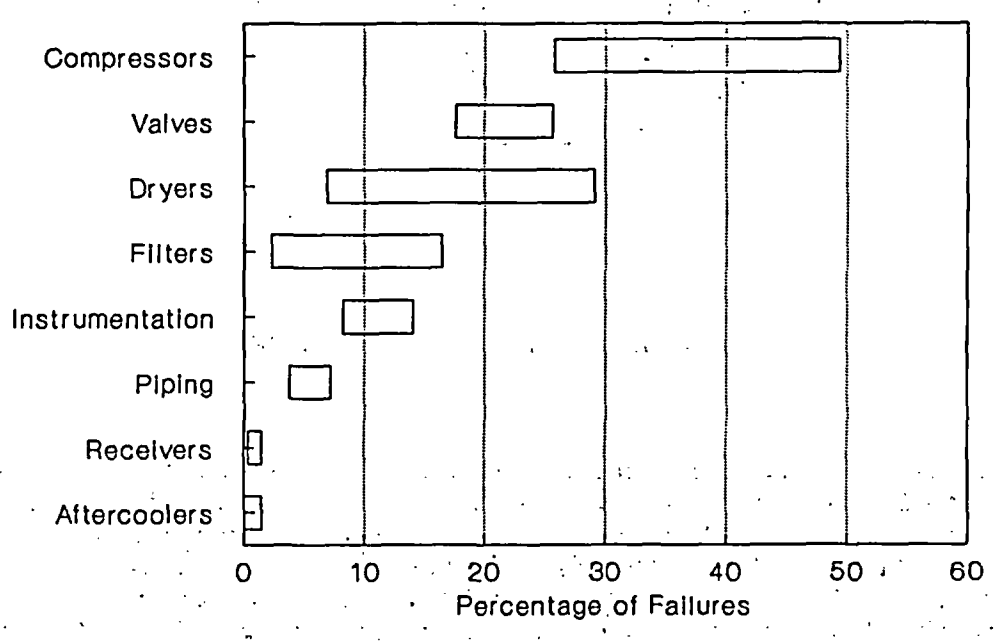

Figure 5 Range of Component Failures

Compressors and dryers exhibited the widest ranges in percentages of failure among the air system components. This may be a reflection of the relative complexity of these components, the active nature of this equipment, or variations resulting from differing types and amounts of maintenance and preventative maintenance received at the various plants in the study.

The failure mechanisms observed in the plant data were most dependent on the component and type, but less influenced by the application. Figure 6 for example, indicates that wear and calibration/setpoint drift were the dominant mechanisms for identical reciprocating air compressors at plant "A", regardless of the application, whether as a service air or an instrument air compressor.

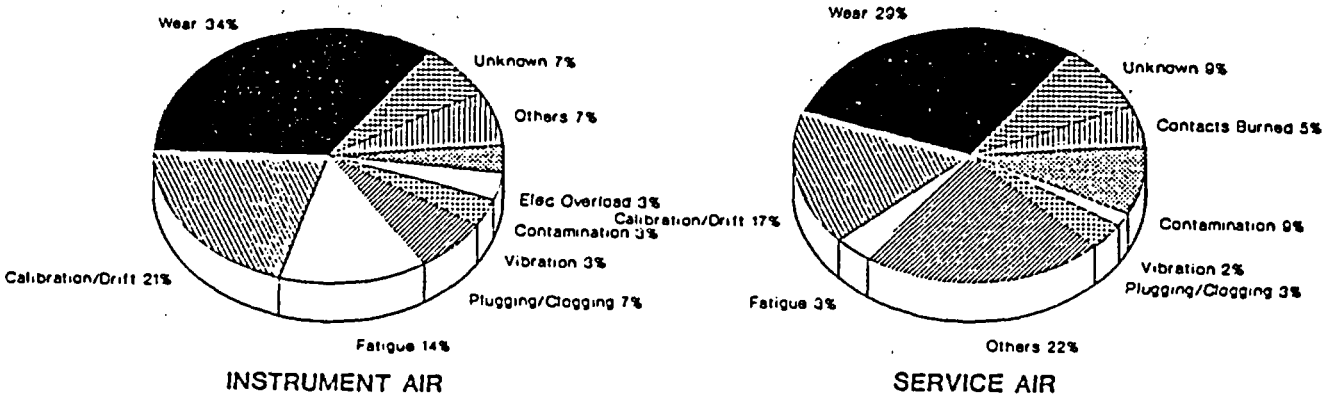

Figure 6 Failure Mechanisms for Reciprocating Compressors

All of the air dryers in use at the six plants for which data were available are of the dual tower, externally heated, regenerative, desiccant type. Analysis of these air dryer failures, yielded the failure mechanism distribution shown in Figure 7. The three dominant failure mechanisms are blocking and/or clogging, corrosion, and deterioration. Other failure mechanisms observed were contamination and instrumentation and controls calibration or setpoint drift.

In order to better understand the failure mechanisms occurring in compressed air distribution system valve failures, the types of valves which are involved must be considered. Typically, the instrument air distribution system will contain 25% of the total number of compressed air system valves in the nuclear plant, the remainder being allocated to the service air distribution network. However, the more complex, power-operated valves will be found primarily in the instrument air distribution system. The majority of failures reported were associated with instrument air. In one of the plants studied, for example, nearly 60% of the reported system valve failures were in the instrument air system, and of that quantity, one-third involved motor-operated valves (MOV's).

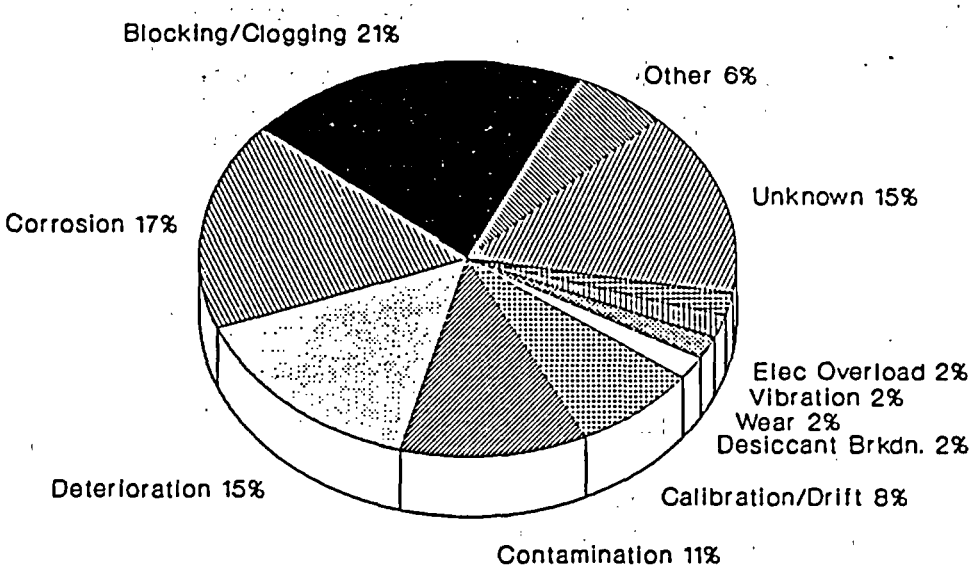

Figure 7 Instrument Air Dryers - Failure Mechanisms

The failure mechanisms observed in air system valves, based on plant data, are depicted in Figure 8. Wear and corrosion are the two dominant processes. Contamination, electrical overloads, and controller calibration or setpoint drift are also significant contributors.

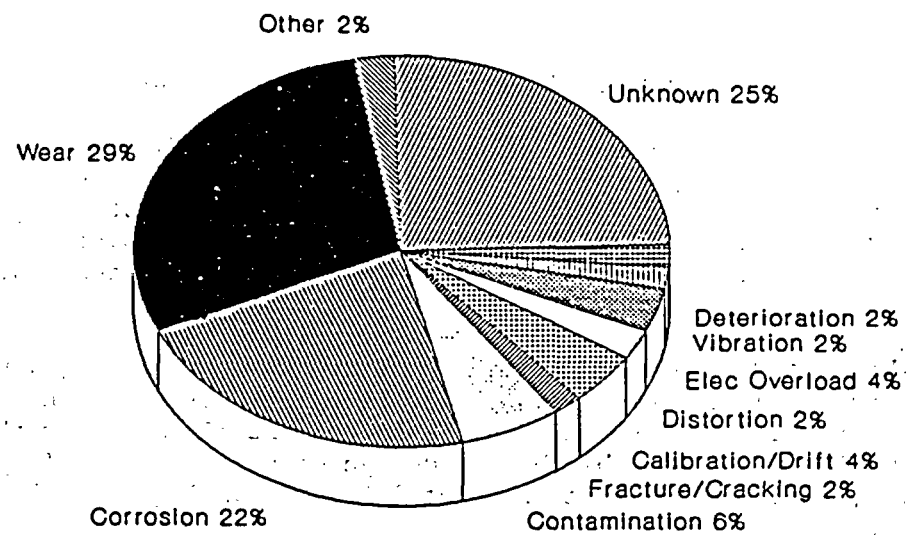

Figure 8 Air System Valves - Failure Mechanisms

Figure 9 shows the distribution of the most typical failure modes encountered during the review of plant maintenance records, separated for each of the major compressor types. The two most common failure modes, failure to load/unload properly and leaks, were found to be dominant in all three compressor types. This failure mode typically results in degraded system operation.

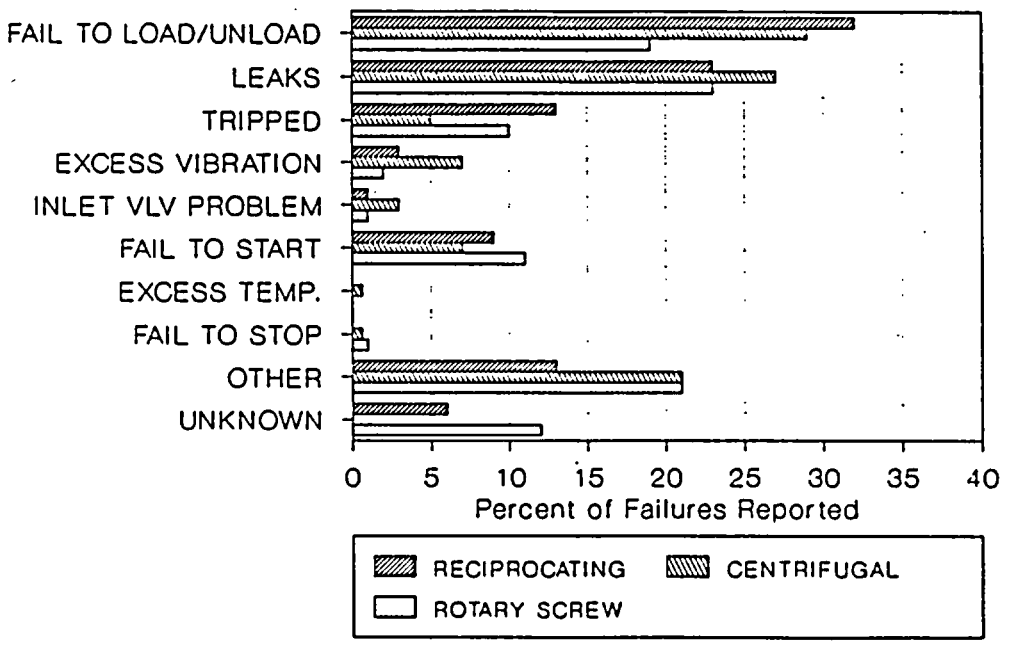

Figure 9 Failure Modes by Compressor Type

Several of the other common failure modes actually involve the immediate loss of a compressor. Depending on the design configuration of the compressed air system, the occurrence of these failure modes requires starting and loading one or more redundant compressors to pick up the load. In systems with only one IA compressor, service air would be called upon to back up the instrument air system.

The most dominant failure mode in the dual tower, regenerative desiccant air dryers was degraded function. The immediate effect of this failure mode is the delivery of compressed air to the instrument air system with a higher pressure dewpoint than allowable by the design specifications. In plants with only one dryer, this might result in a total loss of drying capability for the duration of the maintenance outage.

The dominant failure mode for air system valve failures was "failed to open/close". Seat leaking was the next most common failure mode, followed by leakage from packing, gaskets, or valve body cracks.

Failures that occur on the component level can also affect other parts of the system. The loss of one component will rarely result in the loss of the entire air system since adequate redundancy is designed into most systems to avoid such an occurrence. When a significant compressed air system problem occurs, in most cases it manifests itself as some form of degraded system operation. In the majority of the failure events affecting the air system as a whole, this means operation at some pressure below normal in all or portions of the system. Total loss of system pressure events are rare.

Figure 10 illustrates the effects of failures for the two most critical components in the system. The figure shows that loss of compressor, or loss of redundancy of compressed air source, occurs in about 14% of the failures. Degraded air pressure or quality is a significant factor, resulting from approximately one third of all the air compressor failures. About half of the compressor failures are classified as incipient failures. That is, no immediate loss of a compressor or degraded system pressure has occurred, however, if left unchecked, degraded operation or loss of the component could take place.

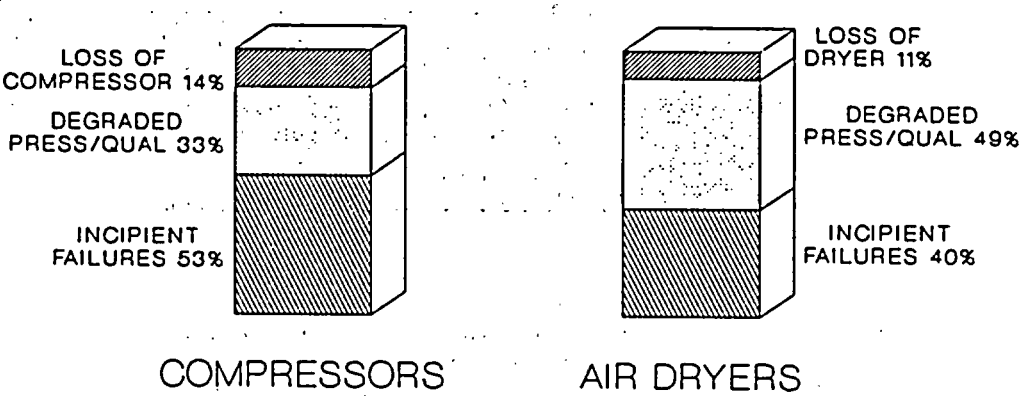

Figure 10 Effects of Component Failures

For air dryers, nearly half of the failures resulted in either degradation or instrument air system pressure or decreased quality of instrument air. Since almost half of the sites surveyed in the FSAR review had only one dryer or less allocated to each nuclear unit, loss of a dryer or malfunctioning of a dryer can often lead to moisture contamination of an instrument air system.

TIME-DEPENDENT FAILURE RATES

For purposes of comparison with commonly used values, time-dependent failure rate plots were developed for the two most critical compressed air components, compressors and air dryers. The failure data from the plant maintenance records were used, together with actual or estimated, weighted operating hours to calculate failure rates as a function of age for each of the six plants. It should be recognized that only those failures originating within the air system, and affecting the air system are reflected in this type of maintenance data.

As plants age, the systems subjected to normal and abnormal operational and environmental stresses become vulnerable to higher failure frequency caused by the aging occurring in components. Hence, a true aging analysis of a system should consider the time-dependent failure rates for all the components within the system contributing to its successful operation. Compressor and filter/-dryer train aging data were extracted from several different plants, for the years available in their computerized maintenance reporting system, each datum was normalized, and then plotted to compile a hypothetical representation of the component's aging characteristic over its life span.

The failure rate plots so obtained are illustrated in Figure 11 for reciprocating air compressors and Figure 12 for the filter/dryer train. The solid horizontal lines drawing in Figures 11 and 12 represent the best estimates of the random failure zones of a typical bath tub representation of aging in equipment. The wearout regions are shown by another straight line starting at a particular year for each component type. The start of wearout was estimated based on the distribution of the data (i.e., departure from the random failure rates) in the later years. The bounds for the linear aging rates are then chosen to include all the scattered data points. The infant mortality part of the bath tub curve is not shown in these plots, since the emphasis of this study was on the aging (i.e, wearout) effects of components on system performance.

It should be noted that these aging representations of failure rates shown in Figures 11 and 12 are not specific to one particular plant. Rather, they represent the bounds of aging rates for the plants included in the data analysis. The shapes of these aging rates may be different industry-wide when all plants are included, because of the great diversity in the way the compressed air systems are designed, operated, maintained and documented.

SYSTEM UNAVAILABILITY WITH AGE

To examine the effects of the increasing failure rates at the system level, a computer program was developed which performs time-dependent probabilistic risk assessment (PRA) calculations. The program PRAAGE-IA, which was adapted specifically for this work from the PRAAGE-1988 set of codes (Lofaro, 1989)[10] used for aging analysis, is based upon a Type II compressed air system modeled in a nuclear plant PRA. This work provides a base case, non-aging reliability analysis of the reference system. Having established the basecase, the nuclear plant experience aging data was introduced into PRAAGE-IA to obtain the estimated effects of aging on the instrument air system reliability.

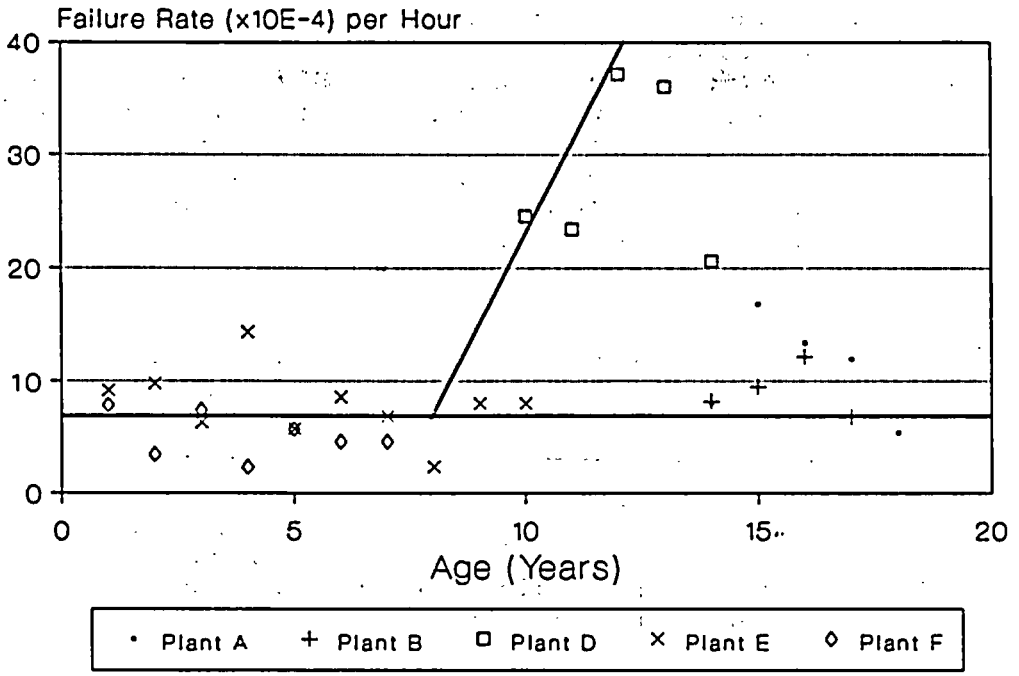

Figure 11 Failure Rates for Reciprocating Air Compressors

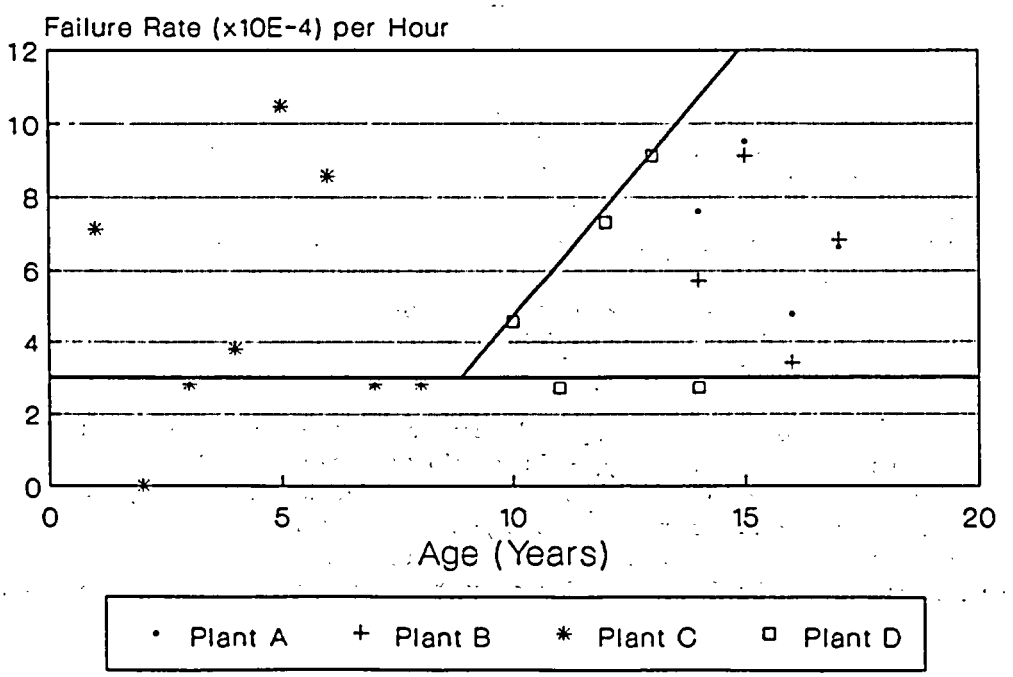

Figure 12 Failure Rates for Filter/Dryer Train

The age-related failure rates for the IA and SA compressors and filter/dryer trains were applied to the PRAAGE-IA model to examine the bounding system unavailabilities due to aging. All other events in the model retained the original PRA failure probabilities. Table 1 summarizes the aging failure probabilities for compressors and dryers which were calculated based on a 24-hour mission duration. The aging fraction increase per year is defined as the increase in failure probability with respect to the constant failure probability per year beyond the age at which the wearout region begins.

Table 1 Failure Probabilities for IA Components

Component	Constant Failure Rates		Aging Failure Rates	
	Failure Rate Per Hr	Failure Probability	Year at which Aging (wearout) Begins	Bounding Aging Fract. Incr. Per Year
IA and SA Compressors	7×10^{-4}	1.68×10^{-2}	8.0	1.0
Dryer/Filter Train	3×10^{-4}	3.1×10^{-4} (For 2 or more air dryer/filter trains)	9.0	0.5

Figure 13 shows the IA system unavailability increase with age using the two component aging data given in Table 1. The non-aging portion of the unavailability increased from 7.1×10^{-4} to 1.0×10^{-3}. After 20 years time-dependent unavailability has increased 4.5 times which represents the bounding effect of aging. The corresponding component contributions to these system unavailabilities are shown in Figure 14. As expected with the higher failure rate for dryers, their contributions remain high for all years. The compressors have also become important in latter years due to aging effects which make them more vulnerable to failure.

The availability of the IA supply is improved through provision of a backup source, i.e., service air in a Type II configuration, and/or redundant components (found in both Types I and II systems). A parametric study reflecting the availability of the backup service air system and various IA system components was performed using higher failure probabilities (i.e., 1.0E-1) for the components which could exhibit larger failure rates over the lifetime of the plant.

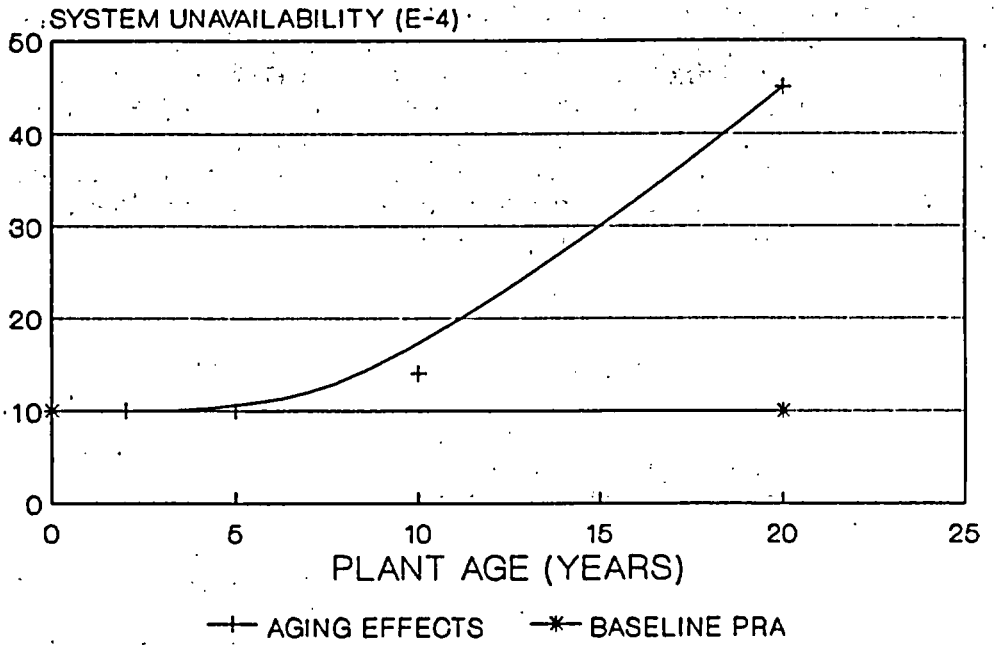

Figure 13 Oconee System Unavailability for Unit 3 IA Supply

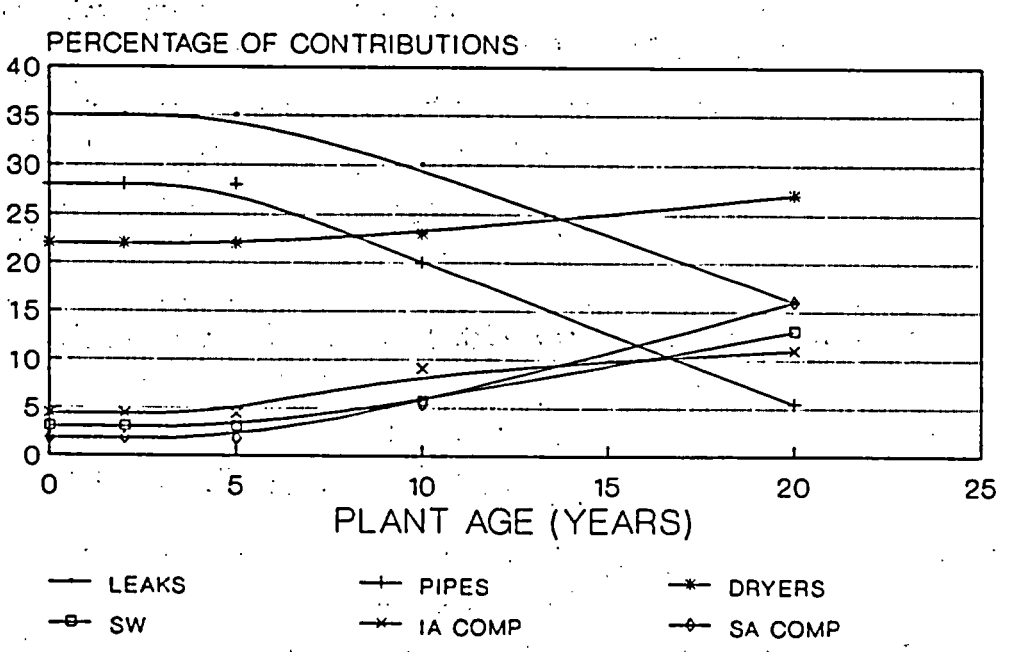

Figure 14 Component Contributions to IA System Availability

The effects of compressors and filter/dryer trains were analyzed separately using their base case aging rates (i.e., 1.0 aging fraction increase[1] for compressors, and 0.5 aging fraction for dryers/filters). Figure 15 illustrates three cases representing: either of the two component types, no aging in the IA compressors, and no aging in the SA compressors, compared with the base case where both component types were subject to aging. For this particular design configuration and PRA model, both compressors and filter/dryer trains were found to be equally important to the system availability.

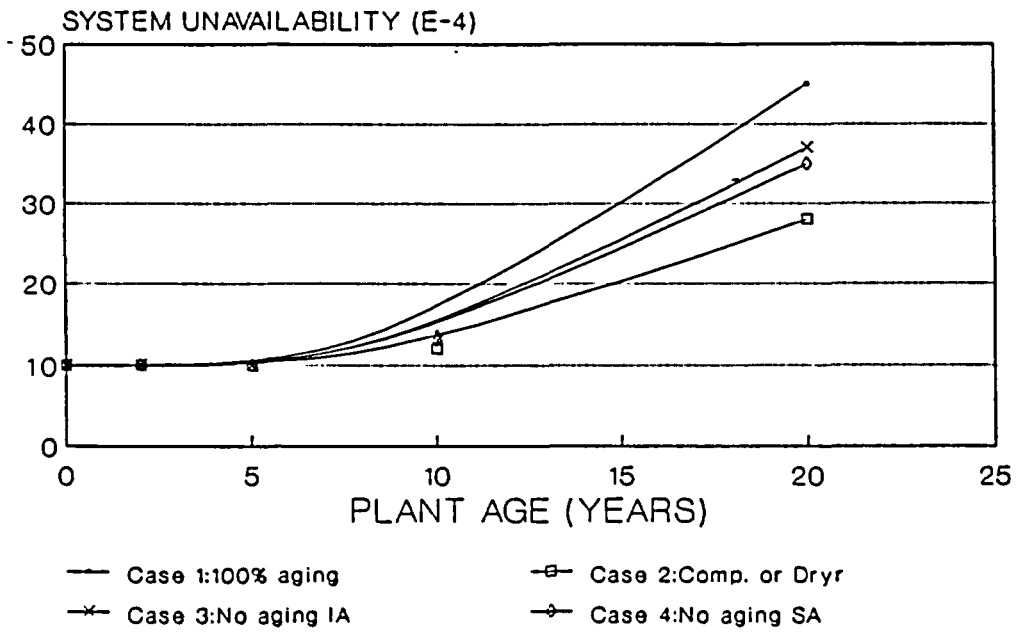

Figure 15 System Unavailability with Age - Different Component Aging

[1] Aging fraction increase is defined as the ratio of the increase in failure rate per year over the constant failure rate for early years.

The other cases examined the effects of enhanced maintenance for either IA or SA compressors such that their aging rates were kept under control. In some plants, the IA compressors are more rigorously maintained than the SA compressors. In this PRA model the SA compressors are assumed to be available to back-up IA in the event that the IA units are not available. Hence, the impact on system availability of SA compressor aging is only marginally higher than that of the IA compressors. Over a 20-year period, the system unavailability for no aging in IA compressors is 3.7×10^{-3} compared to 3.5×10^{-3} for the case where the SA compressors are expected to exhibit no aging. For this PRA model, the importances of both types of compressors (SA and IA) and the dryer/filter trains toward maintaining the overall IA system availability are found to be approximately the same.

CONCLUSIONS

An analysis of past operating experience for IA systems has shown that a significant number of failures are related to aging. The findings from this study have formed a technical basis for understanding the effects of aging in compressed air systems. The major conclusions from this work are highlighted in the following paragraphs.

- This study has identified aging trends in component failure rates, component relative importances, and system unavailability that could have an increasing impact on system availability and consequently affect plant safety in later years.

- Compressors, air system valves, and air dryers were found to make up the majority of failures. The increase in failures found in passive components such as piping, aftercoolers/moisture separators, and receivers was greater over time, but these still constituted only a small percentage of overall failures.

- The effectiveness and quantity of preventive maintenance devoted to a component significantly affected the amount of failures experienced.

- As a continuously operating system, with minimal control room instrumentation due to its non-safety classification, most air system problems are detected by local monitoring and indication, walkdowns and inspection, and preventive maintenance inspection/surveillance.

- Review of compressed air system designs and studies using a PRA based system model revealed that the redundancy of key components (compressors, dryers, IA/SA crossconnect valve) was an important factor in system availability. Overall design configuration had an impact on the pervasiveness of air system problems.

- Total loss of air events are uncommon. The majority of events resulted in degraded operation (low IA pressure, IA quality out of limits). Procedures and testing for the response of personnel and equipment to these conditions should be developed.

- Human error was a significant cause of failures in critical components such as compressors and dryers, as well as at the system and inter-system level. Training should be augmented in two key areas: 1) operation and maintenance of critical air system components, and 2) importance of instrument air to other plant systems particularly safety systems.

- The systems outside of instrument air that were most often affected by IA problems are containment isolation, main feedwater/main steam, auxiliary feedwater, and the BWR scram system. The most commonly affected components were AOV's and SOV's.

- The probabilistic work entailed the development of a computer program (PRAAGE-IA) using a PRA-based IA system model to perform time-dependent PRA calculations. Time-dependent failure rates were developed from the data base findings and input to the program to calculate system unavailability and component importances for various ages. Results from the probabilistic work showed that when the time-dependent effects of aging are accounted for, two significant system effects are seen: 1) system unavailability increases moderately with age, and 2) component relative importances change with age.

The findings presented in this paper form a sound technical basis for understanding and managing the effects of aging in IA systems. Future work will include improvements to current maintenance, monitoring, training, off-normal response procedures, and surveillance practices to mitigate aging degradation.

REFERENCES

1. Gunther, W.E., et al., "Operating Experience and Aging-Seismic Assessment of Battery Chargers and Inverters," NUREG/CR-4564, June 1986.

2. Subudhi, M., et al., "Improving Motor Reliability in Nuclear Power Plants," NUREG/CR-4939, June 1987.

3. Taylor, J., et al., "Seismic Endurance Tests of Naturally Aged Small Electric Motors," BNL Report A-3270-11-85, November 1985.

4. Subudhi, M., et al., "Operating Experience and Aging-Seismic Assessment of Electric Motors," NUREG/CR-4156, June 1985.

5. Greenstreet, W.L., et al., "Aging and Service Wear of Motor Operated Valves Used in Engineered Safety Feature Systems of Nuclear Power Plants," NUREG/CR-4234, June 1985.

6. Greenstreet, W.L., et al., "Aging and Service Wear of Check Valves Used in Engineered Safety Feature Systems of Nuclear Power Plants," NUREG/CR-4302, December 1985.

7. Bacanskas, V.P., "Aging and Service Wear of Solenoid-Operated Valves Used in Safety Systems at Nuclear Power Plants," NUREG/CR-4819, March 1987.

8. Adams, M.L., "Aging and Service Wear of Auxiliary Feedwater Pumps for PWR Nuclear Power Plants,"NUREG/CR-4597, July 1986.

9. Higgins, J., et al., "Operating Experience and Aging Assessment of Component Cooling Water Systems in Pressurized Water Reactors," NUREG/CR-5052, July 1988.

10. Lofaro, R., et al., "Aging Study of Boiling Water Reactor Residual Heat Removal Systems," NUREG/CR-5268, BNL-NUREG-52177, June 1989.

11. Hagen, E.W., "Compressed-Air and Backup Nitrogen Systems in Nuclear Power Plants," NUREG/CR-2796, ORNL/NSIC-206, July 1982.

12. Emrit, R., et al., "A Prioritization of Generic Safety Issues," NUREG-0933, December 1983.

13. NRC Memorandum: Singh, R. to Rossi, C.E., "Forced Shutdowns Induced by Instrument Air Failures," April 1985.

14. Ornstein, H.L., "Operating Experience Feedback Report-Air Systems Problems," NUREG-1275, Vol. 2, USNRC, December 1987.

15. DeMoss, G.M., et al., "A Risk-Based Review of Instrument Air Systems at Nuclear Power Plants," BNL Technical Report No. A-3968-6-23-88, June 1988.

16. Vora, J.P., "Nuclear Plant Aging Research (NPAR) Program Plan," NUREG-1144, Rev. 1, September 1987.

17. Fullwood, R., et al., "Aging and Life Extension Assessment Program (ALEAP)-Systems Level Plan," BNL Report A-3270-12-86, December 1986.

18. "Performance Testing of Nuclear Power Plant Instrument Air Systems," An American National Standard, ANSI/ASME OM-17 (Draft), December 1987.

AGING EFFECTS IN COMPONENT FAILURE AND DOWNTIME DATA AND IMPACTS ON PLANT RISK

W.E. Vesely
Science Applications International Corporation

ABSTRACT

The status results of two related projects are described in this presentation. The first part of the presentation, corresponding to the first project, is entitled "Evaluation of Aging Effects in Component Failure and Downtime Data". The second part of the presentation, corresponding to the second project, is entitled "Evaluation of Core Melt Frequency Effects Due to Component Aging and Maintenance". The work performed to evaluate aging effects in component failure and maintenance downtime data has resulted in an analysis procedure and PC software being developed. The procedure has been applied to diesel data, circuit breaker data, controller data, and starter data. Significant aging effects have been preliminarily identified. The work performed to evaluate core melt frequency impacts from component aging has resulted in approaches and software being developed. The applications to two NUREG 1150 PRAs show the dramatic effects aging and different maintenance programs can have. The detailed contributions which are produced allows the aging contributors to be effectively prioritized. Multiple aging effects are often the dominant contributors. These results are also preliminary and are under review.

1. INTRODUCTION

This paper presents status results from two projects which are being carried out to evaluate aging effects in component failure and downtime data and impacts on plant risk. The presentation is divided into two parts. The first part of the presentation, corresponding to the first project, is entitled "Evaluations of Aging Effects in Component Failure and Downtime Data". The second part of the presentation, corresponding to the second project, is entitled "Evaluations of Core Melt Frequency Effects Due to Component Aging and Maintenance". Two draft reports have been issued on the projects and are currently being reviewed.

The two projects are coupled. The first project is developing and applying approaches to evaluate aging effects and aging rates in failure data and maintenance downtime data. The second project uses estimated component aging rates to evaluate the resulting core melt frequency impacts and risk impacts under given maintenance programs. The first project thus can provide input to the second project.

The work performed to identify aging effects in component failure and maintenance data has resulted in an analysis procedure and software being developed. The procedure has been applied to evaluate plant specific data and data from the Nuclear Plant Reliability Data System (NPRDS). Diesels, circuit breakers, controllers, and starters have specifically been evaluated and significant aging effects have been identified. These results are preliminary and are under review.

The work performed to evaluate core melt frequency impacts from component aging has resulted in approaches and software being developed, and applications being carried out. The results which have been obtained are believed to be significant since they are the first results to be obtained which quantify the effects of aging and the effects of different maintenance programs using full scale probabilistic risk analyses (PRAs). The two PRAs which were used were NUREG 1150 PRAs. The results show the dramatic effects aging and different maintenance programs have. As importantly, the results show how detailed aging contributors can be effectively prioritized with regard to their core melt frequency impacts. The results are also presently under review.

2. EVALUATIONS OF AGING EFFECTS IN COMPONENT FAILURE AND DOWNTIME DATA

This project was carried out to develop and apply methods to evaluate aging effects in component failure and maintenance downtime data. The data analysis methodology which has been developed can be applied to any component failure data or maintenance data which contains times of failures or times of corrective maintenances. The data can be data from a specific plant or can be generic data, consisting of data from multiple plants. If the failure or maintenance data are reported by system, manufacturer, and environment, then these additional variables can also be evaluated for their effects on aging.

For a given set of data, the methodology determines the degree to which aging is exhibited and determines the age dependent failure rate which characterizes the aging behavior. The age dependent failure rate can be linear or nonlinear as determined from the data. The uncertainty bounds (confidence bounds) associated with the failure rate are also determined. The age dependent failure rate and confidence bounds are important information in themselves and quantify the aging behavior. The failure rate and associated confidence bounds which are determined can also be used in reliability and risk analyses. In these reliability and risk applications, the impacts of the aging behavior can be evaluated and the effectiveness of various maintenance programs can be assessed.

The Weibull model is specifically used to evaluate the age dependent failure rate or degradation rate. The Weibull model is a standard reliability model for aging analysis and is the model most generally used for evaluating aging effects in industrial and military applications. The Weibull model includes as a special case the linear aging rate model developed in NRC's Nuclear Plant Aging Research (NPAR) Program. The Weibull model can not only identify aging effects but also can identify improvements in performance, such as decreases in the failure rate, when they exist. The Weibull statistical techniques which are assembled are standard techniques which have been published in the literature and which have been successfully applied in various areas, which is a plus.

One of the objectives of the work is not only to develop a methodology, but to develop a systematic process for evaluating aging effects. As part of the process, standard formats are developed for reporting the data analysis results. Graphical techniques are utilized to illustrate the aging effects which are exhibited in the data. Graphical techniques are also used to illustrate the accuracy of the fitted Weibull model to the data. The graphs which are produced provide effective ways of illustrating and communicating the aging effects which have been identified.

As part of the evaluation process, the statistical techniques and graphical techniques have been computerized for personal computer (PC) applications. By computerizing the techniques, not only are the evaluations made more efficient but evaluation capabilities are enhanced. A given data set can be efficiently analyzed in

a variety of different ways to investigate all the different aging behaviors that might be exhibited in the data.

The evaluation process and software which were developed were applied to plant specific diesel data and to circuit breaker data, controller data, and starter data for a plant obtained from the Nuclear Plant Reliability Data System (NPRDS). Each data set was analyzed in numerous ways by examining different failure severities, different subsystem and piecepart causes, and different model types. In all, 32 cross-sectional cuts of the diesel data were analyzed, and 73 cross-sectional cuts of the NPRDS data were analyzed. The process and software which were developed allow these comprehensive evaluations to be performed.

For each data set, the results are presented in a standard format which summarizes the data evaluated and gives the aging parameters which are determined. Partly due to the comprehensive aging analyses that were performed, significant aging effects were identified in each data set. A significant aging effect as defined here is a failure rate which is identified to significantly increase with age with 95% confidence. There were also numerous marginally significant aging effects identified.

For the diesel data, significant aging effects were identified in the failures and downtimes of the control systems for the diesels. The effects were systematic in that all the control systems exhibited these aging effects. The summary analysis outline and the associated graphical outputs that were obtained for a specific case exhibiting these aging effects are shown on the next pages.

For the circuit breaker, controller, and starter data, significant aging effects were identified for specific systems, particularly for the emergency power system and the essential service water system. These aging effects again were systematic in nature. Particular component manufacturer models also exhibited significant aging effects. The summary analysis output and associated graphical outputs are shown for a specific case that exhibited these aging effects. The outputs are shown after the diesel outputs.

The aging effects which were identified, of course, need to be followed up to determine their causes. The aging effects could be due to data reporting anomalies,

DIESEL GENERATOR
AGING ANALYSIS OUTLINE

PLANT TYPE:	BWR	*DATA ID:*	PS-DGN-1
PLANT ID:	A1	*CASE ID:*	27

COMPONENT ID: DIESEL A

FAILURE MODE: FAIL TO START

SEVERITY: ALL

CAUSES: ALL

CONDITIONS: NORMAL

TIME PERIOD: 01/19/84 TO 12/05/88

AGE PERIOD (yrs.): 1.378 TO 6.328

DATA POINTS: 25 ANALYZED 4TH THROUGH LAST POINT

FAILURE RATE MODE $\lambda \beta t^{\beta - 1}$

METHOD OF ESTIMAT MLE

PARAMETER	*VALUE*	*.05 BOUND*	*.95 BOUND*
BETA	1.742	1.211	2.351
LAMBDA (hr-1)	1.19E-04	7.09E-06	1.75E-03

FITTING CRITERIA: 0.0933

EVIDENCE OF AGING: SIGNIFICANT

COMMENTS:

CASE 27 WEIBULL FIT

OBSERVED DOWNTIME RATE VERSUS AGE
DIESEL GENERATOR A

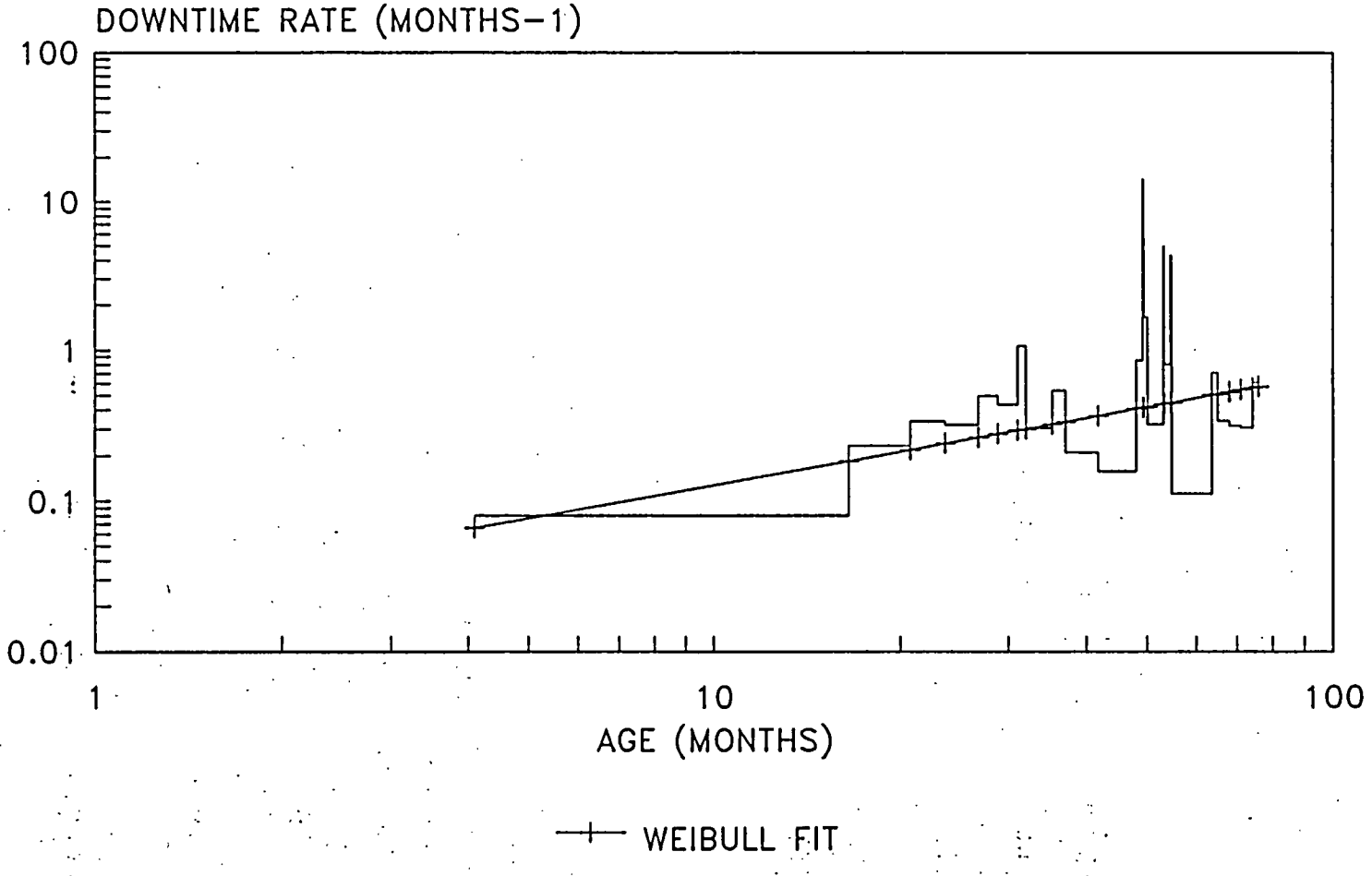

BETA=1.7417 LAMBDA=1.19E-4 Sq=4th DWNTM

CIRCUIT BREAKERS, CONTROLLERS, STARTERS
AGING ANALYSIS OUTLINE

PLANT TYPE:	BWR	DATA ID:	NPRDS-CRB-1
PLANT ID:	B2	CASE ID:	35
COMPONENT ID:	ALL	(12)	
SYSTEM:	ESSENTIAL SERVICE WATER		
FAILURE MODE:	FAIL TO TRANSFER		
SEVERITY:	ALL		
CAUSES:			
CONDITIONS:	NORMAL		

TIME PERIOD:	11/03/75	TO	08/21/89
AGE PERIOD (yrs.):	0	TO	13.8
DATA POINTS:	17	ALL POINTS ANALYZED	

FAILURE RATE MODEL: $\lambda \beta t^{\beta - 1}$

METHOD OF ESTIMATION: MLE

PARAMETER	*VALUE*	*.05 BOUND*	*.95 BOUND*
BETA	5.592	3.563	7.993
LAMBDA (hr-1)	7.16E-11	4.56E-11	1.07E-10

FITTING CRITERIA:	0.1024
EVIDENCE OF AGING:	SIGNIFICANT
COMMENTS:	

OBSERVED DOWNTIME RATE VERSUS AGE
CASE 35 – CIRCUIT BREAKER

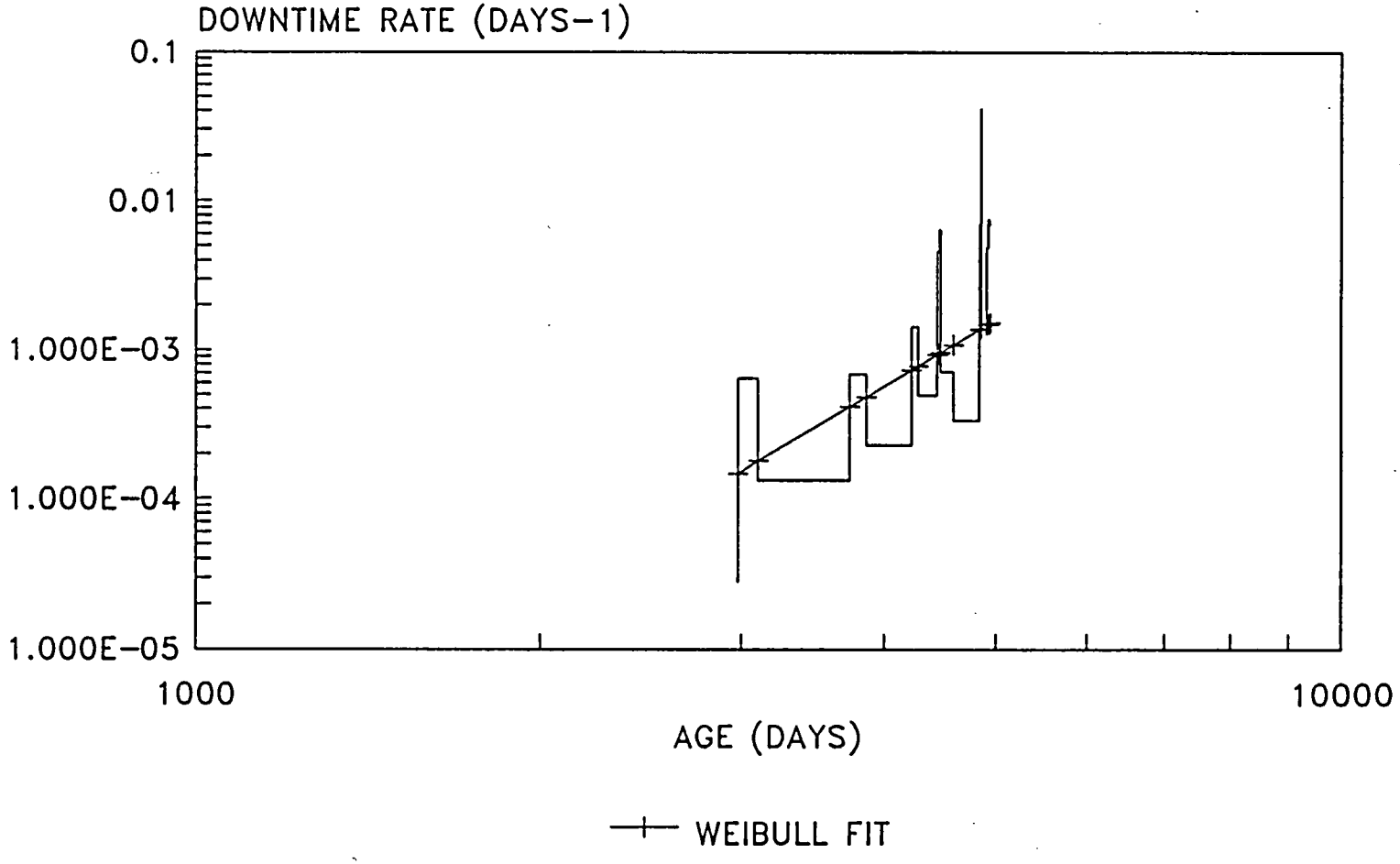

BETA=5.5918 LAMBDA=7.16E-11

which also needs to be checked. However, the applications demonstrated the power of the approaches for identifying aging effects and other trend effects in recorded failure data and maintenance data.

The approaches which have been developed can be used to analyze further NPRDS data and plant specific data in application oriented projects. The applications can be performed to audit data for aging effects, to identify variables and conditions affecting aging, and to develop data bases for risk and reliability analyses to evaluate the implications of aging effects. The age dependent failure rates can be input to risk and reliability models to evaluate the associated risk and reliability implications. In these risk and reliability applications, the procedures and software which have been developed can serve as front-end data analysis processors. The procedures and analyses which have been developed thus can serve as useful tools in aging analyses activities and plant relicensing activities and can usefully complement deterministic approaches and other reliability approaches.

3. EVALUATIONS OF CORE MELT FREQUENCY EFFECTS DUE TO COMPONENT AGING AND MAINTENANCE

This project was carried out to develop an approach to quantify risk effects due to component and structural aging using a probabilistic risk analysis (PRA) and component aging models. The approach which has been developed allows any PRA to be used and allows any aging models to be used for the components and structures. As an important part of the evaluations, the effects of maintenance and surveillance programs in controlling aging are quantified. Maintenance programs and aging surveillance programs can be explicitly evaluated to determine their effectiveness in controlling aging impacts on system unavailability, core melt frequency and public risk. Both point evaluations and uncertainty evaluations can be carried out, and detailed contributors to the aging effects are identified and are prioritized.

The applications which have been performed specifically calculated the increase in core melt frequency which resulted from aging of active components when various maintenance programs were employed. For a given maintenance program the average increase in core melt frequency over time was calculated. The time period over which the core melt frequency increase was averaged was the time period

between component overhauls for a given maintenance program. The average increase in core melt frequency due to aging can be added to the baseline average core melt frequency calculated in the PRA to obtain the projected average core melt frequency when aging is considered.*

Two NUREG 1150 PRAs were used for the applications, one PWR and one BWR. The aging of active components was modeled using the linear failure rate aging model developed in NRC's Nuclear Plant Aging Research (NPAR) Program. In the linear aging model, the component failure rate linearly increases with age according to a characteristic aging rate. For the evaluations, four aging rate data bases were used, which were titled TIRGALEX, MOD1, MOD2, and MOD3. The TIRGALEX aging rate data base was developed in the NPAR program and the other data bases were modifications of the TIRGALEX data base. The TIRGALEX data base involved subjective estimates for certain components and the modifications were constructed to incorporate additional historical data and to serve as sensitivity studies.

For the point evaluations in which point estimates of the core melt frequency changes were calculated, six maintenance programs were evaluated for their effects in controlling aging. The characterizations of the maintenance programs are summarized below.

MAINTENANCE PROGRAMS EVALUATED FOR THE POINT EVALUATIONS OF AGING EFFECTS

1. Each active component has an effective overhaul interval (L) of 18 months at which time aging effects are effectively removed. (L=18)

2. Each active component has an effective overhaul interval (L) of 72 months. (L=72)

3. Each active component has an effective overhaul interval as assigned in the TIRGALEX report (NUREG/CR-5248).

*To be more precise the baseline core melt frequency should be corrected to remove aging effects, however this generally leads to a small difference in the final result.

4. Each active component has an effective overhaul interval (L) of 18 months and, in addition, has an effective aging surveillance interval (T) of 1 month at which time the component is checked for aging effects. (L=18, T=1)

5. Each active component has an effective overhaul interval of 72 months and has an effective aging surveillance interval of 1 month. (L=72, T=1)

6. Each active component has an effective overhaul interval of 72 months and an effective aging surveillance interval of 6 months. (L=72, T=6)

As indicated above, to evaluate its core melt frequency effectiveness or risk effectiveness, a maintenance program needs to be characterized by its effective overhaul intervals and its effective aging surveillance intervals which apply to each component. If overhauls are carried out without intermittent checking for aging effects then the component will only have an overhaul interval (L). If intermittent checking for aging effects is also performed then the component will have an overhaul interval (L) and an aging surveillance interval (T). The particular applicable situation will depend on the plant's maintenance program.

The effective overhaul interval (L) is the interval at which the component is completely renewed of aging effects. At an overhaul, major subassemblies or pieceparts of the component are generally replaced. If surveillance is also carried out for aging effects between overhauls then the component is checked to assure it has not failed from aging effects. If the component is failed, it is restored to an operational status with minimum subassembly or piecepart replacement. In reliability terminology, the overhaul interval L is called the "good as new interval" and the surveillance interval T is called the "good as old interval".

The effective overhaul interval or surveillance interval is the actual interval divided by the efficiency of the overhaul or surveillance in detecting and correcting aging effects. Surveillances which are performed but are not effective in detecting and correcting aging effects will not be included as effective aging surveillances. For a given maintenance program, the values of the effective overhaul intervals and effective surveillance intervals are determined from the maintenance and surveillance schedules, and the effectiveness of the activities in detecting and correcting aging effects.

The maintenance programs that were evaluated for the applications covered a range of programs in terms of the effective overhaul intervals and surveillance intervals which characterized the program. As indicated in the previous table, some programs were characterized as having only overhaul intervals, with surveillance being ineffective in detecting and correcting aging effects. For each aging maintenance program evaluated, the four aging rate data bases (TIRGALEX, MOD1, MOD2, and MOD3) were used to determine the core melt frequency change for different types of aging represented by the data bases. The goal was to determine how much of an effect different maintenance programs could have.

The two figures on the next pages entitled "Core Melt Frequency Increase ΔC Versus Maintenance Program Characteristics", summarize the point results that were obtained for Plant A (the PWR) and for Plant B (the BWR). The y-axis on the figures is the average increase in core melt frequency ΔC due to aging which is calculated to occur under a given maintenance program. The x-axis identifies the different aging maintenance programs that were evaluated, as was described. For example, L=18 T=1 denotes the maintenance program with effective overhaul intervals of 18 months and effective aging surveillance intervals of 1 month on all components. The maintenance programs are arranged in terms of the increasing core melt frequency ΔC they produce. The results for the TIRGALEX overhaul intervals are not shown since they involve a unique interval for each component; the TIRGALEX results are circumscribed by the results shown and are described in the report.

The different results for a maintenance program correspond to the four different aging rate data bases that were used. The horizontal dotted line in each figure is the average baseline core melt frequency that was calculated in the NUREG 1150 PRA without considering aging effects. For Plant A (the PWR) the baseline core melt frequency is 2×10^{-5} per year and for Plant B (the BWR), it is 2×10^{-6} per year.

The two figures show the significant differences in core melt frequency control that result from different aging maintenance programs. These results are significant because they quantify the impacts aging and maintenance can have. These evaluations are the first quantifications of aging and maintenance impacts using full scale, up to date PRAs. It is important to note that the increases in core melt

Core Melt Frequency Increase ΔC Versus Maintenance Program Characteristics

Plant A

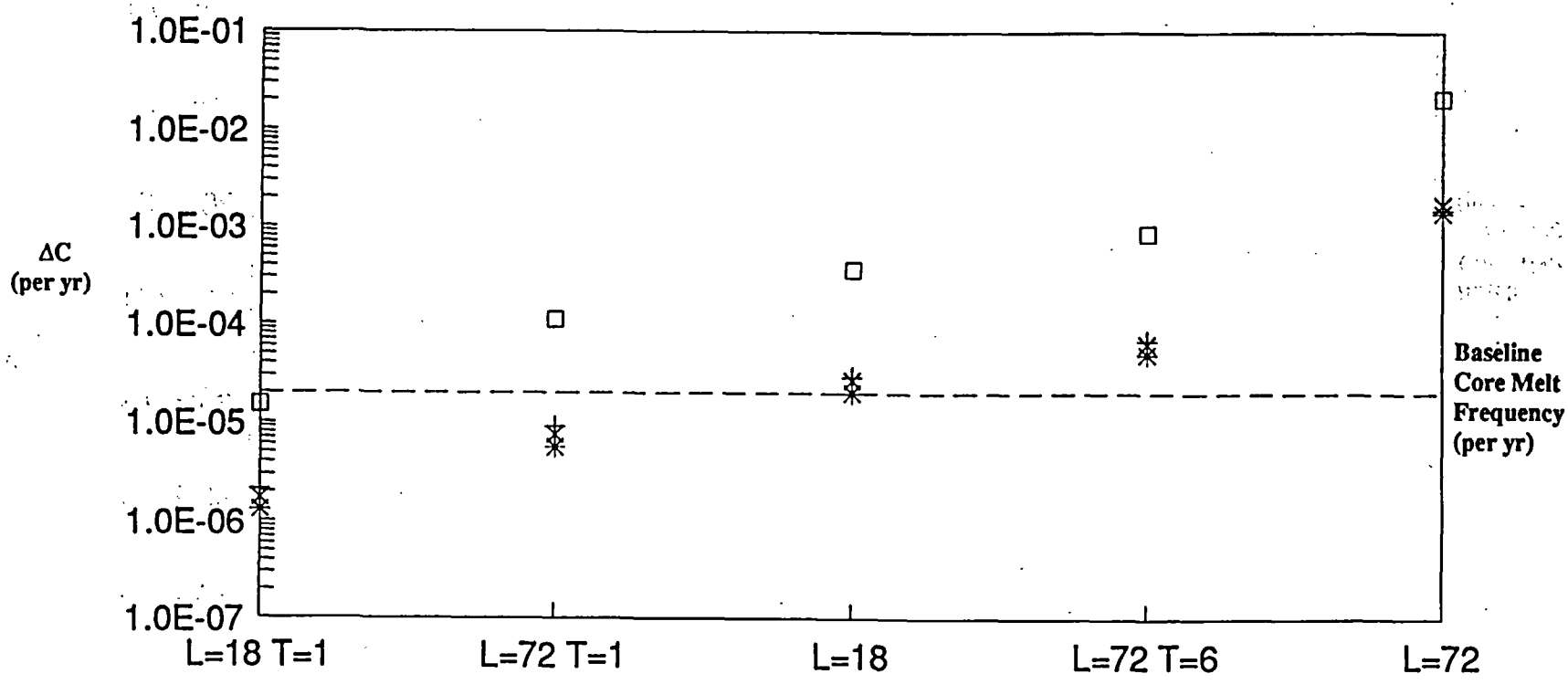

L = Overhaul interval (in months) for all components

T = Surveillance interval (in months) for all components (if intermediate surveillance is performed)

Core Melt Frequency Increase ΔC Versus Maintenance Program Characteristics

Plant B

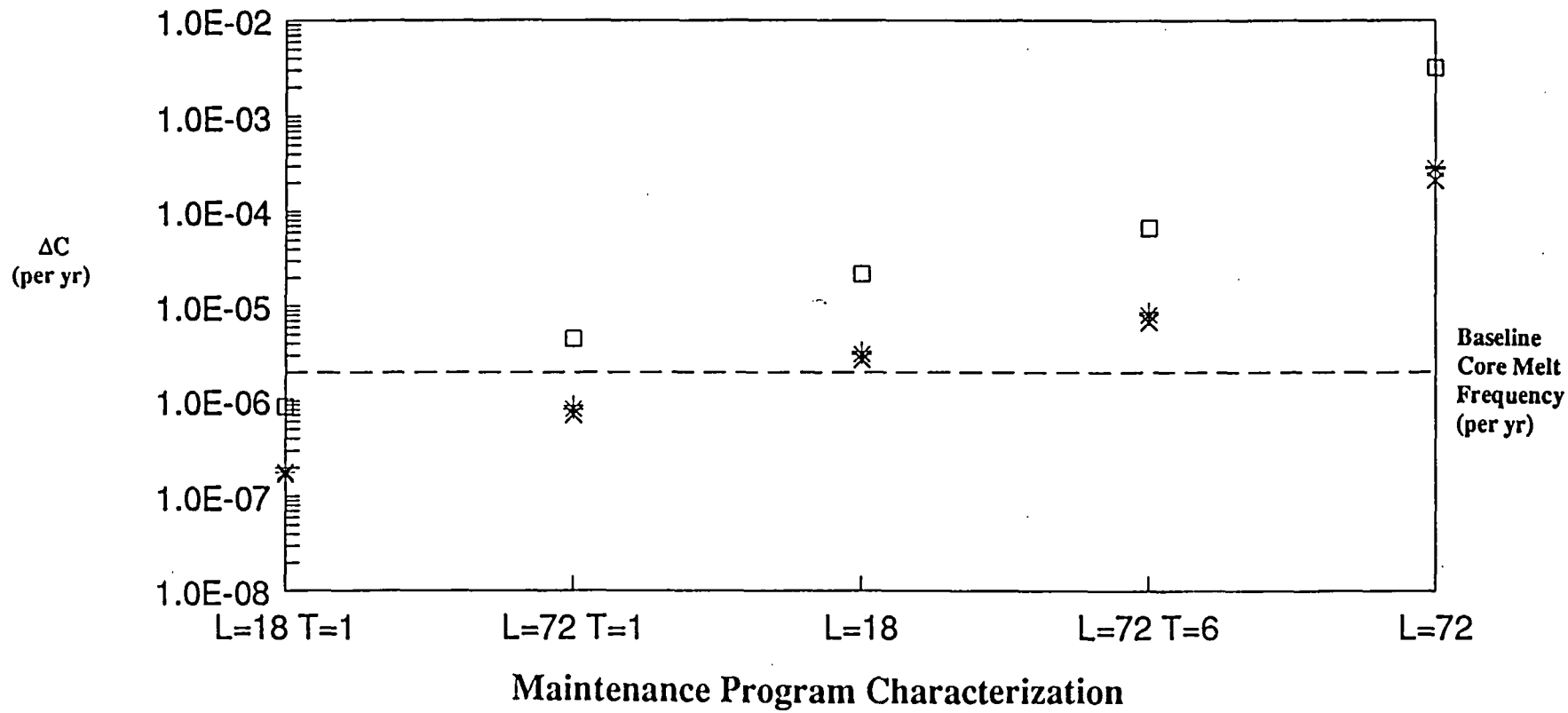

L = Overhaul interval (in months) for all components

T = Surveillance interval (in months) for all components (if intermediate surveillance is performed)

occurred even though the aging rates utilized were generally small to moderate. Even for the largest aging rates producing the largest core melt frequency increases, the aging only corresponded to one additional failure on the average after 5 years.

When the core melt frequency increase ΔC is high for a lower level maintenance program, then examination of the aging contributors showed that relatively few components contribute. This implies that a "graded" maintenance program, or equivalently a "prioritized" maintenance program, can effectively control the core melt frequency increase due to aging. In a graded or prioritized maintenance program, most components can have a lower level of maintenance provided aging-important components have a higher level of maintenance.

The dominant aging contributors for Plant A (the PWR) were found to be diesel generators, specific check valves and motor operated valves in the emergency core cooling system, and motor driven pumps and turbine driven pumps in the aux-feed system. For Plant B (the BWR) the dominant aging contributors were the diesels, the motor driven pumps in the service water system, and the turbine driven pumps in the reactor core isolation system. The aging contribution from every component in the PRA is provided, to the detailed defined in the PRA. Also, the contributions from multiple component interactions are provided; the interactions from multiple aging components were often the dominant contributors to the core melt frequency impacts. These detailed contributors include contributions from specific systems, components, and failure modes and provide a comprehensive means of focusing aging analyses and aging control efforts.

The tables on the next pages illustrate the results that are obtained for the detailed aging contributions. The first table shows the results that are obtained for individual aging contributions. The table gives the component and failure mode as identified in the PRA, the increase in component unavailability due to aging ($\Delta q1$), the core melt frequency importance factor for the component (S1) and the core melt frequency increase (ΔC) from the aging of that component under the given maintenance program. The second table shows similar results for the aging contributions from multiple component aging effects. The particular table shows the contributions from two component interactions. As previously indicated, the multiple component aging interactions are sometimes dominant contributors to the core melt frequency increase.

EFFECTIVE RENEWAL INTERVAL = 72 MONTHS

Plant A
16-Oct-89
02:03 PM

TIRGALEX / 72 MO.
TOP SINGLE CONTRIBUTORS

Total ΔC = 3.3E-04

Rank	Component Name	$\Delta q1$	S1	ΔC
1	HPI-MOV-FT	1.9E-01	3.4E-04	6.4E-05
2	OEP-DGN-FS-DG01	1.9E-01	2.3E-04	4.4E-05
3	OEP-DGN-FR-6HDG1	1.9E-01	2.1E-04	4.0E-05
4	LPR-MOV-FT	1.9E-01	1.3E-04	2.5E-05
5	OEP-DGN-FS-DG02	1.9E-01	1.3E-04	2.4E-05
6	OEP-DGN-FS-DG03	1.9E-01	1.3E-04	2.4E-05
7	OEP-DGN-FR-6HDG3	1.9E-01	1.2E-04	2.3E-05
8	OEP-DGN-FR-6HDG2	1.9E-01	1.1E-04	2.0E-05
9	HPI-MOV-FT-1350	1.9E-01	6.7E-05	1.3E-05
10	OEP-DGN-FR-DG01	1.9E-01	3.8E-05	7.2E-06
11	AFW-TDP-FS-FW2	1.4E-01	2.9E-05	4.1E-06
12	LPR-MOV-FT-1862A	1.9E-01	2.1E-05	4.0E-06
13	LPR-MOV-FT-1862B	1.9E-01	2.1E-05	4.0E-06
14	LPR-MOV-FT-1860B	1.9E-01	2.1E-05	3.9E-06
15	LPR-MOV-FT-1860A	1.9E-01	2.1E-05	3.9E-06
16	OEP-DGN-FR-DG03	1.9E-01	2.0E-05	3.8E-06
17	OEP-DGN-FR-DG02	1.9E-01	2.0E-05	3.7E-06
18	LPI-MDP-FS	1.2E-02	2.2E-04	2.6E-06
19	PPS-MOV-FT-1535	1.9E-01	9.5E-06	1.8E-06
20	AFW-TDP-FR-2P6HR	1.4E-01	1.1E-05	1.6E-06
21	LPR-MOV-FT-1890B	1.9E-01	4.5E-06	8.5E-07
22	LPR-MOV-FT-1890A	1.9E-01	4.5E-06	8.5E-07
23	CVC-MDP-FR-2A1HR	1.2E-02	6.7E-05	7.8E-07
24	HPI-MOV-FT-1115E	1.9E-01	4.1E-06	7.8E-07
25	HPI-MOV-FT-1115B	1.9E-01	4.1E-06	7.8E-07

EFFECTIVE RENEWAL INTERVAL = 72 MONTHS

Plant A
16-Oct-89
02:06 PM

TIRGALEX / 72 MO.
TOP DOUBLE CONTRIBUTORS

Total ΔC = 1.4E-03

Rank	Component Name	Δq1	Component Name	Δq2	S12	Δq1 Δq2	ΔC
1	OEP-DGN-FR-6HDG3	1.9E-01	OEP-DGN-FR-6HDG1	1.9E-01	3.6E-03	3.6E-02	1.3E-04
2	OEP-DGN-FS-DG01	1.9E-01	OEP-DGN-FS-DG03	1.9E-01	3.1E-03	3.6E-02	1.1E-04
3	OEP-DGN-FS-DG01	1.9E-01	OEP-DGN-FS-DG02	1.9E-01	3.1E-03	3.6E-02	1.1E-04
4	OEP-DGN-FS-DG03	1.9E-01	OEP-DGN-FR-6HDG1	1.9E-01	2.4E-03	3.6E-02	8.8E-05
5	OEP-DGN-FS-DG01	1.9E-01	OEP-DGN-FR-6HDG2	1.9E-01	2.4E-03	3.6E-02	8.8E-05
6	OEP-DGN-FS-DG02	1.9E-01	OEP-DGN-FR-6HDG1	1.9E-01	2.4E-03	3.6E-02	8.8E-05
7	OEP-DGN-FS-DG01	1.9E-01	OEP-DGN-FR-6HDG3	1.9E-01	2.4E-03	3.6E-02	8.8E-05
8	OEP-DGN-FR-6HDG2	1.9E-01	OEP-DGN-FR-6HDG1	1.9E-01	2.4E-03	3.6E-02	8.7E-05
9	LPR-MOV-FT-1862B	1.9E-01	LPR-MOV-FT-1860A	1.9E-01	1.5E-03	3.6E-02	5.4E-05
10	LPR-MOV-FT-1862A	1.9E-01	LPR-MOV-FT-1862B	1.9E-01	1.5E-03	3.6E-02	5.4E-05
11	LPR-MOV-FT-1862A	1.9E-01	LPR-MOV-FT-1860B	1.9E-01	1.5E-03	3.6E-02	5.4E-05
12	LPR-MOV-FT-1860A	1.9E-01	LPR-MOV-FT-1860B	1.9E-01	1.5E-03	3.6E-02	5.4E-05
13	LPR-MOV-FT-1890B	1.9E-01	LPR-MOV-FT-1890A	1.9E-01	1.5E-03	3.6E-02	5.4E-05
14	HPI-MOV-FT-1115B	1.9E-01	HPI-MOV-FT-1115D	1.9E-01	1.4E-03	3.6E-02	4.9E-05
15	HPI-MOV-FT-1115C	1.9E-01	HPI-MOV-FT-1115E	1.9E-01	1.4E-03	3.6E-02	4.9E-05
16	OEP-DGN-FR-DG01	1.9E-01	OEP-DGN-FR-DG03	1.9E-01	6.4E-04	3.6E-02	2.3E-05
17	OEP-DGN-FS-DG03	1.9E-01	OEP-DGN-FR-DG01	1.9E-01	6.0E-04	3.6E-02	2.2E-05
18	OEP-DGN-FS-DG02	1.9E-01	OEP-DGN-FR-DG01	1.9E-01	6.0E-04	3.6E-02	2.2E-05
19	OEP-DGN-FS-DG01	1.9E-01	OEP-DGN-FR-DG02	1.9E-01	6.0E-04	3.6E-02	2.2E-05
20	OEP-DGN-FS-DG01	1.9E-01	OEP-DGN-FR-DG03	1.9E-01	6.0E-04	3.6E-02	2.2E-05
21	OEP-DGN-FR-DG02	1.9E-01	OEP-DGN-FR-DG01	1.9E-01	5.8E-04	3.6E-02	2.1E-05
22	OEP-DGN-FS-DG02	1.9E-01	OEP-DGN-FS-DG03	1.9E-01	2.2E-04	3.6E-02	7.8E-06
23	OEP-DGN-FR-6HDG3	1.9E-01	OEP-DGN-FR-6HDG2	1.9E-01	2.0E-04	3.6E-02	7.1E-06
24	OEP-DGN-FS-DG01	1.9E-01	AFW-TDP-FS-FW2	1.4E-01	2.6E-04	2.7E-02	7.0E-06
25	OEP-DGN-FS-DG02	1.9E-01	OEP-DGN-FR-6HDG3	1.9E-01	1.9E-04	3.6E-02	6.9E-06

In addition to the point calculations, uncertainty evaluations were also carried out. For the uncertainty evaluations, ranges were assigned to each component aging rate, each overhaul interval, and each surveillance interval. These ranges described uncertainties and variabilities in the data. Log uniform distributions, which are flat distributions on a log scale, were used for the uncertainty propagations. All the variables were treated as being independent of one another for the evaluations. The table below summarizes the ranges that were assigned to characterize each overhaul interval and surveillance interval for the three cases that were evaluated.

MAINTENANCE PROGRAM CHARACTERIZATIONS FOR THE UNCERTAINTY EVALUATIONS

1. Each active component has an overhaul interval (L) in the range between 12 months and 120 months, which represent 5% and 95% bounds.

2. Each active component has an overhaul interval (L) in a range defined from the TIRGALEX report.

3. Each active component has an overhaul interval (L) in the range between 12 months and 120 months and also has an aging surveillance interval (T) in the range between 1 and 12 months, representing 5% and 95% bounds.

The uncertainty evaluations again showed the large impacts different maintenance programs can have on the control of core melt frequency. The two figures on the subsequent pages, labelled "Probability That the Core Melt Frequency is Larger Than Given Values" show the probability distributions obtained for the different maintenance program characterizations. For each maintenance program characterization, the probability curve is only given for the TIRGALEX aging rates since the other aging rate data sets produced similar probability curves. A given point on a probability curve gives the probability (on the y-axis) that the average core melt frequency increase is larger than a given value (on the x-axis).

As the figures indicate, the characterization of maintenance programs determines the core melt frequency increases which can occur. If aging maintenance programs are characterized as having overhaul intervals in the range of L = 12 - 120 months

Probability that the Aging Increase in Core Melt Frequency is Larger than Given Values

Plant A

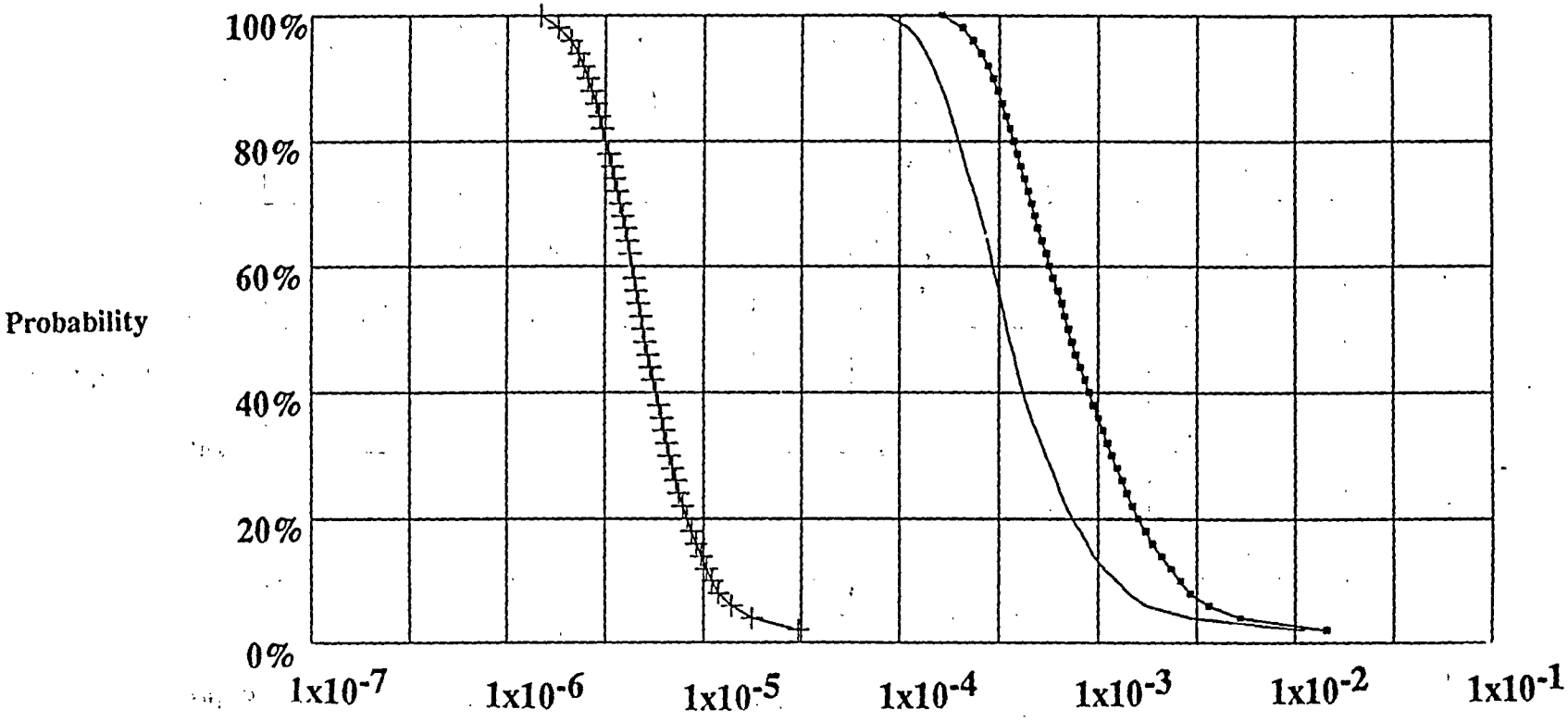

Probability that the Aging Increase in Core Melt Frequency is Larger than Given Values

Plant B

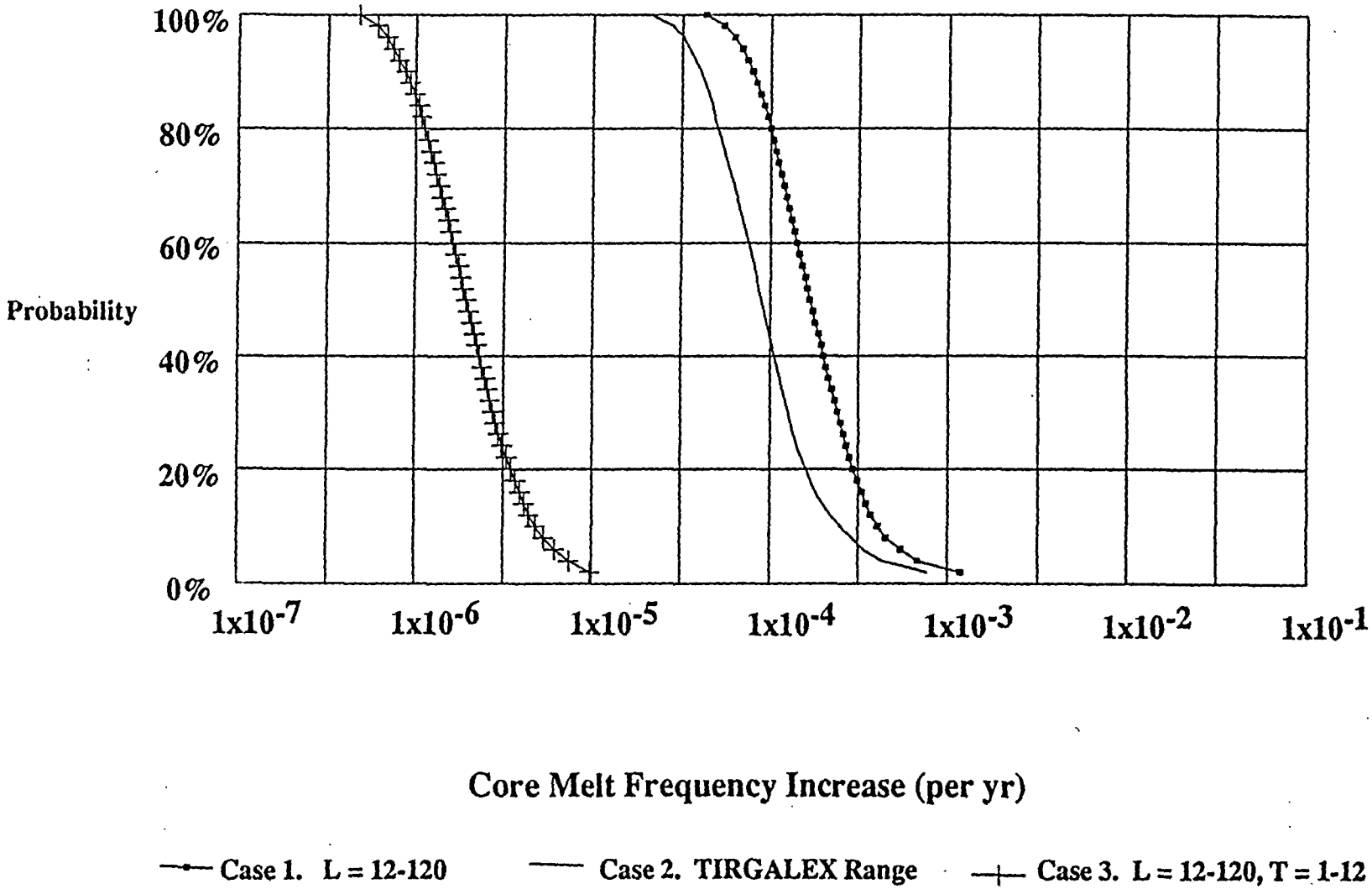

(Case 1) or as having overhaul intervals as characterized by the TIRGALEX ranges (Case 2) then relatively large core melt frequency increases can occur. If the maintenance programs are more effective and are characterized as having overhaul intervals L of 12-120 months and supplemental surveillance intervals T of 1-12 months (Case 3) then relatively smaller core melt frequency increases can occur. As for the previous point results, the larger core melt frequency increases which occur can be reduced by focusing tighter maintenance on the age-important components. Other maintenance program characterizations will produce other results.

Based on the results of the work to date, various recommendations can be made. Plant maintenance programs should be reviewed to determine their characterization in terms of applicable overhaul intervals and aging surveillance intervals for key components. The work identifies ways this can be done. The approaches which have been developed can then be used to evaluate current test and maintenance programs for their core melt frequency effectiveness. The aging rate data which was utilized did not have as large effects as the maintenance program characterizations. However, larger aging rates could produce significantly larger impacts. It is therefore important to collect and analyze component failure and maintenance data to estimate the associated aging rates and as importantly, to determine their projected core melt frequency impacts. The quantification approaches which have been developed can be used in this manner to monitor and audit failure and maintenance data for aging implications.

The PRAs truncated many contributions e.g. contributions from multiple check valve failures were excluded, that could become important when aging is considered. It would be useful to expand the PRA contributions (minimal cut sets) and rerun the aging evaluations to determine the contributions from higher order, multiple component aging effects. It would also be useful to evaluate additional PRAs to determine generic conclusions regarding aging effects and aging contributors.

The aging contributions from passive components and structures are not included in the present evaluations. It is important to include these critical contributors to obtain a more complete picture of aging impacts not only on core melt frequency, but on public health risks. The approaches which have been developed can incorporate passive components and structures if aging data and models are

assembled as they were for the active components. It is important to include these additional contributors since they can have large impacts.

With regard to regulatory applications, the approaches which have been developed can be useful in helping to define maintenance guidelines for controlling core melt frequency impacts and risk impacts from aging. The developed risk quantification approaches can serve as powerful tools to complement deterministic considerations. The approaches can be used to prioritize aging contributors to determine where to focus more detailed deterministic aging analyses and aging maintenance. In the applications which were carried out, there were a relatively small number of important contributors which impacted the core melt frequency, implying that prioritization can be very effective. The quantification approaches which have been developed can also be used to help define guidelines for risk-effective overhaul intervals and surveillance intervals to control aging impacts. The approaches can furthermore be used to define component performance guidelines in terms of component failure rate increases and unavailability increases which require action before risk is impacted. Data collection guidelines can also be developed to define what data should be collected and should be analyzed to audit and monitor aging effects and their risk implications. Finally, the approaches which have been developed can be used as a review tool to evaluate the risk-effectiveness of proposed programs for aging maintenance and aging control.

REFERENCES

1. W.E. Vesely, D.E. Korns, P.L. Appignani, and S.M. Scalzo, "Evaluations of Aging Effects in Component Failure and Maintenance Data", SAIC Draft Report Submitted to NRC, September 28, 1989.

2. W.E. Vesely, R.E. Kurth, G.A. Burlile, and S.M. Scalzo, "Evaluations of Core Melt Frequency Changes Due to Component Aging", SAIC Draft Report Submitted to NRC, August 25, 1989.

The Use of NPAR Results in Plant Inspection Activities[1]

W. Gunther and J. Taylor
Brookhaven National Laboratory
Upton, NY 11973

ABSTRACT

The U.S. NRC's Nuclear Plant Aging Research (NPAR) Program is a hardware oriented research program which has produced a large data base of equipment and system operating, maintenance, and testing information. Equipment and systems which have a propensity for age related degradation are identified, and methods for detecting and mitigating aging effects have been evaluated.

As plants age, it becomes increasingly important that NRC inspectors be cognizant of plant aging phenomena. This paper describes the NPAR information which can enhance inspection activities, and provides a mechanism for making pertinent research available to the inspectors.

BACKGROUND

The NPAR program's goals are to obtain an understanding of the aging degradation processes in components, systems, and structures, and assess methods for detecting and mitigating aging[1]. This hardware-oriented engineering research program uses a two phase approach. The typical output from a two phase study of a component or system includes information such as:

- A detailed assessment and evaluation of operating experience.
- An evaluation of failure modes, causes, and effects.
- A review of current industry maintenance and operating practices.
- An evaluation of operational stresses which could lead to equipment degradation or premature failure.

More than fifty reports have been published through the NPAR program. The potential exists for this output to directly support the NRC regional inspection activities. More specifically, one of the goals of the work described in this paper is to explore the inspection areas where NPAR results could enhance the inspector's understanding of the subject area, thereby contributing to a more effective inspection. Other goals are:

- To identify NPAR information that can help focus inspections on those components and systems vulnerable to age-related degradation, and
- to identify methods for integrating research results into the inspection process.

[1] Work done under the auspices of the U.S. Nuclear Regulatory Commission.

DESCRIPTION OF RESEARCH ACTIVITIES

To achieve the objective of integrating NPAR information into the NRC Inspection Program, a number of activities have been accomplished. It was first necessary to review the Inspection Program to determine relevant inspection guidance. Chapter 2515 of the NRC Inspection Manual was reviewed to determine the areas of emphasis, and to ascertain where aging information could be effective in achieving the inspection goals[2]. Secondly, the NPAR information with potential application to these inspection activities was identified. Four areas of NPAR program results which had applicability to inspection activities are categorized as:

a) component background

b) operating experience

c) recommendations

d) references.

Under the component background category are items such as identification of materials and subcomponents, design specifications, and operating parameters in which age effects dominate. The operating experience heading includes failure data, operational stresses and risk contributions. Recommendations is the area which encompasses the major research results including functional indicators and viable aging detection and mitigation techniques. Also included is an evaluation of current maintenance practices, vendor recommendations, and the results of any testing performed as part of the research. The references area includes NRC documents associated with this component, as well as related industry standards.

Thirdly, the material must be assembled and presented in a format that meets the inspection needs. In this regard, feedback was solicited directly from the inspectors through presentations at regional seminars. This latter activity and its effect on the recommendations are the main emphasis of this paper.

REGIONAL INTERFACE

Presentations were made to Regions 1, 2 and 3 over a 2 month interval between March and May of 1989. These meetings were coordinated with the resident inspector meetings which are held every three to four months. The presentations consisted of two parts, with the first describing the overall goals and objectives of the NPAR program, and the second segment of the presentation providing specific examples of research results and how they could be applied to inspection activities. This latter segment was supported by NPAR report excerpts which were arranged in the four categories described in the previous sections.

The overall response from the regions to the NPAR approach and the type of results achieved to date was favorable. Resident inspectors, especially those assigned to the older plants, supported the need to address aging as a separate issue. Through the use of a survey form they indicated the following preferences:

1. The category of operating experience was felt to be of most value with 60% of the inspectors ranking it "very useful" (5 on a scale of 1 to 5).

2. Most inspectors felt that summaries of the NUREG/CR reports would be the best method of alerting inspectors to NPAR results. The average rating was 3.9 on the 1 to 5 scale.

3. The survey respondents listed a host of systems and components which were of interest to them from the aging perspective. There was only minor commonality, indicating that information needs vary widely depending on the individual's experience, and the problems present at the plants where they are assigned.

RECOMMENDATIONS AND CONCLUSIONS

Based on feedback obtained from these presentations and from discussions with regional management, several recommendations are made to achieve the goal of transferring useful information from the NPAR program to the regions:

1. *Summarize the research from NPAR reports that are applicable to NRC inspection activities.* A summary of the research results coupled with an aging inspection guide will provide the inspector with important insights regarding the aging degradation of various equipment and systems. The summary for each equipment type and system studied in the NPAR Program would include the identification of aging related problems, highlights of the operating experience, solutions to aging problems, and references likely to be available to the inspector. The aging inspection guide is a more concise summary of recommendations with emphasis on visual inspection techniques and activities to evaluate licensee programs for understanding and managing aging. A sample report summary and aging inspection guide have been included as Appendix A and B, respectively.

2. *Establish a schedule of regular regional presentations by NPAR contractors.* Results oriented discussions by NPAR representatives would be of mutual benefit to the regions and NRC research. A workshop type atmosphere for components or systems of particular interest to the region would be of greatest value.

3. Continue to work with the NRC's Data Administration Branch to make NPAR results available through a system such as the Safety Information Network (SINET)[3] With the expanding use of personal computers at NRC offices and the desire to minimize the amount of documentation routinely processed by the NRC inspectors, exploring the application of a data base system is justified.

REFERENCES

1. NUREG-1144, Revision 1, "Nuclear Plant Aging Research (NPAR) Program Plan," September 1987.

2. NRC Inspection Manual, "Light Water Reactor Inspection Program-Operations Phase," Chapter 2515, Appendix D, August 1988.

3. NUREG-1145, Vol. 4, U.S. NRC 1987 Annual Report, pps. 172-177.

AGING REPORT SUMMARY
INVERTERS

SUMMARY

Inverters are used in nuclear power plants to convert dc to ac power for instrumentation, controls, and other equipment necessary for power operation and safety. Research has shown that inverter performance will degrade with time due to the aging susceptibility of some components and materials. This degradation can be detected and mitigated through maintenance, operation, and design activities. This guide summarizes these recommended practices, and identifies areas of inspection importance.

BASED ON:

1. NUREG/CR-4564, *Operating Experience and Aging-Seismic Assessment of Battery Chargers and Inverters*
2. NUREG/CR-5051, *Detecting and Mitigating Battery Charger and Inverter Aging*
3. NUREG/CR-5192, *Testing of a Naturally Aged Battery Charger and Inverter*

AGING RELATED PROBLEMS

Large percentage of inverter failures due to hardware. Components found to be susceptible to aging degradation are:

1. **FILTER CAPACITORS:** These components have experienced a limited service life (approximately 5 years) directly related to ambient temperature, applied voltage, and ripple current.

2. **THYRISTORS (SCRs):** Large SCRs used in the power conversion circuit generate heat which is designed to be dissipated through attached heat sinks. Improper torque of the SCR/heat sink connection has resulted in overheating and failure of the SCR.

3. **FUSES:** Fast acting fuses are used to protect inverter electronics and are subject to a thermal fatigue. Depending on internal cabinet temperature and the proximity of the fuse rating to normal load current, expected life can vary from 5 to 25 years. As the fuses degrade, they are more susceptible to normal plant electrical transients such as starting motors and switching operations.

OPERATING EXPERIENCE

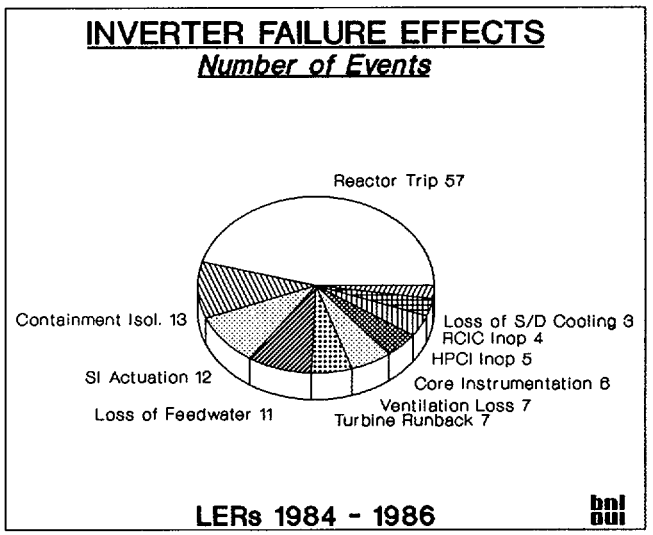

The operating experience data have demonstrated that inverter failures can impact plant safety and availability. One of the most visible and dramatic effects of an inverter failure is reactor trip. From 1984 to 1986, 57 reactor trips resulted from an inverter failure. In addition, safety injection (SI) system actuations, containment isolations, and safety system (HPCI & RCIC) inoperability were directly linked to inverter failures.

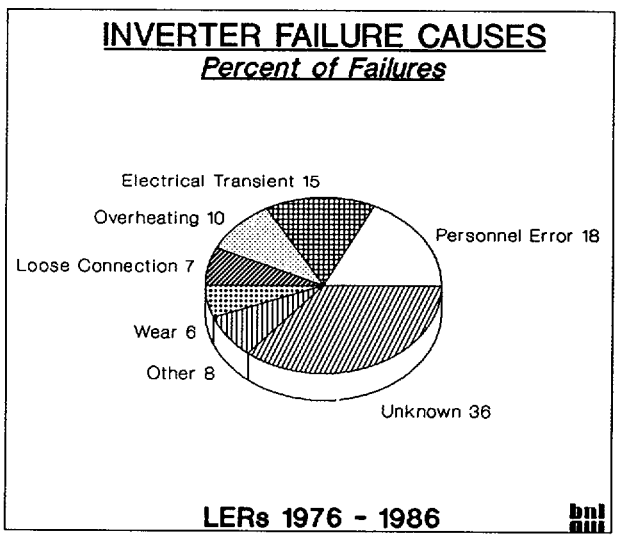

The analysis performed on operating experience data accumulated over 12 years indicates that overheating, electrical transients and personnel errors are the leading causes of inverter failures. Stresses from these occurrences cause aging of critical components. The large percentage of unknown causes may due to 'normal' electrical switching where inverter fuse or circuit breaker operation results.

SOLUTIONS TO AGING PROBLEMS

DESIGN

Four basic designs of inverters are used in the nuclear industry. Improvements have been made in the more recently manufactured units, such as:

1. The use of an automatic transfer switch, which senses an inverter failure and switches to a backup power source without a detectable loss of power to vital equipment.
2. The installation of higher voltage and temperature rated components, especially capacitors & semiconductors. This makes these components less susceptible to operationally induced stresses.
3. Forced air cooling rather than natural convection cooled units tend to have less overheating problems. Several utilities have modified the inverters in this manner.
4. Additional monitoring capabilities, including annunciation of abnormal conditions, such as high temperature, are available in newer units.

MAINTENANCE & MONITORING

Based on the inverter's importance and the effects of its failure on plant safety and availability, a comprehensive inverter maintenance program is recommended. To detect and mitigate the effects of aging on inverters, this program should include inspection, testing, and preventive maintenance.

(continued)

MAINTENANCE & MONITORING

INSPECTION

The inspection of an inverter by experienced personnel can provide a great deal of information about the equipment's overall condition.

1. While operating, observation of cyclical electrical hum, meter oscillation, or cooling fan noise can indicate an impending failure.

2. Component degradation due to overheating, and loose electrical and mechanical connections can be detected when the inverter is off-line.

3. Cleaning can minimize the risk of overheating. The wiping of SCR heat sinks and ventilation flow paths improves heat transfer away from temperature sensitive components.

TESTING/MONITORING

Periodic testing is necessary to verify that design parameters are obtainable under all conditions. The acceptance criteria for such testing should be based on specific plant and manufacturer information.

1. Overheating is an important cause of stress that can reduce the expected life of electrolytic capacitors, thyristors, and inductors. It is prudent to periodically monitor them to detect any increase in temperature.

2. Component performance data may change with time and can indicate degradation. Two parameters for detecting aging of electrolytic capacitors are an increase in the equivalent series resistance (ESR) or a decrease in the value of the capacitance.

3. Capacity testing, especially for standby inverters, is recommended. This verifies that the inverter can supply design loads, and permits inspection and monitoring techniques to be applied at rated conditions.

4. The automatic transfer switch should be tested to verify it is capable of transferring to the alternate supply without interrupting power to critical equipment.

PREVENTIVE & CORRECTIVE MAINTENANCE

Specific requirements from the manufacturer should be incorporated into the maintenance program. These are based on the manufacturer's experience or are generated as a result of equipment qualification. Guidelines are also provided to restore the inverter to an operable condition following a failure.

1. Deviations from equipment qualification requirements require documented engineering analyses. Components which have been identified as having limited service lifes include capacitors, cooling fans, fuses, circuit breakers, and relays.
2. Replacement power electronics, such as SCRs, should be remounted to a cleaned heat sink surface at the torque specified by the vendor.
3. Loose power cable terminal contact surfaces should be cleaned prior to tightening.
4. Fuses identical in rating and design should be used.

REFERENCES

These documents provide additional background information regarding inverters used in nuclear power plants.

1. **AEOD Case Study Report C605,** "Operational Experience Involving Losses of Electrical Inverters", 12/86.
2. **Information Notice 87-24,** "Operating Experience Involving Losses of Electrical Inverters".
3. **Information Notice 88-57,** "Potential Loss of Safe Shutdown Equipment Due to Premature SCR Failures".
4. **IEEE-650-1989,** "IEEE Standard for Qualification of Class 1E Static Battery Chargers and Inverters for Nuclear Power Generating Stations".

AGING INSPECTION GUIDE-*INVERTERS*

I. Visual Inspection Summary

a. External

1. no unusual meter oscillation or electrical hum
2. input and output parameters in spec. (voltage, current, frequency)
3. cooling air filters not clogged

b. Internal

1. no signs of overheating
2. capacitors not bulging or leaking oil
3. cleanliness, especially of SCR heat transfer surfaces

II. Licensee Program Evaluation for Understanding and Managing Aging

a. Maintenance Related Activities

1. Periodic inspections are performed and include cleaning & connection tightness check
2. Preventive maintenance is conducted at least once per cycle and includes calibration, EQ related component replacements, and evaluation of circuit waveforms. Note that electrolytic capacitors are included in EQ program.
3. Personnel responsible for maintenance have been trained, and use approved procedures which have incorporated vendor recommendations.

b. Operations Related Activities

1. Daily logs or round sheets include recording data or observing inverter performance
2. Operating procedures address the response to an inverter failure
3. Periodic checks are made to insure proper electrical alignment - normal supply from the station battery

AGING INSPECTION GUIDE-*INVERTERS*
(continued)

c. Design/Test Related Activities

1. Loading of inverter for normal and postulated accident conditions is within equipment rating.
2. Static switch is functionally tested to assure uninterruptible transfer to alternate supply.
3. Capacity testing, especially recommended for standby inverters, accurately reflects loads.
4. Protective device co-ordination between the inverter and its branch circuits exists.

d. Other Recommended Licensee Activities

1. Replacement or testing of all filter capacitors should be considered when one fails. (Same stress)
2. The ferro-resonant inverters (i.e., SCI, Westinghouse) use magnetic components for waveform shaping and voltage regulation. Special ferro tuning techniques recommended by the manufacturer should be followed.
3. The pulse-width modulated inverters (i.e., Elgar, Cyberrex) generate a near sine wave output through electronic feedback. Photographing the wave shapes for timing and sequence should provide good trouble shooting information.

NPAR APPROACH TO CONTROLLING AGING IN NUCLEAR POWER PLANTS

J. A. CHRISTENSEN
PACIFIC NORTHWEST LABORATORY

ABSTRACT

Aging degradation in nuclear power plants must be controlled to prevent safety margins from declining below limits provided in plant design bases. The NPAR Program and other aging-related programs conducted under the auspices of the NRC Office of Research are developing needed technical guidance for control of aging. Results from these programs, together with relevant information developed by industry and elsewhere, are implemented through various ongoing NRC and industry programs and initiatives as well as by means of conventional regulatory instruments. The aging control process central to these efforts consists of three key elements: 1) selection of components, systems, and structures (CSS) in which aging must be controlled, 2) understanding of the mechanisms and rates of degradation in these CSS, and 3) managing degradation through effective surveillance and maintenance. These elements are addressed in Good Practices Guidance that integrates information developed under NPAR and other studies of aging into a systems-oriented format that tracks directly with the Safety Analysis Reports.

INTRODUCTION

Aging: Cumulative degradation of a component, system, or structure which, if unmitigated, may result in loss of function and impairment of safety.

For several years, the NRC Nuclear Plant Aging Research Program (NPAR) has been developing technical understanding of the time-dependent processes that, through deterioration of components, systems, or structures (CSS), can reduce safety margins in a nuclear power plant (NPP)(1-3). The NPAR program, which is administered by the NRC/RES Electrical and Mechanical Engineering Branch, along with similar efforts performed by the Materials Engineering Branch and the Structural and Seismic Engineering Branch provide for consideration of age-related degradation in all NPP elements that have important safety functions.

The need to mitigate time-dependent deterioration of NPP plant components is not a new or recent concept. Degradation with time is, or should be, a prime consideration in any design effort. The materials specifications and mechanical designs that characterize NPP CSS reflect conscious, detailed concern on the part of the designer over the effects of anticipated service environments and stressors on functionality over time. The major codes and standards upon which NPP designs and inservice inspections are premised (e.g., ASME Boiler and Pressure Vessel Code, Sections III and XI) are based in large measure on recognized needs to achieve acceptable performance over reasonable time.(4)

This is true whether or not age-related degradation is explicitly addressed by the wording in the codes. Given that time-dependent degradation is fundamental to the codes and standards that govern NPP design, construction, and operation, why is additional concern over aging warranted? There are several reasons:

1. Much of the content of codes, standards, and other regulatory instruments that relate to aging is implicit in nature. Aging or time-rates-of-deterioration often are not mentioned or directly addressed, even if proper interpretation of stated requirements should result in their adequately being dealt with. This lack of specificity allows for exercise of considerable judgment in design and other functions. This judgment can be strengthened and made more consistent and defensible by the availability of explicit, detailed information on aging rates and consequences in specific CSS.

2. Codes, standards, and other traditional regulatory instruments evolve slowly. While much developing technology will eventually be reflected in changes to these types of instruments, the process for so doing is too slow. Not only must the frontier of understanding of aging degradation be pushed beyond the state-of-the-art apparent in codes standards and other instruments, but new technical findings must be accessible in a timely way to licensees, regulators, and others who need this information. The NRC aging research programs serve both purposes.

3. Accounting for aging in design and in developing plant operational guidelines is quantitatively very different from attempting to predict actual aging effects and residual lifetimes for CSS. Several conservatisms enter into the process of developing design and operational guidelines. In the case of design, for example, margins of safety are introduced to provide prudent assurance that design-base failures will not occur, i.e., will be mitigated by the end of the service life of the system or by scheduled repair, replacement, or refurbishment of the component in question. In practice, observed degradation rates are usually much lower than would be inferred from design lifetimes because of the need to include safety margins in design computations. (Alternatively, and rarely, degradation rates can be excessively high because of an unanticipated deterioration mode.) The function of aging management is to understand and control the time-dependent degradation that <u>actually</u> occurs in CSS. Management of aging thus focuses on nominal degradation rates as opposed to the upper bound rates associated with design. The nominal approach is needed to implement maintenance programs and to anticipate actual residual lifetimes as is necessary for such considerations as replacement frequency or extended plant life.

4. Most components of NPPs function not as isolated, unique elements but as interactive parts of systems. A given system or its redundant constituents or replicas often includes multiple copies of similar or identical component types. The design process considers, to some extent, single component aging degradation in estimating design lifetimes but does not

take into account common cause failure implications of aging in redundant components or the amplified effect of aging in failure sequences involving multiple component interactions. These effects can be dominant in determining overall level of plant safety. Their evaluation requires accurate failure rate vs time data for each component involved. These data must be applied using probabilistic methods that realistically model NPP systems on plant-specific bases.

Because of these kinds of considerations, specific concerns, independent of plant design and operational parameters, over how and why CSS degrade with age must be resolved. The generic content and structure of programs for addressing these concerns is the subject of the balance of this paper.

PRINCIPLES OF CONTROLLING AGE-RELATED DEGRADATION

Effective control of aging degradation requires a systematic approach that is based upon detailed understanding of CSS functions and their relationship to safety; an awareness of why, how, and where aging occurs; and adequate programs for mitigating the effects of aging. The principal elements of an aging control program structured to respond to these three functional attributes relate to:

1. Selection of CSS in which aging is of significant concern
2. Understanding of aging degradation in these components
3. Managing aging degradation to prevent reductions in safety margins.

These elements and their interfaces are illustrated schematically in Figure 1 and are individually discussed in the following sections.

SELECTION OF CSS

Age-related degradation of some sort occurs in most, if not all, of the CSS that comprise a NPP. It is expected that technical information developed under the NPAR and other NRC-RES aging programs will be useful for maintaining most NPP systems. In general, the CSS of interest are those:

a. That are relied upon to remain functional during or following design basis events to ensure:

   - the integrity of the reactor coolant pressure boundary,
   - the capacity to shut down the reactor and maintain it in a safe shutdown condition, or
   - the capability to prevent or mitigate the consequences of accidents that could result in potential off-site exposures that are unacceptable, e.g., in excess of the guideline exposures cited in 10 CFR 100 and

b. Whose malfunction could interfere with the accomplishment of one or more of these three functions.

Design basis events are those operational conditions and events (including anticipated operational occurrences, design basis accidents, external

events, and natural phenomena) for which the plant was designed to ensure the above.

These criteria are consistent with existing regulations governing environmental qualification and seismic classification. The intent of these criteria is to assure oversight and control of aging degradation in all NPP elements in which aging is of regulatory concern. The net effect of this approach will be to select CSS based upon deterministic assessments of potential aging processes for safety-related CSS and for those balance-of-plant (BOP) CSS whose malfunction could interfere with the functioning of safety-related CSS.

In addition to these deterministic criteria, it will be useful to develop risk-based selection criteria. These can provide a measure of the integrated effects of aging in major CSS on overall plant risk as characterized by factors such as calculated core damage frequency. Risk-based assessments of aging effects can be of value in general or may be useful for screening non-safety-related CSS to ensure that important aging processes have not been overlooked. Considerable progress has been made in developing methods for predicting aging effects on overall plant risk. Models that attempt to characterize aging rates for major components have been developed. These models, together with failure rate data, expert judgment, and estimates of maintenance intervals and effectiveness, have allowed estimates of the risk-based significance of aging in single components and of multiple component aging.(5,6) Incorporated into existing probabilistic-risk assessment (PRAs), these estimates can be used to predict plant- and system-specific effects of aging on hypothetical core damage frequency. These types of analyses can be used for screening CSS to assure that all known, important aging processes are addressed by aging management programs. The interactive elements involved in the selection of CSS are shown in Figure 2.

UNDERSTANDING AGING

The aging processes that occur in NPP CSS must be understood if age-related degradation is to be effectively managed. The requisite understanding may be either empirical or mechanistic depending on the nature and potential consequences of a particular degradation process. An understanding of aging degradation requires a detailed awareness of CSS design, fabrication, installation, testing, inservice operation, and maintenance cycles. All of these elements in the life cycle of CSS involve their interaction with stressors associated with service environment. Age-related degradations of CSS are time-dependent phenomena that depend upon the interactions of materials, environments, and stressors as shown schematically in Figure 3. Aging degradation assessments should consider the integrated effects of these interactions, and all CSS that are important to safety should be evaluated in this context.

Materials

Most materials used in the fabrication of CSS are subject to some level of age-related degradation. Whether this degradation can affect the operability or reliability of CSS such that safety margins are reduced below acceptable limits is a key concern.

It is important to understand how and at what rate the materials (metals, polymers, ceramics, composites, lubricants, etc.) used in plant components degrade with time, environment, and stressors, and how this degradation can be managed to assure the operability and reliability of CSS. This knowledge of material behavior is important in design and operations and in developing quality assurance, plant inspections, condition monitoring, and maintenance programs. As more is learned about the age-related behavior of materials and how to use this knowledge in the design and operation of CSS using these materials, confidence will grow in predictions of CSS lifetime behavior and plant operational safety.

Design and Environmental Conditions

The various environments in which CSS are designed to function affect degradation mechanisms and rates. Environmental elements include ambient operating conditions (air density, humidity, and temperature) within the plant or within a storage facility; chemicals that contact the material (pollutants, acids, lubricants, etc.); radiation, etc. Environmental effects can individually cause degradation such as corrosion or may act in combination with other factors (e.g., material type and condition, heat, and stress).

Stressors

Of the factors that can affect the aging degradation of NPP CSS, the stressors associated with inservice conditions are generally most difficult to characterize. Stressors assume various forms (e.g., mechanical, electrical, thermal), and some originate or are intensified during component fabrication, assembly, transportation, installation, operation, testing, and maintenance.

Mechanical stressors are generally associated with physical movements, pressure differentials, and dimensional changes. The functioning of CSS, either during normal operation (including testing) or under accident conditions, usually induces time-dependent mechanical stresses. These stresses are caused by dynamic loads, internal or external pressure changes, impact, temperature changes, component test loads, and seismically induced motions.

The operational motions of active CSS (e.g., valve operation and pump rotations) produce time-dependent distortions and inertial stresses as well as wear. The effects of these stresses in degrading CSS are generally understood; but the rate of degradation is usually only an estimate obtained from the analysis of inservice monitoring data, inspection reports, and maintenance information. Proper maintenance can mitigate much or all of the degradation that occurs because of mechanical and other stressors.

Internal and external pressure loads approaching operational or accident design limits also can produce high stresses that cause distortions and, with a sufficient number of applications, result in strain hardening and fatigue damage. If these stresses are combined with vibration and thermal stresses, measurable degradation can occur in a period of time that is short relative to the anticipated operational life of the CSS.

The extent of the damage to CSS resulting from external impact must be understood to anticipate any associated reduction in lifetime. Seismic events or similar but more localized events can inflict immediate damage to CSS at

any point during their operational life. Even though the CSS may not fail during the impact, their functional capability may be degraded such that the operational life is shortened.

Vibrational loads can cause fatigue damage. Methods of analyzing vibrational fatigue damage are available; however, the results often include large uncertainties. These uncertainties are associated with material fatigue properties and the distribution and magnitude of the induced dynamic stresses. Vibrational stresses may be induced by plant operational modes, during transportation if a component is not properly isolated, and from ground or seismic vibrations. The source of vibrational loads that develop during the operational life of CSS, the distribution of the associated stresses, and the endurance limit of the materials must be known for lifetime prediction.

Electrical stressors are induced in the insulating materials used in the fabrication of electrical and electromechanical devices. Both passive CSS (cables, connectors, electrical penetrations, transformers, terminal boards, etc.) and active CSS (motors, circuit-breakers, relays, voltage and current activated devices, etc.) experience voltage gradients during normal operation and testing. Of primary concern are the higher levels of electrical stressors that are generated during switching operations and during accident and post-accident situations. The nature of electrical voltage stressors varies depending upon the design and functional application of the device. The voltage may be d.c., a.c., fast (micro-second) transients; or slow, switching transients. The most severe voltage gradients are experienced when a device is subjected to various combinations of these voltages superimposed at the same time. Voltage and current related degradation in plant electrical components and systems must be assessed during normal operating conditions, test conditions, and accident and post-accident situations.

Thermal stressors develop in CSS because of variations in the mechanical and physical properties of materials with temperature. Different materials expand at different rates when heated. These expansions may be resisted internally or by interference with adjacent component surfaces. This resistance results in time-dependent thermal stresses that can cause aging-related degradation, either separately or when combined with the effects of other stressors. Typical of such degradation are the thermal fatigue cracks that have appeared in high temperature coolant water piping and nozzles.

Aging Degradation Mechanisms

Stressors and environments act in concert on CSS constituent materials to cause time-dependent deterioration. Many mechanisms potentially can contribute to deterioration processes. Extensive analytical and experimental efforts by both government and industry have identified numerous aging degradation mechanisms that are operative in nuclear power plants. These mechanisms vary widely in terms of their potential effects. Some mechanisms affect numerous types of CSS over wide variations in environment and stressor level; others are limited in their effects to specific components or materials

over narrow ranges of conditions. Aging degradation mechanisms of concern in NPPs include the following:

Corrosion is the most common form of degradation in NPPs. Bulk corrosion in air, water, or steam causes buildup of corrosion products, loss of materials, and activity transport in irradiated systems but seldom results in major thinning or penetrations. Many localized corrosion processes are operative in NPPs, e.g., crevice corrosion, pitting corrosion, galvanic corrosion, various types of stress-or irradiation-enhanced corrosion, microbially-induced corrosion, etc. These processes can lead to significant local wall thinning and to various, high-consequence failures.

Erosion caused by high velocity steam, water or two-phase mixtures has contributed to major failures in NPP CSS. Special processes of importance include erosion/corrosion (local erosion causing a wearing away of a protective oxide film thus allowing corrosion to proceed) and cavitation.

Embrittlement of metals and plastics because of structural or chemical changes induced by radiation, high temperature, or atmospheric contaminants can lead to fragility and failure under dynamic loading. Radiation embrittlement reflects intense radiation fields thus only those components in close proximity to the reactor core are affected. Organic and electronic materials are particularly susceptible to radiation damage, but embrittlement with loss in toughness for critical components such as pressure vessels and supports represents the most significant contribution of radiation to aging. Thermal embrittlement is associated with chemical or metallurgical changes and results from such processes as high temperature thermal aging leading to reduced toughness of ferrous alloys, high temperature sensitization to intergrannular stress corrosion cracking in austentic stainless steels, and oxidation or cross linking of polymers with a resultant loss in toughness and dielectric strength. Hydrogen absorption by ferrous alloys can also lead to loss of toughness and brittle fracture.

Wear is a general concern for rotating or other sliding surfaces where tolerances can affect performance. Lubricant loss or degradation, e.g., because of contaminants or chemical breakdown, can greatly accelerate wear.

Fatigue is a common degradation process that occurs in rotating equipment or under other service conditions that place periodic or cyclic loads on a system or component. Associated failures may occur at either high or low cycles in response to various kinds of loads, e.g., vibrational loads, thermal cycles, pressure cycles, etc.

Shrinkage or creep can occur in most materials and are common phenomena in metals at high temperatures. Polymers and composites used as electrical insulators, supports, and protective coatings may exhibit dimensional instability caused by exposure to high temperatures, moisture, mechanical stresses, or radiation. These effects can lead to deterioration in insulating and structural properties. Shrinkage of concrete in NPPs is due mainly to long-term dehydration. Dimensional changes in concrete as it ages do not degrade the properties of concrete; however, when these dimensional changes cause interference, e.g., with other components in prestressed reinforced concrete structures, degradation can occur. Shrinkage is the main contributor to the loss of prestressing forces in prestressed concrete containment.

Degradation Sites

Most components are not uniformly susceptible to aging degradation. Certain sites on or within a given component will exhibit more deterioration than other sites; and for many components, degradation is limited to only a specific location. Factors that affect vulnerability to degradation include localized chemical or metallurgical variations, geometry with respect to fluid flow or chemical potential gradients, proximity to mechanically or chemically incompatible materials, localized high stresses, and others. Examples of site-specific degradation include: a) localized erosion/ corrosion in ferritic steel piping because of local high fluid velocities, b) enhanced intergranular stress corrosion cracking in heat-affected zones near welds in austenitic stainless steel due to progressive sensitization during extended operation, c) excessive hinge pin wear in check valves subject to flutter, d) rapid degradation of pump impeller blades when cavitation occurs, e) wear or galling of sliding contacts, f) crevice corrosion, g) fatigue cracking in regions experiencing tensile stresses, and many others. An understanding of aging degradation requires a knowledge of which sites degrade, by what mechanisms, and at what rates. This information is fundamental to selection of monitoring methods and where, how, and with what frequency monitoring must be implemented to reliably trend and mitigate aging degradation processes.

Root Cause Determination

In order to avoid recurrences of excessive aging degradation, it is necessary to understand the basic underlying causes of observed deterioration, i.e., root cause. Root cause is defined as the most basic reason or collection of reasons for the degradation that, if corrected, will prevent future similar deterioration. Root causes may be associated with intrinsic component characteristics, such as composition, metallurgical structure, or design features or may reflect situational factors, i.e., departures from design envelopes, extremes in environmental factors or stressors, operational variables, or combinations of these and other factors. An analysis program should exist to evaluate instances of unexpected or excessive degradation in terms of their root causes. Root cause analysis relies upon the availability of accurate, sufficiently detailed, retrievable records to provide the facts needed to evaluate the potential engineering, procedural, operational, and environmental contributors to the observed degradation. Given this information, knowledgeable staff can generally track causes and effects to successively more basic levels until the root causes are revealed. When the root causes are understood, methods for preventing recurrence of similar degradation will generally become evident.

In summary, the understanding of aging degradation processes should be accomplished on a plant-specific basis by qualified staff using state-of-the-art understanding of age-related degradation in nuclear power plants. The effort to understand aging should be systematically structured in terms of the materials, inservice environments, and stressors that characterize each selected component. These factors and their interactions, when considered in the context of accepted data and analytical approaches, should lead to an identification of potential aging degradation mechanisms, root causes, and sites. This information is the basis for designing and implementing effective programs for monitoring and mitigating aging degradation.

MANAGING AGING

When the interactions that cause degradation are understood, they can be managed to assure that aged CSS will adequately perform their design safety functions. Inspection and surveillance should be implemented to monitor degradation in key CSS. Selectively applied condition monitoring can also be useful in this respect. Effective oversight of aging degradation will permit timely repair, replacement, or servicing through preventive or corrective maintenance.

Condition monitoring, trending, recordkeeping, and maintenance programs are effective tools for managing aging degradation in operating nuclear power plants. Effective maintenance programs require understanding of what to maintain, when to maintain, and how to maintain plant CSS. Depending upon their intended function, these programs take various forms (e.g., corrective maintenance, preventive maintenance, predictive maintenance, reliability centered maintenance, condition monitoring, inspections, tests, surveillances, etc.-see Figure 4). This mix of elements that comprise an overall maintenance program should reflect both the technical nature and the potential consequences of the degradation processes that the program is intended to mitigate.

From an aging degradation perspective, the key steps in determining when to maintain and how to maintain a specific CSS are:

- Identify performance measures/functional indicator(s) for CSS important to safety.
- Apply methods for monitoring performance measures and functional indicators identified above.
- Retain information acquired by monitoring programs in auditable, retrievable form.
- Trend performance measures and functional indicators for each CSS under observation and analyze the impact of rate of change; retain information in auditable, retrievable records until the NPP is decommissioned.
- Determine minimum acceptable functional capability at the end of service life for normal operation and for accident mitigation.
- Develop criteria for effective maintenance, surveillance, and refurbishment programs.
- Interpret, analyze, and make decisions for maintenance or replacement.

Aging management activities should be apportioned between efforts to monitor aging and programs for mitigating aging. The aging degradation management program will provide useful input for making decisions for repair, replacement, and refurbishment of CSS; quality assurance and quality control; engineering support; and plant modifications.

Monitoring Aging

Monitoring and trending of aging degradation is the basis for predictive maintenance. The overall goal of the predictive maintenance program is to provide information concerning degradation rates and residual lifetimes that can be used to predict and prevent failures. Tools used in doing this include non-destructive examination (NDE), condition-monitoring, residual life assessment, and information analysis and trending. Trends and defined action levels provide guidance needed by the preventive maintenance program to schedule services with a frequency that will avoid failure of critical CSS. Observed degradation provides opportunities for identifying and eliminating sources of unnecessary deterioration through root cause analysis and corrective action.

- Non-Destructive Examination[7]

A variety of non-destructive techniques are employed as part of the in-service inspection and testing programs to detect and characterize flaws or other evidence of degradation that may be failure precursors. Commonly used methods include visual inspection, dye-penetrant and magnetic particle treatments, radiography, eddy current testing, ultrasonic testing, electrical signature analysis, and acoustic emission monitoring. Each of these methods has its advantages and limitations. The limitations derive mainly from the fact that NDE techniques were developed primarily as quality control tools for detecting manufacturing flaws. New or improved NDE methods are continuously being developed. It is expected that techniques that will provide the quantitative characterizations of flaws required for fracture mechanics analysis and will allow on-line monitoring of deterioration in mechanical properties during long-term in-service exposure will be available in the future.

- Condition Monitoring

For some important components or systems, integrated monitoring programs that may involve a combination of sensors and evaluation methods to ensure reliability may be in order. Condition monitoring is relatively complex and costly and should be employed only when justified in terms of the consequences of averted failures.

- Surveillance, Testing, and Inspection Programs

Detailed and comprehensive requirements for monitoring degradation in CSS are conveyed by the ISI requirements in Section XI of the ASME Boiler and Pressure Vessel Code and the surveillance testing requirements stated in the plant technical specifications, which are part of the FSAR. These oversight programs can provide useful indications of aging-related deterioration. These programs are supplemented by non-mandatory surveillance, inspections, and tests.

- Residual Life Assessment[7]

For monitored trends to have meaning in terms of service, replacement, or refurbishment frequency, it is necessary to correlate the level of monitored parameters with expected CSS residual lifetimes. These correlations are difficult to establish at best, and, as a consequence, the technology of assessing residual life is not well developed. Methods employed include surveillance specimen testing, monitoring of operational parameters, evalu-

ation of components that have been in service, and mechanistic and empirical modeling to provide bases for predictions. Improvements in the technology, accruing from more sophisticated and reliable models, better archiving, development of miniature specimen testing and reconstituted specimen testing techniques, and on-line damage monitoring, are expected to greatly increase the scope and confidence of future residual lifetime assessments.

In summary, aging monitoring methods (e.g., inspection, surveillance, testing, condition monitoring) should reflect mechanistic and empirical assessments performed by qualified staff in their efforts to understand and mitigate aging degradation. These methods should employ state-of-the-art non-destructive examination, e.g., ultrasonic testing, signature analysis, vibration analysis, dielectric performance measurements, and other measuring techniques performed by qualified or certified staff. Measurement results should be documented and trended and analyzed with respect to implications for residual CSS lifetime and for frequency and nature of preventive and corrective maintenance.

Mitigating Aging

Mitigating of aging degradation through servicing, repair, refurbishment, or replacement of CSS is the prime function of the maintenance program. Some, or all of the monitoring activities discussed in the preceding sections are generally included under the auspices of the Maintenance Department. For present purposes, mitigation of aging is construed as the collection of activities that relate directly to physical maintenance of CSS.

Maintenance activities range from simple, straightforward tasks to complex activities that require extensive coordination, training, and technical expertise. The level of oversight and resources devoted to these activities should reflect their complexity and importance to plant safety and reliability. A maintenance program has many important elements. Those considered here as being particularly relevant to aging degradation include preventive maintenance, corrective maintenance, risk-based or reliability centered maintenance, and recordkeeping and trending. Most of these elements have clear interfaces and interdependencies with aging monitoring activities discussed in the preceding sections. In addition, the scope and nature of the various maintenance elements should reflect the as-built plant design specifications; manufacturer's recommendations; operating experience--both internal and external; relevant recommendations and information from the NRC, the nuclear power industry, and its vendors; and general good engineering practices.

- Corrective Maintenance

Corrective maintenance is performed to restore failed or malfunctioning equipment to service. For some types of equipment or components, e.g., items lacking severe failure consequences, a corrective, as opposed to preventive, approach is preferred (e.g., replacement of light bulbs). Malfunctions that represent significant challenges to plant safety or reliability should be prevented. A major responsibility of the maintenance organization is to be cognizant of the significance of potential malfunctions and to ensure that severe consequence events are normally averted by adequate preventive maintenance. As with other maintenance activities, corrective maintenance priorities should be based on the relative importance of the equipment and on

plant safety and reliability objectives. An added function of corrective maintenance is to determine root causes of malfunctions and carry out appropriate corrective action to prevent unnecessary recurrences.

- Preventive Maintenance

Preventive maintenance includes the planned and scheduled actions performed to prevent equipment failure. Preventive maintenance relies heavily upon information generated by monitoring programs to define necessary activities and the frequency at which they should be performed. In addition to input from monitoring programs, preventive maintenance action should be based on equipment histories, other plant performance experience, vendor recommendations, and good engineering practice including ALARA considerations. Planned actions and schedules should be documented, and departures from these plans should be justified on technical grounds and subject to management review and approval. Clear, comprehensive procedures are vital for preventive maintenance and other oversight and maintenance activities.

- Risk-based and Reliability Centered Maintenance

The traditional approach to defining maintenance program objectives and priorities is based upon engineering judgment supported by vendor and industry data, maintenance and operating histories, and regulatory requirements and guidance. These will continue to be essential considerations in structuring a maintenance program but are likely to be supplemented by new approaches that focus on risk and reliability as key factors in prioritizing maintenance activities. Risk-based methods rely upon quantitative failure mode and effect analyses, e.g., probabilistic risk analysis (PRA), to quantitatively identify CSS, in the context of their service and systems environments, whose malfunction would pose the greatest threat to plant safety. In this way, CSS can be ranked in terms of safety significance, and oversight and maintenance efforts can be commensurately focused upon the most risk significant equipment. Reliability centered maintenance uses formalized decision logic, perhaps employing probabilistic risk-based criteria, to prioritize preventive maintenance activities and to limit maintenance and oversight to those CSS for which safety or economic consequences of failure justify them. The general product of applying RCM criteria to prioritizing preventive maintenance will be:

- A list of CSS whose failure or loss of function could have significant safety consequences. These CSS require scheduled preventive maintenance that may be further prioritized based upon risk or other rankings.

- A list of CSS whose loss of function would not be self-evident. These CSS should also be subject to scheduled oversight and/or maintenance.

- All other CSS: Failure or loss of function for these will have economic consequences only. Preventive maintenance is at the discretion of the plant owner and, presumably, would require justification on economic grounds.

Recordkeeping and Trending

Recordkeeping and trending are essential elements of both monitoring and maintenance programs. The sole product of aging monitoring programs is information. In order to be useful, this information must be translated into effective maintenance practices. This requires 1) that the information obtained by monitoring activities be recorded in adequate, unambiguous detail in a form that allows ready retrievability and 2) that the information be reliably relatable to specific maintenance practices that effectively address the aging-related degradation that is actually occurring. Records that meet these requirements are needed to prioritize maintenance resources and to correlate actual operating environment and stressors with design assumptions and computed lifetimes so that actual CSS lifetimes and maintenance intervals can be anticipated.(8)

Maintenance records serve primarily to establish performance histories for the CSS that comprise the plant. This information and its continuous feedback are useful in specifying what, how, and when equipment should be maintained; what information should be collected; and how it should be recorded. Maintenance histories and equipment performance trends should be documented consistent with regulatory requirements and the licensees' goals and objectives and should be kept current. Requirements for records retention and retrieval should be established by the maintenance program consistent with quality assurance program requirements related to records.

Recordkeeping can be supplemented or requirements offset by conservative maintenance practices based upon equipment history or conservative condition assessments for selected CSS; however, in the context of minimal quality assurance requirements for basic records retention, the requirement for maintaining detailed, usable, and retrievable records must be met at all NPPs. This is a task that, in principle, should be simplified greatly by the "computer revolution," which has enhanced the technical and economic feasibility of maintaining high quality records.

Trending of information obtained by monitoring activities may be a straightforward process that leads directly to maintenance recommendations. More often, however, trending intended to lead to improved oversight and control requires considerable initial development of the basic trending program and qualification of the measures to be trended if results are to be meaningful.(9)

Records of component failure data can be trended and monitored to assess maintenance program effectiveness. Process indicators, such as post-maintenance test results, surveillance test results, ratio of preventive to corrective maintenance, maintenance backlog, and rework frequency, can also be trended to provide indications of problem areas and overall maintenance effectiveness.

In summary, the maintenance program, as the vehicle through which aging degradation is mitigated, is the key to managing aging. Operational and maintenance records and input from monitoring programs should be employed in the maintenance program for scoping and scheduling both preventive and corrective maintenance activities intended to control aging degradation. These activities should be carried out by experienced, qualified maintenance personnel and should lead to needed servicing, repair, refurbishment, or replacement with a frequency sufficient to not significantly compromise CSS reliability.

The primary objective of aging degradation mitigation should be to assure that CSS with important safety functions are subject to surveillance and maintenance that effectively control, at intervals substantially less than expected component lifetimes, processes that could degrade the operability and reliability required to support the safety functions of the CSS. In achieving this objective, goals should be set for utilizing state-of-the-art technology for understanding, monitoring, and controlling aging degradation with the expectation of tailoring aging degradation mitigation to a continuously increasing level of knowledge and standard of quality. In establishing goals, factors such as component function, redundancies, diversity, operating mode (normally active or passive), and plant condition during which the component actively functions (e.g., full power, low power, shutdown, refueling) should be considered. In general, goals for different CSS may differ depending upon their safety functions. An important aspect of plant maintenance and surveillance programs is retention of essential degradation-related data in complete, auditable, easily retrievable records. The records systems and its contents should conform to good maintenance practices as well as the requirements of 10 CFR 50 Appendix B and the plant QA program. Records and related data should be employed, to the extent practicable, in trending degradation processes thereby providing assurance of controlled, timely maintenance. Trends comprised of data contained in the maintenance records should also be used to optimize and monitor the effectiveness of aging degradation management.

APPLICATION TO NUCLEAR POWER PLANT SYSTEMS

A high priority objective of the NPAR program is to integrate the entire body of knowledge related to aging in NPPs into forms that have maximum utility for both regulators and licensees. Most data and other information concerning aging are acquired in laboratory settings by research-oriented professionals. The result is an information base that tends to characterize aging processes very well in materials science terms but is limited in terms of guidance in how to apply what had been learned to the multivariate, interactive complexity typical of NPP systems. The need for practical, system-related guidance on understanding and managing aging is being addressed by transposing the basic aging knowledge base into an engineering-oriented system-based format. The structure chosen mirrors that of the Safety Analysis Reports as specified in Regulatory Guide 1.70, "Standard Format and Content for Safety Analysis Reports" and developed in detail from a regulatory perspective in NUREG 0800, "Standard Review Plan for the Review of Safety Analysis Reports for Nuclear Power Plants."(10,11) The product of this exercise will be a manual entitled "Good Practices for Managing Aging Degradation in Operating Nuclear Power Plants."

The Good Practices Manual (GPM) tracks directly with the Standard Review Plan (SRP) devoting one section to each SRP chapter or sub-chapter that deals with a major NPP system. Each of these GPM sections consolidates what is known about aging degradation for the subject system and presents the information in the following subsections:

1. NRC Requirements: References to and summaries of requirements and guidance related to aging degradation in this system or its components and contained in regulatory instruments.

2. Aging Concerns and Mechanisms: Engineering-based discussion of aging degradation in this system or its components in terms of deterioration processes, rates, and consequences.

3. Managing Aging Degradation - Recommended surveillance and maintenance practices for controlling aging in this system or its components.

4. Non-destructive Evaluation and Residual Life Assessment - Applicable NDE methods and needs and the status of residual life assessment for this system or its components.

5. Recordkeeping and Trending - What records to keep and how to use them in monitoring system performance.

6. References - Available sources that provide more detail concerning aging degradation in this system or its components.

It is expected that the Good Practices Manual will be published as a NUREG report that is revised regularly to reflect advances in the state-of-the-art of understanding and managing aging.

SUMMARY AND CONCLUSIONS

The NPAR program is developing technical understanding of the time-dependent processes that, through deterioration of CSS, can reduce safety margins in nuclear power plants. A major and necessary element of the program involves the application of this basic knowledge in defining functional approaches to managing aging by anticipating and mitigating important deterioration processes.

Fundamental understanding and characterization of aging processes are being accomplished through NPAR-sponsored research projects, review and analysis of aging-related information, integration of NPAR results with those from industry and other aging studies, and interfacing of all of these with the existing body of codes, standards and regulatory instruments that convey aging-related guidance to NPP licensees. Products of these efforts are applied to structuring and providing aging-related technical recommendations in forms that are useful in:

- developing and implementing good aging management practices
- developing regulatory guidance and requirements for understanding and managing aging during normal plant operations and in support of license renewal
- planning and implementing other regulatory actions and initiatives in which aging-related concerns have a bearing on scope or priority.

In developing good practices for managing aging, it is necessary to 1) select the CSS in which aging is an important concern, 2) develop an understanding of the active aging processes and their relationships to specific materials, environments, and stressors; and 3) specify and prioritize monitoring and mitigation programs.

Selection of components is based upon both deterministic and probabilistic considerations. The key overall selection criterion is whether or not aging could lead to a departure from an acceptable safety envelope.

Understanding aging involves developing and applying both empirical and mechanistic relationships at an appropriate level of detail to selected CSS. The variables that govern these relationships reflect CSS design and composition (i.e., materials of construction and their condition); environments to which CSS are exposed, e.g., elevated temperature, corrosive media, ionizing radiation; and the collection of active stressors, e.g., cyclic loading, high stress, thermal gradients, high electrical potentials, to which CSS are subject.

Given an acceptable understanding of the mechanisms and kinetics of aging in important CSS, the final and key step in assuring that aging does not compromise safety is to implement effective practices for monitoring and mitigating aging. These practices, implemented principally through maintenance programs, involve the use of appropriate observational methods in testing, inspection, surveillance, and condition monitoring and preventive and corrective maintenance of the type and frequency needed to avert CSS failures that could threaten plant safety.

The products of NPAR studies, in general, deliberately address each of the key elements discussed above. In addition, good practices for managing aging are being compiled in manuals and documents specifically devoted to that subject. The principal compendium of good aging management practices catalogues all currently available information on understanding and managing aging in a format that mirrors that of the Standard Review Plan (NUREG-0800) and Regulatory Guide 1.70 (Standard Format and Content of Safety Analysis Reports). This systems-oriented format is commonly used and well understood by both licensees and regulators. This approach also provides a needed measure of assurance that aging concerns will be comprehensively addressed throughout the plant. The good practices manual will be a living document that evolves as the state-of-the-art of the understanding of nuclear plant aging expands.

REFERENCES

1. J. P. Vora and J. J. Burns, "Understanding and Managing Aging and Mainenance". International Nuclear Power Plant Aging Symposium. August 1988.

2. J. P. Vora, "Potential Applications of NRC Aging Research Results to License Renewal". Sixteenth Water Reactor Safety Information Meeting. October 1988.

3. J. P. Vora, "Nuclear Plant Aging Research (NPAR) Program Plan", NUREG-1144, Rev. 1, September 1987.

4. E. V. Werry, "Regulatory Instrument Review: Management of Aging of LWR Major Safety-Related Components". NUREG/CR (Pending), August 1989.

5. I. S. Levy et.al., "Prioritization of TIRGALEX Recommended Components for Further Aging Research". NUREG/CR-5248, September 1988.

6. W. E. Vesely et.al. "Evaluation of Core Melt Frequency Changes Due to Component Aging". NUREG/CR (Pending), August 1989.

7. V. N. Shah et.al., "Residual Life Assessment of Major Light Water Reactor Components." Vol. 1, June 1987, Vol. 2, October 1989.

8. J. S. Dukelow, "Recordkeeping Needs to Mitigate the Impact of Aging Degradation During a License Renewal Period." NUREG/CR (Pending), September 1989.

9. J. A. Christensen, "Principles of Performance Trending". Proceedings of the 16th Annual Meeting of the Energy Division of the ASQC, September 1989.

10. "Standard Format and Content of Safety Analysis Reports for Nuclear Power Plants", Regulatory Guide 1.70, Rev. 3, November 1978.

11. "Standard Review Plan for the Review of Safety Analysis Reports for Nuclear Power Plants", NUREG 0800, June 1987.

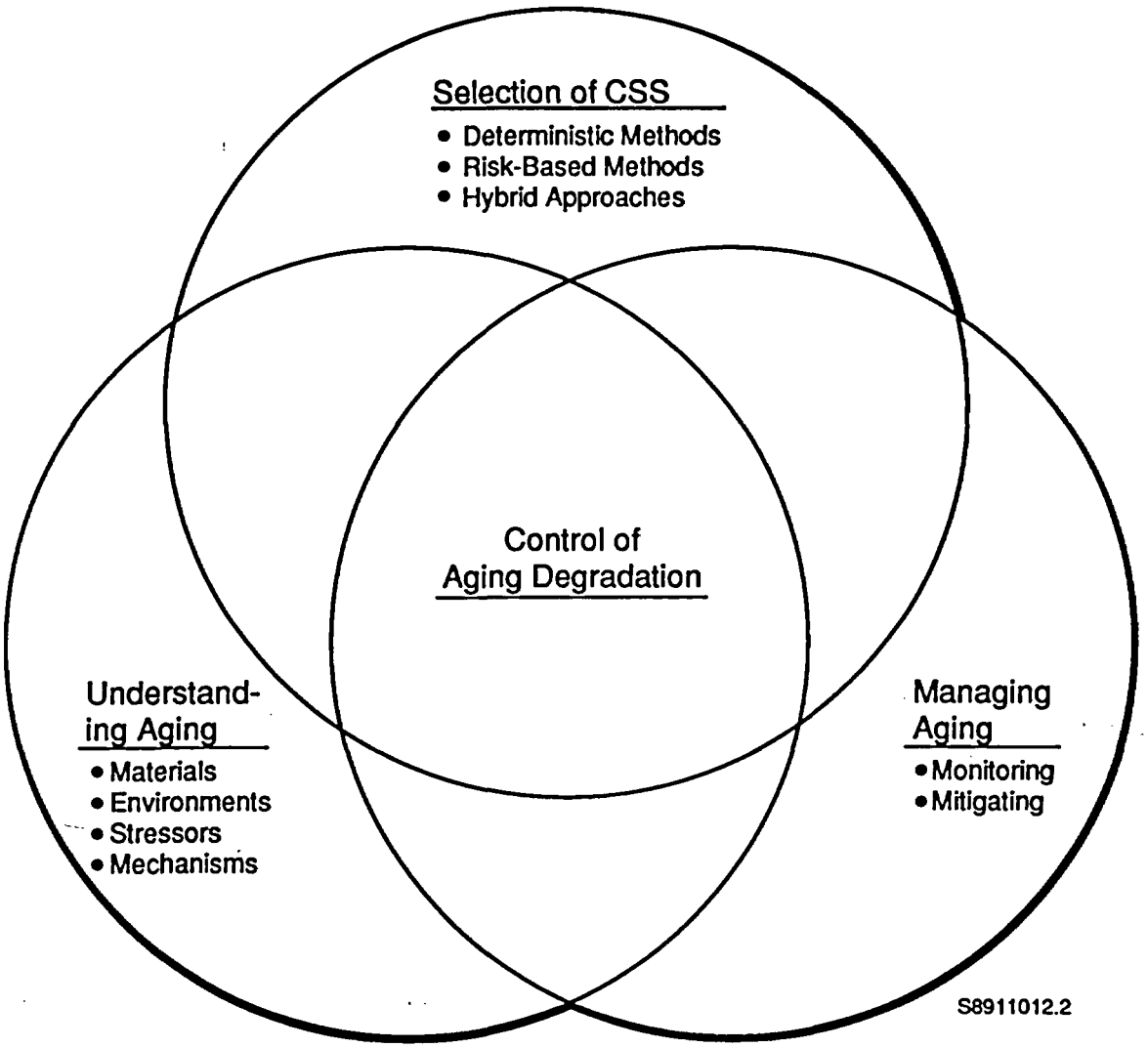

Figure 1. Key Interactive Elements in Total Aging Control Program

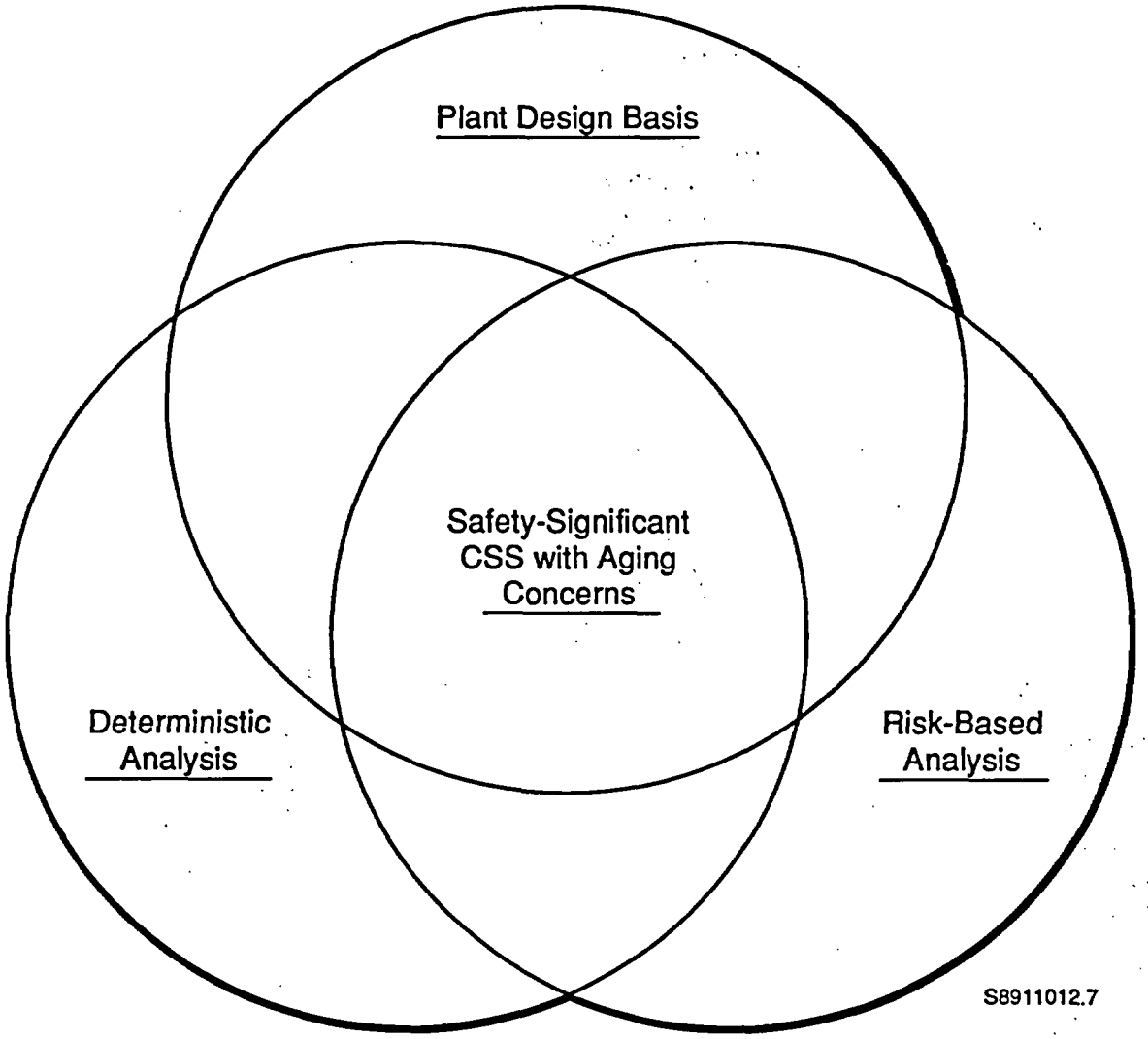

Figure 2. Key Interactive Elements inSelectingSafety-Significant Components, Systems, and Structures for Which Aging is a Potentially Important Issue

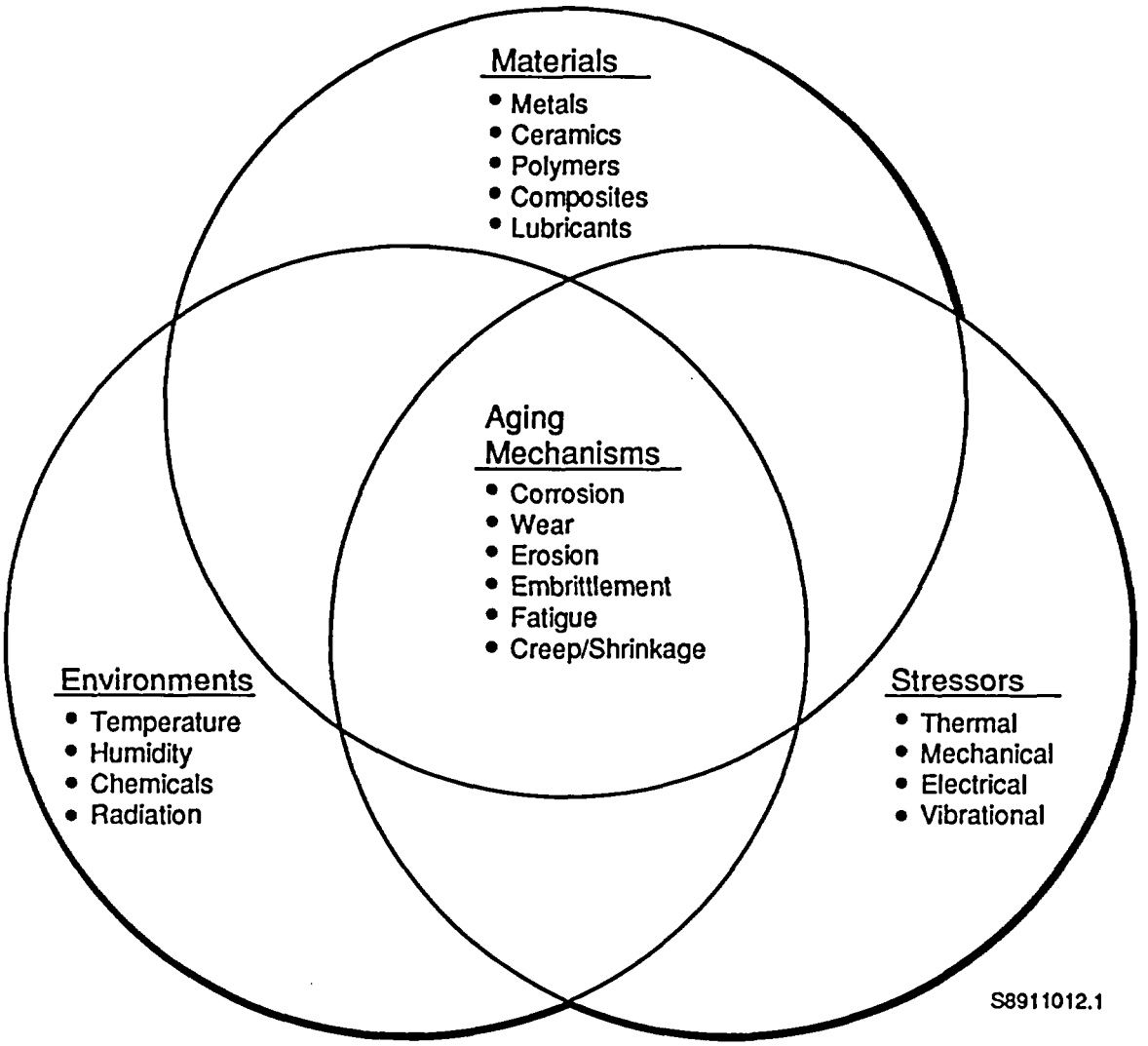

Figure 3. Key interactive elements in understanding aging degradation. Interactions among material type, environment, and stressor nature produce aging by various mechanisms; multiple interactions and variations in stressors and environments with time greatly increase the complexity of quantitatively modeling or anticipating degradation.

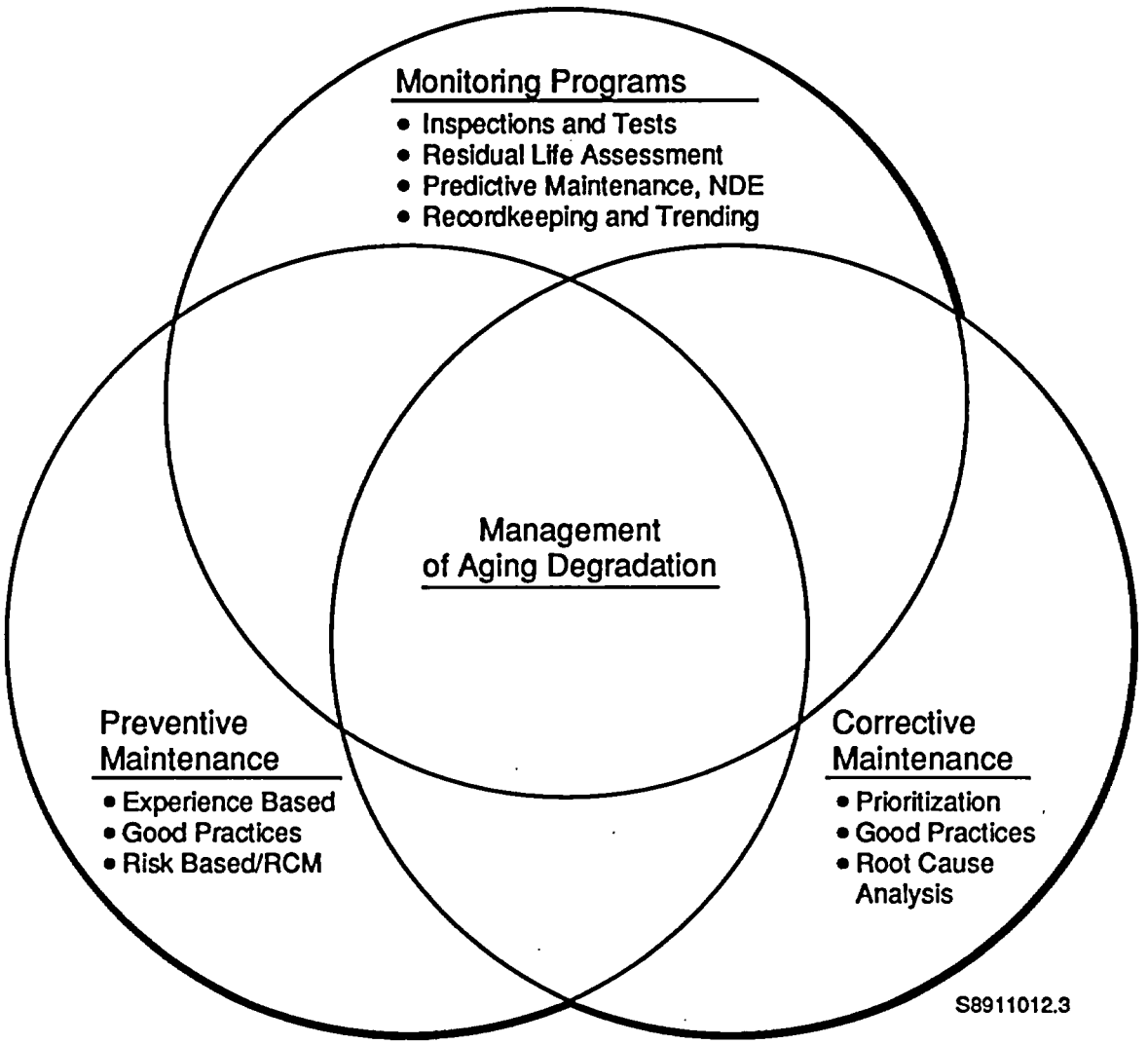

Figure 4. Key Interactive Elements in Managing Aging Degradation

NRC FORM 335 (2-89) NRCM 1102, 3201, 3202

U.S. NUCLEAR REGULATORY COMMISSION

BIBLIOGRAPHIC DATA SHEET

(See instructions on the reverse)

1. REPORT NUMBER (Assigned by NRC, Add Vol., Supp., Rev., and Addendum Numbers, If any.)
NUREG/CP-0105
Vol. 3

2. TITLE AND SUBTITLE
Proceedings of the Seventeenth Water Reactor Safety Information Meeting

3. DATE REPORT PUBLISHED
MONTH: March YEAR: 1990

4. FIN OR GRANT NUMBER
A-3988

5. AUTHOR(S)
Compiled by Allen J. Weiss, BNL

6. TYPE OF REPORT
Proceedings of conference on safety research

7. PERIOD COVERED (Inclusive Dates)
October 23-25, 1989

8. PERFORMING ORGANIZATION – NAME AND ADDRESS (If NRC, provide Division, Office or Region, U.S. Nuclear Regulatory Commission, and mailing address; if contractor, provide name and mailing address.)

Office of Nuclear Regulatory Research
U.S. Nuclear Regulatory Commission
Washington, DC 20555

9. SPONSORING ORGANIZATION – NAME AND ADDRESS (If NRC, type "Same as above"; if contractor, provide NRC Division, Office or Region, U.S. Nuclear Regulatory Commission, and mailing address.)

Same as Item 8 above

10. SUPPLEMENTARY NOTES
Proceedings prepared by Brookhaven National Laboratory

11. ABSTRACT (200 words or less)

This three-volume report contains 84 papers out of the 111 that were presented at the Seventeenth Water Reactor Safety Information Meeting held at the Holiday Inn Crowne Plaza, Rockville, Maryland, during the week of October 23-25, 1989. The papers are printed in the order of their presentation in each session and describe progress and results of programs in nuclear safety research conducted in this country and abroad. Foreign participation in the meeting included ten different papers presented by researchers from France, Germany, Japan, Norway and the United Kingdom. The titles of the papers and the names of the authors have been updated and may differ from those that appeared in the final program of the meeting.

12. KEY WORDS/DESCRIPTORS (List words or phrases that will assist researchers in locating the report.)
Reactor safety--meeting; research programs--reviews; reactor safety reviews; reactor protection systems; reactor cooling systems; reactor components; failures; computer codes; reactor materials; materials testing; performance testing; risk assessment; aging; reactor instrumentation; leading abstract; water cooled reactors; water moderated reactors; Europe; USA; Japan.

13. AVAILABILITY STATEMENT
Unlimited

14. SECURITY CLASSIFICATION
(This Page) Unclassified
(This Report) Unclassified

15. NUMBER OF PAGES

16. PRICE

UNITED STATES
NUCLEAR REGULATORY COMMISSION
WASHINGTON, D.C. 20555

SPECIAL FOURTH-CLASS RATE
POSTAGE & FEES PAID
USNRC
PERMIT No. G-67